D'Angelo M, 2016, Geochemistry, petrography and mineral chemistry of the Guichon Creek Nicola batholiths, south-central British Columbia, MSc Thesis, U Lakehead, ON, 267 p.

Geochemistry, petrography and mineral chemistry of the Guichon Creek and Nicola batholiths, southcentral British Columbia

Michael D'Angelo

Supervisor: Dr. Peter Hollings
Co-Supervisor: Dr. Steve Piercey

A thesis submitted to the Department of Geology in partial fulfilment of the requirements for the degree of

Master of Science in Geology

January 2016

Department of Geology
Lakehead University
Thunder Bay Ontario, Canada

ABSTRACT

The Guichon Creek Batholith (GCB) is a Late Triassic calc-alkaline intrusive complex approximately 60km x 35km in size and located approximately 54km southwest of Kamloops, British Columbia, Canada. The Guichon Creek Batholith forms part of the Quesnel Terrane, comprised of stacked volcanic-arc assemblages and associated sedimentary units, which in addition to the Stikine and Cache Creek terranes, comprise the Intermontane Belt of central British Columbia. The Guichon Creek Batholith intrudes the western volcanic belt of the Upper Triassic Nicola Group and is partially overlain by volcanic and sedimentary rocks belonging to the Kamloops Group and are of Jurassic age and younger.

The Guichon Creek Batholith is host to the Highland Valley Cu-Mo porphyry system comprised of at least five known significant porphyry centers (Valley, Lornex, Highmont, Bethlehem and J.A.). It is one of two mineralized calc-alkaline batholiths that form a Late Triassic belt parallel to younger mineralized, alkaline and calc-alkaline belts to the east. Most of this belt is buried under a thin veneer of Jurassic and younger cover. Understanding the petrogenesis and composition of the Guichon Creek Batholith is important in developing exploration strategies to locate similar buried porphyry deposits along this belt.

The Guichon Creek Batholith consists of six concentrically zoned intrusive facies ranging from diorite in the core to granodiorite in the margin. Field relationships indicate that the facies young towards the centre of the batholith although observable contacts are rare in outcrop. The six intrusive facies are from the margin inward: 1) Border facies;

Highland Valley facies [subdivided into the 2) Guichon sub-facies; and 3) Chataway sub-facies]; 4) Bethlehem facies; 5) Skeena facies; and 6) Bethsaida facies.

The marginal Border facies is the most heterogeneous facies and contains numerous autoliths near the contact between Guichon Creek Batholith and the host Nicola Group basalts which are brecciated and intruded by the Border facies. Rocks belonging to the Border facies are olivine-bearing leuco-gabbros to diorites with equigranular, phaneritic textures.

The Highland Valley facies is comprised of the Guichon and Chataway sub-facies. The composition of both sub-facies is similar, varying from quartz monzodiorite to granodiorite compositions and the Guichon sub-facies is most prominent to the northeast of the batholith whereas the Chataway sub-facies is most prominent to the southeast. The key difference between both sub-facies is the presence of conspicuous pink K-feldspar in the Guichon sub-facies and white K-feldspar in the Chataway sub-facies. Optically continuous, interstitial, sub-ophitic amphibole, K-feldspar and quartz are characteristic of all rocks belonging to the Highland Valley facies.

The three youngest facies are all similar in composition (granodiorite) and show a progressive increase in quartz and K-feldspar, decrease in total mafic minerals (with an increase in biotite relative to hornblende) and nearly constant plagioclase contents progressing from the Bethlehem facies to the Bethsaida facies. The Bethlehem facies is characterized by ophitic amphibole phenocrysts that poikilitically enclose smaller plagioclase chadacrysts, whereas the Bethsaida facies is characterized by biotite and amoeboid quartz phenocrysts. The Skeena facies is texturally and compositionally intermediate to the Bethlehem and Bethsaida facies, lacking both amphibole and biotite

phenocrysts but containing finer-grained amoeboid quartz phenocrysts than those present in the Bethsaida facies.

Weak chlorite-epidote-sericite alteration is ubiquitous across the batholith, and even least altered samples typically contain biotite and amphibole crystals that have been affected by <5 to 60% alteration to chlorite and epidote and plagioclase that has been weakly to moderately sericitized. Alteration is most prominent in samples of the Bethsaida facies, particularly those closest to the mineralized porphyry centers.

The Guichon Creek Batholith is a magnesian, calcic to calc-alkalic (MALI = -5 to 7.3) and metaluminous to weakly peraluminous (ASI = 0.77 to 1.28; AI = 0.02 to 0.13) batholith. Major and trace element geochemistry are consistent with fractional crystallization of the predominant minerals observed petrographically and plots of Zr vs. molar Al/Ti and Al_2O_3 vs. TiO_2 are effective at discriminating between the Border, Highland Valley and Bethlehem-Skeena-Bethsaida facies.

The petrographic and geochemical characteristics of the Guichon Creek Batholith in addition to cross-cutting relationships between facies and recent U-Pb ages suggest that the batholith was emplaced as at least two, but possibly three different magma pulses.

High Sr/Y, low La/Yb, fractionated LREE and HREE relative to MREE and concave primitive-mantle-normalized multi-element diagrams indicate fractional crystallization of hornblende and clinopyroxene in a deep crustal magma reservoir. These geochemical signatures also preclude a significant role for garnet in magma genesis, either as a restite phase left behind by adakite melts of eclogite-facies subducted slabs or by assimilation and contamination by garnetiferous metamorphic

rocks in the deep crust. This is consistent with Sm-Nd systematics ($\epsilon_{Nd(T)}$ = +6.7 to +7.5) which are consistent with <2% contamination of primitive mantle melts by partial melts of subducted sediment, although $^{87}Sr/^{86}Sr_i$ values of 0.703367 to 0.703493 suggest minor contamination of the Border and Guichon facies by radiogenic Sr derived from Nicola Group limestones or contaminated Nicola Group basalts.

Plots of Sr/Y, Al_2O_3 and V/Sc vs. SiO_2 suggest that the parent magmas for the Guichon Creek Batholith were hydrous and oxidized, two criteria key for the production of porphyry deposits. Amphibole chemistry indicates temperature, pressure and fO_2 conditions of crystallization were 712 ± 23.5 to 846 ± 23.5°C, 2.5 ± 0.3 to 0.9 ± 0.1 kbar (equivalent to 7.4 to 2.6km depth) and ΔNNO = 0.03 to 1.81, respectively. Pressure estimates are consistent with gentle tilting to the northeast, and imply that the Valley deposit may have formed at pressures where a single-phase supercritical fluid would have been stable, possibly leading to mineralization styles and an alteration footprint that are atypical of porphyry environments.

"CMIC-NSERC Exploration Footprints Network Contribution 088."

ACKNOWLEDGEMENTS

v

TABLE OF CONTENTS:

List of Figures

List of Tables

CHAPTER 1 INTRODUCTION

1.1 Overview

This study forms part of the copper module of the Canada Mining Innovation Council – National Science and Engineering Research Council (CMIC-NSERC) Exploration Footprints Research Network ("Footprints") Project. The goal of this project is to develop new and innovative approaches to more effectively target hidden ore deposits through multi-parameter integrated exploration. The project has been divided into three modules focused on characterizing the geological, geochemical, geophysical and integrated geoscience footprints created by economic disseminated Au, basinal U and porphyry Cu deposits.

The copper module is focused on the Highland Valley porphyry Cu (±Mo) district in the Upper Triassic Guichon Creek Batholith which is a granitic pluton with a calc-alkaline geochemical differentiation trend (McMillan, 1985). It is host to five major porphyry Cu (±Mo) deposits all majority owned by Teck Resources Limited ("Teck"; Fig. 1.1 and 1.2). These deposits are Valley, Lornex, J.A., Highmont and Bethlehem, and as of December 31, 2014, collectively contain proven and probable reserves of 608,000,000 tonnes at 0.30% Cu and 0.008% Mo (Teck, 2015).

The Guichon Creek Batholith was emplaced into volcanic and sedimentary rocks of the Late Triassic Nicola Group at 210 ± 3 Ma (Mortimer et al., 1990) and is partially overlain by sedimentary and volcanic rocks of the Cretaceous Spences Bridge Group to the southwest and the Jurassic Ashcroft formation and Eocene Kamloops Group to the north (McMillan et al., 2009). At surface, the batholith is exposed as an irregularly
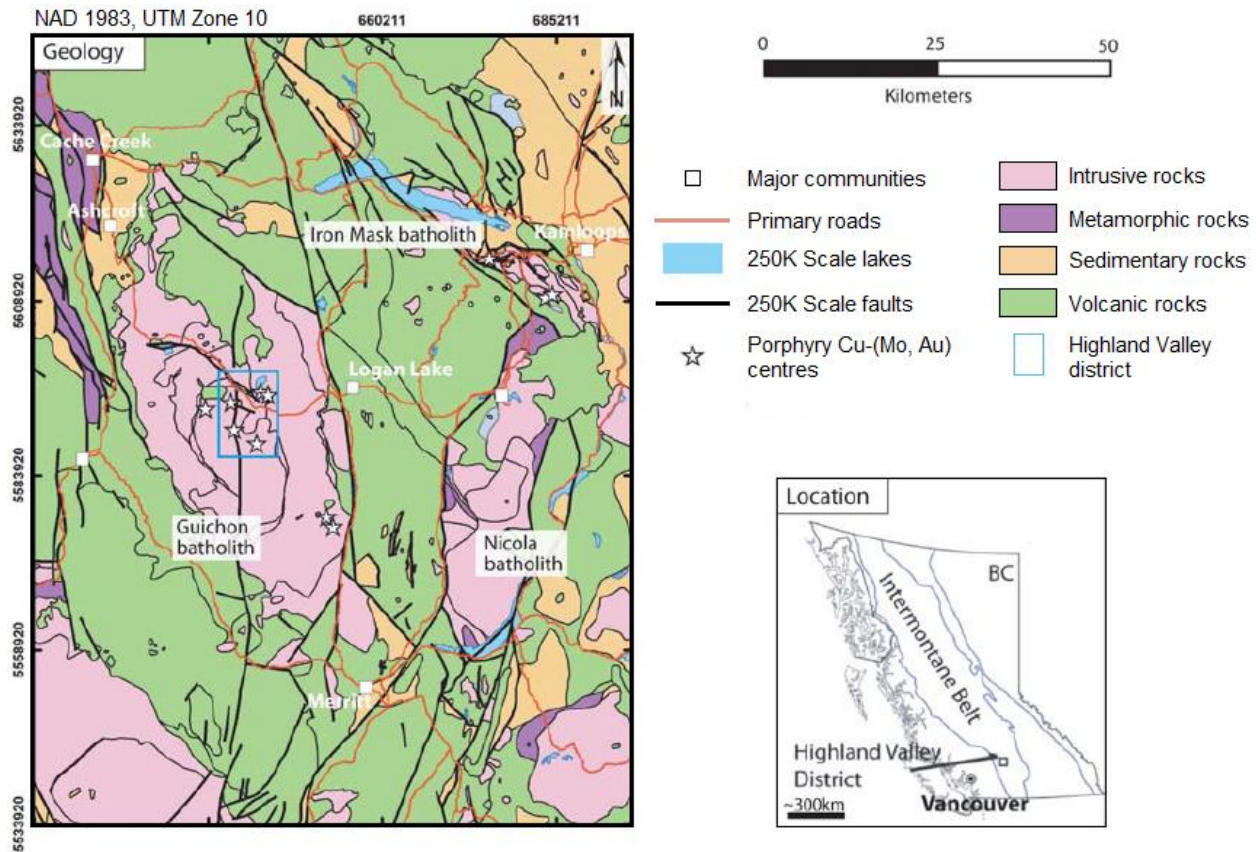
Figure 1.1 Regional map showing the location of the Guichon Creek and Nicola Batholith study areas in the Intermontane Belt of central British Columbia (modified after Massey et al., 2005).

shaped oval body elongated along a north-northeast axis (Fig. 1.1). Gravity models suggest the batholith has a vertical thickness of 6 to >12 km and has a flattened funnel shape with the greatest thicknesses occurring in its feeder zone, located slightly northeast of its centre (Ager et al., 1973). When projected to surface, there is a strong correlation between the location of the feeder zone (as inferred from gravity models) and the location of the major porphyry Cu (±Mo) deposits hosted in the batholith (Ager et al., 1973). Quaternary cover consists of variably thick mid-Wisconsinan age or older glacial deposits as well as Holocene, post-glacial fluvial and lacustrine deposits that formed prior to draining the lake above the Valley pit in 1985 (Bobrowsky et al., 1993).
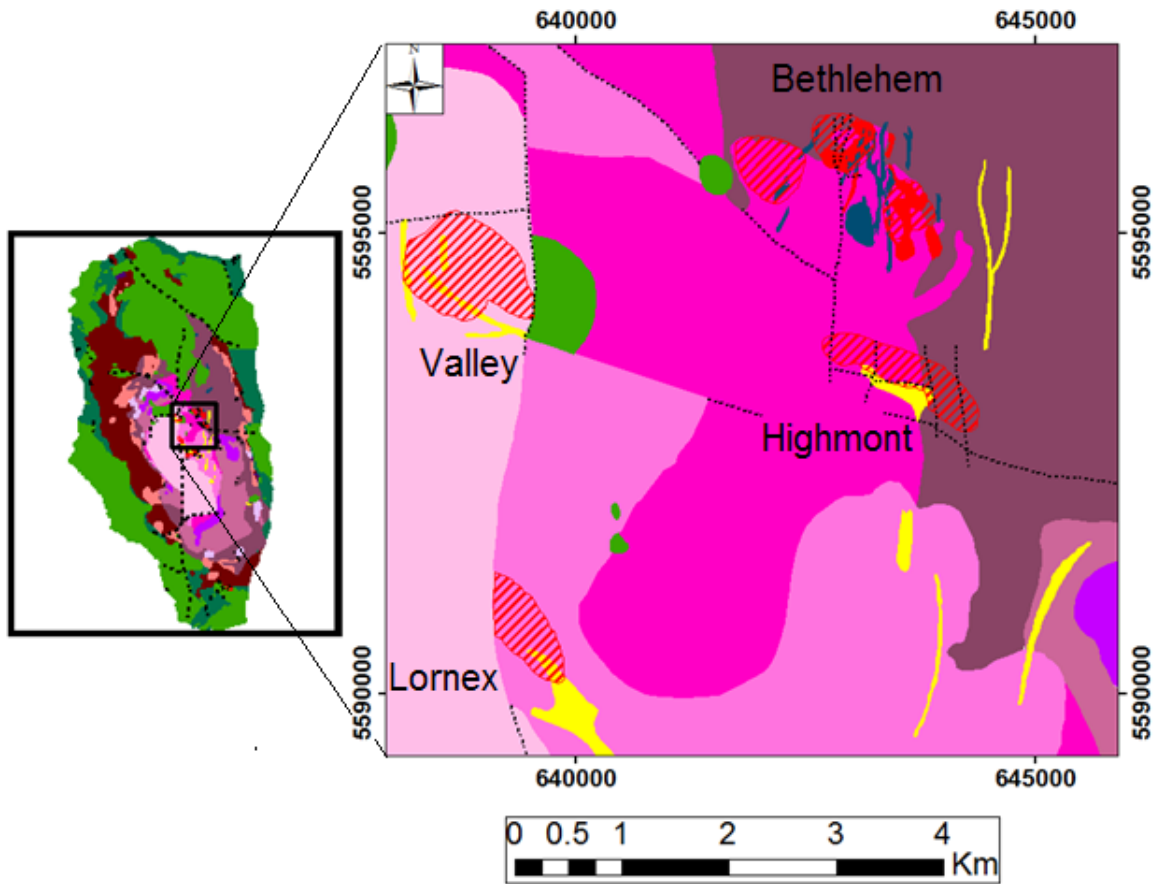
LEGEND

- ┄┄┄ Faults
- ▨ Ore Zones
- ▉ Jurassic and Younger Sedimentary and Volcanic Rocks
- ▉ Hybrid Border and Nicola Facies
- ▉ Transitional Bethlehem and Highland Valley Facies
- ▉ Breccia Bodies
- ▉ Post Bethlehem Porphyry Dykes and Plugs
- ▉ Post-Bethsaida Porphyry Dykes and Plugs
- ▉ Bethlehem Facies
- ▉ Bethsaida Facies
- ▉ Chataway Subfacies
- ▉ Guichon Subfacies
- ▉ Skeena Facies

Figure 1.2 Map showing the location of current and previously mined major porphyry Cu (±Mo) deposits in the Guichon Creek Batholith.

The Guichon Creek Batholith consists of six main intrusive facies that are concentrically zoned from more mafic compositions at the margin, to more felsic compositions in the core. From margin to core these facies are the: 1) Border, 2) Guichon, 3) Chataway, 4) Bethlehem, 5) Skeena and 6) Bethsaida facies. Additional rock types found in the Guichon Creek Batholith are west-northwest and north-northeast trending pre-, syn- and post-mineralization dykes which are most abundant in the areas of the Bethlehem and Valley deposits (Fig. 1.2). Dykes found in the vicinity of the Valley, Lornex and Highmont deposits include the quartz and feldspar-phyric, mafic-bearing porphyry (QFPM), quartz and feldspar-phyric, phenocryst-poor and mafic-poor porphyry (QFPP), quartz and feldspar, quartz-rich porphyry (QFPQ), aplite and lamprophyre varieties. Those in the vicinity of the Bethlehem and J.A. deposits include the feldspar-phyric, hornblende and biotite-bearing porphyry (FPM), feldspar-phyric, mafic poor porphyry (FP), feldspar and quartz-phyric crowded porphyry (FQPC), feldspar-phyric crowded porphyry (FPC), quartz and feldspar porphyry (QFP) and aplite varieties (Byrne et al., 2013). Detailed descriptions of all rock types of the Guichon Creek Batholith have been previously reported by a number of workers (Carr, 1966; Northcote, 1969; McMillan, 1976a, 1985; Byrne et al., 2013) and those sampled for this study are described in Chapter 4.

1.2 Porphyry Deposits

Porphyry deposits are an important source for Cu and Mo and contain ~60 to 70% of global Cu and >95% of global Mo resources (Sinclair, 2007). In Canada they are of similar importance accounting for ~43% of total Canadian Cu production and 100% of total Canadian Mo production (Sinclair, 2007). Porphyry Cu (±Mo) deposits have Cu

and Mo grades that typically range from 0.2% to >1% and 0.005% to 0.03% respectively (Kirkham and Sinclair, 1995; Sinclair, 2007).

Porphyry deposits are characterized as high-tonnage, low- to medium-grade deposits that are spatially and genetically related to intermediate-to-felsic, sub-volcanic, porphyritic intrusions emplaced in magmatic arcs (Kirkham, 1972; Sillitoe, 1972; Sinclair, 2007). Typical porphyry deposits are thought to be emplaced at depths of 1.5 to 3 km and the associated porphyry systems may possess vertical extensions of ≥8 km (Sillitoe, 1973). Many deposits have complex histories with repeated emplacement of porphyry intrusions and overprinting of mineralization and alteration zones (Carten et al., 1988). Telescoping of the porphyry systems and their epithermal environments is similarly common in regions with rapid rates of uplift and exhumation (Cooke et al., 2011). Mineralization and alteration in individual deposits are characteristically zoned, although the intrusion morphology, local structure and host rock character allow for significant variations between deposits (Lowell and Guilbert, 1970; Jones, 1992). The age distribution of deposits shows that most are Phanerozoic (predominantly Cenozoic and Mesozoic) in age (Fig. 1.3; Titley and Bean, 1981; Hunt, 1991, Seedorff et al., 2005). This age distribution is largely a reflection of exposure and preservation, as porphyry environments are typically subject rapid rates of uplift and erosion (Staude and Barton, 2001). Metal and volatiles necessary to form porphyry Cu deposits may come from the parent magma alone (Cline and Bodnar, 1991) or may be elevated by injection of metal- and volatile-rich mafic magmas (Hattori and Keith, 2001), particularly in deposits with significant Au content.
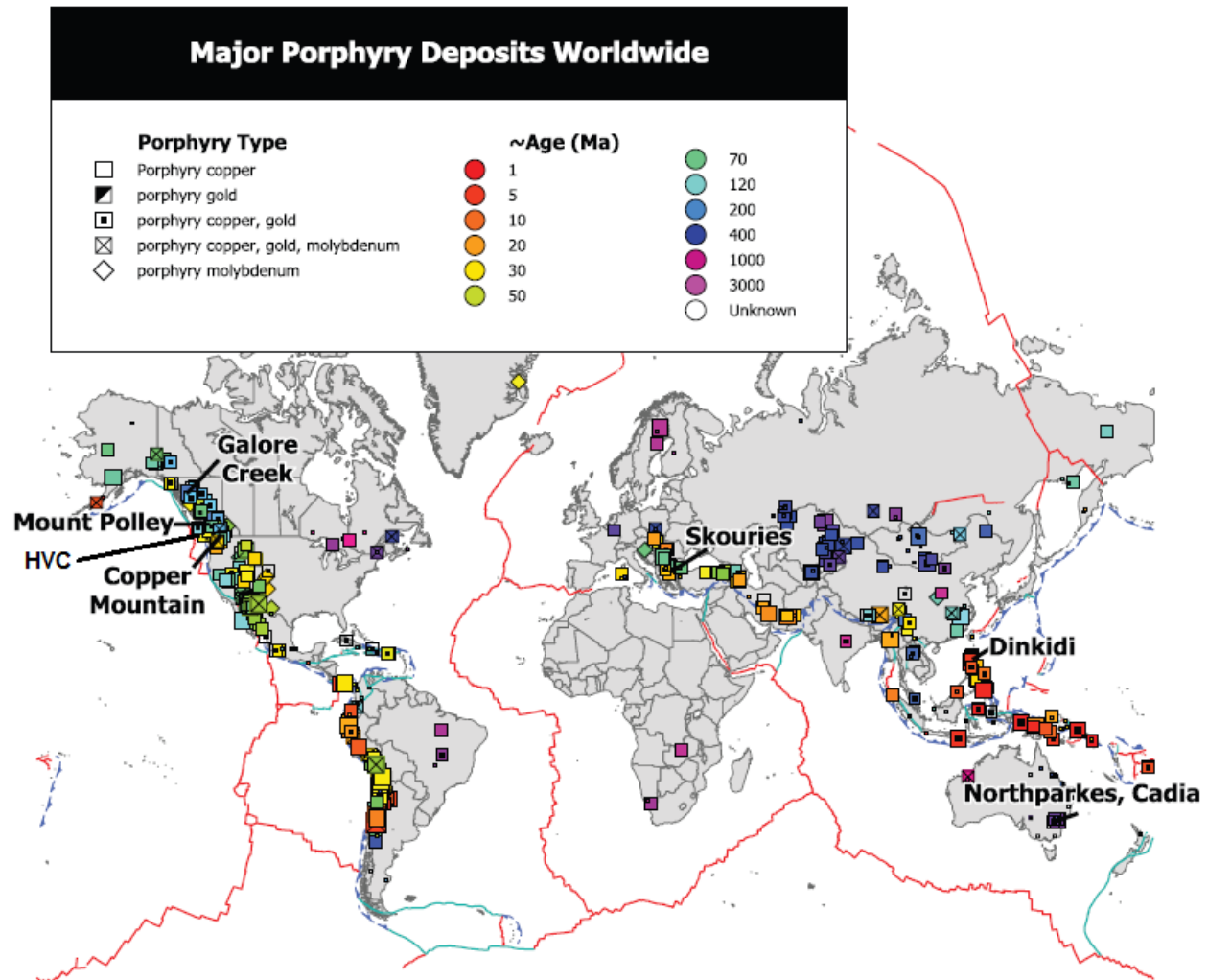
Figure 1.3 Global distribution of porphyry deposits worldwide. Deposits are mostly restricted to convergent plate margins and there is a noticeable absence of deposits in arcs with significant back-arc basins e.g., Japan). The majority of deposits are temporally restricted to the Mesozoic and Cenozoic eras. After Logan and Mihalynuk (2014). Data from Logan and Mihalynuk (2014) and references therein.

Hypogene mineralization is largely hosted in veins and stockworks (Seedorff et al., 2005). Vein morphology is highly varied in most deposits (Gustafson and Hunt, 1975) and early veins, formed in the ductile environment at lithostatic pressures, are commonly overprinted by later brittle veins (Gustafson and Hunt, 1975; Tosdal and Richards, 2001). Vein orientations often form radial patterns centered on the porphyry stocks, or linear arrays which have been interpreted to represent formation at shallow

6

vs. deep levels of a porphyry system (Heidrick and Titley, 1982). The occurrence of younger linear arrays that cross-cut radial fracture sets in many deposits, however, indicates that vein orientations are strongly controlled by the transition from the magmatic to tectonic stress field (Tosdal and Richards, 2001).

Two mechanisms have been proposed for the generation of giant and supergiant porphyry deposits and districts. The first is flat- or shallow-slab subduction caused by the subduction of anomalously buoyant, young and/or hot oceanic lithosphere, such as that generated at mid ocean ridges and oceanic plateaus, acting as a trigger for porphyry formation (Cooke et al., 2005; Hollings et al., 2005, 2013; Rosenbaum et al., 2005). The second is through subduction of oceanic lithosphere with high concentrations of oceanic transform faults and fracture zones aiding in the generation of vertical slab tears which may lead to concentrated mantle flow and elevated temperatures along slab edges liberating large volumes of fluid from serpentinites and inducing slab melting (Richards and Holm, 2013). The generation of large subduction-related porphyry and epithermal deposits, prior to the arrival of buoyant oceanic crust (Rosenbaum et al., 2005), or above steeply dipping subduction zones (Richards and Holm, 2013), poses a problem for the flat-slab subduction model. Both mechanisms likely contribute to porphyry formation, though their relative importance is obscured by the greater presence of both buoyant oceanic lithosphere and major transform faults in the eastern Pacific. Perhaps most importantly, both processes are capable of producing slab tears by: 1) retarded subduction and/or flattening of the slab due to the arrival of low density crust (arcs or oceanic plateaux) on the downgoing slab (Niu et al., 2003); 2) deflection and rapid steepening of the downgoing slab by thick crustal roots in the

upper slab (Sigloch et al., 2008) or; 3) subduction of lithosphere-scale transform faults (Richards and Holm, 2013). Such tears allow an influx of anomalously hot mantle asthenosphere capable of rapidly generating high-degree partial melts (Wortel and Spakman, 2000; Gasparon et al., 2009) and a subsequent thermal relaxation results in widespread partial melting of the oxidized, metal-H_2O-CO_2-S-rich mantle wedge (Mungall, 2002).

1.3 Location and Access

The Guichon Creek Batholith is located in south-central British Columbia, approximately 350 km northeast of Vancouver (Fig. 1.1). The Nicola Batholith is exposed approximately 20 km to the east of the Guichon Creek Batholith (Fig. 1.1). The Guichon Creek Batholith can be accessed either from the HVC mine site directly or through a network of logging roads that cover the batholith. The turnoff to the HVC mine site is located 16 km southwest of Logan Lake along highway 97C.

1.4 Objectives

The principal objective of this M.Sc. study was to investigate the lithogeochemistry and mineralogy of the unmineralized, least-altered intrusive facies of the Guichon Creek Batholith surrounding the Highland Valley porphyry system in order to generate a baseline against which the footprint of the mineralized intrusions could be compared. In addition, the farfield effects of the mineralizing system in the Guichon Creek Batholith were explored. These results were compared and contrasted with the lithogeochemistry and mineralogy of the Nicola Batholith, a calc-alkaline granitic pluton with a similar composition and geochemical differentiation trend to the Guichon Creek

Batholith. The Nicola Batholith is located approximately 20km to the east of the Guichon Creek Batholith but hosts no known porphyry-style mineralization.

Two working hypotheses were tested during the course of this study to help resolve these objectives:

1. Can the geochemical and mineralogical effects of regional metamorphism be distinguished from the hydrothermal overprint from a mineralizing porphyry system.

2. Is there a systematic change in the geochemistry of the intrusive rocks prior to the emplacement of the mineralized intrusions.

1.5 Previous Work

Early exploration was sparked in the 1890's by discovery of the OK (a.k.a. Alwin) deposit and the Snowstorm and Iona showings at the Bethlehem deposit (Casselman et al., 1995). Continued efforts were aimed at exploiting high-grade bornite-chalcopyrite veins through the 1920s and past-producing deposits include the Berthsaida zone (Casselman, 1995), Alwin, Snowstorm and Aberdeen deposits (Carr, 1960; McMIllan, 1976a). Significant exploration for low-grade porphyry deposits did not begin until the mid-1950s with an increase in the price of copper (Carr, 1960). Bethlehem Copper Corporation, in conjunction with American Smelting and Refining Company (ASARCO), conducted extensive trenching and bulk sampling in 1955 followed by 50,000 feet of drilling from 1956 to 1958 (Carr, 1960) which culminated in the first copper production from Highland Valley over the period from 1962 to 1982. Subsequent exploration throughout the 1960s-1980s led to the discovery of the sub-economic Krain (Carr, 1960; McMillan, 1976a), South Seas, Ann Number 1, Minex (McMillan, 1976a) and JA

(Casselman et al., 1995) deposits as well as the currently producing Lornex, Highmont and Valley deposits (Casselman et al., 1995). Production commenced during the 1970s and 1980s at Lornex (1972), Highmont (1980) and Valley (1983) and culminated in the amalgamation of the Lornex Mining Corporation, Highmont Mining Corporation Ltd., Teck Corporation and Cominco Ltd. to form the Highland Valley Copper Partnership from 1985 to 1988 (Casselman et al., 1995).

Extensive mapping of the Guichon Creek Batholith was undertaken by Cockfield (1948), Duffell and McTaggart (1952) and Carr (1960; 1962) and the first complete petrographic and geochronological studies of the batholith were reported by White et al. (1966) and Northcote (1969). Early studies on metal, trace and volatile element distributions in the Highland Valley district (Olade and Fletcher, 1975; 1976; Olade, 1977) showed that they were closely tied to alteration. In 1971 a gravity survey was conducted by the Gravity Division, Earth Physics Branch, Department of Energy, Mines and Resources, Ottawa, Canada and the results were interpreted and reported by Ager et al. (1973). The role of the structural evolution of the district in the formation of the Highland Valley deposits was explored by Hollister et al. (1975) who concluded that the temporal evolution of the intersecting Lornex and Highland Valley faults were critical in creating tensional fractures in which the ore bodies were deposited.

A number of masters and Ph.D. theses (Westerman, 1970; Brabec, 1971; Olade, 1974) were undertaken during the early 1970s to investigate the Guichon Creek Batholith and its copper deposits, culminating in the most complete syntheses of porphyry copper mineralization in the Highland Valley district to date which can be found in the Canadian Institute of Mining and Metallurgy Special Volume 15. This

synthesis includes detailed descriptions of the Highmont (Reed and Jambor, 1976), Lornex (Waldner et al., 1976) Valley (Osatenko and Jones, 1976), Bethlehem (Briskey and Bellamy, 1976) J.A. (McMillan, 1976b) and Krain (Christie, 1976) deposits along with a regional overview (McMillan, 1976a). Minor updates to this work were published by McMillan (1985) with data from additional Ph.D. theses (Briskey, 1980; Tombale, 1984). An update to this work which focused on insights from the Valley deposit was published by Casselman et al. (1995).

Most recently studies by Ash et al. (2007) and Alva Jimenez (2011) attempted to date the mineralization at Highland Valley Copper and studied compositional variations in hydrothermal muscovite and chlorite in the vicinity of the Valley deposit. Byrne et al. (2013) have provided the most recent compilation for geology, mineralization and alteration in the Highland Valley district.

1.6 Sampling Procedures and Sample Locations

Sampling for this study focused on selecting a representative suite of all intrusive facies present in the Guichon Creek and Nicola batholiths. Samples were collected from across the batholiths as part of the CMIC-NSERC Exploration Footprints project. Every effort was made to limit the sample suite to least altered, unmineralized samples where possible.

Initial sampling was conducted with the Teck regional exploration team during a one month period from August 12, 2013 to September 1, 2013. A second round of sampling was conducted from June 28, 2014 to July 9, 2014 to fill in gaps in the original sample distribution.

Samples are a combination of outcrop grab samples and drill core. All outcrop samples were approximately 20cm x 20cm x 20cm to ensure enough material was collected to perform the necessary petrographic, geochemical and petrophysical analyses. The most homogenous samples were taken where possible. Drill core sample lengths were based on the Footprints recommended sample length of 60 cm of whole NQ (47.6 mm diameter) core equivalent. Both drill core and outcrop samples were taken as oriented samples whenever possible, with the azimuth and dip of a downdip arrow recorded on a flat surface for petrophysical analysis.

An attempt was made to obtain a representative sample suite of both study areas with an even distribution across area and facies (Figs. 1.4 and 1.5). Limited access and poor exposure were challenges in both plutons and in particular in the Nicola Batholith. As a result, fewer samples of the Nicola Batholith were collected and samples cluster at the northern and western margins of the batholith (Fig. 1.5). A complete list of sample locations is provided in Appendix A.

Seventy-eight samples were collected from the main intrusive facies of the Guichon Creek and Nicola batholiths as summarized below:

- 45 outcrop samples from the Guichon Creek Batholith including:

    - 7 Border Facies
    - 9 Guichon Sub-facies
    - 7 Chataway Sub-facies
    - 7 Bethlehem Facies
    - 4 Skeena Facies
    - 7 Bethsaida Facies
    - 2 Aplite Dykes
    - 2 Feldspar Porphyry Mafic Dykes

- 20 drill core samples from the Bethlehem and Valley areas:

12

- o 2 Skeena Facies
- o 1 Aplite Dyke
- o 8 Feldspar Porphyry Crowded (FPC) Dykes
- o 5 Feldspar Quartz Porphyry Crowded (FQPC) Dykes
- o 1 Lamprophyre Dyke
- o 3 Tan Porphyry Dykes

- • 13 outcrop samples from the Nicola Batholith

1.7 Structure of Thesis

This thesis is divided into seven chapters: 1) Introduction; 2) Regional Geology; 3) Petrography; 4) Whole Rock Geochemistry; 5) Radiogenic Isotope Chemistry; 6) Mineral Chemistry and; 7) Summary and Conclusions. Chapter 2 provides a summary of the current literature with regards to the tectonic and district setting of the Guichon Creek and Nicola batholiths and the related HVC porphyry copper deposits. Chapter 3 provides detailed petrographic descriptions of all primary intrusive facies in the study areas. Chapter 4 presents major and trace element analyses which are used to interpret the petrogenesis and magmatic history of the Guichon Creek Batholith. Comparisons are also made between the Guichon Creek and Nicola batholiths. Chapter 5 presents the Sm-Nd and Rb-Sr systematics for selected samples from the Guichon Creek Batholith. Chapter 6 documents changes in hornblende, plagioclase, biotite and apatite chemistry over the evolution of the Guichon Creek Batholith. Chapter 7 summarizes the key findings presented in this dissertation and presents an emplacement model for the Guichon Creek Batholith.

LEGEND

- ······ Faults
- Ore Zones
- Jurassic and Younger Sedimentary and Volcanic Rocks
- Triassic Nicola Group Volcanic Rocks
- Hybrid Border and Nicola Facies
- Transitional Bethlehem and Highland Valley Facies
- Transitional Guichon and Chataway Subfacies
- Transitional Highland Valley and Border Facies
- Breccia Bodies

- Post Bethlehem Porphyry Dykes and Plugs
- Post-Bethsaida Porphyry Dykes and Plugs
- Bethlehem Facies
- Bethsaida Facies
- Border Facies
- Chataway Subfacies
- Guichon Subfacies
- Skeena Facies
- Sample Locations

Figure 1.4 Map of the Guichon Creek Batholith with sample locations. Geology modified from McMillan et al. (2009).

14
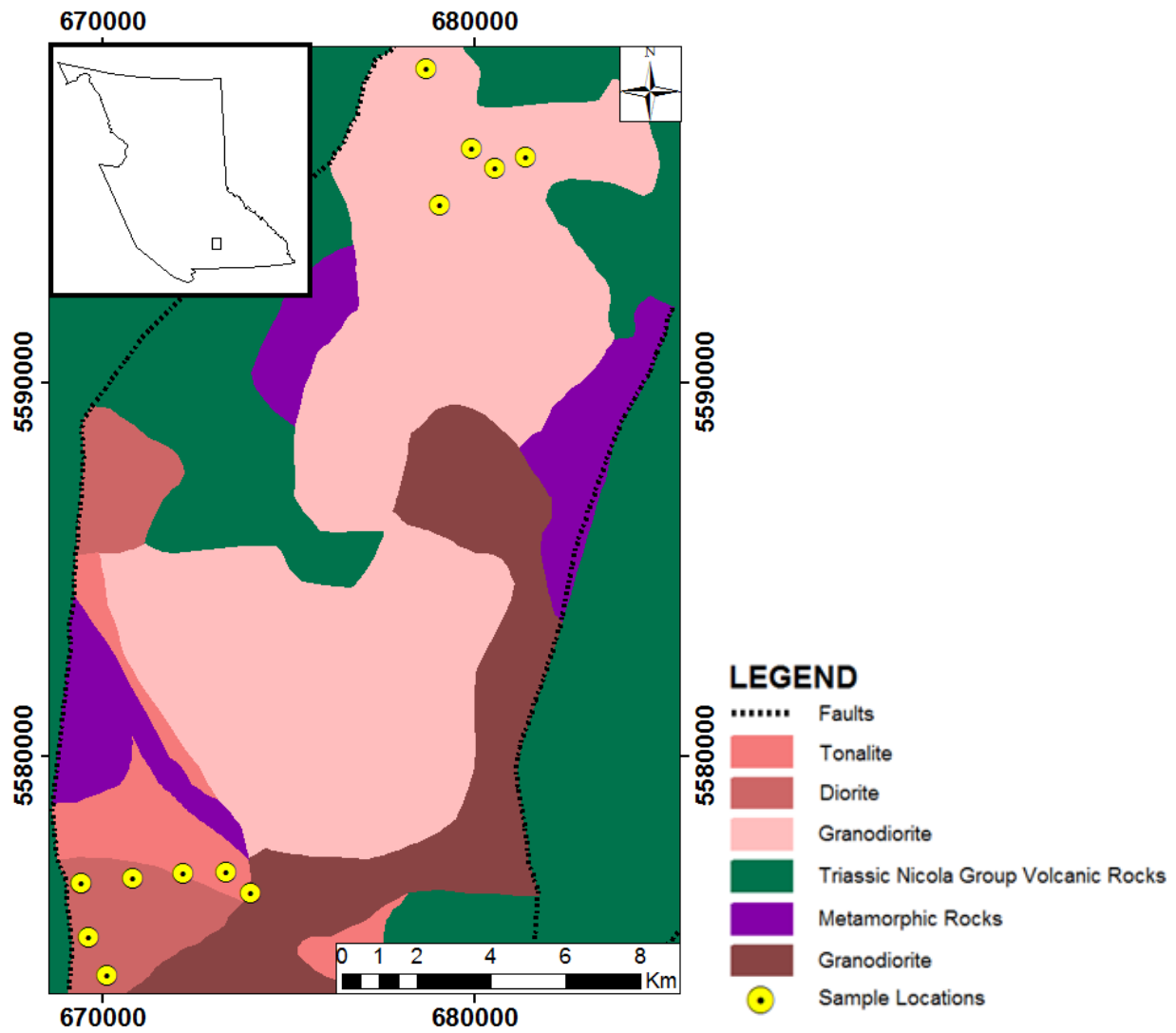
Figure 1.5 A geologic map of the Nicola Batholith with sample locations. Modified from Teck.

CHAPTER 2   REGIONAL GEOLOGY

2.1 Introduction

The Cordillera of western Canada formed as a result of a protracted history of tectonic processes over the course of 1.8 b.y., from the Precambrian to the present (Nelson et al., 2013). The Cordillera has been subdivided into five morphological belts (Foreland, Omineca, Intermontane, Coast and Insular belts; Fig. 2.1; Gabrielse et al., 1991), as well four 'paleogeographic realms', which are comprised of groups of terranes with similar histories (Ancestral North America, Peri-Laurentian, Arctic-Northeast Pacific and Coastal realms; Fig. 2.1; Colpron and Nelson, 2011). Some of the major terranes comprising the North American Cordillera formed a system of interconnected arcs that were in direct contact and influenced by one another at the time of their formation (Nelson and Friedman, 2004). This is in contrast with their original interpretation as regional, fault bounded blocks with geologic histories distinct from adjacent terranes (Jones et al., 1983). This chapter outlines the geology and mineralization in the Quesnel and related peri-Laurentian terranes in detail and gives a brief overview of Cordillera wide geology and tectonic history.

2.2 Peri-Laurentian Realm (Intermontane Superterrane)

The peri-Laurentian realm is composed of six main allochthonous terranes which are from east to west: 1) Slide Mountain, 2) Yukon-Tanana, 3) Quesnel, 4) Stikine, 5) Cache Creek and 6) Bridge River (Fig. 2.1; Monger et al., 1982; Nelson et al., 2013). The peri-Laurentian realm is bounded to the east by the Ancestral North America realm and to the west by the Insular terranes of the Arctic-Northeast Pacific realm (Monger et
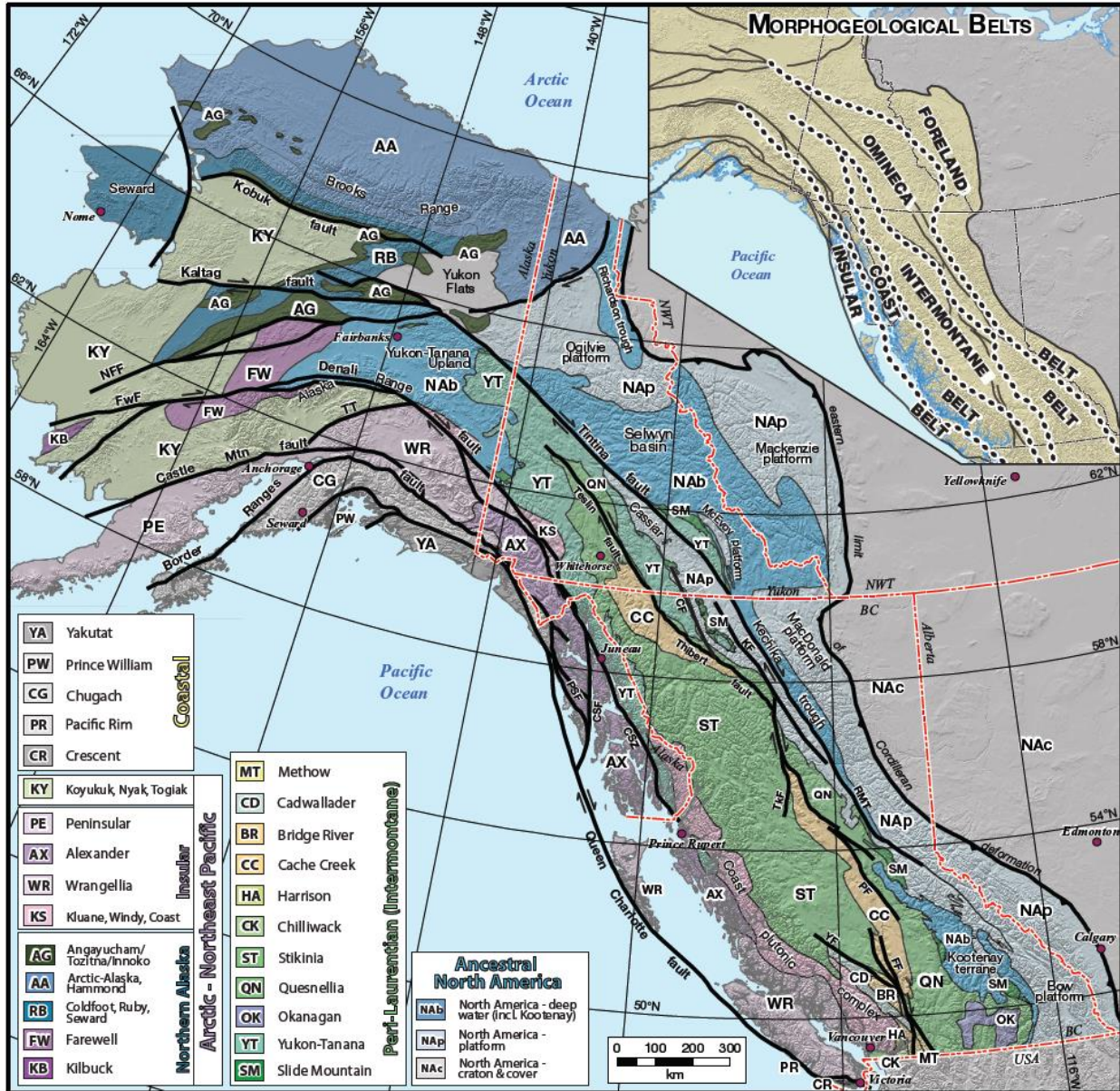
Figure 2.1 Terranes of the Canadian-Alaskan Cordillera (after Nelson et al., 2013). Inset shows morphological belts after Gabrielse et al. (1991). Fault abbreviations: CF = Cassiar fault, CSF = Chatham Strait fault, FF = Fraser fault, FwF = Farewll fault, KF = Kechika fault, NFF = Nixon Fork-Iditarod fault, PF = Pinchi fault, PSF = Peril Strait fault, NMRT = northern Rocky Mountain trench, TkF = Takla-Finlay-Ingenika fault system, TT = Talkeetna thrust, YF = Yalakom fault.

al., 1982; Nelson et al., 2013). Terranes of the peri-Laurentian realm display evidence

for interaction with the western Laurentian margin for their entire history. The terranes of

17

the peri-Laurentian realm are believed to have been assembled to each other by latest Triassic-earliest Jurassic time (Monger et al., 1982; Nelson et al., 2013).

2.2.1 Oceanic Slide Mountain and Cache Creek Terranes

Initially interpreted as a single suite of oceanic rocks formed by continental rifting and subsequent collapse of an ocean basin (Tempelman-Kluit, 1979), the Slide Mountain and Cache Creek terranes (Fig. 2.1) are now recognized to be of North American and Tethyan affinities, respectively, and represent separate ocean basins with differing histories (Monger and Ross, 1971; Monger, 1977; Monger and Price, 1979).

The geology and geochemistry of the Slide Mountain terrane suggests a marginal or back-arc basin origin (Tempelman-Kluit, 1979; Souther, 1991; Nelson, 1993; Smith and Lambert, 1995), with Paleozoic stratigraphic links to Ancestral North America (Klepacki and Wheeler, 1985) and the Yukon-Tanana terrane (Murphy et al., 2006). Slide Mountain rocks are Early Mississipian to Permian in age (Monger, 1977; Monger and Berg, 1987; Nelson, 1993) and comprise an upper volcanic unit of mid-ocean ridge basalts (MORB) and chert (Monger, 1977; Souther, 1977; Nelson, 1993; Roback et al., 1994; Smith and Lambert, 1995), and a lower sedimentary unit of chert, sandstone and conglomerate (Monger, 1977; Souther, 1991). Volcanism in the Slide Mountain terrane occurred from the Early Pennsylvanian to the Late Permian, beginning earlier in the south (Smith and Lambert, 1995). Sedimentary strata contain detrital zircon populations with northwestern Laurentian affinities (Nelson, 1993; Roback et al., 1994) and lie unconformably on and/or are thrust over Upper Devonian to Upper Mississippian continental margin rocks (Monger, 1977).

Rocks of the Cache Creek terrane belong to an accretionary complex that was trapped between the Quesnel and Stikine terranes during closure of the Cache Creek ocean (Mihalynuk et al., 1994; Nelson et al., 2013). Rock types include: late Paleozoic to late Triassic oceanic plateaux (Smith and Lambert, 1995; English et al., 2010); primitive arcs, ophiolites and mafic to intermediate intrusions (English et al., 2010) and; Late Triassic to Middle Jurassic blueschists and eclogite (Monger and Ross, 1971; Orchard et al., 2001; Mihalynuk et al., 2004; Nelson et al., 2013). An origin in the Tethyan realm is indicated by fossils exotic relative to those found in the adjacent Stikine, Quesnel and Yukon-Tanana terranes (Monger and Ross, 1971; Orchard et al., 2001).

The Cache Creek terrane ranges from Mississippian to Late Permian in age and has been subdivided into three subterranes based on lithological differences (Monger, 1977; Monger and Berg, 1987). The eastern Bonaparte subterrane is dominated by basaltic rocks with subordinate gabbro, serpentinite, volcaniclastic rocks, limestone and chert; the central Marble range subterrane is composed of chert, argillite, tuffs and minor basalt whereas chert and minor limestone units comprise the western Pavillion subterrane (Monger and Berg, 1987). Volcanism in the Cache Creek terrane has been dated as Middle Penssylvanian and older in the south and Early Mississippian in the north (Smith and Lambert, 1995).

2.2.2 Yukon-Tanana Terrane

The Yukon-Tanana terrane (Fig. 2.1) is bounded by transcurrent faults that separate it from the Cache Creek and Slide Mountain terranes on either side (Liverton et al., 2005). It originated as a pericratonic arc built upon the western Laurentian margin

(Nelson et al., 2006; Piercey et al., 2006) initiated by Middle to Late Devonian eastward subduction beneath the western Laurentian margin (Rubin et al., 1990; Colpron et al., 2006). Back-arc extension resulted in opening of the Slide Mountain ocean and the frontal arc rifted from North America to become the Yukon-Tanana terrane proper (Nelson et al., 2006; Colpron et al., 2007). A large tract of metamorphosed, siliciclastic sedimentary and Devonian plutonic rocks in the Yukon-Tanana uplands, with lithological, isotopic and detrital zircon characteristics similar to deformed rocks of the western Laurentian continental margin (Samson et al., 1991; Gehrels et al., 1995; Mortensen, 1992), were originally classified as part of the Yukon-Tanana terrane. These rocks have been reclassified, however, as part of the western Laurentian basin based on their structural position and lack of late Paleozoic arc assemblages (Hansen and Dusel-Bacon, 1998; Dusel-Bacon et al., 2006; Nelson et al., 2006). Consequently, only the arc successions that flank the Yukon-Tanana uplands (Roots and Heaman, 2001) are considered part of the Yukon-Tanana terrane proper (Nelson et al., 2013).

Structural relationships between the Yukon-Tanana and Quesnel, Stikine and Cache Creek terranes are complex, with portions of the southern Yukon-Tanana terrane separated from overlying arc assemblages equivalent to the Quesnel terrane (Nelson and Friedman, 2004) by an erosional unconformity (Simard et al., 2003). Complex structural contacts between the Quesnel and Yukon-Tanana terranes are also manifested as imbricate thrust sheets in the Cassiar Mountains of northern British Columbia (Nelson and Friedman, 2004). Part of the Yukon-Tanana terrane envelops the northern ends of the Cache Creek and Stikine terranes and this structural relationship was originally interpreted to represent a possible Stikine and Cache Creek klippe thrust

20

over a pericratonic arc built on a rifted piece of the Laurentian margin (Hansen, 1990; Gehrels et al., 1990). The currently accepted model, however, is the oroclinal bending model of Mihalynuk et al. (1994) where a composite Stikine-Yukon-Tanana-Quesnel arc was rotated around a hinge in the Yukon-Tanana terrane during closure of the Cache Creek ocean.

2.2.3 Quesnel Terrane

The Quesnel terrane is the second easternmost terrane of the Peri-Laurentian Realm in the Canadian Cordillera and bounded by the Slide Mountain terrane to the east and Cache Creek terrane to the west (Fig. 2.1). The Quesnel terrane is characterized by Mesozoic island-arc assemblages comprised of volcanic and sedimentary rocks and associated intrusions, the most important of which belong to the Late Triassic Nicola and Early Jurassic Rossland Groups (Preto et al., 1979; Coney et al., 1980; Roback and Walker, 1995). Peak metamorphic temperatures constrain crustal thickening in the Quesnel terrane to ~25 km with most thickening occurring during the mid-Early Jurassic (Mihalynuk et al., 1999). The basement rocks to the Mesozoic arcs are a complex composite that includes the youngest rocks of the Yukon-Tanana terrane in the Cassiar Mountains (Nelson, 1993; Simard et al., 2003; Nelson and Friedman, 2004) and primitive oceanic rocks (Preto et al., 1979; Smith et al., 1995; Acton et al., 2002) analogous to the Slide Mountain terrane along most of the length of the arc (Nelson and Friedman, 2004).

The oldest rocks in the Quesnel terrane are Late Devonian calc-alkaline arc-volcanic and plutonic rocks (Logan et al., 2000; Beatty et al., 2006), and continental margin assemblages of the Harper Ranch and Okanagan subterranes in southern

British Columbia (Monger, 1977, 1982; Read and Okulitch, 1977; Monger et al., 1991; Nelson, 1993) deposited during the breakup of Rodinia at ~570 Ma (Colpron et al., 2002). Correlative rocks in the Cassiar Mountains to the north, both structurally overlie and underlie the Yukon-Tanana terrane (Nelson, 1993; Nelson and Friedman, 2004) and it is likely that a portion of the Paleozoic Quesnel terrane was partially deposited on top of the youngest parts of the Yukon-Tanana terrane and primitive oceanic basement (Nelson, 1993; Nelson and Friedman, 2004).

2.2.3.1 The Nicola Group

The Late Triassic volcanic and sedimentary rocks of the Nicola Group are the most prominent assemblage in the Quesnel terrane, particularly in southcentral British Columbia (Fig. 2.2; Preto et al., 1979; Mortimer, 1987). The Nicola Group is primarily comprised of submarine volcanic rocks of island-arc affinity and associated sedimentary rocks (Ray et al., 1996; Mortimer, 1987) that were deposited in a rifted marine basin above an east dipping subduction zone (Preto, 1979; Mortimer, 1986, 1987). Radiogenic isotope systematics from the Nicola Group volcanic rocks and associated plutons show no clear evidence for crustal contamination (Smith et al., 1995), and they are interpreted to have been emplaced into primitive oceanic crust (Ghosh, 1995). Prominent high-angle, north-trending faults can be traced along the length of the Nicola Group and are likely basement structures that provided magmatic conduits and focused the construction of the volcanic centres (Preto et al., 1979). Albite-epidote-horfels facies metamorphism is ubiquitous in the Nicola Group (McMillan, 1976a; Preto et al., 1979) and strontium isotope systematics of volcanic rocks indicate that contamination by seawater strontium from carbonate rocks is likely (Preto et al., 1979).
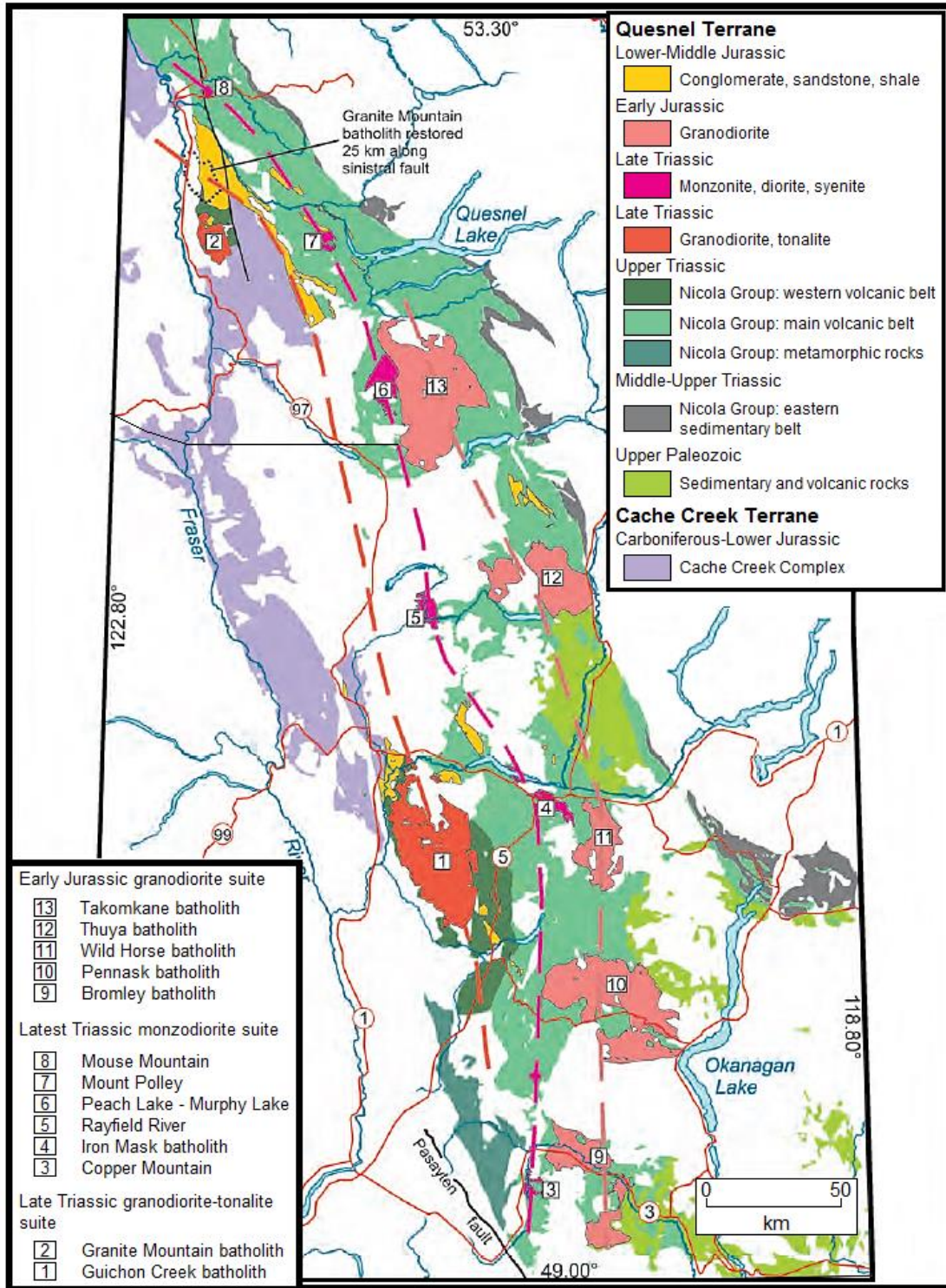
Figure 2.2 Simplified geological map of the Quesnel terrane in central British Columbia. Sub-parallel belts of volcanic and plutonic rocks young to the east where the Paleozoic and sedimentary rocks belonging to the Quesnel Terrane are most abundant. Much of the central Quesnel terrane is obscured by Cretaceous and younger sedimentary and volcanic cover. Modified after Schiarizza (2014).

23

In the eastern Quesnel terrane, the Nicola Group lies unconformably over oceanic rocks similar to the Slide Mountain terrane expressed elsewhere in southern British Columbia (Read and Okulitch, 1977), with some fault-bounded contacts in the eastern most portions (e.g., Hedley District; Ray et al., 1996). Faulted and depositional contact relaionships are also noted with the Cache Creek terrane to the west (Travers, 1977). The thickness of the Nicola group varies significantly from the west to east (~6km to 3km), with the thickest portion associated with mafic volcanic flows and rare limestone packages deposited along the main arc-axis (Preto, 1979). The eastern portion of the Nicola Group is dominated by sedimentary and volcaniclastic rocks and lacks the volcanic flows common in the west (Ray et al., 1996).

The Nicola Group has been subdivided into three distinct, north-south-trending belts in the southern Quesnel terrane (Preto, 1977, 1979; Morrison, 1980; Monger, 1982, 1985; Monger et al., 1982, 1991) that are separated by high-angle Triassic and Tertiary faults (Preto, 1979; Monger, 1985); depositional contacts between the western and central belts have, however, been mapped at some locations (Schau, 1968; McMillan, 1981). The western belt of the Nicola Group is comprised predominantly of basalt and rhyolite flows and volcaniclastic rocks interbedded with subordinate limestones, whereas the central and eastern belts are dominated by subaerial and submarine augite-phyric basalt and andesite flows, breccias and lahars with interbedded limestones, with an increasing proportion of sedimentary rocks to the east (Mortimer, 1987). Localized picrite and absarokite lavas are characteristic of the central to eastern Quesnel terrane and these young to the east (Souther, 1972; Mortimer, 1987).

Volcanic rocks of the Nicola Group have been divided into three lava types on the basis of petrography and geochemistry (Mortimer, 1987). Type 1 lavas are strongly augite-phyric picrite, basalt and andesite that belong to the high-K shoshonitic series. Type 2 lavas are plagioclase- and augite-phyric basalt and andesite with low- to medium-K calc-alkalic affinity. Type 3 lavas are more petrographically variable and range from tholeiitic to transitional basalt and andesite (Mortimer, 1987). Type 1 and Type 2 lavas are characterized by arc-like geochemical signatures with low Ti, Zr, Y and Nb as well as moderate to high K, Rb, Ba and Sr concentrations whereas Type 3 lavas have geochemistry transitional between island-arc and intraplate volcanic rocks (Mortimer, 1987).

2.2.3.2 Sedimentary Assemblages (Nicola, Slocan and Ymir Groups)

Sedimentary rocks of the eastern Nicola Belt are lithologically and temporally correlated to sedimentary rocks of the Slocan and Ymir Groups of the eastern Quesnel terrane (Mortimer, 1987; Monger et al., 1991; Thompson and Daughtry, 1998). The Slocan and Ymir Groups unconformably overlie Paleozoic pericratonic basement rocks (Read and Okulitch, 1977; Thompson and Daughtry, 1996, 1997, 1998) and have been dated between 227 to 210 Ma based on fossil assemblages (Travers, 1977; Preto, 1979; Orchard, 1985; Read, 1996; Thompson and Daughtry, 1996). A wide range of $\epsilon_{Nd(T)}$ values have been reported for the sedimentary rocks of the Slocan, Ymir and Nicola Groups (Ghosh, 1995; Ghosh and Lambert, 1989; Patchett and Gehrels, 1998; Unterschutz et al., 2002) and these overlap the primitive values for the Nicola Group volcanic rocks (Smith et al., 1995) as well as the sedimentary rocks of the ancient Laurentian margin (Jackson, 1992; Boghossian et al., 1996). The isotopic signature is

consistent with derivation of the sedimentary rocks from a mixture of isotopically

primitive and evolved sources (i.e., the Nicola arc and ancient North American western

margin; Patchett and Gehrels, 1998; Unterschutz et al., 2002), and is consistent with a

mixed provenance for sedimentary rocks belonging to the Harper Ranch subterrane

(Roback and Walker, 1995). This implies that the southeastern portion of the Quesnel

terrane was as close as 1500 to 3000 km from the ancient margin of western North

America during the Late Triassic (Patchett and Gehrels, 1998; Unterschutz et al., 2002).

2.2.3.3 Plutonic Belts

The plutonic rocks of the Quesnel terrane occur in two subparallel belts that

young towards the east (Fig. 2.2; Schiarizza, 2014), reflecting ~50 m.y. of arc evolution

above an E-dipping subduction zone (Mortimer, 1987; Parrish and Monger, 1992;

Schiarizza, 2014), and are host to paired belts of calc-alkalic and alkalic style porphyry

deposits (Logan and Mihalynuk, 2014). The oldest, Late Triassic belt is comprised of

calc-alkalic intrusive rocks of granodiorite to tonalite composition (Schiarizza, 2014)

which are geochemically similar to the western volcanic belt of the Nicola Group

(Mortimer, 1987). To the east, a younger (Latest Triassic to Early Jurassic) belt of

monzodiorite to syenite alkalic intrusions (e.g., Copper Mountain, Wild Mask, Mount

Polley; Fig. 2.2) are similar to the Type 1, alkaline Nicola Group lavas of Mortimer

(1987) which intrude the Iron Mask Batholith (Preto, 1972) and have been interpreted to

be co-magmatic (Mortimer, 1987). The youngest plutonic belt is Early Jurassic in age

and consists of calc-alkaline granodiorite and tonalitie similar to the Late Triassic Belt

(e.g., Pennask, Wild Horse, Thuya batholiths, Fig. 2.2; Schiarizza, 2014). Low initial

$^{87}Sr/^{86}Sr$ signatures (0.7025 to 0.7046; Preto et al., 1979) have been measured for a

number of these intrusions indicating a mantle origin, with little contamination by older

continental crust (Preto, 1979). An additional study by Armstrong (1988) found that

initial $^{87}Sr/^{86}Sr$ ratios gradually increase towards the east. Based on their similar

geochemistry and structural relationships, the major batholiths of the Quesnel terrane

are considered the plutonic roots of the Nicola Arc (e.g., Ghosh, 1995).

The Nicola Batholith is located approximately 19km northeast of Merritt, British

Columbia. Potassium-argon dating constrains the minimum emplacement age from the

Paleocene (60.2 ± 1.9 Ma) to the late Eocene (37.3 ± 0.9 Ma), although the late Eocene

age is suspect (Preto et al., 1979). Rock types present in the batholith include

porphyritic quartz monzonite and granodiorite.

2.2.3.4 The Guichon Creek Batholith

The Guichon Creek Batholith is a concentrically zoned, calc-alkaline intrusive

body with a composition varying from diorite and quartz-diorite at the margins to quartz-

monzonite and granodiorite in the core (e.g., McMillan, 1976a; Casselman et al., 1995;

Byrne et al., 2013; this study). It intruded the western volcanic belt of the Nicola Group

and is nonconformably overlain by Early Jurassic sedimentary rocks of the Ashcroft

formation (McMillan, 1976a; McMillan et al., 2009). Six major intrusive facies have been

identified in the Guichon Creek Batholith and described in detail: 1) Border facies,

Highland Valley facies [sub-divided into the 2) Guichon and 3) Chataway sub-facies

based on textural differences], 4) Bethlehem facies, 5) Skeena facies and 6) Bethsaida

facies (Fig. 2.3; e.g., Northcote, 1969; McMillan, 1976a; McMillan et al., 2009).

Additionally, a variety of porphyry dykes occur in and around the Bethlehem and Valley
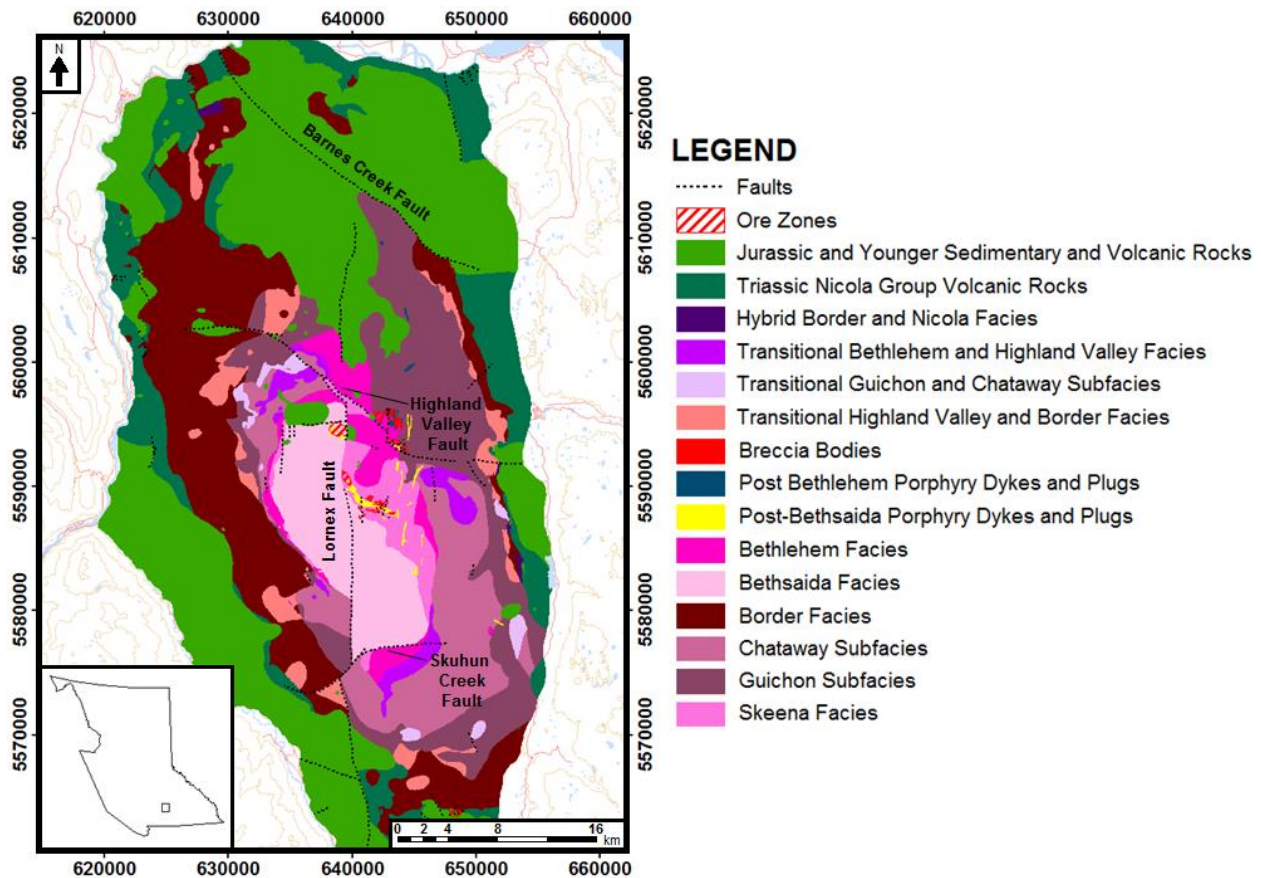
Figure 2.3 Simplified geological map of the Guichon Creek Batholith. Modified after McMillan et al. (2009).

deposits (e.g., Byrne et al., 2013) and, are interpreted to be related to the Bethlehem and Bethsaida facies, respectively (Briskey and Bellamy, 1976; McMillan, 1976a). A single U-Pb zircon crystallization age of 210 ± 3 Ma has been reported for the batholith (Mortimer et al., 1990) but a more detailed dating project conducted by Teck returned ages between ~211 and 206 Ma (Table 2.1; Alfaro, 2013, pers. comm.). Ash et al. (2007) dated molybdenite from the Valley deposit by the Re-Os method at 206.7 ± 1.5 Ma, representing the best estimate for the age of the mineralization event that formed the Valley, Lornex, Highmont and JA deposits, all of which are inferred to be approximately coeval (Casselman et al., 1995). An older mineralization event is inferred

28

at Bethlehem, associated with dyke emplacement and breccia formation following emplacement of the Bethlehem facies (Casselman et al., 1995; Byrne et al., 2013).

Mineralogical and phenocryst flow-alignment evidence suggest that convective overturn occurred in the Border, Guichon and Chataway facies (Westerman, 1970), and that they represent a continuous differentiation sequence (McMillan, 1976a). Cross-cutting contacts between the Bethlehem facies and older Guichon and Chataway sub-facies are often gradational, but sharp contacts have been locally observed, suggesting emplacement prior to complete solidification of the older facies (McMillan, 1976a). The Skeena facies has modal mineralogy and geochemistry intermediate between the Bethlehem and the Bethsaida facies (e.g., McMillan, 1976a; this study) and may represent a gradational contact between the Bethlehem and Bethsaida facies caused either by a single differentiation sequence or mixing between a Bethsaida magma

Table 2.1 U-Pb ages of zircons for different rock types in the Guichon Creek Batholith. Ages from Alfaro (2015, pers comm.) are by the TIMS method.

Facies	Sample	Age (Ma)	± 2σ	Reference
Border	SB123	211.02	0.17	Alfaro (2013, pers. comm.)
Highland Valley[a]	MA026	210.51	0.29	Alfaro (2013, pers. comm.)
Highland Valley[a]	SM059	210.77	0.16	Alfaro (2013, pers. comm.)
Highland Valley[a]	SM060	210.58	0.24	Alfaro (2013, pers. comm.)
Highland Valley[a]	MA038	210.42	0.41	Alfaro (2013, pers. comm.)
Bethlehem	SM058	209.17	0.54	Alfaro (2013, pers. comm.)
Bethlehem	MA099	209.81	0.27	Alfaro (2013, pers. comm.)
Skeena	SM055	208.37	0.29	Alfaro (2013, pers. comm.)
Bethsaida	SB217	208.81	0.21	Alfaro (2013, pers. comm.)
Bethsaida	SM061	208.15	0.22	Alfaro (2013, pers. comm.)
Bethsaida	SB218	208.55	0.20	Alfaro (2013, pers. comm.)
Porphyritic Dyke	SM057	208.71	0.38	Alfaro (2013, pers. comm.)
Porphyritic Dyke	SM056	208.93	0.52	Alfaro (2013, pers. comm.)
Porphyritic Dyke	MA121	206.95	0.22	Alfaro (2013, pers. comm.)
Guichon	Unknown 1	210	3	Mortimer et al. (1990)

[a]No distinction made between Guichon and Chataway sub-facies

emplaced into a partially crystalline Bethlehem magma (McMillan, 1976a). The gradational nature of internal contacts has been interpreted by previous authors (e.g., Northcote, 1969; McMillan, 1976a) to represent a magmatic history characterized by multiple magma pulses in to earlier, partially crystalline magmas.

Gravity (Ager et al., 1973) and seismic (Fig. 2.4; Roy and Clowes, 2000) models have shown the 3D shape of the batholith to be that of a funnel and that the major porphyry deposits are spatially related to the surface projection of the funnel's spout. The gravity model of Ager et al. (1973) also implies tilting of ~10 to 15° to the east-northeast, consistent with magmatic foliations that indicate near-vertical and gentler, east-dipping contacts in the western and eastern portions of the batholith respectively (Alfaro, 2015, pers. comm.). Important batholith-scale structures include the pre-mineralization N-trending Lornex and NW-trending Skuhun Creek, Highland Valley and Barnes Creek faults (Fig. 2.3; McMillan, 1976a; McMillan et al., 2009). These localized mineralization (Logan and Mihalynuk, 2014), and the elongated shape of the batholith may represent the control of magma emplacement by deep seated structures (Carr, 1966).

2.2.4 Stikine Terrane

The Stikine terrane represents a long-lived magmatic-arc assemblage (~130 M.y.; e.g., MacIntyre et al., 2001; Logan and Mihalynuk, 2014) and is presently separated from the Quesnel terrane to the east by the intervening Cache Creek terrane along most of its length. In the north, however, rocks of the Stikine and Quesnel terranes are juxtaposed and in turn surrounded by the Kootenay-Cassiar terrane to the east and the Yukon-Tanana terrane to the north and west (Fig. 2.1; Colpron et al.,
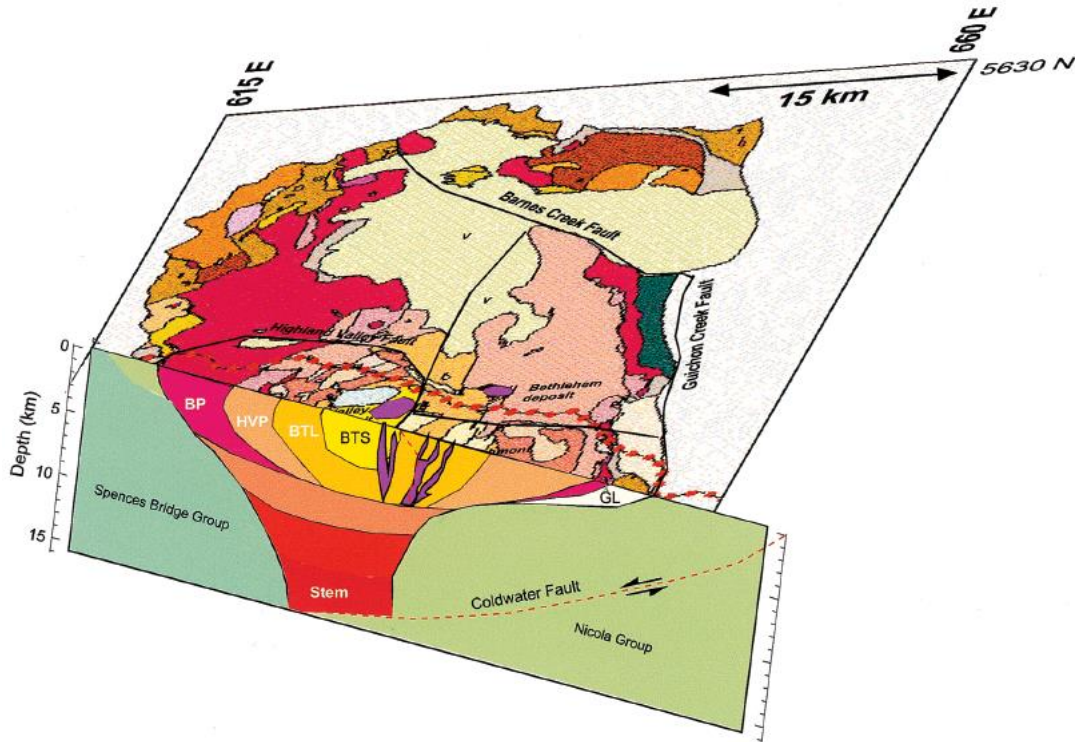
Figure 2.4 A 2D schematic cross-section through the Guichon Creek Batholith along the Southern Canadian Cordillera Transect of LITHOPROBE showing the flattened funnel shape and interpreted internal structures (after Roy and Clowes, 2000). Border facies (BP); Highland Valley facies (HVP); Bethlehem facies (BTL); Bethsaida facies (BTS).

2006). Plutonic belts that cross-cut the Yukon-Tanana-Stikine and Yukon-Tanana-Quesnel terrane boundaries (Wheeler and McFeely, 1991), along with the similarity between terranes suggests that the Stikine terrane was once an arc-axial extension of the Quesnel terrane (Nelson et al., 2013; Logan and Mihalynuk, 2014). The directional migration of magmatism and porphyry deposits characteristic of the southern Quesnel terrane, although present in the northwestern Stikine terrane, is not as well developed and is largely absent from its southern portion (Logan and Mihalynuk, 2014). This ambiguity has been argued to be the result of dual eastward and westward subduction zones beneath the Stikine arc (Thorkelson et al., 1995).

Early Permian to Middle Jurassic volcanism formed three successive, stacked arc assemblages (Asitka, Takla and Hazelton) with intermittent periods of uplift and erosion during the Late Triassic to Early Jurassic (MacIntyre et al., 2001). Hansen (1990) and Gehrels et al. (1991a, 1991b) initially proposed that arcs were built upon a thick basement of Paleo- or Proterozoic continental margin rocks, however, arc-like geochemistry and juvenile Sr initial ratios (Mihalynuk et al., 1992, Whalen et al., 2001) of granitic plutons cross-cutting the Stikine and Cache Creek terranes indicate they overlie an established isotopically primitive reservoir of arc-character and cannot be reconciled with the earlier model. Important mineral deposits in the Stikine Terrane include the Endako porphyry-Mo deposit (Villeneuve et al., 2001).

Granitic plutons dated at 174.1 ± 3.8 to 69.8 ± 0.1 Ma that intrude both the Cache Creek and Stikine terranes (Mihalynuk et al., 1992) and the presence of Cache Creek derived sediment in the northern (Gabrielse, 1991; Ricketts et al., 1992) and southern (MacIntyre et al., 2001) Bowser basin, which overly arc rocks of the Stikine Terrane, constrains closure of the Cache Creek ocean and obduction of Cache Creek rocks westward over the Stikine Terrane to the Early and Middle Jurassic (183 to 172 Ma). Although the Stikine and Cache Creek terranes were joined by the Middle Jurassic, sporadic arc-related magmatism continued into the Cretaceous (Schiarizza and MacIntyre, 1999; Struik et al., 2001; Villeneuve et al., 2001).

2.3 Arctic-northeastern Pacific Realm

The Arctic-northeastern Pacific Realm is comprised of the Insular and Northern Alaska terranes and roughly correlates to the Insular Belt of Gabrielse et al. (1991) in southern and central British Columbia (Fig. 2.1). The most prominent terranes of Arctic-

northeastern Pacific Realm affinity in British Columbia are the Alexander, Wrangell and Peninsular terranes that comprise much of the western coastline (Fig. 2.1). The Alexander and Peninsular terranes are pericratonic in nature and are primarily composed of arc assemblages (Clift et al., 2005). The Wrangell terrane originated as a Late Pennsylvanian-Permian oceanic arc and evolved to a Late Triassic oceanic plateau and Early Jurassic marine basin and volcanic arc (Monger and Price, 1979). Jurassic blueschists in the Penninsular terrane (Plafker et al., 1994) are analogous to those in the Cache Creek terrane and likely represent the trapped remnants of an ancient ocean basin. Faunal and isotopic evidence in terranes of the Arctic-northeastern Pacific Realm provide links to each other and Siberia and/or Baltica during their formation (Beranek et al., 2013a, b). Accretion of the Arctic-northeastern Pacific terranes to the Peri-Laurentian terranes began in the mid-Jurassic and culminated in the formation of a continental arc which developed into the present day Coast Mountains plutonic and metamorphic complex (Nelson et al., 2013).

2.4 Omineca and Coast Metamorphic and Plutonic Belts

The Omineca and Coast Belts (Fig. 2.1) are the two metamorphic and magmatic belts of Monger et al. (1982) resulting from post-accretionary Cretaceous transpression and Tertiary transtension (Nelson et al., 2013). The compressional and extensional regimes were the result of the collision of the peri-Laurentian realm with ancestral North America (Omineca belt) and the Arctic-northeastern Pacific realm with the peri-Laurentian realm (Coast belt) and Omineca and Coast belt metamorphism and deformation are superimposed on rocks from adjacent realms (Monger et al., 1982). Maximum pressures for prograde metamorphism are ~7 kbar in both belts (Pigage,

1976; Ghent et al., 1979; 1982; McClelland et al., 1991) equivalent to burial depths ≥25 km with a thermal metamorphic peak in the Late Cretaceous in the Omineca belt (Carr, 1995).

Metamorphic grade in the Coast Belt is predominantly upper amphibolite to granulite facies (e.g., Stowell and Crawford, 2000; Hollister and Andronicos, 2000; Rusmore et al., 2005) although local lower grade assemblages are evidenced by crinoid stem fragments preserved undeformed rocks hosted in migmatites (Hill, 1985). Magmatism in the Coast Mountains Batholith of the Coast belt represents the roots of a Late Jurassic to Eocene (160-50 Ma) continental arc which migrated eastward (Gehrels et al., 2009; Nelson et al., 2013). Mid-Cretaceous S-type granites dominate the southern Omineca belt (Hart et al., 2004) and were derived from deep burial and melting of continental margin rocks during accretion of the peri-Laurentian realm (Nelson et al., 2013). In contrast, the Coast belt is dominated by Mid-Cretaceous I-type granites (Hart et al., 2004) derived from melting of oceanic crust subducting beneath the newly accreted continental margin (Nelson et al., 2013).

The Mid-Cretaceous stress regime in both belts was predominantly transpressional resulting in eastward-directed shortening manifested as lower- and mid-crustal shortening west of the Omineca belt which transitioned to thin-skinned thrusting in the upper crust to the east of the Omineca belt in the Rocky Mountains of the foreland belt (Evenchick et al., 2007). The structural regime was also expressed by complimentary shear zones (sinistral in the Coast belt, dextral in the Omineca belt) resulting in northward translation of a significant portion of the intervening intermontane block (Nelson et al., 2013). A switch to transtensional stresses during the Paleocene to

Eocene led to extensional collapse of the thickened Omineca and Coast belt crust (Nelson et al., 2013). The subsequent end of subduction beneath much of the west coast of British Columbia during the Late Eocene initiated dextral transform motion along the Queen Charlotte fault that continues to the present (Nelson et al., 2013).

2.5 Tectonic History

Subduction beneath western Laurentia in the Middle to Late Devonian initiated continental and marginal arcs which would later form the peri-cratonic arc terranes of the Peri-Laurentian Realm (Colpron et al., 2006). Late Devonian to Permian back-arc extension caused rifting and ocean-ward migration of the frontal arcs which would become the Yukon-Tanana terrane (Nelson et al., 2006; Colpron et al., 2007) and concurrent opening of the Slide Mountain ocean basin (Nelson et al., 2013). Sedimentary rocks deposited during the Pennsylvanian to Permian transitioned from deep water carbonate assemblages to siliciclastic rocks and chert (Gunning et al., 2006) with Sm-Nd signatures (Patchett and Gehrels, 1998) and faunal assemblages (Belasky and Stevens, 2006) consistent with a maximum distance of 1500 to 3000 km west of the Laurentian margin.

A switch in arc polarity beneath the Yukon-Tanana terrane during the Middle to Late Permian culminated in re-accretion of the Yukon-Tanana terrane to the Laurentian margin during the Early to Middle Triassic (Piercey et al., 2006; Beranek and Mortensen, 2011). Subsequent eastward subduction beneath the Quesnel and Stikine arcs resulted in the emplacement of co-genetic volcanic and plutonic Mesozoic arc rocks of the Stikine and Quesnel terranes (Nelson et al., 2013). Initial closure of the Cache Creek Ocean began at ~175 Ma with complete closure by ~173 Ma in the Middle

Jurassic (Fig. 2.4a-b; Mihalynuk et al., 2004). The initial closure of the Cache Creek Ocean is believed to have occurred in the Late Triassic to Early Jurassic, by counterclockwise oroclinal rotation of the Stikine and Yukon-Tanana terranes, with final closure occurring in the Middle Jurassic (Fig. 2.5a-c; Mihalynuk et al., 1994). Analogous processes are believed to be occurring in the modern day Kurile and Aleutian island arcs (c.f. Mihalynuk et al., 1994; Nelson and Friedman, 2004) and the Molucca Sea region of the southwestern Pacific (Fig. 2.5d; Nelson et al., 2013).

The Mid-Cretaceous and Eocene history of the Intermontane terranes is characterized by transpressional tectonics. Accretion of the peri-Laurentian and Arctic-northeastern Pacific terranes to the Laurentian margin resulted in emplacement of these accreted terranes over the craton margin, causing crustal anatexis in the continental basement and formation of the post-accretionary Coast Mountains Batholith (ca. 160-45 Ma; Nelson et al., 2013) and Omineca arc. Development of the Omineca arc above metamorphosed cratonic basement resulted in emplacement of S-type granitoids, whereas a lack of cratonic basement in the Coast belt resulted in the generation of I-type granitoids (Hart et al., 2004; Massey et al., 2005). Mid-Cretaceous to Eocene dextral strike-slip faults in the Intermontane terranes record ~800km displacement (Gabrielse et al., 2006).

2.6 Porphyry Cu ± Au ± Mo Mineralization of British Columbia

Late Triassic to Early Jurassic porphyry Cu-Au and Cu-Mo deposits are the most significant economic deposits in British Columbia (Nelson et al., 2013). Deposit formation spans the period of 210 to 178 Ma, with more than 90% of copper endowment
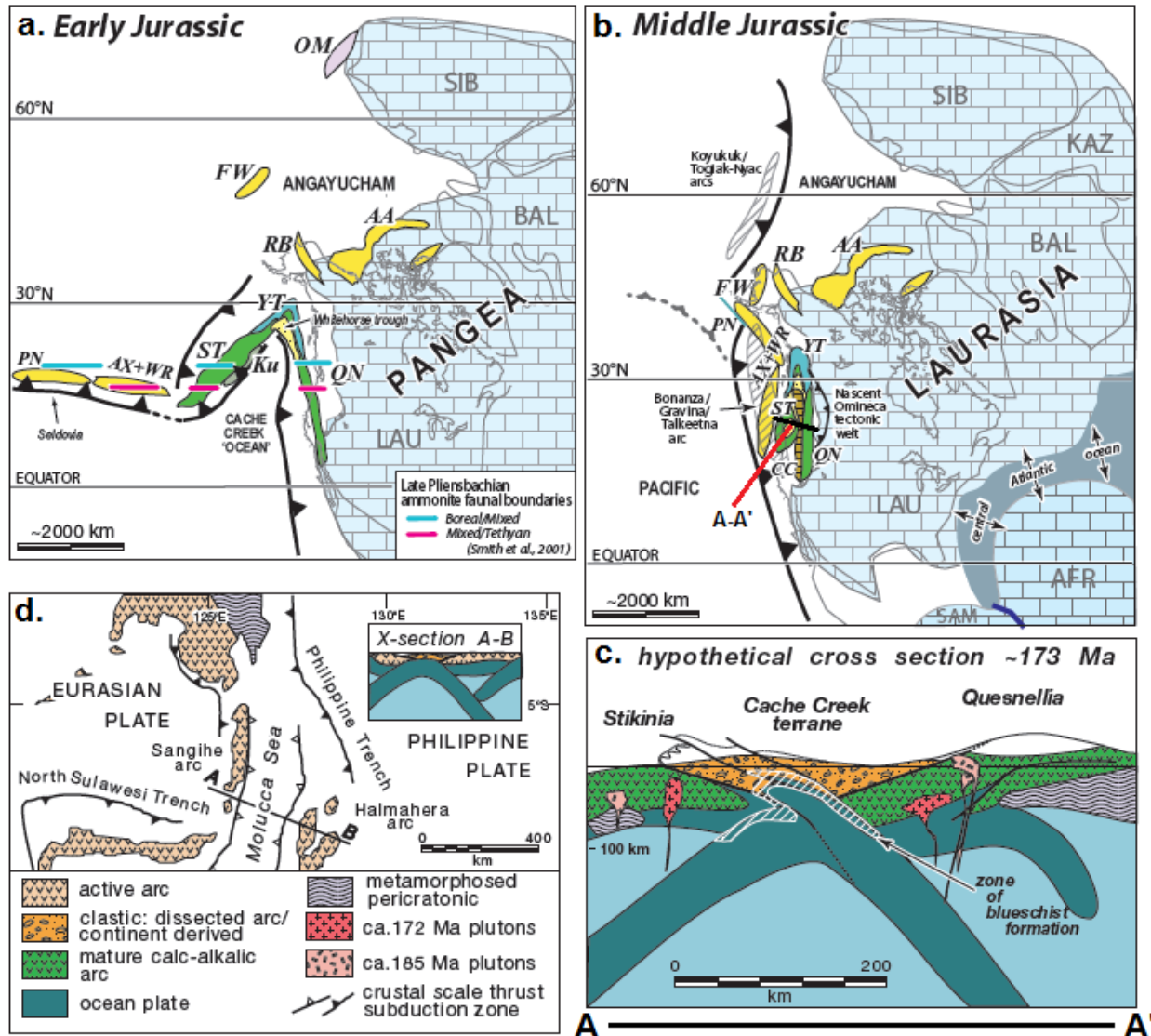
Figure 2.5 A. Early Jurassic paleogeographic reconstruction (after Nelson et al., 2013). Fossil constraints from Smith et al. (2001). Oroclinal closure of the Cache Creek ocean is underway. B. Middle Jurassic schematic reconstruction of the Cache Creek closure modified after (Nelson et al., 2013). C. Schematic cross-section across the Intermontane terranes during the Middle Jurassic (modified after Mihalynuk et al., 2004). D. Tectonic map and cross-section of the modern Molucca Sea region (after Nelson et al., 2013). PN = Peninsular, AX = Alexander, WR = Wrangel, ST = Stikine, Ku = Kutcho, YT = Yukon-Tanana, QN = Quesnel, RB = Ruby, FW = Farewell, AA = Arctic Alaska.
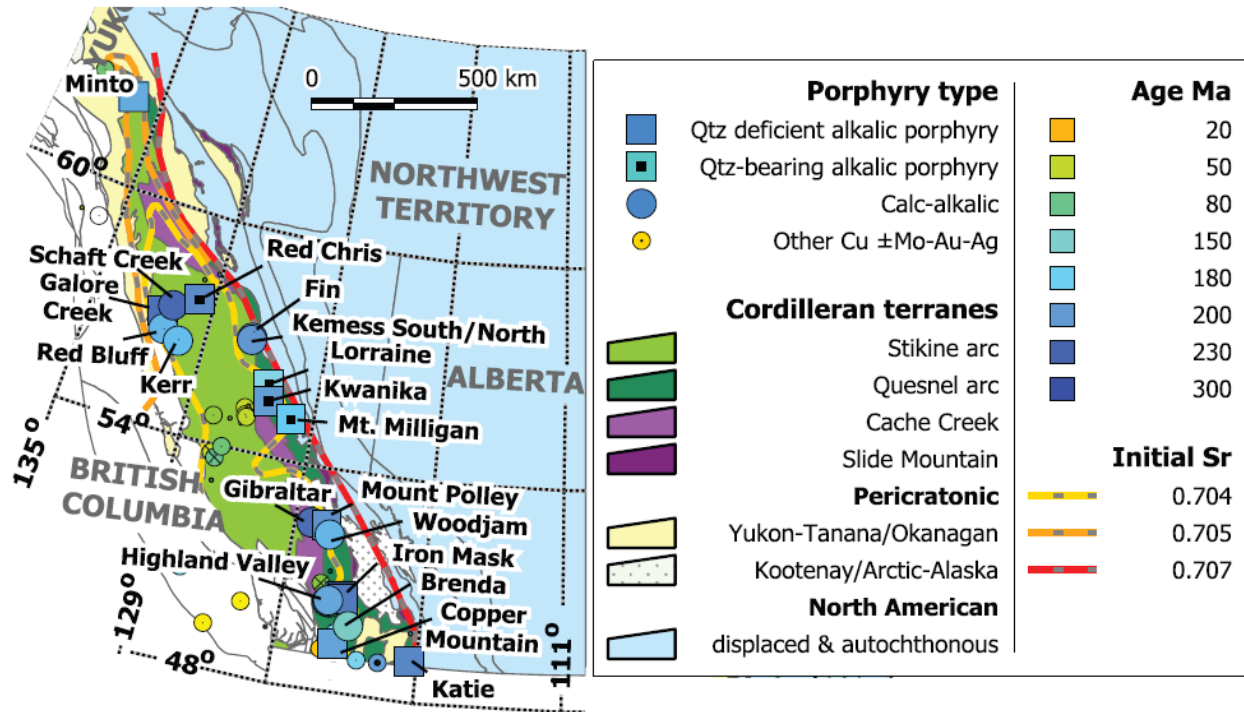
Figure 2.6 Spatial and temporal distribution of porphyry deposits in British Columbia. After Logan and Mihalynuk (2014).

occurring between 205 to 202 Ma (Logan and Mihalynuk, 2014). Historic focus on exploration was on shallow low grade deposits but it has switched in recent years to deeper, higher-grade deposits (Nelson et al., 2013). An excess of $200 billion in metal value is expected to come from combined reserves, resources and past production of BC porphyry deposits (Lydon, 2007).

Porphyry-style mineralization is associated with the subvolcanic intrusions (Nelson and Bellefontaine, 1996) of the Stikine and Quesnel terranes, and occur as paired belts of calc-alkalic and alkalic deposits (Fig. 2.6; Logan and Mihalynuk, 2014). Regular spacing (~100 km) of Triassic and Jurassic alkaline porphyry deposits has been interpreted to represent the spacing of ancient volcanic centres (Panteleyev et al.,

1996). Intrusions with primitive isotopic signatures (Preto et al., 1979; this study) are elongated parallel to the axis of arc-magmatism (e.g., Guichon Creek, Granite Mountain and Wild Horse batholiths; Fig. 2.2), suggesting that deep-seated, arc-axial (N-trending) faults may have been important in channeling porphyry-forming-magmas to shallow crustal levels. However, NW- and E-trending arc-transverse structures control most mineralization on the deposit scale (Preto, 1972, 1979; Northcote, 1977). The formation of subduction-related paired porphyry deposits migrated towards the back-arc until ~195 Ma (e.g., southern Quesnel terrane), and were followed by a number of late (185 to 173 Ma and 80 to 50 Ma; e.g., Endako; Villeneuve et al., 2001) post-accretionary deposits attributed to crustal thickening and decompression melting (Logan and Mihalynuk, 2014). In the southern Quesnel terrane, there is an eastward shift from 210 to 215 Ma calc-alkalic porphyry Cu-Mo deposits (e.g., Highland Valley Copper, Gibraltar; Byrne et al., 2013; Schiarizza, 2014) to slightly younger (~205 Ma) alkalic porphyry Cu-Au ± Ag-Pt-Pd-Mo deposits (e.g., Mount Polley; Barr et al., 1976). A similar pattern of older, calc-alkalic porphyries followed by younger alkalic porphyries has been noted in the northwestern Stikine terrane, but with alkalic deposits developed to the west (Logan and Mihalynuk, 2014).

The Quesnel and Stikine terranes are unique globally for their abundance of quartz-deficient alkalic porphyry deposits (e.g., Galore Creek) with relatively few such deposits located outside of British Columbia (e.g., Wolfe and Cooke, 2011). The abundance of otherwise rare alkalic porphyry deposits in the Quesnel and Stikine terranes has been attributed to the formation of a tear in the subducting slab beneath the Quesnel-Stikine arc, resulting from the collision of the Sitlika-Kutcho-Venables arc

(Logan and Mihalynuk, 2014). The slab tear model for generation of alkalic porphyry deposits is largely based on the abundance of shoshonite series (high-K) picrite and absarokite magmas which are rare in modern arcs. Average Nb and Yb contents of picrite lavas from the Quesnel and Stikine terranes of 0.35 and 0.43 ppm, respectively (Russell and Snyder, 1997), are indicative of large degree mantle partial melts (Logan and Mihalynuk, 2014).

Important alkalic porphyry Cu-Au ± Ag-Pt-Pd-Mo deposits in the Quesnel and Stikine terranes include: Galore Creek (Allen et al., 1976; Enns et al., 1995; Logan and Mihalynuk, 2014; 210 Ma, Mortensen et al., 1995), Afton-Ajax (Iron Mask Batholith, Preto, 1979; Mortimer, 1987; Logan and Mihalynuk, 2005; 204 Ma, Mortensen et al., 1995), Copper Mountain (Copper Mountain Batholith, Preto, 1972; 204 to 200 Ma, Mortensen et al., 1995), Mount Polley (Pass et al., 2014; 205 to 201 Ma, Mortensen et al., 1995; Logan et al., 2007) and Lorraine (Hogem Batholith, Garnett, 1978; Woodsworth et al., 1991; 180 to 177 Ma, Bath et al., 2014; Devine et al., 2014) amongst others. Major calc-alkalic porphyry Cu-Au deposits include Schaft Creek (Hickman Batholith; 222 Ma, Scott et al., 2008), Gibraltar (Granite Mountain Batholith, Schiarizza, 2014), Highland Valley (Guichon Creek Batholith, Casselman et al., 1995; Byrne et al., 2013; 208 to 206 Ma, Ash et al., 2007), Kemess South (Maple Leaf pluton, Logan and Mihalynuk, 2014; 199 Ma, Diakow, 2001), Woodjam (Takomkane, Peters, 2009; 196 Ma, Logan et al., 2011), and Brenda (Pennask Batholith, Soregaroli and Whitford, 1976; 194 Ma, Parrish and Monger, 1992).

Mineralization in the Highland Valley deposits is predominantly controlled by veins, fractures, faults and breccias, with locally important quartz stockworks (Valley and

Lornex) and dykes (Bethlehem; e.g., McMillan, 1976a; Casselman et al., 1995; Byrne et al., 2013). Significant alteration is present in all Highland Valley deposits and includes, silicification, potassic, phyllic, argillic and propylitic assemblages with tourmaline replacement of clasts and matrix occurring in breccias from the Bethlehem deposit (e.g., McMillan, 1976a; Osatenko and Jones, 1976; Casselman et al., 1995; Byrne et al., 2013). The major ore minerals include chalcopyrite, bornite and molybdenite with a small amount of peripheral pyrite (e.g., Byrne et al., 2013). At Valley, the highest Cu-grades are associated with quartz veins with medium- to coarse-grained muscovite selvages of the phyllic zone (Casselman et al., 1995).

CHAPTER 3   PETROGRAPHY

3.1 Introduction

Samples selected for petrographic analysis were chosen to reflect the least altered, unmineralized baseline mineralogy for the different igneous facies that comprise the Guichon Creek and Nicola batholiths. All thin sections were prepared at the Lakehead University lapidary lab in Thunder Bay, Ontario. Grain sizes are reported as very-fine-grained (v.f.g; <0.25mm), fine-grained (f.g.; 0.25 to 1mm), medium-grained (m.g.; 1 to 5mm) and coarse-grained (c.g.; 5 to 50mm). All mineral contents are expressed as modal percent and rock names were determined using the IUGS classification scheme for plutonic igneous rocks (Le Bas and Streckeisen, 1991). Detailed thin section descriptions are provided in Appendix B.

3.2 Border Facies

The Border facies is the outermost unit of the Guichon Creek Batholith. The contact between the batholith and its country rocks was observed in one outcrop on the eastern portion of the batholith, where brecciated blocks of Nicola Group basalts are supported by a matrix of olivine leuco-gabbro of the Border facies (Fig. 3.1). The Border facies is the most heterogeneous of the main facies and is composed of olivine leuco-gabbro, olivine leuco-monzogabbro, quartz leuco-monzogabbro, diorite, quartz diorite and quartz monzodiorite. Textural characteristics are also variable but are dominated by abundant coarse-grained, equigranular textures, with some areas containing rocks with bands of fine-grained rock (Fig. 3.2D) and common autoliths.

Figure 3.1 Brecciated blocks of Nicola Group basalt hosted in a matrix of olivine leuco-gabbro of the Border facies. The photo was taken at a road cut along Highway 97C near the contact between the Guichon Creek Batholith and the Nicola Group country rocks (NAD83, Zone 10U; 0651178E, 5595176N).

3.2.1 Gabbroic Rocks

The most primitive rocks of the Guichon Creek Batholith are gabrroic rocks belonging to the Border facies. These rocks typically contain minor amounts olivine (2 to 5%) and clinopyroxene (2 to 15%). The most primitive gabbroic rocks can contain up to 10% olivine and minor orthopyroxene (2 to 5%). Olivine crystals are typically fine-grained (<0.5mm) and rounded, and have been affected to varying degrees by pervasive alteration to talc (Fig. 3.3A), iddingsite and/or serpentine along internal fractures or grain boundaries resulting in serpentine coronas (Fig. 3.3A). Orthopyroxene and clinopyroxene are generally 0.5 to 2mm and occur as anhedral to subhedral

43
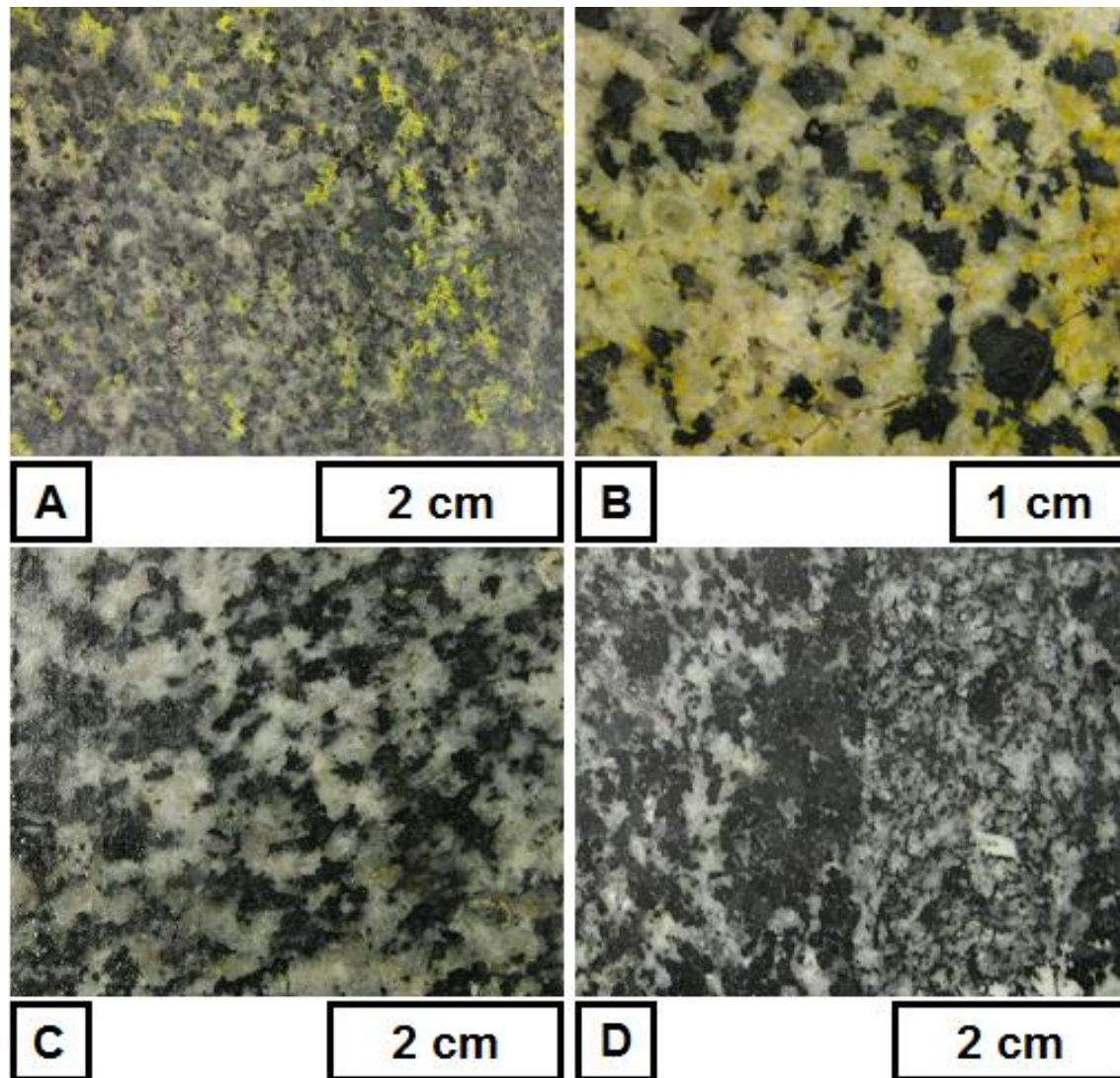
Figure 3.2 Hand sample photos of rocks belonging to the Border facies. All samples have been stained with sodium cobaltinitrite. A. Medium-grained leuco-olivine monzogabbro with secondary K-feldspar (yellow). Mafic minerals are a mixture of olivine, clinopyroxene and abundant biotite (MD001). B. Medium- to coarse-grained quartz monzodiorite (MD057). C. Medium-grained equigranular quartz diorite from the Border facies. Sample is stained and does not contain any K-feldspar (Sample MD046). D. A medium-grained equigranular Border facies diorite with a 2cm band of finer-grained diorite separated by sharp contacts (MD003B).

crystals that are interstitial to abundant plagioclase. Pyroxenes also commonly occur as

relatively coherent cores to amphibole crystals (Fig. 3.3C) or as complex, patchy

intergrowths in the core of amphibole crystals (Fig. 3.3B). Amphibole contents vary

widely, from 2 to 38%, and it is most abundant in samples that contain abundant olivine,
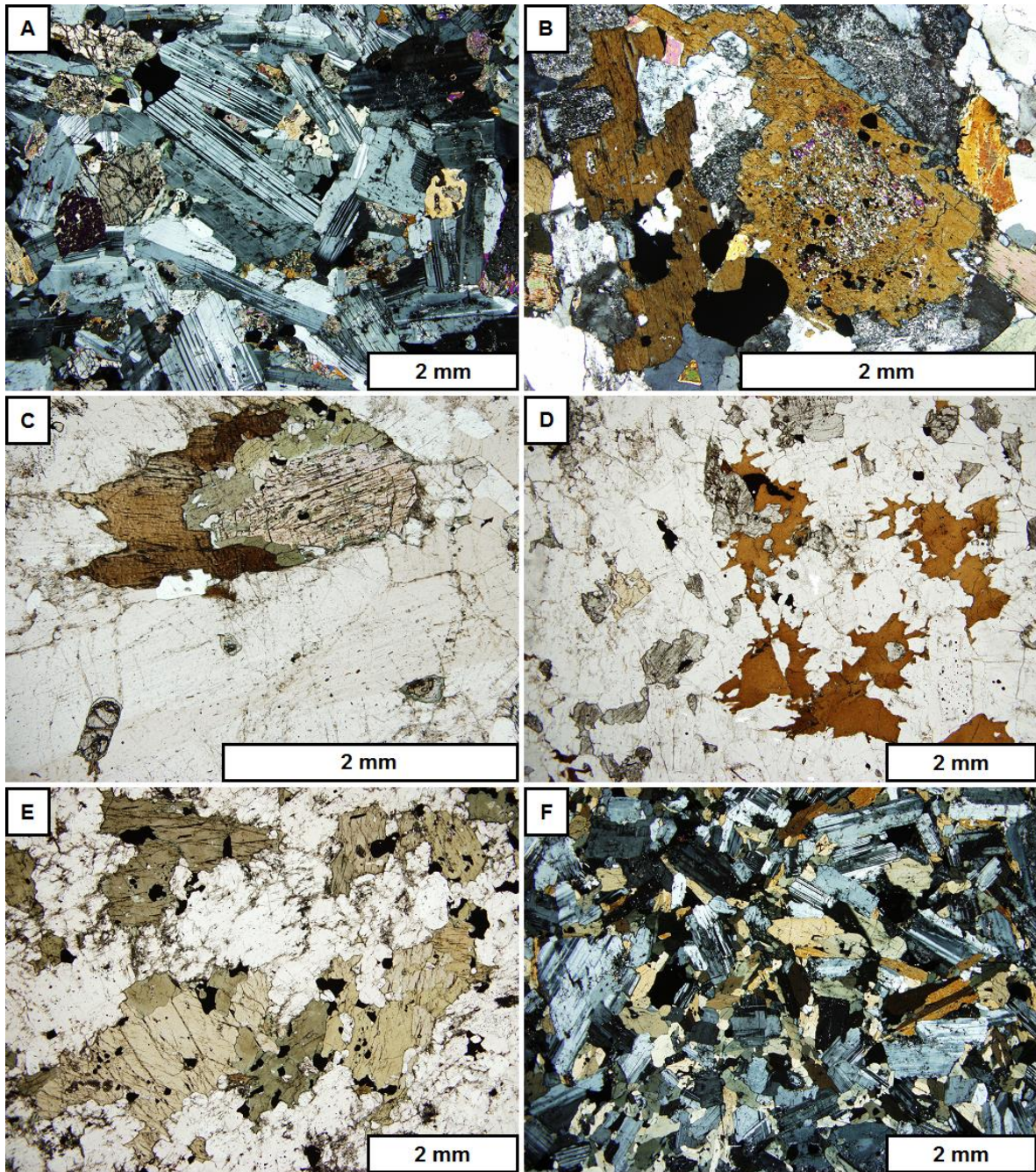
Figure 3.3 Photomicrographs of the Border facies lithologies. A. Weakly altered plagioclase laths with interstitial olivine, amphibole, clinopyroxene and minor biotite in an olivine gabbronorite. Some olivine crystals have been altered to talc and/or weakly serpentinized along fractures (Cross-polarized, transmitted light; MD078). B. Uralitization of pyroxenes common in the Border facies. A core of patchy, altered clinopyroxene and magnetite is surrounded by amphibole (Cross-polarized, transmitted light; MD057). C. Progressive alteration of a clinopyroxene crystal to amphibole and biotite. A single olivine inclusion in plagioclase can be seen to the bottom left (Plane-polarized, transmitted light; MD002). D. Abundant unaltered biotite and K-feldspar from an altered leuco-olivine monzogabbro (Plane-polarized, transmitted light; MD001). E. Interstitial medium- to coarse-grained amphibole with abundant magnetite inclusions typical of Border facies diorites (Plane-polarized, transmitted light; MD003A). F. Medium-grained amphibole and plagioclase from a finer-grained band in a Border facies diorite (Cross-polarized, transmitted light; MD003B).

45

clinopyroxene and orthopyroxene. Amphibole crystals range from 0.5 to 2mm and display two main textural styles. The most common texture in the most evolved samples is anhedral to subhedral crystals interstitial to plagioclase, commonly containing cores of orthopyroxene and clinopyroxene (Fig. 3.3B) and, in the least evolved samples, it predominantly occurs as sub-millimeter thick rims and partial replacements of pyroxene (Fig. 3.3C). These textures are characteristic of uralitization of primary pyroxene to amphibole and are commonly observed in mafic rocks that have been infiltrated by H_2O, either during the late stages of crystallization, or during subsequent deuteric alteration (Winter, 2010). As plagioclase and olivine are relatively less altered than pyroxene in most samples, it is interpreted that uralitization of pyroxenes in the Border facies was an deuteric process related to a progressive increase in magmatic H_2O content during crystallization. This is further supported by the fact that the extent of uralitization and consequent increased amphibole content coincides with progressive evolution towards more intermediate compositions.

All gabbroic rocks from the Border facies contain a significant amount of plagioclase (42 to 58%). Crystals range from 0.5 to 4mm in size and are generally subhedral laths, though in some cases they display serrated grain boundaries (Fig. 3.3A). In amphibole-rich samples, chadacrysts of fine-grained, rounded plagioclase are commonly observed in amphibole crystals. Intense plagioclase alteration is lacking in all samples but some crystals have been affected by patchy sericite alteration (<5% of a given crystal by volume; Fig. 3.3A). Biotite generally occurs in minor amounts (~2%) however two samples (MD001 and MD002) contain ~ 20 to 25% biotite. Biotite crystals are generally <1mm across, flaky and typically occur as secondary alteration of

46

amphibole crystals (Fig. 3.3C) although direct alteration from pyroxenes was less commonly observed. Biotite is particularly abundant in sample MD001 where interstitial, 0.5 to 2mm flakes comprise ~25% of the sample (Fig. 3.3D). This abundant biotite is associated with ~15% interstitial K-feldspar (Fig. 3.3A) which occurs as 0.5 to 4mm anhedral crystals. Olivine in this sample is strongly altered to and rimmed by serpentine coronas indicating that it is not in equilibrium with the K-feldspar. The abundant biotite and K-feldspar in an olivine-bearing gabbroic rock is likely the result of metasomatism by a K-rich fluid, possibly derived from contact metamorphism of the surrounding country rocks.

Accessory minerals include trace titanite, rutile and up to 1% apatite. Titanite occurs as <0.25mm crystals in contact with magnetite, or as inclusions in amphibole. Very-fine-grained rutile and hexagonal apatite occur as inclusions in magnetite and amphibole. Anhedral magnetite crystals <1mm in size most commonly occur interstitially to plagioclase and as inclusions in amphibole and pyroxene, and less commonly in serpentinized fractures in and coronas around olivine. Minor amounts of rounded, fine-grained quartz (2 to 3%) occurs interstitially in two samples.

3.2.2 Dioritic Rocks

Moving inward from the margins of the Guichon Creek Batholith, rocks of the Border facies transition to diorite, quartz diorite and quartz monzodiorite compositions (Fig. 3.2C and D). The primary difference in mineralogy between the Border facies diorites and gabbros is a lack of olivine, the presence of 3 to 8% quartz and a significant increase in amphibole content relative to clino- and orthopyroxene.

Pyroxenes are generally absent from diorites and when present occur as corroded cores to amphibole crystals. Instead, the diorite is dominated by abundant amphibole (20 to 35%) and less than 5% biotite, with sample MD057 containing ~15% biotite. Amphiboles form 1 to 4mm anhedral to subhedral crystals that most commonly occur interstitially to plagioclase laths (Fig. 3.3E and F) and more rarely as radial matts of acicular crystals. Inclusions of magnetite and very fine-grained plagioclase are common in most amphiboles (Fig. 3.3E and F). Biotite typically has a shredded texture and is observed as a patchy replacement in amphibole crystals, especially in acicular amphibole matts. The exception is sample MD057 which contains abundant, coarse-grained biotite (0.25 to 2mm) associated with amphibole and magnetite. In this sample, the biotite has been affected by weak (<5% of a given crystal) chlorite alteration along cleavage planes. Quartz typically occurs as anhedral, rounded to angular crystals (<1mm) interstitial to plagioclase, biotite and amphibole and also as inclusions in biotite.

Common accessory minerals occurring in trace amounts include apatite (<0.2mm) inclusions in magnetite, biotite and amphibole, zircon and rutile. Very-fine-grained titanite (<0.25mm) comprises ~1 to 2% of samples and forms <0.25mm, subhedral sphenoid crystals often with one point. Titanite is most commonly associated with magnetite where it occurs either as inclusions or in contact with magnetite, biotite and quartz and, more rarely as inclusions in amphibole crystals. Approximately 3 to 10% magnetite occurs interstitially to plagioclase and amphibole and also as inclusions in amphibole (Fig. 3.3E and F). Sample MD057 contains 10% interstitial K-feldspar (<1mm) that is strongly altered to clay minerals (60 to 90% of a given crystal). This K-

feldspar coincides with the abundant biotite of MD057 and both were likely formed by subsolidus metasomatism by a K-rich fluid, similar to sample MD001.

3.3 Guichon Sub-Facies

The Guichon sub-facies belongs to the Highland Valley facies, and is most prominent in the northeast portion of the Guichon Creek Batholith where it is more common than the Chataway sub-facies (Fig. 2.3). The Guichon sub-facies is comprised of rocks of granodiorite composition and contains approximately 20 to 25% evenly distributed mafic minerals, predominantly amphibole and biotite in roughly equal abundance, with minor clinopyroxene. Characteristic textures in the Guichon sub-facies are uniform, and consist of medium-grained, phaneritic and equigranular with subhedral plagioclase surrounded by subhedral interstitial biotite and amphibole as well as anhedral quartz and K-feldspar (Fig. 3.4).

The mafic mineralogy of the Guichon sub-facies is comprised of roughly equal amounts of amphibole (8 to 13%) and biotite (12 to 15%). Amphibole typically occurs as sub- to euhedral crystals (0.5 to 2mm) and lacks visible zoning. A small number of crystals have cores that are intergrown with clinopyroxene similar to those observed in the Border facies. Abundant very fine-grained magnetite inclusions are common in the pyroxene cores of such amphiboles, but were not observed in amphiboles without pyroxene cores (Fig.3.4D and F). Biotite is commonly in contact with amphibole crystals, but does not typically display textures that indicate it is an alteration product of amphibole, with the exception of two crystals containing inclusions of fine-grained amphibole in sample MD075, and most biotite occurs by itself with no associated amphibole. Biotite crystals are generally occur as subhedral to anhedral flakes, ranging
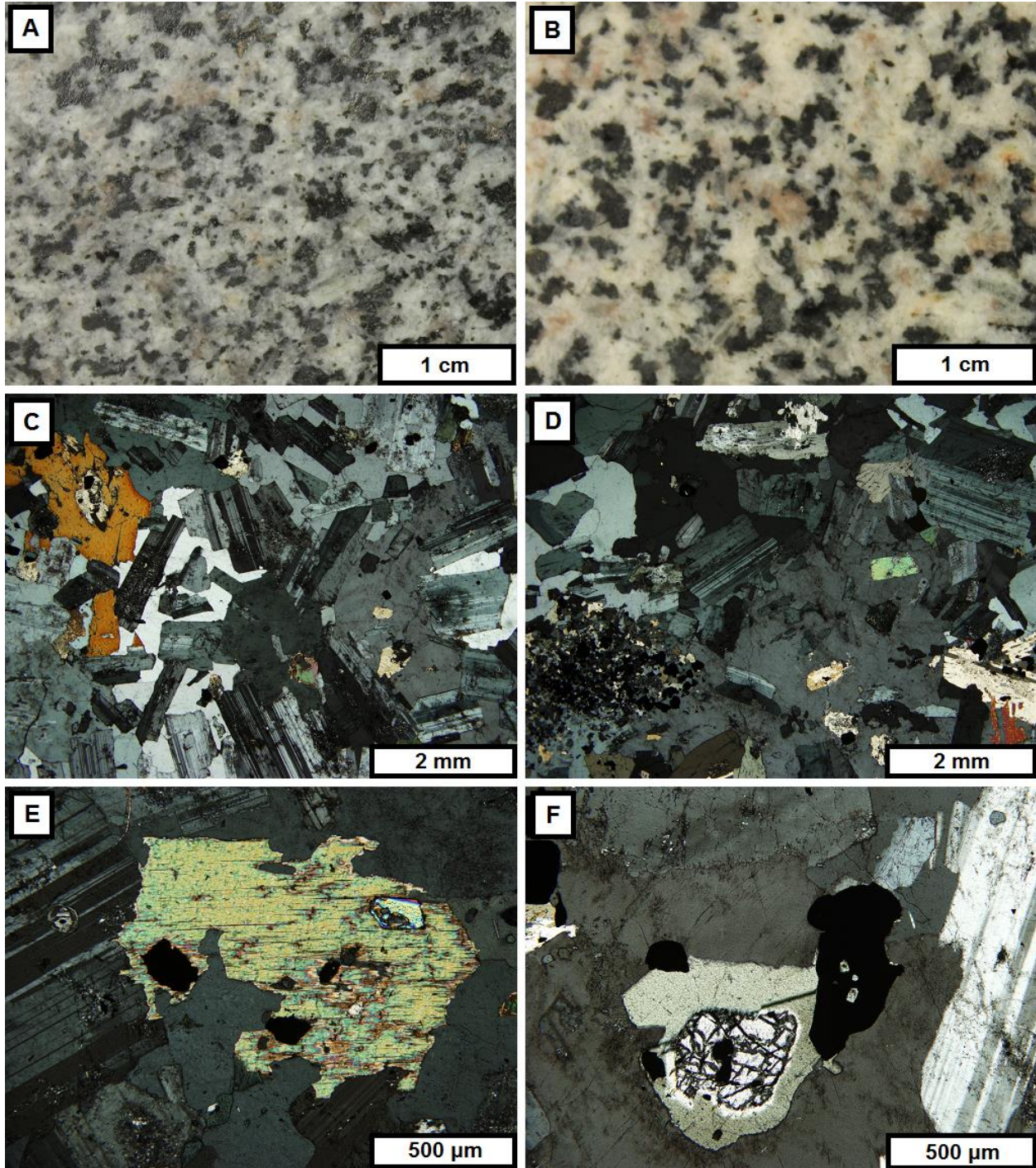
Figure 3.4 Petrography of the Guichon sub-facies. A. and B. Hand sample photos of granodiorite (A. Sample MD074 and B. Sample MD076) C. Sub-ophitic, interstitial quartz and K-feldspar with plagioclase and biotite (Cross-polarized, transmitted light; MD075). D. Ophitic K-feldspar poikilitically enclosing biotite and plagioclase chadacrysts. A Mass of very fine-frained magnetite and altered amphibole can be seen in the bottom left of the figure (Cross-polarized, transmitted light; Sample MD076). E. A chlorite and epidote altered biotite crystal with magnetite inclusions surrounded by plagioclase and interstitial K-feldspar (Cross-polarized, transmitted light; Sample MD075). F. An olivine crystal with an amphibole corona in K-feldspar (Cross-polarized, transmitted light; Sample MD076).

50

in size from 0.5 to 2mm. Alteration of biotite is rare and the most altered crystals are limited to weak chlorite alteration which replaces <5% of a given crystal along cleavage planes (Fig. 3.4E). Small inclusions of epidote were observed along cleavage planes in a few crystals, possibly indicating that the biotite crystals formed by potassic hydrous alteration of calcic-amphibole.

Plagioclase is the dominant felsic mineral and comprises ~35 to 45% of the Guichon sub-facies. Crystals are typically euhedral to subhedral and occur as 2 to 3mm elongated laths as well as 0.5 to 1mm equant, tabular crystals (Fig. 3.4C and D). Fine-grained chadacrysts (<0.5 to 1mm) are commonly poikilitically enclosed by subophitic K-feldspar and quartz (Fig. 3.4C and D). Alteration of plagioclase is generally weak, with sericite replacing <15% of a typical crystal by volume. Sample MD074, however, contains sparse crystals that have been replaced by up to 75% sericite.

Quartz and K-feldspar occur interstitially to plagioclase and the mafic minerals (Fig. 3.4C and D). The size and shape of quartz and K-felsdpar is predominantly controlled by the size and shape of the interstitial spaces between plagioclase and amphibole crystals and both range in size from <1mm to 3mm, and are typically angular in the case of quartz and more irregular for K-feldspar (Fig. 3.4C and D). The K-feldspar is variably altered (5 to 30% of a given crystal) by clay minerals.

The most abundant accessory mineral in the Guichon sub-facies is magnetite (1 to 3%) which occurs as anhedral, fine-grained (<1mm) crystals that are most commonly inclusions or partial inclusions in amphibole and biotite but are also common interstitial to plagioclase. Very-fine-grained magnetite clusters are also common in the cores of

amphibole containing relict clinopyroxene grains (Fig. 3.4D). Other common accessory minerals include trace apatite, which occurs as euhedral inclusions in amphibole and biotite as well as ≤1% euhedral, sphenoid titanite, typically associated with amphibole.

3.4 Chataway Sub-Facies

The Chataway sub-facies of the Highland Valley facies ranges from quartz monzodiorite to granodiorite in composition and contains approximately 13 to 15% evenly distributed mafic minerals. The dominant felsic minerals in this sub-facies are white plagioclase and lesser interstitial quartz. The contrast between the black mafic minerals and white plagioclase gives rocks from the Chataway sub-facies a 'cookies and cream' appearance that is distinct from any of the other facies in the Guichon Creek Batholith (Fig. 3.5A).

Plagioclase contents in the Chataway sub-facies vary between 52 to 66% and exhibit varying degrees of alteration to clay minerals. Moderate to strong replacement of plagioclase crystals by clay minerals (~10 to 25% of primary modal plagioclase) is common, with the most altered sample (MD044) being located near the former Aberdeen Adit in the southwestern portion of the batholith (Fig. 2.3). Clay alteration is weak to moderate, patchy and concentrated in the cores of crystals, suggesting more calcic cores. Plagioclase crystals are fine- to coarse-grained (0.5 to 4.0mm) and predominantly euhedral. Elongate, lath-like crystals are the most common, though equant 0.5 to 1.5mm crystals are also found.

Hornblende dominates the mafic minerals in the Chataway sub-facies and biotite/hornblende ratios vary from 0.1 to 0.4. Crystals are evenly distributed, medium-grained (1.0 to 3.0mm) and anhedral to subhedral. Most of the hornblende is fresh with
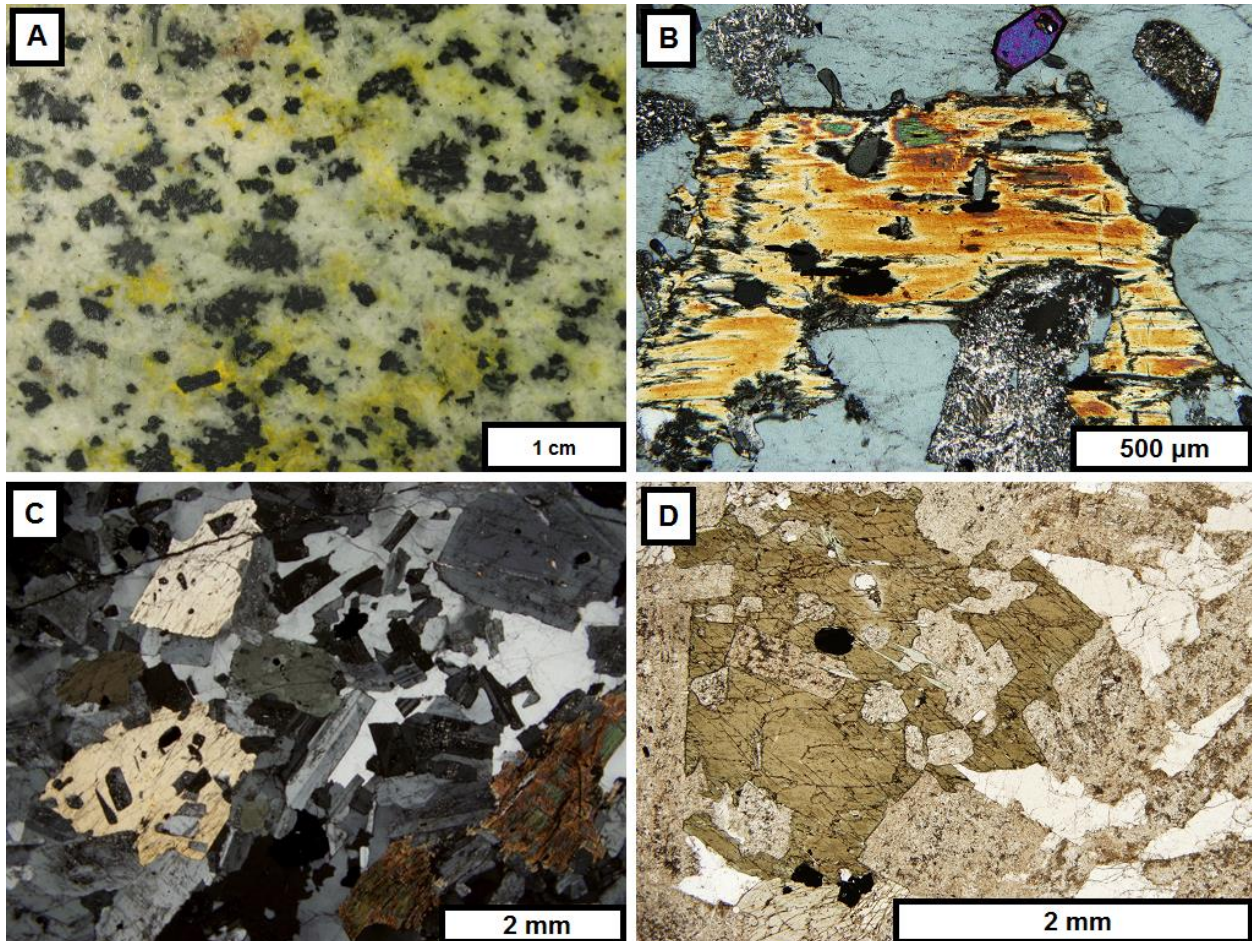
Figure 3.5 Chataway sub-facies petrography. A. A representative sample of the Chataway facies. Sample has been stained with sodium cobaltinitrite to reveal yellow K-feldspar (Sample MD044). B. A biotite crystal with apatite inclusions and weak chlorite alteration along cleavage planes. The biotite crystal is surrounded by K-feldspar which also poikilitically encloses a number of sericitized relict plagioclase chadacrysts (Cross-polarized, transmitted light; Sample MD066). C. Representative ophitic to sub-ophitic amphibole with plagioclase chadacrysts as well as angular, optically continuous quartz interstitial to plagioclase (Cross-polarized, transmitted light; Sample MD066). D. Representative altered sample from the Chataway facies (Cross-polarized, transmitted light; Sample MD044).

rare chlorite alteration along fractures accounting for ≤5% of the volume of the crystal. Hornblende crystals show an interstitial texture with euhedral plagioclase grains impinging upon their crystal faces (Fig. 3.5C and D). Hornblende crystals are commonly observed poikilitically to sub-poikilitically enclosing fine-grained (≤1.5mm) plagioclase grains (Fig. 3.5C and D). Inclusions of fine-grained (≤1.5mm) euhedral opaque crystals are also common.

The quartz content in the Chataway sub-facies varies from 10 to 25%. It most commonly occurs interstitial to plagioclase, orthoclase, hornblende and biotite as optically continuous anhedral crystals (Fig. 3.5C and D). Coarse-grained crystals commonly poikilitically enclose fine-grained (≤0.5mm) euhedral plagioclase crystals (Fig. 3.5C). Inclusions of fine-grained (0.2 to 0.5mm) quartz are also common in biotite and less so in hornblende crystals. Subgrain boundaries and undulatory extinction are commonly observed deformation features in quartz crystals.

Biotite forms 1 to 5% of the rocks and occurs as medium-grained (1.0 to 2.5mm) subhedral grainss with crystal faces that are impinged upon by euhedral plagioclase grains. Crystals are unevenly distributed throughout and exhibit no preferred orientation. The degree of alteration of biotite varies between samples but is generally weak (≤3 to 5% by volume; Fig. 3.5B). In the most altered samples, however, chlorite may have replaced up to 95% of the original biotite crystal and is associated with lenses of fine-grained epidote aligned parallel to cleavage planes.

Accessory minerals in the Chataway sub-facies include fine-grained (≤1.5mm) titanite and magnetite. Titanite is interstitial growing between euhedral plagioclase crystals with rare subhedral faces present in crystals grown into interstitial spaces with no contact with plagioclase crystals. Titanite is less commonly observed as inclusions in hornblende and biotite crystals. Magnetite crystals are disseminated throughout the Chataway sub-facies and commonly found as inclusions in hornblende. Fine-grained apatite aslo commonly occurs as inclusions in magnetite and biotite (Fig. 3.5B).

3.5 Bethlehem Facies

The Bethlehem facies consists of granodiorite that contains between 6.5 and 9% unevenly distributed mafic minerals. Bethlehem facies rocks are characterized by coarse-grained hornblende phenocrysts which poikilitically enclose fine-grained plagioclase crystals. They also lack the distinctive amoeboidal quartz eyes that occur in the Bethsaida and Skeena facies (Fig. 3.6A). A possible secondary unit in the Bethlehem facies has been identified on textural data and has been termed the Fine-grained granodiorite. This unit is mineralogically and texturally similar to the Bethlehem facies, but is much finer-grained (Fig. 3.6B) and is located near the southeast portion of the batholith near the contact between the Chataway and Bethlehem facies (Fig. 2.3).

Plagioclase (55 to 56%), quartz (20 to 25%) and orthoclase (5 to 7%) contents in the Bethlehem facies are similar to those of the Skeena and Bethsaida facies, with a slight increase in bulk plagioclase and a slight decrease in bulk quartz and orthoclase contents. Hornblende and biotite contents vary from 5 to 7% and 1 to 2%, respectively. Biotite/hornblende ratios of ~0.3 show a small decrease relative to the Skeena facies. Minor chlorite (0.5 to 3.0%) is locally present and reflects a greater degree of alteration of a sample. Minor accessory minerals include titanite (1 to 2%), magnetite (~1%) and trace epidote (Fig. 3.6F).

The Bethlehem facies is weakly porphyritic with a medium-grained groundmass comprised of 1.0 to 3.0mm plagioclase, 0.5 to 2.0mm hornblende, 0.5 to 2.0mm biotite and 0.5 to 2.0mm quartz and orthoclase. Phenocrysts consist of coarse-grained plagioclase (5.0 to 6.0mm) and hornblende (4.0 to 8.0mm; Fig. 3.6C-E).

55
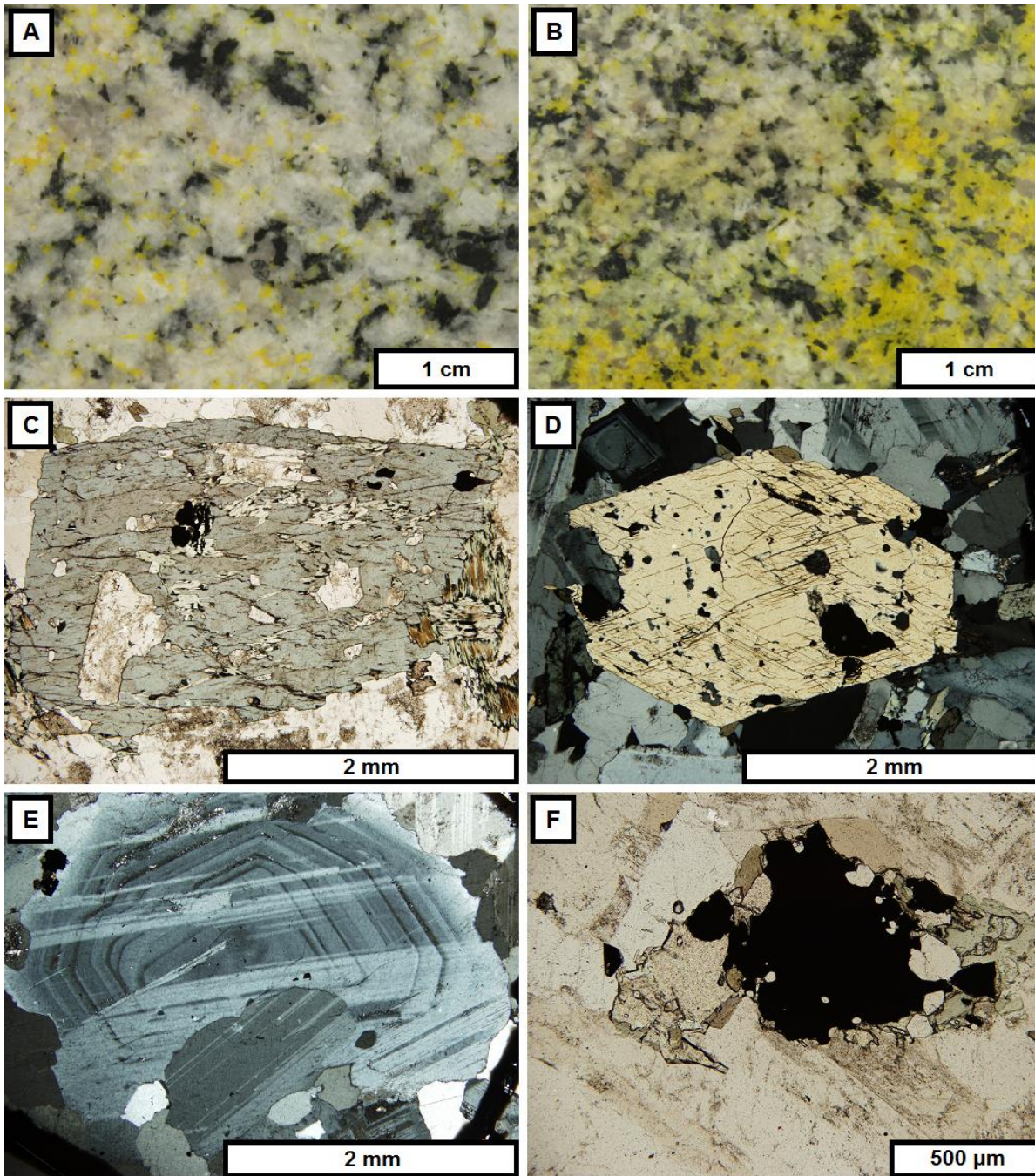
Figure 3.6 Bethlehem facies petrography. A. Sodium cobaltinitrite stained Bethlehem facies sample with yellow K-feldspar (Sample MD059). B. Sodium cobaltinitrite stained sample of the Fine-grained granodiorite variety of the Bethlehem facies (Sample MD063). C. A hornblende oikocryst enclosing partially altered plagioclase chadacrysts and with magnetite and apatite inclusions. Biotite and chlorite alteration has affected the right boundary of the crystal (Plane-polarized, transmitted light; Sample MD049). D. A near euhedral, fresh amphibole crystal with magnetite and apatite inclusions surrounded plagioclase laths and rounded interstitial quartz (Cross-polarized, transmitted light; Sample MD059). E. An oscillatory zoned plagioclase phenocryst typical of the Bethlehem, Skeena and Bethsaida facies. The main phenocryst has been fused with a smaller crystal at the bottom of the photo (Cross-polarized, transmitted light; Sample MD059). F. Magnetite in contact with titanite, chlorite, quartz, plagioclase and K-feldspar. The magnetite also contains inclusions of apatite (Plane-polarized, transmitted light; Sample MD059).

56

Plagioclase size, morphology and textural relationships are similar to those in the Bethsaida and Skeena facies, forming euhedral to subhedral crystals with equant to elongate shape. Concentric zoning and resorption surfaces as well as simple and polysynthetic twins are common and produce complex patterns under cross-polarized light (Fig. 3.6E). Alteration consists of clay minerals and is generally weak though rare crystals have been altered to approximately 90% clay minerals. Clay alteration is patchy and strongest near the cores of crystals. Hornblende crystals are strongly fractured and contain many fine-grained (0.25 to 1.0mm) inclusions of quartz and magnetite (Fig. 3.6C and D). Alteration in hornblende is generally weak with patches of chlorite, epidote and titanite. The hornblende phenocrysts poikilitically enclose fine- to medium-grained (0.5 to 2.5mm) crystals of subhedral plagioclase (Fig. 3.6C and D). Quartz occurs as anhedral rounded grains interstitial to euhedral plagioclase and subhedral hornblende.

Fine-grained (0.5 to 1.0mm), subhedral biotite crystals are unevenly distributed and have undergone varying degrees of alteration to chlorite. Chlorite is preferentially present along cleavage planes in biotite replacing up to 95% of the original grain. Minor epidote is common along cleavage planes in the most strongly altered biotites.

3.6 Skeena Facies

The mineralogy and textural characteristics of the Skeena facies are intermediate between the Bethlehem and Bethsaida facies (Fig. 3.7A). The Skeena facies is on average more felsic than the Bethlehem facies, ranging from granodiorite to monzogranite in composition. Quartz and orthoclase feldspar are less abundant than in the Bethsaida facies with modal compositions falling between 20 to 30% and 6 to 10%, respectively. The plagioclase content (47 to 54%) in the Skeena facies is higher on

average than in the Bethsaida facies. The principal mafic mineral is hornblende with subordinate biotite. This is in contrast with the Bethsaida facies which typically contains more abundant biotite. Biotite/hornblende ratios of the Skeena facies generally fall between 0.4 and 0.75. Alteration minerals include clays (5 to 6%), chlorite (1 to 2%) and epidote (≤0.5%). Other accessory minerals present in the Skeena facies are titanite (1 to 2%), magnetite (1 to 3%) and trace zircon.

The Skeena facies is texturally intermediate to the Bethlehem and Bethsaida facies, and possesses a seriate texture with plagioclase and hornblende crystals varying in size from 0.5 to 7.0mm and 0.5 to 4.0mm, respectively (Fig. 3.7A). Amoeboid quartz eyes are present but they are less abundant and finer-grained (1.5 to 4.0mm) than those observed in the Bethsaida facies (Fig. 3.7B). Finer (0.5 to 1.5mm) anhedral quartz also occurs interstitially between plagioclase crystals. Hornblende crystals are evenly distributed throughout and contain numerous fine-grained inclusions of quartz (≤0.5mm) and opaque crystals (≤0.5mm). Most hornblende crystals are unaltered although weak chlorite alteration is observed in a few crystals along cleavage planes. Simple twinning is common in hornblende. Biotite occurs as medium-grained (0.5 to 2.5mm) subhedral books that are unevenly distributed through the rock. Chlorite alteration of biotite crystals varies between samples but is generally weak and focussed along grain boundaries and cleavage planes (Fig. 3.7D). The most strongly altered biotite crystals commonly contain lenticular pods of fine-grained (0.5 to 1.5mm) epidote aligned parallel to cleavage planes (Fig. 3.7C). Chlorite alteration is strongest in biotite crystals that are in direct contact with opaque minerals and is concentrated at the point of contact. Plagioclase crystals comprise the bulk of the groundmass and form
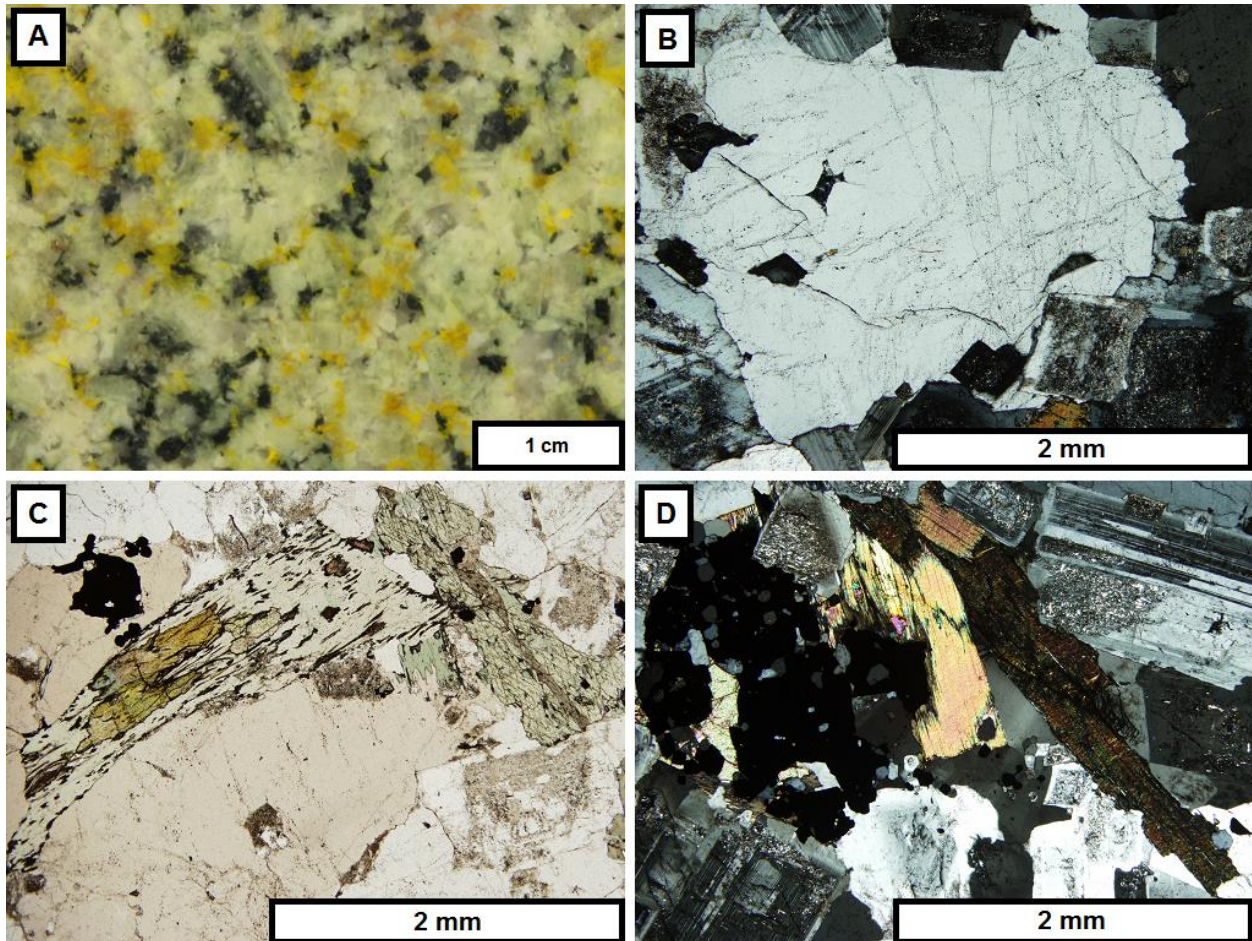
Figure 3.7 Skeena facies petrography. A. Typical hand sample of the Skeena facies. Sample has been stained with sodium cobaltinitrite (Sample; MD034). B. Amoeboidal quartz eye (Cross-polarized, transmitted light; MD035). C. Epidote pods along cleavage planes in chlorite after biotite (Plane-polarized, transmitted light; MD035). D. Magnetite with titanite and apatite inclusions with biotite, plagioclase and quartz (Cross-polarized, transmitted light; Sample MD035).

subhedral to euhedral tabular crystals. Plagioclase crystals are commonly in contact with and supported by other plagioclase crystals with the interstitial spaces filled by quartz. A combination of concentric zoning, resorption surfaces, polysynthetic and synthetic twins combine to create complex patterns under cross-polarized light. Clay alteration of plagioclase is common, though it is highly variable in intensity. Strongly altered crystals may contain up to 95% clay minerals whereas weakly altered crystals typically contain 0 to 15% clay. Patchy, weak clay alteration is most common and is

concentrated in the cores of crystals. Titanite and zircon exhibit similar textures and petrographic sites as in the Bethsaida facies.

3.7 Bethsaida Facies

The Bethsaida facies occupies the interior of, and is the most felsic unit in the Guichon Creek Batholith. Rocks of the Bethsaida facies vary from granodiorite to monzogranite. Mafic minerals are unevenly distributed and comprise 2 to 5% modal abundance. The Bethsaida facies is predominantly weakly porphyritic, with coarse-grained biotite and quartz phenocrysts in a medium-grained groundmass (Fig. 3.8A and B).

Plagioclase forms 32 to 55% of the Bethsaida facies and occurs as medium- to coarse-grained (1.0 to 5.0mm), euhedral to subhedral, tabular crystals. Most crystals are equant with length/width ratios of ~ 1 with less common elongated crystals having length/width ratios of ≈ 2.5. Plagioclase has been affected by varying degrees of alteration with some crystals exhibiting little to no alteration and others being altered almost entirely to clays. Clay mineral alteration is most commonly patchy and concentrated in the cores of crystals (Fig. 3.8E). Concentric zoning, polysynthetic and simple twins are ubiquitous and combine to produce complex patterns under cross-polarized light.

Quartz contents range between 30 – 50%. It occurs as both coarse-grained (3.0 to 8.0mm) amoeboid, anhedral eyes (Fig. 3.8D), and as clusters of fine- to medium-grained (0.5 to 2.0mm) crystals in the groundmass. Undulatory extinction and subgrain boundaries are common in the amoeboid quartz eyes (Fig. 3.8D). Inclusions of fine-
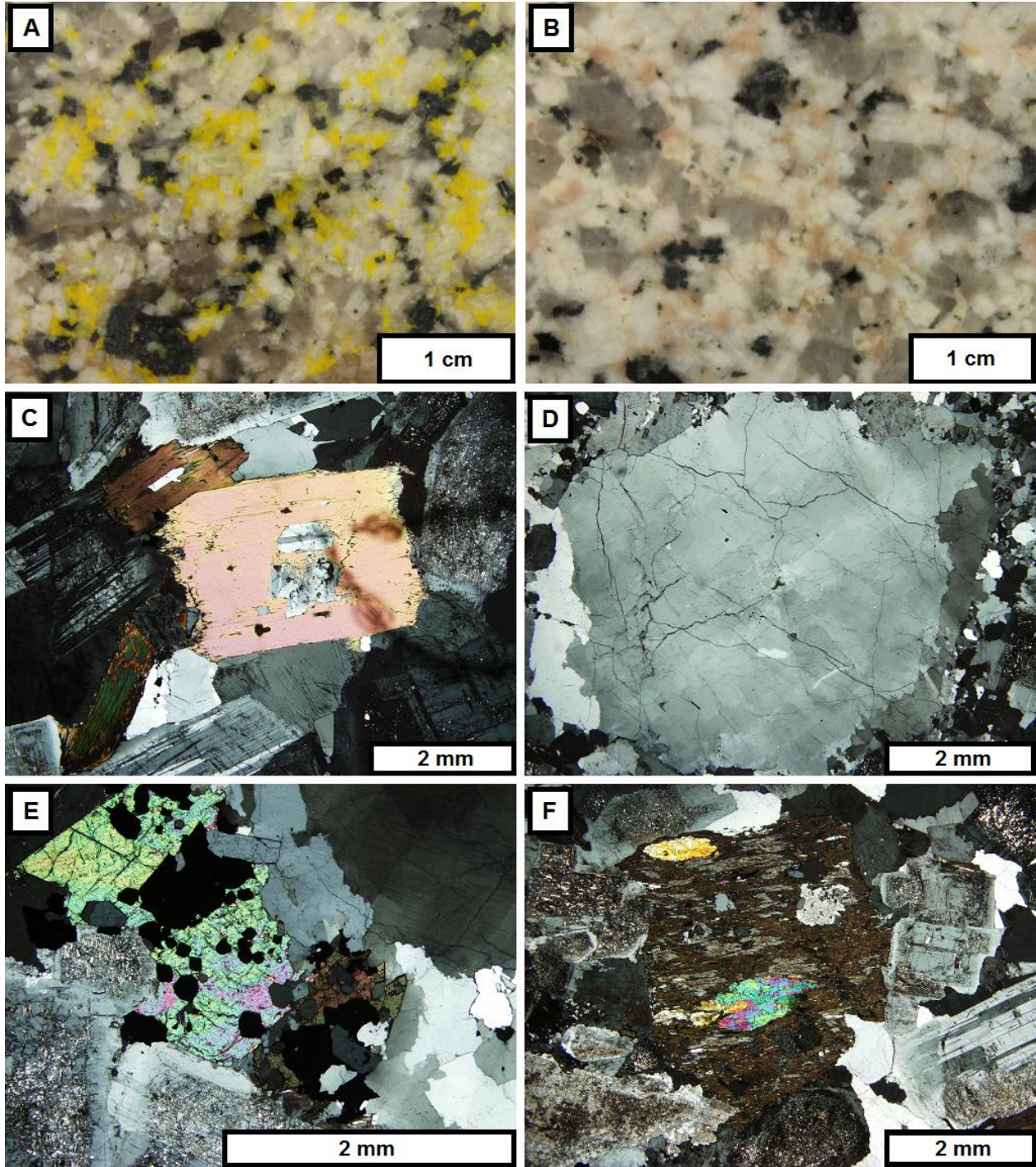
Figure 3.8 Bethsaida facies petrography. A and B. Sodium cobaltinitrite stained and non-stained hand samples from the Bethsaida facies (A. Sample MD072; B. Sample MD069). C. A biotite phenocryst with plagioclase chadacrysts (Cross-polarized, transmitted light; MD069). D. Amoeboid quartz phenocryst with undulatory extinction and subgrains (Cross-polarized, transmitted light; MD004). E. Titanite, apatite and magnetite cluster with plagioclase and quartz (Cross-polarized, transmitted light; MD069). F. Strongly chlorite altered biotite phenocrysts with epidote crystals along cleavage planes (Cross-polarized, transmitted light; MD069).

61

grained (<0.25mm) quartz crystals in the coarse quartz eyes are also common. The fine- to medium-grained quartz is present in <1cm pod-like clusters irregularly dispersed throughout the groundmass.

Orthoclase feldspar contents in the Bethsaida facies range from 8 to 13%. Crystals are generally fine- to medium-grained (0.5 to 2.0mm) and are subhedral to anhedral. Orthoclase is associated with quartz and plagioclase in the groundmass. Albite exsolution lamellae are common and give rise to microperthitic textures.

Biotite is the dominant mafic mineral in the Bethsaida facies (1 to 3%) and occurs as coarse-grained (2.0 to 7.0mm) phenocrysts (Fig. 3.8C). Biotite/hornblende ratios typically fall between 2.0 and 3.0. Some crystals contain numerous fine-grained (<0.5mm) inclusions of quartz and opaque minerals. The degree of alteration varies between samples. The least altered samples contain biotite crystals with little to no alteration, whereas the most altered samples contain relict biotite crystals that have been completely altered to a combination of chlorite, epidote, titanite and opaque minerals (Fig. 3.8F).

Hornblende is the second most abundant primary igneous mafic mineral in the Bethsaida facies. The hornblende content is lower than the biotite content for a given sample and varies from 0.5 to 2%. Hornblende crystals are generally fine-grained (0.25 to 0.5mm), subhedral and display two or more perfect crystal faces in cross-section. Simple twins are rare in a small number of crystals and hornblende mainly occurs as inclusions in the amoeboid quartz eyes, but also occurs interstitially in the groundmass.

Chlorite contents range between 1 and 3%. As it is an alteration product of primary biotite and hornblende, its overall abundance is strongly correlated with the degree of alteration (Fig. 3.8F). Flaky intergrowths with biotite are common where chlorite is concentrated along cleavage planes in primary biotite crystals. In coarse-grained biotite, chlorite alteration along grain boundaries is more common than along cleavage planes. Chlorite also occurs as a local, patchy alteration in hornblende. Up to 1% epidote is commonly found associated with chlorite in altered biotite crystals. The epidote occurs as 0.1 to 2mm crystals grouped together into lenticular bodies along cleavage planes in altered biotite (Fig. 3.8F).

Less abundant accessory minerals include titanite (0.5 to 2%), zircon (<0.5%), apatite (<0.5%), calcite (<0.5%) and opaque minerals (1 to 2%). Titanite occurs as medium-grained (1.0 to 2.5mm) sub- to euhedral crystals and typically forms flattened hexagonal and diamond shaped cross-sections with opaque minerals aligned along grain boundaries. Apatite occurs as fine-grained (0.1 to 0.3mm) euhedral elongate prisms with hexagonal cross-sections. Apatite crystals occur as isolated inclusions or as clusters in some of the quartz eyes as well as in perthitic orthoclase and titanite crystals. Zircon is a rare accessory mineral and crystals are very fine-grained (<0.2mm), occurring as inclusions in both biotite and chlorite and are generally surrounded by metamict haloes. Magnetite occurs as fine- to medium-grained (0.5 to 1.5mm) euhedral crystals with cubic and octahedral crystal habits. Primary igneous magnetite is evenly distributed whereas magnetite replacement of biotite is typically associated with chlorite, epidote and titanite (Fig. 3.8E).

3.8 Crowded Feldspar-Phyric (FPC) and Crowded Quartz- and Feldspar-Phyric Porphyry Dykes (QFPC)

The QFPC and FPC dykes are most commonly found near the Bethlehem deposit, where they exhibit NW and NNE trends parallel to the major faults and fracture sets in the area and are interpreted to have a late- to post-mineralization age of emplacement (Byrne et al., 2013). Thirteen QFPC and FPC dykes were sampled from diamond drill core obtained from the Bethlehem deposit area (five QFPC and eight FPC) of which seven thin sections were made (three QFPC and four FPC) for detailed petrographic analysis. The QFPC and FPC dykes share many compositional and textural similarities with the key difference between the two being their quartz phenocryst content and as such are discussed together.

The FQPC and FPC dykes are characterized by a crowded, porphyritic texture comprising 40 to 60% phenocrysts set in a fine-grained aplitic groundmass (Fig. 3.9). Least altered samples are typically white and grey in appearance owing to the abundance of unaltered plagioclase and quartz phenocrysts with lesser mafic phenocrysts (Fig. 3.9B and D). Altered samples, however, are characteristically pink and green, a result of Fe staining of plagioclase phenocrysts and the aplitic groundmass and prevalent epidote alteration of both primary amphibole and plagioclase phenocrysts (Fig. 3.9A and C).

Least altered samples contain approximately 15% fresh amphibole phenocrysts that are typically 1 to 3mm needle-like prisms with rare outsized phenocrysts (up to 7mm) which occur as optically continuous oikocrysts that poikilitically enclose smaller, altered plagioclase chadacrysts (Fig. 3.10C). In altered samples, the primary
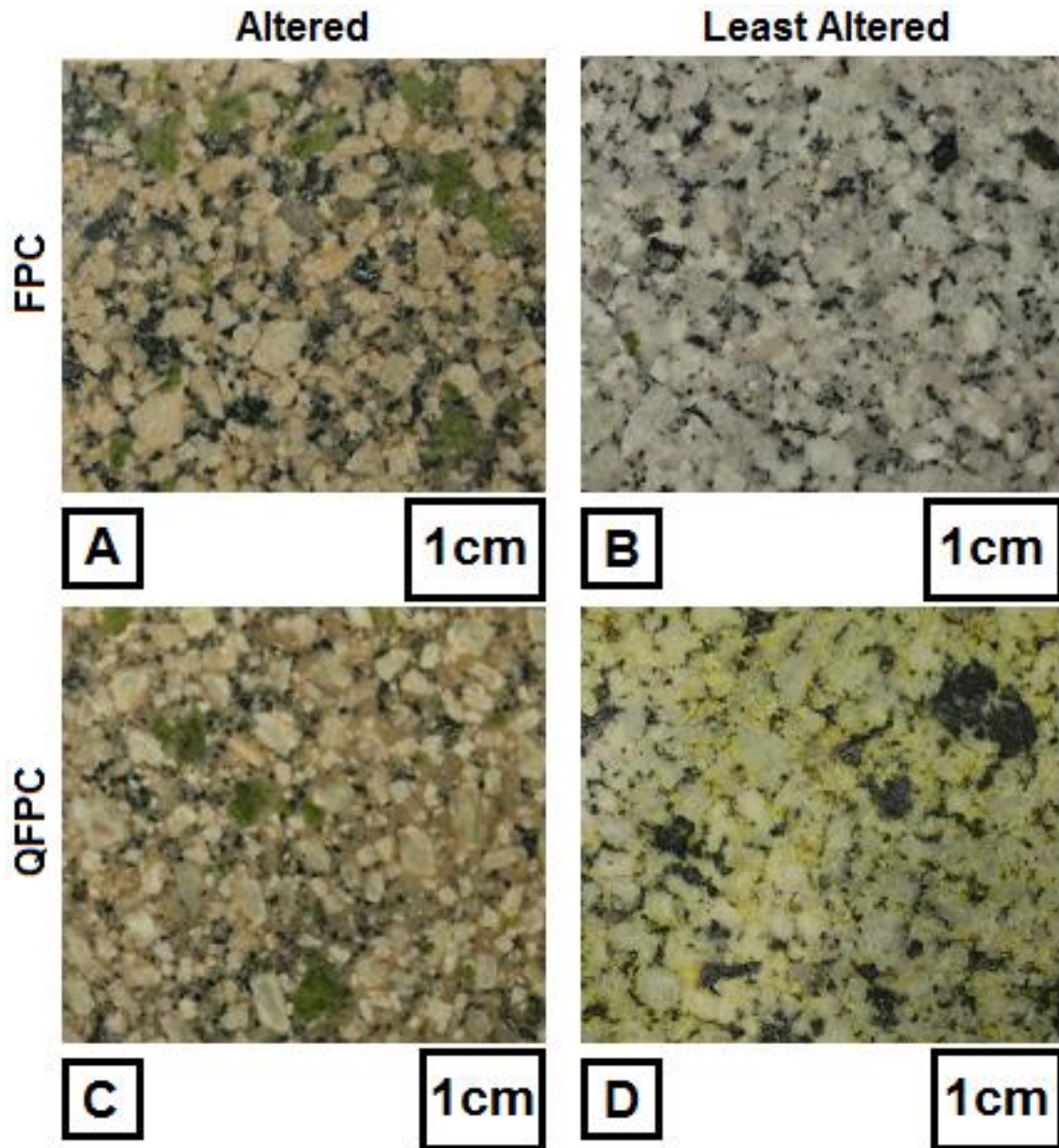
Figure 3.9 Hand sample photos of FPC (A and C) and QFPC (C and D) samples of QFPC dykes. A. Sample MD028. B. Sample MD026. C. Sample MD022. D. Sample MD032. Both rock types are characterized by a crowded porphyritic texture with plagioclase and mafic phenocrysts as well as quartz phenocrysts in the case of the QFPC dykes. Sodium cobaltinitrite staining of samples in photos A., C., and D. reveals yellow interstitial K-feldspar in least altered samples that has been destroyed in the altered samples. Alteration has resulted in an iron dusting of plagioclase phenocrysts and the aplitic groundmass resulting in a pink colour and pervasive epidote alteration has completely altered select mafic and plagioclase crystals (A and C).
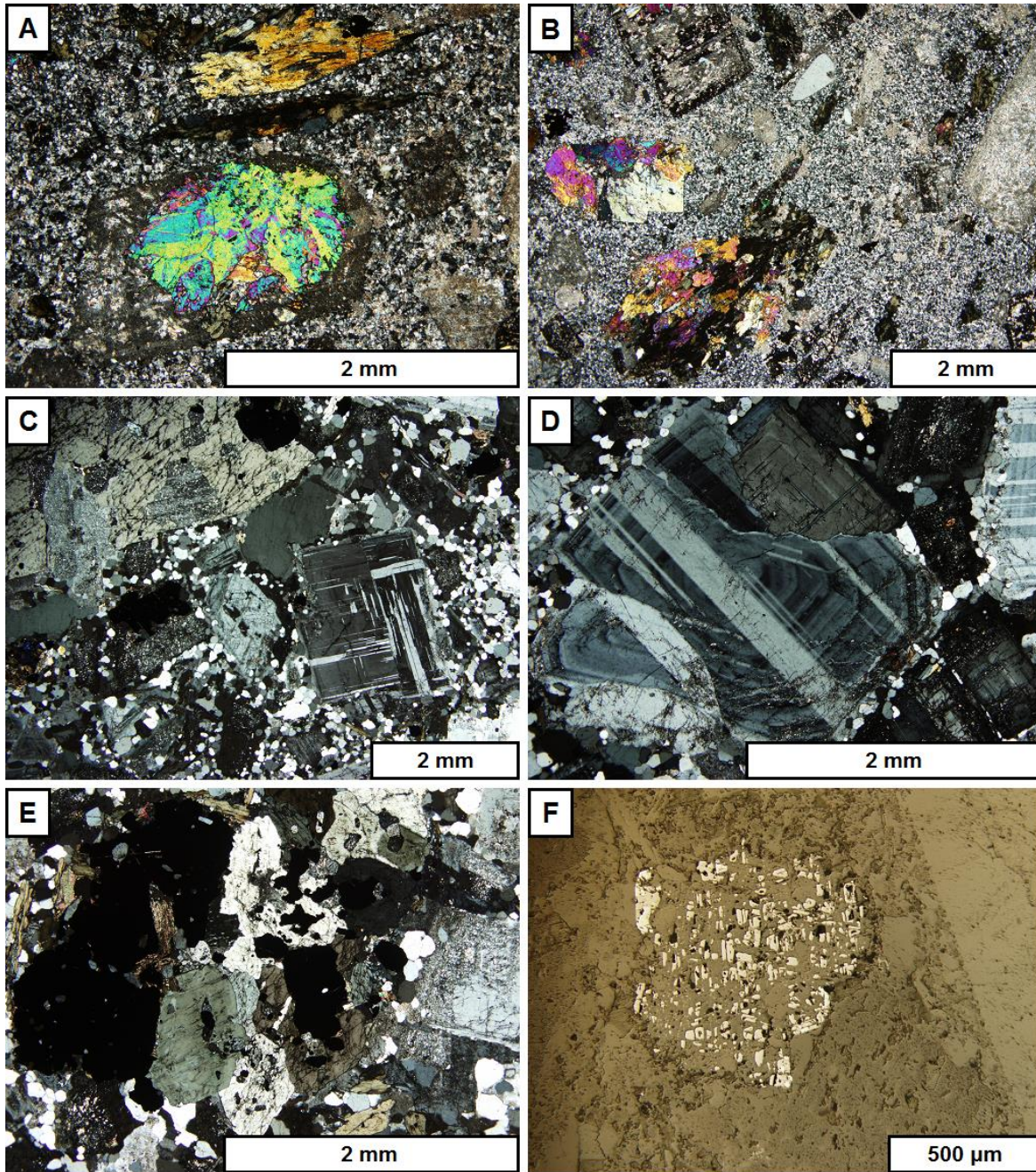
Figure 3.10 Photomicrographs of the altered (A, B and F) and least altered (C,D and E) QFPC and FPC dykes. A. Partial replacement of a plagioclase phenocryst by epidote and complete replacement of an amphibole phenocryst by chlorite in an FPC dyke (Cross-polarized, transmitted light; MD022). B. Complete replacement of a plagioclase phenocryst by epidote and of an amphibole phenocryst by epidote + chlorite in a QFPC dyke (Cross-polarized, transmitted light; MD028). C. Altered plagioclase chadacrysts in an amphibole oikocryst and a plagioclase phenocryst displaying sectors with perpendicular twinning in a fine-grained quartz groundmass. Least altered FPC dyke (Cross-polarized, transmitted light; MD031). D. A composite plagioclase phenocryst comprised of three smaller, fused crystals which all display concentric zoning. Least altered QFPC dyke (Cross-polarized, transmitted light; MD031) E. Magnetite, titanite and amphibole in a least altered FPC dyke (Plane-polarized, transmitted light; MD031). F. Skeletal magnetite with replacement by titanite along fractures in an altered QFPC dyke (Plane-polarized, reflected light; MD028).

66

amphiboles have undergone varying degrees of alteration to biotite, chlorite and epidote (Fig. 3.10B). Secondary biotite is the least abundant mafic alteration mineral with shreddy replacements after amphibole accounting for up to 3% of a sample. Chlorite is the most abundant amphibole alteration product and occurs as replacements along cleavage planes or aggregates of radiating crystals with trace amounts in least altered samples and 7 to 10% in altered samples (Fig. 3.10A and B). Epidote commonly occurs as <1mm crystals disposed along cleavage planes in secondary biotite and chlorite (Fig. 3.10B). Based on these textural and mineralogical relationships it is interpreted that primary amphibole in altered samples has undergone progressive biotitization and chloritization with minor epidote formed from excess Ca released by biotite alteration of the calcic amphiboles.

Plagioclase (30 to 45%) is the most abundant mineral in FPC and QFPC dykes and accounts for up to 70% of the total phenocryst population (Fig. 3.9). Phenocrysts are typically tabular to elongate and range from 1 to 5mm in size. Oscillatory zoning is present in most phenocrysts and is commonly overprinted by polysynthetic and deformation twins (Fig. 3.10D). Plagioclase glomerocrysts comprised of smaller, zoned plagioclase crystals fused together with discontinuous zoning across irregular boundaries are also abundant (Fig. 3.10D). Alteration of plagioclase is ubiquitous, even in least altered samples. Weak sericite and muscovite alteration (<5% of single crystals) is the dominant form of alteration in least altered samples and typically occurs throughout crystals instead of being concentrated in their cores as observed for most dyke rocks. In altered samples, minor sericite and muscovite alteration is common, but saussuritization of plagioclase phenocrysts is predominant. Saussuritized plagioclase is

characterized by abundant replacement by epidote and minor calcite (50 to 100% combined epidote and calcite) that has primarily affected the cores of crystals (Fig. 3.10A) and in many cases completely replaced entire phenocrysts (Fig. 3.10B).

Quartz abundance in FPC and FQPC dykes is similar, although it is more variable in FPC dykes (~30 to 50%) than in FQPC dykes (~30 to 35%). Very fine-grained (<0.25mm) rounded quartz comprises the majority of the aphanitic groundmass, where it occurs interstitially to groundmass K-feldspar (Fig. 3.10C-E). Rounded quartz phenocrysts are 1 to 3mm and have serrated grain boundaries. The abundance of quartz phenocrysts is the key characteristic that distinguishes the FQPC and FPC dykes, with <0.5% in the FPC dykes and between 5 and 20l% in FQPC dykes (Fig. 3.9). Another key difference between the FPC and FQPC dykes is their K-feldspar content. Identification and estimation of K-feldspar content is difficult in thin section, as strong clay alteration (>85%) is common, even in least altered samples. Identification of K-feldspar by staining of hand samples, however, is effective and reveals 10 to 15% interstitial K-feldspar in least altered FPC dykes and <5% in FQPC dykes (Fig. 3.10B and D). Staining of altered samples did not reveal K-feldspar in either the FPC or FQPC dykes suggesting that it has been completely destroyed during progressive alteration (Fig. 3.10A and C).

Apatite is a common accessory mineral (~1%) and occurs as euhedral, hexagonal apatite inclusions in magnetite. Trace chalcopyrite occurs in a few altered samples where it is dispersed irregularly throughout the groundmass. Fine-grained calcite is locally abundant in the groundmass of most samples (3 to 10%) and is likely a by-product of alteration of calcic amphibole and plagioclase. Fine- to medium-grained

(0.5 to 2mm) magnetite is common in least altered samples where it commonly contains very fine-grained apatite inclusions and forms clotted aggregates with amphibole and titanite (Fig. 3.10E). In altered samples, magnetite is typically finer grained (<1mm) and occurs as inclusions in chlorite, or forms skeletal grains along fractures that have been altered to titanite (Fig. 3.10F).

3.9 Quartz- and Feldspar-Phyric, Mafic-Bearing Porphyry Dykes (QFPM)

Two samples of the QFPM dykes were collected and described as part of this study. Both samples were collected in the central portion of the Guichon Creek Batholith where they cut rocks of the Bethsaida facies (Fig. 2.3). The QFPM dykes have been reported from the Valley deposit, tentatively correlated with the Gnawed Mountain porphyry dyke complex and assigned a late mineralization emplacement timing owing to Cu grades lower than associated country rocks (Byrne et al., 2013).

The QFPM dykes are characterized by a matrix supported porphyritic texture comprised of approximately 30 to 40% phenocrysts set in an aphanitic, grey groundmass (Fig. 3.11A). Quartz phenocrysts are generally euhedral and form hexagonal phenocrysts (2 to 7mm) though rounded crystals are also common (Fig. 3.11A). Quartz microphenocrysts (0.1 to 0.5mm) are also common and occur as square to trapezoidal crystals (Fig. 3.11B-D). Very fine-grained, nearly cryptocrystalline quartz comprises the bulk of the aphanitic groundmass (Fig. 3.11B-E). Subhedral to euhedral
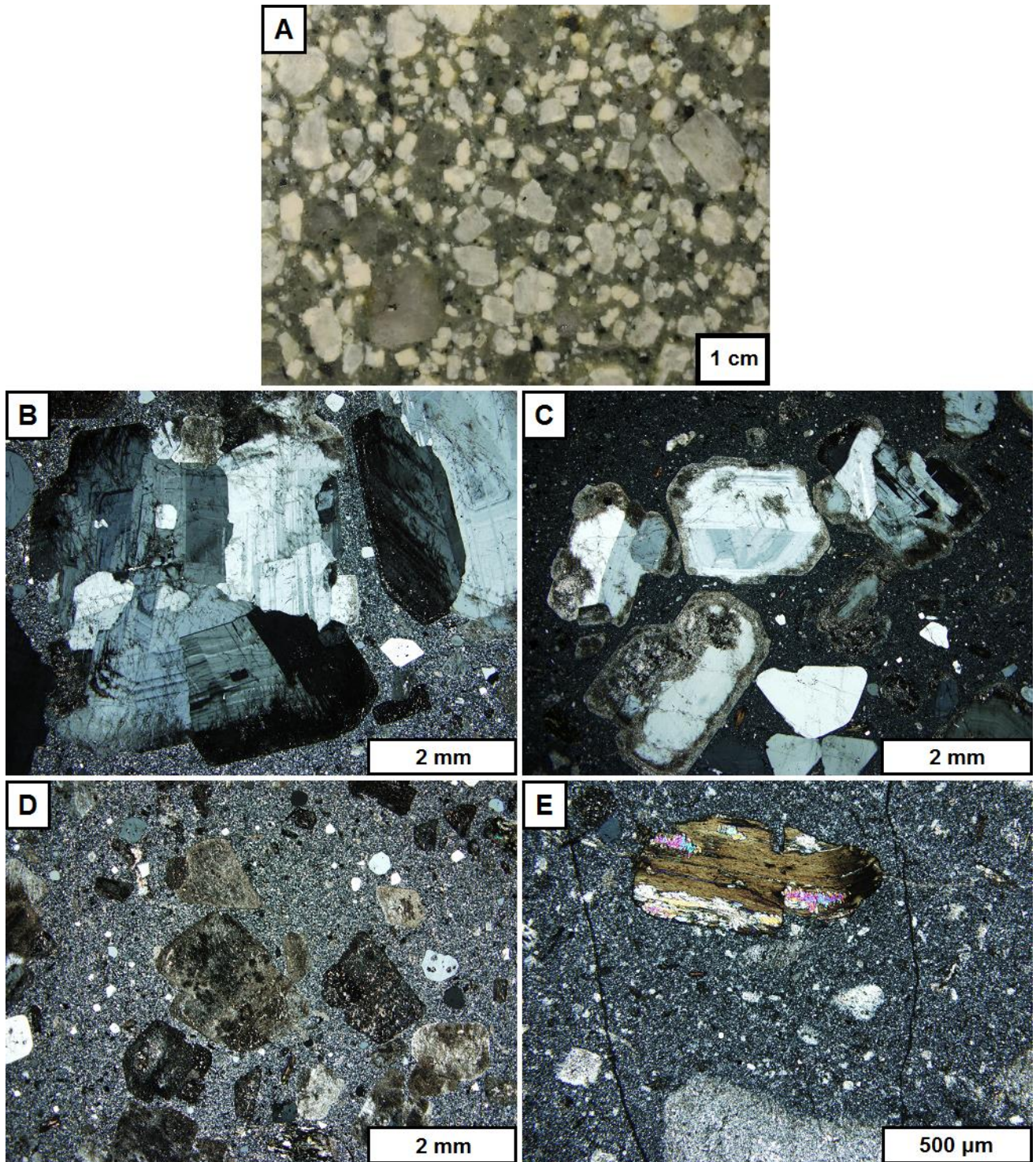
Figure 3.11 Petrography of the QFPM dykes. A. Typical hand sample of a QFPM dyke (Sample MD073). B. A composite plagioclase phenocryst comprised of numerous smaller, fused crystals. The smaller crystals display concentric zoning that is discontinuous across fusion boundaries (Cross-polarized, transmitted light; Sample MD073). C. Plagioclase phenocrysts displaying resorption rims (Cross-polarized, transmitted light; Sample MD077). D. Quartz microphenocrysts and relict plagioclase phenocrysts in an aphanitic groundmass (Cross-polarized, transmitted light; MD073). E. Chloritized biotite microphenocryst with epidote along grain boundaries (Cross-polarized, transmitted light; Sample MD077).

plagioclase is the most abundant phenocryst mineral and has a bimodal size distribution. Small phenocrysts (1 to 2mm) are composed of single plagioclase crystals, whereas large phenocrysts (4 to 10mm) are typically glomerocrysts comprised of two or more smaller crystals that have been fused along irregular boundaries (Fig. 3.11B and C). Oscillatory zoning is ubiquitous in the large, composite phenocrysts and common in the smaller phenocrysts (Fig. 3.11B and C). Replacement of plagioclase phenocrysts by sericite and clays, has resulted in an earthy white lustre in hand sample (Fig. 3.11A). Many small phenocrysts have been completely altered (Fig. 3.11D), and alteration is concentrated along grain boundaries in least altered crystals (70 to 90% alteration; Fig. 3.11C). Minor calcite alteration (3 to 5%) has also affected plagioclase phenocrysts and very fine-grained calcite is common in the groundmass.

Mafic phenocrysts (~0.5 to 1mm) account for approximately 10 modal% on average (Fig. 3.11A and E). All mafic phenocrysts have been completely altered to biotite (≤1%), epidote (1%) and chlorite (~8%). Chlorite is the most abundant mafic mineral and it is interpreted to have formed from primary amphibole by biotitization and subsequent chloritization based on relict crystal shape as well the presence of epidote along cleavage planes (Fig. 3.11E) which commonly occurs as Ca is released by altered calcic amphiboles (Winter, 2010). Accessory minerals in QFPM dykes include ~ 2 to 4% magnetite (0.1 to 1mm) and trace, euhedral (<0.1mm) tourmaline crystals included in quartz. Skeletal magnetite crystals with titanite alteration along fractures are rare.

3.10 Quartz- and Feldspar-Phyric, Phenocryst-Poor Porphyry Dykes (QFPP)

The quartz- and feldspar-phyric, phenocryst-poor porphyry dykes are found in the Valley, Lornex and Highmont deposits and are spatially associated with unidirectional solidification textures (USTs) in the cores of the deposits (Byrne et al., 2013). The dykes described for this study were sampled from drill core that came from the Valley deposit.

The QFPP dykes are characterized by porphyritic textures and are phenocryst-poor (Fig. 3.12). Samples are typically comprised of 3 to 10% phenocrysts which are evenly distributed throughout an aphanitic, siliceous groundmass that varies in colour from tan to purple-brown (Fig. 3.12). The phenocryst population is dominantly comprised of 1 to 3mm corroded plagioclase crystals with lath to tabular shapes (Fig. 3.12). Rounded 1 to 3mm quartz and tabular 1 to 3mm K-feldspar phenocrysts comprise approximately 1 to 3 volume% each. Microphenocrysts of biotite account for less than 1% of the QFFP dykes and are altered to chlorite along cleavage planes (Fig. 3.12E). Biotite phenocrysts are absent from sample MD038 which contains trace crystals of muscovite, potentially replacements after biotite. The groundmass is cryptocrystalline and composed of a mixture of plagioclase, quartz, K-feldspar and their associated alteration products (calcite + white mica).

Alteration of plagioclase phenocrysts is common, with pervasive white mica alteration (randomly oriented sericite + flaky muscovite) affecting the cores of crystals and patchy, fine-grained calcite alteration. Calcite alteration is predominantly comprised of cryptocrystalline aggregates which are nucleated on coarser calcite crystals up to

72
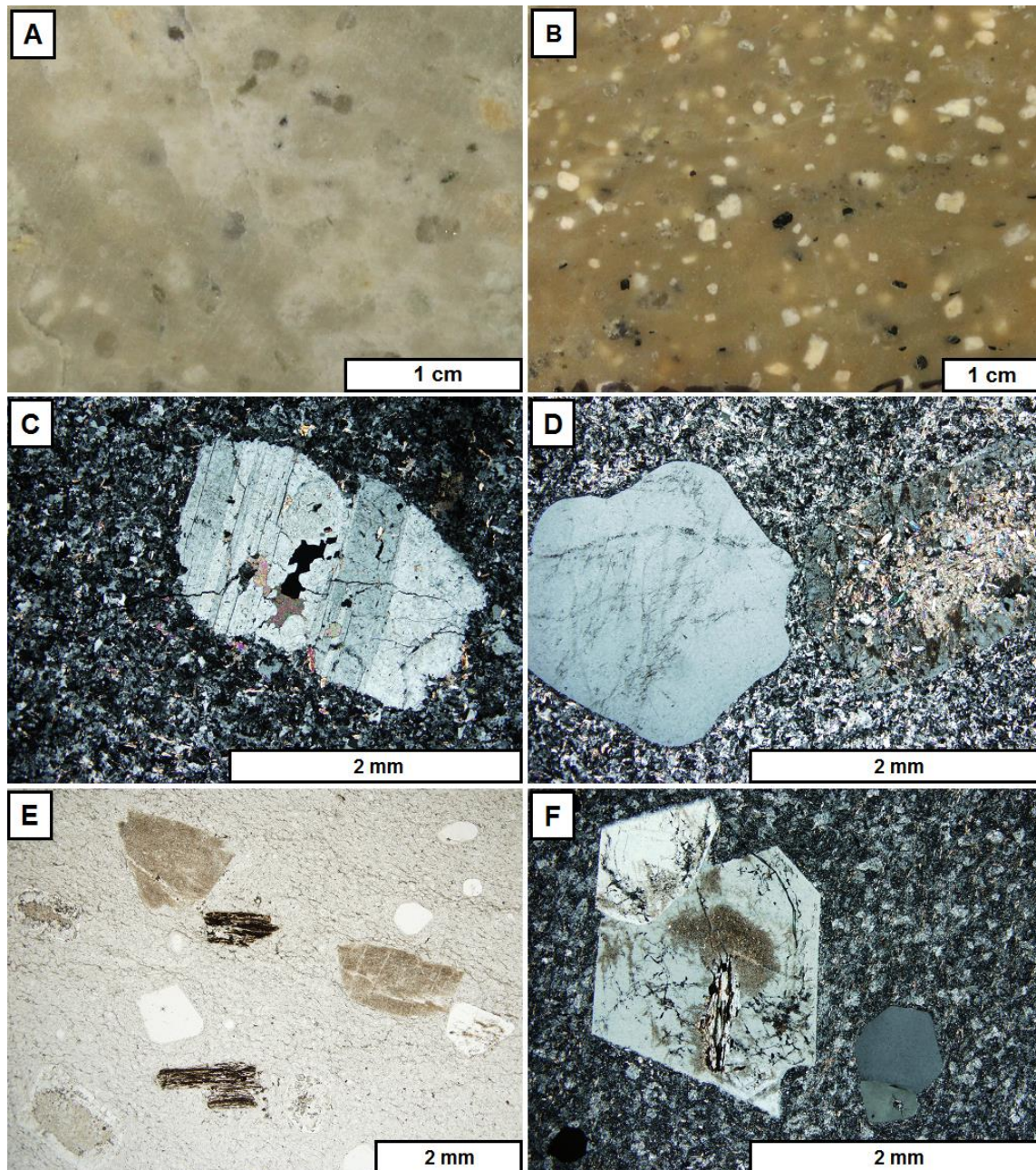
Figure 3.12 QFPP dyke petrography. A. Hand sample MD036 displaying tan coloured groundmass typical of QFPP dykes. B. Hand sample MD037. This sample has an atypical, darker colour and contains more abundant biotite phenocrysts. C. A fractured, corroded plagioclase phenocrysts in a cryptocrystalline groundmass. Patchy calcite alteration is visible in the bottom left portion of the phenocryst (Cross-polarized, transmitted light; MD036). D. An anhedral quartz phenocryst and a relict plagioclase phenocryst whose core has been completely altered to randomly oriented muscovite (Cross-polarized, transmitted light; Sample MD036). E. Quartz, biotite and relict plagioclase phenocrysts in a cryptocrystalline groundmass. Biotite phenocrysts have been partially altered to chlorite along cleavage planes and plagioclase phenocrysts have been completely altered to a mixture of sericite, calcite and epidote (Plane-polarized, transmitted light; Sample: MD037. F. A K-feldspar (likely sanidine) phenocryst with clay alteration in its core in a cryptocrystalline groundmass (Cross-polarized, transmitted light; Sample: MD037).

73

0.25mm in diameter (Fig. 3.12C). One sample contains numerous sub-mm veins that are composed of a mixture of very-fine-grained quartz and slightly coarser calcite.

3.11 Aplite Dykes

Aplite dykes have been reported at the Bethlehem deposit where they are interpreted to have been emplaced either late in the mineralization history or possibly post-mineralization (Byrne et al., 2013). Aplite dykes at the Valley deposit are possibly cogenetic with those at the Bethlehem deposit and were emplaced early in the mineralization history and are associated with localized, pervasive K-feldspar alteration (Byrne et al., 2013). Of the three aplites sampled for this study, one is from drill core in the Valley deposit and two were sampled in the field where they cut rocks of the Bethsaida and Bethlehem facies.

The aplite dykes are inequigranular or phenocryst-poor porphyries with plagioclase and quartz phenocrysts set in a pink, sugary aplitic groundmass (Fig. 3.13). Quartz phenocrysts vary from 3 to 7mm in size and have serrated grain boundaries, undulatory extinction and subgrains indicative of ductile deformation. Finer grained quartz occurs in pods enclosed in and surrounding quartz phenocrysts and the grainsize coarsens away from the phenocrysts and into the groundmass (Fig. 3.13E).

Plagioclase phenocrysts range from 1 to 4mm in size with elongated, prismatic shapes with serrated grain boundaries cut by finer grained (<0.25mm) quartz and plagioclase crystals (Fig. 3.13E). Sample MD041 contains plagioclase phenocrysts that display oscillatory zoning and unusual phenocrysts that appear to be
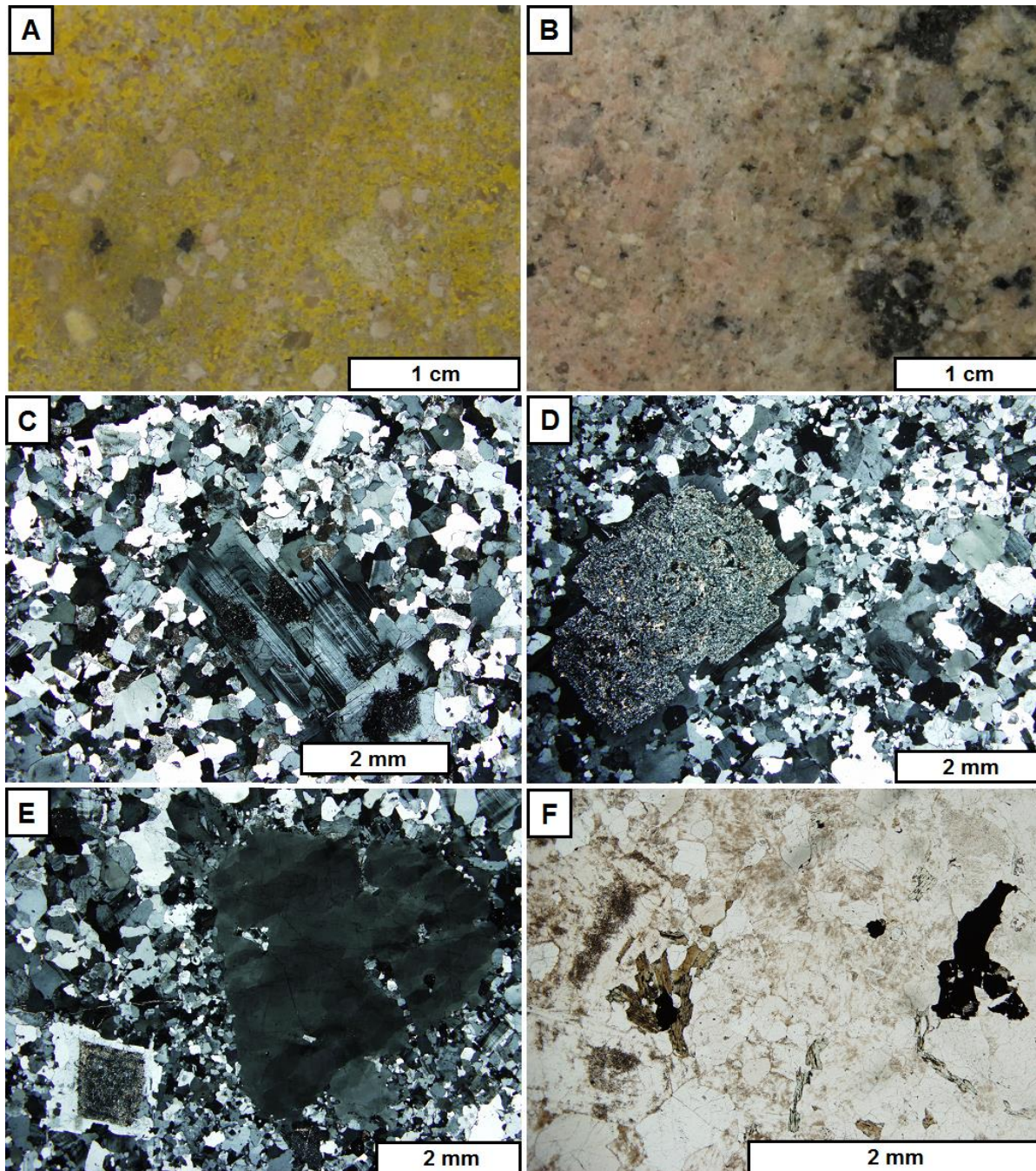
Figure 3.13 Aplite dyke petrography. A. Hand sample MD040. Sample is stained with sodium cobaltinitrite and shows yellow K-feldspar interstitial to quartz and plagioclase in an aplitic groundmass. B. Hand sample MD050 which shows a contact between an aplite dyke and the Bethlehem facies. C. A composite plagioclase phenocryst composed of two fused crystals both displaying oscillatory zoning (Cross-polarized transmitted light; Sample: MD041). D. Pervasive sericite alteration of a plagioclase phenocryst with a narrow, unaltered rim (Cross-polarized transmitted light; Sample: MD040). E. A quartz phenocryst displaying internal subgrains as well as pods of much finer quartz grains both isolated and in contact with the groundmass. Groundmass quartz shows a coarsening in grain size moving away from the phenocryst (Cross-polarized, transmitted light; Sample: MD040). F. Radial biotite crystals centered on a magnetite crystal. The biotite has been altered to chlorite along cleavage planes (Plane-polarized transmitted light: Sample: MD050).

two crystals that are fused together along an irregular grain boundary which are easily identified by twinning and zoning patterns that are not consistent across the contact (Fig. 3.13C). Alteration of plagioclase phenocrysts is variable in and between samples, with pervasive sericite, calcite and epidote alteration affecting between 10 to 85% of individual crystals in sample MD040 (Fig. 3.13D), while phenocrysts from samples MD041 and MD050 display <10% patchy sericite alteration (Fig. 3.13C). Plagioclase alteration in all samples is concentrated in the cores or along fractures in the phenocrysts, with the most altered samples still retaining thin, unaltered rims (Fig. 3.13D). Abundant fine-grained plagioclase occurs in the aplitic groundmass where it forms anhedral, rounded and unaltered crystals <0.5mm in size. Potassium feldspar (microcline) is abundant in all samples (30 to 35%) and occurs interstitial to phenocrysts, as well as groundmass quartz and plagioclase, and is most easily identified in stained hand samples (Fig. 3.13A). Microcline is variably altered, occurring as fresh, unaltered crystals displaying tartan twinning in some samples and with up to 60% patchy clay alteration in others. Biotite is a minor constituent, accounting for 1 to 5% of a sample, and occurs as shredded, <0.5mm crystals throughout the groundmass (Fig. 3.13F). Chlorite and epidote alteration of biotite is ubiquitous and occurs along cleavage planes. Opaque minerals include disseminated magnetite (1 to 3%) and trace pyrite. Accessory minerals include trace amounts of interstitial rutile, zircon inclusions in biotite and quartz, and euhedral, hexagonal apatite, typically observed as inclusions in magnetite. Very-fine-grained epidote and clinozoisite (≤1%) occur disseminated throughout the groundmass.

3.12 Nicola Batholith

The Nicola Batholith is a composite batholith comprised of a number of different rock types. Primary igneous rock types include biotite-quartz diorite (Fig. 3.14A), tonalite, granite, porphyritic granodiorite (Fig. 3.14C) and fine-grained granitic units (Fig. 3.14B). The internal structure of the Nicola Batholith is much more complex than that of the Guichon Creek Batholith as it contains numerous, cm-scale tonalite dykes (Fig. 3.14D) that were observed to cut all of the different rock types of the batholith. In addition to these cross-cutting dykes, a number of outcrops contained rounded to lenticular, fine-grained mafic enclaves which are interpreted to be xenoliths of the host rocks of the Nicola Group trapped during emplacement (Fig. 3.14E).

Alteration in the Nicola Batholith is characterized by weak chlorite after biotite and hornblende as well as epidote after plagioclase. A number of sub-cm, epidote-bearing veins were also noted to cut the batholith (Fig. 3.14F). Many samples are weakly to moderately foliated (Fig. 3.14C and F) indicating deformation at moderately high temperature and pressure conditions. This is consistent with the presence of metamorphic rocks along the margins of the batholith, including amphibolite and biotite-muscovite schist, which suggest the Nicola Batholith itself has undergone upper greenschist to lower amphibolite facies metamorphism.

3.13 Discussion

Excluding the Border facies, the mineralogy of the Guichon Creek Batholith does not significantly vary between facies, with compositional changes being predominantly controlled by the changing modal abundance of the constituent minerals (Fig. 3.15). The
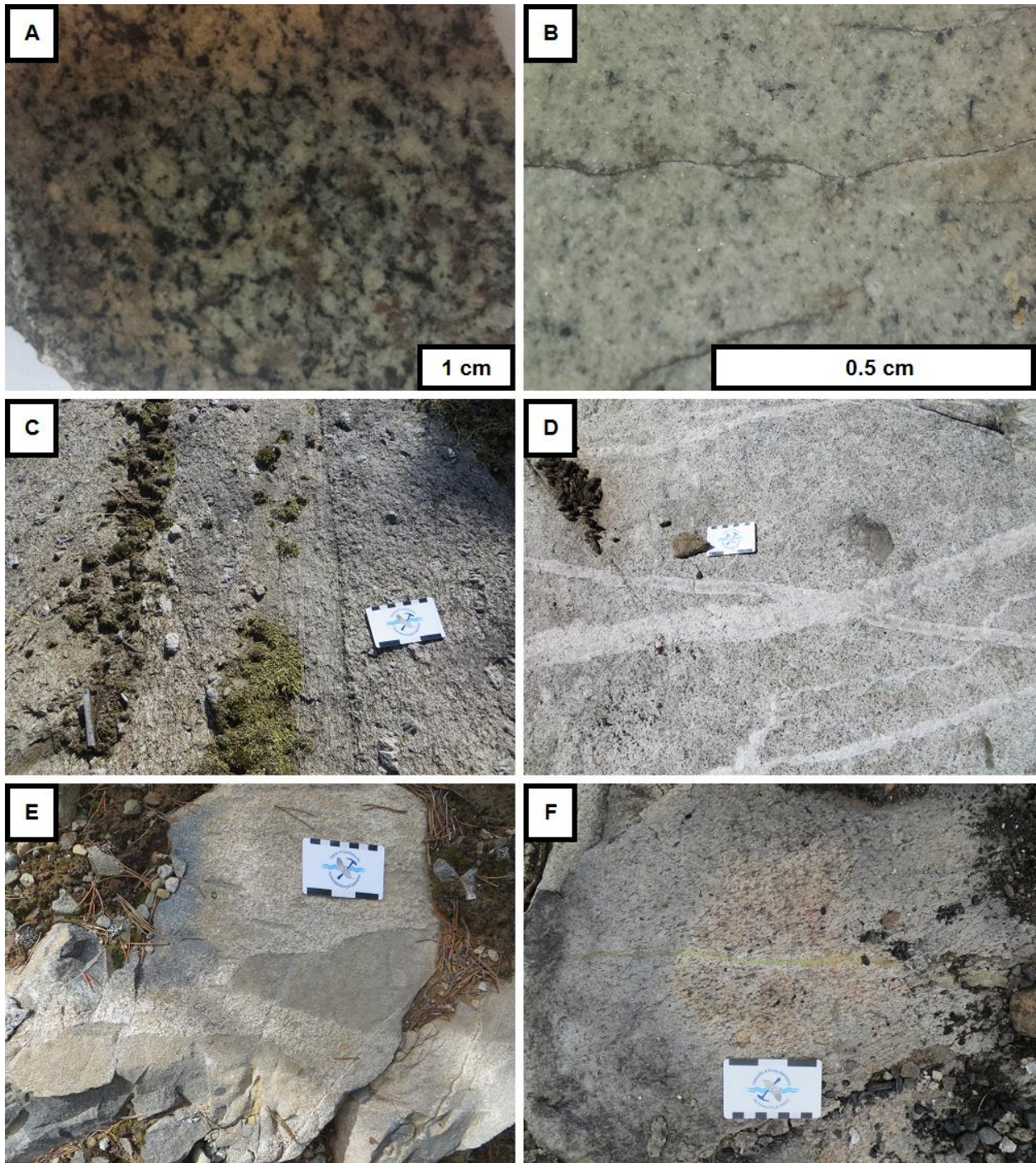
Figure 3.14 Petrography of the Nicola Batholith. A. Biotite-quartz diorite (Sample: MD018). B. Fine-grained felsic unit (Sample: MD 016). C. Foliated porphyritic granodiorite. D. Centimeter-scale tonalite dykes cross-cutting granodiorite. E. Mafic xenoliths in granodiorite. F. A sub-cm epidote vein cross-cutting a foliated granodiorite.

oldest, marginal rocks of the Border facies are characterized by mafic compositions ranging from olivine- and pyroxene-bearing gabbroic rocks to diorite and quartz diorite with the exception of two samples of quartz monzogabbro (Fig. 3.15A and B). Based on disequilibrium textures described early in this chapter (e.g., serpentine coronas around olivine), the K-feldspar and much of the biotite present in the quartz monzogabbro is interpreted to be the product of metasomatism of the Border facies by a K-rich fluid. This fluid was possibly derived from metamorphism or assimilation of the country rocks. The olivine characteristic of gabbroic Border facies samples is absent from all other facies, but pyroxene cores in amphibole are also observed in the Guichon facies, which is the next facies moving towards the core of the batholith. All subsequent facies are characterized by the stable mineral assemblage of quartz, plagioclase, K-feldspar, biotite, amphibole, magnetite, titanite, apatite ± zircon. Key differences between facies include changes in modal abundances of minerals, notably an increase in quartz and K-feldspar (Fig. 3.15A) and an accompanying decrease in hornblende and biotite, as well as textural characteristics (ie. Equigranular vs. porphyritic textures). This is a common trend observed for the modal mineralogy of calcic and calc-alkalic batholiths (as defined by the Modified Alkali Lime Index or MALI; Frost and Frost, 2008).

The most immediately obvious textural difference among facies is the presence of equigranular textures in the older, marginal facies and porphyritic textures in the younger facies in the core of the batholith. The Border facies as well as the Guichon and Chataway sub-facies all display medium-grained equigranular textures with mafic minerals that are spread evenly throughout the samples. The Bethlehem and Bethsaida

79
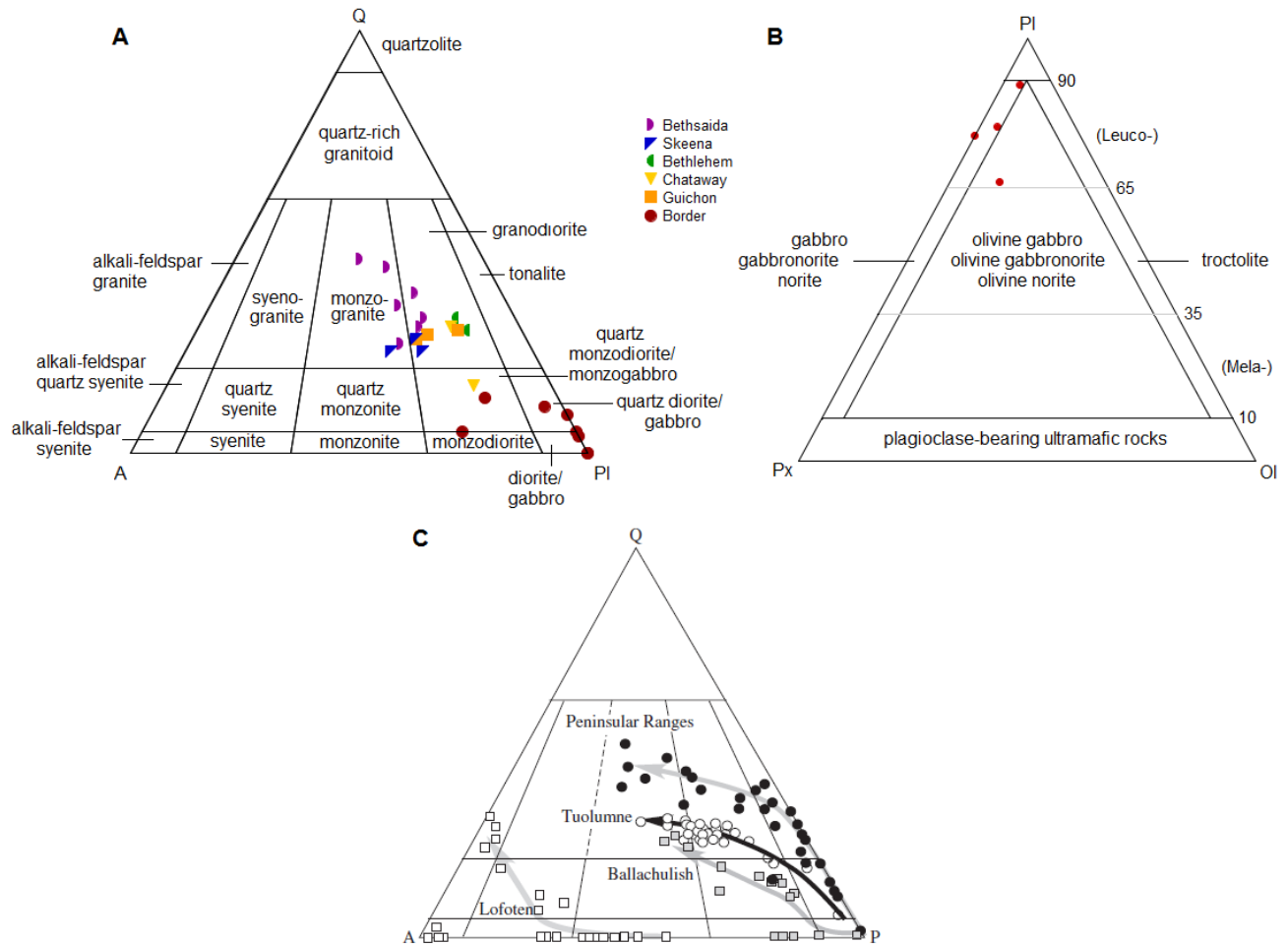
Figure 3.15 A. and B. Evolution of the modal mineralogy of the Guichon Creek Batholith C. Modal mineralogy trends of representative alkalic (Lofoten), alkali-calcic (Ballachulish), calc-alkalic (Tuolumne) and calcic (Peninsular Ranges) batholiths for comparison (after Frost and Frost, 2008).

Facies, however, are weakly porphyritic, with plagioclase phenocrysts in both facies and poikilitic amphibole in the Bethlehem facies but biotite and quartz phenocrysts in the Bethsaida facies. Additionally, all of the dyke rocks are characterized by porphyritic textures with varying phenocryst populations (predominantly plagioclase and/or quartz). The Skeena facies is characterized by a seriate texture intermediate between the equigranular and porphyritc textures of the other facies. Generally, equigranular textures are characteristic of rocks that have undergone a single stage of cooling whereas porphyritic textures are formed either by multi-stage cooling histories or

quenching due to a sudden drop in pressure (Best and Christiansen, 2001). The aplitic

groundmass in aplite, QFPP and QFPM dykes is characteristic of hypabyssal

environments and is almost certainly the result of magma quenching due to a sudden

drop in pressure in a sub-volcanic environment (Best and Christiansen, 2001). The

presence of phenocrysts hosted in a phaneritic groundmass, as in the Bethlehem and

Bethsaida facies, is most likely the result of a two stage cooling history. This may

indicate that the phenocrysts formed in a mid-crustal magma chamber before being

transported into an upper-crustal level during emplacement of the Bethlehem, Skeena

and Bethsaida facies.

A second key difference between facies is the texture of quartz. The Border,

Chataway and Guichon facies are characterized by interstitial quartz, which in the

Guichon and Chataway sub-facies, commonly poikilitically encloses plagioclase

chadacrysts. In these facies, when quartz is not sub-ophitic to ophitic it commonly

appears angular as the interstitial spaces between plagioclase crystals is filled by

single, continuous quartz crystals (Fig. 3.5C). In the Bethlehem, Skeena and Bethsaida

facies, however, interstitial quartz typically occurs as masses of very fine-grained

rounded crystals. The Skeena and Bethsaida facies are additionally characterized by

phenocrysts of amoeboidal quartz (Fig. 3.8D).

Deformation features are common in quartz in all facies, and include undulose

extinction, subgrain boundaries in amoeboid quartz eyes and grainsize reduction (Fig.

3.8D). Some samples also contain plagioclase crystals which display wavy or pinched

out deformation twins. These features are characteristic of the subsolidus redistribution

of strain through the crystal lattice by dislocation creep in response to differential stress

81

at, or above, the homologous temperature (~0.5 $T_{melting}$) of quartz and plagioclase.

These features, in conjunction with abundant secondary biotite and K-feldspar are likely

the result of metasomatism by hot, K-bearing fluids derived from albite-epidote facies

metamorphism of the Nicola Group country rocks as well as slow, post-emplacement

cooling of the fully crystalline batholith under differential stress.

Oscillatory zoning in plagioclase crystals is absent in the older Border, Guichon

and Chataway facies and abundant in the younger Bethlehem, Skeena and Bethsaida

facies (Fig. 3.6E). Oscillatory zoning in plagioclase reflects variations in anorthite

content due to kinetic effects in the crystal-melt boundary layer during crystallization

(e.g., Loomis, 1982; Anderson, 1984). Experiments on the coupled diffusion of CaAl-

NaSi in plagioclase revealed that CaAl-NaSi diffusion occurs slowly and has a high

closure temperature (in the solidus-liquidus temperature interval; Grove et al., 1984)

which could explain the unzoned phenocrysts in the older facies if they were cooled

much more slowly than the younger facies. This scenario is unlikely however, as zoned

amphibole is lacking from all facies, even those containing zoned plagioclase which

indicates slow cooling and continuous re-equilbration to near solidus temperatures in

the presence of melt (Schmidt, 1992). Instead, it is likely that the lack of oscillatory

zoned plagioclase in the Border, Guichon and Chataway facies is a reflection of their

composition, as the higher temperature at which plagioclase begins to crystallize and

cool in more mafic magmas allows for a longer time period for CaAl-NaSi diffusion to

occur and can result in the homogenization of oscillatory zones up to 10µm wide (Grove

et al., 1984). Oscillatory zoning in Bethlehem and younger facies may also indicate

crystallization from a static magma whereas its absence in the older facies may represent magmatic overturn (Westerman, 1970; McMillan, 1976a).

The abundance of amphibole is also an indicator of magmatic water content. The stability of calcic-amphiboles in magmas requires relatively high water contents (≥ 4 wt%; e.g., Naney, 1983; Ridolfi et al., 2010; Ridolfi and Renzulli, 2012). This implies that the magmatic water content of the Guichon Creek Batholith was high enough to stabilize amphibole throughout its entire crystallization history, with the exception of the earliest crystallization of orthopyroxene and clinopyroxene in the Border and Guichon facies. It should be noted, however, whereas most samples are free of significant alteration, all of the pyroxene in these rocks is rimmed or replaced by amphibole (Fig. 3.3B-C). These textures commonly result from the uralitization of pyroxene (Winter, 2010) and are likely the result of the deuteric alteration of pyroxene to secondary amphibole, triggered by an increase in magmatic water content resulting from fractional crystallization of anhydrous phases (olivine + pyroxene + plagioclase). The presence of primary titanite is also an indicator of crystallization conditions, indicating a high magma oxidation state, above the fayalite-magnetite-quartz (FMQ) buffer, particularly when it is in equilibrium with magnetite + quartz ± magnesian amphibole (Lipman, 1971; Czamanske and Wones, 1973; Wones, 1981; Wones, 1989; Foley and Wheller, 1990).

Alteration in samples investigated in this study was mostly minor, and broadly similar across all facies with a few notable exceptions. Two samples from the Border facies contain abundant K-feldspar and biotite that are interpreted to be the result of metasomatism by a K-bearing metamorphic fluid derived via metamorphism of the host Nicola Group; the latter has undergone albite-epidote hornfels to lower greenschist

facies metamorphism. The Border and Guichon facies also commonly contain olivine crystals that have been altered to serpentine and talc as well as pyroxenes which occur as relict cores in amphibole crystals. These are collectively interpreted to be deuteric resulting from late stage igneous uralitization by increased magmatic water contents. Plagioclase and K-feldspar in all facies are weakly altered to sericite and clay minerals (~5 to 40% of single crystals), whereas amphibole and biotite are variably altered to chlorite and epidote. The most strongly altered mafic minerals occur in the Bethsaida facies and one sample of the Chataway facies located near the past-producing Aberdeen Adit. Chlorite and epidote alteration is characteristic of the propylitic alteration assemblage accompanying many porphyry-type deposits, and it is likely that it indicates the distal footprint of the Highland Valley porphyry system. The Nicola Batholith has undergone lower greenschist facies metamorphism as indicated by the alteration of mafic minerals to a combination of chlorite and epidote and the weak to moderately foliated fabrics noted in a number of samples.

CHAPTER 4   LITHOGEOCHEMISTRY

4.1 Introduction

Whole rock geochemical data from the Guichon Creek Batholith was collected to define and characterize the different lithological units described in Chapter 3. The data was used to investigate the evolution of the Guichon Creek Batholith's parent magma(s), as well as any systematic changes in magma chemistry prior to and after formation of the Highland Valley porphyry-Cu deposits.

Additional geochemical data for 179 samples of the Guichon Creek Batholith was provided by Teck, and data from the Nicola Batholith (this study) and volcanic rocks of the Nicola Group (Vaca, 2012) of broadly similar age were also compiled for comparison to the Guichon Creek Batholith. This facilitates the identification of any key differences between the barren and fertile plutons and the investigation of the relationship between the Guichon Creek Batholith's and other Nicola-arc rocks of similar age.

4.2 Methodology

A total of 78 samples were collected over the periods of July 17 to September 8, 2013 and June 19 to July 20, 2014. These included 65 from the Guichon Creek Batholith and an additional 13 from the Nicola Batholith. Guichon Creek Batholith samples include outcrop grab samples and drill core. Nicola Batholith samples are all outcrop grab samples. Complete whole rock analyses for all samples can be found in Appendix C.

All samples were analysed for major element oxides and trace elements at ACME Labs in Vancouver, British Columbia. Major element oxides were analysed by Inductively Coupled Plasma – Emission Spectrometry (ICP-ES) following a lithium borate fusion and dilute acid digestion. Loss on ignition was determined by sintering at 1000°C. Two separate analyses were utilized to optimize trace element determination. Rare earth and refractory elements were analysed by Inductively Coupled Plasma – Mass Spectrometry (ICP-MS) following a lithium borate fusion and dilute acid digestion. Precious metals, base metals and their associated pathfinder elements (Au, Ag, As, Bi, Cd, Cu, Hg, Mo, Ni, Pb, Sb, Se, Tl and Zn) were analysed by ICP-MS following treatment by aqua regia digestion at 95°C. The lower detection limit for major element oxides is 0.01% with the exception of Fe_2O_3 (0.04%) and Cr_2O_3 (0.002%). Lower detection limits for select trace elements are as follows: La (0.1ppm), Sm (0.05 ppm), Gd (0.05ppm), Yb (0.05ppm), Zr (0.1ppm), Hf (0.1ppm), Nb (0.1ppm), Eu (0.02ppm), Cu (0.1ppm), Mo (0.1ppm) and Au (0.5ppb). All analyses were undertaken with external standards and blanks in addition to those used by the analytical facility to ensure quality control. Major element oxide and trace element values were recalculated to a 100% volatile-free composition.

4.3 Results

4.3.1 Major Elements

Geochemical analyses for representative samples of the Guichon Creek and Nicola batholiths are presented in Table 4.1. In the Guichon Creek Batholith, SiO_2 contents increase from the marginal Border facies (49.30 to 62.19 wt%) to the Bethsaida facies (67.49 to 73.95 wt%). The alkali element Na_2O remains relatively

Table 4.1 Representative whole-rock analyses for the Guichon Creek and Nicola batholiths

Locality	Guichon Creek Batholith							
Sample	MD041	MD052	MD053	MD004	MD069	MD003	MD057	MD044
Facies	Aplite Dyke	Bethlehem	Bethlehem	Bethsaida	Bethsaida	Border	Border	Chataway
SiO_2 (wt%)	76.36	65.82	66.05	73.26	68.97	48.77	56.32	61.43
TiO_2	0.10	0.37	0.33	0.17	0.26	1.26	0.94	0.59
Al_2O_3	12.80	16.97	16.97	13.88	16.21	18.19	16.80	16.98
Fe_2O_3	1.39	3.53	3.32	2.23	2.59	11.09	7.84	5.24
MnO	0.03	0.04	0.04	0.06	0.05	0.17	0.13	0.08
MgO	0.13	1.28	1.12	0.36	0.83	5.44	3.72	2.67
CaO	0.77	4.63	4.23	2.10	3.31	9.33	6.25	4.96
Na_2O	3.66	4.76	4.74	4.14	4.63	3.97	4.06	4.34
K_2O	4.63	1.75	1.51	2.81	2.26	0.37	2.08	2.06
P_2O_5	0.05	0.15	0.14	0.06	0.11	0.33	0.25	0.16
LOI	0.00	0.50	1.40	0.70	0.50	0.80	1.30	1.30
Sum	99.92	99.80	99.85	99.77	99.72	99.72	99.69	99.81
Ti (ppm)	599	2218	1978	1019	1558	7553	5635	3537
P	218	654	610	261	480	1440	1091	698
Cr	3.40	5.00	4.00	3.60	4.30	22.10	18.90	9.60
Co	1.10	3.40	5.10	2.10	4.00	14.20	15.30	9.40
Ni	0.80	2.90	3.20	0.90	1.90	14.30	14.30	10.30
Rb	74.20	29.40	17.90	44.80	45.60	1.60	73.30	48.00
Sr	84.00	750	710	399	634	894	716	609
Cs	0.40	0.70	0.20	0.40	1.00	0.10	1.50	0.80
Ba	676	743	722	1171	959	289	637	677
Sc	2.00	5.00	5.00	2.00	3.00	25.00	17.00	10.00
V	17.00	69.00	62.00	23.00	53.00	274	194	128
Ta	0.40	0.10	0.10	0.20	0.10	0.10	0.30	0.20
Nb	2.6	1.7	1.5	1.6	1.6	3.0	3.2	1.9
Zr	58.1	85.9	70.3	61.6	54.0	82.6	155	96.5
Hf	2.9	2.2	1.9	2.2	1.5	1.9	3.9	2.3
Th	5.60	2.20	1.80	2.40	1.50	0.30	4.60	3.20
U	2.20	1.40	0.80	0.60	1.20	0.10	1.90	1.70
Y	5.90	7.10	6.20	7.30	5.00	19.80	16.50	8.80
La	17.2	9.5	9.4	9.7	9.1	15.5	16.9	10.9
Ce	26.70	18.80	18.70	20.20	16.40	34.70	38.10	22.10
Pr	2.59	2.50	2.28	2.21	2.02	4.66	5.00	3.17
Nd	8.60	10.80	8.90	7.30	6.70	22.40	20.60	13.30
Sm	1.04	1.81	1.38	1.31	1.45	5.09	4.06	2.45
Eu	0.14	0.54	0.51	0.36	0.44	1.25	0.94	0.73
Gd	0.79	1.57	1.42	1.25	1.19	4.62	3.77	1.99
Tb	0.12	0.21	0.19	0.16	0.16	0.62	0.54	0.28
Dy	0.84	1.25	1.02	1.03	0.94	3.67	3.14	1.72
Ho	0.17	0.24	0.22	0.17	0.16	0.66	0.53	0.23
Er	0.50	0.78	0.65	0.48	0.57	2.01	1.74	0.77
Tm	0.10	0.11	0.09	0.10	0.08	0.24	0.24	0.12
Yb	0.78	0.74	0.68	0.73	0.60	1.68	1.61	0.84
Lu	0.16	0.09	0.11	0.12	0.10	0.24	0.26	0.13
Cu	4.4	82.8	18.3	24.5	17.2	188	185	75.2
Zn	11.50	7.30	9.80	29.10	17.80	41.40	42.70	32.60
Mo	0.2	1.5	0.5	0.2	0.3	0.2	0.8	0.4
Ag	0.01	0.03	0.00	0.04	0.01	0.07	0.05	0.04
Tl	0.02	0.02	0.02	0.02	0.04	0.02	0.08	0.02
Pb	2.66	1.20	1.49	1.65	0.64	0.53	2.39	1.43
Sn	1.00	1.00	1.00	1.00	1.00	1.00	1.00	1.00
Sb	0.03	0.07	0.06	0.03	0.02	0.02	0.16	0.05
Ga	13.30	16.30	16.60	13.20	16.30	19.90	17.20	18.10
Ge	0.10	0.10	0.10	0.10	0.10	0.10	0.10	0.10
As	0.30	1.50	1.40	0.60	0.40	0.90	3.00	1.30
W	0.50	0.70	0.50	0.50	0.50	0.50	1.00	0.50
Bi	0.02	0.03	0.02	0.02	0.03	0.02	0.09	0.03
Be	0.20	0.10	0.40	0.10	0.20	0.10	0.30	0.20

Table 4.1 Continued…

Locality	Guichon Creek Batholith							
Sample	MD066	MD063	MD022	MD031	MD024	MD026	MD073	MD076
Facies	Chataway	F.g. GRD	FPC	FPC	FQPC	FQPC	Grey Dike	Guichon
SiO_2 (wt%)	63.63	67.19	63.62	66.50	63.73	65.85	71.65	63.10
TiO_2	0.53	0.44	0.33	0.32	0.35	0.32	0.15	0.60
Al_2O_3	16.08	15.26	16.73	16.77	16.42	16.71	15.24	16.09
Fe_2O_3	5.10	3.74	3.88	3.32	4.08	3.91	1.89	5.36
MnO	0.08	0.05	0.05	0.04	0.05	0.03	0.06	0.08
MgO	2.42	1.47	1.14	1.08	1.31	1.13	0.40	2.62
CaO	5.09	3.67	4.31	4.40	3.53	3.79	2.32	4.95
Na_2O	4.02	4.00	4.39	4.77	5.36	5.44	4.95	3.83
K_2O	1.98	3.12	1.88	1.35	1.55	0.45	1.89	2.27
P_2O_5	0.16	0.12	0.12	0.13	0.14	0.13	0.07	0.14
LOI	0.70	0.60	3.30	1.10	3.30	2.00	1.10	0.70
Sum	99.79	99.66	99.75	99.78	99.82	99.76	99.72	99.74
Ti (ppm)	3177	2638	1978	1918	2098	1918	899	3597
P	698	524	523	567	610	567	305	610
Cr	5.80	6.20	4.50	4.10	4.00	4.80	3.80	16.2
Co	8.10	5.90	6.50	3.90	6.80	5.50	1.70	10.6
Ni	6.00	4.80	3.40	2.80	3.90	3.80	0.70	14.7
Rb	46.00	56.80	35.30	18.20	37.30	9.70	29.50	65.1
Sr	720	541	693	813	332	787	625	630
Cs	0.90	0.90	0.70	0.30	0.40	0.40	0.70	2.0
Ba	713	1040	887	882	538	375	1077	717
Sc	8.00	7.00	5.00	4.00	5.00	5.00	2.00	11.00
V	113	81.00	63.00	63.00	74.00	61.00	19.00	138
Ta	0.10	0.30	0.10	0.10	0.10	0.10	0.10	0.2
Nb	2.0	3.0	1.4	1.4	1.4	1.4	1.6	2.7
Zr	101	158	77.3	74.8	68.9	68.0	54.9	146
Hf	3.6	4.7	2.3	2.0	2.0	1.6	1.4	4.1
Th	2.40	2.70	1.30	1.60	1.30	1.30	0.60	5.40
U	1.70	1.40	0.70	0.80	0.80	0.90	0.60	2.20
Y	9.70	13.90	6.00	6.70	6.00	5.90	4.90	12.30
La	11.1	14.1	9.2	9.0	8.1	8.5	7.8	13.8
Ce	24.40	37.60	18.50	19.20	16.40	17.10	13.60	30.90
Pr	3.30	5.05	2.25	2.22	2.03	2.13	1.53	3.83
Nd	14.50	21.40	10.40	7.90	8.50	8.40	6.10	16.70
Sm	2.69	4.13	1.74	1.49	1.69	1.56	0.96	2.99
Eu	0.71	0.81	0.55	0.55	0.53	0.48	0.28	0.79
Gd	2.30	3.39	1.42	1.53	1.33	1.33	0.82	2.63
Tb	0.31	0.50	0.20	0.20	0.20	0.17	0.13	0.38
Dy	1.80	2.85	1.03	1.22	1.16	1.02	0.74	2.10
Ho	0.32	0.55	0.24	0.23	0.21	0.20	0.16	0.47
Er	1.06	1.42	0.70	0.57	0.65	0.48	0.59	1.32
Tm	0.15	0.21	0.09	0.10	0.09	0.08	0.07	0.21
Yb	1.06	1.46	0.73	0.68	0.59	0.69	0.65	1.24
Lu	0.17	0.23	0.11	0.11	0.11	0.11	0.09	0.20
Cu	12.3	198	403	75.9	1.9	90.0	9.5	123
Zn	26.00	19.80	20.10	7.40	19.70	16.90	16.20	39.40
Mo	0.3	0.8	4.8	0.3	0.3	0.6	0.2	0.7
Ag	0.01	0.08	0.03	0.02	0.00	0.02	0.02	35.00
Tl	0.03	0.04	0.02	0.02	0.02	0.02	0.02	0.06
Pb	1.06	1.21	1.12	1.56	0.59	2.04	2.37	3.35
Sn	1.00	1.00	1.00	1.00	1.00	1.00	1.00	1.00
Sb	0.06	0.03	0.15	0.07	0.31	0.10	0.10	0.10
Ga	16.40	14.50	16.30	16.10	17.20	16.20	13.40	17.40
Ge	0.10	0.10	0.10	0.10	0.10	0.10	0.10	0.10
As	0.60	0.30	0.90	1.30	1.30	1.50	0.70	1.40
W	0.50	0.50	0.50	0.80	0.50	0.60	0.50	0.30
Bi	0.03	0.07	0.02	0.02	0.06	0.02	0.02	0.06
Be	0.20	0.20	0.20	0.30	0.20	0.40	0.20	0.10

Table 4.1 Continued…

Locality	Guichon Creek Batholith					Nicola Batholith		
Sample	MD048	MD039	MD049	MD006	MD037	MD013	MD008	MD016
Facies	Guichon	Lamprophyre	Skeena	Skeena	QFPP	Nicola	Nicola	Nicola
SiO_2 (wt%)	68.53	37.09	65.50	70.79	74.35	50.39	67.62	73.42
TiO_2	0.42	1.91	0.39	0.22	0.06	1.13	0.35	0.11
Al_2O_3	14.80	10.61	16.99	15.11	14.04	17.72	15.92	14.54
Fe_2O_3	3.67	10.75	3.65	2.52	1.18	10.88	2.82	1.38
MnO	0.04	0.15	0.06	0.04	0.04	0.20	0.05	0.01
MgO	1.37	8.60	1.32	0.76	0.23	4.34	1.01	0.29
CaO	2.94	12.69	4.45	2.83	0.92	9.07	2.71	0.96
Na_2O	3.70	0.18	4.84	4.13	4.15	2.79	4.92	4.37
K_2O	3.29	1.54	1.65	2.74	3.68	0.82	3.18	4.02
P_2O_5	0.12	1.28	0.15	0.08	0.11	0.18	0.14	0.05
LOI	0.90	14.40	0.80	0.50	1.10	2.30	1.00	0.50
Sum	99.78	99.20	99.80	99.72	99.86	99.82	99.72	99.65
Ti (ppm)	2517	11450	2338	1318	359	6774	2098	659
P	523	5585	654	349	480	785	610	218
Cr	7.70	232	4.00	4.40	3.30	6.10	10.60	4.90
Co	6.60	42.90	5.20	4.30	0.50	13.50	4.80	1.80
Ni	7.60	274	2.70	2.50	1.10	3.60	5.70	3.00
Rb	98.50	36.50	27.90	29.50	52.70	17.60	71.60	57.50
Sr	438	1296	758	500	185	406	779	479
Cs	1.10	24.80	0.50	0.40	0.60	0.90	3.40	1.10
Ba	813	2195	1015	1197	672	311	1361	1733
Sc	6.00	21.00	5.00	3.00	1.00	30.00	4.00	2.00
V	82.00	203	75.00	43.00	8.00	280	45.00	12.00
Ta	0.20	2.20	0.10	0.10	0.50	0.10	0.90	0.60
Nb	3.2	35.8	1.6	1.2	3.9	1.3	11.9	5.1
Zr	190	144	84.4	77.5	21.5	47.0	141	64.0
Hf	5.6	3.6	2.2	2.2	0.8	1.5	3.9	2.4
Th	9.60	8.20	1.80	1.80	0.20	0.70	5.20	4.90
U	2.30	2.80	0.70	0.50	1.20	0.60	1.70	2.10
Y	12.50	16.90	6.40	5.30	6.70	18.70	8.40	4.70
La	17.7	74.2	9.4	7.5	3.4	5.3	24.0	15.0
Ce	37.90	161	18.70	16.60	6.50	12.60	41.30	26.00
Pr	4.72	21.06	2.34	2.06	1.01	1.81	4.59	2.84
Nd	19.40	87.30	8.90	7.00	3.30	9.50	16.70	9.60
Sm	3.30	11.85	1.77	1.51	0.95	2.64	2.76	1.56
Eu	0.64	3.24	0.54	0.35	0.09	0.97	0.77	0.45
Gd	2.79	8.23	1.46	1.24	0.98	3.34	2.20	1.23
Tb	0.38	0.85	0.20	0.19	0.17	0.56	0.31	0.16
Dy	2.08	3.71	1.16	1.04	0.98	3.23	1.33	0.87
Ho	0.46	0.59	0.21	0.19	0.22	0.70	0.33	0.13
Er	1.29	1.29	0.63	0.73	0.53	2.15	0.92	0.48
Tm	0.20	0.19	0.09	0.09	0.08	0.29	0.14	0.06
Yb	1.37	1.14	0.65	0.56	0.72	2.21	0.95	0.51
Lu	0.21	0.15	0.10	0.10	0.09	0.30	0.13	0.09
Cu	117	62.3	21.3	8.5	223	21.5	4.7	2.7
Zn	14.50	104	21.70	24.60	11.70	35.00	44.40	13.10
Mo	0.5	0.2	0.3	0.2	18.6	0.3	2.7	0.1
Ag	0.02	0.04	0.02	0.01	0.09	0.02	0.01	0.00
Tl	0.02	0.02	0.02	0.02	0.03	0.06	0.31	0.05
Pb	1.68	5.90	0.89	1.07	0.96	0.56	2.33	1.45
Sn	1.00	1.00	1.00	1.00	1.00	1.00	1.00	1.00
Sb	0.06	0.13	0.02	0.02	0.04	0.02	0.04	0.02
Ga	14.80	14.40	17.50	14.20	15.20	15.40	16.80	15.80
Ge	0.10	0.20	0.10	0.10	0.10	0.10	0.10	0.10
As	1.00	7.30	0.40	1.60	1.10	0.50	0.50	0.90
W	0.50	1.00	0.50	0.80	0.60	0.50	0.50	0.50
Bi	0.09	0.04	0.02	0.02	0.07	0.02	0.06	0.16
Be	0.30	1.60	0.10	0.30	0.10	0.10	0.30	0.10

constant, varying from 3.32 to 4.73 wt% in the Border facies to 3.55 to 4.99 wt% in the Bethsaida facies. Most other major elements decrease moving inward from the Border to the Bethsaida facies and vary as follows: TiO_2 (0.80-1.27 to 0.09-0.35 wt%), Fe_2O_3 (6.66-11.21 to 1.33-3.44 wt%), MgO (2.93-5.55 to 0.19-1.16 wt%), CaO (5.73-9.43 to 1.07-4.42 wt%) and P_2O_5 (0.14-0.36 to 0.02-0.15 wt%). The Al_2O_3 content decreases from the Border (15.91 to 20.75 wt%) to Chataway (13.36 to 16.94 wt%) facies and then increases in the Bethlehem (16.00 to 18.02 wt%) facies before decreasing again to the Bethsaida (13.36 to 16.94 wt%) facies. The K_2O content follows a similar pattern, increasing from 0.26 to 2.20 wt% in the Border facies to 1.36 to 3.47 wt% in the Chataway facies and 1.34 to 2.95 wt% in the Bethlehem to 1.13 to 4.78 in the Bethsaida facies.

In the Nicola Batholith, SiO_2 contents vary from 51.67 to 74.05 wt%, and most major element contents decrease with increasing SiO_2 [Al_2O_3 (14.20 to 18.65 wt%), CaO (0.97 to 9.47 wt%), Fe_2O_3 (1.39 to 11.16 wt%), MgO (0.29 to 4.45 wt%), TiO_2 (0.11 to 1.16 wt%) and P_2O_5 (0.05 to 0.23 wt%)] with decreasing K_2O (0.55 to 4.05 wt%) and Na_2O (2.86 to 5.02 wt%).

Major element contents of porphyry dykes in the Guichon Creek Batholith are broadly similar to the main facies with SiO_2 (65.56 to 77.34 wt%), TiO_2 (0.06 to 0.38 wt%, Al_2O_3 (12.47 to 17.65 wt%), CaO (0.77 to 7.03 wt%), Fe_2O_3 (0.97 to 6.97 wt%), MgO (0.13 to 1.58 wt%), P_2O_5 (0.03 to 0.17 wt%), K_2O (0.09 to 4.76 wt%) and Na_2O (0.08 to 6.48 wt%).

4.3.2 Trace Elements

Key trace element ratios were calculated for the main intrusive facies and porphyry dykes of the Guichon Creek Batholith as well as for the Nicola Batholith. These are presented in Table 4.2 and summarized below. Zirconium (Zr/Zr*), niobium (Nb/Nb*), titanium (Ti/Ti*) and europium (Eu/Eu*) anomalies are calculated following the logarithmic method of McCuaig et al. (1994) except that Nb/Nb* is calculated relative to Th and La and Zr/Zr* is calculated using Gd in place of Eu. La/Sm$_{cn}$ ratios arenormalized to chondritic values (i.e. cn = chondrite normalized). Zirconium anomalies in the Border facies range from 0.19 to 1.37 with an anomalous value of 10.06 for sample MD002. All samples show negative Nb anomalies between 0.21 and 0.08. La/Sm$_{cn}$ and Gd/Yb$_{cn}$ ratios for the Border facies range from 1.32 to 2.69 and 1.38 to 2.63, respectively. Negative Ti anomalies are also present in all samples and range between 0.43 and 0.90. Eu/Eu* ratios vary from 0.67 to 1.24 indicating a negative to slightly positive europium anomaly.

Table 4.2 Select trace element ratios for the intrusive rocks of the Guichon Creek and Nicola batholiths.

Facies	Nb/Nb*	Zr/Zr*	Ti/Ti*	Eu/Eu*	La/Sm$_{cn}$	Gd/Yb$_{cn}$
Border	0.08 to 0.21	0.19 to 10.06	0.43 to 0.90	0.67 to 1.24	1.32 to 2.69	1.38 to 2.63
Guichon	0.11 to 0.18	1.23 to 1.70	0.33 to 0.60	0.61 to 0.94	2.83 to 3.76	1.40 to 2.11
Chataway	0.08 to 0.24	0.45 to 2.04	0.25 to 0.67	0.48 to 1.18	1.88 to 3.95	1.48 to 2.52
Bethlehem	0.10 to 0.25	1.15 to 1.64	0.26 to 0.63	0.57 to 1.19	2.21 to 4.40	1.19 to 2.35
Skeena	0.03 to 0.19	0.76 to 1.87	0.31 to 0.70	0.55 to 1.73	2.89 to 9.56	1.31 to 2.39
Bethsaida	0.05 to 0.56	0.71 to 2.37	0.20 to 0.62	0.61 to 1.41	2.37 to 8.88	0.81 to 2.62
F.g. granodiorite	0.17 to 0.21	1.17 to 1.25	0.27 to 0.28	0.57 to 0.64	2.21 to 2.62	1.64 to 1.92
Porphyry Dykes	0.06 to 0.90	0.84 to 4.52	0.15 to 0.74	0.28 to 1.27	2.31 to 12.85	0.71 to 2.51
Lamprophyre	0.39	0.31	0.46	0.95	4.05	5.97
Nicola Batholith	0.06 to 0.50	0.65 to 3.13	0.19 to 0.90	0.86 to 1.85	1.30 to 6.21	1.13 to 7.66

The Guichon and Chataway sub-facies possess negative Nb and Ti anomalies as well as positive to negative Eu anomalies. Nb/Nb* values range from 0.08 to 0.24 (Chataway) and 0.11 to 0.18 (Guichon), Ti/Ti* from 0.25 to 0.67 (Chataway) and 0.33 to 0.60 (Guichon) and Eu/Eu* from 0.61 to 0.94 (Guichon) and 0.48 to 1.18 (Chataway; Table 4.2). The Guichon (La/Sm$_{cn}$ = 2.83 to 3.76; Gd/Yb$_{cn}$ = 1.40 to 2.11) and Chataway

 (La/Sm$_{cn}$ = 1.88 to 3.95; Gd/Yb$_{cn}$ = 1.48 to 2.52) sub-facies are characterized by LREE enrichment and fractionated HREE, respectively (Table 4.1). Key ratios for the fine-grained granodiorite unit are similar to the Guichon and Chataway facies (Nb/Nb* = 0.17 to 0.21, Ti/Ti* = 0.27 to 0.28, Eu/Eu* = 0.57 to 0.64, La/Sm$_{cn}$ = 2.21 to 2.62 and Gd/Yb$_{cn}$ = 1.64 to 1.92; Table 4.1).

Bethlehem samples are characterized by negative Nb (Nb/Nb* = 0.10 to 0.25) and Ti anomalies (Ti/Ti* = 0.26 to 0.63). Europium anomalies vary from negative to positive (Eu/Eu* = 0.55 to 1.73). LREE and HREE ratios for the Bethlehem facies vary from 2.21 to 4.40 (La/Sm$_{cn}$) and 1.19 to 2.35 (Gd/Yb$_{cn}$), respectively.

The Skeena and Bethsaida facies are similar with respect to trace element characteristics, with negative Nb and Ti anomalies (Nb/Nb* = 0.03 to 0.56 and Ti/Ti* = 0.20 to 0.70) and moderately negative to strongly positive Eu anomalies (Eu/Eu* = 0.55 to 1.73). LREE and HREE ratios for the Skeena and Bethsaida facies vary from 2.37 to 9.56 (La/Sm$_{cn}$) and 0.81 to 2.62 (Gd/Yb$_{cn}$), respectively.

The aplite, FPC, QFPC and QFP (tan porphyry) dykes all exhibit weak to strong negative Nb (Nb/Nb* = 0.06 to 0.90) and Ti anomalies (Ti/Ti* = 0.15 to 0.74) and strongly negative to positive Eu anomalies (Eu/Eu* = 0.28 to 1.27). The single

lamprophyre dyke has Nb/Nb* = 0.39 and Ti/Ti* = 0.46. La/Sm$_{cn}$ ratios of the dykes are

as follows: lamprophyre (4.04), FPC (2.76 to 3.90), FQPC (3.10 to 3.52), tan porphyry

(2.31 to 2.65) and aplite (7.67 to 12.85). Gd/Yb$_{cn}$ ratios of the dykes are as follows:

lamprophyre (5.97), FPC (1.32 to 2.51), FQPC (1.59 to 2.03), tan porphyry (1.13 to

1.33) and aplite (0.71 to 1.19).

Samples from the Nicola Batholith have negative Nb and Ti anomalies with

Nb/Nb* values of 0.06 to 0.50 and Ti/Ti* values of 0.19 to 0.90. Small negative to

positive Eu anomalies are indicated by Eu/Eu* of 0.86 to 1.85. La/Sm$_{cn}$ and Gd/Yb$_{cn}$

ratios for the Nicola Batholith range from 1.30 to 6.21 and 1.12 to 7.66, respectively.

4.4 Discussion

4.4.1 Major and Trace Elements

On Harker variation diagrams, major element oxides from the Guichon Creek and

Nicola batholiths display smooth geochemical trends. Plots of Al_2O_3, CaO, MgO, Fe_2O_3,

TiO_2 and P_2O_5 vs. SiO_2 wt% define tight negative correlations (Figs. 4.1 to 4.3) and the

alkali elements Na_2O and K_2O show a weak positive trend, albeit with significant scatter

(Fig. 4.3a-b, e-f).

The post-mineralization dykes display a similar geochemical evolution to the

main intrusive facies (Figs. 4.1 to 4.3). The FPM, FPC and QFPC dykes all display

mutually comparable geochemistry and are similar to the Bethlehem facies (Figs. 4.1 to

4.3). The Bethlehem Porphyry and QFP dykes display a more evolved geochemistry

similar to the Skeena and Bethsaida facies (Fig. 4.1 to 4.3). The QFPP and aplite dykes
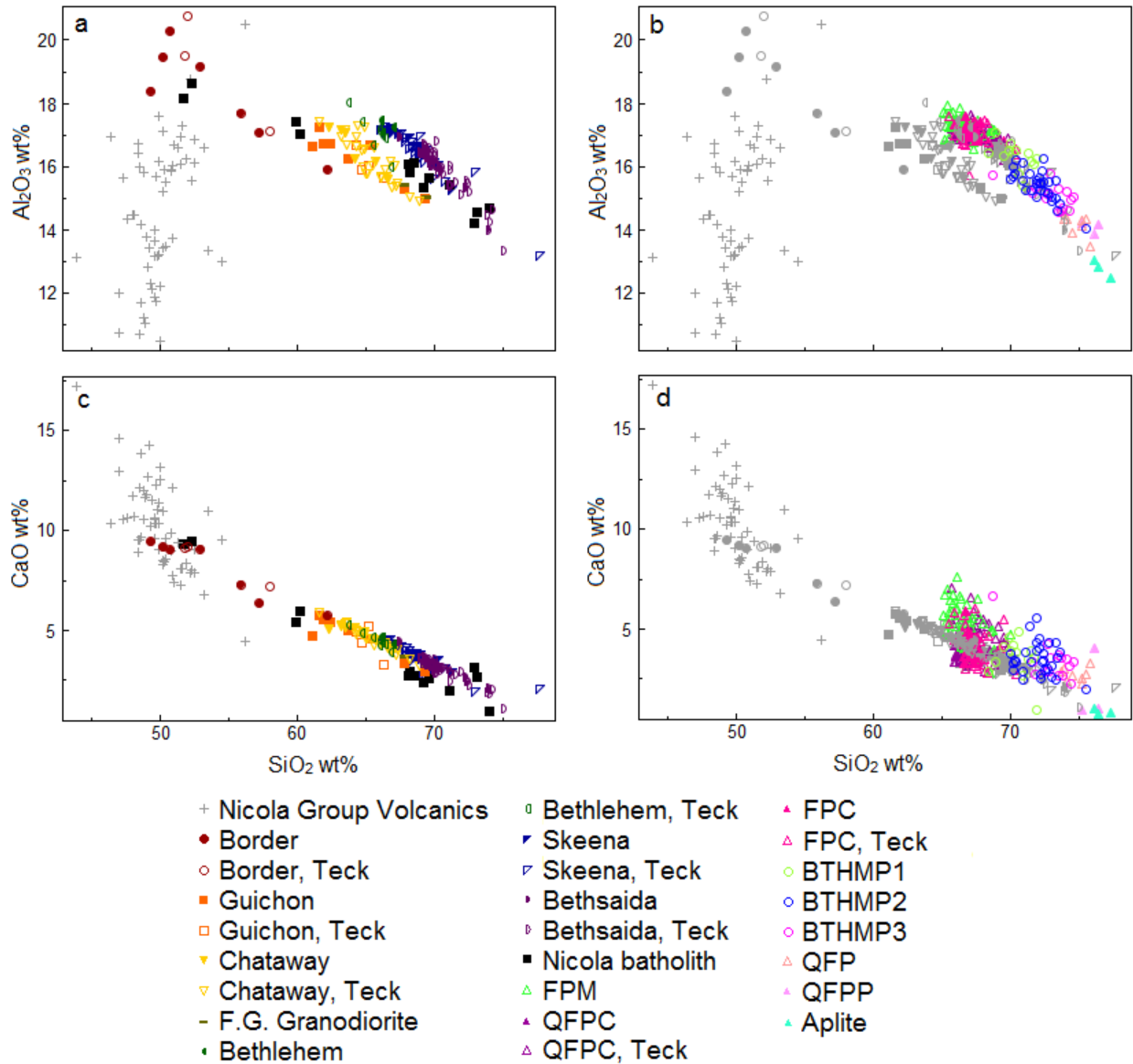
Figure 4.1 Harker variation diagrams for select major element oxides of the Nicola and Guichon Creek batholiths main facies and porphyry stocks and dykes. Solid symbols represent data acquired for this study. Open symbols are data provided by Teck. Legend symbols are the same for all subsequent figures. Data for the Nicola Group Volcanics from Vaca (2012). Symbols for the main intrusive facies have been coloured grey (b and d) for clarity when comparing dyke geochemistry to the main facies.
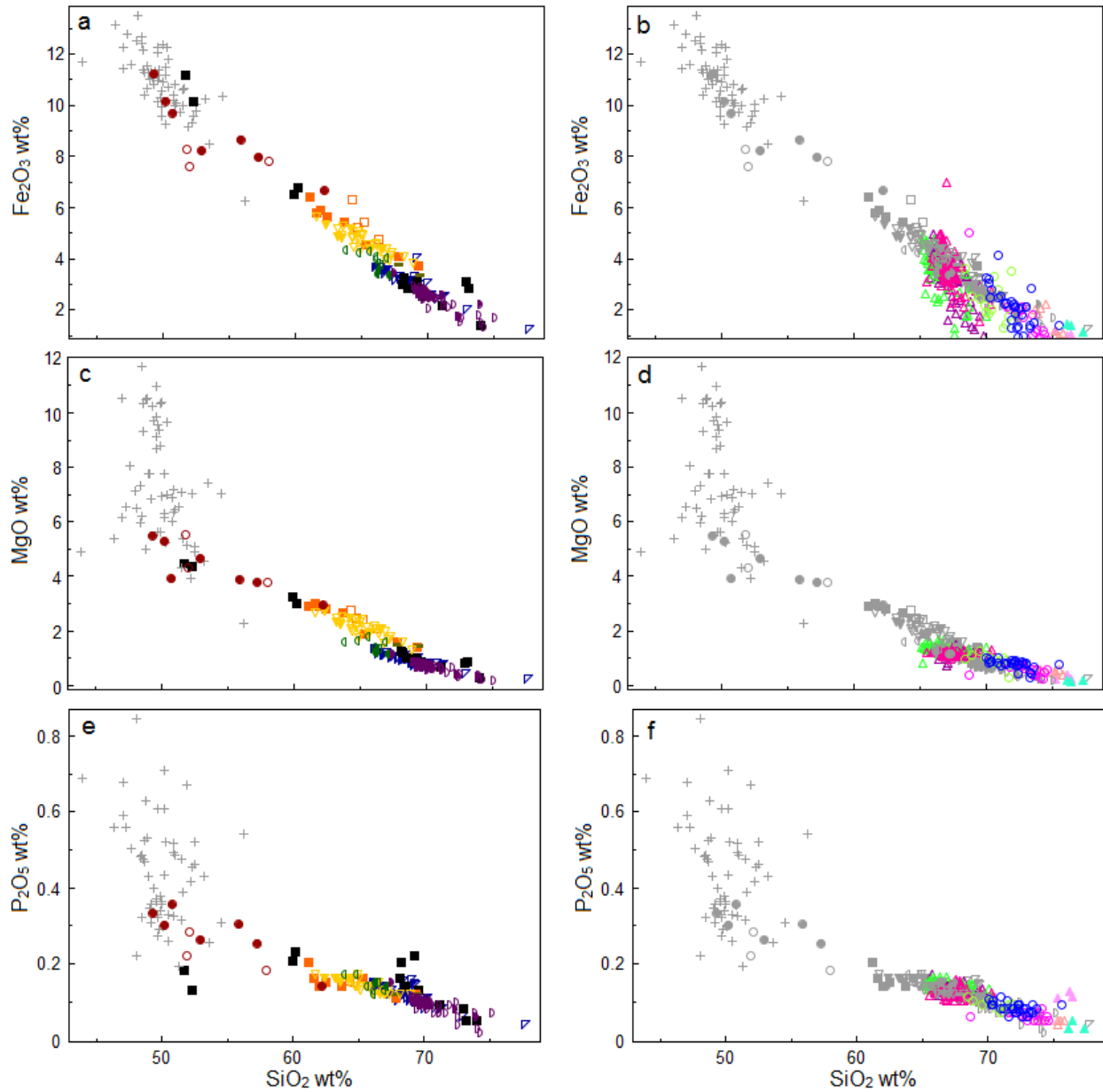
Figure 4.2 Harker variation diagrams for select major element oxides of the Nicola and Guichon Creek batholiths main facies and porphyry stocks and dykes. See Figure 4.1 for legend. Symbols for the main intrusive facies have been coloured grey (b, d and f) for clarity when comparing dyke geochemistry to the main facies.

95
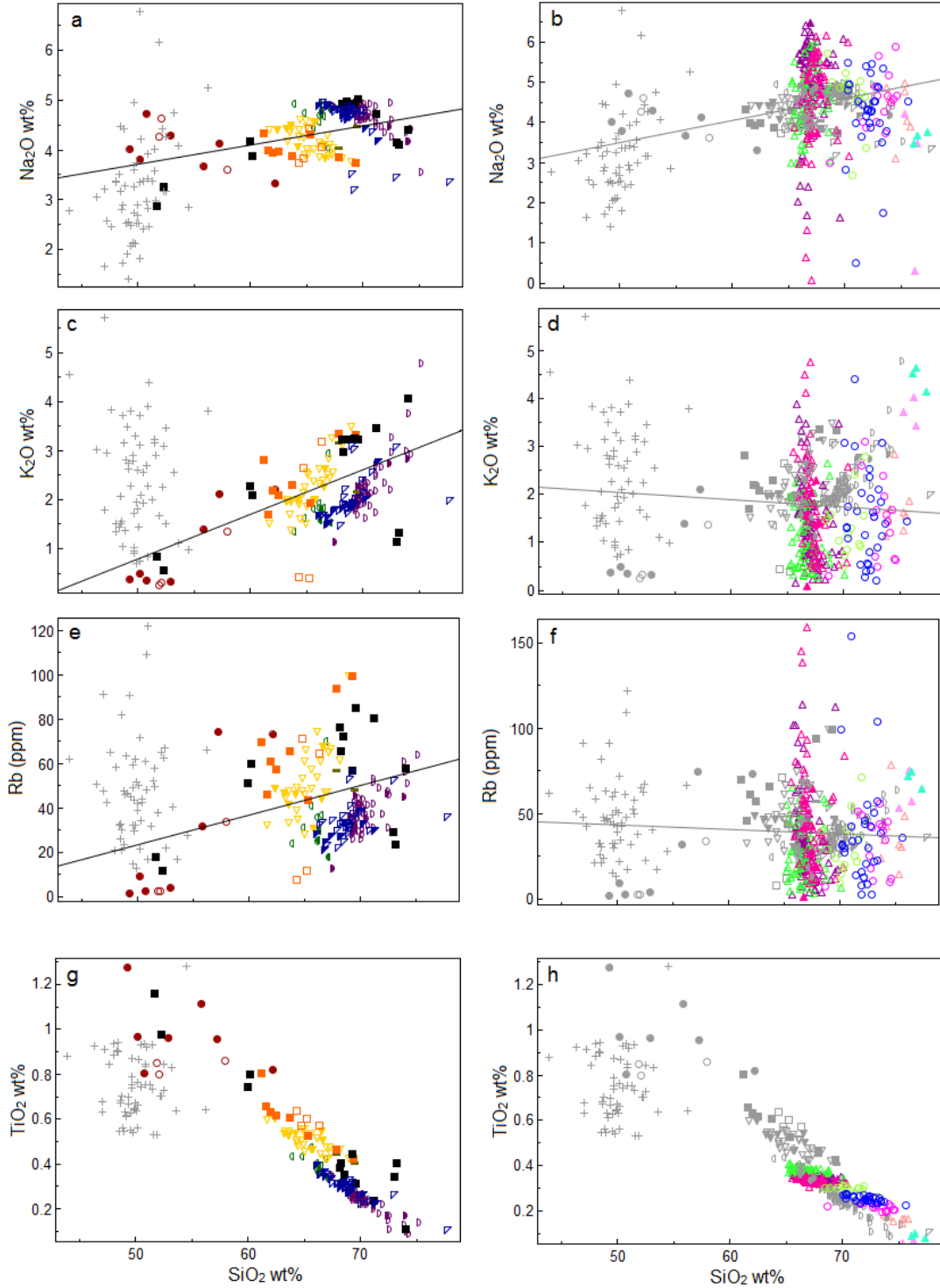
Figure 4.3 Harker variation diagrams for alkali elements, large ion lithophile elements (LILE) and high field strength element (HFSE) from the Guichon Creek and Nicola batholiths. a-d the main intrusive facies. e-h Porphyry stocks and dykes. Lines are best fits through the Guichon Creek Batholith data set. See Figure 4.1 for legend. Symbols for the main intrusive facies have been coloured grey (b, d, f and h) for clarity when comparing dyke geochemistry to the main facies.
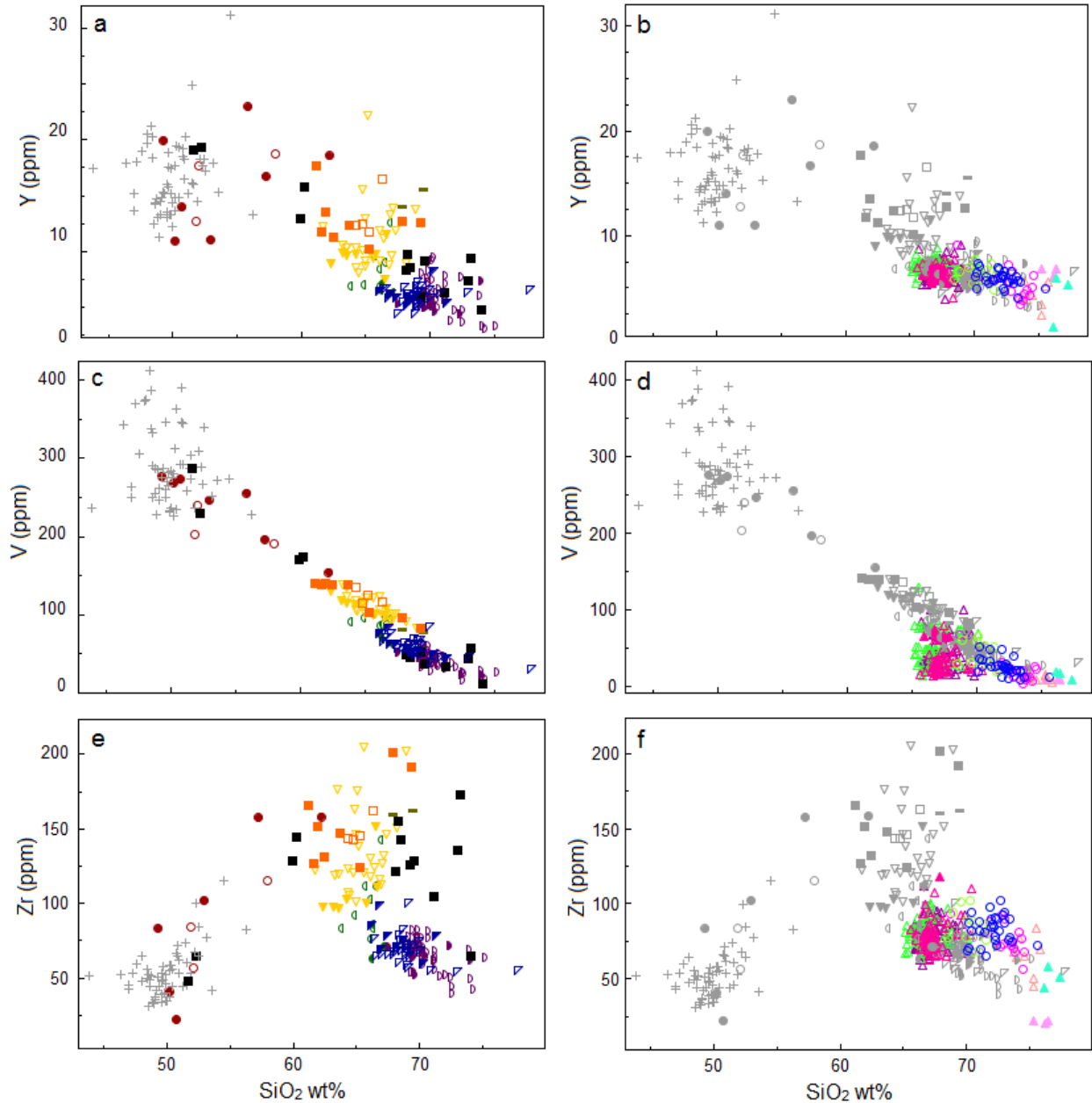
Figure 4.4 Harker variation diagrams for select trace elements of the Nicola and Guichon Creek batholiths main facies and porphyry stocks and dykes. See Figure 4.1 for legend. Symbols for the main intrusive facies have been coloured grey (b, d and f) for clarity when comparing dyke geochemistry to the main facies.

show the most evolved geochemistry and follow the evolution trend observed for the

rest of the batholith (Figs. 4.1 to 4.3).

97

On trace element Harker diagrams, the Guichon Creek and Nicola batholiths display smooth geochemical evolution trends consistent with those observed for the major element oxides (Fig. 4.4). Negative correlations are observed for Zr (Fig. 4.4), Th and U (not shown) with significant scatter between 62 and 70 wt% SiO_2. A negative correlation with moderate scatter can be observed for Y, whereas V and Sc (not shown) display a tight negative correlation (Fig. 4.4).

The trends observed on Harker diagrams (Figs. 4.1 to 4.4) for both the Guichon Creek and Nicola batholiths are consistent with the processes of crystal fractionation and/or partial melting. Strong, negative linear trends are observed for all major element oxides with the exception of Al_2O_3, Na_2O and K_2O (Figs. 4.1 to 4.3). The least evolved rocks of the Border facies have the highest CaO (5.73 to 9.43%), MgO (2.93 to 5.55%) and Fe_2O_3 (6.66 to 11.21%) and, these values smoothly decrease with increasing SiO_2 until the lowest values are reached in the Bethsaida facies (CaO; 1.07 to 4.42%, MgO; 0.19 to 1.16%; and Fe_2O_3; 1.33 to 3.44%). These trends can be explained by the fractional crystallization of the ferromagnesian minerals, particularly hornblende and later biotite, as well as olivine, clinopyroxene and Fe-Ti oxides during the early evolution of the batholith. Crystallization of these phases caused a depletion of Fe_2O_3 and MgO in the melt and in turn, the subsequently crystallizing facies. This interpretation is consistent with the observed decrease in the abundance of mafic minerals from the most primitive Border facies to the most evolved Bethsaida facies (Chapter 3). The decrease in CaO is consistent with plagioclase fractionation, with a continuous change from anorthitic to albitic plagioclase, moving from the margins to the core of the Guichon Creek Batholith as well as fractionation of calcic-amphibole. Smooth patterns displayed

on Harker diagrams for the Nicola Batholith (Figs. 4.1 to 4.3) are consistent with fractionation of ferromagnesian minerals and plagioclase. The negative corelations between TiO_2, P_2O_5 and SiO_2 wt% are consistent with fractionation of titanite ± Fe-Ti oxides and apatite which is consistent with the observed mineral paragenesis (Fig. 4.1 and 4.3; Chapter 3).

Harker diagrams for Na_2O and K_2O wt% display positive correlations with a high degree of scatter (Fig. 4.3a-d). The overall increase in both components as the rocks become more evolved is likely an artifact of their conservation in the melt as other components were removed. The degree of scatter is attributed to remobilization during subsequent hydrothermal alteration which is evident from the alteration of hornblende and biotite to chlorite and epidote as well as deformation structures present in quartz as observed from petrographic analysis (Chapter 3).

A negative correlation is observed for Al_2O_3 against SiO_2 though it is not a single tight trend as observed for the other major element oxides (Fig. 4.1a). Two subparallel but offset trends can be discerned on the Al_2O_3 vs. SiO_2 plot (Fig. 4.1a). The Border through Chataway facies fall along a line that displays lower Al_2O_3 for a given SiO_2 content than that defined by the Bethlehem through Bethsaida facies. A disconnect between the pre- and post-Bethlehem facies is also observed on a plot of K_2O vs. SiO_2, with lower K_2O contents for a given wt% SiO_2 in the Bethlehem, Skeena and Bethsaida facies relative to the earlier Border through Chataway facies (Fig. 4.3c). The broad trends of decreasing Al_2O_3 and increasing K_2O can be explained by fractional crystallization of plagioclase and later K-feldspar, though the offset in the trend would require an increase in the Al_2O_3 content and concurrent decrease in the K_2O content of

99

the magma prior to crystallization of the Bethlehem facies. This suggests that there may be different origins and/or histories for the Chataway and preceding facies vs. the post-Chataway facies, which is permissive by the statistically significant age gap between emplacement of the Highland Valley (210.51 ± 0.29 Ma) and Bethlehem (209.81 ± 0.27 Ma) facies (Table 2.1).

Trace elements similarly display trends that are consistent with fractionation (Fig. 4.4). Plots of Zr, Th and U (Th and U not shown) show a switch from incompatible to compatible behaviour between 58 to 63 wt% SiO_2, which is consistent with zircon saturation. This occurs at approximately 67 wt% SiO_2 in felsic magmas with slight changes dependent on the water content of a magma (Watson and Harrison, 1983). The synchronous change to compatible behaviour of U and Th with Zr is also consistent with zircon saturation as it is a common sink for these elements (Rollinson, 1993). The higher degree of scatter observed for Zr, Th and U between 62 and 70 wt% SiO_2 may be the result of a non-homogeneous distribution of Zr and/or H_2O in the Guichon Creek and Nicola batholith magmas as they cooled. The negative trends observed for V and Sc are consistent with the fractionation of hornblende and Fe-Ti-oxides, respectively (Winter, 2010; Chapter 3). Although Y is generally an incompatible element, it may concentrate into titanite, apatite and hornblende (Winter, 2010), and the negative trend displayed by Y is consistent with the observed fractionation of titanite and apatite (Chapter 3). It is unlikely that hornblende is a major reservoir for Y in the Guichon Creek Batholith as Y displays incompatible behavior for most of the Border facies samples even though they contain greater modal hornblende than any other intrusive facies (Chapter 3). The transition to compatible Y behaviour with crystallization of the Guichon

and Chataway sub-facies is consistent with the crystallization of titanite and apatite observed in thin section (Chapter 3).

4.4.2 Element Mobility

The use of proper geochemical classification methods is strongly dependent on a solid understanding of the degree of alteration and metamorphism that have affected the samples. First order screening of samples was done on the macroscopic scale through petrographic observation of hand samples and thin sections for the presence, texture and intensity of alteration minerals (Chapter 3). Second order screening for alteration and element mobility utilized the geochemical data and is discussed below.

Harker plots of K_2O, Na_2O, Rb and TiO_2 (Fig. 4.3) were constructed to test the mobility of the Large Ion Lithophile Elements (LILE) and High Field Strength Elements (HFSE) for the main facies and porphyry dykes and stocks of the Guichon Creek Batholith. In the main facies, LILEs (K_2O, Na_2O and Rb; Fig. 4.3 a-f) define weak positive correlations with significant scatter whereas TiO_2 defines a tightly clustered, negative correlation with much less scatter (Fig. 4.3g-h). The tight correlation between TiO_2 and SiO_2 and moderate scatter of the LILE data in the Guichon Creek Batholith suggests relatively high and low mobility of the LILE and HFSE, respectively. Samples of the porphyry stocks and dykes show a larger variation in Na_2O, K_2O and Rb contents for a given SiO_2 wt.% than is observed for the main intrusive facies whereas TiO_2 defines a tight, negative correlation. These trends indicate high mobility of the LILEs, consistent with petrographic evidence for alteration caused by hydrothermal activity in close proximity to mineralized porphyry centers. Similar trends are observed for the Nicola Batholith and are consistent with their lower greenschist facies metamorphism.

As significant mobility of the alkali and LILEs in the analyzed porphyry stocks and dykes is indicated, these rocks are excluded from further discussion as their altered nature precludes proper comparison to the least altered igneous rocks of the Guichon Creek Batholith.

4.4.3 Geochemical Classification

A geochemical classification used in conjunction with the IUGS petrographic classification of Le Bas and Streckeisen (1991) of granitic rocks can be used to examine the role and abundance of mafic minerals instead of limiting classification to only quartz, plagioclase and alkali feldspar. Both the Guichon Creek and Nicola batholiths are subalkaline and follow a calc-alkaline differentiation trend when samples are plotted on an alkalis-iron-magnesium (AFM) diagram (Fig. 4.5). On the K_2O vsersus SiO_2 wt% discrimination diagram (Peccerillo and Taylor, 1976: Fig. 4.6) the Guichon Creek and Nicola batholiths display medium- to high-K calc-alkaline affinities with six Border facies, two Guichon sub-facies, one Bethsaida facies and two Nicola Batholith samples displaying low-K tholeiitic character. The previously noted remobilization of K, however, calls into question the validity of the discriminations obtained from the K_2O vs. SiO_2 diagram. To test the accuracy of this classification, a P_2O_5/Al_2O_3 vs. K_2O/Al_2O_3 diagram (Fig. 4.7) was constructed as proposed by Crawford et al. (2007). On this diagram, most sampes are also classified as medium-K calc-alkalic with a small number of samples plotting in the high- and low-K fields, confirming the classifications of Figure 4.6. However, the majority of samples on the P_2O_5/Al_2O_3 vs.. K_2O/Al_2O_3 plot to the right of the field for unaltered rocks from the Vanuata and Sunda arcs, suggesting that they have experienced an addition of K. In light of the apparent addition of K to the Guichon
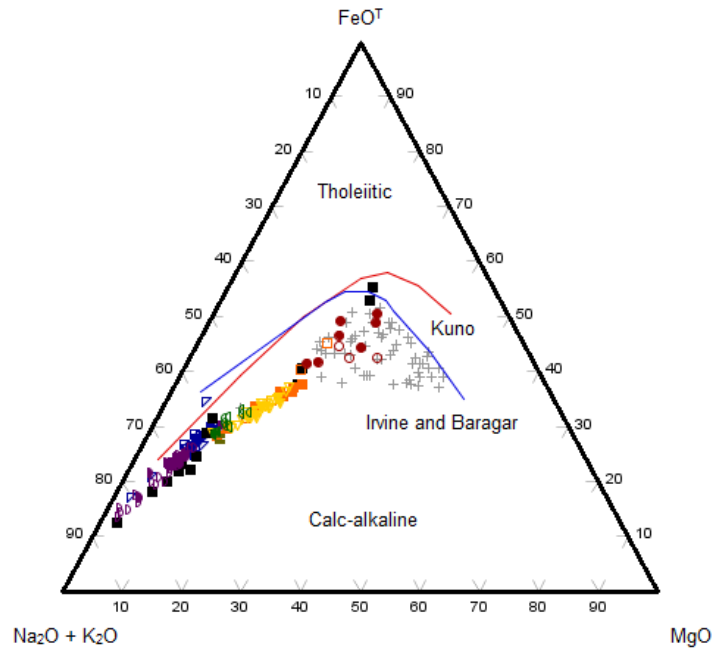
Figure 4.5 AFM diagram for the Guichon Creek and Nicola batholiths. The lines separating the tholeiitic and calc-alkaline fields are from Kuno (1968; red) and Irvine and Baragar (1971; blue). Fe_2O_3 is plotted as FeO^T. Refer to Figure 4.1 for legend.
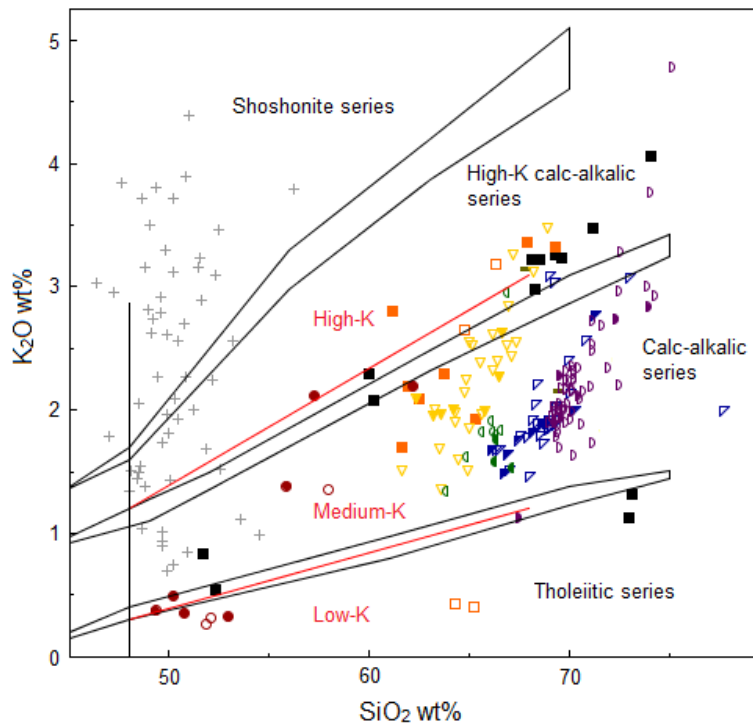
Figure 4.6 Subdivision of subalkalic rocks based on K_2O vs. SiO_2 wt% for the Guichon Creek and Nicola batholiths. Diagram after Peccerillo and Taylor (1976). Red lines and labels are the subdivions of Le Maitre et al. (1989). Outlined boundaries after Rickwood (1989). Refer to Figure 4.1 for legend.

Creek Batholith rocks, it is not possible classify them using the plutonic total-alakalis-silica (TAS) diagram (Middlemost, 1994).

A number of schemes have been proposed for the geochemical classification of granitic rocks such as the alphabetic (Chappell and White, 1974; Loiselle and Wones, 1979; White, 1979; Kilpatrick and Ellis, 1992), magnetite- and ilmenite-series (Ishihara, 1977) and trace element discrimination (Pearce et al., 1984). One problem with all of these schemes is that they implicitly specify tectonic or genetic origins. For example, the alphabetic scheme of Chappell and White (1974) classifies peraluminous granites as S-type, implying derivation via partial melting of sedimentary rocks. Rocks with mildly peraluminous compositions, however, can be generated from a
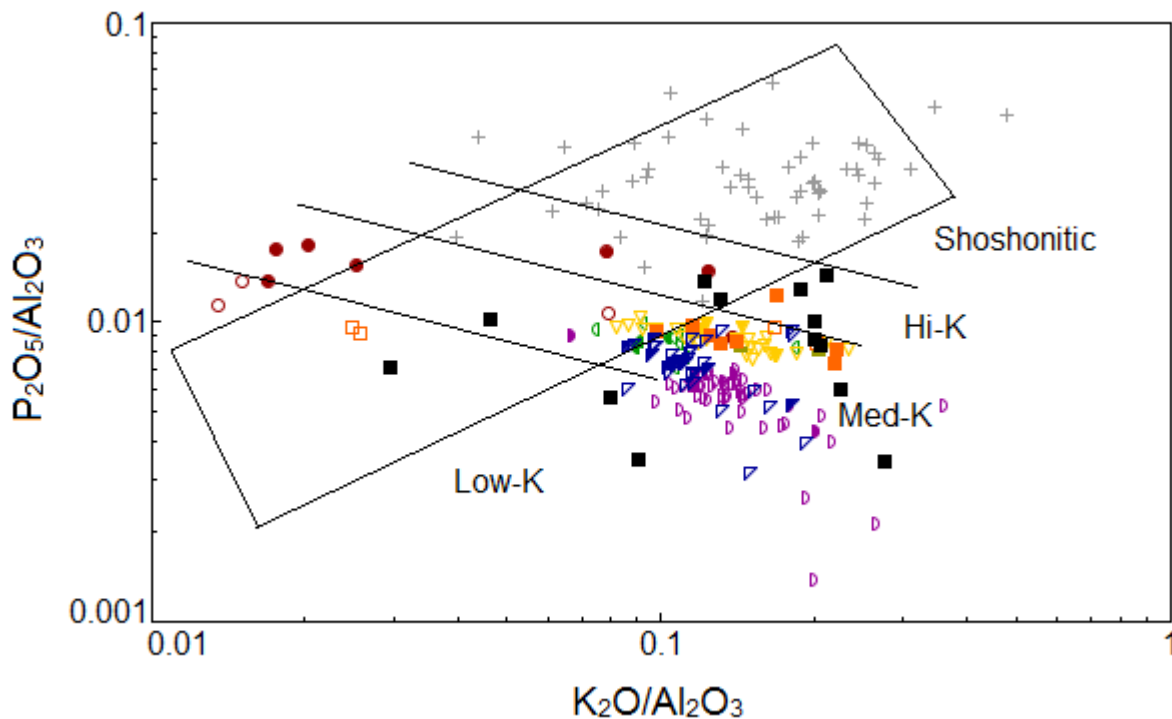
Figure 4.7 K-series classification of the Guichon Creek and Nicola batholiths based on the scheme of Crawford et al. (2007).

metaluminous melt by fractional crystallization of aluminous biotite (Zen, 1986; 1988). Because of this problem, the classification scheme of Frost et al. (2001) with updates from Frost and Frost (2008) has been chosen for this study as it does not presume a tectonic setting or formation process for the rocks it classifies.

The Guichon Creek and Nicola batholiths were classified in three steps (Fig. 4.8), based on the parameters FeO* (FeO* = FeO + $0.9Fe_2O_3$/(FeO + $0.9Fe_2O_3$ + MgO; Frost et al., 2001), Modified Alkali Lime Index (MALI = Na_2O + K_2O – CaO; Frost et al., 2001), Aluminum Saturation Index (ASI = molecular Al/(Ca – 1.67P + Na + K; Shand, 1947; Zen, 1988) and the Alkalinity Index (AI = molecular Al – (K+ Na); Shand, 1947). The majority of rocks from both batholiths are classified as magnesian with a few of the most evolved samples (>72 wt% SiO_2) plotting in the ferroan field (Fig. 4.8a). On the MALI diagram (Fig. 4.8b), the Guichon Creek Batholith straddles the boundary between calcic and calc-alkalic compositions and samples with <60 wt% SiO_2 (Border facies) are typically calc-alkalic in nature. The Nicola Batholith follows a different trend, however, evolving from more calcic compositions at low SiO_2 to calc-alkalic and then alkali-calcic compositions with increasing SiO_2 with the exception of two outlier samples that lie in the calcic field at ~72 to 74 wt% SiO_2 (Fig. 4.8b). On the ASI vs.. AI plot both batholiths evolve from metaluminous to peraluminous compositions with decreasing AI (Fig. 4.8c). For the Guichon Creek Batholith this corresponds to a metaluminous composition for the Border through Bethlehem facies and a weakly peraluminous composition for most of the Bethsaida facies (Fig. 4.8c). The Skeena facies straddles the boundary between the metaluminous and weakly peraluminous fields (Fig. 4.8c).
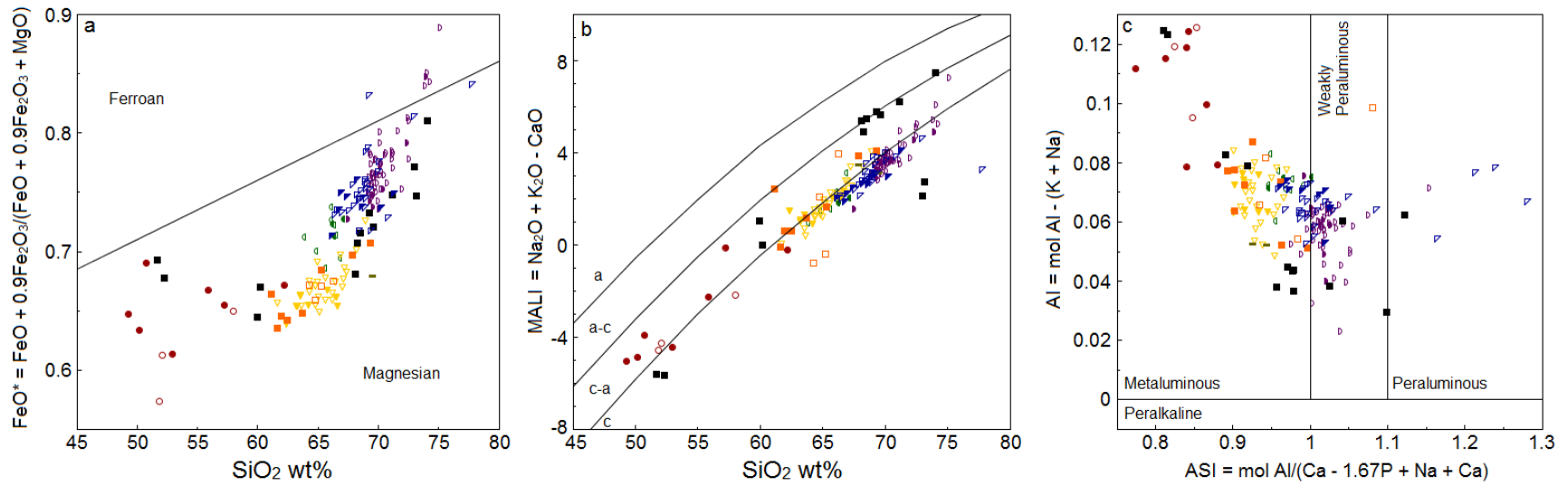
Figure 4.8 Granite classification scheme of Frost et al. (2001). A. Fe-index diagram. The boundary between ferroan and magnesian granites is defined by the line FeO*/(FeO* + MgO) = 0.46 + 0.005SiO$_2$ wt%. B. The modified alkali-lime index (MALI) vs SiO$_2$ wt.%. a, alkali; a-c, alkali-calcic; c-a, calc-alkalic; c, calcic; boundaries after Frost et al. (2001). C. Plot of the aluminum-saturation index (ASI) vs. the alkalinity-index (AI). Refer to Figure 4.1 for legend.

The magnesian signature of the Guichon Creek and Nicola batholiths is likely a reflection of differentiation under oxidizing, hydrous conditions (Osborn, 1959, Frost and Lindsley, 1992) resulting in magnetite crystallization and fractionation of Fe. Such conditions are common in arcs and 'post-collisional' environments or, via partial melting of such rocks (Frost and Frost, 2008).

The MALI signature is affected by either the source composition or the differentiation history of a magma (Frost et al., 2001). The Guichon Creek Batholith follows a trend parallel to the calcic and calc-alkalic boundary on the MALI diagram (Fig. 4.8b) which is consistent with fractional crystallization of a feldspathic melt (Frost and Frost, 2008). The Nicola Batholith however crosses two boundaries with samples lying in the calcic, calc-alkalic and alkali-calcic fields (Fig. 4.8b). Possible explanations for this are accumulation of albite and K-feldspar, magma mixing or assimilation of host rocks with a different MALI signature or a change in the composition of the source region for the magma. It has been noted that as the source region for parental melts in continental arcs moves continent-ward, melts become progressively more potassic and alkalic, resulting in a transition from calcic to calc-alkalic and then alkali-calcic plutons (Moore, 1959; Bateman and Dodge, 1970; Anderson and Cullers, 1990; John and Wooden, 1990). This trend is also observed in island arc magmas with no continental contribution (Dickenson, 1975) and is likely a reflection of their mantle source region. As the scant geochronology data available for the Nicola Batholith suggests it may represent a composite batholith constructed on the order of hundreds of millions of years, one possibility is that the shift to more a alkalic MALI signature is a reflection of the changing architecture of the subduction zone through time and a transition to post-collisional

magmatism. More likely however, it may represent higher degree partial melting of the mantle in response to a slab tear as proposed by Logan and Mihalynuk (2014) to be the source of the alkalic porphyries common to central British Columbia.

The shift from metaluminous compositions in the Border through Bethlehem facies to slightly peraluminous compositions in the Skeena and Bethsaida facies can be attributed to fractional crystallization of aluminous biotite. The crystallization of biotite with a deficiency in A-site alkalis and excess octahedral and tetrahedral Al (ASI = 1.3 to 1.4) along with hornblende (ASI = 0.3 to 0.5) in proportions greater than 3:1 as observed in the Skeena and Bethsaida facies (Chapter 3) could account for their weakly peraluminous nature (Zen, 1986; 1989). The decreasing Al values observed in the Guichon Creek Batholith can be explained by the "plagioclase effect", or preferential removal of Al relative to Na by plagioclase and alkali feldspar fractionation (Bowen, 1945). Similar trends are observed for the Nicola Batholith and it is likely that the same processes are responsible for imparting its ASI and Al signatures.

A purely geochemical division of the various facies of the Guichon Creek Batholith is complicated by the geochemically and texturally transitional nature of the main intrusive facies. Byrne et al. (2013) proposed a classification scheme based on a plot of Zr vs. molar Al/Ti which is effective at discriminating the various rock types for facies found in the vicinity of the Bethlehem deposit (Figure 4 from Byrne et al., 2013). The expanded data set utilized in the current study (with supplemental regional and Bethlehem area samples provided by Teck) has a greater sample density, particularly for the marginal Border, Guichon and Chataway facies, resulting in considerable overlap between the Guichon and Chataway sub-facies as well as the Bethlehem, Skeena and

Bethsaida facies (Fig. 4.9a). Utilizing the expanded data set compiled for this study, it is proposed that the Zr vs. molar Al/Ti diagram can be used to effectively discriminate between three distinct groups among the main intrusive facies of the Guichon Creek Batholith which are the 1) Border facies, 2) Highland Valley Facies (including the Guichon and Chataway sub-facies, and the fine-grained granodiorite dykes) and, 3) Post-Highland Valley Facies (including the Bethlehem, Skeena and Bethsaida facies): (Fig. 4.9a). The Border facies group is characterized by a narrow range of molar Al/Ti (22 to 41) with a wide range of Zr content (22 to 158 ppm) whereas the Highland Valley facies group is characterized by a slightly higher, narrow range of molar Al/Ti (32 to 60) and greater Zr contents (97 to 205 ppm). The Post-Highland Valley facies group is characterized by a much wider range in molar Al/Ti (63 to 253) and a lower, more restricted range in Zr content (40 to 112 ppm).

The various porphyry stocks and dykes located in the vicinity of the Bethlehem, J.A., Valley, Lornex and Highmont deposits are more easily discriminated based on Zr content and molar Al/Ti than the main intrusive facies and display decreasing Zr content with increasing molar Al/Ti (Fig. 4.9b)

On a plot of Al_2O_3 vs.. TiO_2, the data similarly falls into three distinct groups (Fig. 4.9a). Three possible batholith-scale geochemical evolution trends are also visible and follow a concurrent increase in Al_2O_3 content with increasing TiO_2 content (Fig. 4.9b). The Border facies as well as the Guichon and Chataway sub-facies follow the Highland Valley facies trend separately from the Bethlehem and later facies. Both the Bethlehem and Valley trends start at Bethlehem Facies compositions but follow slightly different
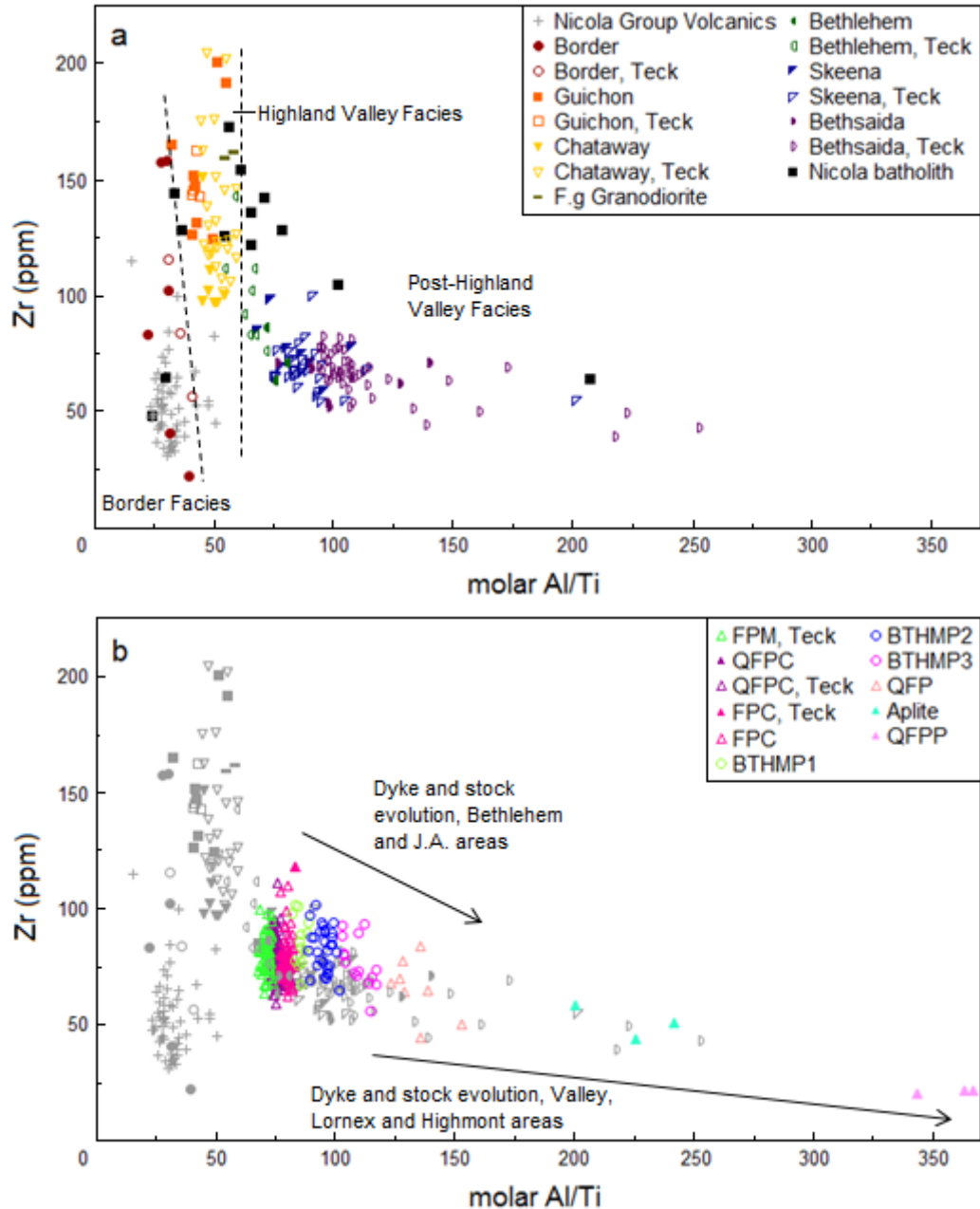
Figure 4.9 Plot of Zr (ppm) vs.. molar Al/Ti for A. the main intrusive facies and B. the porphyry dyke and stock facies of the Guichon Creek Batholith. The batholith-scale facies can be sub-divided into three groups on the basis of molar Al/Ti and Zr with moderate overlap between facies/sub-facies in each group. Porphyry stocks and dykes in the Bethlehem area can be defined by their molar Al/Ti ratios and compositions overlap with the Bethlehem sub-facies and evolve towards the Bethsaida facies. Dykes from the Valley, Lornex and Highmont areas overlap with Bethsaida compositions and evolve to high molar Al/Ti with decreasing Zr. Data is a compilation of samples collected as part of this study with additional regional and deposit scale samples provided by Teck. Figures modified after Byrne et al. (2013). All lines fit by hand.
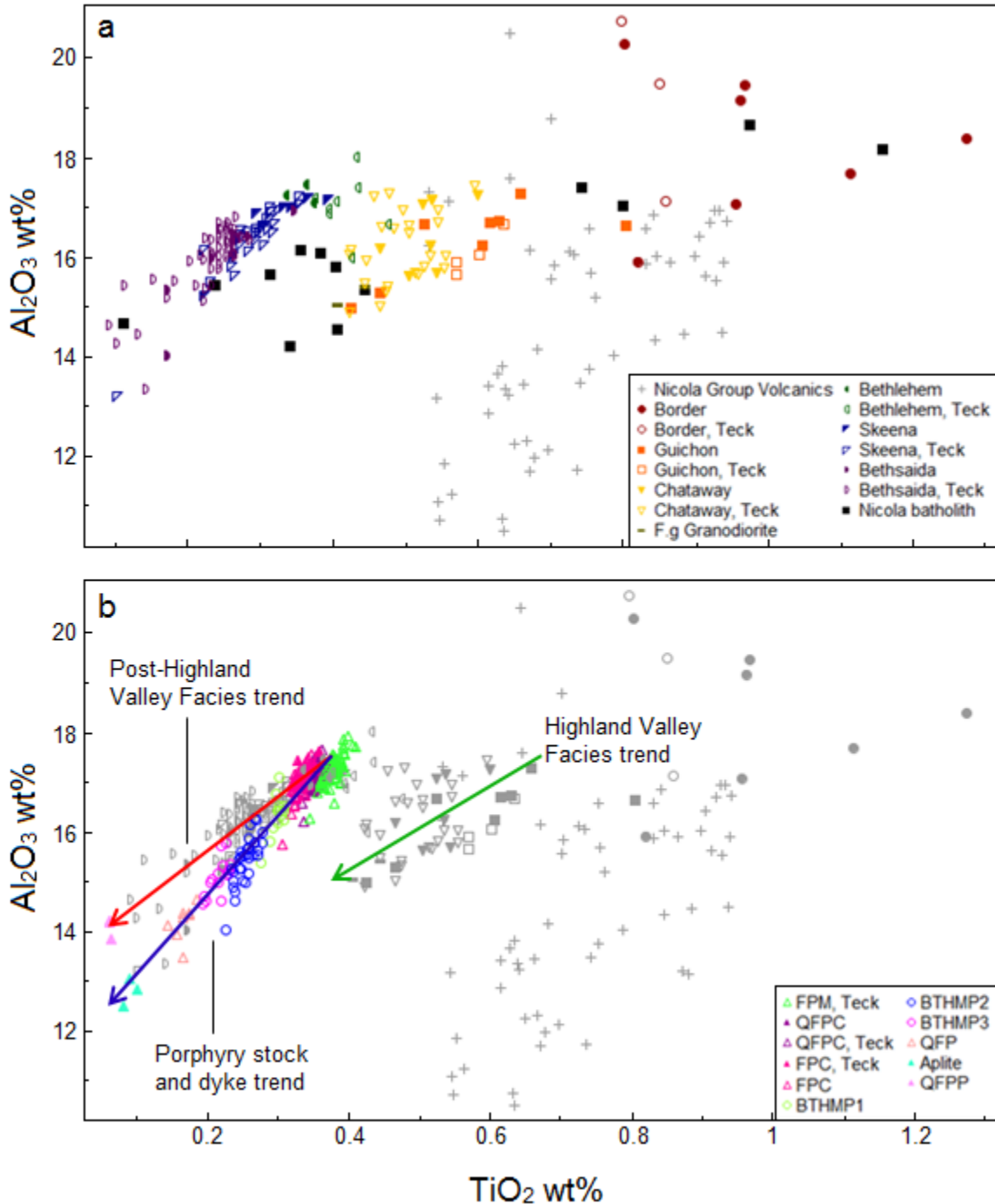
Figure 4.10 Plot of Al_2O_3 vs. TiO_2 for A. the main intrusive facies and B. the porphyry stocks and dykes of the Guichon Creek Batholith. A. Samples are subdivided into three groups as in the Zr vs. Al/Ti_{mol} diagram. B. Three possible batholith-scale geochemical evolution trends. The Highland Valley Trend is followed by the Guichon and Chataway sub-facies separately from the Bethlehem and later facies. Both the Post-Highland Valley facies and Porphyry stock and dyke trends start at Bethlehem Facies compositions but evolve along slightly different paths. The three evolution trends have been delineated graphically and there is no statistical significance ascribed to the lines that define them.

fractionation paths for rocks in the Bethlehem and J.A. area (Bethlehem Trend) and

Valley, Lornex and Highmont area (Valley Trend; Fig. 4.9b). This suggests that the

Bethlehem and Valley deposits share a broadly similar parental magma source, but

were isolated from each other prior to and during crystallization and subsequent

mineralization, possibly as two separate apophyses derived from a deep seated pluton.

4.4.4 Magma Fertility and Genesis

Plots of Al_2O_3/TiO_2, Sr/Y and V/Sc vs. SiO_2 wt% were constructed to assess the

fertility of the Guichon Creek and Nicola Batholith magmas and the potential for

porphyry-Cu exploration. Samples were screened for those that were least altered and

without significant plagioclase accumulation and 22 samples were excluded; 20 of

which belonged to the expanded dataset provided by Teck. The selection criteria were

those set out by Loucks (2014) and are summarized as follows:

1. Loss on ignition (LOI) <3.5 wt%

2. Volatile-free analytical totals between 97.5 to 101.5 wt%

3. Absence of significant plagioclase destructive alteration based on inspection of hand samples and thin sections when available

4. Samples do not represent plagioclase crystal cumulates, with no samples having >20 wt% Al_2O_3 or positive europium anomalies (Eu/Eu* > 1.3)

5. All samples belong to the calc-alkalic magma series as defined by Irvine and Baragar (1971)

6. No samples are of the alkali or absarokite-shoshonite-banakite series as defined by Peccerillo and Taylor (1976; Fig. 4.6)

These plots were selected as they have been shown by Loucks (2014) to be effective at discriminating between average infertile arc magmas and fertile arc magmas rich in H_2O (5 to 6 wt%) and other volatiles which can be contributed to a porphyry Cu-Au-($\pm$Mo) system. In hydrous magmas, the plagioclase saturation point is suppressed and hornblende begins to fractionate early causing elements that partition into hornblende (Ti, Y, Sc) to be depleted and those that partition into plagioclase (Al, Sr) to be concentrated in the residual melt (Loucks, 2014). As a result, element ratios reflecting the modal proportions of hornblende and plagioclase crystallizing from a melt can be used as a proxy for the H_2O content of a magma (Loucks, 2014). Consequentially, Al_2O_3/TiO_2 and Sr/Y ratios should increase in wet magma series and remain flat or decrease in dry magma series with increasing SiO_2 wt% (Loucks, 2014). If hornblende begins to fractionate before titanomagnetite in H_2O-rich magmas, it can deplete much of the Fe^{3+} and Fe^{2+} and leave V in the residual melt (Loucks, 2014). The depletion in Fe further suppresses the formation of titanomagnetite and the result should be an increase in V/Sc ratios over time as Sc is partitioned into hornblende and V left in the melt (Loucks, 2014).

Samples from all facies of the Guichon Creek Batholith show increasing Al_2O_3/TiO_2, Sr/Y and V/Sc with increasing SiO_2 wt% (Figs. 4.11 and 4.12). The Nicola Batholith displays Al_2O_3/TiO_2 and Sr/Y trends similar to the Guichon Creek Batholith (Figs. 4.11 and 4.12). The V/Sc ratio for the Nicola Batholith increases until ~65 to 70 wt% SiO_2 and then decreases with further increases in SiO_2 wt% (Fig. 4.11). The increase in Al_2O_3/TiO_2 and Sr/Y ratios with increasing magma differentiation (Figs. 4.11 and 4.12) is indicative of the early suppression of plagioclase crystallization followed by
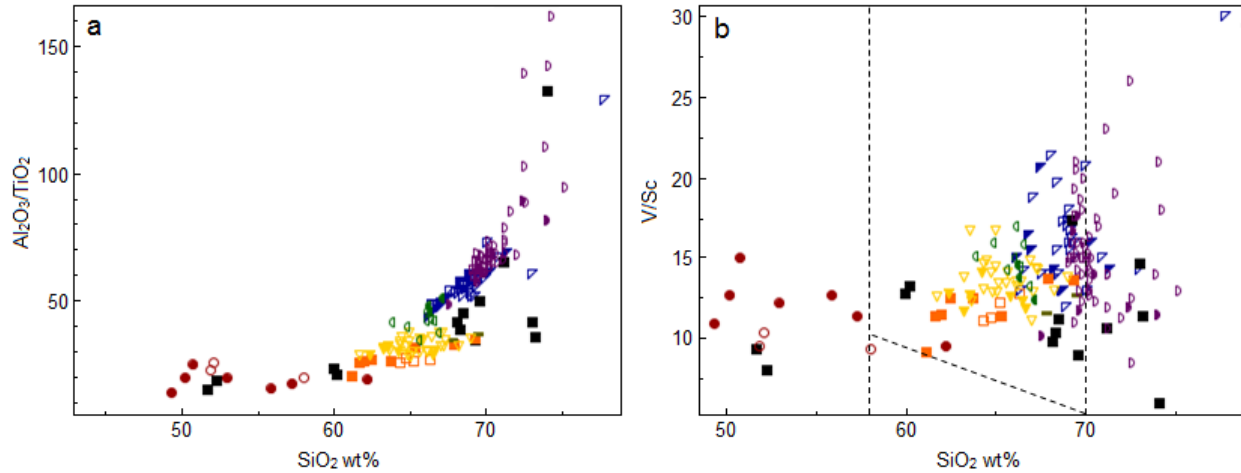
Figure 4.11 A. A plot of Al_2O_3/TiO_2 vs. SiO_2 wt% for the Guichon Creek and Nicola batholiths. A sharp increase in the Al_2O_3/TiO_2 ratio indicates the depletion of Ti and concentration of Al in the residual melt. B. A plot of V/Sc vs. SiO_2 wt% for the Guichon Creek and Nicola batholiths. A modest increase in the V/Sc ratio indicates the depletion of Sc and concentration of V in the residual melt during crystallization. The sloped line is defined by the equation $32.5 - 0.385 \times SiO_2$ wt%. Samples that fall above this line and between 58 and 70 SiO_2 wt% are considered to represent fertile magmas prospective for porphyry copper mineralization (Loucks, 2014). Refer to Figure 4.1 for legend.
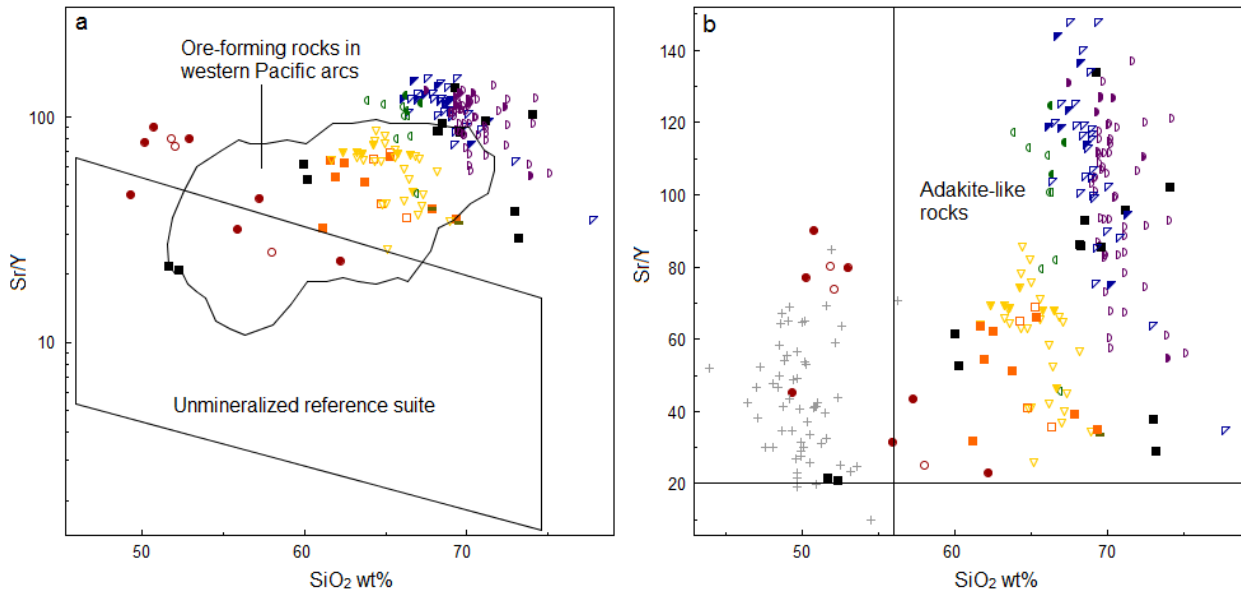
Figure 4.12 Plots of Sr/Y vs. SiO_2 wt% for the Guichon Creek and Nicola batholiths. A. An increase in the Sr/Y ratio indicates the depletion of Y and concentration of Sr in the residual melt during crystallization. The majority of samples plot in or well above the ore-forming igneous suite defined by Loucks (2014). B. Most samples display adakite-like affinities (after Richards and Kerrich, 2007; Richards et al., 2012; boundaries from Defant and Drummond, 1990; 1993). Solid circles represent samples collected as part of the CMIC footprints project. Hollow circles represent unpublished data provided by Teck. Refer to Figure 4.1 for legend.

114

increased plagioclase crystallization in both the Guichon Creek and Nicola batholiths. This can be caused by differentiation of magmas with high water contents (5-6 wt% H_2O) in the magma or by increasing the pressure of crystallization up to ~1GPa (Moore and Carmichael, 1998; Müntener et al., 2001; Loucks, 2014) and it is likely most effective in continental arcs with thick overriding plates (Chiaradia, 2014). Using Loucks (2014) cutoff values of Sr/Y > 40, and SiO_2 > 58 and increasing, it can be observed that most of the samples from the Guichon Creek and Nicola batholiths should be considered fertile and prospective for porphyry copper mineralization. It should be noted, however, that high Sr/Y magmas have been reported in apparently barren volcanic complexes (e.g. the Chachimbiro volcanic complex in Ecuador; Bellver-Baca and Chiaradia, 2015) which formed over relatively small timescales (<0.5 Ma). Long lasting magmatic cycles (several Ma) may be required to generate fertile high Sr/Y magmas through generation of larger magma reservoirs (Bellver-Baca and Chiaradia, 2015) and/or by favouring metal and volatile enrichment in late high Sr/Y magmas (Rohrlach and Loucks, 2005).

The increase in V/Sc with increasing SiO_2 observed for the Guichon Creek and Nicola batholiths (Fig. 4.11) is likely the result of high water contents and oxygen fugacities in their parent magmas. High water contents can lead to early hornblende crystallization acting as a sink for Sc, Fe^{3+} and Fe^{2+} thereby supressing titanomagnetite crystallization (Loucks, 2014). Although V and Sc behave similarly during mantle melting, they are not mobile in fluids and both mildly incompatible (Lee et al., 2005); the speciation and partition coefficient for V, however, is strongly dependent on fO_2 (Lindstrom, 1976; Lee et al., 2005). Partition coefficients for oxidized V^{4+} and V^{5+} are

significantly greater than those for V^{3+} in all minerals and are an order of magnitude lower in silicate minerals than in titanomagnetite (Lindstrom, 1976). Fractional crystallization of a hydrous, oxidized magma at depth results in removal of Sc from the residual melt by hornblende crystallization and a buildup of V as titanomagetite crystallization is suppressed and it is incompatible in silicates in the oxidized state (V^{4+} and V^{5+}). The V/Sc ratios suggest that both batholiths are fertile and prospective for porphyry copper mineralization as all samples in the 58 to 70 wt% SiO_2 wt% range plot above the fertile/infertile cutoff line 32.5 – 0.385 x SiO_2 wt% (Loucks, 2014).

In Sr/Y vs. SiO_2 and Sr/Y vs. Y diagrams, most samples from both batholiths lie in the field for adakite-like rocks (Figs. 4.12b and 4.13a). Previous workers have noted a spatial association between high Sr/Y "adakites" and porphyry Cu-Au deposits (Thiéblemont et al., 1997; Sajona and Maury, 1998). In some cases, it has been inferred that the production of adakites by slab melting of eclogite facies subducted aseismic ridges, seamounts and oceanic plateaus is critical to the formation of giant and supergiant porphyry-Cu deposits (Mungall, 2002; Cooke et al., 2005). Mungall (2002) argued that adakite magmas produced by slab melting may be a key factor in oxidizing the mantle wedge in fertile porphyry-Cu-Au subduction zones by introducing high Fe^{3+} contents derived from the subduction and melting of oxidized seafloor basalts. Work by Cline and Bodnar (1991), Cline (1995) and Richards (2011) has shown that normal evolutionary processes involving amphibole (± garnet) fractionation in hydrous calc-alkaline magmas can also produce oxidized, high Sr/Y magmas with Cu budgets favourable for porphyry-Cu formation, indicating that melting of oceanic lithosphere is not required to produce fertile porphyry magmas and in fact may be a special case.

116
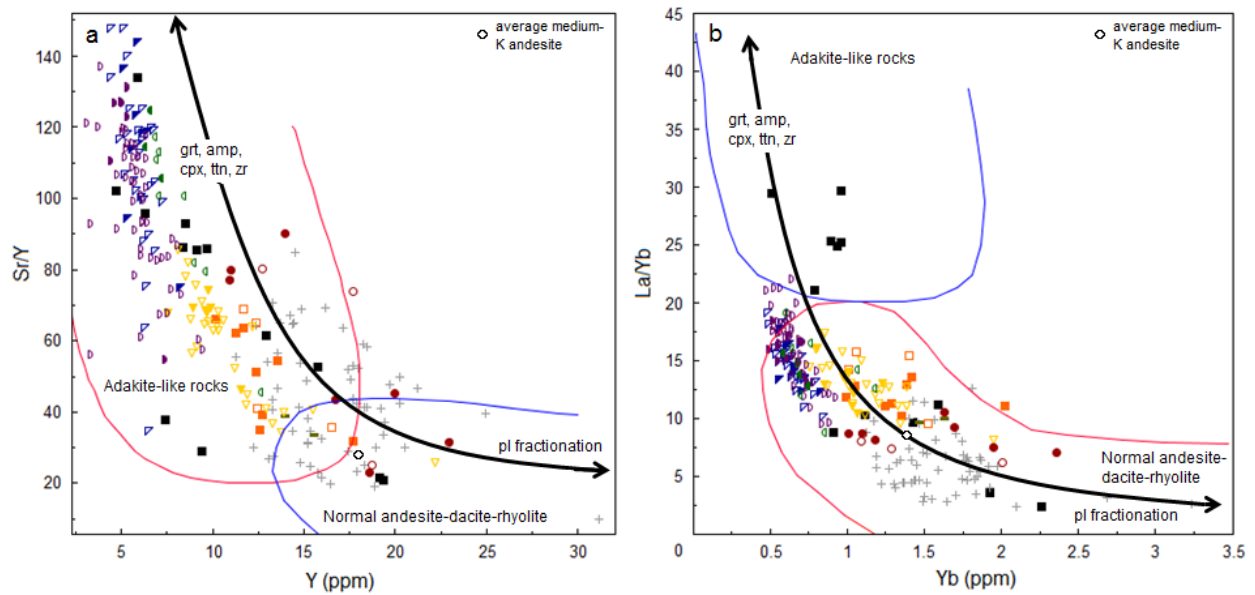
Figure 4.13 Plots of A. Sr/Y vs Y and B. La/Yb vs Yb for the Guichon Creek and Nicola batholiths. Adakite fields from Richards and Kerrich (2007). Normal island-arc andesite-dacite-rhyolite fields from Castillo et al. (1999). Fractionation trends from Castillo et al. (1999) and Richards and Kerrich (2007) modeled assuming an average medium-K calc-alkaline andesite (Gill, 1981) and partition coefficient values from Bachman et al. (2005). Refer to Figure 4.1 for legend.

Additionally, the melting of trench-fill sediments, likely to accompany slab melting, produce reducing mixed melts rather than the oxidized melts typical of porphyry settings if these sediments contain significant organic matter (Wang et al., 2007).

Direct evidence for shallow subduction of hot lithosphere beneath the Quesnel Terrane during the Late Triassic is lacking unlike in younger porphyry-Cu-Au provinces (e.g., the Inca Plateau in Northern Peru and the Nazca and Juan Fernandez Ridges in Northern and Central Chile; Cooke et al., 2005). It is therefore critical to evaluate whether or not the Guichon Creek and Nicola Batholith magmas represent true adakites as this interpretation can have significant impact on any model considering the formation of the Highland Valley porphyry deposits. A comparison of the Guichon Creek and Nicola

Table 4.3 Test of the Guichon Creek and Nicola batholiths against select geochemical characteristics of adakites. Criteria compiled by Richards and Kerrich (2007).

Unit	n=	Sr (≥400 ppm)	Y (≤18 ppm)	Yb (≤1.9 ppm)	Ni (≥20 ppm)	Cr (≥30 ppm)	Sr/Y (≥20)	La/Yb (≥20)	Mg# (≈0.5)
Guichon Creek Batholith									
Border	10	Yes	Some	Most	No	No	Yes	No	0.34
Guichon	12	Yes	Yes	Most	One	No	Yes	No	0.31
Chataway	32	Yes	Most	Most	No	No	Yes	No	0.31
Bethlehem	13	Yes	Yes	Yes	No	No	Yes	No	0.27
Skeena	36	Most	Yes	Yes	No	No	Yes	No	0.23
Bethsaida	58	Most	Yes	Yes	No	No	Yes	Few	0.21
FQPC	5	Most	Yes	Yes	No	No	Yes	No	0.24
FPC	8	Most	Yes	Yes	No	No	Yes	No	0.24
Tan Porphyry	3	No	Yes	Yes	No	No	Most	No	0.21
Aplite	3	No	Yes	Yes	No	No	One	Yes	0.11
FPM	1	Yes	Yes	Yes	No	No	Yes	No	0.18
Nicola Batholith	13	Most	Most	Most	No	No	Yes	~Half	0.26

batholiths against some key geochemical characteristics of adakites as compiled by Richards and Kerrich (2007) is shown in Table 4.3. Most samples pass the major and trace element tests for SiO_2, Na_2O, K_2O, Rb, Sr, Y and Yb content as well as Sr/Y ratio (see also: Fig. 4.12b and 4.13a), however, they fail the critical tests for Ni and Cr content as well as La/Yb ratios and Mg# (Table 4.3). Furthermore, on the La/Yb vs. Yb plot (Fig. 4.13b) most samples lie in the field for normal andesite-dacite-rhyolite. This is consistent with the assimilation-fractional-crystallization (AFC; DePaolo, 1981b), and/or deep crustal melting in the melting-assimilation-storage-homogenization (MASH; Hildreth and Moorbath, 1988) models involving a combination of garnet, amphibole, clinopyroxene, titanite and/or zircon with little to no plagioclase fractionation in a deep- to mid-crustal magma reservoir prior to emplacement (Kerrich and Richards, 2007; Richards, 2011). The large number of samples plotting outside the adakite-like rock field

on the plot of La/Yb vs. Yb relative to the Sr/Y vs. Y plot is likely due to the similar behaviour of La and Yb during fractional crystallization and different behaviour of Sr and Y dependent upon the fractionating mineral phases.

Chondrite normalized La/Sm$_{cn}$ and Gd/Yb$_{cn}$ (Fig. 4.14) increase from ~1 to ~13 and a slight decrease from ~3 to ~0.5, respectively, with increasing SiO$_2$. This is consistent with hornblende fractionation (increasing LREE/MREE and steady or decreasing MREE/HREE ratios). It is not, however, consistent with garnet fractionation or melt separation in a restite which would result in increasing LREE/MREE and increasing MREE/HREE ratios. These expected trends result from hornblende's moderate affinity for MREE and garnet's strong affinity for HREE (Rollinson, 1993). La/Sm$_{cn}$ values are generally >2.0 and show a small increase with decreasing age, peaking during the emplacement of the Bethsaida facies and aplite dykes (Fig. 4.15). The progressive enrichment of the LREE most likely results from
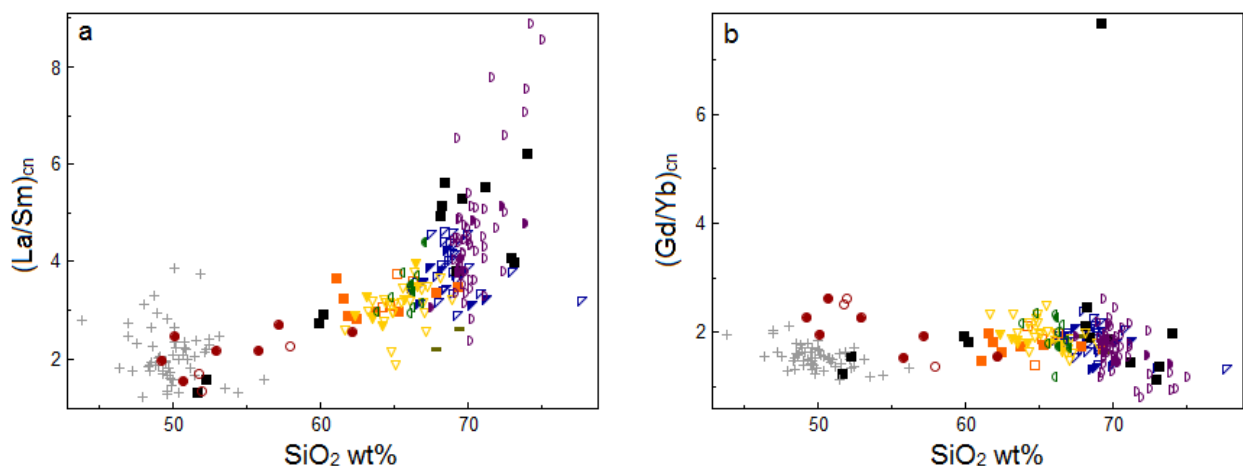
Figure 4.14 C1 chondrite-normalized La/Sm$_{cn}$ and Gd/Yb$_{cn}$ ratios vs. SiO$_2$ wt% for the Guichon Creek and Nicola batholiths. Normalization values of Sun and McDonough (1989). Refer to Figure 4.1 for legend.

progressive fractionation in a magma chamber. Gd/Yb$_{cn}$ values are generally low, <2.0,

implying melting in a relatively shallow source region above the garnet stability zone.

There are two progressive decreases in Gd/Yb$_{cn}$ values with decreasing age starting

around the time of mineralization at the Bethlehem and Valley deposits (Fig. 4.16). This

change cannot be tied to a concurrent change in La/Sm$_{cn}$ values and is likely the result

of the MREEs fractionating into hornblende on a deposit-scale.

Primitive mantle normalized multi-element diagrams for the main facies and dyke

rocks of the Guichon Creek Batholith as well as those for the Nicola Batholith (Figs.

4.17 and 4.18) are broadly similar to those of basalts from the Nicola Group and all

display large negative Ta, Nb and Ti anomalies which are characteristic features of arc

magmas (Pearce et al., 1984). The coherent patterns observed for the Guichon through
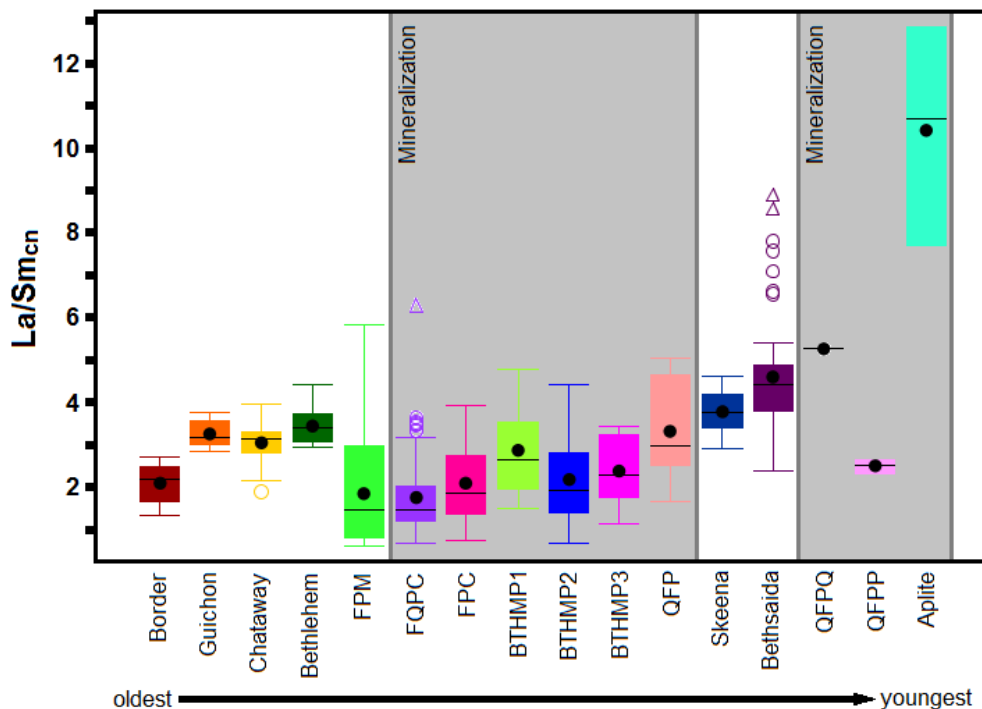
Figure 4.15 Tukey plot of La/Sm$_{cn}$ vs. relative age for the intrusive facies of the Guichon Creek Batholith. Data set is a compilation of data acquired for this study with additional data provided by Teck.
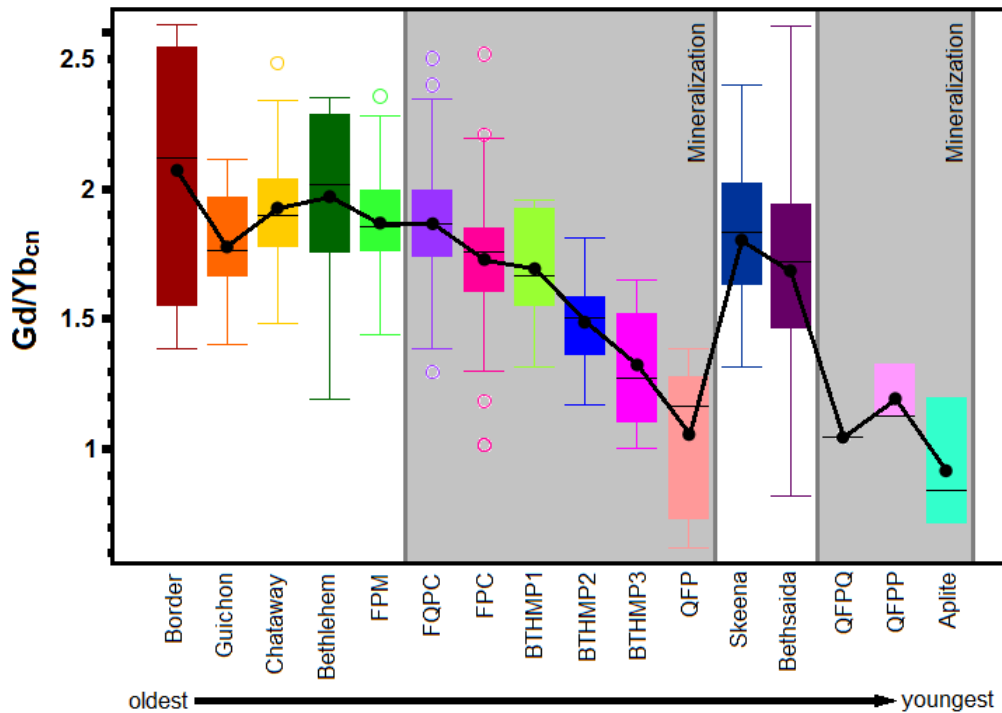
Figure 4.16 Tukey plot of Gd/Yb$_{cn}$ vs. relative age for the intrusive facies of the Guichon Creek Batholith. Data set is a compilation of data acquired for this study with additional data provided by Teck.

Bethsaida facies (Fig. 4.17 b-f) are consistent with limited alteration. The variation in the LILEs and large positive to negative Hf-Zr anomalies of the Border facies (Fig. 4.17a) are likely the result of varying degrees of localized contamination and assimilation of the country rocks during emplacement. A clear evolution from flat-lying REE patterns in the older Border and Guichon facies to increasingly concave-upwards REE patterns in the Chataway through Bethsaida facies (including the porphyry stocks and dykes) as well as a gradual decrease in MREE and HREE abundances relative to the reference Nicola Group basalts is also evident on these plots (Fig. 4.17 and Fig. 4.18). A similar variation is also observed for primitive mantle normalized multi-element diagrams for the Nicola Batholith (Fig. 4.18). Such concave-upwards REE patterns with small Eu anomalies are

121

observed for rocks of many of the porphyry copper deposits in the southwestern United States (Leveille and Stegen, 2012) where they have been attributed to fractionation of hornblende and Fe-Ti oxides with little to no plagioclase fractionation.

4.5 Summary and Conclusions

Geochemically, the Guichon Creek Batholith is classified as magnesian, calcic to calc-alkalic (MALI = -5 to 7.3) and metaluminous to weakly peraluminous (ASI = 0.77 to 1.28; AI = 0.02 to 0.13). Major and trace element variations are consistent with progressive fractional crystallization of the contained mineral phases. Rocks of the Guichon Creek Batholith belong predominantly to the medium-K calc-alkaline series, with the exception of a number of Border facies samples, which are low-K tholeiitic. A number of samples from the remaining facies are high-K calc-alkalic. A plot of Zr vs. molar Al/Ti has been effective to discriminate between the Border, Highland Valley and Bethlehem-Skeena-Bethsaida facies, and on a plot of Al_2O_3 vs. TiO_2, these three groups all follow similar but different trends of decreasing Al_2O_3 with decreasing TiO_2.

High magmatic H_2O contents and relatively oxidizing conditions in the Guichon Creek Batholith magmas are suggested by geochemical indicators of magmatic fertility (Sr/Y, V/Sc, Al_2O_3/TiO_2). The high Sr/Y ratios observed for the Guichon Creek Batholith are accompanied by low La/Yb ratios, indicating adakitic slab melts did not play an important role in generating fertile porphyry magmas. Instead, the high Sr/Y ratios are the result of fractionation of amphibole and clinopyroxene, but suppression of plagioclase fractionation from a hydrous magma at depth and on the timescale of ~3 m.y. Amphibole fractionation at depth is also supported by MREE fractionation relative
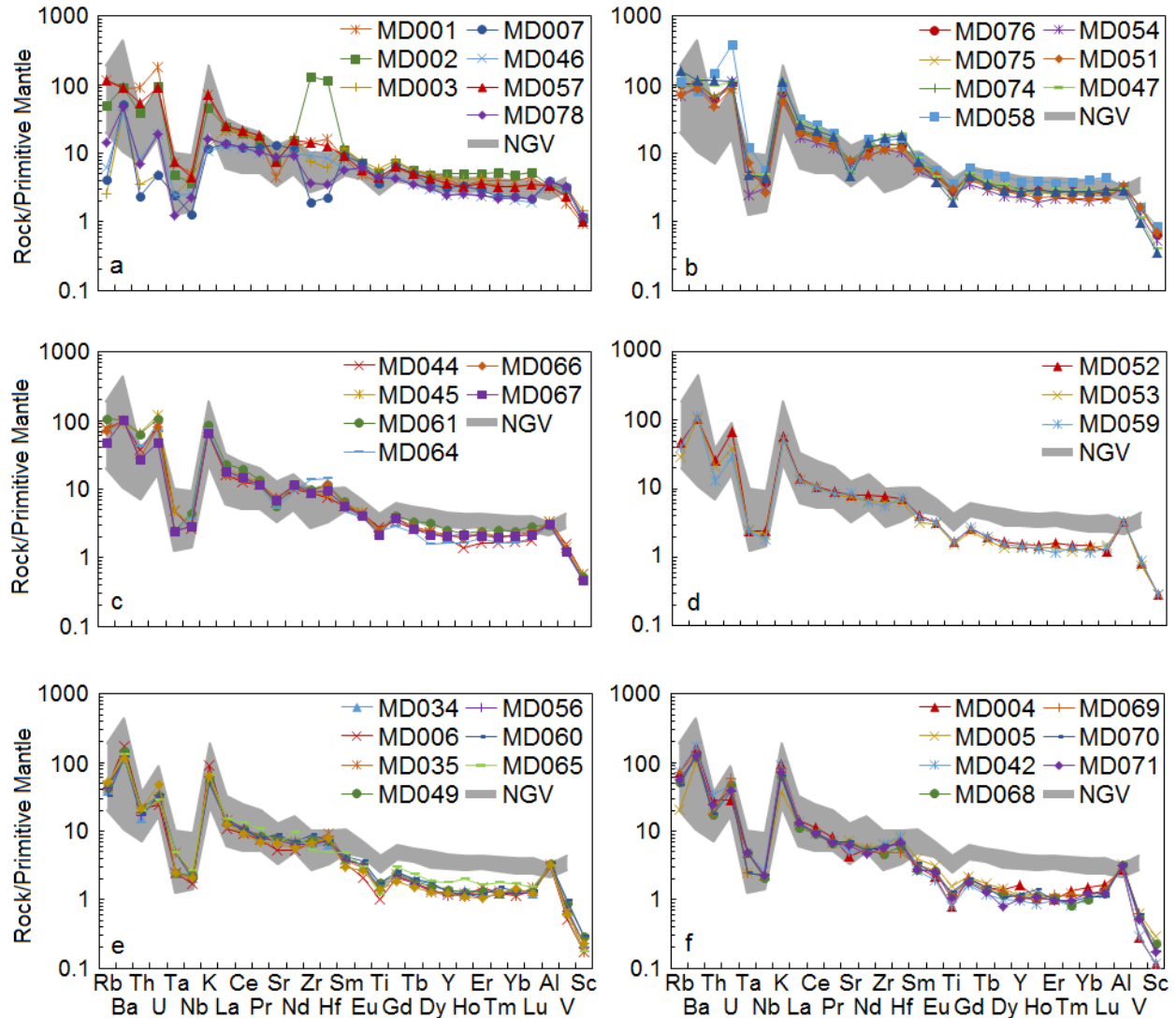
Figure 4.17 Primitive mantle normalized multi-element diagrams for the main intrusive facies of the Guichon Creek Batholith. A. Border facies, B. Guichon sub-facies, C. Chataway sub-facies, D. Bethlehem facies, E. Skeena facies and F. Bethsaida facies. Normalizing values from Sun and McDonough (1989). NGV = Nicola Group Volcanics, data from Vaca (2012).

to the LREE and HREE (Fig. 4.13) producing concave-upwards primitive mantle normalized multi-element patternss (Fig. 4.17).

The Nicola Batholith is geochemically similar to the Guichon Creek Batholith. It is also magnesian and metaluminous to weakly peraluminous in composition, but the rocks exhibit a compositional trend that crosses from the calcic field into the calc-alkalic
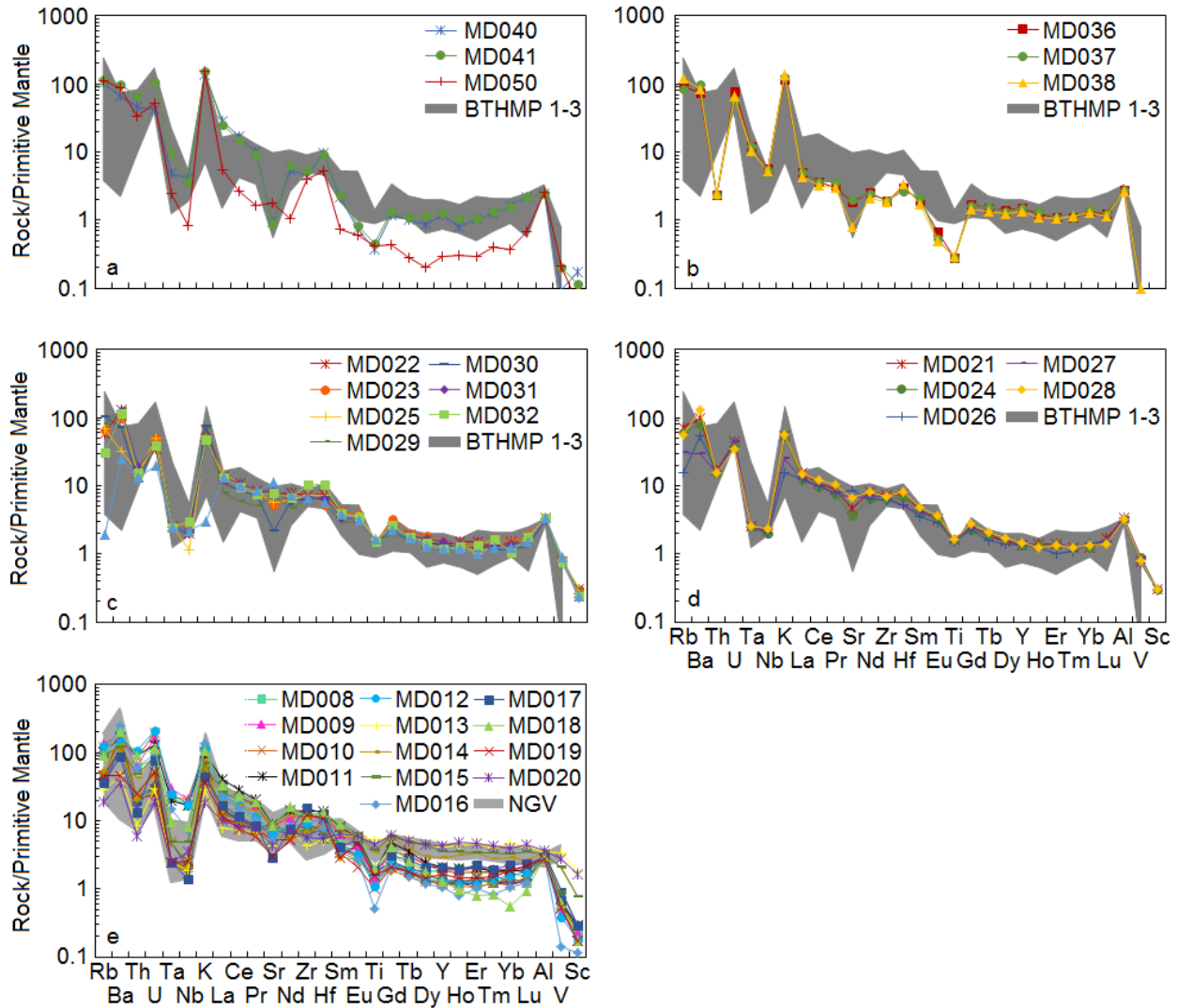
Figure 4.18 Primitive mantle normalized multi-element diagrams for the porphyry stocks and dykes of the Guichon Creek and Nicola batholiths. A. aplite dykes, B. QFPP (Tan Porphyry) dykes, C. FPC dykes, D. QFPC dykes and E. Nicola Batholith. Normalizing values from Sun and McDonough (1989). NGV = Nicola Group Volcanics, data from Vaca (2012). BTHMP 1-3 = Bethlehem Porphyry 1,2 and 3 dykes, data provided by Teck.

and alkali-calcic fields on the MALI diagram. This is likely due to contamination by a

crustal source with an alkali-calcic or alkalic MALI composition, although no such source

has yet been identified due to poor exposure in the area. High and increasing Sr/Y,

Al_2O_3/TiO_2 and V/Sc with increasing SiO_2 suggest that the Nicola Batholith magmas

were fertile and should be favourable for porphyry-Cu (±Au) exploration. However, the

124

Paleocene to late Eocene crystallization ages reported by Preto et al. (1979) indicate

that it was emplaced after the ~173 Ma Middle Jurassic accretion of the Intermontane

Superterrane onto western Laurentia (Mihalynuk et al., 2004), meaning that any

porphyry-style mineralization would have to be of the post-accretionary type.

CHAPTER 5   RADIOGENIC ISOTOPE GEOCHEMISTRY

5.1 Introduction

Fourteen samples from the Guichon Creek Batholith were analyzed for Rb-Sr, and Sm-Nd isotopes at Memorial University, St. John's, Newfoundland (Fig. 5.1). The sample suite is representative of the six main intrusive facies comprising the Guichon Creek Batholith, including four samples of the Border facies and two samples each from the Guichon, Chataway, Bethlehem, Skeena and Bethsaida facies. Regional data sets from the adjacent Nicola Group, the Quesnel terrane, the oceanic Slide Mountain and Cache Creek terranes, as well as the Precambrian to Late Triassic sedimentary rocks of the paleomargin of western North America were compared to data for the Guichon Creek Batholith from this study to help constrain the emplacement of the batholith in the geologic framework of the Intermontane Superterrane and southern Canadian Cordillera.

5.2 Previous Studies

Previous isotopic studies in the Quesnel terrane have largely focused on the Sm-Nd systematics of the sedimentary rocks of the Nicola, Slocan and Ymir Groups which have $\in_{Nd(140-220Ma)}$ values that vary from -12.4 to +6.4 (Unterschutz et al., 2002; Ghosh and Lambert, 1989; Patchett and Gehrels, 1998; Petersen et al., 2004). Volcanic rocks of the Nicola Group have a tighter range (+3.6 to +7.9) of $\in_{Nd(222Ma)}$ values (Smith et al., 1995; Patchett and Gehrels, 1998). The Paleozoic basement to the younger, Triassic Nicola arc consists of volcanic and sedimentary rocks of the
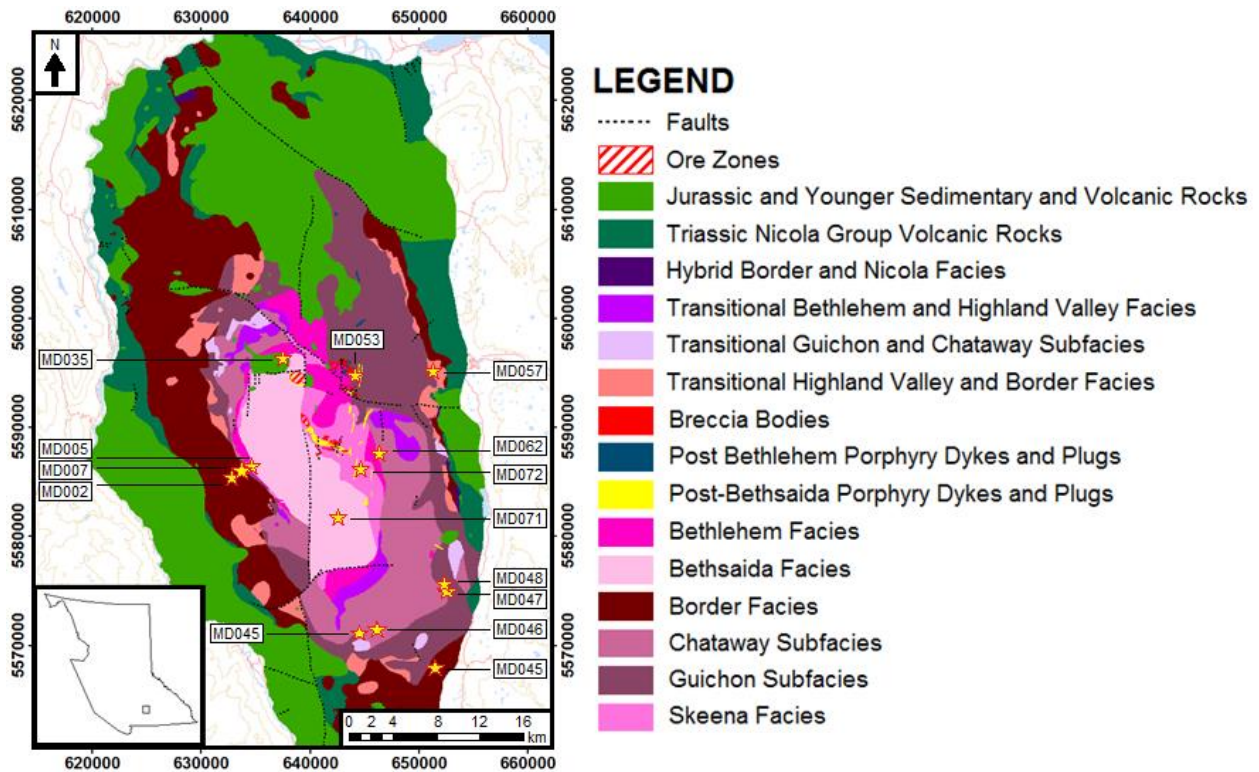
Figure 5.1 Locations of samples selected for radiogenic isotope analysis.

Harper Ranch and Okanagan subterranes and have a large variation in

$\epsilon_{Nd(270-300Ma)}$ values from +3.4 to +11.6 (Patchett and Gehrels, 1998; Dostal et al.,

2001). A transition from primitive $\epsilon_{Nd(140-220Ma)}$ values in the west to more evolved

values in the east has been observed in sedimentary rocks of the Quesnel terrane

(Patchett and Gehrels, 1998; Unterschutz et al., 2002). It has been suggested that this

isotopic variation reflects derivation of Quesnel terrane sediments from a primitive

(Nicola arc) source to the west and an evolved (western North American passive margin

sediments with $\epsilon_{Nd(217-600Ma)}$ = -6.8 to -10.7; Jackson, 1992; Boghossian et al.,

1996) source to the east (Patchett and Gehrels, 1998; Unterschutz et al., 2002) which is

consistent with a provenance study of Paleozoic sedimentary rocks from the Harper Ranch assemblage (Roback and Walker, 1995).

5.3 Methodology

5.3.1 Analytical Procedure

Prior to acid digestion, a mixed ^{150}Nd/^{149}Sm spike was added to each sample. Whole rock powders were then dissolved in Teflon beakers using an 8 ml (4:1) mixture of 29 M HF – 15 M HNO$_3$. After five days of digestion, the solutions were evaporated to dryness and re-dissolved in 6M HCl for three days. Samples were dried down and re-dissolved in 1.0 ml of 2.5 M HCL before being loaded onto a column containing cation exchange resin AG-50W-X8, H+ form, (200-400 mesh) to isolate a Sr fraction, followed by collection of bulk rare earth elements (REE). This solution was then dried, taken up in 0.18 M HCl and loaded on a second column containing Eichrom© Ln resin (50-100 mesh) to isolate Sm and Nd separately from the other REE. The Sr fraction was also evaporated to dryness and then taken up in 3M HNO$_3$ and loaded onto a column containing Eichrom© Sr resin to separate out the Sr and remove Rb and other remaining elements.

Samarium and Nd concentrations and the Nd and Sr isotopic compositions were determined using a multi-collector Finnigan Mat 262 mass spectrometer in static mode for concentration determination, and dynamic mode for isotopic composition determination. Samarium and Nd were loaded onto a double rhenium filament assembly whereas Sr was loaded onto a single tungsten filament with 2 µL of Sr activator (tantalum fluoride). Instrumental mass fractionation of Sm and Nd isotopes were corrected using a Raleigh law relative to ^{146}Nd/^{144}Nd = 0.7219 and ^{152}Sm/^{147}Sm = 1.783.

Measured values were adjusted to the JNdi-1 standard (^{143}Nd/^{144}Nd = 0.512115;

Tanaka et al., 2000). Measured values of JNdi-1 yielded a mean ^{143}Nd/^{144}Nd =

0.512098 ± 8 (1σ, n=20). Sr ratios were normalized to ^{88}Sr/^{86}Sr = 8.375202 and

measured values were adjusted to the NBS-987 standard. Measured values of NBS-

987 yielded a mean ^{87}Sr/^{86}Sr = 0.710251 ± 14 (1σ, n=20).

Reproducibility of the Sm-Nd analyses was evaluated by analyzing USGS whole

rock reference material BCR-2 with each analysis as a separate dissolution. The mean

values of BCR-2 were as follows, where the relative two standard deviations of the

mean (n = 12) are given in percent in parenthesis; ^{143}Nd/^{144}Nd = 0.512636 (0.0026%);

^{147}Sm/^{144}Nd = 0.1383 (0.346%); Nd ppm=27.7 (0.7%); Sm = 6.32 (0.6%).

Reproducibility of the Rb-Sr analyses was evaluated by analyzing USGS whole rock

reference material BCR-2 with a mean value of ^{87}Sr/^{86}Sr = 0.704987 ± 0.000013 (1σ) for

n = 5 analyses.

5.3.2 Data Presentation

Isotopic data for Nd is presented in terms of $\in_{Nd(T)}$ or the deviation in parts per

10^4 of the sample's initial ^{143}Nd/^{144}Nd ratio from the ^{143}Nd/^{144}Nd ratio of the chondritic

uniform reservoir (CHUR) as defined by DePaolo and Wasserburg (1976, 1977):

$$\in_{Nd(T)} = \ 10^4 \left[\frac{^{143}Nd/^{144}Nd_{Rock}(T)}{^{143}Nd/^{144}Nd_{CHUR}(T)} - 1 \right]$$

The ratio ^{143}Nd/^{144}Nd$_{CHUR}$(T) was calculated using the following equation (DePaolo,

1981a):

$$^{143}Nd/^{144}Nd_{CHUR}(T) = 0.512638 - 0.1966(e^{\lambda_{Sm}T} - 1)$$

where λ_{Sm} = 6.54 x 10^{-12} yr^{-1} (Dickin, 2005), T is time measured backward from the present and the constants are $^{143}Nd/^{144}Nd_{CHUR}(0)$ and $^{147}Sm/^{144}Nd_{CHUR}(0)$, where 0 – the present day, respectively (Dickin, 2005). Strontium isotope data is presented as initial $^{87}Sr/^{86}Sr$ ratios ($^{87}Sr/^{86}Sr_i$).

5.4 Results

The isotopic analyses are presented in Table 5.1. Initial $^{143}Nd/^{144}Nd$ and $^{87}Sr/^{86}Sr$ ratios were calculated assuming the average U-Pb zircon age reported for the respective facies from Alfaro (2015, pers. comm.).   Nd isotope data is reported as values of epsilon Nd at the time of formation ($\epsilon_{Nd(T)}$) and at present day ($\epsilon_{Nd(0)}$). All facies exhibit consistently positive $\epsilon_{Nd(T)}$ values and there is little variation in and between facies, with the exception of the Border facies: Border facies (+6.7 to +7.1), Guichon facies (+7.1 to +7.5), Chataway facies (+7.1), Bethlehem facies (+7.1 to +7.2), Skeena facies (+7.0) and Bethsaida facies (+7.1). Initial $^{87}Sr/^{86}Sr$ ratios define a narrow range with values as follows: Border (0.70340 to 0.70356), Guichon (0.70348 to 0.70349), Chataway (0.70337 to 0.70339), Bethlehem (0.70339 to 0.70348), Skeena (0.70337 to 0.70341) and Bethsaida (0.70340).

5.5 Discussion

Figure 5.2 shows the composition of the Guichon Creek Batholith relative to Nicola Group volcanic rocks and the key mantle reservoirs (Zindler and Hart, 1986) in $^{143}Nd/^{144}Nd_i$ vs. $^{87}Sr/^{86}Sr_i$ space. The Guichon Creek Batholith is depleted relative to the

Table 5.1 Results of Sm-Nd and Rb-Sr analyses for samples from the Guichon Creek Batholith.

Sample	Facies	Age (Ma)	Sm (ppm)	Nd (ppm)	$^{147}Sm/^{144}Nd$	$^{143}Nd/^{144}Nd_{(m)}$	± 2σ	$^{143}Nd/^{144}Nd_{(i)}$	$\epsilon_{Nd(0)}$	$\epsilon_{Nd(T)}$
MD002	Border	211.02	4.58	20.21	0.137	0.512921	7	0.51273	5.5	7.1
MD005	Bethsaida	208.5	1.68	8.67	0.1173	0.512895	7	0.51274	5	7.1
MD007	Border	211.02	4.08	16.98	0.1452	0.512929	6	0.51273	5.7	7.1
MD035	Skeena	208.37	1.83	9.49	0.1167	0.512889	6	0.51273	4.9	7
MD045	Chataway	210.57	3	15.34	0.1182	0.512892	7	0.51273	5	7.1
MD046	Border	211.02	2.88	12.91	0.135	0.512896	7	0.51271	5	6.7
MD047	Guichon	210.57	3.5	18.63	0.1137	0.512907	28	0.51275	5.2	7.5
MD048	Guichon	210.57	3.69	19.4	0.1151	0.51289	7	0.51273	4.9	7.1
MD053	Bethlehem	209.49	1.8	9.29	0.1168	0.512893	6	0.51273	5	7.1
MD057	Border	211.02	4.32	21.04	0.1242	0.512903	6	0.51273	5.2	7.1
MD062	Bethlehem	209.49	4.35	22.32	0.1179	0.5129	7	0.51274	5.1	7.2
MD071	Bethsaida	208.5	1.31	7.39	0.1072	0.512879	7	0.51273	4.7	7.1
MD072	Skeena	208.37	1.53	8.19	0.1129	0.512882	6	0.51273	4.8	7

Table 5.1 Continued…

Sample	Facies	Age (Ma)	Rb (ppm)	Sr (ppm)	$^{87}Sr/^{86}Sr_{(m)}$	± 2σ	$^{87}Sr/^{86}Sr_{(i)}$
MD002	Border	211.02	31.62	726.01	0.703846	10	0.703467
MD005	Bethsaida	208.5	13.01	691.79	0.703566	10	0.703404
MD007	Border	211.02	2.63	1258.56	0.703416	10	0.703398
MD035	Skeena	208.37	26.99	719.95	0.703734	10	0.703412
MD044	Chataway	210.57	48.63	617.95	0.704054	10	0.703371
MD045	Chataway	210.57	46.47	686.28	0.703977	10	0.703389
MD046	Border	211.02	3.94	877.70	0.703471	15	0.703432
MD047	Guichon	210.57	93.65	498.10	0.705114	9	0.703481
MD048	Guichon	210.57	99.40	442.59	0.705443	10	0.703493
MD053	Bethlehem	209.49	18.15	720.50	0.703603	10	0.703385
MD057	Border	211.02	74.27	726.27	0.704449	10	0.703559
MD062	Bethlehem	209.49	47.93	525.29	0.704267	12	0.703479
MD071	Bethsaida	208.5	35.46	589.21	0.703921	10	0.703404
MD072	Skeena	208.37	33.17	639.40	0.703813	10	0.703367
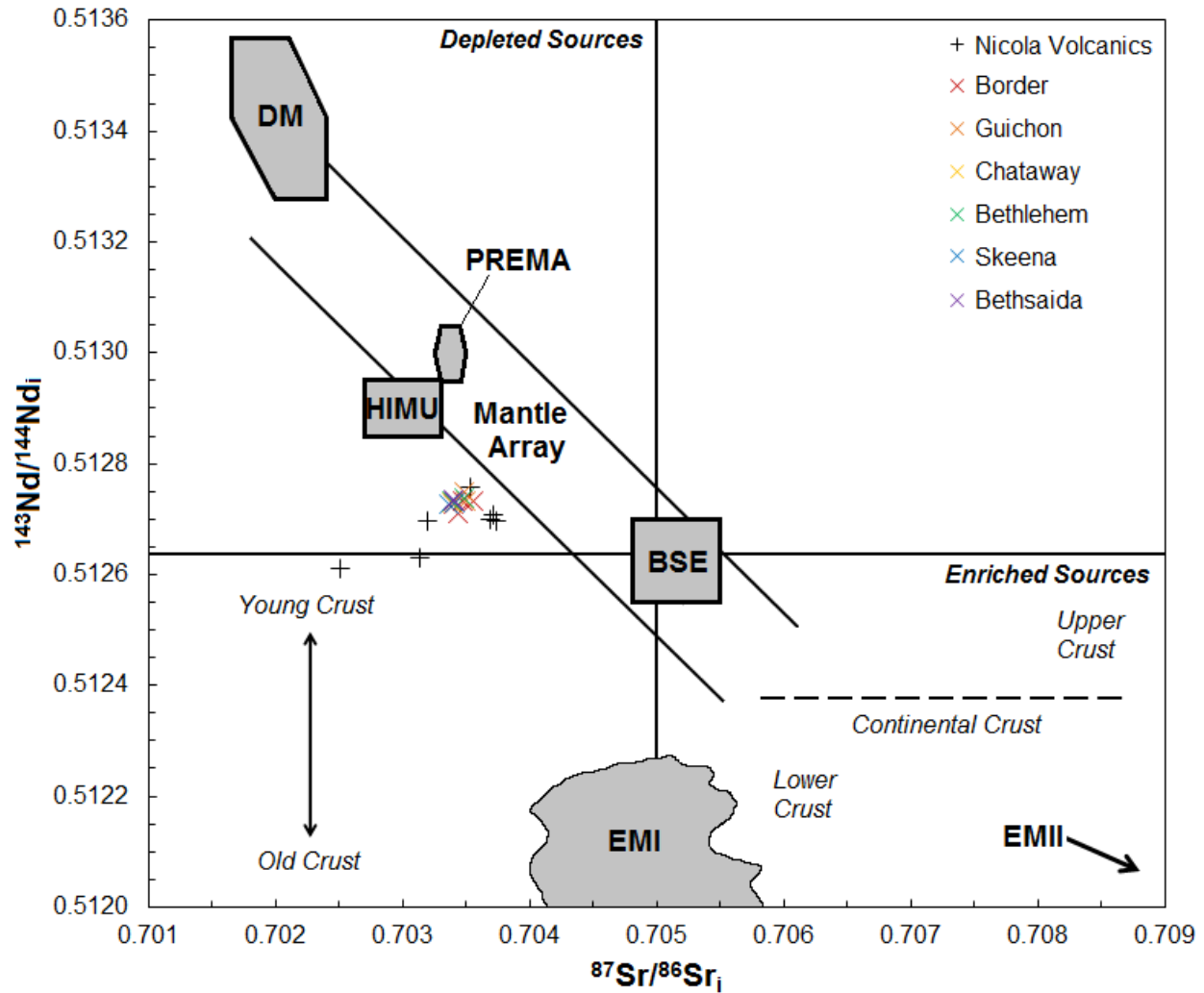
Figure 5.2 A plot of $^{143}Nd^{/144}Nd_i$ vs. $^{87}Sr/^{86}Sr_i$ for the Guichon Creek Batholith and volcanic rocks of the Nicola Group showing the location of the main mantle reservoirs of Zindler and Hart (1986). DM = Depleted Mantle, BSE = Bulk Silicate Earth, PREMA = frequently observed PREvalent Mantle composition, HIMU = mantle with high U/Pb ratio, EMI and EMII = Enriched Mantle I and II. The mantle array is defined by data compiled from many oceanic basalts (e.g., DePaolo and Wasserburg, 1976; O'Nions et al., 1977) and a bulk earth value for $^{87}Sr/^{86}Sr_i$ can be obtained from this trend. Also shown are the fields for enriched and depleted sources relative to BSE. Crustal rocks tend to plot in the lower right enriched quadrant with upper and lower crust plotting in different areas in the field (line separating upper and lower crust is schematic and from DePaolo and Wasserburg, 1979).

Bulk Silicate Earth (BSE) and is slightly enriched in $^{143}Nd/^{144}Nd_i$ and/or depleted in

$^{87}Sr/^{86}Sr_i$ relative to the mantle array (Fig. 5.2).

All samples have positive $\epsilon_{Nd(T)}$ values and plot near the depleted mantle (DM) field which at the time of emplacement had an $\epsilon_{Nd(T)}$ range of +7.9 to +9.5 (Fig. 5.3). These values suggest that the Guichon Creek Batholith magmas were derived from a primitive source that was depleted in REEs. The small degree of variation between samples suggests that the parental magmas of all six facies were derived from a similar, and most likely, the same source. The primitive nature of the $\epsilon_{Nd(T)}$ values indicates that the Guichon Creek Batholith magmas were most likely derived from a depleted mantle source with a minimal contribution from a more radiogenic source that could include terrigenous or pelagic sediments introduced to the mantle wedge during subduction, or a small degree of crustal contamination during ascent and residence at mid- to upper-crustal levels.

Samples from the Guichon Creek Batholith do not show a consistent change in $\epsilon_{Nd(T)}$ with increasing Nb/Y (Fig. 5.4d) which suggests a lack of significant crustal contamination as this ratio is typically high in continental crust. On plots of radiogenic isotope against time, however, a small decrease in $(^{87}Sr/^{86}Sr)_i$ with time is observed (Fig. 5.5). Preto et al. (1979) argued that elevated radiogenic Sr contents in select samples of volcanic rocks from the Nicola Group are the result of contamination by Nicola Group limestones $(^{87}Sr/^{86}Sr_i = 0.70730$ to $0.70750)$ which coincide with Sr contents of Late Triassic seawater (Prokoph et al., 2008). It is possible that the Sr isotope signature of the Guichon Creek Batholith reflects contamination of the older, marginal facies by either limestone or contaminated basalt units, whereas the younger facies which were intruded as a second pulse of magma were largely buffered from

133
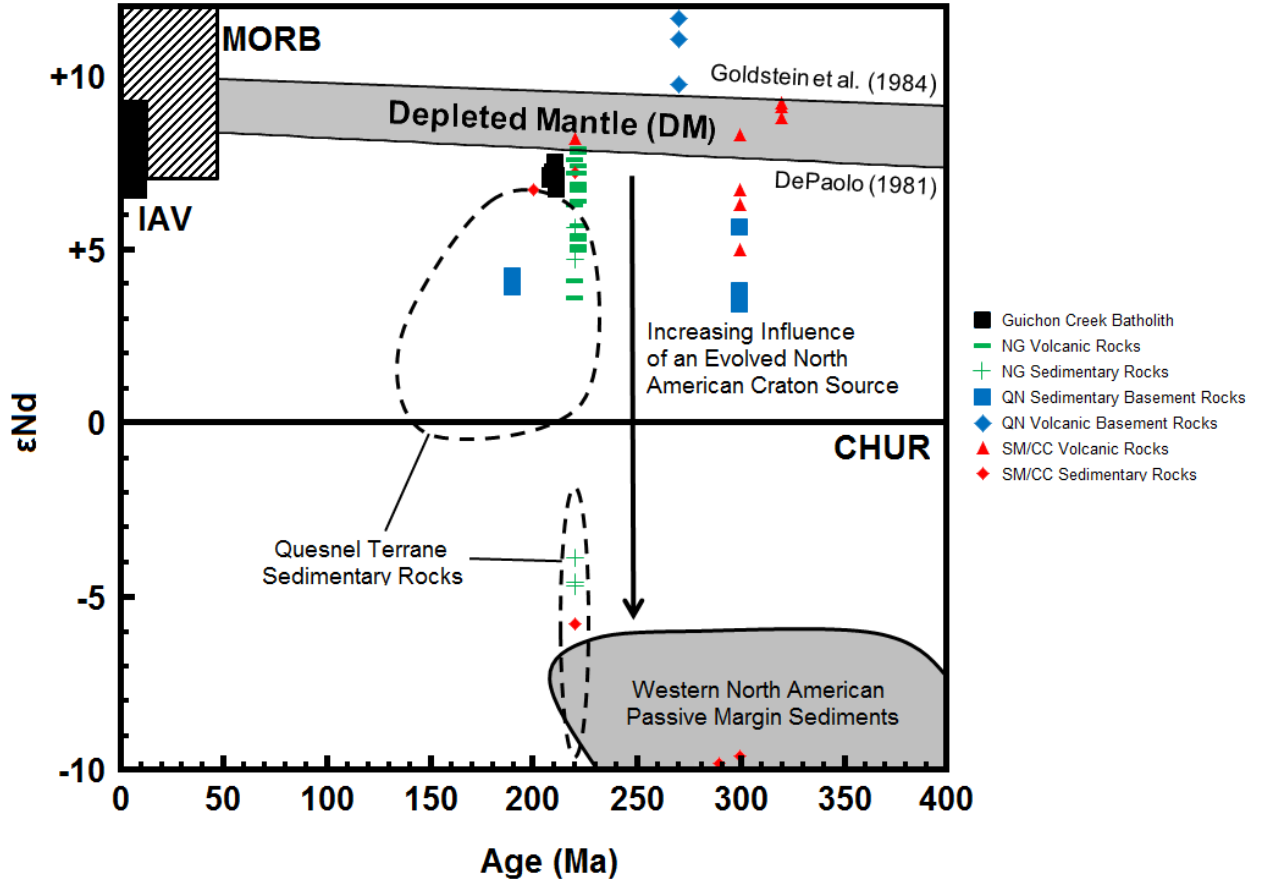
Figure 5.3 Time vs. $\epsilon_{Nd(T)}$ for samples from the Guichon Creek Batholith with comparison fields for volcanic and sedimentary rocks from the Nicola Group (NG; Unterschutz et al., 2002; Smith et al., 1995; Patchett and Gehrels, 1998), Quesnel Terrane (QN) basement rocks of the Harper Ranch subterrane and Attwood Group (Patchett and Gehrels, 1998; Dostal et al., 2001), Quesnel Terrane sedimentary rocks of the Slocan and Ymir Groups (Patchett and Gehrels, 1998; Petersen et al., 2004; Unterschutz et al., 2002; Ghosh and Lambert, 1989), Slide Mountain and Cache Creek terranes (SM/CC; Patchett and Gehrels, 1998) and Precambrian to Late Triassic Western North American passive margin sediments (Jackson, 1992; Boghossian et al., 1996). Present day MORB (DePaolo and Wasserburg, 1976) and IAV (DePaolo and Johnson, 1979; White and Patchett, 1984) compositions and the depleted mantle field (boundary lines from DePaolo, 1981a and Goldstein et al., 1984) plotted for comparison.

contamination by the older facies. The $^{143}Nd/^{144}Nd$ systematics of the Guichon Creek

Batholith remain broadly similar over time which is not consistent with contamination by

older crust which should result in lower $^{143}Nd/^{144}Nd_i$ values with increasing

contamination (Fig. 5.4d), suggesting a decoupling of the Rb-Sr and Sm-Nd isotope

systems. The lack of correlation between the two systems could be the result of either
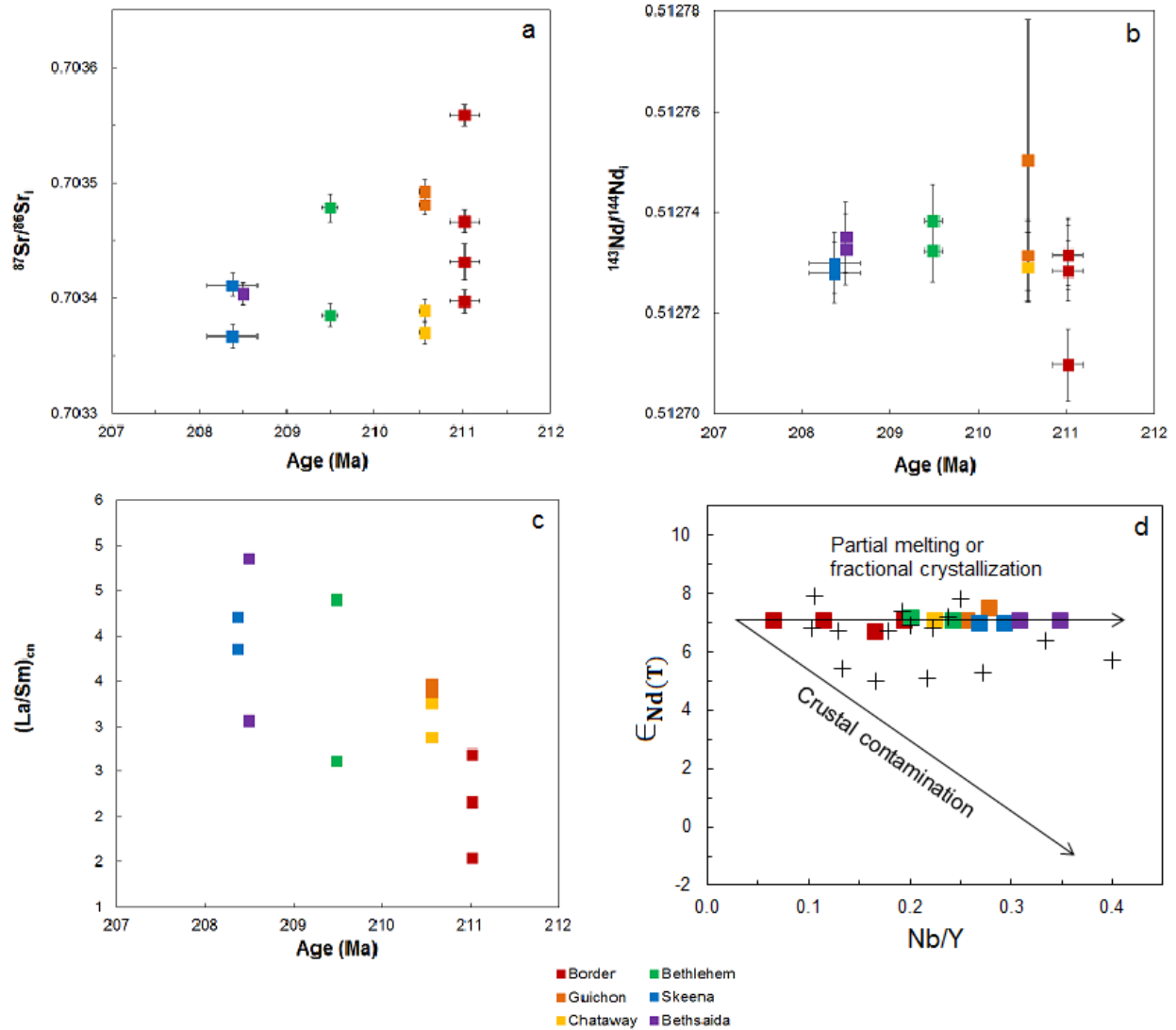
Figure 5.4 Plots of A. $^{87}Sr/^{86}Sr$, B. $^{143}Nd/^{144}Nd$, C. $(La/Sm)_{cn}$ vs. age and D. $\varepsilon Nd_{(T)}$ vs. Nb/Y for the Guichon Creek Batholith. Crustal contamination and magma mixing are indicated by decreasing $\varepsilon Nd_{(T)}$ with increasing Nb/Y. Lines are schematic and illustrate the relative effects of contamination by radiogenic sources.

contamination by young, contaminated basaltic crust of the Nicola Group that has not

had sufficient time to evolve a distinct Nd signature (Fig. 5.4d) or direct contamination

by assimilation of limestone units in the Nicola Group. The increase in La/Sm$_{cn}$ with

decreasing age (Fig. 5.4c) is consistent with progressive fractionation rather than crustal

contamination and supports a limestone contaminant to account for the variability in the Sr isotope values.

The slightly more radiogenic $\epsilon_{Nd(T)}$ values reported for the Guichon Creek Batholith relative to depleted mantle possibly reflect derivation from a depleted mantle source contaminated to varying degrees by subducted sediment. This model is similar to that proposed by Samson et al. (1989) for volcanic rocks of the neighbouring Stikine terrane. This argument is supported by modelling the mixing of a depleted mantle source at 210 Ma. Assuming the average $^{143}Nd/^{144}Nd_{DM}$ at 210 Ma [0.512806 from the depleted mantle curves of DePaolo (1981) and Goldstein et al. (1984)] and the average $^{143}Nd/^{144}Nd$ of present day Global Subducting Sediment (GLOSS) of (0.51218; Plank and Langmuir, 1998) the $\epsilon_{Nd(T)}$ values for the Guichon Creek Batholith can be explained by <2% contamination of the depleted mantle source by GLOSS. Mixing with subducted sediments is also supported by the fact that the Guichon Creek Batholith lies on a mixing line between the mantle array and Enriched Mantle I (EMI) reservoir (Fig. 5.2). The EMI reservoir is believed to represent subducted pelagic sediment (Weaver, 1991) and high Ba/Th and Th/Ta ratios (Fig. 5.5) which are proxies for mantle metasomatism by slab derived fluids and siliceous sediment melts, respectively (Keppler, 1996; Johnson and Plank, 1999; Pearce et al, 2005).

5.6 Summary and Model

Isotopic evidence supports a model whereby the Guichon Creek Batholith magmas were derived from a primitive mantle source depleted in REEs. It is proposed that a primitive, sub-arc mantle, with a composition intermediate between N-MORB and
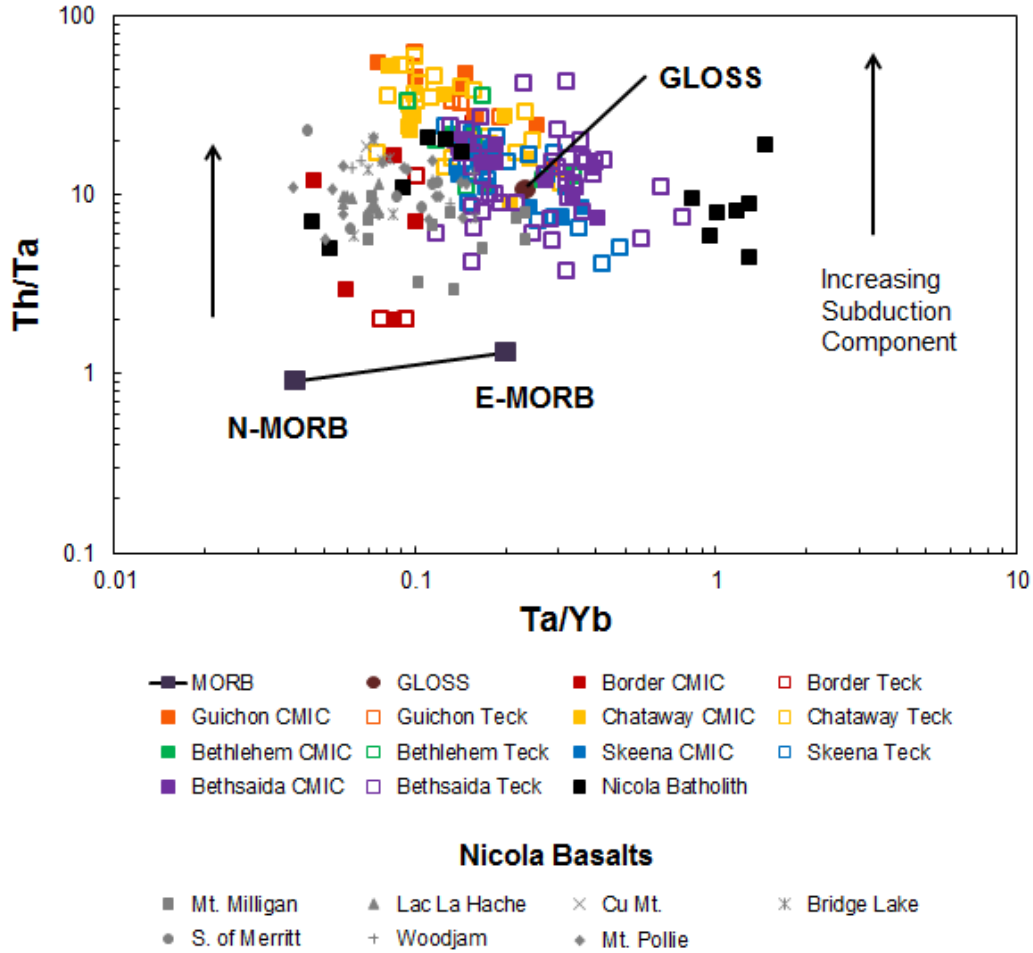
Figure 5.5 Plot of Th/Ta vs. Ta/Yb for the Guichon Creek and Nicola batholiths and Nicola Group basalts. High Ta/Yb ratios reflect enrichment relative to a depleted mantle source. Increasing mantle metasomatism by dehydrating slab fluids and partial melts of subducted sediments are reflected by high Th/Ta ratios. The data for Guichon Creek and Nicola batholiths are from this study with supplemental data provided by Teck. The data for N-MORB and E-MORB are from Sun and McDonough (1989), average Global Subducting Sediment (GLOSS) from Plank and Langmuir (1998) and Nicola Group basalts from Vaca (2012).

E-MORB, was metasomatized by fluids sourced from the subducting slab and partial

melts of sediment with a similar composition to present day GLOSS resulting in <2%

contamination with sediment derived Nd. Decoupling of the Sm-Nd and Rb-Sr systems

supports additional contamination of the Guichon Creek magmas during their ascent to

mid- and upper-crustal levels by radiogenic Sr, most likely sourced from limestone units

of the Nicola Group, although contamination by previously contaminated Nicola Group

volcanic rocks cannot be ruled out. Decreasing $^{87}Sr/^{86}Sr_i$ and constant $\epsilon_{Nd(T)}$ with

decreasing age can be explained by increased contamination of the older Border,

Guichon and Chataway facies by radiogenic Sr from Nicola Group limestone or volcanic

units. These buffered the younger Bethlehem, Skeena and Bethsaida facies during their

emplacement.

CHAPTER 6   MINERAL CHEMISTRY

6.1 Introduction

Igneous amphibole, plagioclase, biotite, magnetite and apatite from 15 samples representing the six main intrusive facies of the Guichon Creek Batholith (Fig. 6.1) were analyzed by electron microprobe micro-analysis (EPMA) to assess changes in mineral chemistry during crystallization of the batholith and establish baseline characteristics for least altered minerals. A complete data set for all minerals analyzed on the EPMA can be found in Appendix D. Amphibole compositions were used to estimate the temperature, pressure and oxygen fugacity of emplacement via the Ti-in-hornblende geothermometer of Otten (1984), Al-in-hornblende geobarometer of Anderson and Smith (1995) and thermobarometric equations of Ridolfi and Renzulli (2012). An estimate of dissolved S in the melt was made using apatite saturation temperatures and SO_3 content in cores of apatite grains.

6.2 Methodology

Polished and carbon-coated thin sections were analyzed in wavelength-dispersion mode (WDS) using a JEOL JXA-8230 electron probe micranalyzer (EPMA) equipped with four energy dispersive spectrometers (EDS) at Memorial University of Newfoundland in St. John's, Newfoundland and Labrador, Canada. Beam conditions included an accelerating voltage of 15 kV and a beam current of 20 nA. Data were corrected on-line using the ZAF correction procedure to account for matrix effects using the Astimex standards of known composition: apatite, rutile, willemite, barite, magnetite, jadeite, diopside, tugtupite, biotite, almandine, rhodonite, plagioclase, celestite,
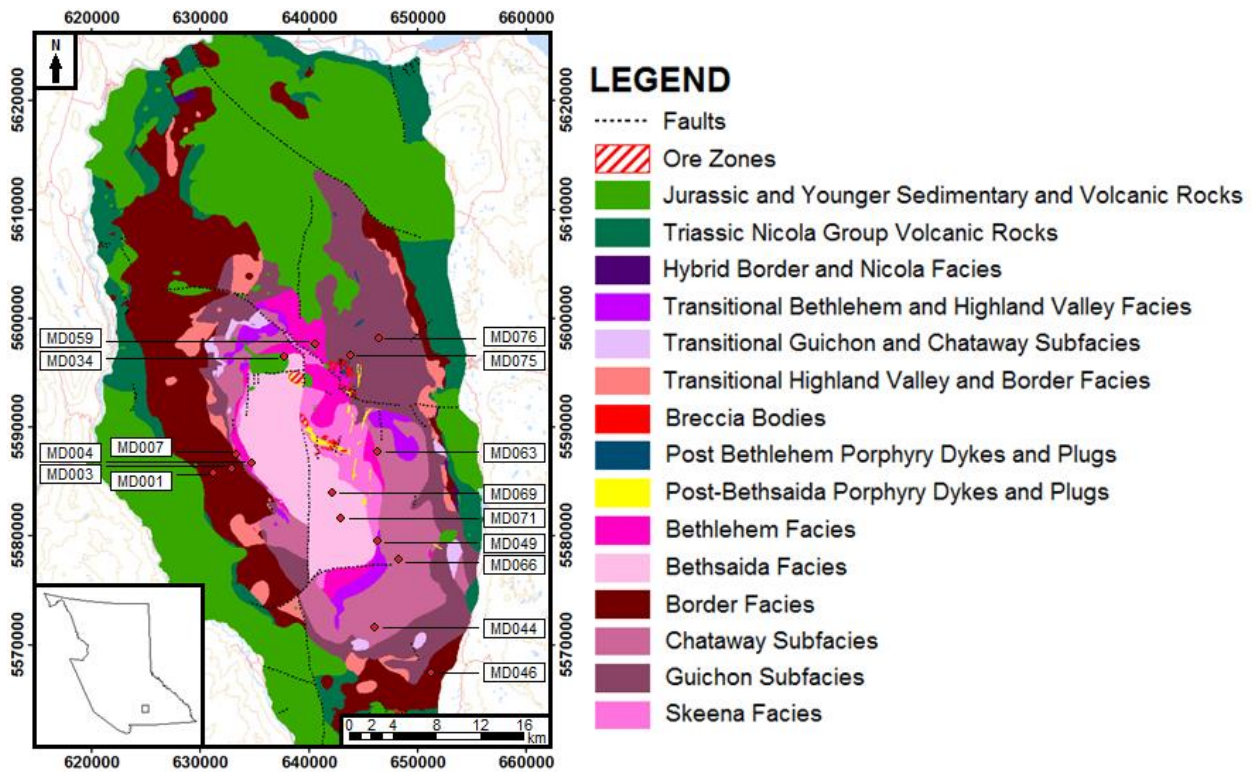
Figure 6.1 Map of the Guichon Creek Batholith with locations for samples selected for EPMA analysis.

chromium oxide, metallic vanadium and synthetic zircon. A defocused beam diameter of 10 µm was used to avoid volatilization of alkali elements in feldspars. For apatite analyses, grains that had their c axis approximately parallel to the beam were preferentially chosen to minimize the effects of fluorine migration towards the beam (Stormer et al., 1993). Apatite grains hosted in anhydrous (e.g., magnetite, titanite) and hydrous (e.g., biotite, amphibole) minerals were both analysed and documented in an attempt to detect potential effects of sub-solidus chlorine-hydroxyl exchange (cf. Piccoli and Candela, 1994).

Elements analyzed were Si, Ti, Al, Fe, Mn, Mg, K, Ca, Na, F, Cl, Ba, Sr, P, S, Cr, V and Zr. The elements Sr, Ba and Zr were measured using the Lα line with a PETJ (Sr,

Table 6.1 A summary of minerals and elements analyzed by EPMA

Element	Crystal	Emission Line	Plagioclase	Amphibole	Biotite	Titanite	Apatite	Fe-Ti oxides
Ba	PETJ	Lα	√					
Sr	PETJ	Lα	√					
Ca	PETL	Kα	√	√		√	√	
Na	TAP	Kα	√	√		√	√	
K	PETL	Kα	√	√	√	√		
Si	TAP	Kα	√	√	√	√	√	√
Ti	LIFL	Kα		√	√	√	√	√
Al	TAP	Kα	√	√	√	√	√	√
Fe	LIFH	Kα		√	√	√	√	√
Mn	LIFL	Kα		√	√		√	√
Mg	TAP	Kα		√	√		√	√
Cr	LIFL	Kα						√
V	LIFH	Kα						√
Zr	PETH	Lα				√		
F	LDE1	Kα		√	√	√	√	
Cl	PETL	Kα		√	√	√	√	
P	PETL	Kα					√	
S	PETL	Kα					√	

Ba) and PETH (Zr) crystal. All other elements were measured using the Kα line with the PETL (Ca, K, Cl, P, S), TAP (Na, Si, Mg, Al), LIFH (Fe, V), LIFL (Ti, Mn, Cr) and LDE1 (F) crystals. All minerals and elements analyzed are summarized in Table 6.1. Peak counting times were 20 s for major elements and 60 s for minor elements and determined on a mineral by mineral basis. Background counting times were typically half the peak counting times. Natural and synthetic known standards were analyzed at the start and end of each run to assess accuracy and correct for machine drift during analyses. Lower detection limits for S and P in apatite were approximately 30 and 75 ppm, respectively. Lower detection limits for F were approximately 246 ppm (apatite), 326 ppm (biotite), 310 ppm (hornblende), and 455 ppm (titanite). Lower detection limits

for Cl were approximately 150 ppm (apatite), 26 ppm (biotite), 25 ppm (hornblende), and 29 ppm (titanite). All spots analyzed were from least altered samples and performed on mineral crystals that had been affected by <1% alteration by volume.

6.3 Plagioclase

Plagioclase belongs to the feldspar group of minerals and is a solid solution between the three components albite (Ab), $NaAlSi_3O_8$, anorthite (An), $CaAl_2Si_2O_8$ and minor orthoclase (Or), $KAlSi_3O_8$. Compositions are most commonly expressed by anorthite content (An_{xx}) and subdivided into six varieties (anorthite, bytownite, labradorite, andesine, oligoclase and albite). Anorthite and albite are the dominant components with significant orthoclase contents restricted to albitic plagioclase formed at high temperatures (Deer et al., 2013). The transition from anorthite to albite requires the coupled substitution of Na^+ and Si^{4+} for Ca^{2+} and Al^{3+} to maintain charge balance (Deer et al., 2013). Other common substitutions include Ba, Sr, Mn and Mg for Ca and Ti, Fe^{3+}, Fe^{2+} for Al and Si (Deer et al., 2013). A total of 140 spots were analyzed for characterization of plagioclase in the Guichon Creek Batholith.

6.3.1 Textures

Plagioclase crystals display a variety of textures in the Guichon Creek Batholith (Fig. 6.2). The most common form are subhedral crystals that are abundant in the groundmass of all facies, that range in size from approximately 0.5 to 2mm, are not visually zoned, but are altered to clay and sericite to varying degrees (Fig. 6.2d). Optically zoned plagioclase is found in all facies, though it is rare in the Border, Guichon
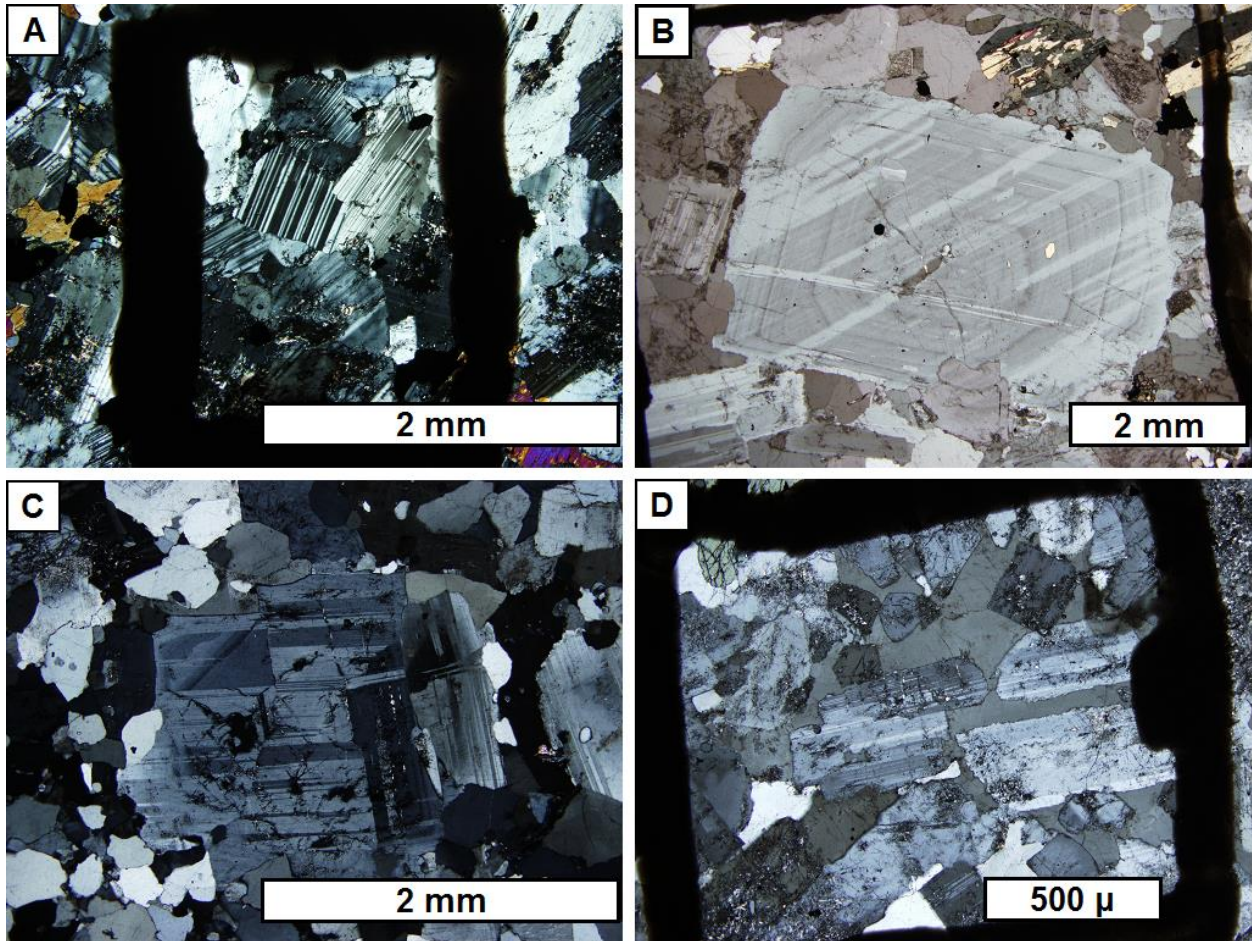
Figure 6.2 Photomicrographs of plagioclase (Pl) crystals under XPL, transmitted light. A. Plagioclase phenocryst displaying oscillatory zoning (MD059); B. Complex growth domains in subhedral plagioclase, Bethsaida facies (MD004); C. Subhedral plagioclase surrounder by interstitial orthoclase, Chataway facies (MD044); D. Fresh groundmass plagioclase, Border facies (MD003a).

and Chataway facies where it occurs predominantly as small (0.2 to 2mm), unzoned crystals in the groundmass. Zoned plagioclase is more common in the Bethlehem, Skeena and Bethsaida facies where it forms 2.5 to 8mm phenocrysts with oscillatory zoning (Fig. 6.2a). Also restricted to the Bethlehem, Skeena and Bethsaida facies are subhedral plagioclase crystals that display complex growth domains and twinning patterns (Fig. 6.2b). The final type of plagioclase occurs as sub-millimeter crystals rimmed by orthoclase (Fig. 6.2c) and are restricted to the Chataway facies.

143

6.3.2 Results

The composition of Guichon Creek Batholith plagioclase is predominantly andesine with subordinate labradorite, oligoclase and albite (Fig. 6.3). Most plagioclase display a narrow compositional range from $An_{0.17}Ab_{0.80}Or_{0.04}$ to $An_{0.56.0}Ab_{0.43}Or_{0.01}$, with four analyses from $An_{0.08}Ab_{0.90}Or_{0.02}$ to $An_{0.12}Ab_{0.86}Or_{0.02}$.

On Figure 6.4, plagioclase crystals that display normal zoning lie to the right of the line $An_{core}/An_{rim} = 1$ while those that display reverse zoning lie to the left of it. All plagioclase crystals from the Guichon, fine-grained Granodiorite, Bethlehem, and Skeena facies are normally zoned (An-rich core to lower-An rim; Fig. 6.4). The Border, Chataway and Bethsaida facies contains plagioclase that ranges from normally zoned to reversely zoned (Fig. 6.4). No statistically significant systematic variations in An, Ab and Or content were observed between facies, though the Border facies is generally the most An-rich and the Bethsaida facies is the most Ab-rich. Barium and Sr contents are low (< lower detection limit (l.d.l.) to 0.13 and 0 to 0.24 wt%, respectively) and do not vary systematically with SiO_2 or anorthite content (Fig. 6.5).

6.3.3 Discussion

Negative correlations between Al_2O_3 and CaO with SiO_2 and a positive correlation between Na_2O and SiO_2 are consistent with the coupled substitution of $Si^{4+} + Na^+$ for $Al^{3+} + Ca^{2+}$ as plagioclase evolves to more albitic compositions during fractionation (Fig. 6.5). A similar positive trend with greater scatter is observed for K_2O wt%, also consistent with limited substitution of K^+ for Na^+ in more albitic plagioclase (Fig. 6.5). No clear trend is observed for BaO or SrO wt% with evolution (Fig. 6.5). Plagioclase compositions evolve smoothly from Al_2O_3- and CaO-rich (Na_2O- and K_2O-
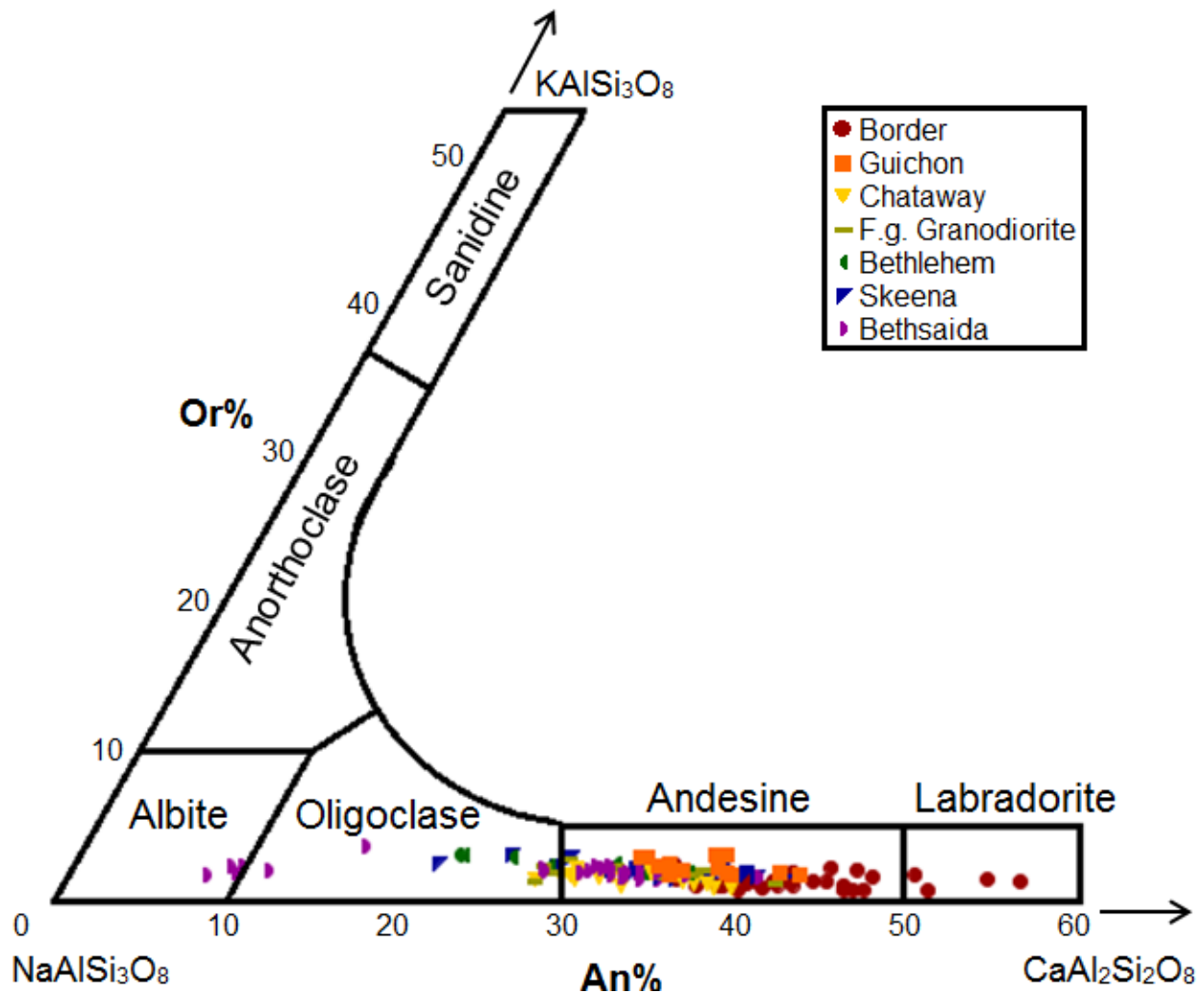
Figure 6.3 Albite (Ab)-anorthite (An)-orthoclase (Or) ternary diagram showing plagioclase compositions from the Guichon Creek Batholith.

poor) compositions at low SiO_2 in the Border facies, to Al_2O- and Ca-poor (Na_2O- and

K_2O-rich) compositions at high SiO_2 in the Guichon and Chataway facies with little

compositional overlap (Fig. 6.5). This trend is consistent with simple fractional

crystallization processes resulting from the coupled substitution mechanisms described

above. Plagioclase compositions in the Bethlehem, Skeena and Bethsaida facies,

however, display much more overlap (Fig. 6.5), which cannot be easily explained by

progressive fractionation in a single magma. Most of the plagioclase in the
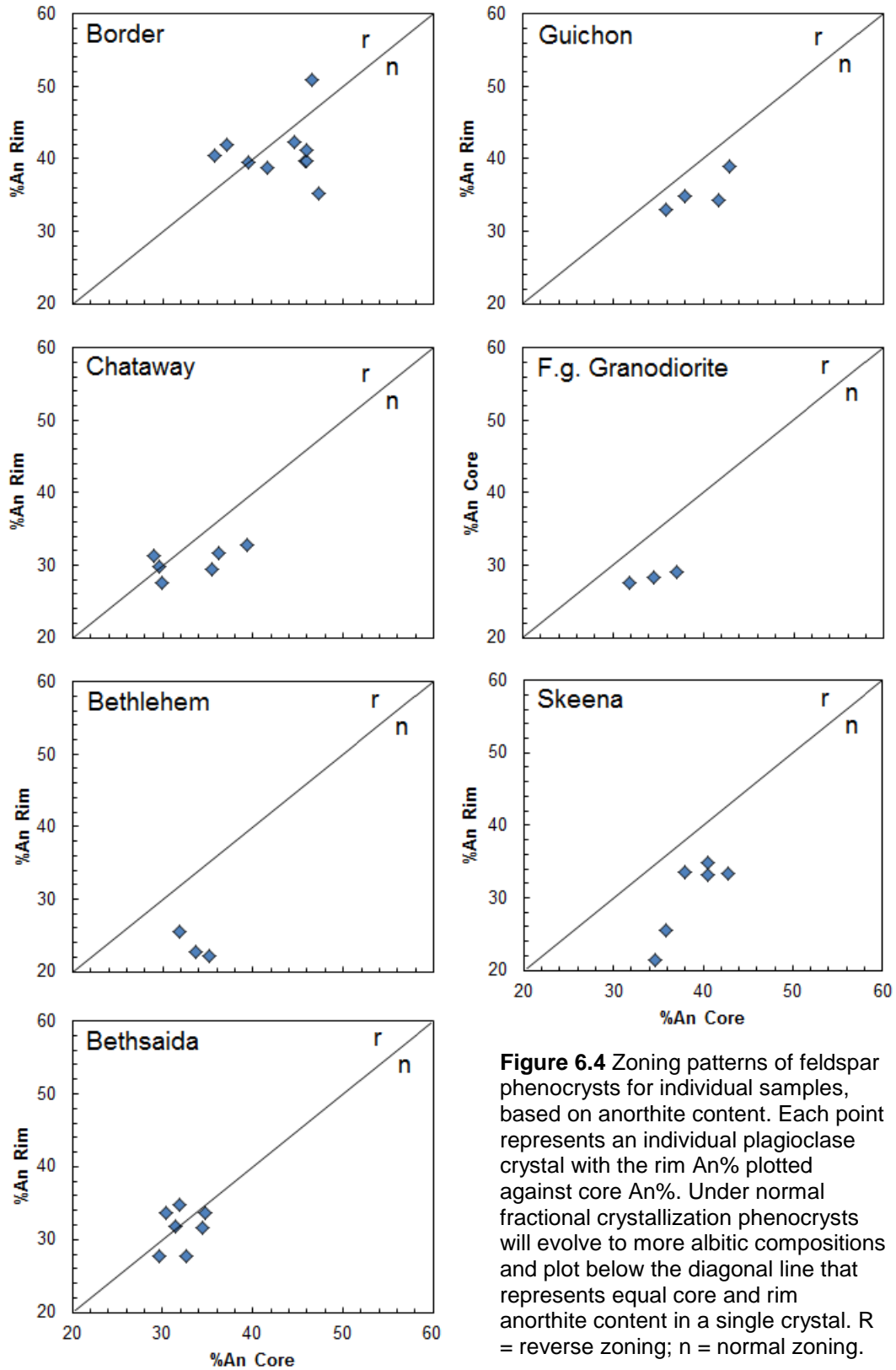
Figure 6.4 Zoning patterns of feldspar phenocrysts for individual samples, based on anorthite content. Each point represents an individual plagioclase crystal with the rim An% plotted against core An%. Under normal fractional crystallization phenocrysts will evolve to more albitic compositions and plot below the diagonal line that represents equal core and rim anorthite content in a single crystal. R = reverse zoning; n = normal zoning.

146
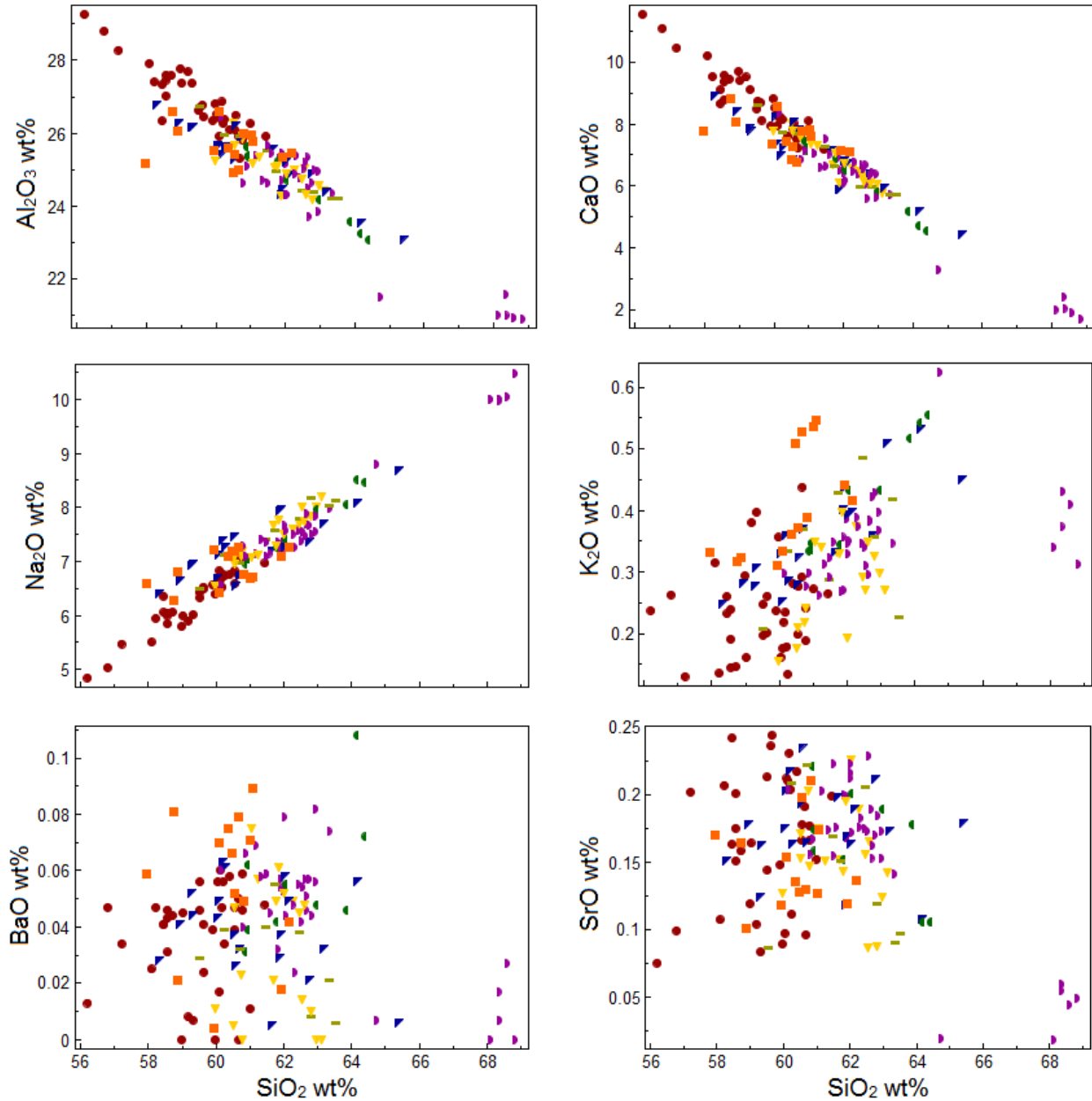
Figure 6.5 Harker variation diagrams for major element oxides in plagioclase from the Guichon Creek Batholith. Refer to Figure 6.3 for legend.

Bethlehem through Bethsaida facies is present as sub- to euhedral phenocrysts that display concentric, oscillatory zoning and are present in a finer-grained groundmass. In light of their phenocrystic nature and similar compositions, it is suggested that the plagioclase phenocryst population of the Bethlehem, Skeena and Bethsaida facies

represents plagioclase crystals that formed at depth in the parental magma chamber. These crystals may have been transported in a crystal mush to their present crustal levels during the emplacement of a Highland Valley facies magma pulse that subsequently underwent fractional crystallization to produce the Bethlehem, Skeena and Bethsaida facies.

Plagioclase crystals from the Border, Chataway and Bethsaida facies are dominantly normally zoned with cores enriched in anorthite relative to rims, but a number of crystals are reversely zoned, with anorthite-rich rims relative to their cores (Fig. 6.4). Plagioclase crystals from all other facies are normally zoned (Fig. 6.4). The albitic component in plagioclase rims generally increases with evolution from the Guichon through Bethsaida facies (Fig. 6.4) consistent with progressive magmatic fractionation.

Oscillatory zoning in plagioclase is a common feature in many intrusive igneous rocks (e.g., Loomis and Welber, 1982; Blundy and Shimizu, 1991; Brophy et al., 1996) and is characterized by changes in anorthite content on the order of 1 to 30 mol% (Ginibre et al., 2002). Oscillations may be present as low-amplitude, high-frequency (LAHF) oscillations or high-amplitude, low-frequency (HALF) oscillations. These have been interpreted to represent kinetic effects at the plagioclase crystal-melt interface and crystallization in a dynamic, convecting magma regime, respectively, for volcanic rocks erupted from Mt. Etna, Italy (Viccaro et al., 2010). The oscillations observed in phenocrysts from the Bethlehem, Skeena and Bethsaida facies is characterized by thin tightly spaced oscillations. This is characteristic of LAHF oscillatory zoning, which is generally attributed to periodic convection in a boundary layer at the crystal-melt

148

interface and require relatively rapid cooling and/or a high crystal-melt partition coefficient for a given element (Loomis, 1982). Another interpretation for the formation of LAHF oscillatory zoning is the periodic destruction of the crystal-melt boundary layer (Loomis, 1982; Anderson, 1984). Experiments on the coupled diffusion of CaAl-NaSi in plagioclase revealed that CaAl-NaSi diffusion occurs slowly and has a high closure temperature (in the solidus-liquidus temperature interval; Grove et al., 1984). This can explain the lack of oscillatory zoning in the Border, Guichon and Chataway facies, as although the entire batholith is interpreted to have experienced slow cooling rates, the higher temperature at which cooling initiates in gabbroic and dioritic intrusions relative to granodiorite intrusions allows for the homogenization of oscillatory zones up to approximately 10μm (Grove et al., 1984).

Detailed studies of zoning in plagioclase phenocrysts have proven useful in interpreting the role of magma recharge, assimilation and hybridization in many orogenic magma systems (e.g., Tepley III et al., 1999; Browne et al., 2006; Ginibre and Worner, 2007; Andrews et al., 2008). However, most interpretations of magma recharge and mixing hinge on variations in $^{87}Sr/^{86}Sr$, Fe, Mg and anorthite concentrations over micron-scale distances. The lack of a dense dataset for individual plagioclase phenocrysts (3 to 4 spot analyses per crystal) and data for $^{87}Sr/^{86}Sr$, Fe and Mg precludes a similar attempt at delineating multiple recharge events. Regardless, changes in anorthite content can still be used to examine broad magma chamber processes responsible for coarse zoning patterns in plagioclase crystals.

Normal zoning of plagioclase crystals (high-An core to low-An rim) is expected from fractional crystallization under constant or increasing rate of undercooling, which is

promoted by rapid cooling, contemporaneous crystallization of other phases and/or loss of volatiles (Loomis, 1982). In contrast, reverse zoning can be expected in crystals that have experienced decreasing rate of undercooling which can result in melts that are slowly cooled or with high concentration of volatile elements (Loomis, 1982). Plagioclase from all facies displays normal zoning with the exception of the Border, Chataway and Bethsaida facies (Fig. 6.4). This is consistent with crystallization from a poorly convecting magma producing a constant or increasing undercooling rate. For the Border and Chataway facies it is proposed that reverse zoning in select plagioclase crystals is the result of convective overturn, where crystals formed near the rapidly cooled contact with the surrounding country rocks are convected back into the hotter magma in the center of the magma chamber resulting in a decreased rate of undercooling. Such convective overturn has been proposed for the Border and Highland Valley facies of the Guichon Creek Batholith based on mineralogical and flow alignment evidence (Westerman, 1970) and is consistent with the presence of autoliths in the Border facies (Chapter 3). Reverse zoning in a number of plagioclase phenocrysts from the Bethsaida facies are likely the result of a high concentration of volatile elements during the latest stages of crystallization.

6.4 Amphibole

The amphibole group minerals are double-chain silicates with the general formula $A_{0-1}B_2C_5T_8O_{22}W_2$, where the A, B, C, T cations are found in the (A), (M4), (M1, M2 and M3) octahedral and (T) tetrahedral sites (Leake et al., 1997). Following the International Mineralogical Association (IMA) guidelines, amphiboles were originally classified into five main subgroups based on the dominant charge-arrangements and type of B site

cations (Leake et al., 1997; 2003), with a recent update by Hawthorne et al. (2012) bringing the total number of subgroups to eight [Mg-Fe-Mn, Ca, Na-Ca, Na, Li, Na-(Mg-Fe-Mn), Li-(Mg-Fe-Mn) and Li-Ca amphiboles]. Hawthorne et al. (2012) also added a higher order group division based on the dominant W-site species: ^{W}(OH,F,Cl)-dominant and ^{W}O-dominant amphiboles (oxo-amphiboles).

Amphiboles are most commonly found in greenschist to lower granulite facies metamorphic rocks and plutonic igneous rocks (Deer et al., 2013). Compositions vary greatly under a wide range of pressure and temperature conditions which makes them useful indicators of temperature (Blundy and Holland, 1990; Ernst and Liu, 1998; Féménias et al., 2006), pressure (Hammarstrom and Zen, 1986; Johnson and Rutherford, 1989; Rutter et al., 1989; Schmidt, 1992; Anderson and Smith, 1995; Ernst and Liu, 1998), fO_2, (Anderson and Smith, 1995) and, magmatic halogen content (Zhang et al., 2012; Giesting and Filiberto, 2014). A total of 123 spots were analysed for amphibole chemistry.

Classification of amphiboles is complicated by the fact that most modern analyses are conducted by EPMA, which cannot account for varying valence states of certain cations (e.g., Fe and Mn) or H_2O content. As the Fe^{2+} and Fe^{3+} content of an amphibole is required to accurately classify amphiboles, some estimation of Fe^{3+} content is generally performed utilizing one, of a number of, cation normalization schemes (Leake et al., 1997; Hawthorne et al., 2012). Cosca et al. (1991) demonstrated that the 13eCNK (13 cation normalization scheme, excluding Ca, Na and K) provides the best approximation for hornblende formulae compared to compositions determined by wet chemistry. All hornblende formulae presented in this study are calculated on an

anhydrous basis assuming 23 O atoms utilizing the 13eCNK normalization scheme and assume OH + F + Cl = 2, ignoring possible substitutions of O^{2-} at the OH site in oxo-amphiboles.

6.4.1 Results

All amphiboles were Mg-rich [Mg/(Mg + Fe^2) = 0.699 to 0.906] and calcic [^{B}(Ca + ΣM^{2+})/$\Sigma B \geq 0.75$, ^{B}Ca/$\Sigma B \geq$ $^B\Sigma M^{2+}$/ΣB] according to the most recent IMA classification scheme of Hawthorne et al. (2012). These and the additional parameters ^{C}(Al + Fe^{3+} + 2Ti) apfu = 0.642 to 1.712 and ^{A}(Na + K + 2Ca) apfu = 0.023 to 0.297 allowed for the assignment of the root names magnesiohornblende (116 analyses) and tschermakite (7 analyses; Fig. 6.6). Amphiboles are generally Al-poor (3.35 to 10.94 Al_2O_3 wt%) with TiO_2 contents from 0.32 to 2.17 wt%. Other important constituents are MgO (13.45 to 16.98), FeO^T (9.46 to 13.26), CaO (10.66 to 12.25), Na_2O (0.38 to 1.75) and K_2O (0.13 to 0.73). Halogen contents are generally low, with no F analyses above the lower detection limit and <0.25 wt% Cl.

6.4.2 Discussion

Calcic amphiboles in igneous systems are characteristic of fluid saturated (high-H_2O) magmas and their stability is believed to increase with increasing water pressure (Ridolfi and Renzulli, 2012). Magnesiohornblende and tschermakite species have only been demonstrated to be in equilibrium with calc-alkaline melts at equilibrium pressures up to ~ 1GPa and magnesiohornblendes are specifically confined to crystallization conditions of ≤300MPa and <930°C (Ridolfi and Renzulli, 2012). The presence of magnesiohornblende and subordinate tschermakite indicates that the Guichon Creek
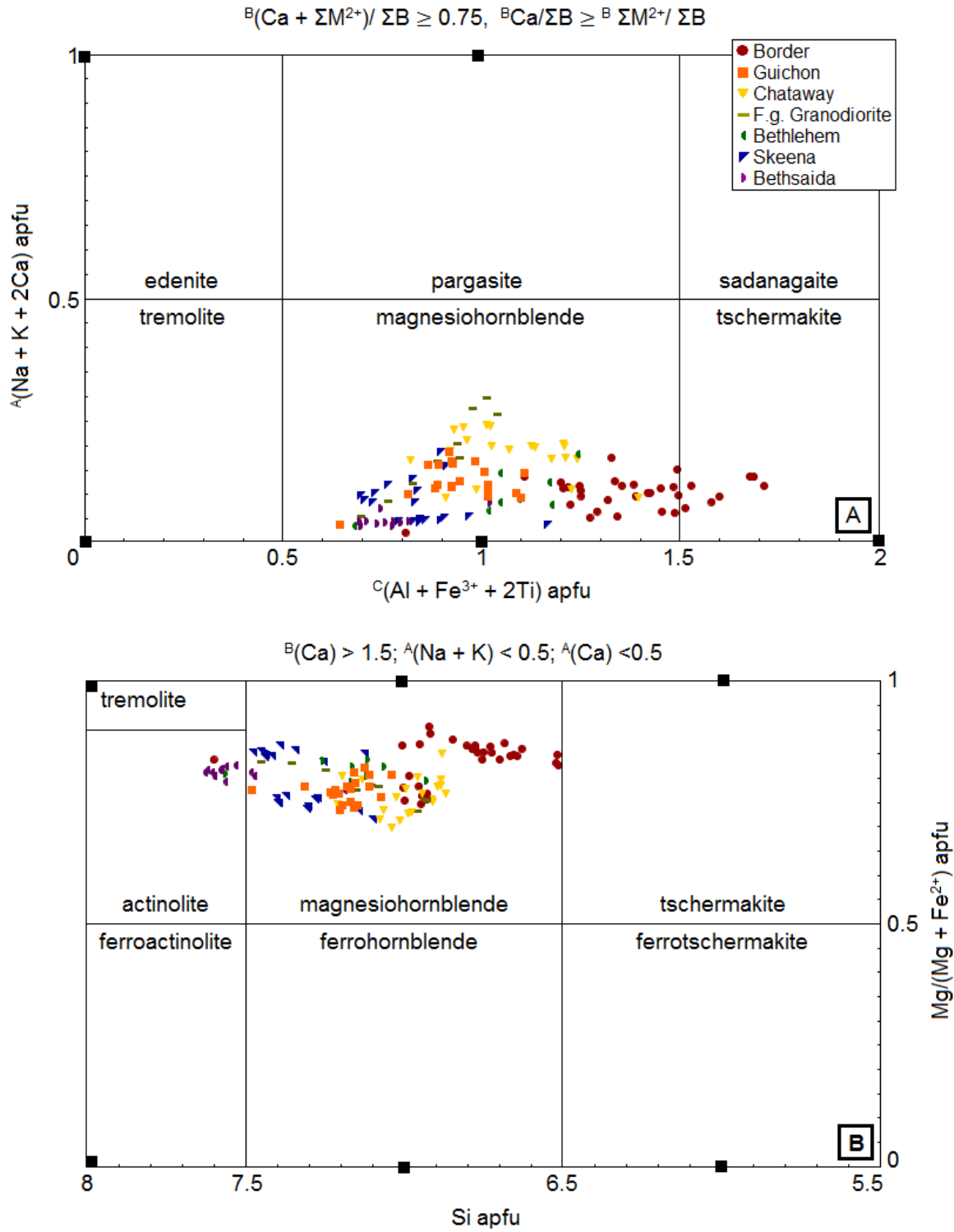
Figure 6.6 Amphibole compositions from the Guichon Creek Batholith. Black squares represent pure end-member compositions. After the IMA classification schemes of A. Hawthorne et al. (2012) and B. Leake et al. (1997).

153

Batholith magmas possessed relatively high-H_2O contents and crystallized at upper

crustal conditions, consistent with a porphyry-type setting (e.g., Hollings et al., 2011;

Richards, 2011). The evolution of amphibole compositions in the Guichon Creek

Batholith can be seen in Figure 6.7, where a number of key constituents are plotted

against Al^{iv} apfu. Most analyses fall in the range defined by experimental and natural

magnesiohornblendes in calc-alkaline melts (Al^{iv} = 0.8 to 1.5) reported by Ridolfi and

Renzulli (2012), although analyses from the Skeena and Bethsaida facies typically

contain lower Al^{iv} contents (~0.4 to 0.8). When these samples are plotted on an Al^T vs.

Al^{iv} diagram (Fig. 6.8) they follow a trend towards the ideal cummingtonite composition

(Al^t = Al^{iv} = 0), which is a low-Ca and –Al amphibole in solid solution with

magnesiohornblende and typical of rhyolite melts (Ridolfi et al., 2010). An evolution

towards the low-Al cummingtonite end-member is not unexpected as the Skeena and

Bethsaida facies represent the most evolved magmas present in the Guichon Creek

Batholith with compositions lying in the granite (plutonic equivalent of rhyolite) field of

the QAPF diagram (Fig. 3.14).

6.5 Biotite

6.5.1 Results

Figure 6.9 is a plot of X_{Mg} [X_{Mg} = Mg/(Mg+Fe)] vs. Al^{iv} and shows the composition

of the 62 biotite analyses relative to the four end-member bioitite compositions

(phlogopite, annite, eastonite and siderophyllite) which are summarized in Table 6.2. All

biotites are phlogopitic (X_{Mg} > 0.5) with a narrow range of magnesium numbers (X_{Mg})

from 0.54 to 0.66. Analyzed biotite can be subdivided into low-X_{Mg} (0.54 to 0.55),

medium-X_{Mg} (0.59 to 0.62) and high-X_{Mg} (0.63 to 0.66) groups (Fig. 6.9). Biotites from
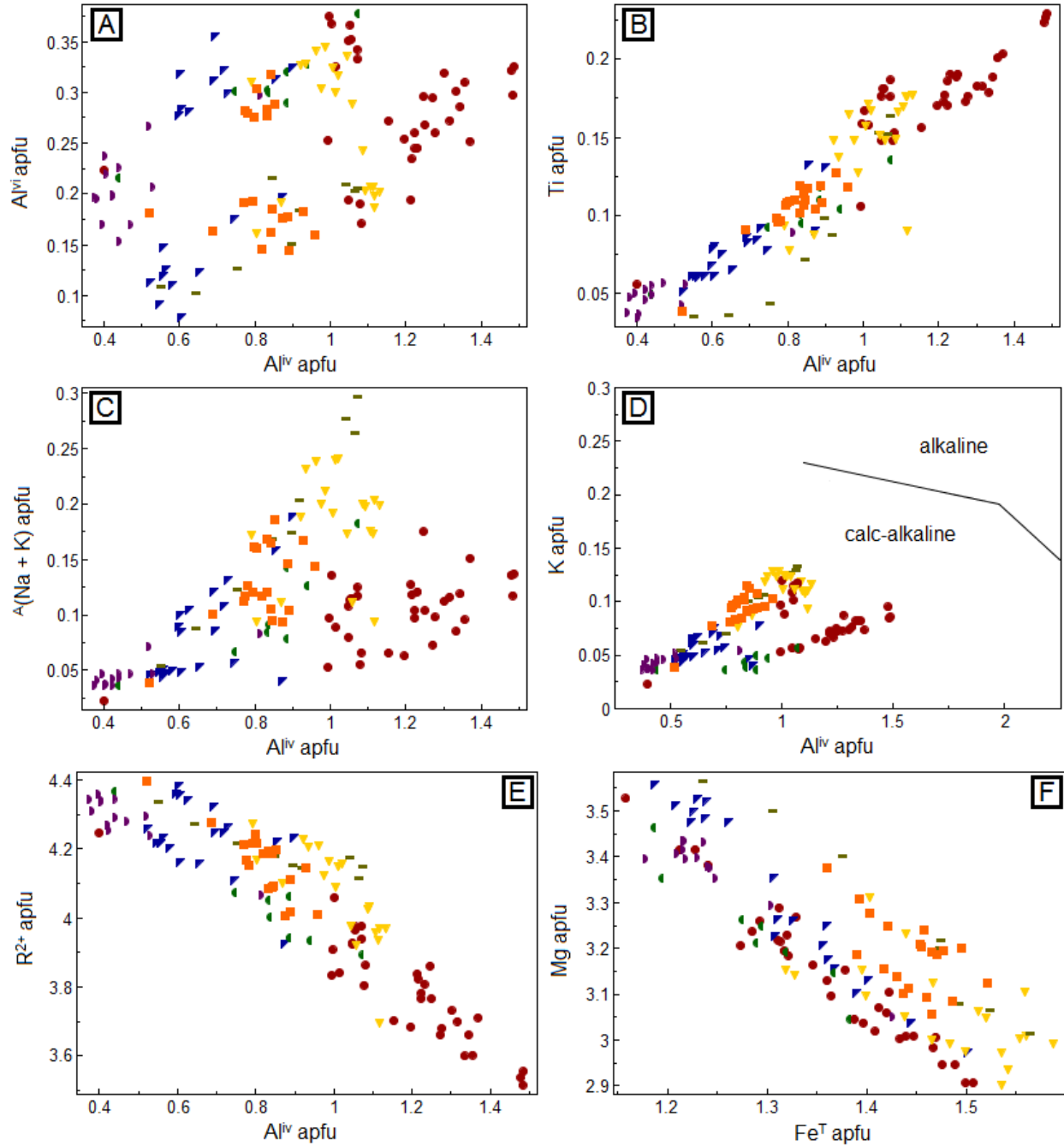
Figure 6.7 Cation variation diagrams for amphiboles from the Guichon Creek Batholith. The line on D. separating the stability fields for amphibole compositions in equilibrium with calc-alkaline and alkaline melts is from Ridolfi and Renzulli (2012). R^{2+} = the sum of cations with 2+ charges in the C-site. See Figure 6.6 for legend.
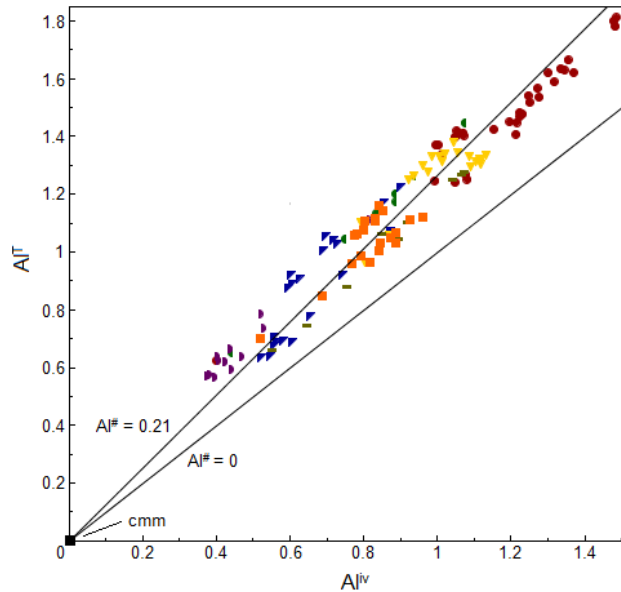
Figure 6.8 Al^T vs. Al^{iv} diagram for Guichon Creek Batholith amphiboles. The majority of volcanic amphiboles from Ridolfi et al. (2010) plot between the lines for $Al^\# = 0$ and $Al^\# = 0.21$ whereas crustal and a small number of volcanic amphiboles plot above $Al^\# = 0.21$. $Al^\# = Al^{vi}/Al^T$ calculated on the basis of 13 cations. See Figure 6.6 for legend.

the fine-grained granodiorite sample fall in the high-X_{Mg} group, whereas the medium-X_{Mg} group contains all of the Guichon and Bethsaida biotites (Fig. 6.9). Chataway biotites are mostly medium-X_{Mg} with one analysis falling in the lower bounds of the high-X_{Mg} field (Fig. 6.9). Similarly, biotites from the Skeena facies straddle the boundary between medium- and high-X_{Mg} values (Fig. 6.9). A small subset of Border facies analyses plot with different compositions to all other samples and they are closer to end-member eastonite (Fig. 6.9). All three analyses belong to a single biotite crystal from sample MD046, and their anomalous compositions have been attributed to chlorite alteration (Fig. 6.10). These spots were initially chosen regardless of their altered nature due to the general lack of biotite in most Border facies samples in hopes that usable data could be obtained from them.

Table 6.2 Summary of biotite end-member compositions.

Name	Formula	Mg/(Mg+Fe$_{tot}$)	Al^{iv} (a.p.f.u.)
Phlogopite	K$_2$Mg$_6$[Al$_2$Si$_6$O$_{20}$](OH)$_4$	1	2
Annite	K$_2$Fe$^{2+}_6$[Al$_2$Si$_6$O$_{20}$](OH)$_4$	0	2
Eastonite	K$_2$Mg$_4$Al$_2$[Al$_4$Si$_4$O$_{20}$](OH)$_4$	1	4
Siderophyllite	K$_2$Fe$^{2+}_4$Al$_2$[Al$_4$Si$_4$O$_{20}$](OH)$_4$	0	4

Halogens are dominated by Cl, with F below the lower limit of detection, with the exception of one fine-grained granodiorite facies analyses (MD063 Bt-1.3). Chlorine contents are highest in biotite from the Border facies with 0.14 to 0.16 atoms per formula unit (apfu), whereas all subsequent facies have low chlorine contents (0.01 to 0.08 apfu).

Figure 6.11 shows changes in X$_{Mg}$ and various elements with decreasing relative age. X$_{Mg}$ increases with decreasing age up to the emplacement of the Bethlehem facies followed by a progressive decrease to the Bethsaida facies (Fig. 6.11). Al^{iv} and K apfu remain relatively constant with decreasing age with the exception of the fine-grained granodiorite facies, which shows anomalously high K contents (Fig. 6.11). The Ti content in biotite decreases from the Border to fine-grained granodiorite facies and slightly increases in the Bethsaida facies (Fig. 6.11). Manganese contents increase in younger facies (0.01 to 0.08 apfu), whereas Cl contents show a sharp decrease between the Border and Guichon facies and a more gradual decrease from the Guichon through the Bethsaida facies (Fig. 6.11). The exception to the above is the fine-grained granodiorite facies, which has higher Cl contents, similar to the Guichon facies. Biotite from all facies have a minimal range of Cl contents with the exception of the Guichon and fine-grained granodiorite facies (Fig. 6.11).
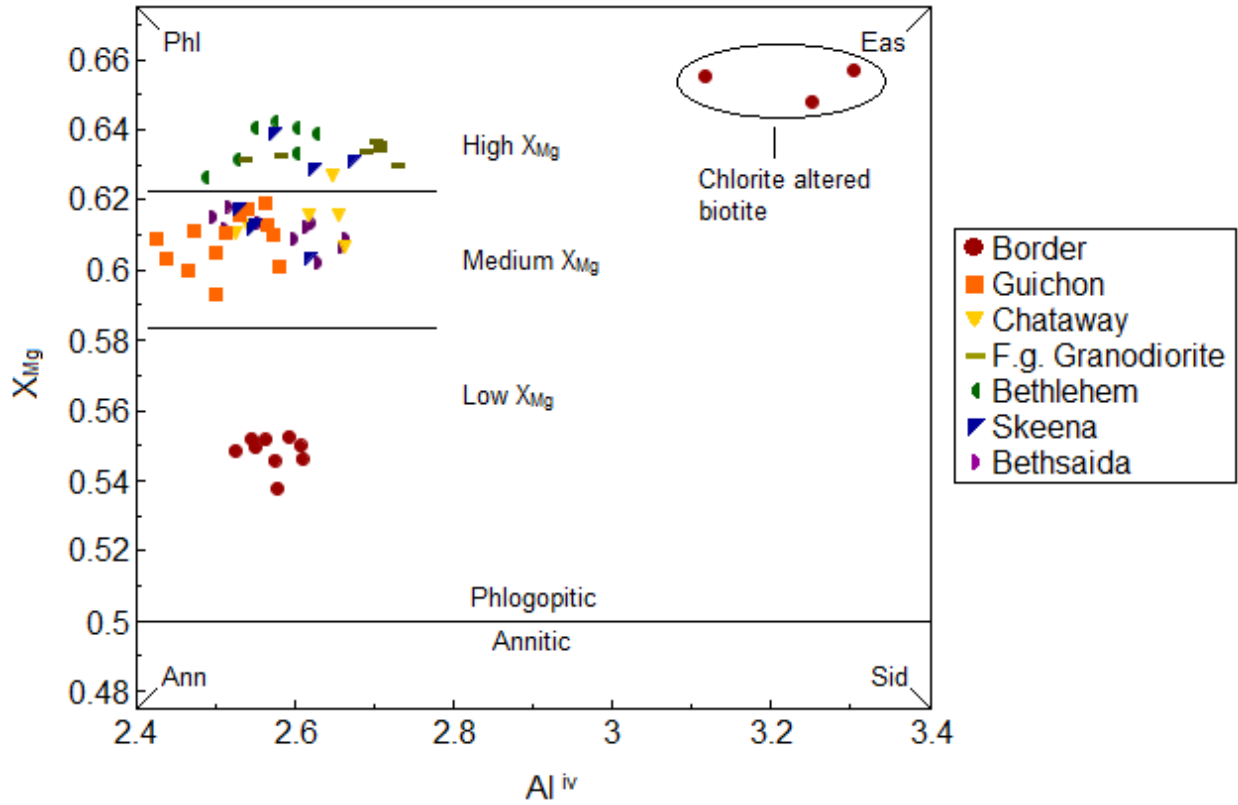
Figure 6.9 Biotite compositions for the Guichon Creek Batholith. Classification is based on the end-member X_{Mg} and Al^{iv} compositions reported in Table 6.2 with a cutoff of $X_{Mg} > 0.5$ for phlogopitic biotite.
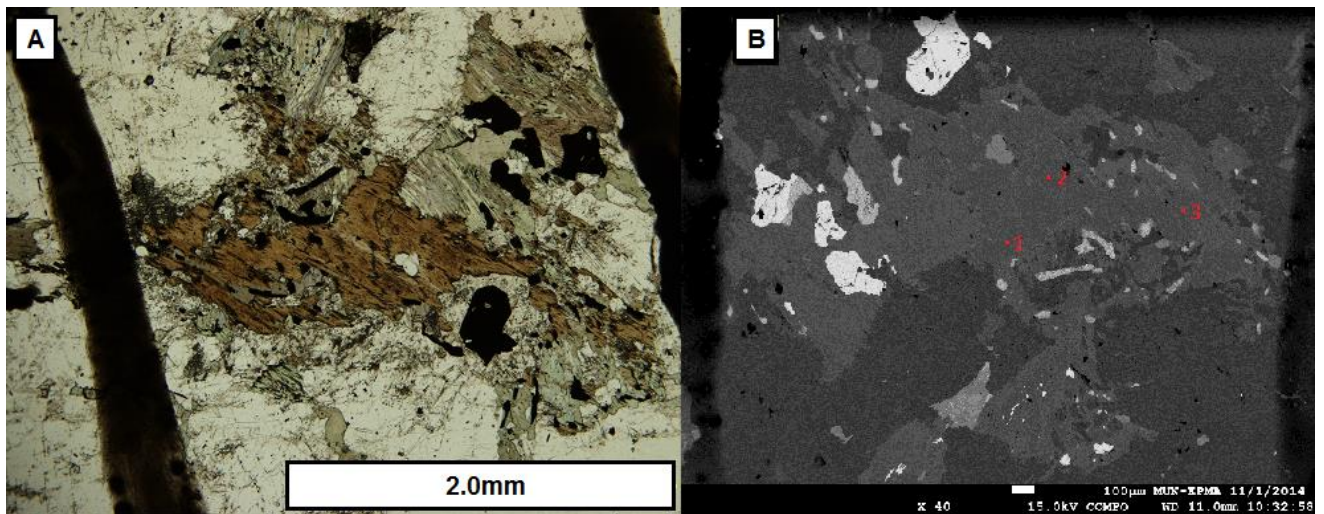
Figure 6.10 A. Photomicrograph of MD046-Bt-1. PPL, transmitted light. B. Backscatter electron image of MD046-Bt-1. Numbered points indicate the locations of spot analyses. The spots analyzed are those that plot with altered compositions in Fig. 6.9.

6.5.2 Discussion

Because Mn increases and Cl decreases with decreasing age in a given X_{Mg} group, the ratio Mn/Cl was used to illustrate the compositional differences between biotites from each intrusive facies as a function of evolution of the Guichon Creek Batholith (Fig. 6.12). The low X_{Mg} in the Border facies biotites, relative to the later facies, is interpreted to result from the sharp decrease in modal amphibole in the Guichon and later facies. The high X_{Mg} in biotites from the Bethlehem facies (MD059) and the three Skeena analyses (all from MD034) are interpreted to reflect leaching of Fe to circulating hydrothermal fluids as they are located proximal to the Bethlehem and Valley deposits, respectively (Fig. 6.13).

Chlorine content in igneous biotite is strongly dependant on pressure, temperature (higher-T favours partitioning of Cl$^-$ into biotite; Zhu and Sverjensky, 1991) and pH (Munoz, 1974), as well as total Cl$^-$ concentration in the melt. It is likely that the decrease in Cl in biotite between emplacement of the Border and Guichon facies is caused by the loss of Cl$^-$ from the melt resulting from exsolution of an aqueous/vapour phase. The subsequent gradual decrease is probably a result of a temperature decrease during crystallization of the progressively younging intrusive facies. The large range in Cl content for the Guichon facies biotite (Fig. 6.11) is interpreted to represent variable fluid exsolution resulting from varying pressure during emplacement. This interpretation is favoured over re-equilibration and losses resulting from post-emplacement alteration because the Border facies retains high Cl contents and is also exposed at the surface. It is also unlikely that the range of Cl values is the result of
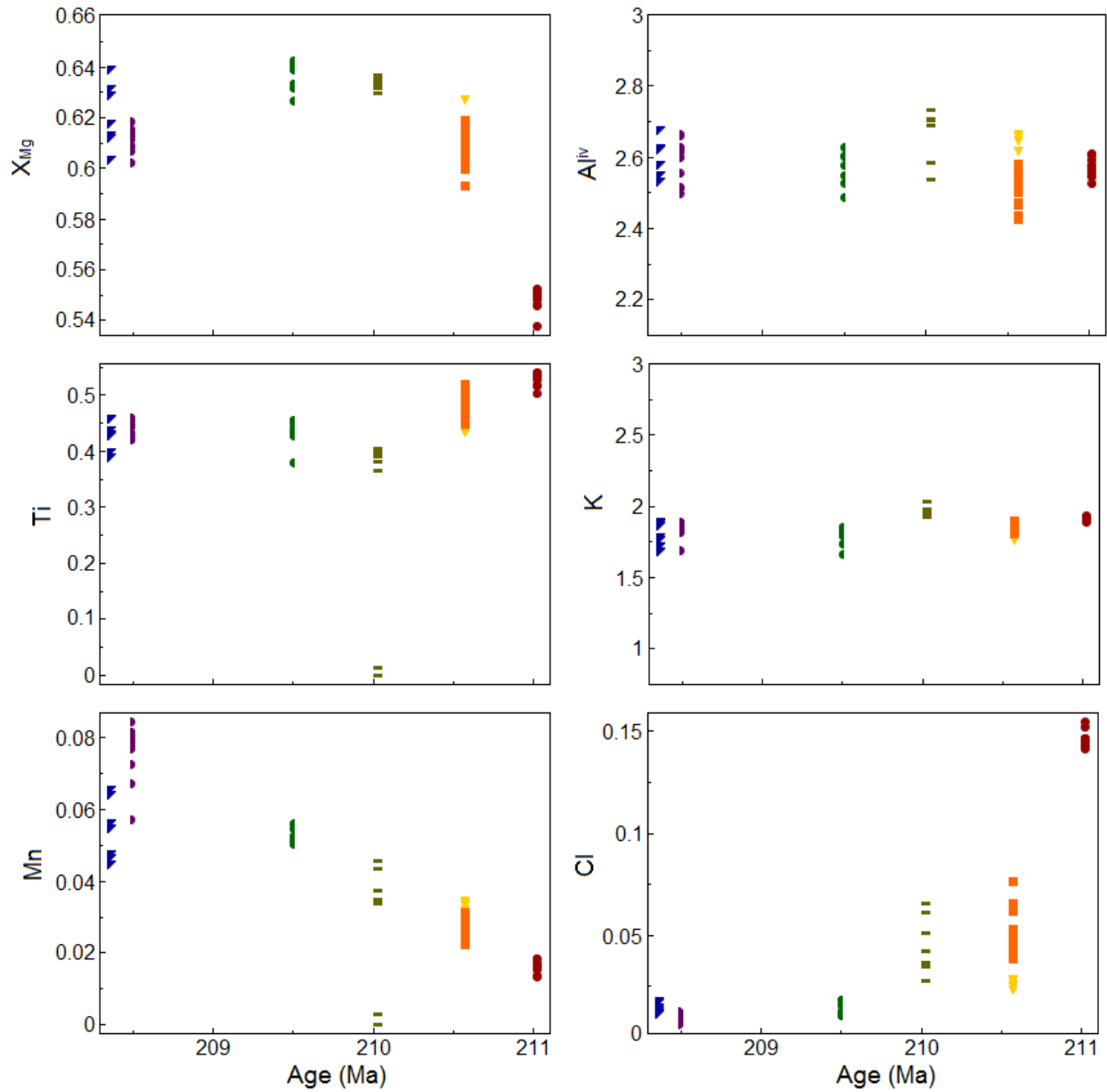
Figure 6.11 Plots showing changes in element concentrations with decreasing age for biotite analyses from the Guichon Creek Batholith. See Figure 6.9 for legend.
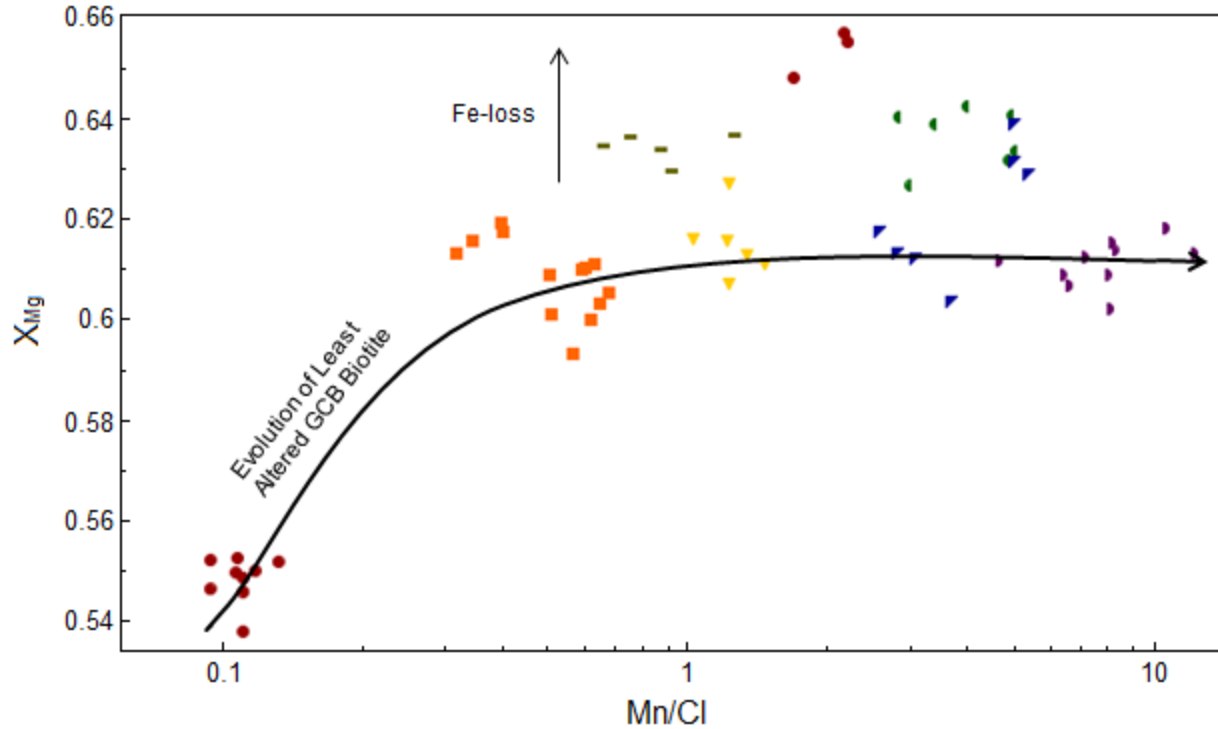
Figure 6.12 Plot of X_{Mg} vs Mn/Cl for biotites from the Guichon Creek Batholith. Trend for biotite evolution fit by hand. See text for discussion, See Figure 6.9 for legend.

multiple magma pulses as there is no coinciding variability in any other major element.

The spread of Cl contents in the fine-grained Granodiorite facies is harder to explain as

all analyses are from a single sample. It is argued to be the result of fluid exsolution

during crystallization, as in the Guichon facies, which is consistent with petrographic

evidence suggesting the fine-grained Granodiorite samples represent dykes intruded

into the Highland Valley facies. An increase in Mn with decreasing age is likely due to

normal fractionation as it follows a smooth trend from low to high contents (Fig. 6.11).

6.6 Apatite

Apatite, $Ca_5(PO_4)_3(OH,F,Cl)$, is the most abundant phosphorous-bearing mineral

in igneous rocks (Deer et al., 2013). Common substitutions in cation and anion sites
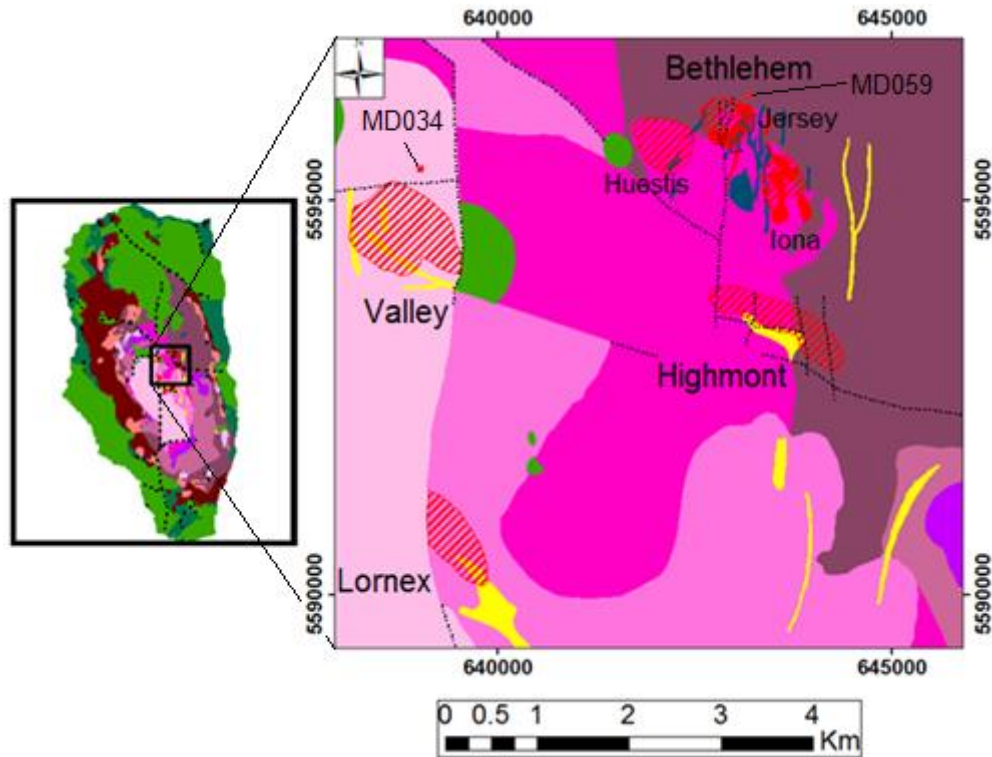
Figure 6.13 Map of the Guichon Creek Batholith with an inset of the Bethlehem and Valley areas showing the location of samples MD034 and MD059.

result in a complete solid solution between fluor-, chlor- and hydroxylapatite with varying

degrees of incorporation of REEs, C and S (Table 6.3). Because of the variety of trace

and volatile elements that can be incorporated into its structure, apatite can be used for

determining apatite saturation temperatures (AST; Piccoli and Candela, 1994),

estimating halogen fugacities (Zhu and Sverjensky, 1992; Piccoli and Candela, 1994;

Coulsen et al., 2001), crystallization temperature (Munoz, 1984) and estimating

magmatic sulphur contents (Streck and Dilles, 1998; Parat et al., 2002). Trace element

contents are dependent on αSiO_2, fO_2, total alkalis, aluminum saturation index (ASI)

and alteration (Sha and Chappell, 1999; Belousova et al., 2002). All of these factors are

important in the generation of fertile porphyry copper magmas (Blevin and Chappell,

Table 6.3 Common substitution mechanisms in apatite.

	Substitution	Reference
1	$CO_3^{2-} + F^- = PO^{4-}$	Deer et al.)2013)
2	$Sr^{2+}, Mn^{2+}, Fe^{2+}, REE, Y^{3+}, Na^+ = Ca^{2+}$	Waychunas (2002)
3	$Si^{4+}, As^{5+}, S^{6+}, C^{4+} = P^{5+}$	Waychunas (2002)
4	$Cl^-, OH^- = F^-$	Waychunas (2002)
5	$2Ca^{2+} = Na^+ + REE^{3+} + Si^{4+}$	Waychunas (2002)
6	$S^{6+} + Si^{4+} = 2P^{5+}$	Rouse and Dunn (1982)
7	$REE^{3+} + Si^{4+} \rightarrow Ca^{2+} + P^{5+}$	Rønsbo (1989)
8	$S^{6+} + Na^+ \rightarrow P^{5+} + Ca^{2+}$	Liu and Comodi (1993)

1995) suggesting that geochemical signatures in apatite may be utilized to aid in porphyry exploration.

Previous work on apatites from the Guichon Creek Batholith by Bouzari et al. (2011) characterized textural characteristics of apatite in fresh, K-silicate altered and grey muscovite (phyllic) altered host rocks using cathodoluminescence. They determined that fresh rocks are characterized by apatite with yellow and brown fluorescence, K-silicate altered rocks by apatite with green fluorescence replacing yellow fluorescence and, grey apatite in rocks that underwent phyllic alteration. Yellow fluorescence was attributed to high MnO (0.3 to 0.5 wt%), brown to low MnO (<0.2 wt%), green to lower MnO/FeO ratios regardless of absolute MnO and, grey due to significant Mn and trace element loss during phyllic alteration on the basis of Mn^{2+} and Fe^{2+} excitation (Mariano, 1988; Waychunas, 2002). Chlorine, Na and S contents were also highest in apatite from least altered rocks, with significant depletion in apatite from altered samples (Bouzari et al., 2011). A total of 110 spots were analyzed for apatite chemistry.

6.6.1 Textures

Apatite crystals are generally euhedral and <0.25mm. It occurs as inclusions in hornblende, biotite, plagioclase, Fe-Ti oxides and titanite and is easily distinguished by its hexagonal profile when cut perpendicular to the c-axis. Zoning was not observed in individual crystals under the optical or scanning electron microscope in this study; however, complex zoning in apatite from the Guichon Creek Batholith has been previously described using cathodoluminescence (Bouzari et al., 2011).

6.6.2 Results

All grains are fluorapatite (Fig. 6.14), which is characteristic of an igneous origin (Nash, 1984); however, they may be are classified into two groups (Fig. 6.14): a low-Cl group has X(Fap) from 0.55 to 0.93 and X(Cap) from 0.01 to 0.12; and a high-Cl group that has X(Fap) from 0.33 to 0.62 and X(Cap) from 0.13 to 0.23. Concentrations of CaO and P_2O_5 exhibit a narrow range from 53.9 to 56.3 wt% and 39.0 to 40.8 wt% respectively. Other major element oxides values are Al_2O_3 (<ldl to 0.07 wt%), Na_2O (0.02 to 0.21), SiO_2 (0.05 to 0.64 wt%), SO_3 (0.02 to 0.66 wt%), MnO (0.01 to 0.43 wt%), FeO (0.01 to 1.83 wt%), MgO (<ldl to 0.04 wt%), F (1.23 to 3.40 wt%), Cl (0.05 to 1.55 wt%) and MnO/FeO ratios vary significantly from 0.05 to 8.67.

Apatites lack consistent chemical zonation with the exception of SO_3 contents, which are consistently zoned from sulfur-rich cores to sulfur-poor rims (Fig. 6.15) with the exception of one apatite from the Guichon facies (Fig. 6.15b), two from the Skeena facies (Fig. 6.15e) and two from the Bethsaida facies (Fig. 6.15f), which display reverse zoning.

6.6.3 Discussion

High Cl contents and low F/Cl ratios are characteristic of apatites from the Border and Guichon facies (Fig. 6.16a-c), whereas apatites from the Bethlehem, fine-grained granodiorite, Skeena and Bethsaida facies all exhibit low Cl contents and high F/Cl ratios (Fig. 6.16a-c). Most Chataway apatites exhibit low Cl and high F/Cl, however, three analyses display high Cl and low F/Cl similar to the Guichon and Border facies (Fig. 6.16a-c). The three low Cl, high F/Cl analyses all belong to sample MD044 and are inclusions in anhydrous minerals. Another small group of apatites from the Guichon and Border facies display intermediate-Cl contents (Fig. 6.16a) and are mostly inclusions in hydrous minerals. The correlation of high- and low-Cl with low- and high-Cl/F ratios,
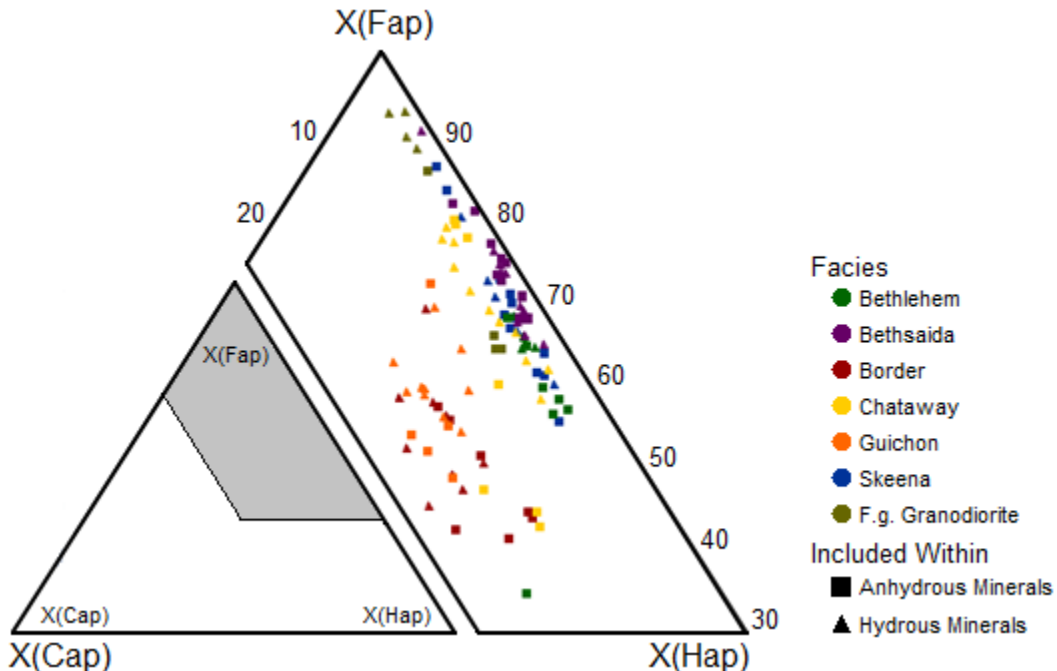
Figure 6.14 Ternary plot of apatite compositions for the Guichon Creek Batholith. Samples group into Cl-rich and Cl-poor fluorapatites.

165
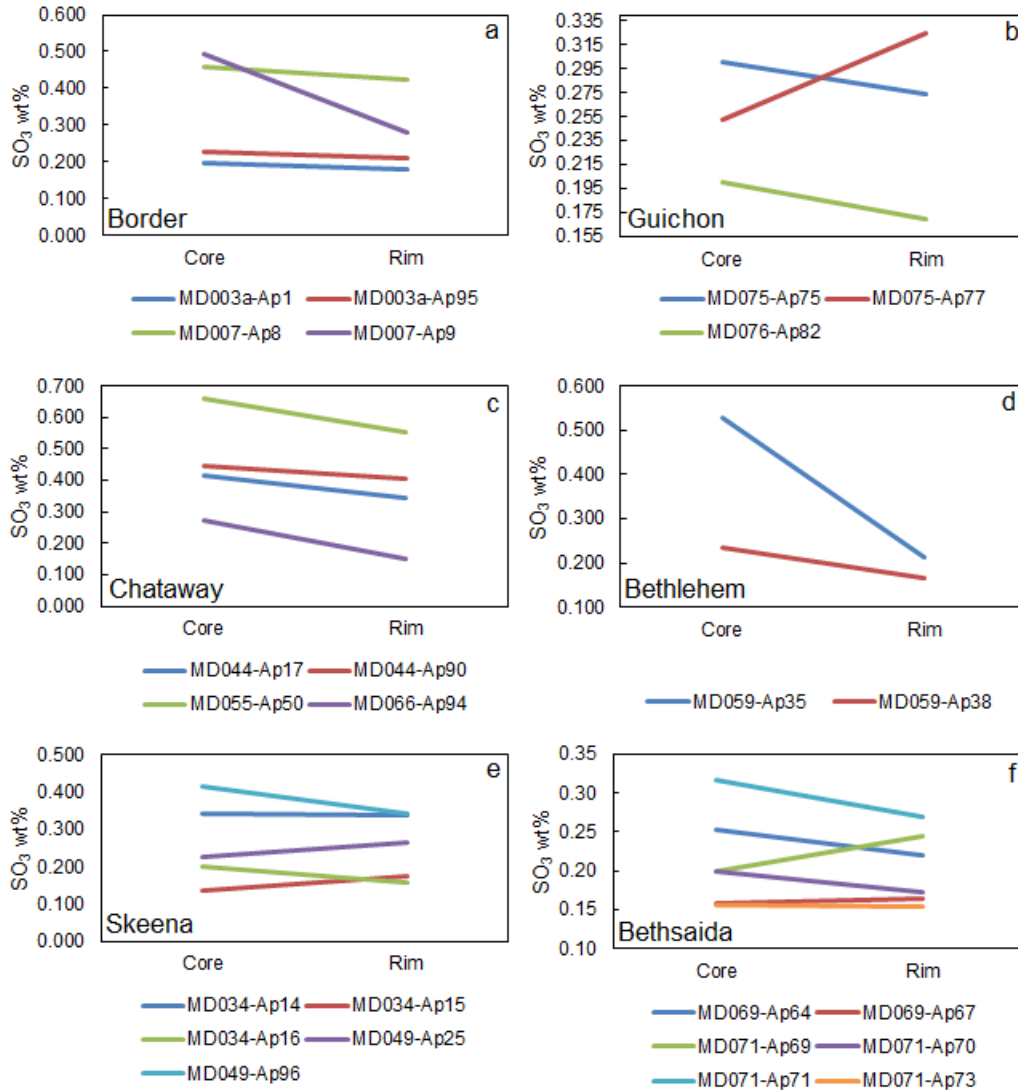
Figure 6.15 SO$_3$ zoning in apatite from the Guichon Creek Batholith.

respectively, is likely related to a loss of Cl relative to F due to interactions with an aqueous fluids as Cl is more soluble in water (Brehler and Fuge, 1974). If Cl-contents were governed by meteoric fluids and weathering processes, the high- and low-Cl groups would be restricted to inclusions in anhydrous and hydrous minerals, respectively. As this is not the case, it is argued that the low-Cl content in later crystallized apatite resulted from separation of an aqueous fluid as Cl is strongly
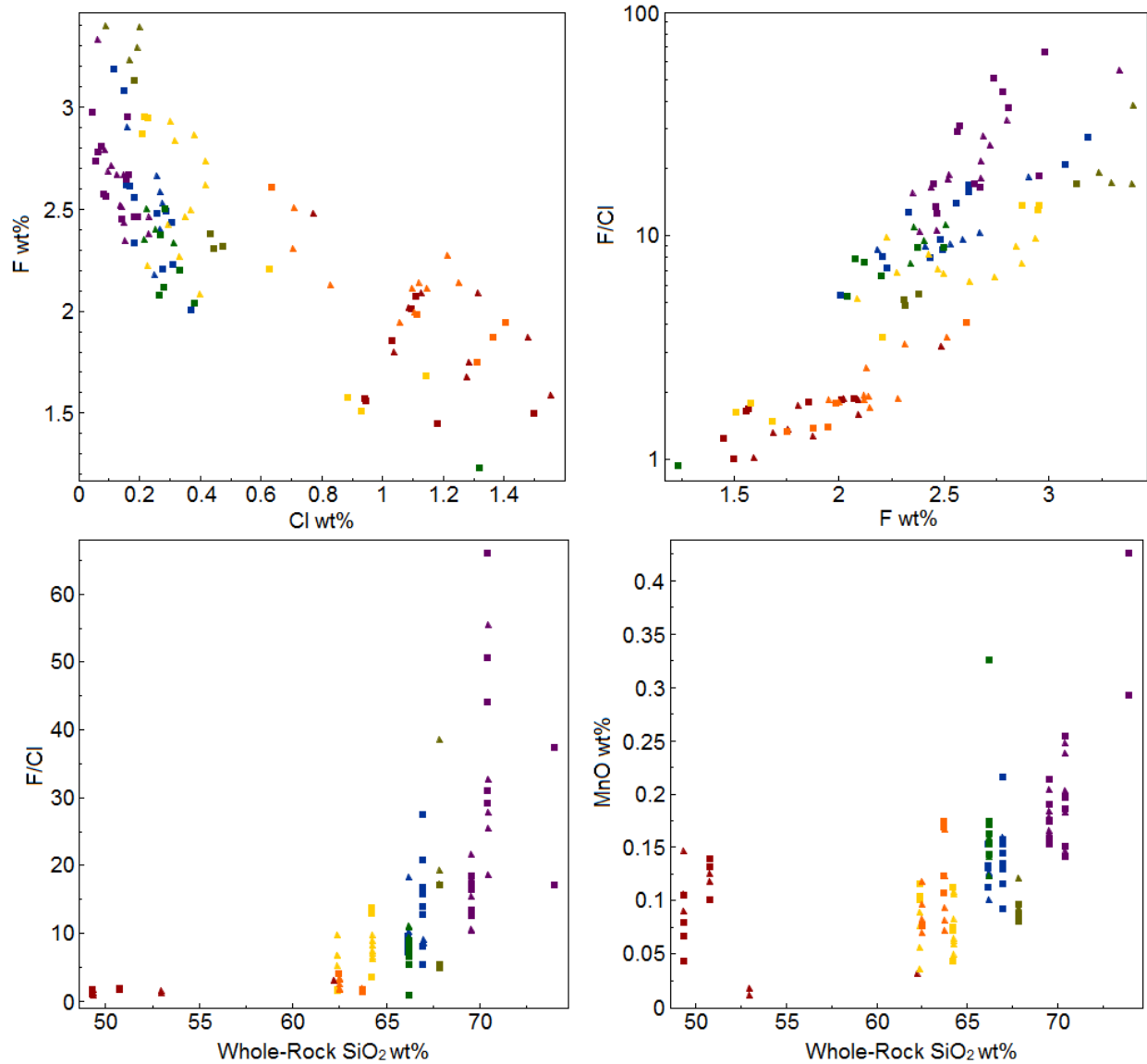
Figure 6.16 Trace element plots for apatites from the Guichon Creek Batholith: a) F vs. Cl wt%; b) F/Cl vs. F wt%; c) F/Cl vs. whole rock SiO_2 wt%; d) MnO wt% vs. whole rock SiO_2 wt%. See Figure 6.14 for legend.

partitioned into a fluid phase with respect to F (Candela, 1986; Boudreau and Kruger, 1990). Re-equilibration with a fluid phase can also explain the medium-Cl apatite inclusions in anhydrous phases of the Guichon and Border phases.

A positive correlation between MnO content in apatite and whole-rock SiO_2 is observed in Figure 6.16d and has also been reported for other igneous rocks (Belousova et al., 2002; Cao, 2012) where it has been interpreted to reflect magmatic differentiation. A similar positive correlation is observed for F/Cl vs. whole-rock SiO_2 (Fig. 6.16c), which is also attributed to differentiation.

Figure 6.17 shows trace element compositions plotted against CaO wt% for apatite from all facies as well as the field for the maximum/minimum reported values from Bouzari et al. (2011). Na_2O shows a weak negative correlation whereas SO_3 shows no correlation with increasing CaO (Fig. 6.17a,e). There is also no systematic change in Na_2O or SO_3 content between facies with all showing significant overlap (Fig. 6.17a,e). Border, Guichon and rare Chataway (MD044) samples display Cl and SiO_2 contents significantly higher than those previously reported (Fig. 6.17b,d; Bouzari et al., 2011). Similarly, the majority of analyses (mostly Border, Guichon and Chataway facies) exhibit MnO and P_2O_5 contents lower than any reported by Bouzari et al. (2011; Fig. 6.17c,f). On a plot of MnO/FeO ratio vs. MnO wt% the majority of samples lie well outside of the ranges observed by Bouzari et al. (2011) due to low MnO/FeO and/or MnO (Border, Guichon and Chataway facies; Fig. 6.17g) or elevated MnO/FeO at a given MnO wt% (Skeena and Bethsaida facies; Fig. 6.17g). It has been suggested that MnO and MnO/FeO contents will affect luminescence colours in apatite associated with B.C porphyry deposits with the lowest MnO/FeO ratios associated with phyllic and K-silicate altered host rocks imparting green luminescence and high MnO wt% and MnO/FeO values associated with apatites in fresh rocks imparting brown/yellow luminescence (Bouzari et al., 2011). The new data presented in this study suggests that some of the

168
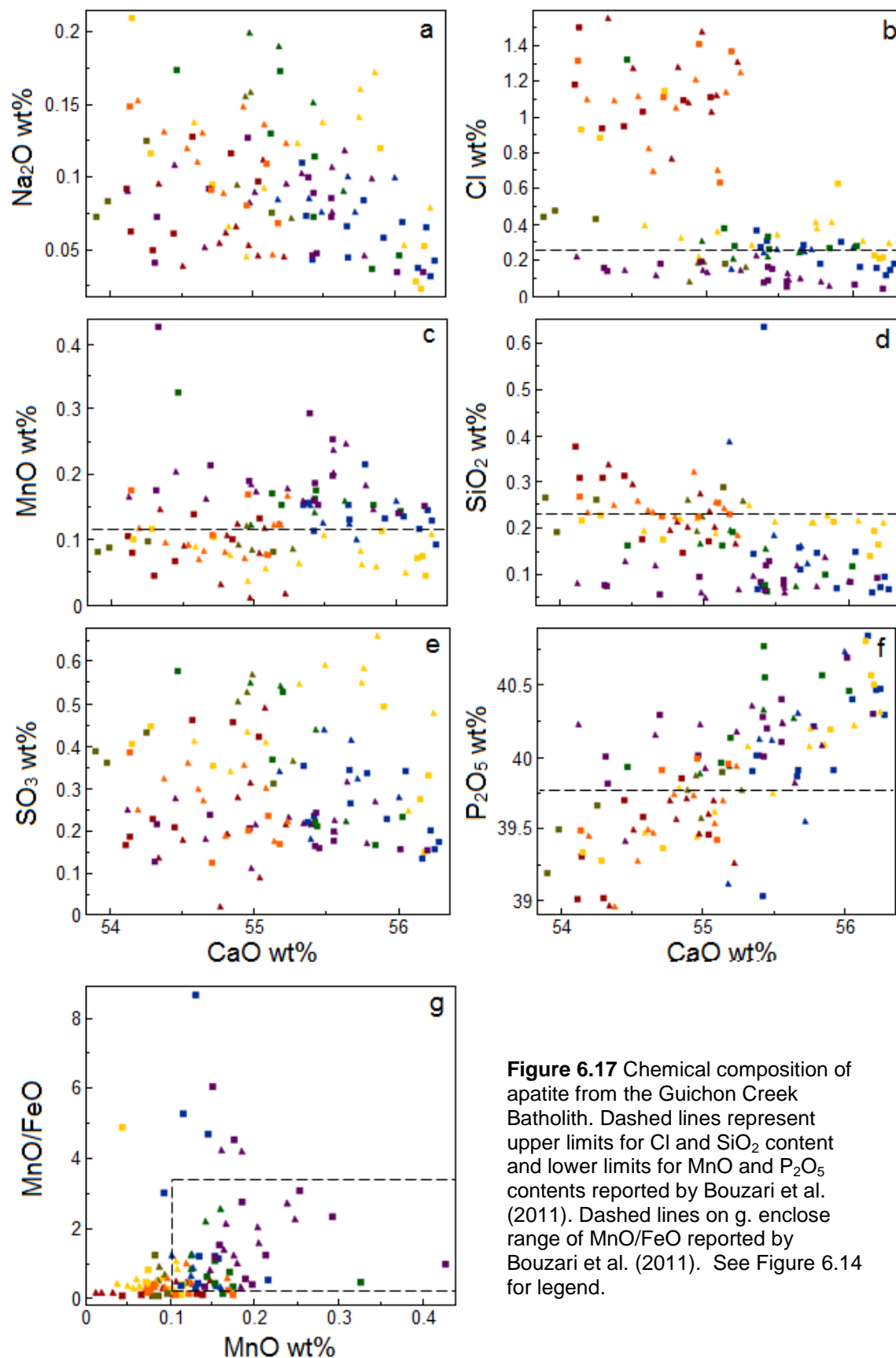
Figure 6.17 Chemical composition of apatite from the Guichon Creek Batholith. Dashed lines represent upper limits for Cl and SiO$_2$ content and lower limits for MnO and P$_2$O$_5$ contents reported by Bouzari et al. (2011). Dashed lines on g. enclose range of MnO/FeO reported by Bouzari et al. (2011). See Figure 6.14 for legend.

freshest host rocks in the Guichon Creek Batholith have the lowest MnO/FeO ratios and should display green or grey luminescence attributed to alteration in proximity to a porphyry-Cu deposit though they are found in fresh host rocks and suggests that the scheme of Bouzari et al. (2011) may need to be re-evaluated. The low MnO/FeO ratios in these samples is attributed to low total MnO as they are from the least evolved facies (Fig. 6.16d). Further examination of these apatites under cathodoluminescence would be needed to confirm luminescence colours, which may render use of apatite luminscence from glacial tills as a porphyry indicator mineral more difficult. However, most of the least altered Border, Guichon and some of the Chataway samples with low MnO also contain high Cl content (Fig. 6.18), which may enable the use of trace element chemistry of apatite in glacial tills as a tool for porphyry-Cu exploration in British Columbia.
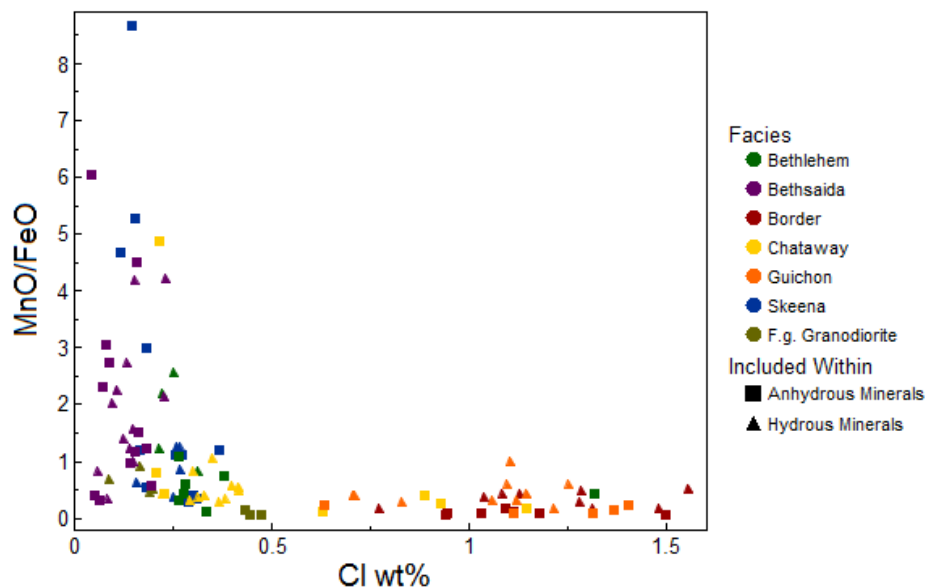
Figure 6.18 MnO/FeO ratio vs. Cl wt% for apatite. See Figure 6.14 for legend.

6.7 Oxides

The oxides consist of magnetite ($Fe^{2+}Fe_2^{3+}O_4$) and ilmenite ($Fe^{2+}TiO_3$). Magnetite is a member of the magnetite series of the spinel group ($A^{2+}B_2^{3+}O_4$) with Fe^{3+} and Fe^{2+} as the prevalent tri- and divalent cations, respectively (Deer et al., 2013). Small amounts of Al, Cr and V may substitute for Fe^{3+} and replacement of Fe^{2+} by Ca, Mn and Mg is also common (Deer et al., 2013). A solid solution also exists between magnetite and ulvöspinel ($Fe_2^{2+}TiO_4$) and intermediate compositions containing a significant ulvöspinel component are often termed titanomagnetite (Deer et al., 2013). Ilmenite is characterized by a rhombohedral crystal structure and the most common substitutions are Mg, Mn, Cr, and V for Fe^{2+} and Fe^{3+} and Zr for Ti (Deer et al., 2013). When pairs of coexisting magnetite and ilmenite are present and in equilibrium in igneous rocks, their compositions may be used as a geothermometer and oxygen barometer (Carmichael, 1967; Andersen and Lindsley, 1988; Ghiorso and Sack, 1991; Ghiorso and Evans, 2008).

A total of 114 spot analyses were conducted to characterize oxide chemistry in the Guichon Creek Batholith. Of these, 94 were on magnetite crystals and 20 were on ilmenite. Ilmenite crystals coexisting and in contact with magnetite were prioritized for analysis and a total of 11 magnetite-ilmenite pairs were suitable for assessment of equilibrium conditions in order to evaluate equilibrium which is necessary for oxide thermometry and estimation of fO_2.

6.7.1 Textures

Oxides in the Guichon Creek Batholith occur in a number of textural styles (Fig. 6.19a-f). Magnetite crystals are sub- to euhedral and occur in all facies. Unaltered

magnetite is commonly in contact with magnetite grains containing significant ilmenite exsolution (Fig. 6.19a-c) and more rarely pure ilmenite (Fig. 6.19c) in granular aggregates, particularly in the Guichon facies. Mottled textures are also common in magnetite crystals with small subgrains of hematite concentrated along grain boundaries (Fig. 6.19d). In the Bethsaida and Skeena facies, aggregates of magnetite, apatite, titanite are common and these aggregates contain rare barite (Fig. 6.19b,e). Magnetite crystals in all facies commonly contain inclusions of euhedral apatite (Fig. 6.19e). Ilmenite mainly occurs as exsolutions in magnetite grains (Fig. 6.19a,f), and are commonly affected by patchy alteration (Fig. 6.19a). Patchy alteration of shredded ilmenite rarely occurs in some samples associated with altered biotite (Fig. 6.19d).

6.7.2 Results

As EPMA analysis is only capable of measuring FeO, Fe^{3+} contents were estimated using the method of Droop (1987), which assumes perfect stoichiometry and charge balance. This method is appropriate as neither magnetite nor ilmenite contain vacant cation sites and Fe is the only element with varying valence states present in a significant amount. The formula used in this estimation was:

$$F = 2X\left(1 - \frac{T}{S}\right)$$

where T and X are the ideal number of cations and oxygens per formula unit, S is the observed cation total assuming all iron to be Fe^{2+} and F is the number of Fe^{3+} ions per X oxygens.
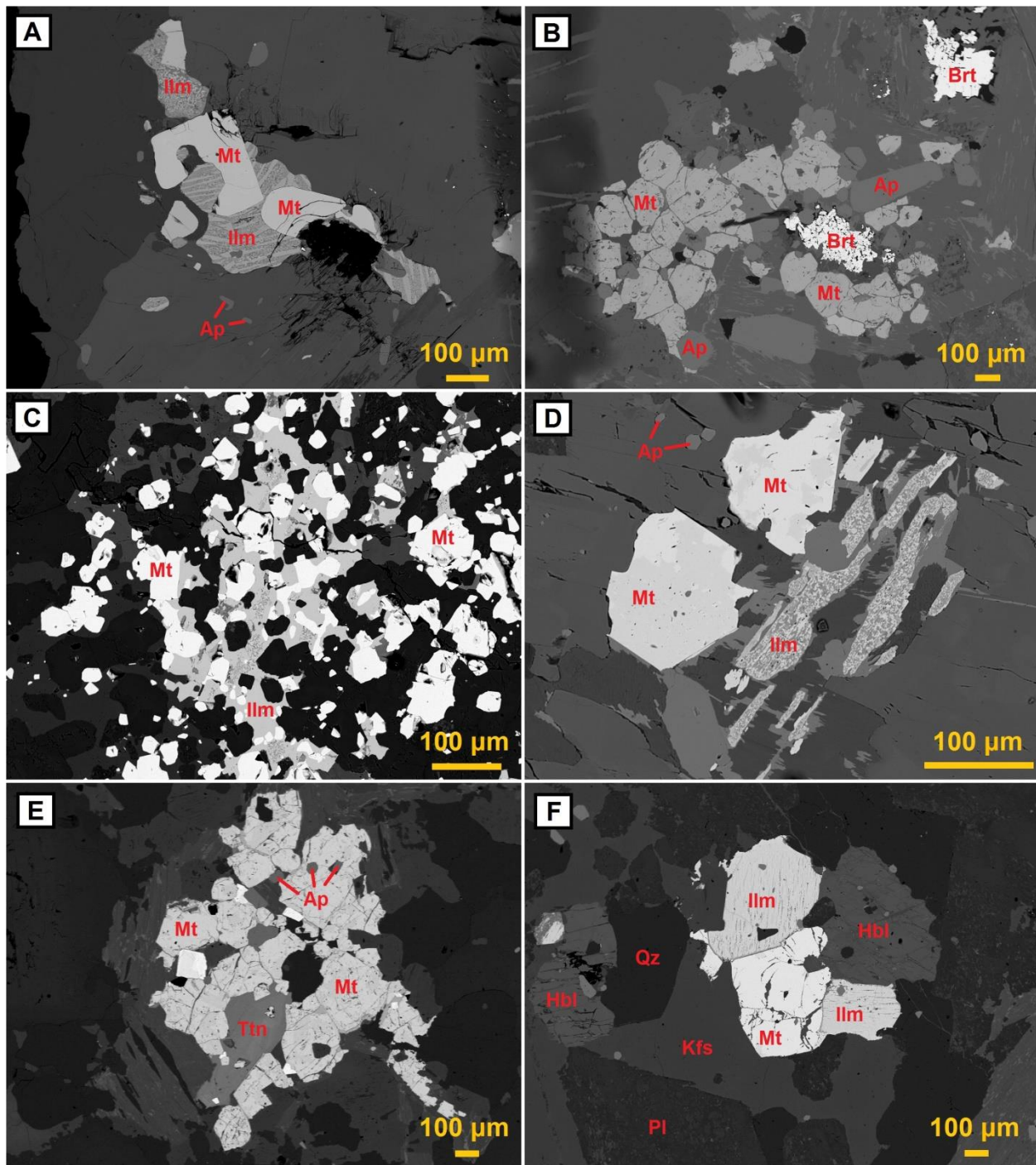
Figure 6.19 Backscatter electron images (BSE) of oxides from the Guichon Creek Batholith. A. Pure magnetite crystals co-existing with magnetite crystals containing ilmenite exsolutions; MD003a. B. A cluster of magnetite crystals and associated apatite and barite; MD071. C. Patch of 'Speckled' magnetite (white) and ilmenite (grey); MD076. D. Magnetite with mottled zoning and ilmenite with patchy alteration; MD049. E. Magnetite with apatite inclusions and titanite; MD004. F. Unaltered magnetite crystal in contact with ilmenite; MD044. Mt – magnetite, Ilm – ilmenite, Brt – barite, Ap – apatite, Ttn – titanite, Qz-quartz, Kfs – K-feldspar, Pl – plagioclase, Hbl – hornblende.

Magnetites are characterized by low Mn (<0.008 apfu), Cr (<0.005 apfu), V (<0.025 apfu) and Ti (<0.031 apfu) contents. Similarly, Mg (<0.002 apfu), Si (<0.003 apfu), Al (<0.05 apfu) contents are also typically low, but a few outlier analyses are present for these elements (<4 analyses). Ferric and ferrous iron contents are relatively restricted (Fe^{3+} = 1.810 to 1.989 and Fe^{2+} = 0.994 to 1.024 apfu) and close to stoichiometric proportions.

Ilmenite compositions are more varied than magnetite (Fig. 6.20). The variability in ilmenite compositions likely reflects disequilibrium and alteration as indicated by the predominance of exsolution and patchy alteration textures (Fig. 6.19a,d,f).

6.7.3 Discussion

Oxide compositions are plotted in Ti-Fe^{2+}-Fe^{3+} space on Figure 6.21. Increasing Fe^{2+} is strongly correlated with a decrease in Fe^{3+} and an increase in Ti (Fig. 6.22a,d). This is consistent with the substitution of Fe^{2+} + Ti^{4+} for Fe^{3+}, resulting in a greater ulvöspinel ($Fe_2^{2+}TiO_4$) component common in titanomagnetite. Aluminum content decreases with increasing Fe^{3+} indicating limited substitution of a spinel component in some grains (Fig. 6.22f). Manganese contents display a strong negative correlation with
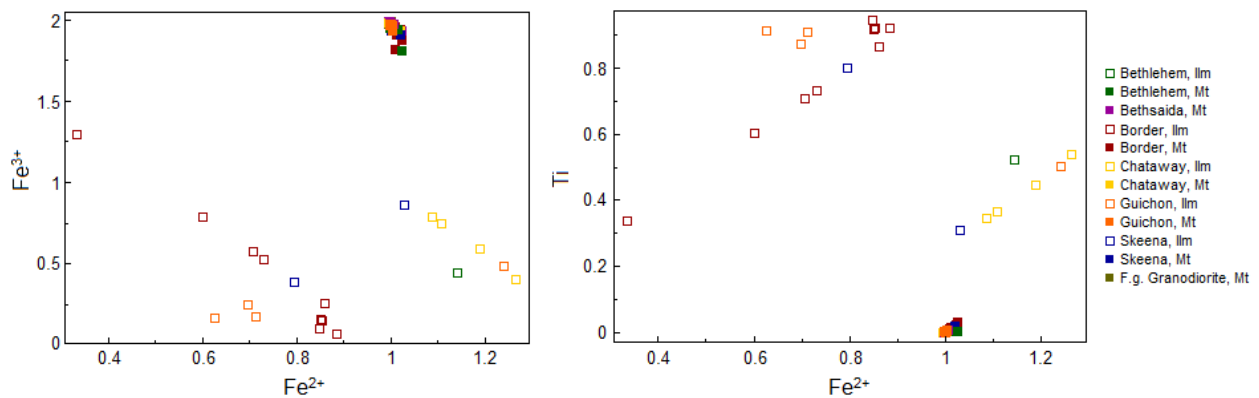
Figure 6.20 Chemical variation diagrams for Ti-rich iron oxides in the Guichon Creek Batholith.
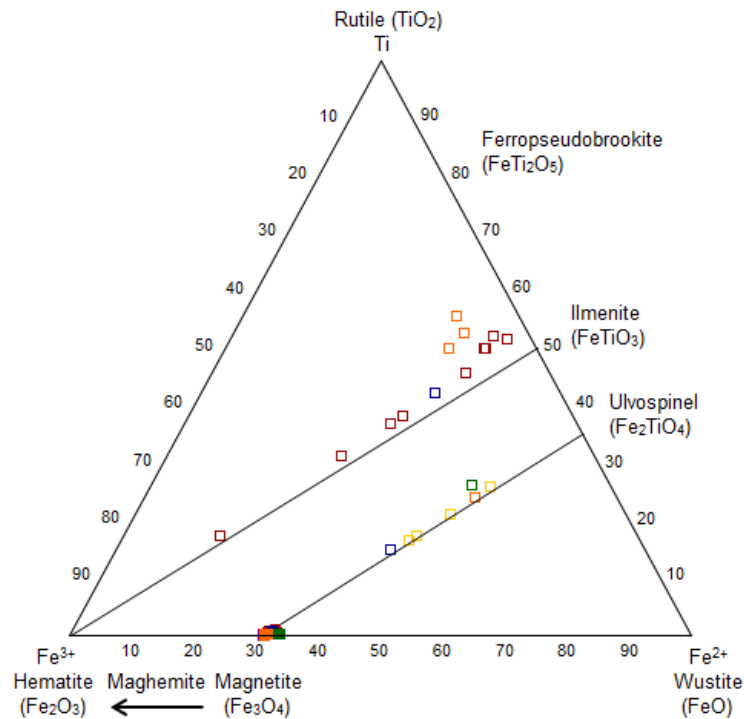
Figure 6.21 Oxide compositions of the Guichon Creek Batholith in Ti-Fe^{2+}-Fe^{3+} space from Taylor (1964). See Figure 6.20 for legend.

Fe^{2+} at low Fe^{2+} apfu (<0.1005) and more scatter at higher Fe^{2+} contents (Fig. 6.22c). This is consistent with the substitution of Mn^{2+} for Fe^{2+} in the magnetite structure.

Magnetite can be subdivided into two groups based on V content (Fig. 6.22e). Magnetite from the Border and Guichon facies belong to the high V group and magnetite from the remaining facies belong to the low V group (Fig. 6.22b). Chromium contents are also variable between different facies, with high Cr present in magnetite from the Border and Guichon facies, as well as sample MD044 from the Chataway facies (Fig. 6.22f). Lower Cr contents are typical for magnetite from the Bethlehem through Bethsaida facies and Chataway sample MD066 (Fig. 6.22f). Excluding the

difference in Cr and V, there are no other systematic variations in chemistry between the different facies.

The Ti-rich oxides are characterized by lamellar and patchy exsolution textures as well as highly varied and scattered geochemical trends (Fig. 6.20). A wide range of Fe^{2+} and Ti contents (Fig. 6.20), varying greatly from stoichiometric values for ilmenite and ulvöspinel, in conjunction with textural evidence indicates disequilibrium. Equilibrium between coexisting magnetite and Ti-rich oxides was tested by the method of Bacon and Hirschmann (1988) with a plot of log(Mg/Mn) in magnetite vs. log(Mg/Mn) for coexisting Ti-rich oxides (Fig. 6.23). All coexisting oxide pairs except for one plot outside of the 2σ error bars for the equilibrium line, confirming textural and stoichiometric evidence for disequilibrium. The oxides likely represent exsolution of ilmenite and ulvöspinel from Ti-rich magnetite under subsolidus conditions as the continuous solid solution between magnetite and ulvöspinel becomes unstable at temperatures below 600°C (Deer et al., 2013).
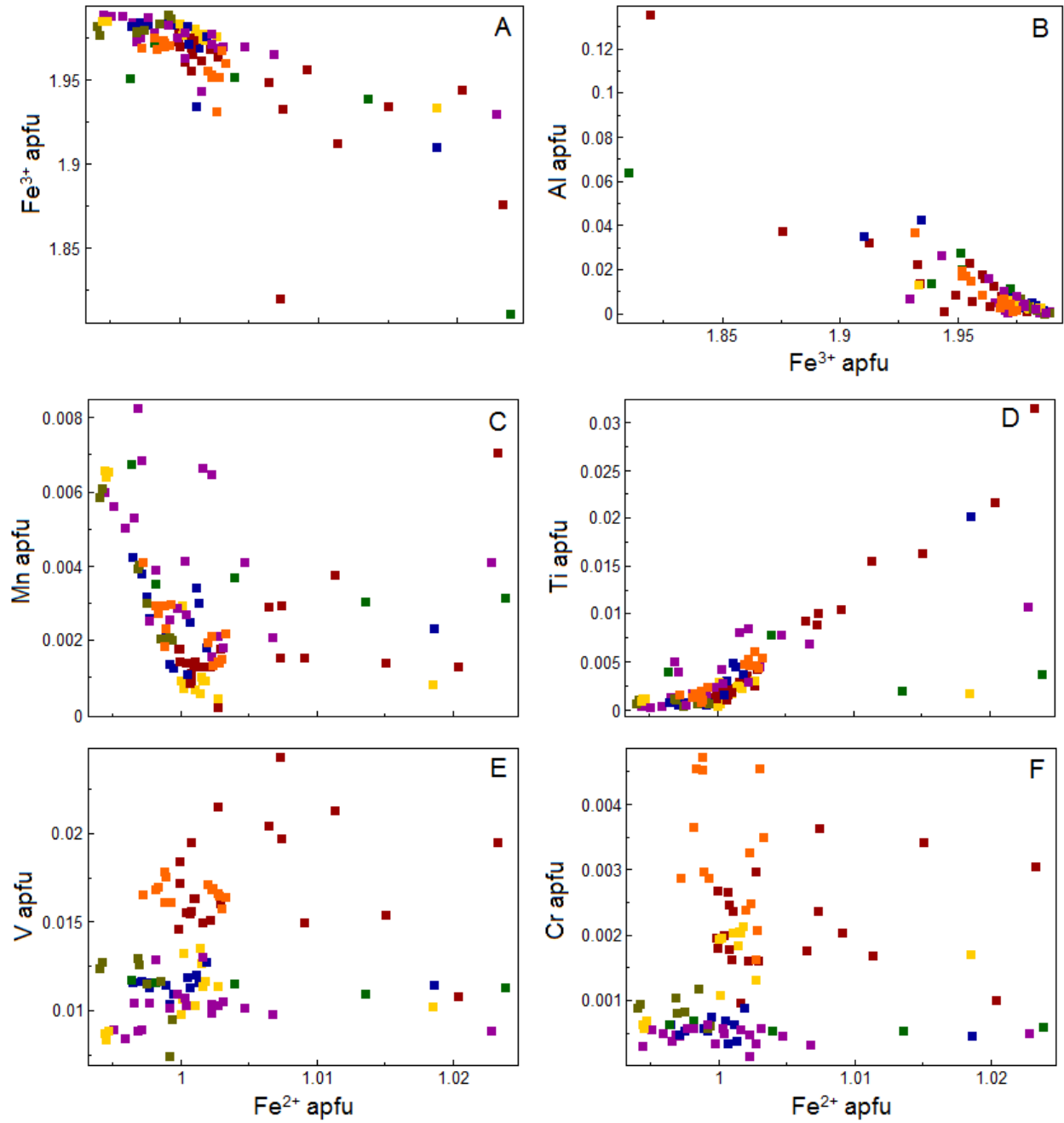
Figure 6.22 Chemical variation diagrams for magnetite in the Guichon Creek Batholith. See Figure 6.20 for legend.

177
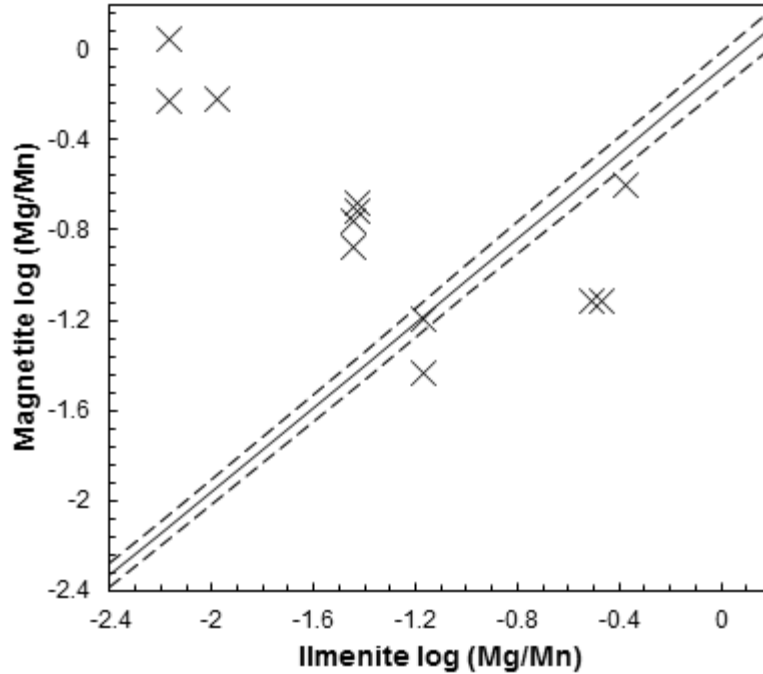
Figure 6.23 Plot of the atomic Mg/Mn ratio of oxide pairs compared to the equilibrium line of Bacon and Hirschmann (1988) with dashed lines representing the 2σ error envelope.

6.8 Estimation of Intensive Parameters

6.8.1 Temperature and Pressure

A number of empirical and experimental geobarometers and geothermometers have been developed for calcic amphibole- and plagioclase-bearing plutonic rocks (e.g., Otten, 1984; Hammarstrom and Zen, 1986; Johnson and Rutherford, 1989; Rutter et al., 1989; Blundy and Holland, 1990; Schmidt, 1992; Anderson and Smith, 1995; Ernst and Liu, 1998; Féménias et al., 2006; Ridolfi et al., 2010; Ridolfi and Renzulli, 2012).

Geothermometers available for use in calc-alkaline granitic rocks include the Ti-in-hornblende thermometer (Otten, 1984), amphibole-plagioclase thermometer (Blundy and Holland, 1990), combined Al_2O_3-TiO_2 thermobarometer (Ernst and Liu, 1998) and the amphibole stability and chemical equilibrium thermobarometric and chemometric

calculations of Ridolfi et al. (2010) and Ridolfi and Renzulli (2012). This study utilized and compared temperature estimates from the geothermometer of Otten (1984), geobarometer of Anderson and Smith (1995) and the thermobarometric equations of Ridolfi and Renzulli (2012). The thermobarometric equations of Ridolfi and Renzulli (2012) were chosen as they have been shown to be the most accurate and precise thermobarometers and are not reliant on a particular buffering mineral assemblage, although it must be noted that the crystallization temperatures and pressures for Guichon Creek Batholith amphiboles were expected to be slightly lower than the range of values used in their empirical calibrations (i.e., P = 130 to 2200 MPa and T = 800 to 1130°C) as they formed formed in a hypabyssal environment. The Al-in-hbl geobarometer of Anderson and Smith (1995) and Ti-in-hbl geothermometer of Otten (1984) were selected as they are valid for all amphibole-bearing granitic rocks (with the appropriate buffer assemblage) and all igneous and sub-solidus amphiboles respectively, allowing for a check on the accuracy of the Ridolfi and Renzulli (2012) estimates.

The equations of Ridolfi and Renzulli (2012), used to estimate pressure and temperature as well as fO_2, H_2O_{melt} and anhydrous melt compositions (sections 6.8.3 and 6.8.4). The conditions under which they are valid are presented in Table 6.4. The equations were determined empirically through statistical analysis of natural and experimental calcic-amphiboles and are only valid for igneous amphiboles formed in equilibrium with calc-alkaline melts in volcanic or sub-volcanic/plutonic environments and should not be applied to amphiboles affected by hydrothermal processes (Ridolfi and Renzulli, 2012). Crystals were therefore screened for disequilibrium textures (e.g.,

skeletal and swallow-tailed microstructures) and only analyses with Ti apfu > 0.1 were selected for estimation of intensive parameters as this is typically the cutoff value for igneous amphiboles (pers. comm., Dilles, 2015). Representative amphibole compositions are presented in Table 6.5. The resulting pressure and temperature estimates are presented in Table 6.6 as well as estimates for depths of intrusion, which were estimated by assuming an average specific weight for oceanic crust of $2.89g/cm^3$ (Carlson and Raskin, 1984) and leveling all resulting depths to an equal elevation of 1500m (Table 6.6). Although the Guichon Creek Batholith is now part of the North American continent, the average specific weight of oceanic crust was chosen as it was formed on top of the Nicola island arc in the Late Triassic.

The Ti-in-hbl thermometer of Otten (1984) was derived utilizing the experimental data of Helz (1973) who showed that the Ti content of hornblende as a function of temperature is controlled by crystal-chemical limitations of the amphibole crystal structure and not melt composition. Lower than expected Ti contents may occur when the fO_2 is too close to the hematite-magnetite (HM) buffer (Helz, 1973) or if there is a Ti deficiency in the melt (Otten, 1984); therefore, the thermometer is only applicable when fO_2 is near the fayalite-magnetite-quartz (FMQ) and nickel-nickel-oxide (NNO) buffers and a titanium-bearing phase is present in the stable mineral assemblage. As the presence of quartz + magnetite + titanite with magnesian amphibole implies fO_2 conditions above the fayalite-magnetite-quartz (FMQ) buffer (Wones, 1989), all samples meet the criteria necessary for the thermometer's use. Temperatures are reported in Table 6.6 and were calculated using the equation:

Table 6.4 Thermobarometric and chemometric equations used in calculation of intensive parameters from Ridolfi and Renzulli (2012).

Eq	Dependent Variable	Constant	Independent Variables											
			Si	Ti	Al	Fe	Mg	Ca	Na	K	Pressure	$\sigma_{(est)}$	$\sigma_{(est)}$(%)
1a	lnP (130/2,200 MPa)	125.93	-9.5876	-10.116	-8.1735	-9.2261	-8.7934	-1.666	2.4835	2.5192	–	160	19.3
1b	lnP (130/500 MPa)	38.723	-2.6957	-2.3565	-1.3006	-2.778	-2.4838	-0.661	-0.2705	0.1117	–	43	13.1
1c	P (130/500 MPa)	24,023	-1,925.30	-1,720.60	-1,478.50	-1,843.20	-1,746.90	-158.3	-40.444	253.52	–	37	14.9
1d	P (400/1,500 MPa)	26,106	-1,991.90	-3,035.00	-1,472.20	-2,454.80	-2,125.80	-830.6	2,708.80	2,204.10	–	–	
1e	lnP (930/2,200 MPa)	26.543	-1.2085	-3.8593	-1.1054	-2.9068	-2.6483	0.5134	2.9752	1.8147	–	–	
2	T(°C) (800/1130 °C)	17,098	-1,322.30	-1,035.10	-1,208.20	-1,230.40	-1,152.90	-130.4	200.54	29.408	24.41	23.5	
3	ΔNNO (-2.1/3.6 log units)	214.39	-17.042	-26.08	-16.389	-18.397	-15.152	0.2162	6.1987	14.389	–	0.37	
4	lnH$_2$O$_{melt}$ (2.8/12.2 wt%)	-65.907	5.0981	3.1308	4.9211	4.9744	4.6536	1.0018	-0.789	-0.539	0.4642	0.78	14.4
5	SiO$_2$ (52.6/78.1 wt%)	-142.31	22.008	-15.306	2.188	16.455	12.868	0.4085	6.71	20.98	-9.6423	1.25	
6	lnTiO2 (0.1/2.4 wt%)	97.954	-9.0415	-4.2383	-4.4955	-8.4409	-7.2865	-1.926	-0.5651	0.1928	42.139	0.16	27.6
7	Al$_2$O$_3$ (12.2/19.8 wt%)	-52.839	3.3116	6.8641	8.64	6.076	6.9081	-0.34	1.9713	-0.7151	4.8816	0.48	
8	lnFeO (0.5/10.8 wt%)	-8.6576	0.007	4.5518	1.8145	1.1984	1.2713	0.3236	-0.803	-5.3301	–	0.85	23.6
9	MgO (0.0/4.9 wt%)	73.818	-6.2053	-0.32	-3.9986	-6.2767	-5.3359	1.1256	-2.8936	-5.5058	8.6765	0.26	
10	CaO (0.4/8.7 wt%)	130.54	-12.941	-2.2341	3.0863	-12.813	-10.362	-4.016	-7.4515	-13.561	224.48	0.58	
11	lnK$_2$O (0.8/5.8 wt%)	7.1059	-0.1302	-2.1327	-1.0459	-0.5768	-0.5424	-0.996	1.0093	9.231	-0.00051	0.42	13

Each dependent variable is calculated by adding the constant to the sum of the products of the independent variables (total apfu of elements calculated on the basis of 13 cations) and their coefficients.

[II]The coefficients in the pressure column must be multiplied by the following values: [a]lnP; [b]10^8P^{-4}; [c]$P^{-1/3}$; [d]$10^{28}P^{-14}$; [e]$10^{-62}P^{20}$; [f]$P^{-0.5}$; [g]P

Table 6.5 Representative amphibole analyses used for the estimation of intensive melt parameters. Each sample is the average of n spots performed on a single amphibole crystal.

Facies	Border						Guichon			
Sample	MD003A-Hbl1		MD007-Hbl1		MD046-Hbl1		MD075-Hbl1		MD076-Hbl1	
n =	3		3		3		2		3	
	x̄	σ	x̄	σ	x̄	σ	x̄	σ	x̄	σ
SiO_2	47.08	0.49	48.32	0.69	48.67	0.11	50.68	0.23	50.13	0.38
Al_2O_3	10.00	0.62	8.49	0.73	8.38	0.03	6.47	0.12	6.16	0.37
TiO_2	1.90	0.20	1.65	0.18	1.69	0.04	0.96	0.06	1.04	0.12
FeO	12.31	0.27	10.85	0.26	12.16	0.11	11.88	0.16	12.51	0.25
MnO	0.34	0.02	0.29	0.01	0.24	0.02	0.39	0.00	0.40	0.02
MgO	14.38	0.28	15.52	0.42	14.12	0.05	14.84	0.25	14.97	0.17
CaO	11.04	0.06	11.37	0.12	11.33	0.09	11.36	0.10	11.46	0.23
Na_2O	1.30	0.08	1.12	0.08	0.97	0.03	1.14	0.03	1.05	0.08
K_2O	0.47	0.01	0.37	0.04	0.64	0.00	0.55	0.01	0.50	0.04
F	0.00	0.00	0.00	0.00	0.00	0.00	0.00	0.00	0.00	0.00
Cl	0.08	0.01	0.06	0.01	0.14	0.02	0.17	0.00	0.13	0.03
Sum	98.91	0.37	98.05	0.07	98.34	0.14	98.43	0.05	98.35	0.36
-O=F	0.00	0.00	0.00	0.00	0.00	0.00	0.00	0.00	0.00	0.00
-O=Cl	0.02	0.00	0.01	0.00	0.03	0.01	0.04	0.00	0.03	0.01
Total	98.89	0.38	98.03	0.07	98.30	0.14	98.39	0.05	98.32	0.36
Si	6.629	0.085	6.827	0.090	6.935	0.007	7.208	0.011	7.139	0.067
Al-T	1.371	0.085	1.173	0.090	1.065	0.007	0.792	0.011	0.861	0.067
Sum T	*8.000*	*0.000*	*8.000*	*0.000*	*8.000*	*0.000*	*8.000*	*0.000*	*8.000*	*0.000*
Al^{vi} (M)	0.289	0.021	0.240	0.033	0.342	0.008	0.292	0.012	0.173	0.021
Ti	0.202	0.021	0.175	0.019	0.181	0.004	0.103	0.006	0.111	0.012
Fe^{3+}	0.910	0.035	0.766	0.023	0.516	0.018	0.420	0.051	0.590	0.100
Fe^{2+}	0.540	0.010	0.516	0.021	0.933	0.023	0.993	0.075	0.900	0.094
Mn	0.041	0.002	0.035	0.001	0.029	0.002	0.047	0.001	0.048	0.003
Mg	3.019	0.065	3.268	0.084	2.999	0.010	3.145	0.043	3.178	0.038
Cr	0.000	0.000	0.000	0.000	0.000	0.000	0.000	0.000	0.000	0.000
Sum C	*5.000*	*0.000*	*5.000*	*0.000*	*5.000*	*0.000*	*5.000*	*0.000*	*5.000*	*0.000*
Mg-B	0	0	0	0	0	0	0	0	0	0
Ca-B	1.665	0.012	1.721	0.017	1.730	0.013	1.731	0.021	1.748	0.037
Na-B	0.335	0.012	0.279	0.017	0.266	0.012	0.269	0.021	0.252	0.037
Sum B	*2.00*	*0.00*	*2.00*	*0.00*	*2.00*	*0.00*	*2.00*	*0.00*	*2.00*	*0.00*
Na-A	0.019	0.010	0.029	0.004	0.003	0.004	0.045	0.014	0.038	0.026
K	0.085	0.002	0.067	0.007	0.116	0.001	0.099	0.002	0.090	0.007
Sum A	*0.104*	*0.010*	*0.096*	*0.011*	*0.119*	*0.004*	*0.144*	*0.017*	*0.128*	*0.028*
Total	*15.104*	*0.010*	*15.096*	*0.011*	*15.115*	*0.008*	*15.144*	*0.017*	*15.128*	*0.028*
F	0.000	0.000	0.000	0.000	0.000	0.000	0.000	0.000	0.000	0.000
Cl	0.020	0.003	0.015	0.002	0.035	0.006	0.040	0.000	0.032	0.007
OH	0.980	0.003	0.985	0.002	0.965	0.006	0.960	0.000	0.968	0.007
Sum W	*1.000*	*0.000*	*1.000*	*0.000*	*1.000*	*0.000*	*1.000*	*0.000*	*1.000*	*0.000*

Table 6.5 Continued…

Facies	Chataway				F.g. Granodiorite		Bethlehem		Skeena
Spot	MD044-Hbl1		MD066-Hbl1		MD063-Hbl1		MD059-Hbl1		MD049-Hbl2
n =	3		3		2		3		1
	x̄	σ	x̄	σ	x̄	σ	x̄	σ	x̄
SiO$_2$	48.58	0.05	48.66	0.20	48.66	0.10	50.18	0.37	49.48
Al$_2$O$_3$	7.86	0.06	7.92	0.18	7.48	0.05	7.12	0.31	7.24
TiO$_2$	1.54	0.11	1.48	0.07	1.42	0.00	0.99	0.09	1.21
FeO	12.72	0.28	11.52	0.65	12.92	0.17	10.92	0.12	12.51
MnO	0.40	0.02	0.40	0.04	0.48	0.01	0.49	0.03	0.59
MgO	14.48	0.26	14.45	0.42	14.28	0.11	15.30	0.19	13.90
CaO	11.37	0.14	11.25	0.16	11.59	0.09	10.79	0.04	11.79
Na$_2$O	1.28	0.10	1.27	0.04	1.33	0.02	1.52	0.06	1.08
K$_2$O	0.62	0.03	0.66	0.03	0.71	0.01	0.23	0.03	0.42
F	0.00	0.00	0.00	0.00	0.00	0.00	0.00	0.00	0.00
Cl	0.13	0.07	0.16	0.00	0.20	0.02	0.06	0.00	0.03
Sum	98.97	0.10	97.77	0.28	99.07	0.21	97.59	0.24	98.23
-O=F	0.00	0.00	0.00	0.00	0.00	0.00	0.00	0.00	0.00
-O=Cl	0.03	0.02	0.04	0.00	0.05	0.00	0.01	0.00	0.01
Total	98.94	0.11	97.74	0.28	99.03	0.20	97.58	0.24	98.22
Si	6.897	0.012	6.980	0.016	6.948	0.012	7.116	0.041	7.100
Al-T	1.103	0.012	1.020	0.016	1.052	0.012	0.884	0.041	0.900
Sum T	*8.000*	*0.000*	*8.000*	*0.000*	*8.000*	*0.000*	*8.000*	*0.000*	*8.000*
Al^{vi} (M)	0.212	0.023	0.320	0.015	0.206	0.003	0.306	0.016	0.324
Ti	0.165	0.012	0.160	0.009	0.152	0.000	0.106	0.010	0.130
Fe^{3+}	0.639	0.038	0.450	0.066	0.496	0.035	0.630	0.019	0.315
Fe^{2+}	0.872	0.072	0.932	0.140	1.047	0.055	0.666	0.029	1.187
Mn	0.049	0.002	0.049	0.006	0.058	0.001	0.059	0.003	0.072
Mg	3.064	0.050	3.090	0.081	3.040	0.025	3.234	0.030	2.973
Cr	0.000	0.000	0.000	0.000	0.000	0.000	0.000	0.000	0.000
Sum C	*5.000*	*0.000*	*5.000*	*0.000*	*5.000*	*0.000*	*5.000*	*0.000*	*5.000*
Mg-B	0	0	0	0	0	0	0	0	0.000
Ca-B	1.729	0.024	1.729	0.025	1.773	0.013	1.639	0.009	1.812
Na-B	0.271	0.024	0.271	0.025	0.227	0.013	0.361	0.009	0.188
Sum B	*2.00*	*0.00*	*2.00*	*0.00*	*2.00*	*0.00*	*2.00*	*0.00*	*2.000*
Na-A	0.081	0.010	0.081	0.027	0.142	0.007	0.058	0.015	0.112
K	0.112	0.005	0.120	0.006	0.129	0.001	0.041	0.005	0.077
Sum A	*0.193*	*0.012*	*0.201*	*0.028*	*0.271*	*0.006*	*0.098*	*0.020*	*0.188*
Total	*15.193*	*0.012*	*15.201*	*0.028*	*15.271*	*0.006*	*15.098*	*0.020*	*15.188*
F	0.000	0.000	0.000	0.000	0.000	0.000	0.000	0.000	0.000
Cl	0.031	0.017	0.039	0.001	0.049	0.005	0.015	0.000	0.007
OH	0.969	0.017	0.961	0.001	0.951	0.005	0.985	0.000	0.993
Sum W	*1.000*	*0.000*	*1.000*	*0.000*	*1.000*	*0.000*	*1.000*	*0.000*	*1.000*

Table 6.6 Temperature and pressure estimates for amphiboles from the Guichon Creek Batholith.

Facies	Sample	T1 (°C)[a]	±	T2 (°C)[b]	±[f]	Elevation (m)	P1 (kbar)[c]	±	Depth 1 (km)[d]	P2 (kbar)[e]	±[f]
Border	MD003A-Hbl1	844.2	23.5	787.7	80.6	1592	2.5	0.3	7.3	2.9	0.5
	MD003A-Hbl2	846.8	23.5	795.2	102.2	1592	2.5	0.3	7.5	2.9	0.6
	MD003A-Hbl3	821.3	23.5	756.0	53.3	1592	2.2	0.3	6.4	3.2	0.4
	MD003A-Hbl4	796.4	23.5	716.4	184.0	1592	1.8	0.2	5.4	3.4	1.3
	MD007-Hbl1	802.4	23.5	755.5	82.7	1655	1.8	0.2	5.2	2.6	0.5
	MD007-Hbl2	798.8	23.5	738.8	70.5	1655	1.7	0.2	4.9	2.7	0.6
	MD007-Hbl3	805.2	23.5	759.2	38.6	1655	1.8	0.2	5.3	2.7	0.2
	MD007-Hbl4	822.2	23.5	773.5	43.6	1655	2.1	0.2	6.0	2.8	0.3
	MD046-Hbl1	756.1	23.5	763.3	18.2	1008	1.6	0.2	5.4	2.4	0.1
	MD046-Hbl2	749.9	23.5	754.5	29.7	1008	1.6	0.2	5.3	2.5	0.1
	MD046-Hbl3	761.2	23.5	742.8	39.2	1008	1.6	0.2	5.4	2.6	0.2
Guichon	MD075-Hbl1	740.5	23.5	668.8	40.3	1569	1.1	0.1	3.2	2.2	0.2
	MD075-Hbl2	737.8	23.5	682.7	28.3	1569	1.1	0.1	3.2	2.2	0.1
	MD075-Hbl3	742.1	23.5	669.3	50.0	1569	1.1	0.1	3.3	2.3	0.3
	MD076-Hbl1	742.5	23.5	678.6	75.2	1463	1.0	0.1	3.1	1.9	0.4
	MD076-Hbl2	748.2	23.5	680.3	22.5	1463	1.0	0.1	3.1	1.9	0.2
	MD076-Hbl3	757.5	23.5	676.9	42.3	1463	1.1	0.1	3.2	1.9	0.2
	MD076-Hbl4	712.0	23.5	663.5	53.5	1463	0.9	0.1	2.6	1.4	0.2
Chataway	MD044-Hbl1	797.6	23.5	743.3	53.2	1403	1.5	0.2	4.5	2.4	0.2
	MD044-Hbl2	795.6	23.5	751.7	22.2	1403	1.5	0.2	4.5	2.2	0.1
	MD044-Hbl3	809.4	23.5	756.7	0.0	1403	1.5	0.2	4.7	2.2	0.0
	MD066-Hbl1	793.4	23.5	737.5	39.3	1357	1.6	0.2	4.8	2.6	0.2
	MD066-Hbl2	777.4	23.5	737.6	40.0	1357	1.5	0.2	4.6	2.5	0.3
	MD066-Hbl3	764.6	23.5	710.4	52.9	1357	1.4	0.2	4.4	2.8	0.3
	MD066-Hbl4	750.4	23.5	716.3	26.7	1357	1.3	0.1	4.1	2.5	0.1
F.g. GRD	MD063-Hbl1	795.2	23.5	728.6	2.1	1569	1.3	0.1	4.0	2.4	0.0
	MD063-Hbl2	759.3	23.5	663.4	0.0	1569	1.0	0.1	3.1	2.0	0.0
	MD063-Hbl3	815.1	23.5	741.8	0.0	1569	1.4	0.2	4.2	2.3	0.0
Bethlehem	MD059-Hbl1	810.4	23.5	672.1	61.5	1465	1.4	0.2	4.1	2.7	0.4
	MD059-Hbl2	828.4	23.5	692.4	72.4	1465	1.6	0.2	4.8	3.1	0.6
	MD059-Hbl3	805.0	23.5	666.1	0.0	1465	1.3	0.1	3.9	2.4	0.0
Skeena	MD049-Hbl2	765.9	23.5	701.7	0.0	1427	1.3	0.1	3.9	2.6	0.0
	MD049-Hbl3	777.7	23.5	703.6	0.0	1427	1.2	0.1	3.8	2.3	0.0

[a]Ridolfi and Renzulli (2012) estimate
[b]Otten (1984) estimate
[c]Ridolfi and Renzulli (2012) estimate
[d]Depth of crystallization calculated assuming 1kbar = 3km and levelled to a common sample elevation of 1500m
[e]Anderson and Smith (1995) estimate
[f]Uncertainties calculated based on 1σ error in Ti (apu) and Al (apu)

$$T(°C) = 1204 \, x \left(\frac{Ti}{23 \, O} \right) + 545$$

where Ti/23O is the number of Ti cations per 23O formula unit.

The Al-in-hbl barometer was first empirically derived by Hammarstrom and Zen (1986) for use in granitic, amphibole-bearing calc-alkaline plutonic rocks on the premise that Al_{tot} in calcic amphiboles is buffered by the tschermack-exchange reaction ($^{vi}Mg^{2+}$ + $^{iv}Si^{4+} \leftrightharpoons$ $^{vi}Al^{3+}$ + $^{iv}Al^{3+}$) and is an indicator of the pressure of crystallization. As other factors may contribute to the Al_{tot} present in amphiboles (e.g., temperature, fO_2, bulk composition, αSiO_2) they suggested that the barometer should be restricted to rocks that meet the following criteria: 1) crystallized at near solidus temperatures; 2) show evidence for fO_2 conditions between the nickel-bunsite (NB) and hematite-magnetite (HM) buffers; and 3) contain the stable mineral assemblage quartz + K-feldspar + plagioclase + amphibole + titanite +apatite + biotite + magnetite and/or ilmenite. These restrictions effectively limit the Al_{tot} content in amphibole to be dependent on pressure, as changes in bulk chemistry at a given pressure can only be accommodated by changes in modal proportions, not by compositions of individual minerals (Hammarstrom and Zen, 1986). Additionally, samples should be screened for alteration by a fluid phase and only amphiboles that are in equilibrium with quartz ($\alpha SiO_2 < 1$ results in excess Al^{iv} substituting for Si) should be analyzed to avoid erroneously low and high pressure estimates respectively (Hammarstrom and Zen, 1986).

The original empirical barometer was subsequently modified by Hollister et al. (1987) and experimentally tested (Rutter et al., 1989) and calibrated to pressures and temperatures between 2 to 8 kbar and 740 to 780 °C (Johnson and Rutherford, 1989)

and 2.5 to 13 kbar and 700 to 655 °C (Schmidt, 1992). The most recent expression is that of Anderson and Smith (1995), which was revised to incorporate temperature effects using the experimental data of Johnson and Rutherford (1989) and Schmidt (1992) and is the version of the barometer used in this study.

Previous pressure estimates for the Guichon Creek Batholith (Dilles, 2013 pers. comm.) assumed an equilibrium temperature of 700°C. This temperature represents the wet granitic solidus (± 20°C; Piwinskii, 1975) and is a valid assumption as hydrous tonalite and granodiorite magmas have nearly pressure independent solidus temperatures between 700 and 900°C (Kenah and Hollister, 1983) and the relatively narrow range in TiO_2 (0.11 to 0.19 wt%) implies a narrow range of crystallization temperatures (Anderson, 1980; Otten, 1984). Because analyzed amphiboles in this study lacked zoning, they are interpreted to have undergone slow cooling and continuous re-equilibration to solidus temperatures in the presence of the remaining melt (Schmidt, 1992). Additionally, amphibole should retain magmatic Al-contents in large, slow-cooling plutons based on the aluminum diffusion coefficient (Hammarstrom and Zen, 1986). Temperature estimates from the Otten (1984) Ti-in-hbl thermometer used in this study (Table 6.6) are close to the near solidus temperatures implied by petrographic evidence and pressure estimates were therefore calculated using the equation:

$$P(\pm 0.6\text{kbar}) = 4.76Al - 3.01 - \left(\frac{T(°C) - 675}{85}\right) \times [0.530Al + 0.005294(T(°C) - 675)]$$

where Al is Al apfu in amphibole using the Ti-in-hbl equilibrium temperatures and are presented in Table 6.6.

Figures 6.24A and B, respectively, show the temperature and pressure estimates of the Ti-in-hbl thermometer and Al-in-hbl thermometer vs. those of the Ridolfi and Renzulli (2012) thermobarometric equations. Temperature estimates from both methods are positively correlated at a ratio parallel to a perfect one to one correlation, but the Ti-in-hbl thermometer (Otten, 1984) yields consistently lower temperatures (Fig. 6.24A). This is likely due to inaccuracies in the Ti-in-hbl thermometer as it was not as rigorously constrained or calibrated to natural and experimental amphiboles as the thermometer of Ridolfi and Renzulli (2012). Pressure estimates are positively correlated and the Al-in-hbl barometer consistently yields higher pressures, although there does not appear to be a systematic reason for these overestimates as evidenced by the relatively wide range of pressure estimates relative to those of the Ridolfi and Renzulli (2012) method (Fig. 6.24B). This can partly be explained by the lower temperatures yielded by the Ti-in-hbl thermometer. These were used in pressure calculations and lower input temperatures will yield higher pressures using this method. If this were the only cause of overestimation, however, it would be expected that there should be a systematic variation in the overestimation of pressures by the Al-in-hbl method. Instead, it is most likely that the overestimation of pressure by the Al-in-hbl method is an indication that the K-feldspar present in the Chataway facies, and some samples of the Border facies, is in fact secondary, as proposed in Chapter 3. As a result, the required equilibrium buffering mineral assemblage is not present and the barometer is not valid for use in pressure estimation.
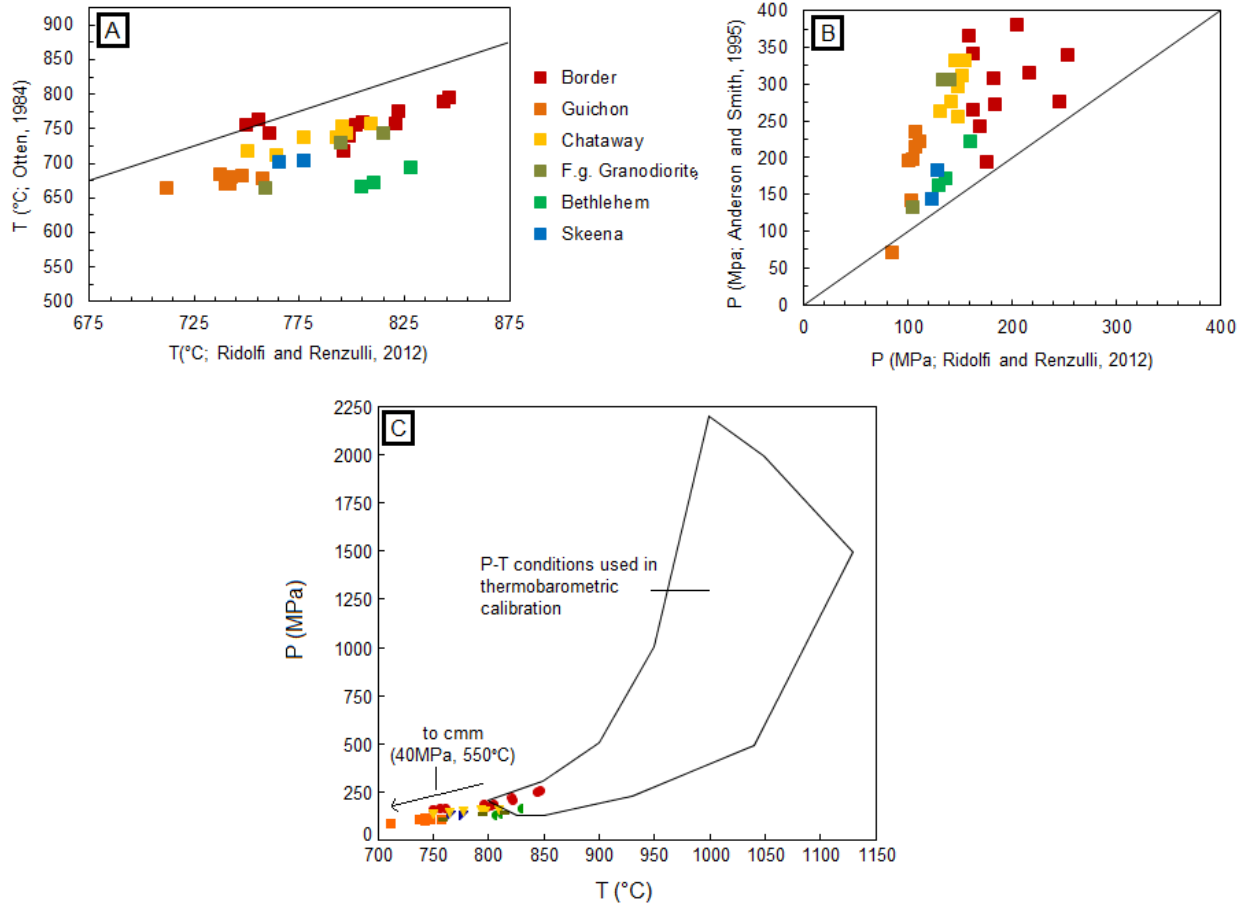
Figure 6.24 A. and B. Comparison of temperature and pressure estimates from the two methods used in this study. C. Comparison of pressure and temperature estimates from the equations of Ridolfi and Renzulli (2012) and the pressure and temperature conditions of synthetic amphiboles used in the calibration of their equations. Cmm = cummingtonite.

The pressure and temperature estimates obtained from the equations of Ridolfi and Renzulli (2012) for the Guichon Creek Batholith do not lie in the field of experimentally calibrated data, but do follow the projected continuation of this field to lower pressure and temperature towards the stability conditions for cummingtonite (Fig. 6.2; 40MPa, 550°C; Evans and Ghiorso, 1995). As the majority of samples have the composition of magnesiohornblende and tschermakite, which form a solid-solution with cummingtonite, it is reasonable to conclude that the estimated pressure and temperature values are realistic in nature. In summary, the Guichon Creek Batholith is

estimated to have crystallized at temperatures between 712 ± 23.5 and 846.8 ± 23.5 and at pressures between 2.5 ± 0.3 and 0.9 ± 0.1 kbar.

6.8.2 Oxygen Fugacity (fO_2)

Estimation of oxygen fugacities for granitic rocks under magmatic crystallization conditions is difficult as primary magnetite and ilmenite compositions are commonly altered in slow cooling plutons by sub-solidus re-equilibration and Ti-cleansing of magnetite (Buddington and Lindsley, 1964). Evidence for re-equilibration of Fe-Ti-oxides in the Guichon Creek Batholith has been documented (this study) so it was not possible to make absolute estimates of fO_2 using the ilmenite-magnetite geothermometers (Carmichael and Nicholls, 1967; Andersen and Lindsley, 1988; Ghiorso and Sack, 1991; Ghiorso and Evans, 2008).

Oxygen fugacity was, therefore, estimated using the method of Ridolfi and Renzulli (2012) by the equation presented in Table 6.4 with results presented in Table 6.7. The estimated fO_2 values are all close to the nickel-nickel oxide (NNO) buffer and range from ΔNNO = 0.03 to 1.81 (Table 6.7; Fig. 6.25) which is consistent with the expected fO_2 values for calc-alkaline magmas between NNO - 1 and NNO + 2.7 (Carmichael, 1991; Martel et al., 1999; Behrens and Gaillard, 2006). This is also consistent with the stable mineral assemblage of titanite + magnetite + quartz, which implies oxygen fugacities above the fayalite-magnetite-quartz (FMQ) buffer (Wones, 1981; Lipman, 1971; Czamanske and Wones, 1973) and even higher oxygen fugacities are implied by coexisting amphibole with low $Fe_{tot}/(Fe_{tot} + Mg)$ =0.25 to 0.35 (Wones, 1989).

Table 6.7 Estimated fO$_2$, H$_2$O$_{melt}$, and anhydrous melt compositions for the Guichon Creek Batholith.

Facies	Sample	ΔNNO[a]	H$_2$O$_{melt}$[b]	SiO$_2$	TiO$_2$	Al$_2$O$_3$	FeO	MgO	CaO	K$_2$O
	MD003A-Hbl1	0.31	6.35	71.40	1.17	14.57	2.01	1.16	3.41	2.61
	MD003A-Hbl2	0.17	6.41	70.78	1.20	14.66	2.16	1.26	3.65	2.43
	MD003A-Hbl3	0.42	6.60	73.17	0.99	14.01	1.70	1.10	3.06	2.56
	MD003A-Hbl4	0.40	6.68	75.69	0.82	13.36	1.32	0.77	2.47	2.80
	MD007-Hbl1	0.46	6.26	74.68	0.94	13.52	1.49	0.94	2.64	2.65
Border	MD007-Hbl2	0.57	6.25	75.23	0.92	13.40	1.41	0.88	2.50	2.68
	MD007-Hbl3	0.39	6.42	74.06	0.98	13.72	1.61	1.03	2.81	2.55
	MD007-Hbl4	0.56	6.41	72.84	1.06	14.13	1.80	1.16	3.06	2.47
	MD046-Hbl1	0.03	6.86	76.63	0.79	12.91	1.04	0.54	2.15	4.14
	MD046-Hbl2	0.05	6.99	76.97	0.74	12.75	1.00	0.52	2.13	4.01
	MD046-Hbl3	0.04	6.73	77.11	0.74	12.62	1.01	0.60	2.11	3.76
	MD075-Hbl1	1.20	5.87	78.71	0.59	12.97	0.50	-0.43	0.63	5.72
	MD075-Hbl2	1.01	5.98	78.24	0.62	13.04	0.53	-0.38	0.78	5.64
	MD075-Hbl3	1.15	5.96	79.28	0.59	12.41	0.51	-0.40	0.62	5.80
Guichon	MD076-Hbl1	0.80	5.70	76.10	0.67	15.58	0.58	-0.32	1.01	4.98
	MD076-Hbl2	0.91	5.62	76.65	0.68	14.51	0.58	-0.29	0.93	5.12
	MD076-Hbl3	1.21	5.42	77.60	0.67	13.69	0.55	-0.38	0.66	5.57
	MD076-Hbl4	0.64	5.85	69.44	0.65	53.77	0.50	-0.41	1.37	4.88
	MD044-Hbl1	0.95	5.64	77.54	0.82	12.88	0.92	0.19	1.23	4.66
	MD044-Hbl2	0.71	5.64	77.31	0.83	12.82	0.94	0.22	1.30	4.54
	MD044-Hbl3	0.89	5.35	77.32	0.86	12.93	0.95	0.21	1.20	4.65
Chataway	MD066-Hbl1	1.35	5.80	78.24	0.76	12.72	0.80	0.20	1.05	5.18
	MD066-Hbl2	0.80	6.09	78.26	0.72	12.44	0.80	0.23	1.21	4.94
	MD066-Hbl3	1.11	6.41	78.98	0.67	12.31	0.70	0.12	1.03	5.32
	MD066-Hbl4	0.90	6.41	78.82	0.66	12.15	0.68	0.08	1.11	5.21
	MD063-Hbl1	1.45	5.46	78.49	0.77	12.57	0.72	-0.06	0.64	5.73
F.g. GRD	MD063-Hbl2	1.45	5.60	77.36	0.66	14.02	0.54	-0.32	0.59	5.58
	MD063-Hbl3	1.81	5.12	78.39	0.82	12.73	0.74	-0.03	0.47	6.00
	MD059-Hbl1	1.57	5.08	79.81	0.65	12.24	0.72	-0.11	0.70	3.69
Bethlehem	MD059-Hbl2	1.67	5.26	78.86	0.69	12.71	0.84	0.12	0.93	3.58
	MD059-Hbl3	1.34	5.12	79.88	0.60	11.61	0.66	0.09	0.67	3.55
Skeena	MD049-Hbl2	0.62	6.15	78.46	0.63	11.86	0.76	0.29	1.33	3.62
	MD049-Hbl3	0.56	5.65	78.05	0.64	11.82	0.80	0.32	1.39	3.02

[a] ΔNNO = difference between estimated fO$_2$ and the nickel-nickel oxide buffer
[b] H$_2$O$_{melt}$ = H$_2$O content of the melt at the time of amphibole crystallization
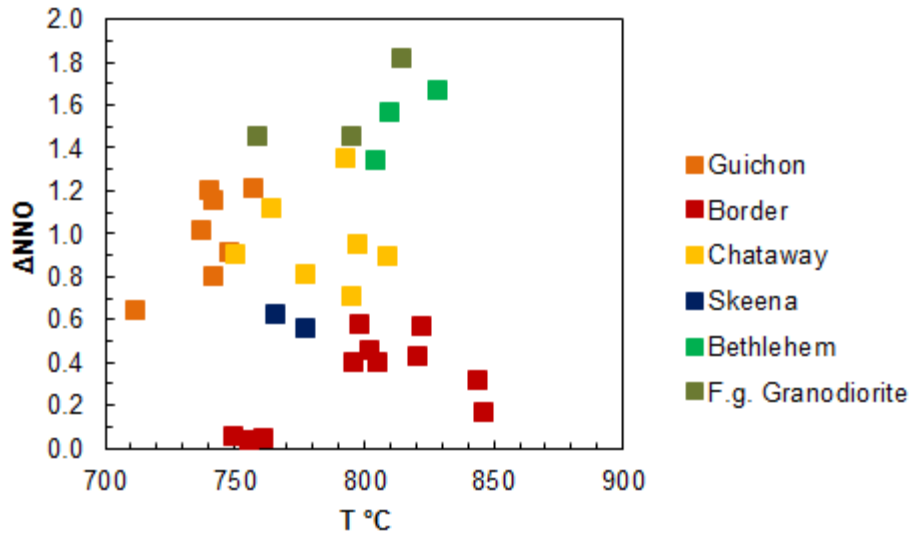
Figure 6.25 Estimated oxygen fugacities relative to the Ni + NiO buffer (ΔNNO) vs. temperature.

6.8.3 H_2O_{melt} and Anhydrous Melt Composition

Estimation of the anhydrous composition of the Guichon Creek Batholith magma was possible using the equations of Ridolfi and Renzulli (2012) in Table 6.4 and the results are presented in Table 6.7. Magmatic water contents are relatively high and vary from 5.08 to 6.99 wt%. Estimated anhydrous wt% for the major elements in the Guichon Creek Batholith magmas are as follows: SiO_2 (69.44 to 79.88), TiO_2 (0.59 to 1.20), Al_2O_3 (11.61 to 53.77), FeO (0.50 to 2.16), MgO (-0.43 to 1.26), CaO (0.47 to 3.65) and K_2O (2.43 to 6.00). The estimates for all elements fall in the permissible ranges set out by Ridolfi and Renzulli (2012) with the exception of MgO, although the negative MgO values all fall, in error, of the lower permissible bound (0 wt%).

6.8.4 Apatite Saturation Temperature (AST)

Harrison and Watson (1984) showed that in metaluminous (ASI < 1) to mildly peraluminous melts (1 < ASI < 1.1) apatite precipitation can be approximated as a

function of P_2O_5 and SiO_2. Harrison and Watson's (1984) data was recast by Piccoli et al. (1999) as the empirical solubility expression:

$$T = \frac{[26{,}400 C_{SiO_2}^1 - 4800]}{[12.4 C_{SiO_2}^1 - \ln(C_{P_2O_5}^1) - 3.97]}$$

where T (in Kelvin) is the temperature at which apatite begins to crystallize (apatite saturation temperature: AST), and $C_{SiO_2}^1$ and $C_{P_2O_5}^1$ are the concentrations of SiO_2 and P_2O_5 expressed as weight fractions (wt%/100). Most of the apatite present in a granodioritic to quartz-dioritic rock crystallizes in 60°C of the AST, making it a useful initial estimate of the temperature of crystallization for the majority of the apatite present in a rock (Piccoli and Candela, 1994).

Apatite saturation temperatures were calculated for all 15 samples for which EPMA data for apatite was collected and are presented in Table 6.8. Whole rock SiO_2 and P_2O_5 concentrations were assumed to represent melt SiO_2 and P_2O_5 contents at the time of apatite saturation (e.g., Harrison and Watson, 1984; Coulsen et al., 2001; Parat et al., 2002). This has been shown to be a reasonable assumption for granitic rocks, but significant magma crystallization prior to apatite saturation and the concurrent change in the instantaneous SiO_2 content of the melt can significantly alter calculated ASTs in more mafic tonalites and quartz-monzodiorites (Piccoli and Candela, 1994; Piccoli et al., 1999). Piccoli et al. (1999) estimated that apatite saturation began after approximately 33% magma crystallization in the Rush Creek quartz-monzodiorite of the Sierra Nevada Batholith, and the corrected SiO_2 concentrations lead to AST's 30 to 50°C greater than when assuming bulk rock SiO_2 compositions. The lower AST's

calculated for the older, more mafic facies of the Guichon Creek Batholith relative to the

younger, more evolved facies are, therefore attributed to significant crystallization prior

to apatite saturation (up to 30% crystallinity). Therefore resulting AST's presented in

Table 6.8 should be considered minimum temperatures.

6.8.5 Magmatic Sulfur Content

Sulfur rich arc-magmas are characteristically difficult to identify, as much of the

original S contained in the magmas is lost due to shallow volatile degassing and rapid

dissolution of magmatic anhydrite by meteoric and hydrothermal fluids (Luhr et al.,

1984; Barth and Dorais, 2000). The discovery of anhydrite inclusions in silicate

phenocrysts from volcanic (Luhr et al. 1984; Fournelle, 1990; Pallister et al. 1996;

Matthews et al., 1999; Parat et al., 2002) and intrusive (Barth and Dorais, 2000) arc-

magma related rocks

Table 6.8 Whole rock geochemistry and results of apatite saturation temperature (AST) calculations for the Guichon Creek Batholith

Sample no.	Border				Guichon		Chataway	
	MD001	MD003a	MD007	MD046	MD075	MD076	MD066	MD044
SiO_2 (wt%)	62.19	49.30	50.74	52.94	62.47	63.71	64.21	62.36
TiO_2	0.82	1.27	0.80	0.96	0.62	0.61	0.53	0.60
Al_2O_3	15.91	18.39	20.28	19.17	16.71	16.25	16.23	17.24
Fe_2O_3	6.66	11.21	9.69	8.22	5.64	5.41	5.15	5.32
MnO	0.10	0.17	0.11	0.10	0.08	0.08	0.08	0.08
MgO	2.93	5.50	3.91	4.66	2.83	2.65	2.44	2.71
CaO	5.73	9.43	9.02	9.07	5.44	5.00	5.14	5.04
Na_2O	3.32	4.01	4.73	4.29	3.98	3.87	4.06	4.41
K_2O	2.20	0.37	0.36	0.32	2.09	2.29	2.00	2.09
P_2O_5	0.14	0.33	0.36	0.26	0.15	0.14	0.16	0.16
ASI	0.87	0.76	0.82	0.80	0.89	0.90	0.89	0.92
AST (°C)	854.7	773.9	806.5	802.0	865.4	872.5	893.0	871.9

Table 6.8 Continued…

Sample no.	F.g. Granodiorite	Bethlehem	Skeena		Bethsaida		
	MD063	MD059	MD034	MD049	MD004	MD069	MD071
SiO$_2$ (wt%)	67.83	66.18	66.96	66.16	73.95	69.51	70.40
TiO$_2$	0.44	0.36	0.34	0.39	0.17	0.26	0.23
Al$_2$O$_3$	15.40	17.46	17.01	17.16	14.01	16.34	15.99
Fe$_2$O$_3$	3.78	3.42	3.59	3.69	2.25	2.61	2.53
MnO	0.05	0.07	0.06	0.06	0.06	0.05	0.06
MgO	1.48	1.18	1.08	1.33	0.36	0.84	0.75
CaO	3.70	4.66	4.31	4.49	2.12	3.34	3.16
Na$_2$O	4.04	4.92	4.88	4.89	4.18	4.67	4.67
K$_2$O	3.15	1.58	1.64	1.67	2.84	2.28	2.12
P$_2$O$_5$	0.12	0.15	0.13	0.15	0.06	0.11	0.10
ASI	0.91	0.95	0.96	0.95	1.01	1.01	1.01
AST (°C)	901.6	907.7	900.9	907.8	894.5	909.9	909.6

Average AST = 871.5 °C (n=15), σ = ± 42.6

indicate that S-rich, oxidized and hydrous evolved arc magmas may be more common than once believed. As S-rich apatite has been observed to co-exist with anhydrite ± pyrrhotite (Parat et al., 2002; Chambefort et al., 2008), and anhydrite + S-rich apatite-bearing volcanic rocks have been found associated with large hydrothermal Cu and Au mineral deposits (e.g., Yanacocha, Peru; Chambefort et al., 2008), attempts at estimating magmatic sulfur contents, as well as evaluating sulfate saturation as a contributor to the sulfur budget of porphyry and epithermal deposits, have met with varying success (Streck and Dilles, 1998; Parat et al., 2002; Chambefort et al., 2008). Controls on sulfur content in Guichon Creek Batholith apatites are evaluated in Figure 6.26a-c. In Figure 6.26a, a slope m = 1 would indicate that the sulfur content is predominantly controlled by the substitution $S^{6+} + Si^{4+} \rightarrow 2P^{5+}$ (Rouse and Dunn, 1982). The samples that lie along the line with a slope of m = 0.5 could be explained by the coupled exchange reaction $S^{6+} + Na^+ \rightarrow P^{5+} + Ca^{2+}$ (Liu and Comodi, 1993), which is

supported by the positive correlation between SO_3 and Na_2O wt% (Fig. 6.26b). When both of these substitutions are taken into account and plotted as Si + Na vs. S apfu most samples lie along a line of slope m = 1 (Fig. 6.26c). The remaining samples define a steeper slope and a non-zero intercept (Fig. 6.26c), likely the result of coupled substitutions such as $REE^{3+} + Si^{4+} \rightarrow Ca^{2+} + P^{5+}$ (Rønsbo, 1989). Although REE contents were not analyzed, coupled substitution of $REE^{3+} + Si^{4+}$ for $Ca^{2+} + P^{5+}$ has been observed in other apatites from the Yerington Batholith (Streck and Dilles, 1998).

Zonation observed in the majority of apatite displays decreasing sulfur from core to rim with a minority of samples displaying increasing sulfur concentration (Fig. 6.15). Decreasing sulfur content may have resulted from local kinetic effects, such as S-depletion in proximity to a crystallizing sulphate or sulphide phase (i.e., anhydrite, pyrrhotite; Baker and Rutherford, 1996). Saturation of a sulphate phase has been argued as the cause for similarly zoned apatite in both felsic plutonic and volcanic rocks, which may contain or lack preserved magmatic anhydrite (Streck and Dilles, 1998; Parat et al., 2002). The presence of barite ($BaSO_4$) associated with apatite and magnetite in two samples of the Bethsaida facies (Fig. 6.27) supports sulphate saturation as the cause of S-poor rims. Because lower temperatures favour sulfur partitioning into apatite (Peng et al., 1997), rare zonation from S-poor cores to more S-rich rims is possibly the result of decreasing temperature in the absence of sulphate minerals.
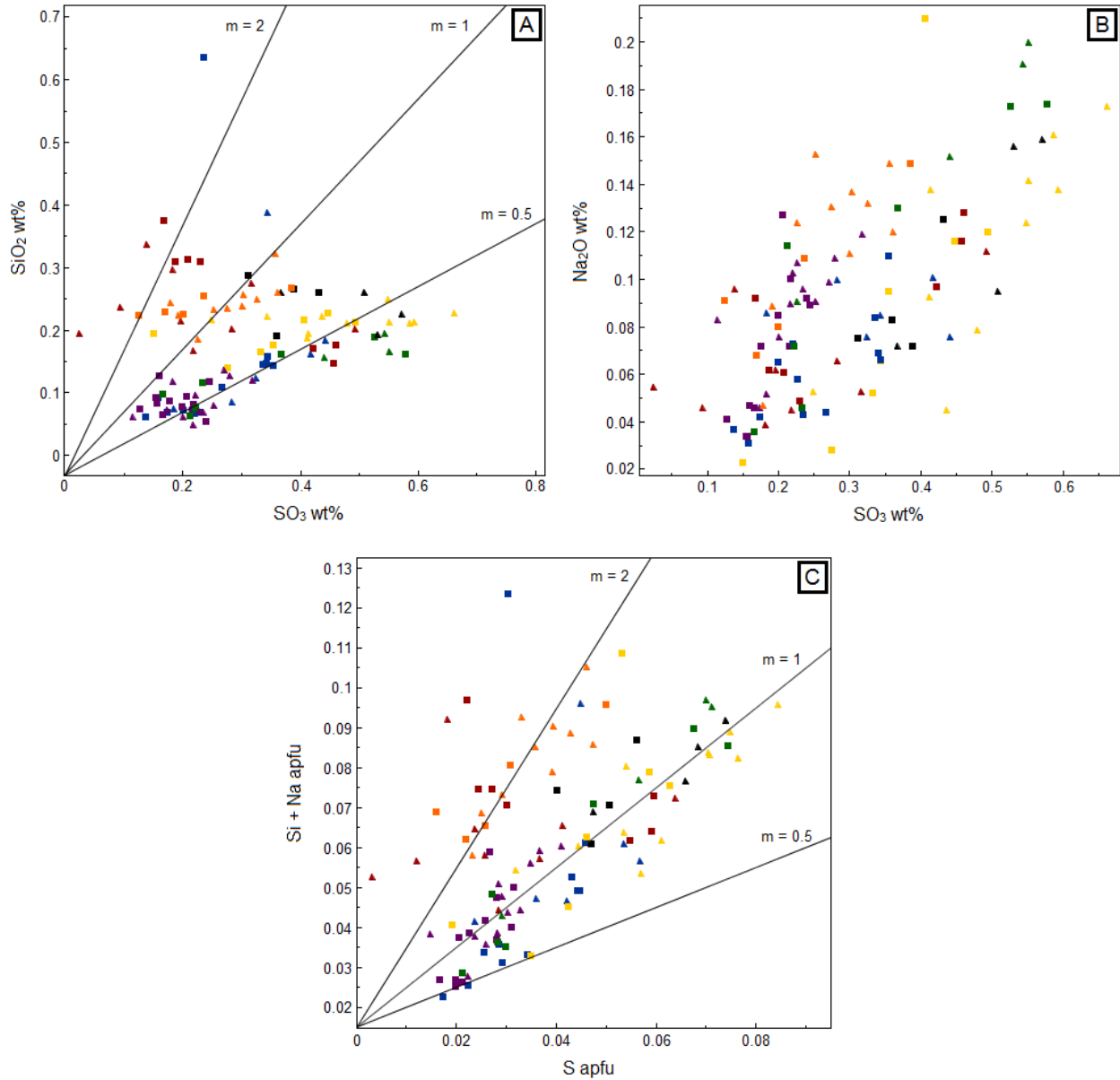
Figure 6.26 Plots of a) SiO_2 vs. SO_3, b) Na_2O vs. SO_3 and c) Si + Na (apfu) vs. S (apfu). See text for discussion. See Figure 6.14 for legend.

Estimates of the S-content in the melt prior to apatite saturation have been made based on the average AST, apatite sulfur content and the partition coefficient for SO_3 between apatite and silicate melt ($D_{SO_3}{}^{ap/m}$). Experiments by Peng et al. (1997)

196
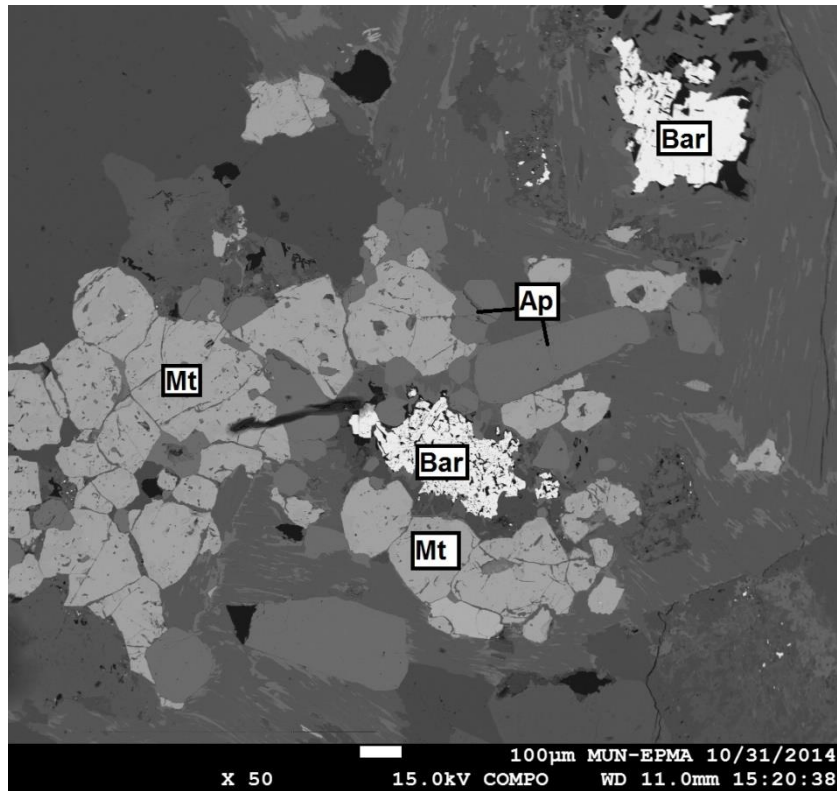
Figure 6.27 Backscattered electron (BSE) image of barite associated with apatite and magnetite from the Bethsaida facies. Sample MD071.

showed that $D_{SO_3}^{ap/m}$ increases with decreasing temperature, is largely independent of

pressure and can be described by the equation:

$$ln\ D_{SO_3}^{ap/m} = \frac{21130}{T(K)} - 16.2$$

Assuming an average AST of T = 871°C, this yields an apatite-melt partition coefficient

for SO_3 of $D_{SO_3}^{ap/m}$ = 9.6 for the Guichon Creek Batholith. Using the most frequent

apatite core compositions of 0.2 and 0.55 wt% SO_3 (Fig. 6.28a), this approach yields an

estimated range between 80 and 230 ppm, respectively, for dissolved sulfur in the melt
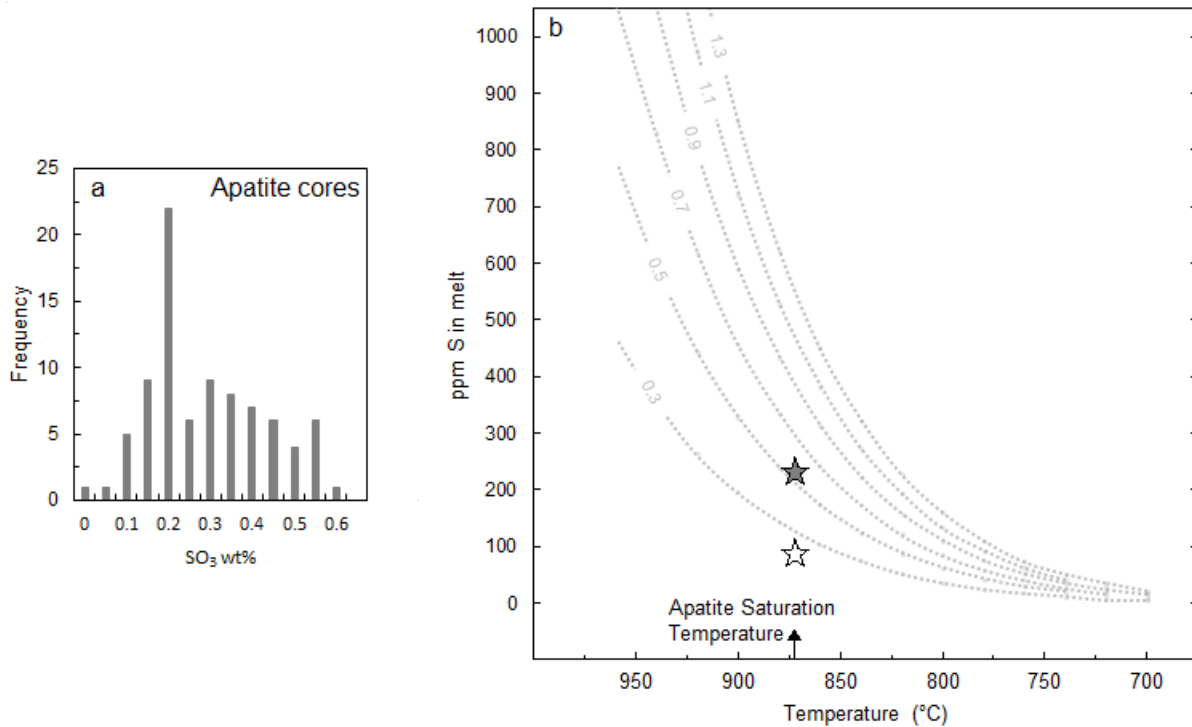
Figure 6.28 A. Histogram of SO$_3$ content in apatite cores. B. Plot of temperature vs. S content of melt. Stars show calculated initial melt sulfur content at the apatite saturation temperature assuming 0.2 wt% SO$_3$ (white star) and 0.55 wt% SO$_3$ (grey star) in apatite. Dashed lines represent SO$_3$ content of apatite as a function of T and S in melt according to the equation of Peng et al. (1997).

(Fig. 6.28b). This range should be considered a minimum estimate because the ASTs for the older facies are likely underestimated.

6.8.6 Summary and Discussion

Temperature, pressure and depth estimates are summarized and plotted on a map of the Guichon Creek Batholith (Figure 6.29) where a northeastward decrease in pressure and inward decrease in temperature is observed. This distribution of pressure estimates implies that there is a significant difference in the level of exposure on either side of the Lornex fault (~1.8 to 2.7km) as well as between the southern and northern ends of the batholith (~1km). This is consistent with cross-sections based partially on internal magmatic foliations in the batholith (Alfaro, 2015 pers. comm.) and the gravity

model of Ager et al. (1973), which implies gentle tilting of approximately 10 to 15° to the east/northeast. In the Lornex pit, fault surface striations on the north-trending Lornex fault indicate oblique to dip-slip motion and the fault dips to the east in the Lornex pit and at depth in the Valley Pit (Byrne, 2015 pers. comm.). The structural evidence suggests that oblique, dextral strike-slip movement with a normal component along the Lornex fault and a down-dropped eastern hanging wall block is also consistent with pressure estimates. Additionally, reactivation of the Lornex and Highland Valley fault systems and north-northeast extension is supported by the presence of a west-northwest trending Tertiary and Quaternary sedimentary basin in the northern portion of the batholith (Byrne et al., 2013).

In addition to gravity, barometric and structural evidence, differing mineralization styles at the Valley and Bethlehem deposits provide strong evidence that deeper levels of the HVC system are exposed to the south, as well as west of the Lornex fault. Much of the mineralization in the Bethlehem deposit is hosted in elongate breccia bodies (Byrne et al., 2013). Breccia zones are common to many porphyry deposits and are generally attributed to shallow level emplacement in the upper parts of the system (Lowell and Guilbert, 1970; Sillitoe, 1973; Gustafson and Hunt, 1975), consistent with low-pressure estimates in the vicinity of the Bethlehem deposit (Fig. 6.29). The Valley and to a lesser extent Lornex deposits contain significant amounts of sinuous quartz veins with well-developed haloes of coarse-grained silver muscovite (Byrne et al., 2013). These veins are similar to the early-halo type (EHT) veins in other porphyry systems (e.g., Chuquicamata, Lomos Bayas, and Los Pelambres, Chile; Haquira, Peru;

199
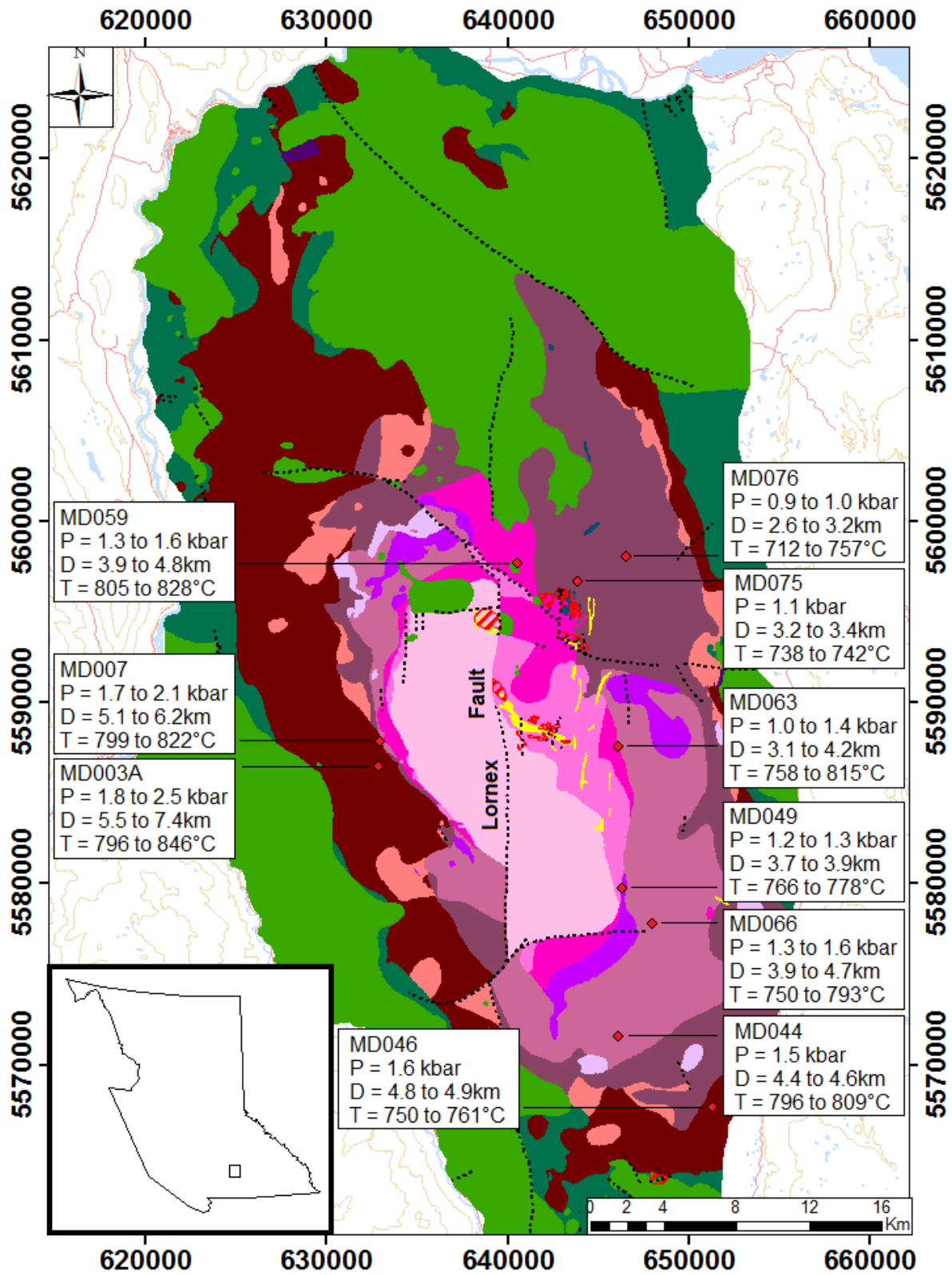
Figure 6.29 Map of the Guichon Creek Batholith showing the location of temperature and pressure estimates.

200

Copper Creek, Arizona; and Ann-Mason Pass, Nevada; Proffett, 2009; Riedell and Proffett, 2014) and contrast with the more typical A-veins originally described by Gustafson and Hunt (1975). At depths of >4 km, early-halo veins are interpreted to have formed above deeper magmatic sources than typical A-type veins (Proffett, 2009; Riedell and Proffett, 2014; Cooke, 2015). At these depths, pressures are above the critical point of saline water and exsolved magmatic-hydrothermal fluids are supercritical, affecting metal transport and deposition processes (Riedell and Proffett, 2014; Cooke, 2015). A summary of characteristics common to deposits formed at different depths shows that shallow deposits are characterized by abundant A-veins, secondary feldspar alteration and high Fe/Fe + Cu, low Se/Fe + Cu sulfide-oxide mineral assemblages whereas deeper deposits have swarms of veinlets with coarse muscovite ± secondary feldspar ± biotite haloes and low Fe/Fe + Cu and high S/Fe + Cu ore assemblages (Proffett, 2009). These differences are attributed to a change from a two-phase, Cl-bearing aqueous fluid to a one phase supercritical fluid exsolved at depth (Proffett, 2009). This has implications for studying the footprint surrounding the Valley and Bethlehem deposits, as they may look significantly different because of differences in depth of emplacement and the nature of the ore forming fluids.

CHAPTER 7   SUMMARY AND CONCLUSIONS

The Guichon Creek Batholith is a composite batholith that is concentrically zoned and comprised of six distinct facies and sub-facies which are: 1) Border facies; Highland Valley facies, subdivided into the 2) Guichon sub-facies and 3) Chataway sub-facies; 4) Bethlehem facies; 5) Skeena facies and; 6) Bethsaida facies. Least altered samples of each facies were selected for petrographic, geochemical, and mineralogical analysis in order to provide better insight into the igneous history of the batholith and to quantify the baseline geological characteristics of the Guichon Creek Batholith for future studies of the alteration footprint of the Highland Valley porphyry-Cu (±Mo) deposits.

The marginal facies of the batholith is the Border facies which varies in composition from olivine-bearing leuco-gabbro to diorite. The Border facies is the most heterogeneous unit as evidenced by abundant autoliths and an outcrop of brecciated Nicola Group basalt host rocks in a matrix of Border facies olivine leuco-gabbro. The Border facies is characterized by equigranular phaneritic textures and a mineralogy comprised of plagioclase, calcic-amphibole, clinopyroxene, orthopyroxene, olivine and accessory magnetite, apatite, rutile biotite and quartz.

The Highland Valley facies is the second unit progressing inwards to the core of the batholith and is comprised of the Guichon and Chataway sub-facies. The Guichon sub-facies is most prominent in the northeast portion of the batholith whereas the Chataway sub-facies is most prominent in the southeast. The mineralogy of both facies is nearly identical, but they can be subdivided on the basis of textural differences and variations in the modal abundance of minerals. The Guichon facies is characterized by

granodiorite, an equigranular phaneritic texture and ~ 20 to 25% evenly distributed mafic minerals. The Chataway facies is characterized by quartz monzodiorite to granodiorite, an equigranular phaneritic texture and ~13 to 15% evenly distributed mafic minerals. The most noteworthy textural differences between the Guichon and Chataway sub-facies are the presence of pink K-feldspar in the Guichon facies and white K-feldspar in the Chataway sub-facies, significantly more amphibole than biotite in the Chataway sub-facies and approximately equal amounts of biotite and amphibole in the Guichon sub-facies. The primary mineralogy of the Highland Valley facies consists of plagioclase, calcic-amphibole, biotite, K-feldspar and quartz. Minor amounts of clinopyroxene are also present in the Guichon sub-facies where it occurs as cores to amphibole crystals. In both sub-facies, quartz and amphibole typically occur as optically continuous oikocrysts that are interstitial to, and sub-ophitically enclose, small euhedral plagioclase crystals. Accessory minerals present in the Highland Valley facies include magnetite, titanite, and apatite.

The rock forming and accessory mineralogy of the Bethlehem, Skeena and Bethsaida facies are nearly identical and the only variation is in the relative abundance of their constituent minerals. The primary mineralogy of all three facies is comprised of plagioclase, quartz, K-feldspar, amphibole and biotite. Accessory minerals include magnetite, titanite, rutile, zircon and apatite. Relative to the other facies, these are characterized by an increase in the modal abundance of quartz and K-feldspar, relatively consistent plagioclase contents and a decrease in modal mafic minerals. Although there is an overall decrease in mafic mineral content, biotite content increases relative to amphibole from the Bethlehem to Bethsaida facies. On the basis of their

mineralogy, the Bethlehem, Skeena and much of the Bethsaida facies are granodiorite, however, an increase in K-feldspar content in a number of Bethsaida samples indicates these are monzogranite. The Bethlehem and Bethsaida facies are characterized by phaneritic, weakly porphyritic textures whereas the Skeena facies has a phaneritic and seriate texture. Both the Bethlehem and Bethsaida facies contain oscillatory zoned plagioclase phenocrysts, but the Bethlehem facies also contains amphibole phenocrysts that poikilitically enclose plagioclase chadacrysts, whereas the Bethsaida facies has biotite phenocrysts. The Bethsaida facies also contains abundant amoeboidal quartz phenocrysts that are absent in the Bethlehem facies. Fine-grained granodiorite dykes that intruded the Chataway facies near its contact with the Bethlehem facies are petrographically and geochemically similar to, and interpreted to be related to, the Bethlehem facies.

As a function of planned sampling bias towards least altered rocks, alteration in samples analyzed in this study was minor and broadly similar across all facies with a few notable exceptions. Two samples from the Border facies contain abundant K-feldspar and biotite. These are interpreted to be the result of metasomatism by a K-bearing metamorphic fluid derived by metamorphism of the host Nicola Group which has undergone albite-epidote hornfels to lower greenschist facies metamorphism. The Border and Guichon facies also commonly contain olivine crystals that have been altered to serpentine and talc as well as pyroxenes which occur as relict cores to amphibole crystals. These are interpreted to be deuteric, resulting from late stage igneous uralitization by increased magmatic water contents. Plagioclase and K-feldspar in all facies are weakly altered to sericite and clay minerals (~5 to 40% of single

204

crystals), whereas amphibole and biotite are variably altered to chlorite and epidote. The most strongly altered mafic minerals occur in the Bethsaida facies and in one sample of the Chataway facies located near the past-producing Aberdeen Adit. Chlorite and epidote alteration is characteristic of the propylitic alteration assemblage associated with many porphyry-type deposits and it is likely that its presence indicates the distal footprint of the Highland Valley porphyry-Cu (±Mo) system.

Geochemically, the Guichon Creek Batholith is classified as magnesian, calcic to calc-alkalic (MALI = -5 to 7.3) and metaluminous to weakly peraluminous (ASI = 0.77 to 1.28; AI = 0.02 to 0.13). Major and trace element variation diagrams are consistent with progressive fractional crystallization of the mineral phases observed petrographically. Rocks of the Guichon Creek Batholith belong predominantly to the medium-K calc-alkaline series, with the exception of a number of Border facies samples, which are low-K tholeiitic and a number of samples from the remaining facies which are high-K calc-alkalic. A plot of Zr vs. molar Al/Ti has been effective to discriminate between the Border, Highland Valley and Bethlehem-Skeena-Bethsaida facies and, on a plot of Al_2O_3 vs. TiO_2, these three groups all follow similar but different trends of decreasing Al_2O_3 with decreasing TiO_2.

Cross-cutting relationships between facies in the Guichon Creek Batholith suggest that it is a composite batholith constructed by at least two magmatic pulses. The first pulse followed a continuous differentiation from olivine-bearing gabbroic rocks in the most marginal rocks of the Border facies to the granodiorites of the Guichon and Chataway sub-facies of the Highland Valley facies, and is consistent with the previous interpretation of McMillan (1976a). The proposed second pulse of magma was likely

205

emplaced prior to complete solidification of the Highland Valley facies as contacts between the Bethlehem and older Highland Valley facies vary from gradational to sharp contacts (e.g., McMillan, 1976a) and the crystallization ages of both facies overlap, within uncertainty (Fig. 7.1). Internal contacts between the Bethlehem, Skeena and Bethsaida facies are all gradational (e.g., Northcote, 1969; McMillan, 1976a) and the Skeena facies has mineralogical, petrographic and geochemical characteristics that are intermediate between those of the Bethlehem and Bethsaida facies. These features may represent the continuous differentiation of a single magma pulse or mixing between a third, Bethsaida facies magma and a partially crystalline Bethlehem magma as initially proposed by McMillan (1976a). Similar gradational contacts have been observed in other large silicic arc plutons (e.g., the Mount Stuart Batholith; Matzel et al., 2006) and can be explained by the intrusion of a young, low crystallinity magma into an older magma transitional between the mush- and melt-impregnated regimes and the resulting
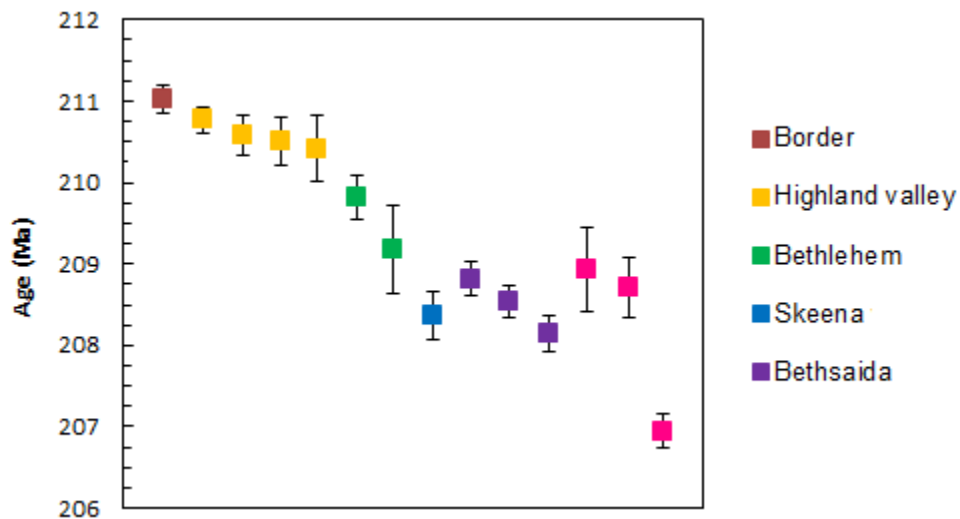
Figure 7.1 U-Pb zircon crystallization ages for the rocks comprising the Guichon Creek Batholith (pers. comm., Alfaro, 2015).

disaggregation and mixing of the mush zone and the intruding magma (Bergantz, 2000).

Further evidence for multiple magma pulses during the construction of the Guichon Creek Batholith includes petrographic and geochemical differences between facies. Key petrographic differences include a transition from angular, optically continuous interstitial quartz in the Border and Highland Valley facies, to very fine-grained rounded interstitial and large amoeboid quartz phenocrysts in the Bethlehem and younger facies as well as a lack of oscillatory zoned plagioclase in the Border and Highland Valley facies. Although the lack of zoning in amphiboles from all facies indicates history of slow cooling and re-equilibration in the presence of melt (Schmidt, 1992), thermal models suggest that such large plutons should cool below their solidus in hundreds of thousands of years rather than millions (e.g., Harrison and Clarke, 1979). The emplacement of multiple magma pulses over the course of ~2.5 m.y. is, therefore, a plausible explanation for the continued supply of heat to the batholith. Geochemical indicators for multiple pulses of magma include the delineation of at least two distinct fractionation trends on plots of Al_2O_3 vs. TiO_2 and Zr vs. mol Al/Ti (Figs. 4.5 and 4.6) and, the separate grouping of pre- and post-Bethlehem facies rocks on a number of classification diagrams (e.g. Al_2O_3 vs. SiO_2 and Sr/Y vs. SiO_2).

High magmatic H_2O contents and relatively oxidizing conditions in the Guichon Creek Batholith magmas are suggested both by geochemical indicators of magmatic fertility (Sr/Y, V/Sc, Al_2O_3/TiO_2) as well as petrographic evidence such as abundant magnesian calcic-amphibole and the stable mineral assemblage quartz-magnetite-titanite (Lipman, 1971; Czamanske and Wones, 1973; Wones, 1981; Wones, 1989; Ridolfi and Renzulli, 2012). Spot analysis of amphiboles allowed for estimates of H_2O_{melt}

and fO_2 which yielded values of 5.08 to 6.99 wt% and ΔNNO = 0.03 to 1.81, respectively (Table 6.7). These estimates are consistent with the expected H_2O (1 to 8 wt%; Sobolev and Chaussidon, 1996; Wallace, 2005; Plank et al., 2013) and fO_2 values (NNO - 1 to NNO + 2.7; Carmichael, 1991; Martel et al., 1999; Behrens and Gaillard, 2006) for calc-alkaline magmas. Both water content and oxygen fugacity are critical to the formation of porphyry-style deposits from arc magmas as large volumes of water are needed to establish the hydrothermal cells responsible for large-scale metal deposition and alteration, and oxidizing conditions prevent the removal of Cu by sulphide saturation.

In addition to magmatic H_2O and fO_2 estimates, amphibole chemistry allowed for an estimate of temperature and pressure conditions at crystallization. Temperature estimates range from 712 to 846°C. Pressure estimates vary from 2.5 ± 0.3 to 0.9 ± 0.1 kbar and the greatest pressures are present in the southeast and southern part of the batholith. These are consistent with gentle tilting to the northeast as proposed by gravity and seismic models. Assuming an average density for oceanic crust of 2.89 g/cm^3, these estimates correspond to emplacement depths of 7.4 to 2.6 km. The large variation in depth has implications for the mineralization and alteration of the Highland Valley porphyry system, as depth-of-crystallization estimates in the vicinity of the Valley deposit suggest that it may have formed from a single-phase supercritical fluid in contrast to the two-phase saline brine and vapour model responsible for most porphyry deposits.

Biotite compositions show a progressive increase in Mn/Cl ratios from the oldest to youngest facies as well as a sharp increase from low X_{Mg} in the Border facies (0.54 to

0.55) to medium X_{Mg} in the Guichon through Bethsaida facies (0.59 to 0.62). Chlorine contents in biotite from all facies are generally tightly clustered with the exception of the more variable Guichon sub-facies and fine-grained granodiorite dyke variety of the Bethlehem facies. As all facies have been exposed to the same degree of surface weathering, the variable Cl content in the Guichon and fine-grained granodiorite samples is likely the result of the exsolution of an aqueous fluid phase rather than alteration by meteoric fluids.

Apatites are all fluorapatites and can be divided into low-Cl [X(Cap) = 0.01 to 0.12] and high-Cl [0.13 to 0.23] groups. Apatite chemistry allowed for the determination of an average apatite saturation temperature of 871.5°C and the presence of S-bearing apatite enable an estimation of the S content of the Guichon Creek Batholith melt of 80 to 230ppm. An accurate estimation of the instantaneous SiO_2 content of the melt at apatite saturation temperature was complicated by the more mafic compositions of the Border and Highland Valley facies. This resulted in an underestimation of the AST and $D_{SO_3}^{ap/m}$, and the resulting estimates for magmatic S content for these facies should be considered conservative.

Plagioclase compositions vary from labradorite (An_{56}) to albite (An_8) with andesine comprising the majority of analyses (An_{29-47}). An content generally decreases with evolution, although there is significant overlap between facies. The dominant Fe-Ti oxide present in the Guichon Creek Batholith is magnetite, although ilmenite with variable solid solution with hematite is also present in most samples. Exsolution of an ulvöspinel component in many magnetites has been observed in a number of samples

indicating that exsolution from Ti-rich titanomagnetite occurred under subsolidus conditions.

The high Sr/Y ratios of the Guichon Creek Batholith are accompanied by low La/Yb ratios indicating adakitic slab melts did not play an important role in generating the fertile porphyry magmas. Instead, the high Sr/Y ratios are the result of fractionation of amphibole, clinopyroxene and suppression of plagioclase fractionation from a hydrous magma at depth and on the timescale of ~3 m.y. Amphibole fractionation at depth is also supported by MREE depletion relative to the LREE and HREE (Fig. 4.14) and resultant concave-upwards primitive mantle normalized multi-element diagrams (Fig. 4.17).

Isotopic evidence supports a model where the Guichon Creek Batholith magmas were derived from a primitive source depleted in REEs. It is proposed that a primitive, sub-arc mantle with a composition intermediate to N-MORB and E-MORB was metasomatized by fluids and partial melts of sediment derived from the subducting slab and <2% contamination derived from sediments with a composition similar to present day GLOSS. Decoupling of the Sm-Nd and Rb-Sr systems supports contamination of the Guichon Creek magmas during their ascent to mid- and upper-crustal levels by radiogenic Sr, most likely derived from limestone units in the Nicola Group. Contamination by previously contaminated Nicola Group volcanic rocks, however, cannot be ruled out. Decreasing $^{87}Sr/^{86}Sr_i$ and constant $\in_{Nd(T)}$ with decreasing age can be explained by increased contamination of the older Border, Guichon and Chataway facies by radiogenic Sr from Nicola Group limestone or volcanic units that subsequently

buffered the younger Bethlehem, Skeena and Bethsaida facies during their emplacement.

A close examination of the REE characteristics of the Guichon Creek and Nicola batholiths, combined with their primitive Sm-Nd isotope systematics, rule out significant garnet fractionation and/or melting of garnetiferous deep crustal material or eclogite facies slab melts as an oxidant or metal source in the Highland Valley district. Instead, it is proposed that the geochemical characteristics of the Guichon Creek and Nicola batholiths are the result of assimilation-fractional crystallization processes involving hornblende ± titanite ± titanomagnetite at depth in a hydrous (5 to 8 wt% H_2O) parent magma.

7.1 Petrogenetic Model

Based on the petrographic, geochemical, mineralogical and isotopic evidence, the following petrogenetic model is proposed for the emplacement of the Guichon Creek Batholith (Fig. 7.2):

(1) Fluids derived by dehydration of the downgoing slab, with <2% contribution by melted pelagic sediments, metasomatise the sub-arc mantle with a composition intermediate to N-MORB and E-MORB (Fig. 7.2A).

(2) Partial melting of the metasomatized mantle generated primitive mafic magmas that rose to the crust-mantle boundary and underwent assimilation-fractional-crystallization. This magma was hydrous enough to stabilize and promote significant amphibole fractionation while suppressing plagioclase fractionation and driving the magma to high Sr/Y ratios. The elevated water

content of this magma may have been primary, resulting from subduction of an aseismic ridge, oceanic plateau or fractured and serpentinized oceanic crust associated with oceanic transcurrent faults. Alternatively, it may have resulted from the evolution towards more hydrous compositions by fractional crystallization of anhydrous silicates over the course of a minimum of 3 m.y., as indicated by U-Pb ages for the Guichon Creek Batholith (Fig. 7.2B).

(3) Emplacement of the Guichon Creek Batholith occurred in at least two pulses, with an early magmatic pulse crystallizing to form the gabbros, diorites and granodiorites of the Border and Highland Valley facies, followed by a second pulse that formed the Bethlehem, Skeena and Bethsaida facies granodiorites (Fig. 7.2C). Alternatively, the Bethsaida facies represents a third pulse that was intruded into a partially crystalline Bethlehem facies, with the transitional Skeena facies representing a mixing zone between the two magmas. Emplacement of the Guichon Creek Batholith magmas likely utilized older, arc-parallel structures that facilitated emplacement of the Nicola basalt host rocks.

(4) The primary magmas fractionated at depth, retained their high Sr/Y signatures and experienced very little crustal contamination as evidenced by primitive Rb-Sr and Nd-Sm isotopic signatures. The exceptions are the Border, Guichon and Chataway facies which have marginally elevated $^{97}Sr/^{86}Sr_i$ ratios that resulted from minor contamination by limestone and previously contaminated Nicola Group basalt country rocks (Fig. 7.2C). Unfractionated HREE signatures also indicate that deep crustal melts of garnetiferous metamorphic rock in a MASH
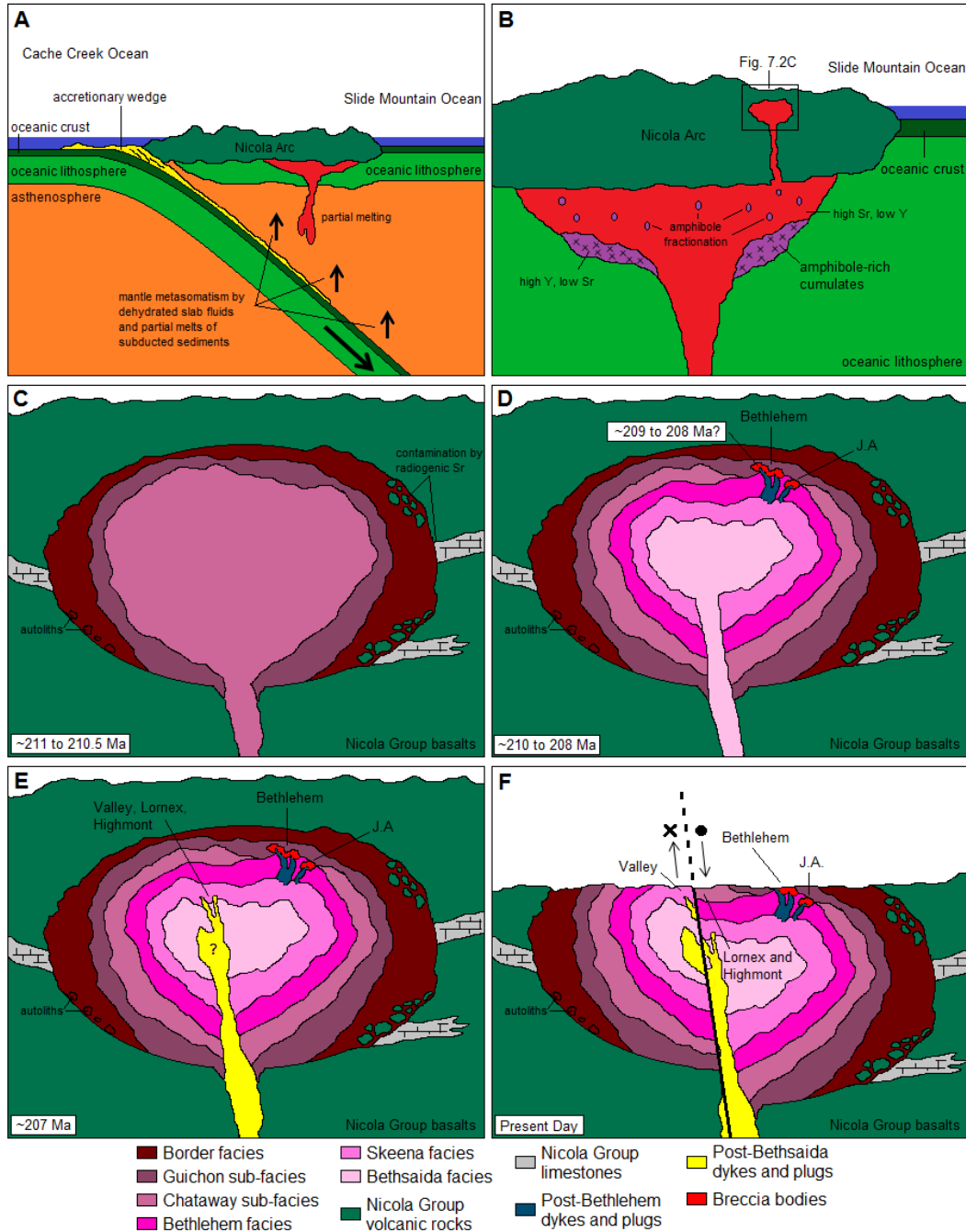
Figure 7.2 Schematic petrogenetic model for the Guichon Creek Batholith, not to scale. A. Metasomatism of the sub-arc mantle lithosphere by partial melting of subducted sediment and fluids derived from dehydration of the downgoing slab leads to partial melting. B. Fractional crystallization of amphibole in a deep crustal magma chamber over ~3 m.y. generates a high and increasing Sr/Y signature. C. Emplacement of the Border, and Highland Valley facies resulting in contamination with radiogenic Sr from Nicola Group volcanic rocks and limestones. D. Emplacement of the Bethlehem, Skeena and Bethsaida facies as well as the mineralizing dykes associated with the Bethlehem and J.A. deposits. E. Emplacement of post-Bethsaida dykes and stocks associated with the mineralizing event at the Valley, Highmont and Lornex deposits. F. Oblique slip along the Lornex fault resulting in dextral-normal motion and juxtaposition of the Valley and Bethlehem structural levels on opposite sides of the Lornex fault.

213

zone did not play a significant role in the genesis of the Guichon Creek

Batholith magmas.

(5) Mineralization at the Bethlehem and Valley deposits coincides with the

emplacement of porphyry stocks and dykes into the Bethlehem and Bethsaida

facies, respectively (Fig. 7.2D and E). The first appearance of these stocks and

dykes closely coincides with the emplacement of the Bethlehem facies, and

they have similar geochemical compositions and follow a similar evolutionary

trend to the main facies of the batholith, indicating they likely share the same

source.

(6) Thermobarometric calculations utilizing amphibole chemistry provide estimates

between 2.6 and 7.4 km for the depth of crystallization that increases towards

the south and southwest of the batholith. This is consistent with previous

gravity and seismic models that predicted ~12 to 15° of tilting to the northeast,

as well as dextral, dip-slip oblique movement along the Lornex Fault (Fig.

7.2F). The greater depth estimates east of the Lornex fault may have important

implications for possible differences and interpretations of mineralization and

alteration styles as well as processes at the Valley and Bethlehem deposits. At

depths of >4km, it is likely that a single-phase supercritical fluid was exsolved,

consistent with the abundance of early muscovite halo veins at Valley, and in

contrast to the typical two-phase Cl-bearing aqueous brine + vapour

predominant in most porphyry-Cu (±Mo) systems.

(7) Chemometric estimates indicate the magmas were hydrous (5.08 to 6.99 wt%

H_2O) and moderately oxidized (ΔNNO = 0.03 to 1.81). Their oxidized nature

would have allowed S to occur as dissolved SO_3^{2-} preventing sulfide saturation and significant loss of Cu before reaching the porphyry environment. The presence of sulfate and possible sulfate saturation is evident as S-bearing apatite and rare associated barite may indicate sulfate saturation, indicating that abundant, easily dissolvable magmatic anhydrite may have provided S to the hydrothermal systems responsible for formation of the Highland Valley porphyry-Cu (±Mo) deposits. The presence of S-bearing apatite also permitted an estimate of the S content of the melt, yielding a result of 80 to 230ppm. This estimate was complicated by the difficulty in determining the instantaneous SiO_2 and P_2O_5 content of the magmas at apatite saturation. The reported estimates of magmatic S content should, therefore, be considered a minimum.

REFERENCES

Acton, S.L., Simony, P.S. and Heaman, L.M., 2002. Nature of the basement to Quesnel Terrane near Christina Lake, southeastern British Columbia. Canadian Journal of Earth Sciences. v.39, p.65-78.

Ager, C.A., Ulrych, T.J. and McMillan, W.J., 1973. A gravity model for the Guichon Creek Batholith, south-central British Columbia. Canadian Journal of Earth Sciences. v.10, p.920-935.

Allen, D.G., Panteleyev, A. and Armstrong, A.T., 1976. Galore Creek. Canadian Institute of Mining and Metallurgy. Special Volume 15, p.402–414.

Alva Jimenez, T.R., 2011. Variation in hydrothermal muscovite and chlorite composition in the Highland Valley porphyry Cu-Mo district, British Columbia, Canada. Unpublished M.Sc. thesis, University of British Columbia, Vancouver, British Columbia, 233p.

Anderson, A.T., 1984. Probable relations between plagioclase zoning and magma dynamics, Fuego Volcano, Guatemala. American Mineralogist. v.69, p.660-676.

Andersen, D.J. and Lindsley, D.H., 1988. Internally consistent solution models for Fe-Mg-Mn-Ti oxides: Fe-Ti oxides. American Mineralogist. v.73, p.714-726.

Anderson, J.L., 1980. Mineral equilibria and crystallization conditions in the late Precambrian Wolf River rapakivi massif, Wisconsin. American Journal of Science. v.280, p.289-332.

Anderson, J.L. and Cullers, R.L., 1990. Middle to upper crustal plutonic construction of a magmatic arc; an example from the Whipple Mountains metamorphic core complex. In: Anderson, J.L. (ed.), The Nature and Origin of Cordilleran Magmatism. Geological Society of America, Memoir. v.174, p.47-69.

Anderson, J.L. and Smith, D.R., 1995. The effects of temperature and fO_2 on the Al-in-hornblende barometer. American Mineralogist. v.80, p.549-559.

Andrews, B.J., Gardner, J.E. and Housh, T.B., 2008. Repeated recharge, assimilation, and hybridization in magmas erupted from El Chichón as recorded by plagioclase and amphibole phenocrysts. Journal of Volcanology and Geothermal Research. v.175, p.415-426.

Armstrong, R.L., 1988. Mesozoic and early Cenozoic magmatic evolution of the Canadian Cordillera. Geological Society of America, Special Paper 218, p.55–91.

Ash, C.H., Reynolds, P.H., Creaser, R.A. and Mihalynuk, M.G., 2007. ^{40}Ar/^{39}Ar and Re O isotopic ages for hydrothermal alteration and related mineralization at the Highland Valley Cu-Mo deposit (NTS 092I), southwestern British Columbia. Geoscience BC Report 2007-1. p.19-24.

Bachmann, O., Dungan, M.A. and Bussy, F., 2005. Insights into shallow magmatic processes in large silicic magma bodies: the trace element record in the Fish Canyon magma body, Colorado. Contributions to Mineralogy and Petrology. v.149, p.338–349.

Bacon, C.R. and Hirschmann, M.M., 1988. Mg/Mn partitioning as a test for equilibrium between coexisting Fe-Ti oxides. American Mineralogist. v.73, p.57-61.

Baker, L. and Rutherford, M.J., 1996. Sulfur diffusion in rhyolite melts. Contributions to Mineralogy and Petrology. v.123, p.335–344.

Bateman, P.C. and Dodge, F.C.W., 1970. Variations of major chemical constituents across the central Sierra Nevada batholith. Geological Society of America Bulletin. v.81, p.409-420.

Barr, D.A., Fox, P.E., Northcote, K.E. and Preto, V.A., 1976. The alkaline suite porphyry deposits: A summary. Canadian Institute of Mining and Metallurgy Special Volume 15. p.359–367.

Barth, A.P. and Dorais, M.J., 2000. Magmatic anhydrite in granitic rocks: First occurrence and potential petrologic consequences. American Mineralogist. v.85, p.430-435.

Bath, A.B., Cooke, D.R., Friedman, R.M., Faure, K., Kamenetsky, V.S., Tosdal, R.M. and Berry, R.F., 2014. Mineralization, U-Pb geochronology, and stable isotope geochemistry of the Lower Main zone of the Lorraine deposit, north-central British Columbia: A replacement-style alkalic Cu-Au porphyry. Economic Geology. v.109, p.979–1004.

Beatty, T.W., Orchard, M.J. and Mustard, P.S., 2006. Geology and tectonic history of the Quesnel terrane in the area of Kamloops, British Columbia. Geological Association of Canada Special Paper 45. p.483–504.

217

Behrens, H. and Gaillard, F., 2006. Geochemical aspects of melts: Volatiles and redox behaviour. Elements. v.2., p.275-280.

Belasky, P. and Stevens, C.H., 2006. Permian faunas of westernmost North America: Paleobiogeographic constraints on the Permian positions of Cordilleran Terranes. Geological Association of Canada Special Paper 46. p.71-80.

Bellver-Baca, M.T. and Chiaradia, M., 2015. High Sr/Y magmas and porphyry-type deposits: What is the role of timescales of magmatic processes? 13th Society for Geology applied to Mineral Deposits Biennial Meeting 2015. v.1, p.259-262.

Belousova, E.A., Griffin, W.L., O'Reilly, S.Y. and Fisher, N.I., 2002. Apatite as an indicator mineral for mineral exploration: Trace-element compositions and their relationship to host rock type. Journal of Geochemical Exploration. v.76, p.45–69.

Beranek, L.P. and Mortensen, J.K., 2011. The timing and provenance record of the Late Permian Klondike orogeny in northwestern Canada and arc-continent collision along western North America. Tectonics. v.30, TC5017, 23p.

Beranek, L.P., van Staal, C., McClelland, W.C., Israel, S. and Mihalynuk, M., 2013a. Baltican crustal provenance for Cambrian-Ordovician sandstones of the Alexander terrane, North American Cordillera: Evidence from detrital zircon U-Pb geochronology and Hf isotope geochemistry. Journal of the Geological Society of London. v.170, p.7-18.

Beranek, L.P., van Staal, C., McClelland, W.C., Israel, S. and Mihalynuk, M., 2013b. Detrital zircon Hf isotopic compositions indicate a northern Caledonian connection for the Alexander terrane. Lithosphere. v.5, p.163–168.

Bergantz, G.W., 2000. On the dynamics of magma mixing by reintrusion: Implications for pluton assembly processes. Journal of Structural Geology. v.22, p.1297–1309.

Best, M. and Christiansen, E., 2001. Igneous Petrology. Blackwell Science. 458p.

Blevin, P. and Chappell, B., 1995. Chemistry, origin, and evolution of mineralized granites in the Lachlan fold belt, Australia: The metallogeny of I- and S-type granites. Economic Geology. v.90, p.1604–1619.

Blundy, J.D. and Holland, T.J.B., 1990. Calcic amphibole equilibria and a new amphibole-plagioclase geothermometer. Contributions to Mineralogy and Petrology. v.104, p.208-224.

Blundy, J.D. and Shimizu, N., 1991. Trace element evidence for plagioclase recycling in calc-alkaline magmas. Earth and Planetary Science Letters. v.102, p.178-197.

Bobrowsky, P.T., Kerr, D.E. and Sibbick, S.J., 1993. Drift exploration studies, Valley Copper pit, Highland Valley copper mine, British Columbia: Stratigraphy and sedimentology (92I/6, 7, 10 and 11). British Columbia Geological Survey Geological Fieldwork 1992. Paper 1993-1, p.427-437.

Boghossian, N.D., Patchett, P.J., Ross, G.M. and Gehrels, G.E., 1996. Nd isotopes and the source of sediments in the miogeocline of the Canadian Cordillera. The Journal of Geology. v.104, p.259-277.

Boudreau, A. and Kruger, F., 1990. Variation in the composition of apatite through the Merensky cyclic unit in the western Bushveld Complex. Economic Geology. v.85, p.737–745.

Bouzari, F., Hart, C.J.R., Barker, S. and Bissig, T., 2011. Porphyry indicator minerals (PIMS): A new exploration tool for concealed deposits in south-central British Columbia. Geoscience B.C. Report 2011-17. 31p.

Bowen, N.L., 1945. Phase equilibria bearing on the origin and differentiation of alkaline rocks. American Journal of Science. v.243, p.75-89.

Brabec, D., 1971. A geochemical study of the Guichon Creek Batholith, British Columbia. Unpublished Ph.D. thesis, University of British Columbia, Vancouver, British Columbia, 148p.

Brehler, B. and Fuge, R., 1974. Chlorine. In: Wedepohl, K.H. (ed.), Handbook of geochemistry. Springer-Verlag, Berlin, II-2, 17A–17O.

Briskey, J.A.Jr., 1980. Geology, petrology, and geochemistry of the Jersey, East Jersey, Huestis, and Iona porphyry copper-molybdenum deposits, Highland Valley, British Columbia. Unpublished Ph.D. thesis, Oregon State University, Corvallis, Oregon, 399p.

Briskey, J.A.Jr. and Bellamy, J.R., 1976. Bethlehem Copper's Jersey, East Jersey, Huestis and Iona deposits. In Sutherland Brown, A., (ed.), Porphyry Deposits of the Canadian Cordillera: Canadian Institute of Mining and Metallurgy, Special Volume 15, p.105-119.

Brophy, J.G., Dorais, M.J., Donnelly-Nolan, J. and Singer, B., 1996. Plagioclase zonation in hornblende gabbro inclusions from Little Glass Mountain, Medicine Lake volcano, California: Implications for fractionation mechanisms and the formation of composition gaps. Contributions to Mineralogy and Petrology. v.126, p.121-136.

Browne, B.L., Eichelberger, J.C., Patino, L.C., Vogel, T.A., Uto, K. and Hoshizumi, H., 2006. Magma mingling as indicated by texture and Sr/Ba ratios of plagioclase phenocrysts from Unzen volcano, SW Japan. Journal of Volcanology and Geothermal Research. v.154, p.103-116.

Buddington, A.F. and Lindsley, D.H., 1964. Iron-titanium oxide minerals and synthetic equivalents. Journal of Petrology. v.54, p.310-357.

Byrne, K., Stock, E., Ryan, J., Johnson, C., Nisenson, J., Jimenez, T.A., Lapointe, M., Stewart, H., Grubisa, G. and Sykora, S., 2013. Porphyry Cu-(Mo) deposits in the Highland Valley district, south-central British Columbia. In: Logan, J. and Schroeter, T., (ed.), Society of Economic Geologists Field Trip Guidebook, Series 43, p.99-116.

Candela, P., 1986. Toward a thermodynamic model for the halogens in magmatic systems: An application to melt-vaporapatite equilibria. Chemical Geology. v.57, p.289–301.

Cao, M., Li, G., Qin, K., Seitmuratova, E.Y. and Liu, Y., 2012. Major and trace element characteristics of apatites in granitoids from central Kazakhstan: Implications for petrogenesis and mineralization. Resource Geology. v.62, p.63-83.

Carlson, R.L. and Raskin, G.S., 1984. Density of the ocean crust. Nature. v.311, p.555-558.

Carmichael, I.S.E., 1967. The iron-titanium oxides of salic volcanic rocks and their associated ferromagnesian silicates. Contributions to Mineralogy and Petrology. v.14, p.36-64.

Carmichael, I.S.E., 1991. The redox state of basic and silicic magmas: A reflection of their source regions? Contributions to Mineralogy and Petrology. v.106, p.106-141.

Carmichael, I.S.E. and Nicholls, J., 1967. Iron-titanium oxides and oxygen fugacities in volcanic rocks. Journal of Geophysical Research. v.72, p.4665-4687.

Carr, J. M., 1960. Porphyries, breccias and copper mineralization in the Highland Valley, B.C. Canadian Mining Journal. v.81, p.71-73.

Carr, J.M., 1962. The geology of part of the Thompson River Valley between Ashcroft and Spences Bridge. British Columbia Ministry of Mines and Petroleum Resources Annual Report. p.28-45.

Carr, J.M., 1966. Geology of the Bethlehem and Craigmont copper deposits. Tectonic History and Mineral Deposits of the Western Cordillera. CIM Special Volume 8. p.321-328.

Carr, S.D., 1995. The southern Omineca Belt, British Columbia: New perspectives from the Lithoprobe Geoscience Program. Canadian Journal of Earth Sciences. v.32, p.1720-1739.

Carten, R.B., Geraghty, E.P. and Walker, B.M., 1988. Cyclic development of igneous features and their relationship to high-temperature hydrothermal features in the Henderson porphyry molybdenum deposit, Colorado. Economic Geology. v.83, p.266-296.

Casselman, M.J., McMillan, W.J. and Newman, K.M., 1995. Highland Valley porphyry copper deposits near Kamloops, British Columbia: A review and update with emphasis on the Valley deposit. In: Schroeter, T.G., (ed.), Porphyry Deposits of the Northwestern Cordillera of North America. Canadian Institute of Mining and Metallurgy, Special Volume 46, p.161-191.

Castillo, P.R., Janney, P.E. and Solidum, R.U., 1999. Petrology and geochemistry of Camiguin Island, southern Philippines: Insights to the source of adakites and other lavas in a complex arc setting. Contributions to Mineralogy and Petrology. v.134, p.33–51.

Chambefort, I., Dilles, J.H. and Kent, A.J.R., 2008. Anhydrite-bearing andesite and dacite as a source for sulfur in magmatic-hydrothermal mineral deposits. Geology. v.36, p.719-722.

Chappell, B.W. and White, A.J.R., 1974. Two contrasting granite types. Pacific Geology. v.8, p.173-174.

Chiaradia, M., 2014. Copper enrichment in arc magmas controlled by overriding plate thickness. Nature Geoscience. v.7, p.43-46.

Christie, J.S., 1976. Krain. In: Sutherland Brown, A., (ed.), Porphyry Deposits of the Canadian Cordillera. Canadian Institute of Mining and Metallurgy, Special Volume 15, p.182-185.

Clift, P.D., Pavlis, T., Debari, S.M., Draut, A.E., Rioux, M. and Kalemen, P.B., 2005. Subduction erosion of the Jurassic Talkeetna-Bonanza arc and the Mesozoic accretionary tectonics of western North America. Geology. v.33, p.881-884.

Cline, J.S., 1995. Genesis of porphyry copper deposits: The behavior of water, chloride, and copper in crystallizing melts. Arizona Geological Society Digest. v.20, p.69–82.

Cline, J.S. and Bodnar, R.J., 1991. Can economic porphyry copper mineralization be generated by a typical calc-alkaline melt? Journal of Geophysical Research. v.96, p.8113–8126.

Cockfield, W.E., 1948. Geology and mineral deposits of the Nicola map-area. Geological Survey of Canada Memoir 249.

Colpron, M., Logan, J.M. and Mortensen, J.K., 2002. U-Pb zircon age constraint for late Neoproterozoic rifting and initiation of the lower Paleozoic passive margin of western Laurentia. Canadian Journal of Earth Sciences. v.39, p.133–143.

Colpron, M., Nelson, J.L. and Murphy, D.C., 2006. A tectonostratigraphic framework for the pericratonic terranes of the northern Canadian Cordillera. Geological Association of Canada Special Paper 45. p.1–23.

Colpron, M., Nelson, J.L. and Murphy, D.C., 2007. Northern Cordilleran terranes and their interactions through time. GSA Today. v.17, p.4-10.

Colpron, M. and Nelson, J.L., 2011. A digital atlas of terranes for the northern Cordillera: Yukon Geological Survey, www.geology.gov.yk.ca/bedrock_terrane .html, accessed September 2015.

Coney, P.J., Jones, D.L. and Monger, J.W.H., 1980. Cordilleran suspect terranes. Nature. v.288, p.329-333.

Cooke, D.R., Braxton, D.P., White, N.C. and Rinne, M., 2015. Metal transport and ore deposition in porphyry copper ± gold ± molybdenum deposits – Contrasting behaviour between deep and shallow environments. 13th Society for Geology applied to Mineral Deposits Biennial Meeting 2015. v.1, p.275-278.

Cooke, D.R., Deyell, C.L., Waters, P.J., Gonzales, R.I. and Zaw, K., 2011. Evidence for magmatic-hydrothermal fluids and ore-forming processes in epithermal and porphyry deposits of the Baguio district, Philippines. Economic Geology. v.106, p.1399-1424.

Cooke, D.R., Hollings, P. and Walshe, J.L., 2005. Giant porphyry deposits: Characteristics, distribution, and tectonic controls. Economic Geology. v.100, p.801–818.

Cosca, M.A., Essene, E.J. and Bowman, J.R., 1991. Complete chemical analyses of metamorphic hornblendes: Implications for normalizations, calculated H_2O activities, and thermobarometry. Contributions to Mineralogy and Petrology. v.108, p.472-484.

Coulsen, I.M., Dipple, G.M. and Raudsepp, M., 2001. Evolution of HF and HCl activity in magmatic volatiles of the gold-mineralized Emerald Lake pluton, Yukon Territory, Canada. Mineralium Deposita. v.36, p.594-606.

Crawford, A.J., Meffre, S., Squire, L.M., Barron, L.M. and Falloon, T.J., 2007. Middle and Late Ordovician magmatic evolution of the Macquarie Arc, Lachlan Orogen, New South Wales. Australian Journal of Earth Sciences. v.54, p.181-214.

Czamanske, G.K. and Wones, D.R., 1973. Oxidation during magmatic differentiation: Finnmarka Complex, Oslo Area, Norway. Part 2. The mafic silicates. Journal of Petrology. v.14, p.349-380.

Deer, W.A., Howie, R.A. and Zussman, J., 2013. An Introduction to the Rock-forming Minerals. Mineralogical Society, London, 510p.

Defant, M.J. and Drummond, M.S., 1990. Derivation of some modern arc magmas by melting of young subducted lithosphere. Nature. v. 347, p.662–665.

Defant, M.J. and Drummond, M.S., 1993. Mount St. Helens: Potential example of the partial melting of the subducted lithosphere in a volcanic arc. Geology. v.21, p.547–550.

DePaolo, D.J., 1981a. A neodymium and strontium isotopic study of the Mesozoic calc alkaline granitic batholiths of the Sierra Nevada and Peninsular Ranges, California. Journal of Geophysical Research. v.86, p.10470-10488.

DePaolo, D.J., 1981b. Trace element and isotopic effects of combined wallrock assimilation and fractional crystallization. Earth and Planetary Science Letters. v. 53, p. 189–202.

DePaolo, D.J. and Johnson, R.W., 1979. Magma genesis in the New Britain island-arc: Constraints from Nd and Sr isotopes and trace-element patterns. Contributions to Mineralogy and Petrology. v.70, p.367-379.

DePaolo, D.J. and Wasserburg, G.J., 1976. Inferences about magma sources and mantle structure from variations of ^{143}Nd/^{144}Nd. Geophysical Research Letters. v.3, p.743-746.

DePaolo, D.J. and Wasserburg, G.J., 1977. The sources of island arcs as indicated by Nd and Sr isotopic studies. Geophysical Research Letters. v.4, p.465-468.

DePaolo, D.J. and Wasserburg, G.J., 1979. Petrogenetic mixing models and Nd-Sr isotopic patterns. Geochimica and Cosmochimica Acta. v.43, p.615-627.

Devine, F.A.M., Chamberlain, C.M., Davies, A.G.S., Friedman, R. and Baxter, P., 2014. Geology and district-scale setting of tilted alkalic porphyry Cu-Au mineralization at the Lorraine deposit, British Columbia. Economic Geology. v.109, p.939–977.

Diakow, L.J., 2001. Geology of the southern Toodoggone River and northern McConnell Creek map areas, north-central British Columbia. British Columbia Ministry of Energy, Mines. Geoscience Map 2001-1, 1:50,000 scale, 1 sheet.

Dickin, A.P., 2005. Radiogenic Isotope Geology. 2nd Ed. Cambridge University Press, New York.

Dickenson, W.R., 1975. Potash-depth (K-h) relations in continental margins and intra oceanic magmatic arcs. Geology. v.3, p.53-56.

Dostal, J., Church, B.N. and Hoy, T., 2001. Geological and geochemical evidence for variable magmatism and tectonics in the southern Canadian Cordillera: Paleozoic to Jurassic suites, Greenwood, southern British Columbia. Canadian Journal of Earth Sciences. v.38, p.75-90.

Droop, G.T.R., 1987. A general equation for estimating Fe^{3+} concentrations in ferromagnesian silicates and oxides from microprobe analyses, using stoichiometric criteria. Mineralogical Magazine. v.51, p.431-435.

Duffell, S. and McTaggart, K.C., 1952. Ashcroft map-area, British Columbia. Geological Survey of Canada Memoir 262.

Dusel-Bacon, C., Hopkins, M.J., Mortensen, J.K., Williams, I., Heslop, K., Dashevsky, S.S., Bressler, J.R. and Day, W.C., 2006. Paleozoic tectonic and metallogenetic evolution of the Yukon-Tanana terrane, east-central Alaska. Geological Association of Canada Special Paper 45. p.25-74.

English, J.M., Mihalynuk, M.G. and Johnston, S.T., 2010. Geochemistry of the northern Cache Creek terrane and implications for accretionary processes in the Canadian Cordillera. Canadian Journal of Earth Sciences. v.47, p.13–34.

Enns, S.G., Thompson, J.F.H., Stanely, C.R. and Yarrow, E.W., 1995. The Galore Creek porphyry copper-gold deposits, northwestern British Columbia. Canadian Institute of Mining, Metallurgy and Petroleum. Special Volume 46, p.630–644.

Ernst, W.G. and Liu, J., 1998. Experimental phase-equilibrium study of Al- and Ti-contents of calcic amphibole in MORB - A semiquantitative thermobarometer. American Mineralogist. v.83, p.952-969.

Evans, B.W. and Ghiorso, M.S., 1995. Thermodynamics and petrology of cummingtonite. American Mineralogist. v.80, p.649-663.

Evenchick, C.A., McMechan, M.E., McNicoll, V.J. and Carr, S.D., 2007. A synthesis of the Jurassic-Cretaceous tectonic evolution of the central and southeastern Canadian Cordillera: Exploring links across the orogeny. Geological Society of America Special Paper 433. p.117–145.

Féménias, O., Mercier, J-C. C., Nkono, C., Diot, H., Berza, T., Tatu, M. and Demaiffe, D., 2006. Calcic amphibole growth and compositions in calc-alkaline magmas: Evidence from the Motru Dike Swarm (Southern Carpathians, Romania). American Mineralogist. v.91, p.73-81.

Foley, S.F. and Wheller, G.E., 1990. Parallels in the origin of the geochemical signatures of island arc volcanics and continental potassic igneous rocks: The role of residual titanites. Chemical Geology. v.85, p.1–18.

Fournelle, J., 1990. Anhydrite in Nevado del Ruiz November 1985 pumice: Relevance to the sulfur problem. Journal of Volcanology and Geothermal Research. v.42, p.189–201.

Frost, B.R., Arculus, R.J., Barnes, C.G., Collins, W.J., Ellis, D.J. and Frost, C.D., 2001. A geochemical classification of granitic rocks. Journal of Petrology. v.42, p.2033-2048.

Frost, B.R. and Frost, C.D., 2008. A geochemical classification for feldspathic igneous rocks. Journal of Petrology. v.49, p.1955-1969.

Frost, B.R. and Lindsley, D.H., 1992. Equilibria among Fe-Ti oxides, pyroxenes, olivine, and quartz: Part II. Application. American Mineralogist. v.77, p.1004-1020.

Gabrielse, H., Monger, J.W.H., Wheeler, J.O. and Yorath, C.J., 1991. Part A-Morphogeological belts, tectonic assemblages and terranes, Chapter 2. In: Gabrielse, H. and Yorath, C.J., (eds.), Geology of the Cordilleran Orogen in Canada. Geological Survey of Canada. Geology of Canada. no.4, p.15-28.

Gabrielse, H., Murphy, D.C. and Mortensen, J.K., 2006. Cretaceous and Cenozoic orogen-parallel displacements, magmatism and paleogeography in the northern Canadian Cordillera. Geological Association of Canada Special Paper 46. p.255-276.

Garnett, J.A., 1978. Geology and mineral occurrences of the southern Hogem batholith. British Columbia Department of Mines and Petroleum Resources. Bulletin 70, 75p.

Gasparon, M., Rosenbaum, G., Wijbrans, J. and Manetti, P., 2009. The transition from subduction to slab tearing: Evidence from Caraia Island, northern Tyrrhenian Sea. Journal of Geodynamics. v.47, p.30–38.

Gehrels, G.E., Dickinson, W.R., Ross, G.M., Stewart, J.H. and Howell, D.G., 1995. Detrital zircon reference for Cambrian to Triassic miogeoclinal strata of western North America. Geology. v.23, p.831–834.

Gehrels, G.E., McClelland, W.C., Samson, S.D., Patchett, P.J. and Jackson, J.L., 1990. Ancient continental margin assemblage in the northern Coast Mountains, southeast Alaska and northwest Canada. Geology. v.18, p.208-211.

Gehrels, G.E., McClelland, W.C., Samson, S.D., Patchett, P.J. and Brew, D.A., 1991a. U-Pb geochronology of Late Cretaceous and early Tertiary plutons in the northern Coast Mountains batholith. Canadian Journal of Earth Sciences. v.28, p.899-911.

Gehrels, G.E., McClelland, W.C., Samson, S.D. and Patchett, P.J. 1991b. U-Pb geochronology of detrital zircons from a continental margin assemblage in the northern Coast Mountains, southeastern Alaska. Canadian Journal of Earth Sciences. v.28, p.1285-1300.

Gehrels, G., Rusmore, M., Woodsworth, G., Crawford, M., Andronicos, C., Hollister, L., Patchett, J., Ducea, M., Butler, R., Klepeis, K., Davidson, C., Friedman, R., Haggart, J., Mahoney, B., Crawford, W., Pearson, D. and Girardi, J., 2009. U-Th-Pb geochronology of the Coast Mountains batholith in north-coastal British Columbia: Constraints on age and tectonic evolution. Geological Society of America Bulletin. v.121, p.1341-1361.

Ghent, E.D., Knitter, C.C., Raeside, R.P. and Stout, M.Z., 1982. Geothermometry and geobarometry of pelitic rocks, upper kyanite and sillimanite zones, Mica Creek area, British Columbia. Canadian Mineralogist. v.20, p.295-305.

Ghent, E.D., Robbins, D.B. and Stout, M.Z., 1979. Geothermometry, geobarometry, and fluid compositions of metamorphosed calc-silicates and pelites, Mica Creek, British Columbia. American Mineralogist. v.64, p.874-885.

Ghiorso, M.S. and Evans, B.W., 2008. Thermodynamics of rhombohedral oxide solid solutions and a revision of the Fe-Ti two-oxide geothermometer and oxygen-barometer. American Journal of Science. v.308, p.957-1039.

Ghiorso, M.S. and Sack, R.O., 1991. Fe-Ti oxide geothermometry: Thermodynamic formulation and the estimation of intensive variables in silicic magmas. Contributions to Mineralogy and Petrology. v.108, p.485-510.

Ghosh, D.K., 1995. Nd-Sr isotopic constraints on the interactions of the Intermontane superterrane with the western edge of North America in the southern Canadian Cordillera. Canadian Journal of Earth Sciences. v.32, p.1740–1758.

Ghosh, D.K. and Lambert, R. St. J., 1989. Nd-Sr isotopic study of Proterozoic to Triassic sediments from southeastern British Columbia. Earth and Planetary Science Letters. v.94, p.29-44.

Giesting, P.A. and Filiberto, J., 2014. Quantitative models linking igneous amphibole composition with magma Cl and OH content. American Mineralogist. v.99, p.852-865.

Gill, J.B., 1981. Orogenic andesites and plate tectonics. New York, Springer-Verlag, 390p.

Ginibre, C., Kronz, A. and Wörner, G., 2002. High-resolution quantitative imaging of plagioclase composition using accumulated backscattered electron images: New constraints on oscillatory zoning. Contributions to Mineralogy and Petrology. v.142, p.436-448.

Ginibre, C. and Wörner, G., 2007. Variable parent magmas and recharge regimes of the Parinacota magma system (N. Chile) revealed by Fe, Mg and Sr zoning in plagioclase. Lithos. v.98, p.118-140.

Goldstein, S.L., O'Nions, R.K. and Hamilton, P.J., 1984. A Sm-Nd study of atmospheric dusts and particulates from major river systems. Earth and Planetary Science Letters. v.70, p.221-236.

Grove, T.L., Baker, M.B. and Kinzler, R.J., 1984. Coupled CaAl-NaSi diffusion in plagioclase feldspar: Experiments and applications to cooling rate speedometry. Geochimica et Cosmochimica Acta. v.48, p.2113-2121.

Gunning, M.H., Hodder, R.W.H. and Nelson, J.L., 2006. Contrasting volcanic styles in the Paleozoic Stikine assemblage, western Stikine terrane, northwestern British Columbia. Geological Association of Canada Special Paper 45, p.201-227.

Gustafson, L.B. and Hunt, J.P., 1975. The porphyry copper deposit at El Salvador, Chile. Economic Geology. v.70, p.857-912.

Hammarstrom, J.M. and Zen, E.-A., 1986. Aluminium in hornblende: An empirical igneous geobarometer. American Mineralogist. v.71, p.1297-1313.

Hansen, V.L., 1990. Yukon-Tanana terrane: A partial acquittal. Geology. v.18, p.365-369.

Hansen, V.L. and Dusel-Bacon, C., 1998. Structural and kinematic evolution of Yukon-Tanana upland tectonites, east-central Alaska: A record of late Paleozoic to early Mesozoic crustal assembly. Geological Society of America Bulletin. v.110, p.211–230.

Harrison, T.M. and Clarke, G.K.C., 1979. A model of the thermal effects of igneous intrusion and uplift as applied to Quottoon Pluton, British Columbia. Canadian Journal of Earth Sciences. v.16, p.411–420.

Harrison, T.M. and Watson, E.W., 1984. The behavior of apatite during crustal anatexis: Equilibrium and kinetic considerations. Geochimica and Cosmochimica Acta. v.48, p.1467–1477.

Hart, C.J.R., Goldfarb, R.J., Lewis, L.L. and Mair, J., 2004. The northern Cordilleran mid-Cretaceous plutonic province: Ilmenite-magnetite series granitoids and intrusion-related mineralization. Resource Geology. The Ishihara Volume. v.54, p.253-280.

Hattori, K.H. and Keith, J.D., 2001. Contribution of mafic melt to porphyry copper mineralization: Evidence from Mount Pinatubo, Philippines, and Bingham Canyon, Utah, USA. Mineralium Deposita. v.36, p.799-806.

Hawthorne, F.C., Oberti, R., Harlow, G.E., Maresch, W.V., Martin, R.F., Schumacher, J.C. and Welch, M.D., 2012. Nomenclature of the amphibole supergroup. American Mineralogist. v.97, p.2031-2048.

Heidrick, T.L. and Titley, S.R., 1982. Fracture and dike patterns in Laramide plutons and their structural and tectonic implications: American southwest. In: Titley, S.R., (ed.), Advances in Geology of the Porphyry Copper Deposits. Tucson, University of Arizona Press, p. 73–91.

Helz, R.T., 1973. Phase relations of basalts in their melting range at P_{H2O} = 5 kb as a function of oxygen fugacity. Part I. Mafic phases. Journal of Petrology. v.14, p.249-302.

Hildreth, W. and Moorbath, S., 1988. Crustal contributions to arc magmatism in the Andes of central Chile. Contributions to Mineralogy and Petrology. v.98, p.455–489.

Hill, M.L., 1985. Remarkable fossil locality: Crinoid stems from migmatite of the Coast Plutonic Complex, British Columbia. Geology. v.13, p.825-826.

Hollings, P., Cooke, D. and Clark, A., 2005. Regional geochemistry of Tertiary igneous rocks in central Chile: Implications for the geodynamic environment of giant porphyry copper and epithermal gold mineralization. Economic Geology. v.100, p.887-904.

Hollings, P., Cooke, D.R., Waters, P.J. and Cousens, B., 2011. Igneous geochemistry of mineralized rocks of the Baugio district, Philippines: Implications for tectonic evolution and the genesis of porphyry-style mineralization. Economic Geology. v.106, p.1317-1333.

Hollings, P., Sweet, G., Baker, M., Cooke, D.R. and Friedman, R., 2013. Tectonomagmatic controls on porphyry mineralization: Geochemical evidence from the Black Mountain porphyry system, Philippines. Society of Economic Geologists Special Publication 17. p.301-335.

Hollister, L.S. and Andronicos, C., 2000. The Central Gneiss Complex, Coast Mountains, British Columbia. In: Stowell, H.H. and McClelland, W.C., (eds.), Tectonics of the Coast Mountains, SE Alaska and British Columbia. Geological Society of America. Special Paper 343, p.45-59.

Hollister, L.S., Grissom, G.C., Peters, E.K., Stowell, H.H. and Sisson, V.B., 1987. Confirmation of the empirical correlation of Al in hornblende with pressure of solidification of calcalkaline plutons. American Mineralogist. v.72, p.231-239.

Hollister, V.F., Allen, J.M., Anzalone, S.A. and Seraphim, R.H., 1975. Structural evolution of porphyry mineralization at Highland Valley, British Columbia. Canadian Journal of Earth Sciences. v.12, p.807-820.

Hunt, J.P., 1991. Porphyry copper deposits. Economic Geology Monograph 8. p.192-206.

Irvine, T.N. and Baragar, W.R.A., 1971. A guide to the chemical classification of the common volcanic rocks. Canadian Journal of Earth Sciences. v.8, p.523-548.

Ishihara, S., 1977. The magnetite-series and ilmenite-series granitic rocks. Mining Geology. v.27, p.293-305.

Jackson, J.L., 1992. Tectonic analysis of the Nisling, northern Stikine and northern Cache Creek terranes, Yukon and British Columbia. Unpublished Ph.D thesis, The University of Arizona, Tucson, Arizona, 200p.

John, B.E. and Wooden, J., 1990. Petrology and geochemistry of the metaluminous to peraluminous Chemehuevi Mountains Plutonic suite, southeastern California. In: Anderson, J.L. (ed.), The Nature and Origin of Cordilleran Magmatism. Geological Society of America, Memoir. v.174, p.71-98.

Johnson, M.C. and Plank, T., 1999. Dehydration and melting experiments constrain the fate of subducted sediments. Geochemistry, Geophysics, Geosystems. v.1, 26p.

Johnson, M.C. and Rutherford, M.J.,1989. Experimental calibration of the aluminium-in-hornblende geobarometer with application to Long Valley caldera (California) volcanic rocks. Geology. v.17, p.837-841.

Jones, D.L., Howell, D.G., Coney, P.J. and Monger, J.W.H., 1983. Recognition, character and analysis of tectonostratigraphic terranes in western North America. In: Hashimoto, M. and Uyeda, S., (eds.), Accretion Tectonics in the Circum-Pacific Regions. Tokyo, Terra Scientific Publishing Company. p.21–35.

Jones, B.K., 1992. Application of metal zoning to gold exploration in porphyry copper systems. Journal of Geochemical Exploration. v.43, p.127-155.

Kenah, C., and Hollister, L.S., 1983. Anatexis in the central gneiss complex, British Columbia. In: Artherton, M.P. and Gribble, C.D., (eds.), Migmatites, Melting and Metamorphism. Shiva, Nantwich. p.142-162.

Keppler, H., 1996. Constraints from partitioning experiments on the composition of subduction-zone fluids. Nature. v.380, p.237-240.

Kilpatrick, J.A. and Ellis, D.J., 1992. C-type magmas: Igneous charnockites and their extrusive equivalents. Transactions of the Royal Society of Edinburgh: Earth Sciences. v.83, p.155-164.

Kirkham, R.V., 1972. Porphyry deposits. In: Blackadar, R.G., (ed.), Report of Activities Part B, November 1971 to March 1972. Geological Survey of Canada, Paper 72-1b, p.62-64.

Kirkham, R.V., and Sinclair, W.D., 1995. Porphyry copper, gold, molybdenum, tungsten, tin, silver. In: Eckstrand, O.R., Sinclair, W.D. and Thorpe, R.I., (eds.), Geology of Canadian Mineral Deposit Types. Geological Survey of Canada, Geology of Canada, no. 8, p.421-446.

Klepacki, D.W. and Wheeler, J.O., 1985. Stratigraphic and structural relations of the Milford, Kaslo and Slocan Groups, Goat Range, Lardeau and Nelson map areas, British Columbia. Geological Survey of Canada. Paper 85-1A, p.277–286.

Kuno, H., 1968. Differentiation of basalt magmas. In: Hess, H. H. and Poldervaart, A. A., (eds.), Basalts: The Poldervaart Treatise on Rocks of Basaltic Composition. Interscience, New York. p.623-688.

Le Bas, M.J. and Streckeisen, A.L., 1991. The IUGS systematics of igneous rocks. Journal of the Geological Society. v.148, p.825-833.

Le Maitre, R.W. (Ed.), Bateman, P., Dubek, A., Keller, J., Lameyre, J., Le Bas, M.J., Sabine, P.A., Schmid, R., Sorensen, H., Streckeisen, A,, Woolley, A.R. and Zanettin, B., 1989. A Classification of Igneous Rocks and Glossary of Terms: Recommendations of the International Union of Geological Sciences Subcommission on the Systematics of Igneous Rocks. Blackwell, Oxford, 193p and Wall Chart.

Leake, B. E., Woolley, A. R., Arps, C. E. S., Birch, W. D.,Gilbert, M. C., Grice, J.D., Hawthorne,F.C., Kato, A., Kisch, H.J., Krivovichev, V.G., Linthout, K., Laird, J., Mandarino J., Maresch, W.V., Nickel, E.H., Rock, N.M.S., Schumacher, J.C., Smith, D.C.,Stephenson, N.C.N., Ungaretti, L., Whittaker, E.J.W. and Youzhi, G., 1997. Nomenclature of amphiboles: Report of the subcommittee on amphiboles of the International Mineralogical Association commission on new minerals and mineral names. Mineralogical Magazine. v.61, p.295-321.

Leake, B. E., Woolley, A. R., Birch, W. D., Burke, E. A.J., Ferraris, G., Grice, J.D., Hawthorne, F.C., Kisch, H.J., Krivovichev, V.G., Schumacher, J.C., Stephenson, N.C.N. and Whittaker, E.J.W., 2003. Nomenclature of amphiboles: Additions and revisions to the International Mineralogical Association's 1997 recommendations. The Canadian Mineralogist. v.41, p.1355-1362.

Lee, C-T.A., Leeman, W.P., Canil, D. and Li, Z-X., A., 2005. Similar V/Sc systematics in MORB and arc basalts: Implications for the oxygen fugacities of their mantle source regions. Journal of Petrology. v.46, p.2313-2336.

Leveille, R.A. and Stegen, R.J., 2012. The southwestern North America porphyry copper province. Economic Geology Special Publication 16. p.361-401.

Lindstrom, D.J., 1976. Experimental study of the partitioning of the transition metals between clinopyroxene and coexisting silicate liquids. Unpublished Ph.D. thesis, University of Oregon, Eugene, Oregon, 188p.

Lipman, P.W., 1971. Iron-titanium oxide phenocrysts in compositionally zoned ash-flow sheets from southern Nevada. Journal of Geology. v.79, p.438-456.

Liu, Y. and Comodi, P., 1993. Some aspects of the crystal-chemistry of apatites. Mineralogical Magazine. v.57, p.709–719.

Liverton, R., Mortensen, J.K. and Roots, C.F., 2005. Character and metallogeny of Permian, Jurassic and Cretaceous plutons in the southern Yukon-Tanana Terrane. In: D.S. Emond, L.L. Lewis and G.D. Bradshaw (eds.), Yukon Exploration and Geology 2004. Yukon Geological Survey. p.147-165.

Logan, J.M. and Mihalynuk, M.G., 2005. Porphyry Cu-Au deposits of the Iron Mask batholith, southeastern BC. British Columbia Ministry of Energy and Mines, Geological Fieldwork 2004. Paper 2005-1, p.271–290.

Logan, J.M. and Mihalynuk, M.G., 2014. Tectonic controls on early Mesozoic paired alkaline porphyry deposit belts (Cu-Au ± Ag-Pt-Pd-Mo) in the Canadian Cordillera. Economic Geology. v.109, p.827-858.

Logan, J.M., Drobe, J.R. and McClelland, W.C., 2000. Geology of the Forrest Kerr-Mess Creek area, northwestern British Columbia (NTS 104B/10, 15 & 104G/2 & 7W). British Columbia Ministry of Energy, Mines and Petroleum Resources Bulletin 104. 164p.

Logan, J.M., Mihalynuk, M.G., Ullrich, T. and Friedman, R.M., 2007. U-Pb Ages of intrusive rocks and [40]Ar/[39]Ar plateau ages of copper-gold-silver mineralization associated with alkaline intrusive centres at Mount Polley and the Iron Mask batholith, southern and central British Columbia. British Columbia Ministry of Energy, Mines and Petroleum Resources, Geological Fieldwork 2006. Paper 2007-1, p.93–116.

Logan, J.M., Mihalynuk, M.G., Friedman, R.M. and Creaser, R.A., 2011. Age constraints of mineralization at the Brenda and Woodjam Cu-Mo ± Au porphyry deposits— An Early Jurassic calc-alkaline event, south-central British Columbia. British Columbia Ministry of Forests, Mines and Lands, Geological Fieldwork 2010. Paper 2011-1, p.129–144.

Loiselle, M.C. and Wones, D.S., 1979. Characteristics and origin of anorogenic granites. Geological Society of America, Abstracts with Programs. v.11, p.468.

Loomis, T.P., 1982. Numerical simulations of crystallization processes of plagioclase in complex melts: The origin of major and oscillatory zoning in plagioclase. Contributions to Mineralogy and Petrology. v.81, p.219-229.

Loomis, T.P. and Welber, P.W., 1982. Crystallization processes in the Rocky Hill granodiorite pluton, California: An interpretation based on compositional zoning of plagioclase. Contributions to Mineralogy and Petrology. v.81, p.230-239.

Loucks, R.R., 2014. Distinctive composition of copper-ore-forming arc magmas. Australian Journal of Earth Sciences. v.61, p.5-16.

Lowell, J.D. and Guilbert, J.M., 1970. Lateral and vertical alteration-mineralization zoning in porphyry ore deposits. Economic Geology. v.65, p.373-408.

Luhr, J.F., Carmichael, I.S.E. and Varekamp, J.C., 1984. The 1982 eruptions of El Chichón volcano, Chiapas, Mexico: Mineralogy and petrology of the anhydrite-bearing pumices. Journal of Volcanology and Geothermal Research. v.23, p.69–108.

Lydon, J.W., 2007. An overview of the economic and geological contexts of Canada's major mineral deposit types. Geological Association of Canada, Mineral Deposits Division. Special Publication 5, p.3-48.

MacIntyre, D.G., Villeneuve, M.E. and Schiarizza, P., 2001. Timing and tectonic setting of Stikine Terrane magmatism, Babine-Takla lakes area, central British Columbia. Canadian Journal of Earth Sciences. v.38, p.579-601.

Mariano, A.N., 1988. Some further geological applications of cathodoluminescence. In: Marshall, D.J., (ed.), Cathodoluminescence of Geological Materials. Unwin Hyman, Boston. p. 94–123.

Martel, C., Pichavant, M., Holtz, F., Scaillet, B., Bourdier, J.L. and Traineau, H., 1999. Effects of fO_2 and H_2O on andesite phase relation between 2 and 4kbar. Journal of Geophysical Research. v.104, p.29453-29470.

Massey, N.W.D., MacIntyre, D.G., Desjardins, P.J. and Cooney, R.T., 2005. Digital geology map of British Columbia. B.C. Ministry of Energy and Mines, Whole Province. Geofile 2005-1.

Matthews, S.J., Sparks, R.S.J. and Gardeweg, M.C., 1999. The Piedras Grandes–Soncor eruptions, Lascar volcano, Chile: Evolution of a zoned magma chamber in the Central Andean upper crust. Journal of Petrology. v.40, p.1891–1919.

Matzel, J.E.P., Bowring, S.A. and Miller, R.B., 2006. Time scales of pluton construction at differing crustal levels: Examples from the Mount Stuart and Tenpeak intrusions, North Cascades, Washington. Geological Society of America Bulletin. v.118, p.1412-1430.

McClelland, W.C., Anovitz, L.M. and Gehrels, G.E., 1991. Thermobarometric constraints on the structural evolution of the Coast Mountains batholith, central southeastern Alaska. Canadian Journal of Earth Sciences. v.28, p.912-928.

McMillan, W.J., 1976a. Geology and genesis of the Highland Valley ore deposits and the Guichon Creek batholith. In: Sutherland Brown, A., (ed.), Porphyry Deposits of the Canadian Cordillera. Canadian Institute of Mining and Metallurgy, Special Volume 15, p.85-104.

McMillan, W.J., 1976b. J.A.. In: Sutherland Brown, A., (ed.), Porphyry Deposits of the Canadian Cordillera. Canadian Institute of Mining and Metallurgy, Special Volume 15, p.144-162.

McMillan, W.J., 1981. Nicola project-Merritt area. British Columbia Ministry of Energy, Mines and Petroleum Resources. Preliminary Map 47 (2 sheets), scale 1:25 000.

McMillan, W. J., 1985. Geology and ore deposits of the Highland Valley camp. In: Sinclair A.J., (ed), Mineral Deposits Division Field Guide and Reference Manual Series, no. 1, Geological Association of Canada, 121p.

McMillan, W.J., Anderson, R.G., Chen, R. and Chen, W., 2009. Geology and mineral occurences (MINFILE), the Guichon Creek Batholith and Highland Valley porphyry copper district, British Columbia, Geological Survey of Canada, Open file 6079, 2 sheets. http://geoscan.ess.nrcan.gc.ca/cgibin/starfinder/0?path =geoscan.fl&id=fastlink&pass=&search=R%3D248060&format=FLFULL

McCuaig, T.C., Kerrich, R. and Xie, Q., 1994. Phosphorous and high field strength anomalies in Archean high-magnesian magmas as possible indicators of source mineralogy and depth. Earth and Planetary Science Letters. v.124, p.221– 239.

Middlemost, E.A.K., 1994. Naming materials in the magma/igneous rock system. Earth Science Reviews. v.37, p.215-224

Mihalynuk, M.G., Smith, M.T., Gabites, J.E., Runkle, D. and Lefebure, D., 1992. Age of emplacement and basement character of the Cache Creek terrane as constrained by new isotopic and geochemical data. Canadian Journal of Earth Sciences. v.29, p.2463-2477.

Mihalynuk, M.G., Nelson, J.L. and Diakow, L.J., 1994. Cache Creek terrane: Oroclinal paradox in the Canadian Cordillera. Tectonics. v.13, p.575-595.

Mihalynuk, M.G., Mountjoy, K.J., Smith, M.T., Currie, L.D., Gabites, J.E., Tipper, H.W., Orchard, M.J., Poulton, T.P. and Cordey, F., 1999. Geology and mineral resources of the Tagish Lake area (NTS 104M/ 8,9,10E, 15 and 104N/ 12W), northwestern British Columbia. British Columbia Ministry of Energy and Mines Bulletin 105. 217p.

Mihalynuk, M.G., Erdmer, P., Ghent, E.D., Cordey, F., Archibald, D.A., Friedman, R.M. and Johannson, G.G., 2004. Coherent French Range blueschist: Subduction to exhumation in <2.5 m.y.? Geological Society of America Bulletin. v.116, p.910-922.

Monger, J.W.H., 1977. Upper Paleozoic rocks of the western Canadian Cordillera and their bearing on Cordilleran evolution. Canadian Journal of Earth Sciences. v.14, p.1832-1859.

Monger, J.W.H., 1982. Geology of Ashcroft map area, southwestern British Columbia. In: Current research, part A. Geological Survey of Canada, Paper 82-I A, p.293-297.

Monger, J.W.H., 1985. Structural evolution of the southwestern Intermontane belt, Ashcroft and Hope map areas, British Columbia. In: Current research, part A. Geological Survey of Canada, Paper 85-I A, p.349-358

Monger, J. W.H. and Berg, H.C. 1987. Lithotectonic terrane map of western Canada and southeastern Alaska. In: Silberling, N. J. and Jones, D. L. (eds.), Lithotectonic Terrane Map of the North American Cordillera. United States Geological Survey, Map 1874B.

Monger, J.W.H. and Price, R. A., 1979. Geodynamic evolution of the Canadian Cordillera-Progress and problems. Canadian Journal of Earth Sciences. v.16, p.770-791.

Monger, J.W.H., Price, R.A. and Tempelman-Kluit, D.J., 1982. Tectonic accretion and the origin of the two major metamorphic and plutonic welts in the Canadian Cordillera. Geology. v.10, p.70-75.

Monger, J.W.H. and Ross, C. A., 1971. Distribution of fusulinaceans in the western Canadian Cordillera. Canadian Journal of Earth Sciences. v.8, p.259-278.

Monger, J.W.H., Wheeler, J.O., Tipper, H.W., Gabrielse, H., Harms, T., Struik, L.C., Campbell, R.B., Dodds, C.J., Gehrels, G.E. and O'Brian, J., 1991. Part B: Cordilleran terranes. In: Gabrielse, H. and Yorath, C.J. (eds.), Geology of the Cordilleran Orogen in Canada. Geological Survey of Canada, Geology of Canada, no. 4.

Moore, J.G., 1959. The quartz diorite boundary line in the western United States. Journal of Geology. v.67, p.198-210.

Moore, G.M. and Carmichael, I.S.E., 1998. The hydrous phase equilibria (to 3 kbar) of an andesite and basaltic andesite from western Mexico: Constraints on water content and conditions of phenocryst growth. Contributions to Mineralogy and Petrology. v.130, p.304–319.

Morrison G.W., 1980. Stratigraphic control of Cu-Fe skarn ore distribution and genesis at Craigmont, British Columbia. Canadian Mining and Metallurgical Bulletin. v.73, p.109-123.

Mortensen, J.K., 1992. Pre-mid-Mesozoic tectonic evolution of the Yukon-Tanana terrane, Yukon and Alaska. Tectonics. v.11, p.836-853.

Mortensen, J.K., Ghosh, D.K. and Ferri, F., 1995. U-Pb geochronology of intrusive rocks associated with copper-gold porphyry deposits in the Canadian Cordillera. Canadian Institute of Mining, Metallurgy and Petroleum Special Volume 46, p.142–158.

Mortimer, N., 1986. Late Triassic, arc-related, potassic igneous rocks in the North American Cordillera. Geology. v.14, p.1035-1038.

Mortimer, N., 1987. The Nicola Group: Late Triassic and early Jurassic subduction related volcanism in British Columbia. Canadian Journal of Earth Sciences. v.24, p.2521-2536.

Mortimer, N., Van Der Heyden, P., Armstrong, R.L. and Harakal, J., 1990. U-Pb and K-Ar dates related to timing of magmatism and deformation in the Cache Creek Terrane and Quesnellia, southern British Columbia. Canadian Journal of Earth Sciences. v.27, p.117-123.

Mungall, J.E., 2002. Roasting the mantle: Slab melting and the genesis of major Au and Au-rich Cu deposits. Geology. v.30, p.915–918.

Munoz, J.L., 1974. Measurements of quenched fluoride in synthetic hydrothermal fluids. Geological Society of America Abstracts Program. v.4, p.882.

Munoz, J.L., 1984. F-OH and Cl-OH exchange in micas with applications to hydrothermal ore deposits. In: Bailey, S.W. (ed.), Micas: Reviews in Mineralogy 13, Chapter 11, Mineralogical Society of America, p.469-493.

Müntener, O., Kelemen, P.B. and Grove, T.L., 2001. The role of H_2O during crystallization of primitive arc magmas under uppermost mantle conditions and genesis of igneous pyroxenites: An experimental study. Contributions to Mineralogy and Petrology. v.141, p.643–658.

Murphy, D.C., Mortensen, J.K., Piercey, S.J., Orchard, M.J. and Gehrels, G.E., 2006. Mid-Paleozoic to early Mesozoic tectonostratigraphic evolution of Yukon-Tanana and Slide Mountain terranes and affiliated overlap assemblages, Finlayson Lake massive sulfide district, southeastern Yukon. Geological Association of Canada Special Paper 45. p.75–105.

Naney, M.T., 1983. Phase equilibria of rock-forming ferromagnesian silicates in granitic systems. American Journal of Science. v.283, p.993–1033.

Nash, W.P., 1984. Phosphate minerals in terrestrial igneous and metamorphic rocks. In: Nriaguand, J. O. and Moore, P. B. (eds.), Phosphate Minerals. Springer-Verlag, Berlin, p.215–241.

Nelson, J.L., 1993. The Sylvester Allochthon: upper Paleozoic marginal basin and island arc terranes in northern British Columbia. Canadian Journal of Earth Sciences. v.30, p.631–643.

Nelson, J.L. and Bellefontaine, K.A., 1996. The geology and mineral deposits of north-central Quesnellia: Tezzeron Lake to Discovery Creek, central British Columbia. BC Ministry of Energy, Mines and Petroleum Resources Bulletin 99. 112p.

Nelson, J.L. and Friedman, R., 2004. Superimposed Quesnel (late Paleozoic-Jurassic) and Yukon-Tanana (Devonian-Mississippian) arc assemblages, Cassiar Mountains, northern British Columbia: Field, U-Pb and igneous petrochemical evidence. Canadian Journal of Earth Sciences. v.41, p.1201–1235.

Nelson, J.L., Colpron, M., Piercey, S.J., Dusel-Bacon, C., Murphy, D.C. and Roots, C.F., 2006. Paleozoic tectonic and metallogenetic evolution of pericratonic terranes in Yukon, northern British Columbia and eastern Alaska. Geological Association of Canada Special Paper 45. p.323–360.

Nelson, J.L., Colpron, M. and Israel. S., 2013. The Cordillera of British Columbia, Yukon, and Alaska: Tectonics and Metallogeny. In: Colpron, M., Bissig, T., Rusk., G. and Thompson, J.F.H. (eds.), Tectonics, Metallogeny, and Discovery: The North American Cordillera and Similar Accretionary Settings. Society of Economic Geologists Special Publication 17, p.53-109.

Niu, Y.L., O'Hara, M.J. and Pearce, J.A., 2003. Initiation of subduction zones as a consequence of lateral compositional buoyancy contrast in the lithosphere: A petrological perspective. Journal of Petrology. v.44, p.851–866.

239

Northcote, K.E., 1969. Geology and geochronology of the Guichon Creek Batholith. B.C. Department of Mines and Petroleum Resources, Bulletin 56.

Northcote, K.E., 1977. Iron Mask batholith. B.C. Ministry of Energy, Mines and Petroleum Resources. Preliminary map 26, 1:15,840 scale, 1 sheet, with accompanying notes.

O'Nions, R.K., Hamilton, P.J. and Evensen, N.M., 1977. Variations in ^{143}Nd/^{144}Nd and ^{87}Sr/^{86}Sr ratios in oceanic basalts. Earth and Planetary Science Letters. v.34, p.13-22.

Olade, M.A., 1974. Bedrock geochemistry of porphyry copper deposits, Highland Valley, British Columbia. Unpublished Ph.D. thesis, University of British Columbia, Vancouver, British Columbia, 496p.

Olade, M.A., 1977. Nature of volatile element anomalies at porphyry copper deposits, Highland Valley, B.C., Canada. Chemical Geology. v.20, p.235-252.

Olade, M.A. and Fletcher, W.K., 1975. Primary dispersion of Rubidium and Strontium around porphyry copper deposits, Highland Valley, British Columbia. Economic Geology. v.70, p.15-21.

Olade, M.A. and Fletcher, W.K., 1976. Trace element geochemistry of the Highland Valley and Guichon Creek Batholith in relation to porphyry copper mineralization. Economic Geology. v.71, p.733-748.

Orchard, M.J., 1985. Carboniferous, Permian and Triassic conodonts from the central Kootenay arc, British Columbia: Constraints on the age of the Milford, Kaslo, and Slocan Groups. Geological Survey of Canada, Current Research, Part A, Paper 85–1A, p.287–300.

Orchard, M., Struik, L.C., Rui, L., Bamber, E.W., Mamet, B.L., Sano, H. and Taylor, H., 2001. Palaeontological and bioigeographical constraints on the Carboniferous to Jurassic Cache Creek terrane in central British Columbia. Canadian Journal of Earth Sciences. v.38, p.551–578.

Osatenko, M.J. and Jones, M.B., 1976. Valley Copper. In: Sutherland Brown, A. (ed.), Porphyry Deposits of the Canadian Cordillera. Canadian Institute of Mining and Metallurgy, Special Volume 15. p.130-143.

Osborn, E.F., 1959. Role of oxygen pressure in the crystallization and differentiation of basaltic magma. American Journal of Science. v.257, p.609-647.

Otten, M.T., 1984. The origin of brown hornblende in the Artfjallet gabbro and dolerites. Contributions to Mineralogy and Petrology. v.86, p.189-199

Pallister, J.S., Hoblitt, R.P., Meeker, G.P., Knight, R.J. and Siems, D.F., 1996. Magma mixing at Mount Pinatubo: Petrographic and chemical evidence from the 1991 deposits. In: Newhall, C.G. and Punongbayan, R.S. (eds.), Fire and Mud: Eruptions and Lahars of Mount Pinatubo. University of Washington Press, Seattle, p.687–731.

Panteleyev, A., Bailey, D.G., Bloodgood, M.A. and Hancock, K.D., 1996. Geology and mineral deposits of the Quesnel River-Horsefly map area, central Quesnel trough, British Columbia (NTS 93A/5, 6, 7, 11, 12, 13; 93B/9, 16; 93G/1; 93H/4). British Columbia Ministry of Energy, Mines and Petroleum Resources Bulletin 97, 156p.

Parat, F., Dungan, M.A. and Streck, M.J., 2002. Anhydrite, pyrrhotite, and sulfur-rich apatite: Tracing the sulfur evolution of an Oligocene andesite (Eagle Mountain, CO, USA). Lithos. v.64, p.63-75.

Parrish, R.R. and Monger, J.W.H., 1992. New U-Pb dates from southwestern British Columbia, radiogenic age and isotopic studies. Geological Survey of Canada. Report 5, p.87–108.

Pass, H.E., Cooke, D.R., Davidson, G., Maas, R., Dipple, G., Rees, C., Ferreira, L., Taylor, C. and Deyell, C.L., 2014. Isotope geochemistry of the Northeast zone, Mount Polley alkalic Cu-Au-Ag porphyry deposit, British Columbia: A case for carbonate assimilation. Economic Geology. v.109, p.859–890.

Patchett, P.J. and Gehrels, G.E., 1998. Continental influence on Canadian Cordilleran terranes from Nd isotope study, and significance for crustal growth processes. The Journal of Geology. v.106, p.269-280.

Pearce, J.A., Harris, N.B.W. and Tindle, A.G., 1984. Trace element discrimination diagrams for the tectonic interpretation of granitic rocks. Journal of Petrology. v.25, p.956-983.

Pearce, J.A., Stern, R.J., Bloomer, S.H. and Fryer, P., 2005. Geochemical mapping of the Mariana arc-basin system: Implications for the nature and distribution of subduction components. Geochemistry, Geophysics, Geosystems. v.6, 27p.

Peccerillo, A. and Taylor, S.R., 1976. Geochemistry of Eocene calcalkaline volcanic rocks from the Kastamonu area, Northern Turkey. Contributions to Mineralogy and Petrology. v.58, p.63–81.

Peng, G, Luhr, J.F. and McGee, J.J., 1997. Factors controlling sulfur concentrations in volcanic apatite. American Mineralogist. v.82, p.1210-1224.

Peters, L.J., 2009. Assessment report including diamond drilling on the Woodjam claims. British Columbia Ministry of Energy, Mines and Petroleum Resources, Assessment Report 26242, 40p.

Petersen, N.T., Smith, P.L., Mortensen, J.K., Creaser, R.A. and Tipper, H.W., 2004. Provenance of Jurassic sedimentary rocks of south-central Quesnellia, British Columbia: Implications for paleogeography. Canadian Journal of Earth Sciences. v.41, p.103-125.

Piccoli, P. and Candela, P., 1994. Apatite in felsic rocks: A model for the estimation of initial halogen concentrations in the Bishop Tuff (Long Valley) and Tuolumne Intrusive Suite (Sierra Nevada Batholith) magmas*. American Journal of Science. v.294, p.92-135.

Piccoli, P.M., Candela, P.A. and Williams, T.J., 1999. Estimation of aqueous HCl and Cl concentrations in felsic systems. Lithos. v.46, p.591-604.

Piercey, S.J., Nelson, J.L., Colpron, M., Dusel-Bacon, C., Murphy, D.C., Simard, R.-L. and Roots, C.F., 2006. Paleozoic magmatism and crustal recycling along the ancient Pacific margin of North America, northern Cordillera. Geological Association of Canada Special Paper 45. p.281–322.

Pigage, L.C., 1976. Metamorphism of the Settler Schist, southwest of Yale, British Columbia. Canadian Journal of Earth Sciences. v.13, p.405-421.

Piwinskii, A.J., 1975. Experimental studies of granitoid rocks near the San Andreas Fault zone in the Coast and Transverse Ranges and Mojave Desert, California. Tectonophysics. v.25, p.217-231.

Plafker, G., Moore, J.C. and Winkler, G.R., 1994. Geology of the southern Alaska margin. In: Plakfer, G. and Berg, H.C. (eds.), The Geology of Alaska. Geological Society of America, The Geology of North America. v.G-1, p.389–450.

Plank, T. and Langmuir, C.H., 1998. The chemical composition of subducting sediment and its consequences for the crust and mantle. Chemical Geology. v.145, p.325-394.

Plank, T., Kelley, K.A., Zimmer, M.M., Hauri, E.H. and Wallace, P.J., 2013. Why do mafic arc magmas contain ~4 wt% water on average? Earth and Planetary Science Letters. v.364, p.168-179.

Preto, V.A., 1972. Geology of Copper Mountain, British Columbia. British Columbia Ministry of Energy, Mines and Petroleum Resources Bulletin 59. 87p.

Preto, 1977. The Nicola Group: Mesozoic volcanism related to rifting in southern British Columbia. In: Baragar, W.R.A., Coleman, L.C. and Hall, J.M. (eds.), Volcanic Regimes in Canada. Geological Association of Canada, Special Paper No. 16. p.39-57.

Preto, V.A., 1979. Geology of the Nicola Group between Merritt and Princeton. British Columbia Ministry of Energy, Mines and Petroleum Resources, Bulletin 69.

Preto, V.A., Osatenko, M.J., McMillan, W.J. and Armstrong, R.L., 1979. Isotopic dates and strontium isotopic ratios for plutonic and volcanic rocks in the Quesnel Trough and Nicola Belt, south-central British Columbia. Canadian Journal of Earth Sciences. v.16, p.1658-1672.

Proffett, J.M., 2009. High Cu grades in porphyry Cu deposits and their relationship to emplacement depth of magmatic sources. Geology. v.37, p.675-678.

Prokoph, A., Shields, G.A. and Veizer, J., 2008. Compilation and time-series analysis of a marine carbonate $\delta^{18}O$, $\delta^{13}C$, $^{87}Sr/^{86}Sr$ and $\delta^{34}S$ database through Earth history. Earth-Science Reviews. v.87, p.113-133.

Ray, G.E., Dawson, G.L. and Webster, I.C.L., 1996. The stratigraphy of the Nicola Group in the Hedley district, British Columbia, and the chemistry of its intrusions and Au skarns. Canadian Journal of Earth Science. v.33, p.1105-1126.

Read, P.B., 1996. Kamloops to Vernon: Tertiary stratigraphy and structure, industrial mineral and precious metal potentials, Kamloops, Nicola, and Vernon mining divisions. British Columbia Geological Survey, Assessment Report 25361, 2v., 49p.

Read, P.B. and Okulitch, A.V., 1977. The Triassic unconformity of south central British Columbia. Canadian Journal of Earth Sciences. v.14, p.1127-1145.

Reed, A.L. and Jambor, J.L., 1976. Highmont: Linearly zoned copper-molybdenum porphyry deposits and their significance in the genesis of the Highland Valley ores. In: Sutherland Brown, A. (ed.), Porphyry Deposits of the Canadian Cordillera. Canadian Institute of Mining and Metallurgy, Special Volume 15. p.163-181.

Richards, J.P., 2011. High Sr/Y arc magmas and porphyry Cu ± Mo ± Au deposits: Just add water. Economic Geology. v.106, p.1075-1081.

Richards, J.P. and Kerrich, R., 2007. Adakite-like rocks: Their diverse origins and questionable role in metallogenesis. Economic Geology. v.102, p.537-576.

Richards, J.P., Spell, T., Rameh, E., Razique, A. and Fletcher, T., 2012. High Sr/Y magmas reflect arc maturity, high magmatic water content, and porphyry Cu ± Mo ± Au potential: Examples from the Tethyan arcs of central and eastern Iran and western Pakistan. Economic Geology. v.107, p.295-332.

Richards, S.W. and Holm, R.J., 2013. Tectonic preconditioning and the formation of giant porphyry deposits. Society of Economic Geologists Special Publication 17. p.265-275.

Ricketts, B.C., Evenchick, C.A., Anderson, R.G. and Murphy, D.C., 1992. Bowser basin, northern British Columbia: Constraints on the timing of initial subsidence and Stikinia-North America terrane interactions. Geology. v.20, p.1119-1122.

Rickwood, P.C., 1989. Boundary lines in petrologic diagrams which use oxides of major and minor elements. Lithos. v.22, p.247-263.

Ridolfi F., Renzulli A. and Puerini M., 2010. Stability and chemical equilibrium of amphibole in calc-alkaline magmas: An overview, new thermobarometric formulations and application to subduction-related volcanoes. Contributions to Mineralogy and Petrology. v.160, p.45–66.

Ridolfi, F. and Renzulli, A., 2012. Calcic amphiboles in calc-alkaline and alkaline magmas: Thermobarometric and chemometric empirical equations valid up to 1,130°C and 2.2 GPa. Contributions to Mineralogy and Petrology. v.163, p.877-895.

Riedell, B.K. and Proffett, J.M., 2014. Batholithic and early halo type copper-molybdenum deposits. Geological Society of America, Abstracts with Programs. v.11, p.468.

Roback, R.C., Sevigny, J.H. and Walker, N.W., 1994. Tectonic setting of the Slide Mountain terrane, southern British Columbia. Tectonics. v.13, p.1242–1258.

Roback, R.C. and Walker, N.W., 1995. Provenance, detrital zircon U-Pb geochrnometry, and tectonic significance of Permian to lower Triassic sandstone in southeastern Quesnel Terrane, British Columbia and Washington. Geological Society of America Bulletin. v.107, p.665-675.

Rohrlach, B.D. and Loucks, R.R., 2005. Multi-million year cyclic ramp-up of volatiles in a lower crustal magma chamber trapped below the Tampakan copper-gold deposit by Mio-Pliocene crustal compression in the Southern Philippines. In: Porter, T.M. (ed.) Super Porphyry Copper and Gold Deposits: A Global Perspective. PGC Publishing, Adelaide, p.270-313.

Rollinson, H.R., 1993. Using Geochemical Data: Evaluation, Presentation, Interpretation. Routledge, New York, 352p.

Rønsbo, J. G., 1989. Coupled substitution involving REEs and Na and Si in apatites in alkaline rocks from the Ilimaussaq intrusion, South Greenland, and the petrological implications. American Mineralogist. v.74, p.896–901.

Roots, C.F. and Heaman, L., 2001. Mississippian U-Pb dates from Dorsey Terrane assemblages in the upper Swift River area, southern Yukon Teritory. Geological Survey of Canada Current Research. Paper 2001-A1.

Rosenbaum, G., Giles, D., Saxon, M., Betts, P.G., Weinberg, R.F., and Duboz, C., 2005. Subduction of the Nazca Ridge and the Inca Plateau: Insights into the formation of ore deposits in Peru. Earth and Planetary Science Letters. v.239, p.18–32.

Rouse, R. C. and Dunn, P. J., 1982. A contribution to the crystal chemistry of ellestadite and the silicate sulfate apatites. American Mineralogist. v.67, p.90–96.

Roy, B. and Clowes, R.M., 2000. Seismic and potential-field imaging of the Guichon Creek batholith, British Columbia, Canada, to delineate structures hosting porphyry copper deposits. Geophysics. v.65, p.1418-1434.

Rubin, C.M., Miller, M.M. and Smith, G.M., 1990. Tectonic development of mid-Paleozoic volcanic-plutonic complexes: Evidence for convergent margin tectonism. Geological Society of America Special Paper 255. p.1–16.

Rusmore, M.E., Woodsworth, G.J. and Gehrels, G.E., 2005. Two-stage exhumation of midcrustal arc rocks, Coast Mountains, British Columbia. Tectonics. v.24, TC5013, 25p.

Russell, J.K. and Snyder, L.D., 1997. Petrology of picritic basalts from Kamloops, British Columbia: Primary liquids from a Triassic-Jurassic arc. Canadian Mineralogist. v.35, p.521–541.

Rutter, M.J., Van der Laan, S.R. and Wyllie, P.J., 1989. Experimental data for a proposed empirical igneous geobarometer: Aluminium in hornblende at 10 kbar pressure. Geology. v.17, p.897-900.

Sajona, F.G. and Maury, R.C., 1998. Association of adakites with gold and copper mineralization in the Philippines. Earth and Planetary Science. v.326, p.27-34.

Samson, S.D., McClelland, W.C., Patchett, P.J., Gehrels, G.E. and Anderson, R.G., 1989. Evidence from neodymium isotopes for mantle contributions to Phanerozoic crustal genesis in the Canadian Cordillera. Nature. v.337, p.705-709.

Samson, S.D., Patchett, P.J., McClelland, W.C. and Gehrels, G.E., 1991. Nd and Sr isotopic constraints on the petrogenesis of the west side of the northern Coast Mountains batholith, Alaskan and Canadian Cordillera. Canadian Journal of Earth Sciences. v.28, p.939-946.

Schau, M.P., 1968. Geology of the Upper Triassic Nicola Group in south central British Columbia. Unpublished Ph.D. thesis. The University of British Columbia, Vancouver, British Columbia.

Schiarizza, P., 2014. Geological setting of the Granite Mountain batholith, host to the Gibraltar porphyry Cu-Mo deposit, south-central British Columbia. In: Geological Fieldwork 2013, British Columbia Ministry of Energy and Mines, British Columbia Geological Survey Paper 2014-1, p.95-110.

Schiarizza, P. and MacIntyre, D.G. 1999. Geology of the Babine Lake-Takla Lake area, central British Columbia (93 K/11, 12, 13, 14; 93 N/3, 4, 5, 6). In: Geological fieldwork 1998. British Columbia Ministry of Employment and Investment. Paper 1999–1, p.33-68.

Schmidt, M.W., 1992. Amphibole composition in tonalite as a function of pressure: An experimental calibration of the Al-in-hornblende barometer. Contributions to Mineralogy and Petrology. v.110, p.304-310.

Scott, J.E., Richards, J.P., Heaman, L.M., Creaser, R.A. and Salazar, G.S., 2008. The Schaft Creek porphyry Cu-Mo-(Au) deposit, northwestern British Columbia. Exploration and Mining Geology. v.17, p.163–196.

Seedorf, E., Dilles, J.H., Proffett, J.M. Jr., Einaudi, M.T., Zurcher, L., Stavast, W.J.A., Johnson, D.A. and Barton, M.D., 2005. Porphyry deposits: Characteristics and origin of hypogene features. Economic Geology 100th Anniversary Volume. p.251-298.

Sha, L. K. and Chappell, B. W., 1999. Apatite chemical composition, determined by electron microprobe and laser-ablation inductively coupled plasma mass spectrometry, as a probe into granite petrogenesis. Geochimica and Cosmochimica. Acta. v.63, p.3861–3881.

Shand, S. J., 1947. The Eruptive Rocks, 3rd edition. John Wiley, New York, 444p.

Sigloch, K., Mcquarrie, N. and Nolet, G., 2008. Two-stage subduction history under North America inferred from multiple-frequency tomography. Nature Geoscience. v.1, p.458–462.

Simard, R.-L., Dostal, J. and Roots, C. F., 2003. Development of late Paleozoic volcanic arcs in the Canadian Cordillera: An example from the Klinkit Group, northern British Columbia and southern Yukon. Canadian Journal of Earth Sciences. v.40, p.907-924.

Sillitoe, R.H., 1972. Relation of metal provinces in western Americas to subduction of oceanic lithosphere. Geological Society of America Bulletin. v. 83, p.813–818.

Sillitoe, R.H., 1973. The tops and bottoms of porphyry copper deposits. Economic Geology. v.68, p.700-815.

Sinclair, W.D., 2007. Porphyry deposits. In: Goodfellow, W.D. (ed.), Mineral Deposits of Canada: A Synthesis of Major Deposit-Types, District Metallogeny, the Evolution of Geological Provinces, and Exploration Methods. Geological Association of Canada, Mineral Deposits Division, Special Publication No. 5, p.223-243.

Smith, A.D. and Lambert, R.St.J., 1995. Nd, Sr, and Pb isotopic evidence for contrasting origins of late Paleozoic volcanic rocks from the Slide Mountain and Cache Creek terranes, south-central British Columbia. Canadian Journal of Earth Sciences. v.32, p.447-459

Smith, A.D., Brandon, A.D. and Lambert, R.St. J., 1995. Nd-Sr isotope systematics of Nicola Group volcanic rocks, Quesnel terrane. Canadian Journal of Earth Science. v.32, p.437-446.

Smith, P.L., Tipper, H.W. and Ham, D.M., 2001. Lower Jurassic amaltheidae (ammonitina) in North America: Paleobiogeography and tectonic implications. Canadian Journal of Earth Sciences. v.38, p.1439-1449.

Sobolev, A. and Chaussidon, M., 1996. H_2O concentrations in primary melts from supra-subduction zones and mid-ocean ridges: Implications for H_2O storage and recycling in the mantle. Earth and Planetary Science Letters. v.137, p.45–55.

Soregaroli, A.E. and Whitford, D.F., 1976. Brenda. In: Sutherland Brown, A., (ed.), Porphyry Deposits of the Canadian Cordillera. Canadian Institute of Mining and Metallurgy, Special Volume 15. p.186-194.

Souther, J.G., 1972. Telegraph Creek map area, British Columbia. Geological Survey of Canada Paper 71-44, 38p.

Souther, J. G., 1977. Volcanism and tectonic environments in the Canadian Cordillera - A second look. In: Baragar, W.R.A., Coleman, L.C. and Hall, J.M. (eds.), Volcanic Regimes in Canada. Geological Association of Canada Special Paper 16, p.3-24.

Souther, J.G., 1991. Volcanic regimes. In: Geology of the Cordilleran Orogen in Canada. Geological Survey of Canada, Geology of Canada. No.4, p.459-490.

Staude, J.-M.G. and Barton, M.D., 2001. Jurassic to Holocene tectonics, magmatism, and metallogeny of northwestern Mexico. Geological Society of America Bulletin. v.113, p.1357-1374.

Stormer, J.C. Jr., Pierson, M.L. and Tacker, R.C., 1993. Variation of F and Cl X-ray intensity due to anisotropic diffusion in apatite during electron microprobe analysis. American Mineralogist. v.78, p.641-648.

Stowell, H.H. and Crawford, M.L., 2000. Metamorphic history of the Coast Mountains orogen, western British Columbia and southeastern Alaska. In: Stowell, H.H. and McClelland, W.C. (eds.), Tectonics of the Coast Mountains, SE Alaska and British Columbia. Geological Society of America. Special Paper 343, p.257-284.

Streck, M.J. and Dilles, J.H., 1998. Sulfur evolution of oxidized arc magmas as recorded in apatite from a porphyry copper batholith. Geology. v.26, p.523-526.

Struik, L.C., Schiarizza, P., Orchard, M.J., Cordey, F., Sano, H., MacIntyre, D.G., Lapierre, H. and Tardy, M., 2001. Imbricate architecture of the upper Paleozoic to Jurassic oceanic Cache Creek Terrane, central British Columbia. Canadian Journal of Earth Sciences. v.38, p.495-514.

Sun, S.-S., and McDonough, W.F., 1989. Chemical and isotopic systematics of oceanic basalts: Implications for mantle composition and processes. Geological Society of London Special Publication 42, p.313–345.

Tanaka, T., Togashi, S., Kamioka, H., Amakawa, H., Kagami, H., Hamamoto, T., Yuhara, M., Orihashi, Y., Yoneda, S., Shimizu, H., Kunimaru, T., Takahashi, K., Yanagi, T., Nakano, T., Fujimaki, H., Shinjo, R., Asahara, Y., Tanimizu, M. and Dragusanu, C., 2000. JNdi-1: A neodymium isotopic reference in consistency with LaJolla neodymium. Chemical Geology. v.168, p.279-281.

Taylor, R.W., 1964. Phase equilibriums in the system $FeO-Fe_2O_3-TiO_2$ at 1300°C. American Mineralogist. v.49., p.1016-1030.

Teck Resources Limited, 2015. Annual information form. 102p.

Tempelman-Kluit, D. J., 1979. Transported cataclastite, ophiolite and granodiorite in Yukon: Evidence of arc-continent collision. Geological Survey of Canada Paper 79-14.

Tepley III, F.J., Davidson, J.P. and Clynne, M.A., 1999. Magmatic interactions as recorded in plagioclase phenocrysts of Chaos Crags, Lassen Volcanic Center, California. Journal of Petrology. v.40, p.787-806.

Thiéblemont, D., Stein, G. and Lescuyer, J.-L., 1997. Epithermal and porphyry deposits: The adakite connection. C.R. Académie des Science Paris. Earth and Planetary Sciences. v.325, p.103–109.

Thompson, R.I. and Daughtry, K.L., 1996. New stratigraphic and tectonic interpretations, north Okanagan Valley, British Columbia. Geological Survey of Canada, Current Research 1996-A. p.132–141.

Thompson, R.I. and Daughtry, K.L., 1997. Anatomy of the Neoproterozoic-Paleozoic continental margin, Vernon map-area, British Columbia. Geological Survey of Canada, Current Research 1997-A. p.145–150.

Thompson, R.I. and Daughtry, K.L., 1998. Stratigraphic linkages across Vernon map area (82L), British Columbia. Geological Survey of Canada, Current Research 1998-A. p.181–187.

Thorkelson, D.J., Mortensen, J.K., Marsden, H. and Taylor, R.P., 1995. Age and tectonic setting of early Jurassic episodic volcanism along the northeastern margin of the Hazelton Trough, northern British Columbia. In: Miller, D.M. and Busby, C. (eds.), Jurassic Magmatism and Tectonics of the North American Cordillera. Geological Society of America. Special Paper 299, p.83-94.

Titley, S.R. and Beane, R.E., 1981. Porphyry copper deposits. Economic Geology 75th Anniversary Volume. p.214-269.

Tombale, A.K., 1984. An interpretation of lithogeochemical data of the Guichon Creek Batholith. Unpublished Ph.D. thesis, University of British Columbia, Vancouver, British Columbia, 150p.

Tosdal, R.M. and Richards, J.P., 2001. Magmatic and structural controls on the development of porphyry Cu ± Mo ± Au deposits. Society of Economic Geologists Reviews. v.14, p.157-181

Travers, W.B., 1977. Overturned Nicola and Ashcroft strata and their relation to the Cache Creek Group, southwestern Intermontane belt, British Columbia. Canadian Journal of Earth Sciences. v.15, p.99–116.

Unterschutz, J.L.E., Creaser, R.A., Erdmer, P., Thompson, R.I. and Daughtry, K.L., 2002. North American margin origin of Quesnel terrane strata in the southern Canadian Cordillera: Inferences from geochemical and Nd isotopic characteristics of Triassic metasedimentary rocks. Geological Society of America Bulletin. v.114, p.462-475.

Vaca, S., 2012. Variability in the Nicola/Takla Group basalts and implications for alkalic Cu-Au porphyry prospectivity in the Quesnel terrane, British Columbia, Canada. Unpublished M.Sc. thesis, University of British Columbia, Vancouver, British Columbia, 148p.

Viccaro, M., Giacomoni, P.P., Ferlito, C. and Cristofolini, 2010. Dynamics of magma supply at Mt. Etna volcano (Southern Italy) as revealed by textural and compositional features of plagioclase phenocrysts. Lithos. v.116, p.77-91.

Villeneuve, M., Whalen, J.B., Anderson, R.G. and Struik, L.C., 2001. The Endako Batholith: Episodic plutonism culminating in formation of the Endako porphyry molybdenite deposit, north-central British Columbia. Economic Geology. v.96, p.171-196.

Waldner, M.W., Smith, G.D. and Willis, R.D., 1976. Lornex. In: Sutherland Brown, A. (ed.), Porphyry Deposits of the Canadian Cordillera. Canadian Institute of Mining and Metallurgy, Special Volume 15. p.120-129.

Wallace, P.J., 2005. Volatiles in subduction zone magmas: Concentrations and fluxes based on melt inclusion and volcanic gas data. Journal of Volcanology and Geothermal Research. v.140, p.217-240.

Wang, J. Hattori, K.H., Kilian, R. and Stern, C.R., 2007. Metasomatism of sub-arc mantle peridotites below southernmost South America: Reduction of fO_2 by slab-melt. Contributions to Mineralogy and Petrology. v.153, p.607–624.

Watson, E. B. and Harrison, T. M., 1983. Zircon saturation revisited: Temperature and composition effects in a variety of crustal magma types. Earth and Planetary Science Letters. v.64, p.295-304.

Waychunas, G.A., 2002 Apatite luminescence. In: Kohn, M.L., Rakovan, J. and Hughes, J.M. (eds.), Phosphates– Geochemical, Geobiological, and Materials Importance. Mineralogical Society of America, Reviews in Mineralogy and Geochemistry. v.48, p.710–742.

Weaver, B.L., 1991. The origin of ocean island basalt end-member compositions: Trace element and isotopic constraints. Earth and Planetary Science Letters. v.104, p.381-397.

Westerman, C.J., 1970. A petrogenetic study of the Guichon Creek Batholith, B.C. Unpublished M.Sc. thesis, University of British Columbia, Vancouver, British Columbia, 116p.

Whalen, J.B., Anderson, R.G., Struik, L.C. and Villeneuve, M.E., 2001. Geochemistry and Nd isotopes of the François Lake plutonic suite, Endako batholith: Host and progenitor to the Endako molybdenum camp, central British Columbia. Canadian Journal of Earth Sciences. v.38, p.603-618.

Wheeler, J.O. and McFeely, P., 1991. Tectonic assemblage map of the Canadian Cordillera and adjacent parts of the United States of America. Geological Survey of Canada Map 1712A. 1:2000000.

White, A.J.R., 1979. Sources of granite magmas. Geological Society of America, Abstracts with Programs. v.11, p.539.

White, Wm.H., Erickson, G.P., Northcote, K.E., Dirom, G.E. and Harakal, J.E., 1966. Isotopic dating of the Guichon Batholith, B.C. Canadian Journal of Earth Sciences. v.4, p.677-690.

White, W.M. and Patchett, J., 1984. Hf-Nd-Sr isotopes and incompatible element abundances in island arcs: Implications for magma origins and crust-mantle evolution. Earth and Planetary Science Letters. v.67, p.167-185.

Whitney, D.L. and Evans, B.W., 2010. Abbreviations for names of rock-forming minerals. American Mineralogist. v.95, p.185-187.

Winter, J.D., 2010, An Introduction to Igneous and Metamorphic Petrology. Prentice Hall, Upper Saddle River, New Jersey, 697p.

Wolfe, R.C. and Cooke, D.R., 2011. Geology of the Didipio region and genesis of the Dinkidi alkalic porphyry Cu-Au deposit and related pegmatites, northern Luzon, Philippines. Economic Geology. v.106, p.1279–1315.

Wones, D.R., 1981. Mafic silicates as indicators of intensive variables in granitic magmas. Mining Geology (Japan). v.31, p.191-212.

Wones, D.R., 1989. Significance of the assemblage titnite + magnetite + quartz in granitic rocks. American Mineralogist. v.74, p.744-749.

Woodsworth, G.J., Anderson, R.G. and Armstrong, R.L., 1991. Plutonic Regimes. Geological Survey of Canada. Geology of Canada Series no.4, p.491–531.

Wortel, M.J.R. and Spakman, W., 2000. Subduction and slab detachment in the Mediterranean-Carpathian region. Science. v.290, p.1910–1917.

Zen, E., 1986. Aluminum enrichment in silicate melts by fractional crystallization: Some mineralogic and petrologic constraints. Journal of Petrology. v.27, p.1095-1117.

Zen, E., 1988. Phase relations of peraluminous granitic rocks and their petrogenetic implications. Annual Review of Earth and Planetary Sciences. v.16, p.21-52.

Zhang, C., Holtz, F., Ma, C., Wolff, P.E and Li, X., 2012. Tracing the evolution and distribution of F and Cl in plutonic systems from volatile-bearing minerals: A case study from the Liujiawa pluton (Dabie orogeny, China). Contributions to Mineralogy and Petrology. v.164, p.859-879.

Zhu, C. and Sverjensky, D.A., 1991. Partitioning of F-Cl-OH between minerals and hydrothermal fluids. Geochimica and Cosmochimica Acta. v.55, p.1837-1858.

Zhu, C. and Sverjensky, D.A., 1992. F-Cl-OH partitioning between biotite and apatite. Geochimica and Cosmochimica Acta. v.56, p.3435-3467.

Zindler, A and Hart, S., 1986. Chemical Geodynamics. Annual Reviews in Earth and Planetary Science. v.14, p.493-571.

APPENDIX A: SAMPLE LOCATIONS

Sample Name	Datum	Zone	Easting	Northing	Rock Type
MD001	NAD83	10U	630527	5585709	Border Facies
MD002	NAD83	10U	632119	5585738	Border Facies
MD003	NAD83	10U	633013	5586244	Border Facies
MD004	NAD83	10U	634574	5586650	Bethsaida
MD005	NAD83	10U	634269	5586686	Bethsaida
MD006	NAD83	10U	633878	5586151	Skeena
MD007	NAD83	10U	633702	5586786	Border Facies
MD008	NAD83	10U	679926	5596324	Nicola Batholith
MD009	NAD83	10U	679073	5594782	Nicola Batholith
MD010	NAD83	10U	678696	5598435	Nicola Batholith
MD011	NAD83	10U	681395	5596085	Nicola Batholith
MD012	NAD83	10U	680556	5595793	Nicola Batholith
MD013	NAD83	10U	669646	5575149	Nicola Batholith
MD014	NAD83	10U	670133	5574124	Nicola Batholith
MD015	NAD83	10U	669453	5576600	Nicola Batholith
MD016	NAD83	10U	669439	5576582	Nicola Batholith
MD017	NAD83	10U	672183	5576873	Nicola Batholith
MD018	NAD83	10U	673996	5576345	Nicola Batholith
MD019	NAD83	10U	673334	5576909	Nicola Batholith
MD020	NAD83	10U	670822	5576742	Nicola Batholith
MD021	NAD83	10U	643090.7	5595812	FQPC
MD022	NAD83	10U	643179	5596061	FPC
MD023	NAD83	10U	642847.5	5596043	FPC
MD024	NAD83	10U	642998	5595759	FQPC
MD025	NAD83	10U	642998	5595759	FPC
MD026	NAD83	10U	643034.9	5595930	FQPC
MD027	NAD83	10U	642974.1	5595807	FQPC
MD028	NAD83	10U	643179	5596061	FQPC
MD029	NAD83	10U	643179	5596061	FPC
MD030	NAD83	10U	642963.2	5596004	FPC
MD031	NAD83	10U	642703.6	5595927	FPC
MD032	NAD83	10U	642703.6	5595927	FPC
MD033	NAD83	10U	642479.7	5595740	FPC
MD034	NAD83	10U	637545.1	5596507	Skeena
MD035	NAD83	10U	637545.1	5596507	Skeena
MD036	NAD83	10U	638761.3	5595434	Tan Porphyry
MD037	NAD83	10U	638701.1	5594335	Tan Porphyry
MD038	NAD83	10U	639012.7	5595494	Tan Porphyry
MD039	NAD83	10U	638789.3	5594175	Lamprophyre
MD040	NAD83	10U	637591.4	5595076	Aplite
MD041	NAD83	10U	641899	5577302	Aplite
MD042	NAD83	10U	641899	5577300	Bethsaida

Sample Name	Datum	Zone	Easting	Northing	Rock Type
MD043	NAD83	10U	646997	5573977	Chataway
MD044	NAD83	10U	645994	5571430	Chataway
MD045	NAD83	10U	644469	5571255	Chataway
MD046	NAD83	10U	651601	5567979	Border Facies
MD047	NAD83	10U	652476	5574640	Guichon
MD048	NAD83	10U	652212	5575358	Guichon
MD049	NAD83	10U	646049	5579507	Bethlehem
MD050	NAD83	10U	646039	5579501	Aplite
MD051	NAD83	10U	643498	5596292	Guichon
MD052	NAD83	10U	643253	5595463	Bethlehem
MD053	NAD83	10U	644010	5594729	Bethlehem
MD054	NAD83	10U	644305	5594875	Guichon
MD055	NAD83	10U	644034	5594779	Bethlehem
MD056	NAD83	10U	640177	5590440	Skeena
MD057	NAD83	10U	651124	5595137	Border Facies
MD058	NAD83	10U	651759	5595590	Guichon
MD059	NAD83	10U	640339	5597621	Bethlehem
MD060	NAD83	10U	640557	5598038	Skeena
MD061	NAD83	10U	646741	5588152	Chataway
MD062	NAD83	10U	646480	5587710	Bethlehem
MD063	NAD83	10U	646203	5587555	Bethlehem
MD064	NAD83	10U	646086	5587438	Chataway
MD065	NAD83	10U	645294	5587028	Skeena
MD066	NAD83	10U	648505	5577836	Chataway
MD067	NAD83	10U	646217	5579581	Chataway
MD068	NAD83	10U	645172	5578265	Bethsaida
MD069	NAD83	10U	641865	5584335	Bethsaida
MD070	NAD83	10U	642558	5584809	Bethsaida
MD071	NAD83	10U	642347	5581907	Bethsaida
MD072	NAD83	10U	644625	5585972	Skeena
MD073	NAD83	10U	643717	5580032	QFPM
MD074	NAD83	10U	643459	5596335	Guichon
MD075	NAD83	10U	643753	5596304	Guichon
MD076	NAD83	10U	646571	5598260	Guichon
MD078	NAD83	10U	651178	5595176	Border

APPENDIX B: THIN SECTION DESCRIPTIONS

Grain sizes are reported as very-fine-grained (v.f.g; <0.25mm), fine-grained (f.g.; 0.25 to 1mm), medium-grained (m.g.; 1 to 5mm) and coarse-grained (c.g.; 5 to 50mm). All mineral contents are expressed as modal percent and rock names were determined using the IUGS classification scheme for plutonic igneous rocks (Le Bas and Streckeisen, 1991). Mineral abbreviations are from Whitney and Evans (2010) and are summarized as follows: Ab = albite; Amp = amphibole; Ap = apatite; Brt = barite; Bt = biotite; Cal = calcite; Chl = chlorite; Ccp = chalcopyrite; Ep = epidote; Hem = hematite; Ilm = ilmenite; Kfs = K-feldspar; Mag = magnetite; Mc = microcline; Ms = muscovite; Ol = olivine; Cpx = clinopyroxene; Opx = orthopyroxene; Pl = plagioclase; Py = pyrite; Qz= quartz; Ser = sericite; Srp = serpentine; Tlc = talc; Ttn = titanite; Zrn = zircon.

Sample: MD057   **Facies:** Border   **Name:** hornblende-quartz monzodiorite

Hand Sample Description: A medium-grained, equigranular texture with ~ 30% evenly distributed mafic minerals. Mafic minerals are a mixture of fresh amphibole and biotite and are generally anhedral. The primary felsic mineral is 0.5 to 3mm plagioclase which makes up ~60% of the sample. Plagioclase crystals are generally sub- to euhedral elongate prisms with glassy cores and chalky, white rims. Approximately 10% K-feldspar occurs interstitially to the plagioclase, biotite and amphibole.

Mineral Name and Abundance	Description
	Primary Mineralogy
Plagioclase 44%	Sub- to euhedral crystals 0.5 to 3.0mm. Weak to moderate sericite alteration (<5 to 40% of a crystal) is most common, though smaller crystals may be up to 95% altered. Uncommonly contain saussuritized cores that have been altered to calcite and epidote (<5% of single crystals) with sericite/muscovite alteration occurring throughout the same crystals but focused just around the calcite + epidote cores. Lack of zoning.
Biotite 14%	Subhedral crystals 0.25 to 2.5mm in size. Often found in contact with hbl and mt. Some f.g. bt in hbl crystals may be secondary alteration. Inclusions of mt, rt and qz common. Weak chlorite alteration (<5% replacement) is present along cleavage planes in some crystals.
Quartz 8%	Occurs as anhedral crystals interstitial subhedral pl. Many crystals display undulose extinction.
Hornblende 20%	1 to 4mm sub- to anhedral crystals occur interstitially to plagioclase. Many crystals contain small cores of orthopyroxene. Some crystals show complex intergrowths with orthopyroxene. These textures likely represent late-stage magmatic or subsolidus alteration of primary opx to hbldue to increased magmatic water content resulting by early crystallization of anhydrous phases. Inclusions of v.f.g. biotite (often chloritized), plagioclase and magnetite are common.
Rutile (Tr.)	Trace rutile is typically associated with magnetite or as inclusions in biotite with long axes aligned to cleavage planes
Titanite (<1%)	<0.25mm subhedral, sphenoid crystals, often with one pointed side. Normally associated with bt, qz and mt
Apatite (Tr.)	V.f.g. (<0.2mm) hexagonal crystals included in some bt and mt crystals
Magnetite 3%	Sub- to euhedral crystals varying from 0.1 to 1.5mm across. Mostly associated with hbl and bt as finer-grained inclusions or partially enclosed when coarser-grained. A subordinate amount of v.f.g. (<0.2mm) crystals occur as inclusions in plagioclase.
Orthopyroxene 2%	0.5 to 2.0mm anhedral crystals with irregular, corroded grain

	boundaries. Mostly observed in cores of hbl crystals but occasionally seen in the groundmass unassociated with hbl. Sometimes seen as complex intergrowths with hbl.
K-feldspar 10%	Anhedral crystals generally <1mm in size that occur interstitially to plagioclase and mafics. Moderately to strongly altered to clays (60 to 90% of a single crystal)

Textures: Medium-grained equigranular with subhedral plagioclase and interstitial mafics, quartz and K-spar

Alteration: Near complete uralitization of opx to hbl. Trace to weak chloritization of biotite. Strong to complete clay alteration of K-feldspar, weak to moderate sericitization of plagioclase and rare saussuritization of plagioclase cores.

Mineralization: None observed.

Normalized QAP:

Quartz	13	Alkali Feldspar	16	Plagioclase	71

Sample: MD046   **Facies:** Border   **Name:** Quartz Diorite

Hand Sample Description: This sample has a medium-grained equigranular texture and is black and white in colour. It is composed of approximately 40% mafic minerals (mostly amphibole with lesser biotite) which are evenly distributed. The remainder of the sample is comprised predominantly of anhedral plagioclase with subordinate quartz (<5%).

Mineral Name and Abundance	Description
	Primary Mineralogy
Plagioclase 48%	Occurs as 0.5 to 3mm anhedral crystals. Grain boundaries are often serrated. Primary polysynthetic twinning is rarely preserved and most crystals contain wavy or pinched out deformation twins. Trace sericitization (<5% of each crystal) has affected most crystals.
Biotite 5%	Patchy and shreddy biotite occurs as an alteration product of amphibole. It is most abundant in mats of v.f.g. acicular amphibole.
Quartz 5%	V.f.g. (<1mm) angular quartz occurs interstitially to plagioclase, amphibole and biotite.
Amphibole 35%	Possibly two populations? Two distinctive sets of interference colours. Most abundant colour is 1st order orange. Second set of hbl crystals have mottled 1st order purple to 2nd order blue colours. Many hbl crystals contain f.g (0.2 to 0.5mm) inclusions of rounded, anhedral opx. Crystals are generally anhedral and occur interstitially to pl and or(?). Inclusions of v.f.g. qz and f.g. pl are common. Some areas contain patches of finer (~0.1 to 0.7mm) acicular an- to subhedral crystals arranged in radiating mats and associated with bt. Acicular amphibole may be actinolite?
Rutile (Tr.)	V.f.g. accessory mineral
Titanite 1%	V.f.g. anhedral crystals commonly included in or in contact with magnetite. Less commonly as inclusions in amphibole. <0.25mm subhedral, sphenoid crystals, often with one pointed side. Normally associated with bt, qz and mt
Apatite (Tr.)	V.f.g. (<0.2mm) hexagonal crystals included in or in direct contact with some mt crystals
Zircon (Tr.)	One 0.5 x 2mm zircon crystal observed.
Magnetite 5%	Anhedral crystals general <1mm in size. Occur throughout the sample interstitial to amphibole and plagioclase, but is most abundant as inclusions with amp or along grain boundaries between two or more amp crystals. Commonly associated with titanite and apatite both of which may occur as inclusions.
Orthopyroxene 2%	Occurs as v.f.g to f.g. (0.2 to 0.5mm) anhedral, rounded inclusions in the cores of hbl crystals.

Textures: Phaneritic, equigranular.

Alteration: Trace sericitization of plagioclase crystals. Amphibole (tremolite?) has replaced primary orthopyroxene which in turn has been replaced by biotite.

Mineralization: None observed.

Normalized QAP:

Quartz	9	Alkali Feldspar	0	Plagioclase	91

Sample: MD007   **Facies:** Border   **Name:** hornblende-bearing leuco-gabbronorite

Hand Sample Description: Fine- to medium-grained equigranular texture. ~40% wormy, anhedral mafics (biotite + amphibole) occur interstitially to plagioclase. ~60% an- to subhedral plagioclase. Rusted brown and orange material occurs interstitially with mafic minerals.

Mineral Name and Abundance	Description
	Primary Mineralogy
Plagioclase 49%	0.5 to 3mm elongate, subhedral crystals with serrated grain boundaries. Some rounded, f.g. (~0.5) crystals are included in amphiboles. Most crystals are fresh with the most altered crystals displayin <5% alteration to sericite.
Olivine 2%	Rounded, v.f.g. (<0.5mm) highly fractured crystals occur interstitially to plagioclase. Commonly altered to grungy, orange coloured alteration (iddingsite).
Biotite 2%	Patchy alteration of select amphibole crystals
Quartz 2%	V.f.g. rounded quartz crystals occur interstitially to plagioclase.
Amphibole 38%	0.5 to 2mm anhedral crystals occurring interstitially to subhedral plagioclase
Rutile (Tr.)	V.f.g. accessory mineral
Titanite (Tr.)	V.f.g. anhedral crystals commonly in contact with magnetite. Less commonly as inclusions in amphibole. <0.25mm subhedral, sphenoid crystals, often with one pointed side. Normally associated with bt, qz and mt
Apatite (Tr.)	V.f.g. (<0.2mm) hexagonal crystals included in or in direct contact with some mt crystals
Clinopyroxene 2%	Minor subhedral crystals occur interstitially to plagioclase. Commonly being altered to amphibole
Magnetite 3%	<1mm, anhedral crystals occur interstitially to plagioclase crystals as well as inclusions in amphiboles.
Orthopyroxene 2%	Minor, anhedral opx occurs as the core of some amphibole crystals

Textures: Phaneritic and equigranular with interstitial orthopyroxene, clinopyroxene, olivine and amphibole.

Alteration: Alteration of olivine to iddingsite, orthopyroxene and clinopyroxene to amphibole and amphibole to biotite. Weak (<5%) alteration of plagioclase to sericite.

Mineralization: None observed

Normalized QAP:

Quartz	4	Alkali Feldspar	0	Plagioclase	96
Plagioclase	89	Pyroxene	7	Olivine	4

Sample: MD001   **Facies:** Border   **Name:** biotie-bearing olivine leuco-monzogabbronorite

Hand Sample Description: Medium-grained equigranular texture. Approximately 15% K-feldspar occurs interstitial to subhedral plagioclase (~45%) and biotite (~40%).

Mineral Name and Abundance	Description
	Primary Mineralogy
Plagioclase 42%	Commonly contains inclusions of v.f.g. cpx. Crystals range from 0.5 to 2mm and are generally tabular to elongate in shape and have serrated anhedral grain boundaries.
Biotite 25%	Flaky, anhedral biotite occurs interstitially to plagioclase and K-feldspar. Crystals range from 0.5 to 2mm in size. Many crystals contain inclusions of v.f.g. apatite, magnetite and plagioclase. Biotite commonly partially surrounds irregularly shaped amphibole crystals indicating biotite may be secondary after amphibole.
Quartz 3%	V.f.g. anhedral quartz occurs interstially to all other minerals
Amphibole 2%	Minor amphibole occurs as an alteration product of clinopyroxene. Most amphibole appears to have been altered to biotite.
Apatite (Tr.)	V.f.g. euhedral, hexagonal crystals occur throughout the sample, commonly as inclusions or in contact with grain boundaries of magnetite
K-feldspar 15%	0.5 to 4mm, anhedral crystals occurring interstitially to plagioclase.
Magnetite 2%	V.f.g. inclusions in cpx, and along grain boundaries of serpentinized olivine. Also occurs as coarser (0.25 to 0.5mm) inclusions in K-spar, biotite and plagioclase. Also occurs interstitially to all other minerals.
Clinopyroxene 9%	Elongate, anhedral crystals occur interstitially to plagioclase and quartz(? Possibly K-spar?). Chlorite, serpentine and talc alteration is common along grain-boundaries.
Olivine 2%	0.25 to 0.5mm rounded olivine crystals occur interstitially to plagioclase, and K-spar. All crystals are altered along fractures and rimmed by serpentine.

Textures: Phaneritic and equigranular with interstitial orthopyroxene, clinopyroxene, olivine and minor amphibole.

Alteration: Alteration of olivine to serpentine + magnetite and in some cases talc, clinopyroxene to chlorite, serpentine, talc and minor amphibole and amphibole and clinopyroxene to biotite. Weak (<2%) alteration of plagioclase to sericite.

Mineralization: None observed.

Paragenetic Comments: K-feldspar and biotite are likely secondary possibly a result of subsolidus K-bearing alteration (NOT classic potassic alteration associated with

porphyries however) based on strange mineral association of olivine + cpx + K-spar + qz. Similarly, quartz is interstitial to all other minerals and likely formed late in the samples history, possibly subsolidus.

Normalized QAP:

Quartz	5	Alkali Feldspar	25	Plagioclase	70
Plagioclase	79	Pyroxene	17	Olivine	4

Sample: MD002   **Facies:** Border   **Name:** biotite-bearing leuco-quartz monzogabbronorite

Hand Sample Description: A medium-grained, equigranular texture with a black and white colour. Mineralogy consists of ~40% anhedral mafics (amp + bt) and ~60% anhedral plagioclase. Sample is not stained, but has a nearly identical appearance to MD046 and is interpreted to have little to no K-feldspar.

Mineral Name and Abundance	Description
	Primary Mineralogy
Plagioclase 48%	0.5 to 4mm crystals. Larger crystals are elongated and have serrated grain-boundaries and smaller crystals are rounded and equant. Carlsbad and deformation twins that pinch out or are wavy. Undulatory extinction and subgrains present but less common than deformation twins. Smallest grains are generally strain-free. Melting temperature of 600 to 1000, so implies temperature of deformation of >300. Typically unaltered (<1% patchy sericite), except when in close proximity to a thin fracture that cuts through the centre of the sample bisecting many plagioclase crystals affecting by moderate sericite alteration (25 to 60% alteration of individual crystals).
Biotite 20%	Flaky, anhedral <1mm crystals occur interstitially to plagioclase. Often contains abundant inclusions and partial inclusions. Biotite appears to be altering from amphibole and in some cases directly from cpx.
Quartz 6%	V.f.g. (0.25 to 0.5mm) anhedral crystals generally in contact with plagioclase and amphibole.
Amphibole 5%	Anhedral patchy amphibole occurs as rims and partial rims surrounding cores of cpx and also complexly intergrown with cpx. Complex intergrowths with cpx are likely secondary, formed by uralitization of the primary cpx but 'cleaner' looking amphibole rims may be primary reflecting an increase in magmatic water content. Rarely seen without associated cpx and occur interstitially to plagioclase.
Rutile (Tr.)	V.f.g. ruby red crystals
Apatite (Tr.)	V.f.g. inclusions in plagioclase and magnetite
K-feldspar 2%	<1mm crystals with weak to moderate (<5% of individual crystals) clay alteration. Crystals are anhedral with serrated grain boundaries and they occur interstitially to other minerals.
Magnetite 5%	V.f.g. crystals are abundant as inclusions in altered cpx crystals often occurring and elongated along cleavage planes. 0.25 to 1mm anhedral crystals occur interstitially to plagioclase, biotite and cpx.
Clinopyroxene 14%	0.5 to 2mm anhedral crystals with irregular boundaries. Occurs interstitially to plagioclase and often contains v.f.g. inclusions of serpentine and talc with thin (<<<1mm) rims of amphibole. Also found in larger amphiboles where they may be irregulary shaped

Textures: Medium-grained equigranular with mafic minerals occurring interstitially to subhedral plagioclase.

Alteration: Trace to weak sericitization of plagioclase except in close proximity to a fracture, where moderate sericitization is observed. Primary clinopyroxenes contain inclusions of v.f.g. serpentine and talc, and are often seen as cores to or complex intergrowths with amphiboles (uralitized). Biotite is observed altering from secondary amphibole and rarely directly from clinopyroxene.

Mineralization: None observed.

Normalized QAP:

Quartz	11	Alkali Feldspar	4	Plagioclase	85
Plagioclase	77	Pyroxene	23	Olivine	0

Sample: MD003A   **Facies:** Border   **Name:** diorite

Hand Sample Description: Medium-grained equigranular texture. Comprised of approximately 40% anhedral amphibole and ~60% anhedral plagioclase. Much of the plagioclase has been bleached white (albitized) around a fracture that cuts across the sample. Sample is stained and reveals no K-feldspar.

Mineral Name and Abundance	Description
	Primary Mineralogy
Plagioclase 57%	0.5 to 4mm anhedral crystals with serrated grain boundaries comprise most of the sample. Polysynthetic and deformation twins are ubiquitous and crystals lack zoning. Weak sericite alteration (<5 to 15% of a given crystal) is primarily concentrated in cores.
Biotite 1%	Alteration along rims of amphibole.
Quartz 3%	Angular crystals (0.5 to 2mm) occurring interstitially plagioclase and amphibole. Typicaaly displays undulatory extinction and subgrains.
Amphibole 29%	0.5 to 3mm anhedral crystals. Mostly occurs interstitially to subhedral plagioclase which impinges upon amphibole grain boundaries. Cleavages are commonly well developed. Olive green pleochroism. Commonly contains 0.1 to 1mm inclusions of magnetite which also occurs sandwiched between amphibole crystals along grain boundaries. V.f.g. apatite occurs as inclusions in some crystals.
Rutile (Tr.)	V.f.g. inclusions in plagioclase and amphibole.
Apatite (Tr.)	Euhedral, hexagonal, v.f.g. crystal occur as inclusions in amphibole and magnetite.
Chlorite (Tr.)	Alteration of biotite crystals at grain boundaries and along cleavage planes.
Magnetite 10%	0.1 to 1mm, anhedral crystals. Commonly occurs as interstitial crystals to plagioclase as well as partial or full inclusions in amphiboles.

Textures: Phaneritic, equigranular texture.

Alteration: Amphiboles are generally fresh with trace biotite alteration along grain margins. Rare chlorite alteration of biotite is present along cleavage planes. Plagioclase is affected by weak sericite alteration. Plagioclase is albitized surrounding a fracture in the hand sample.

Mineralization: None observed.

Normalized QAP:

Quartz	5	**Alkali Feldspar**	0	**Plagioclase**	95

Sample: MD003B   **Facies:** Border   **Name:** diorite

Hand Sample Description: Medium- to coarse-grained equigranular texture comprises most of the sample, but a 2cm band of medium- to fine-grained, equigranular material cuts across the sample. The band is mostly equigranular with a single 5mm, euhedral plagioclase crystal and a 5mm, anhedral amphibole crystal. The contacts between the finer-grained band are sharp and well defined, with coarse-grained amphiboles concentrated along them. The composition of the finer-grained band is identical to the rest of the sample, which is composed of ~40% anhedral amphibole and ~60% anhedral plagioclase. Sample is stained and reveals no K-feldspar.

Mineral Name and Abundance	Description
	Primary Mineralogy
Plagioclase 60%	Anhedral, 0.25 to 4mm crystals with serrated grain boundaries. Polysynthetic and deformation twins are present in most crystals but zoning is absent. Weak patchy sericite alteration (<5% of individual crystals).
Amphibole 33%	Anhedral1 to 3mm crystals with no preferred orientation occur in the main part of the sample with finer-grained (0.5 to 1mm) anhedral crystals in the finer-grained band.
Apatite 1%	Euhedral, hexagonal crystals included in amphiboles and magnetite.
Magnetite 7%	0.25 to 1mm anhedral crystals occur interstitially to plagioclase and amphibole crystals, as well as inclusions in amphibole.

Textures: Medium- to coarse-grained, equigranular texture dominates most of sample. A 2cm band with a fine- to medium-grained equigranular textures cuts across the sample with sharp contacts.

Alteration: Weak sericite alteration plagioclase.

Mineralization: None observed.

Normalized QAP:

Quartz	0	**Alkali Feldspar**	0	**Plagioclase**	100

Sample: MD078   **Facies:** Border   **Name:** leuco-olivine gabbronorite

Mineral Name and Abundance	Description
	Primary Mineralogy
Plagioclase 58%	0.5 to 4mm sub- to anhedral plagioclase crystals with random orientations comprises the majority of the sample. Polysynthetic twinning is abundant and deformation twinning is fairly common. <5% alteration of individual crystals to sericite.
Biotite 2%	V.f.g., flaky, anhedral replacements after amphibole and pyroxenes.
Amphibole 5%	Anhedral amphibole partially replaces clinopyroxene and forms thin, interstitial growths between plagioclase and pyroxenes. Some larger, better developed crystals contain remnant cores of cpx.
Olivine 10%	Highly fractured crystals with irregular grain boundaries. Many crystals have been completely altered to v.f.g. talc and the rest are serpentinized and/or surrounded by serpentine coronas.
Magnetite 10%	An- to subhedral (0.5 to 1mm) crystals occur interstitially to plagioclase, pyroxene and olivine crystals.
Orthopyroxene 5%	0.5 to 2mm anhedral crystals occur interstitial to plagioclase, as well as in cores of amphibole.
Clinopyroxene 15%	0.5 to 2mm anhedral crystals occur interstitial to plagioclase, as well as in cores of amphibole.

Textures: Fine- to medium-grained equigranular texture.

Alteration: Weak (<5%) sericite alteration of plagioclase. Olivine crystals are often completely altered to talc. Serpentine coronas or alteration along fractures is also common in olivine. Pyroxenes are often partially rimmed by secondary amphibole which is in turn partially replaced by biotite.

Mineralization: None observed.

Normalized QAP:

Quartz	0	Alkali Feldspar	0	Plagioclase	100
Plagioclase	66	Pyroxene	23	Olivine	11

Sample: MD075   **Facies:** Guichon   **Name:** granodiorite

Hand Sample Description: Light coloured, medium-grained, equigranular, phaneritic rock with ~75% felsic and 25% mafic minerals. Felsic minerals are predominantly subhedral plagioclase (white), interstitial K-feldspar (pink) and quartz (transparent). Mafics are roughly half biotite and half amphibole. Average grainsize is ~3mm.

Mineral Name and Abundance	Description
	Primary Mineralogy
K-feldspar 18%	Anhedral, often wormy shaped K-feldspar is found interstitial to plagioclase and the mafic minerals. Crystal size is predominantly controlled by the size of interstitial spaces between plagioclase crystals. Typically affected by 10 to 30% alteration of individual crystals by clays. Often sub-ophitically encloses plagioclase crystals.
Quartz 20%	Anhedral quartz occurs interstitially to plagioclase and the mafic minerals. Grain boundaries are generally straight, and controlled by crystal habit of the minerals it is interstitial to. Generally strain-free, although undulose extinction is not uncommon. Sometimes optically continuous quartz is observed sub-ophitically enclosing plagioclase crystals. Generally 0.5 to 3mm, but dominantly controlled by the size of interstitial space between plagioclase crystals.
Biotite 13%	Anhedral, flaky crystals ranging from 1 to 2mm in size. A number of crystals have inclusions of epidote along cleavage planes, posibbly resulting from biotitization of primary amphibole. Biotites with epidote inclusions are also commonly being altered to chlorite along grain boundaries and cleavage planes (<5% replacement). Commonly in direct contact with amphibole, growing along grain boundaries of and sometimes containing small partial or total inclusions of amphibole.
Amphibole 8%	Sub- to euhedral crystals (1 to 2mm) with prismatic longitudinal- or elongate-diamond cross-sections. Cross-sections are generally more subhedral and longitudinal sections are serrated and subhedral. Smaller (0.5mm) crystals are rarely included in biotites. Many amphiboles contain cores that are complexly intergrown with cpx and magnetite, indicating secondary nature resulting from uralitization of primary pyroxene. Amphiboles with no pyroxene in the core are generally free of v.f.g. magnetite inclusions, indicating that primary amphibole is also present.
Plagioclase 37%	Occurs as ~3mm eu- to subhedral, elongate lath-like crystals and ~0.25 to 1mm euhedral, equant, tabular crystals randomly oriented throughout the sample. Most crystals are partially surrounded by interstitial quartz and k-feldspar, although smaller crystals (<0.5mm, both elongate and tabular types) are completely surrounded by

	poikilitic K-feldspar. Alteration is primarily sericite and clay, and is variable, typically affecting <5 to 15% of individual crystals, although more altered crystals (up to ~75%) are not rare.
Magnetite 2%	V.f.g. (<0.5mm) crystals, typically anhedral and occurring as inclusions in or along grain boundaries of amphibole and biotite. Less commonly occurs as inclusions in feldspars and quartz.
Titanite 1%	~0.5mm euhedral sphenoid crystals, typically associated with amphibole
Epidote <1%	Trace v.f.g. (<0.1mm) anhedral crystals associated with biotite and chlorite
Chlorite <1%	Trace chlorite occurs as alteration along biotite grain boundaries and cleavage planes. Alteration accounts for <1% of affected biotite crystals
Apatite <1%	V.f.g. eushedral, hexagonal crystals included in amphibole and biotite.

Textures: Equigranular, phaneritic rock with interstitial K-feldspar and quartz

Alteration: Trace to weak chlorite and epidote alteration of biotite. Uralitization of relict cpx to amphibole. Possibly biotitization of amphiboles. Weak clay and sericite alteration of feldspars.

Mineralization: None observed

Normalized QAP:

Quartz	27	**Alkali Feldspar**	24	**Plagioclase**	49

Sample: MD074   **Facies:** Guichon   **Name:** granodiorite

Hand Sample Description: Dark grey, equigranular, phaneritic sample with an average grain size of ~2mm. Approximately 30% mafic minerals and 70% felsic minerals. Interstitial K-feldspar and quartz accounts for 7-10% and 20% of the sample respectively. Subhedral, 1-3mm plagioclase makes up ~40% and subhedral amphibole and biotite make up ~13 and ~12% of the sample respectively.

Mineral Name and Abundance	Description
	Primary Mineralogy
Quartz 20%	F.g. (<1mm) anhedral crystals interstitial to plagioclase and mafic minerals. Often has an angular shape with straight grain boundaries controlled by the shape of interstitial spaces between plagioclase.
K-feldspar 10%	Irregular, anhedral crystals interstitial to plagioclase and mafic minerals. Often weakly altered (<5%) to clay minerals. Shape of crystals controlled by shape of interstitial spaces.
Amphibole 13%	Occurs as 0.5 to 2mm anhedral crystals, often with an angular shape due to impingement of crystal faces by plagioclase crystals. Often in contact with biotite and magnetite, the latter of which are commonly partially or fully included in the amphibole.
Biotite 12%	Occurs as 0.5 to 2mm, flaky an- to subhedral crystals throughout the sample. Most crystals are weakly altered to chlorite along cleavage planes (<5% of individual crystals). Often contain v.f.g. inclusions of magnetite, plagioclase, quartz and apatite.
Plagioclase 40%	Occurs as ~3mm eu- to subhedral, elongate lath-like crystals and ~0.25 to 1mm euhedral, equant, tabular crystals randomly oriented throughout the sample. Most crystals are partially surrounded by interstitial quartz and k-feldspar, although smaller crystals (<0.5mm, both elongate and tabular types) are completely surrounded by poikilitic K-feldspar. Alteration is primarily sericite and clay, and is variable, typically affecting <5 to 15% of individual crystals, although more altered crystals (up to ~75%) are not rare.
Magnetite 3%	V.f.g. (<0.5mm) crystals, typically anhedral and occurring as inclusions in or along grain boundaries of amphibole and biotite. Also commonly occurs as inclusions in and interstitial to feldspars and quartz.
Apatite <1%	V.f.g. eushedral, hexagonal crystals included in amphibole and biotite.
Titanite 1%	~0.5mm euhedral sphenoid crystals, typically associated with amphibole
Chlorite <1%	Trace chlorite occurs as alteration along biotite grain boundaries and cleavage planes. Alteration accounts for <1% of affected biotite crystals

Textures: Medium-grained, phaneritic, equigranular with interstitial quartz and K-feldspar.

Alteration: Trace to weak chlorite and epidote alteration of biotite. Uralitization of relict cpx to amphibole. Possibly biotitization of amphiboles. Weak clay and sericite alteration of feldspars.

Mineralization: None observed.

Normalized QAP:

Quartz	29	Alkali Feldspar	14	Plagioclase	57

Sample: MD076   **Facies:** Guichon   **Name:** granodiorite

Hand Sample Description: Light coloured, medium-grained, equigranular, phaneritic rock with ~75% felsic and 25% mafic minerals. Felsic minerals are predominantly subhedral plagioclase (white), interstitial K-feldspar (pink) and quartz (transparent). Mafics are roughly half biotite and half amphibole. Average grainsize is ~3mm.

Mineral Name and Abundance	Description
	Primary Mineralogy
K-feldspar 15%	Anhedral, sometimes wormy shaped K-feldspar is found interstitial to plagioclase and the mafic minerals. Crystal size is predominantly controlled by the size of interstitial spaces between plagioclase crystals. Typically affected by 5 to 15% alteration of individual crystals by clays. Often sub-ophitically encloses plagioclase, biotite and amphibole crystals.
Quartz 20%	Anhedral quartz occurs interstitially to plagioclase and the mafic minerals. Grain boundaries are generally straight, and controlled by crystal habit of the minerals it is interstitial to but there is more rounded qtz present than in sample MD075. Generally strain-free, although undulose extinction is not uncommon. Optically continuous quartz is commonly observed sub-ophitically enclosing plagioclase crystals. Generally 0.5 to 3mm, but dominantly controlled by the size of interstitial space between plagioclase crystals.
Biotite 15%	Anhedral, flaky crystals ranging from 0.5 to 2mm in size. A number of crystals have inclusions of epidote along cleavage planes, possibly resulting from biotitization of primary amphibole. Biotites with epidote inclusions are also commonly being altered to chlorite along grain boundaries and cleavage planes (<5% replacement). Commonly in direct contact with amphibole, growing along grain boundaries of and sometimes containing small partial or total inclusions of amphibole.
Amphibole 10%	Sub- to euhedral crystals (1 to 2mm) with prismatic longitudinal- or elongate-diamond cross-sections. Cross-sections are generally more subhedral and longitudinal sections are serrated and subhedral. Smaller (0.5mm) crystals are rarely included in biotites. Many amphiboles contain cores that are complexly intergrown with cpx and magnetite, indicating secondary nature resulting from uralitization of primary pyroxene. Amphiboles with no pyroxene in the core are generally free of v.f.g. magnetite inclusions, indicating that primary amphibole is also present.
Plagioclase 36%	Occurs as ~1 to 3mm subhedral, elongate crystals and ~0.25 to 1mm euhedral, equant, tabular crystals randomly oriented throughout the sample. Elongated crystals are not as lath-shaped as in MD075, and are a little bit wider on average. Grain boundaries

	are also more irregular than in MD075 and appear serrated in some cases. Oscillatroy zoning is rare, but was observed in ~3-5 crystals. Most crystals are partially surrounded by interstitial quartz and k-feldspar, although smaller crystals (<0.5mm, both elongate and tabular types) are completely surrounded by poikilitic K-feldspar. Alteration is primarily sericite and clay, and is variable, typically affecting <5 to 15% of individual crystals, although more altered crystals (up to ~75%) are not rare.
Magnetite 2%	V.f.g. (<0.5mm) crystals, typically anhedral and occurring as inclusions in or along grain boundaries of amphibole and biotite. Also commonly occurs as inclusions in and interstitial to feldspars and quartz.
Titanite 1%	~0.5mm euhedral sphenoid crystals, typically associated with amphibole and magnetite
Epidote <1%	Trace v.f.g. (<0.1mm) anhedral crystals associated with biotite and chlorite
Chlorite <1%	Trace chlorite occurs as alteration along biotite grain boundaries and cleavage planes. Alteration accounts for <1% of affected biotite crystals
Apatite <1%	V.f.g. eushedral, hexagonal crystals included in amphibole and biotite.
Olivine Tr.	One rounded olivine crystal (~1mm) observed completely surrounded by amphibole (near one of the mineral chemistry spots for reference).

Textures: Medium-grained, phaneritic, equigranular with interstitial quartz and K-feldspar.

Alteration: Trace to weak chlorite and epidote alteration of biotite. Uralitization of relict cpx to amphibole. Possibly biotitization of amphiboles. Weak clay and sericite alteration of feldspars.

Mineralization: None observed.

Normalized QAP:

Quartz	28	**Alkali Feldspar**	21	**Plagioclase**	51

Sample: MD044   **Facies:** Chataway   **IUGS Classification:** quartz monzodiorite

Mineral Name and Abundance	Description
	Primary Mineralogy
Plagioclase 40%	Plagioclase occurs as subhedral to euhedral crystals with a continuous variation in size from 0.5 to 5.0mm. Many of the crystals have been completely altered to clay minerals and this is most common where they are in proximity to chlorite altered biotites although it is also observed in many of the f.g. crystals poikilitically enclosed by hornblendes. Simple twinning is common in crystals that have not been to strongly altered to clays and concentric zoning appears to be absent. Clay alteration ranges from 5 – 100%, with most crystals containing between 40 to 60% clay by volume.
Amphibole 13%	Hornblende occurs as m.g. (1.0 to 4.0mm) subhedral to anhedral crystals evenly distributed throughout the sample. Textures indicate a later crystallization relative to more abundant plagioclase. Hornblende is seen as interstitial crystals growing between and impinged upon by subhedral to euhedral plagioclase. Many larger hornblende crystals poikilitically enclose f.g. (≤1.5mm) euhedral plagioclase crystals which is most commonly observed in basal sections. Inclusions of f.g. (≤1.0mm) opaque and titanite crystals are also common in the hornblende. Most crystals are fresh with rare crystals exhibiting minor alteration to chlorite. This contrasts with the high degree of alteration in biotite and plagioclase.
Quartz 10%	Quartz occurs as f.g. to m.g. (0.5 to 2.0mm) anhedral crystals interstitial to euhedral plagioclase crystals. Some quartz-rich pockets exist in the sample which at first glance appear as single crystals that sub-poikilitically enclose f.g. crystals of euhedral plagioclase. Upon closer inspection however it is concluded that they consist of many finer-grained quartz crystals that partially surround the plagioclase crystals.
Chlorite 6%	Chlorite occurs predominantly as an alteration mineral along cleavage planes in primary biotite crystals ranging in size from 1.5 to 4.5mm and rarely as a f.g (≤1.0mm) trace alteration product of hornblende crystals. Chlorite now accounts for upwards of 90% volume of the primary biotites
Epidote 2%	Epidote is found as v.f.g. lenses occurring along cleavage planes in mica books. It is interpreted to be an alteration product of the primary biotite as is chlorite.

Biotite 1%	Biotite occurs as thin, wispy plates parallel to primary cleavage planes surrounded chlorite in what were originally m.g. (1.5 to 4.5mm) biotite crystals. Typically, less than 10% of the primary biotite remains with chlorite, epidote and quartz having replaced it. Thin lenticular pods of v.f.g quartz and epidote are common along cleavage planes.
Titanite 1%	Titanite occurs as f.g. (≤1.5mm) subhedral crystals both in the groundmass and less commonly as inclusions in the mafic minerals. It is interstitial in nature often growing up against euhedral plagioclase crystals though it's f.g. nature often allows for multiple well-defined crystal faces to have formed in the interstitial space where it is not in contact with other crystals.
Magnetite 1%	
Orthoclase 10%	Occurs as m.g. (2.0 to 4.0mm) subhedral crystals sparsely dispersed throughout the sample. Crystals are weakly altered to clay minerals. Wavy albite exsolution lamellae present in some crystals.
Clays 16%	Clay minerals occur as a v.f.g. alteration product of the plagioclase feldspar. Clay alteration varies from weak to strong but is generally strong throughout the sample as a whole. Complete alteration of plagioclase crystals to clay is common with relict grainshape being the only way to determine the original crystal.

Normalized QAP:

Quartz	16	Alkali Feldspar	17	Plagioclase	67

Sample: MD066   **Facies:** Chataway   **IUGS Classification:** granodiorite

Mineral Name and Abundance	Description
	Primary Mineralogy
Plagioclase 40%	Plagioclase crystals vary greatly in size and shape. Coarser crystals are generally sub- to euhedral and lath shaped ranging from 1.5 to 4.0mm in size. Finer-crystals (0.5 to 1.5mm) are also sub- to euhedral and are predominantly lath shaped although tabular, equant crystals are also common. Finer-grained plagioclase crystals are often poikilitically enclosed by coarser hornblende crystals or completely surround by a single interstitial quartz crystal. Concentric zoning is noticeably absent unlike the Bethsaida phase. Polysynthetic twinning is ubiquitous. Clay alteration varies between individual crystals but is generally weak to moderate, patchy and progresses from crystal cores to rims.
Quartz 25%	Quartz occurs as f.g. to m.g. (0.2 to 2.5mm) anhedral crystals. Inclusions of f.g. (0.2 to 0.5mm) quartz crystals are common in biotite and to a lesser extent hornblende. Quartz most commonly occurs interstitially to the other major minerals (plagioclase, orthoclase, biotite and hornblende) and commonly a single crystal will poikilitically enclose many f.g. (~0.5mm) euhedral crystals of plagioclase and opaque minerals. Subgrain boundaries and undulatory extinction are common.
Clay 5%	Clay minerals occur as v.f.g. (too small to reliably distinguish between different types) alteration products of the feldspars present. Clay alteration of feldspars varies greatly between crystals but is generally weak to moderate, patchy and progresses from cores to rims. Clay mierals are most abundant in f.g. plagioclase crystals poikilitically enclosed by hornblende crystals.
Amphibole 9%	Hornblende occurs as m.g. (1.0 to 3.0mm) an- to subhedral crystals with crystals occasionally possessing one or two good crystal faces. Crystals are mostly fresh with rare chlorite alteration up to a few percent of the entire crystal (≤5%). Crystal faces are typically impinged upon by euhedral plagioclase crystals. Hornblende crystals poikilitically enclose f.g. (≤1.5mm) plagioclase crystals and contain inclusions of f.g. (≤1.5mm) sub- to euhedral opaque mineral crystals. Distributed evenly throughout sample.
Orthoclase 12%	Occurs as m.g. (2.0 to 4.0mm) subhedral crystals sparsely dispersed throughout the sample. Crystals are weakly altered to clay minerals. Wavy albite exsolution lamellae present in some crystals.

Biotite 5%	Biotite occurs as f.g. to m.g. (0.5 to 2.5mm) crystals with the predominant crystal size ranging between 1.0 to 2.0mm. Crystals are typically subhedral with crystal faces often impinged upon by euhedral plagioclase crystals. Inclusions of v.f.g. (≤0.25mm) quartz crystals are common in the biotite. Biotite crystals are randomly oriented and evenly distributed throughout the sample. Minor chlorite alteration up to a few percent of the crystals total are occurs is visible in some crystals but is rare.
Magnetite 2%	
Chlorite 1%	Chlorite occurs as a v.f.g. (≤0.25mm) alteration mineral in a small number of hornblende and biotite crystals. Found along fractures in hornblende and along grain boundaries and cleavage planes in biotite. Chlorite occurs in very low percentages (up to 3 to 5% of the total volume of host crystal).
Titanite 1%	Titanite occurs as v.f.g. (0.1 to 0.5mm) sub- to euhedral pseudohexagonal crystals. Crystals are sparsely scattered throughout the sample.

Normalized QAP:

Quartz	30	**Alkali Feldspar**	15	**Plagioclase**	55

Sample: MD049   **Facies:** Bethlehem   **IUGS Classification:** granodiorite

Mineral Name and Abundance	Description
	Primary Mineralogy
Plagioclase 44%	Plagioclase varies continuously from f.g. to c.g. (0.5mm to 7.0mm) in size and crystal habit ranges from tabular equant crystals to elongate prisms. Concnetric zoning, polysynthetic and simple twins are common and can combine to produce complex patterns in XPL. Most crystals that make up the groundmass are m.g. (1.0 to 3.0mm) in size with coarser phenocrysts irregularly dispersed throughout. Clay alteration varies from weak to strong (0% to 95% clay) and is patchy, progressing from the cores of crystals to their rims. Plagioclase crystals are mostly supported by each other with small areas with significant interstitial quartz.
Quartz 25%	Quartz forms anhedral crystals that occur interstitially to euhedral plagioclase crystals as well as in ameboidal quartz eyes. The interstitial quartz is f.g. to m.g. (0.5 to 2.0mm). Quartz eyes are rare and are typically 2.0 to 3.0mm in size.
K-feldspar 10%	Occurs as m.g. (1.0 to 2.0mm) subhedral crystals sparsely dispersed throughout the sample. Crystals are weakly altered to clay minerals. Wavy albite exsolution lamellae present in some crystals.
Clay 5%	Clays occur as alteration products in plagioclase crystals and their abundances vary with degree of alteration. Alteration is patchy and progresses from the cores to rims of crystals.
Amphibole 5%	Hornblende occurs as m.g. (1.0 to 3.0mm) subhedral crystals. Crystals occur as two distinct groups. The first group is composed of finer (1.0 to 1.5mm) crystals that are free of euhedral plagioclase inclusions and distributed evenly throughout the sample. The second group consists of coarser (2.5 to 3.0mm) irregularly distributed phenocrysts that poikilitically enclose f.g. (≤1.0mm) euhedral plagioclase crystals. Inclusions of f.g. (≤1.0mm) opaque and titanite crystals are common in both groups.
Biotite 2%	Biotite occurs as m.g. (1.5 to 2.5mm) subhedral crystals with an uneven distribution. Inclusions of f.g. (≤1.0mm) opaque crystals are common. Weak to moderate chlorite alteration is common.
Magnetite 2%	
Chlorite 1%	Chlorite occurs most commonly along grain boundaries as well as along cleavage planes in the host biotite crystals.
Titanite 1%	Titanite occurs as f.g. (≤1.0mm) euhedral to subhedral crystals

unevenly distributed through the sample. It can be found as inclusions in hornblende and biotite crystals as well as in the groundmass.

Normalized QAP:

Quartz	32	Alkali Feldspar	13	Plagioclase	55

Sample: MD059   **Facies:** Bethlehem   **IUGS Classification:** granoidiorite

Mineral Name and Abundance	Description
	Primary Mineralogy
Plagioclase 51%	Plagioclase occurs as subhedral to euhedral crystals that comprise most of the groundmass. Crystals are often supported by other plagioclase crystals with quartz filling the interstitial spaces. Crystals vary continuously in size from f.g. to c.g. (0.5mm to 6.0mm) with most falling in the 2.0 to 3.0mm range. Concentric zoning, simple twinning and polysynthetic twinning are ubiquitous and combine to produce complex patterns under XPL. Crystal shape ranges from tabular, equant crystals to prismatic crystals with length:width ratios of approximately 2:1. Tabular equant crystals are more abundant than elongate prisms. Minor clay alteration is present in many crystals but generally accounts for <5% of the total volume of an individual crystal. Clay alteration is patchy and concentrated in the cores of crystals.
Quartz 25%	Quartz occurs as m.g. (1.0 to 2.0mm) anhedral to rounded crystals interstitial to the uhedral/subhedral plagioclase and subhedral hornblende crystals. Quartz is less abundant than in samples from the Skeena phase and the quartz eyes observed in both the Skeena and Bethsaida phases are noticeably absent.
K-feldspar 10%	Orthoclase textures are typical of those documented for other Bethlehem, Bethsaida and Skeena samples.
Amphibole 5%	Hornblende occurs as f.g. to m.g. (0.5 to 3.0mm) subhedral unevenly distributed crystals with most crystals being between 1.5 and 2.5mm. Rare phenocrysts 5.0 to 6.0mm in size occur sporadically throughout the sample. Phenocrysts contain numerous inclusions of f.g. (≤1.0mm) opaques and v.f.g. (≤0.25mm) quartz. The more abundant finer-grained hornblende crystals also commonly contain these inclusions as well as f.g. inclusions of plagioclase and rarely titanite.
Clay 5%	
Biotite 1.5%	Biotite occurs as f.g. (0.5 to 1.5mm) subhedral books. Biotite crystals are mostly fresh with some crystals showing up to 30% chlorite alteration. Biotite is unevenly distributed throughout the sample and commonly contains rounded inclusions of quartz ~0.5mm across.
Chlorite <1%	Chlorite is found as an alteration product in a small amount of the primary biotite crystals. It typically replaces <5% of the biotite but may reach up to ~30% replacement in rare cases. Chlorite alteration

	is concentrated along cleavage planes in the biotites.
Titanite 1%	Titanite textures are typical of those documented for other Bethlehem, Bethsaida and Skeena samples.
Magnetite 1%	

Normalized QAP:

Quartz	29	**Alkali Feldspar**	12	**Plagioclase**	59

Sample: MD035   **Facies:** Skeena   **IUGS Classification:** granodiorite

Mineral Name and Abundance	Description
	Primary Mineralogy
Plagioclase 41%	Plagioclase crystals are subhedral to euhedral and vary continuously in size from 1.0 to 4.0mm. Plagioclase comprises the bulk of the groundmass, are often in contact with multiple other plagioclase crystals and interstitial spaces between crystals are filled with quartz. Crystal shape varies from equant tabular crystals to more elongate prisms with tabular crystals being dominant. Concnetric zoning is common along with polysynthetic and to a lesser extent simple twins. Overprinting of these features generates complex patterns in XPL in many crystals. Clay alteration is common and variable. Strongly altered crystals may be up to 95% v.f.g. clay minerals whereas weakly altered crystals contain 0 to 15% clay minerals. Weak clay alteration is most common and alteration is patchy progressing from the cores to rims of crystals.
Quartz 23%	Quartz occurs both as anhedral m.g. (1.5 to 2.0mm) crystals in aggregates forming ameboidal quartz eyes as well as f.g. to m.g. (0.5 to 1.5mm) crystals interstitial to euhedral plagioclase crystals. Quartz is less abundant than in the Bethsaida samples. Quartz eyes are generally smaller and less abundant. The amount of interstitial quartz is also significantly lower.
K-Feldspar 20%	Occurs as m.g. (2.0 to 3.0mm) subhedral crystals sparsely dispersed throughout the sample. Crystals are weakly altered to clay minerals. Wavy albite exsolution lamellae present in some crystals.
Clay 5%	
Amphibole 3%	Hornblende occurs as f.g. to m.g. (0.5 to 2.0mm) subhedral crystals evenly distributed throughout the sample. Most crystals are unaltered although some show weak alteration to chlorite along cleavage planes. Inclusions of f.g. (~0.5mm) quartz and opaque minerals are common with the opaque inclusions more common. Simple twinning is common in the hornblende.
Biotite 2%	Biotite occurs as m.g. (1.0 to 3.0mm) subhedral books distributed irregularly throughout the sample. Crystals are mostly fresh with some showing weak alteration to chlorite. Chlorite alteration is focussed along grain-boundaries and cleavage planes. Inclusions of epidote are common in chloritized crystals. F.g. quartz inclusions are present in some crystals. Chlorite alteration is closely associated with

	biotites crystals in contact with opaque minerals and appears to spread from the point of contact between the two minerals.
Chlorite 2%	Chlorite occurs as f.g. (≤1.0mm) anhedral crystals. Chlorite is observed in subhedral biotite and hornblende crystals and appears to be an alteration product of the two host minerals. It is predominantly focused along cleavage planes and along grain-boundaries in biotite crystals as well as cleavage planes in hornblendes.
Magnetite 2%	
Titanite 1.5%	Titanite occurs as subhedral f.g. (0.5 to 1.0mm) crystals. Crystals are hexagonal to pseudohexagonal in shape and are associated with hornblende and opaque minerals usualliy in contact with them or partially surrounded by opaques.
Epidote <1%	Epidote occurs as f.g. (0.5 to 1.5mm) anhedral crystals in chlorite altered biotite crystals. The epidote forms elongated pods parallel to and along cleavage planes in the micas.
Zircon (Tr.)	Zircon crystals occur as rare v.f.g. (<≤0.1mm) in biotite crystals. They are easily identified by their extreme relief. Pleochroic halos surrounding the zircon inclusions are not present.

Normalized QAP:

Quartz	27	**Alkali Feldspar**	24	**Plagioclase**	49

Sample: MD034   **Facies:** Skeena   **IUGS Classification:** granodiorite

Mineral Name and Abundance	Description
	Primary Mineralogy
Plagioclase 44%	Textures are similar to MD035. Deformation twins that crosscut internal zoning and pinch out instead of continuing across the crystals are common. Grainsize ranges continuously from 1.0 to 4.0mm with elongate 2.0 to 3.0mm crystals being the most common.
Quartz 20%	Textures are similar to those observed in MD035. One quartz eye is 4.0mm in size but the rest are between 1.5 and 2.0mm as in MD035.
K-feldspar 20%	Orthoclase has a similar grainsize, shape and texture to MD035.
Clay 6%	Clays occur as alteration products in plagioclase crystals and their abundances vary with degree of alteration. Alteration is patchy and progresses from the cores to rims of crystals.
Amphibole 4%	Textures are similar to MD035 with a few exceptions. Chlorite alteration of hornblende crystals is greater than MD035 with altered patches in crystals more abundant and up to 1.0mm in size. One anomalously large crystal is present (5.0mm) which contains numerous inclusions of f.g. (≤1.0mm) opaque and plagioclase crystals.
Biotite 2%	Textures are similar to those observed in MD035. Biotite crystals are slighltly finer-grained (0.5 to 2.5mm) and lack epidote inclusions.
Magnetite 2%	
Chlorite 1%	Chlorite occurs as f.g. (≤1.5mm) anhedral crystals. Unlike MD035, chlorite is concentrated in altered hornblende crystals, not biotite crystals. It is especially prevalent in one large hornblende crystal where patchy chlorite alteration has replaced up to 20% of the original crystal.
Titanite 1%	Titanite has a similar grainsize, shape, texture and occurrence to MD035.

Normalized QAP:

Quartz	24	**Alkali Feldspar**	24	**Plagioclase**	52

Sample: MD060   **Facies:** Skeena   **IUGS Classification:** granodiorite

Mineral Name and Abundance	Description
	Primary Mineralogy
Plagioclase 37%	Plagioclase varies continuously from f.g. to c.g. (0.5mm to 6.0mm) in size and crystal habit ranges from tabular equant crystals to elongate prisms. Concnetric zoning, polysynthetic and simple twins are common and can combine to produce complex patterns in XPL. Most crystals that make up the groundmass are m.g. (1.0 to 3.0mm) in size with coarser phenocrysts irregularly dispersed throughout. Clay alteration varies from weak to strong (0% to 95% clay) and is patchy, progressing from the cores of crystals to their rims.
Quartz 20%	Quartz forms anhedral crystals that occur interstitially to euhedral plagioclase crystals as well as in ameboidal quartz eyes. The interstitial quartz is f.g. to m.g. (0.5 to 2.0mm). Quartz eyes are rare and are typically 2.0 to 3.0mm in size.
K-feldspar 25%	Occurs as m.g. (1.0 to 2.0mm) subhedral crystals sparsely dispersed throughout the sample. Crystals are weakly altered to clay minerals. Wavy albite exsolution lamellae present in some crystals.
Clay 5%	Clays occur as alteration products in plagioclase crystals and their abundances vary with degree of alteration. Alteration is patchy and progresses from the cores to rims of crystals.
Amphibole 5%	Hornblende occurs as f.g. to m.g. (0.25 to 8.0mm) subhedral crystals. Crystals are highly fractured and contain many f.g. (0.25 to 1.0mm) inclusions of quartz and opaque minerals. Many crystals have been partially altered to chlorite and some contain inclusions of associated epidote and titanite. Most crystals are between 0.5 and 2.0mm with one large phenocryst that is 8.0mm across. The large phenocryst poikilitically encloses f.g. to m.g. (0.5 to 2.5mm) subhedral plagioclase crystals that have been strongly altered to clay minerals.
Chlorite 3%	Chlorite occurs as f.g. (0.5 to 1.0mm) crystals in hornblendes as an alteration product and coarser (up to 2.0mm) books where it has partially or completely altered from biotite. Chlorite alteration in biotite crystals is focused along cleavage planes and grain-boundaries and ranges from a few percent to near complete alteration of the host biotite crystal. In hornblende crystals, chlorite alteration is patchy and f.g. Fine-grained epidote (≤1.0mm) crystals are often associated with chlorite.
Biotite 2%	Biotite occurs as wavy bands in books of chlorite. There are no

	weakly to unaltered biotite crystals present with original biotite crystals containing between 50 and 100% chlorite. Epidote and quartz crystals are common in books of biotite and chlorite and are likely associated with the alteration of the biotite to chlorite.
Titanite 1%	Titanite occurs as f.g. (0.5 to 1.0mm) subhedral to euhedral crystals interstitial to euhedral plagioclase crystals and as inclusions in some of the coarser hornblende crystals. Crystals form hexagonal to pseudohexagonal shapes.
Magnetite 1.5%	
Epidote <1%	Epidote occurs as f.g. (0.25 to 1.0mm) subhedral to anhedral crystals in chlorite altered biotite and hornblende crystals. Epidote is concentrated along cleavage planes in mica books.

Normalized QAP:

Quartz	24	**Alkali Feldspar**	31	**Plagioclase**	45

Sample: MD071   **Facies:** Bethsaida   **IUGS Classification:** monzogranite

Hand Sample Description: Light, white coloured rock with evenly scattered mafic minerals. Holocrystalline, weakly porphyritic texture. Approximately 40% tabular to lath-like plagioclase (1 to 8mm) with clay and sericite dusting. 35% anhedral quartz phenocrysts (1 to 6mm; amoeboidal). 15% f.g. (<1mm) interstitial orthoclase. 1 to 2% interstitial magnetite. 7%

Mineral Name and Abundance	Description
	Primary Mineralogy
30% Quartz	Quartz crystals are anhedral and range from 0.5 to 5.0mm in size. The coarsest crystals form ameboidal eyes in the groundmass and characteristically exhibit undulatory extinction and subgrain boundaries. Finer-grained crystals may be strain-free but typically also exhibit undulatory extinction and subgrain boundaries. Finer-grained quartz occurs as anhedral interstitial material to subhedral orthoclase and sub- to euhedral plagioclase crystals.
35% Plagioclase	Plagioclase occurs as sub- to euhedral m.g. to c.g. (1.0 to 5.0mm) crystals distributed evenly throughout the groundmass. Rare phenocrysts up to 7.0mm in size are present. Finer-grained plagioclase often occurs as strongly sericitized inclusions in chlorite altered biotites as well as fresh, euhedral inclusions poiklitically enclosed by hornblende crystals. Sericitization of plagioclase in the groundmass is common ranging from weak to strong. Sericitization is patchy progressing from the cores of crystals outwards. Plagioclase inclusions associated with chlorite altered biotites are the most altered and those poikilitically enclosed by hornblendes are the least altered. Concentric zoning, simple and polysynthetic twinning are common and can combine to produce complex patterns in XPL.
20% Orthoclase	Orthoclase occurs as m.g. (1.0 to 2.5mm) subhedral crystals irregularly distributed throughout the groundmass. Crystals are typically weakly altere to sericite. Wavy albite exsolution lamellae are common and produce perthitic textures when present.
3% Chlorite	Chlorite occurs as an alteration product of c.g. (3.0 to 5mm) subhedral biotite books. Chlorite crystals contain f.g. (≤0.5mm) inclusions of opaque crystals and f.g. (0.5 to 1.0mm) elongate epidote inclusions. Chlorite alteration of biotites varies from weak to strong. Weakly chlorite altered crystals are characterized by chlorite alteration around the crystal margins progressing inward along cleavage planes. Strongly altered biotites range from 60 to 90% chlorite and associated epidote. Inclusions of strongly sericitized

	plagioclase are common.
2% Biotite	Biotite occurs as c.g. (3.0 to 5mm) subhedral mica books. Biotite crystals contain f.g (0.1 to 1.5mm) inclusions quartz and plagioclase (anhedral quartz, sub- to euhedral plagioclase) and f.g. (≤0.5mm) opaque crystals. Chlorite alteration varies from weak to strong. Weakly chlorite altered crystals are characterized by chlorite alteration around the crystal margins progressing inward along cleavage planes. Strongly altered biotites range from 60 to 90% chlorite and associated epidote. Cleavage planes in altered biotites are wavy epidote inclusions occur along some of them. Inclusions of plagioclase have been strongly altered to sericite.
2% Hornblende	Hornblende occurs as f.g. to m.g. (0.5 to 2.0mm) crystals unevenly distributed throughout the groundmass. Crystals are generally subhedral forming elongate prisms or diamond-shaped cross-sections with imperfect crystal faces. Most hornblende crystals are observed to poikilitically enclose f.g. (0.5 to 1.0mm) crystals of euhedral plagioclase. There does not appear to be significant chlorite alteration of the hornblende in this sample as is common in other samples from the Bethsaida phase.
1% Titanite	Tiatanite occurs as f.g. (0.5 to 1.5mm) crystals and crystal clusters. Clusters of titanite are associated with clusters of f.g. (0.5mm) opaque minerals
1% Epidote	Epidote occurs as f.g. (0.5 to 1.0mm) elongate crystals included in chlorite and chlorite altered biotite. It is typically observed along cleavage planes in the sheet silicates. It is interpreted to be an alteration product of the biotite as it is absent in the least altered biotite crystals and abundant in those that have been partially or completely altered to chlorite.

1% Opaques

Textures: Weakly porphyritic, phenocryst-rich. Interstitial K-feldspar

Alteration: Weak clay alteration of plagioclase (pale greenish colour)

Mineralization: None observed

Paragenetic Comments: Interstitial K-feldspar after plagioclase, quartz, and mafic phenocrysts. Pervasive clay/sericite alteration after igneous plagioclase.

Normalized QAP:

Quartz	35	**Alkali Feldspar**	24	**Plagioclase**	41

Sample: MD072   **Facies:** Bethsaida   **IUGS Classification:**

Hand Sample Description: Light, white coloured rock with scattered black minerals. Holocrystalline, coarse-grained (1 to 7mm) with a weakly porphyritic texture. Approximately 44% tabular to lath-shaped, white plagioclase phenocrysts with many appearing to be zoned. Approximately 29% anhedral, 1 to 6mm quartz phenocrysts (amoeboid). 2% hornblende phenocrysts (1 to 6mm) which poikilitically enclose sub-mm chadacrysts of plagioclase. 5% biotite phenocrysts distributed evenly throughout the sample. 18% K-feldspar (f.g., sub to 1mm) occurs interstitially to phenocrysts of all other minerals. 2% magnetite.

Textures: Weakly porphyritic, phenocryst-rich. Interstitial K-feldspar.

Alteration: Weak pervasive clay/sericite alteration of plagioclase phenocrysts.

Mineralization: None observed.

Paragenetic Comments: Interstitial K-feldspar formed late after crystallization of plagioclase, quartz and mafic phenocrysts.

Normalized QAP:

Quartz	32	**Alkali Feldspar**	20	**Plagioclase**	48

Sample: MD069   **Facies:** Bethsaida   **IUGS Classification:** granodiorite

Mineral Name and Abundance	Description
	Primary Mineralogy
Plagioclase 40%	Plagioclase occurs as euhedral to subhedral tabular crystals. Most crystals are equant with less common elongated prisms with lengths up to 2.5x their width. Varying degrees of sericitization have affected the crystals ranging from common completely sericitized to rare unaltered crystals, but most commonly they are partially altered to sericite to varying degrees. Sericitization of plag is patchy, but generally has affected the cores of crystals. Concentric compositional zoning, polysynthetic twins and simple twins are ubiquitous and combine to produce complex patterns under XPL. The Michel-Levy test indicates a composition of the Labradorite variety of plagioclase although due to the degree of alteration and complexity of zoning and twins, this may be unreliable.
Quartz 35%	Quartz occurs both as c.g. (4.0 to 6.0mm) ameboid eyes as well as smaller clusters of crystals (0.5 to 2mm) in the groundmass. The large Qz eyes exhibit ubiquitous undulatory extinction and subgrains indicating conditions conducive to dislocation creep. Inclusions of finer-grained Qz (≤0.25mm) in eyes may be the result of grainsize reduction. Finer-grained Qz is generally characterized as being strain-free, especially the small Qz inclusions in the coarser strained eyes. Qz is observed in contact with all other minerals.
K-feldspar 17%	Crystals occur as f.g. (0.5 to 2mm) sub- to anhedral crystals in the groundmass associated predominantly with Qz and plag. Observed in contact with tit, plag, qz, bt, chl, ap, opaques and hbl. Perthitic textures are observed in most crystals with thin albite exsolution lamellae.
Biotite 3%	Biotite occurs as m.g. (1.5 to 3.5mm) crystals with a platy, subhedral texture. Crystals display strong pleochroism from dark brown to pale yellow. Some crystals contain numerous small (<0.5mm) inclusions of Qz and opaque minerals. The degree of alteration varies considerably between individual crystals with some showing no alteration, some being partially altered to chlorite along grain boundaries and cleavage planes and others (smallest) almost completely altered to chlorite. Bitotite is observed in contact with Qz, K-Spar, Plag, Tit, Chl, opaques, Ap and Hbl.
Amphibole 1%	Hornblende occurs as f.g. (0.25 to 0.5mm) subhedral crystals. Two or more perfect crystal faces usually visible in cross-section with remaining faces being altered to chl. Most crystals have been partially altered to chlorite. Simple twinning is present in some crystals. Mainly occurs as small inclusions in Qz eyes but also occurs in the groundmass with finer-grained Qz and feldspars.

293

Chlorite 1%	Chlorite occurs as f.g. (≤0.5mm), flaky inclusions in Qz phenocrysts. Interference colours are typical of chlorite exhibiting first order greys and yellows with some crystals displaying anomalous third order blues. Flaky intergrowths with biotite are common where chlorite appears to be replacing biotite along cleavage planes. Chlorite alteration of biotite along grain boundaries is common in coarser biotites. Chlorite is also observed to be partially replacing 0.25 to 0.5mm hornblende crystals.
Titanite 1%	Titanite occurs as m.g. (1.0 to 2.5mm) crystals. Crystals are generally subhedral to euhedral and form flattened hexagons with multiple distinct crystal faces which may be disrupted by abundant inclusions of apatite and opaque minerals along grain boundaries. Crystals display moderate pleochroism with colours ranging from light brown to light grey. Titanite is observed in contact with Bt, Ap, opaques, Chl, Hbl,Plag, Qz and K-Spar.
Calcite (Tr.)	
Apatite (<1%)	Apatite occurs as a v.f.g. (0.1 to 0.3mm) accessory mineral. Crystals are generally euhedral displaying elongate prisms in longitudinal section or hexagonal cross-sections. Crystals occur as isolated inclusions or clusters in Qz and perthitic K-Spar. It is also observed as inclusions in biotite, titanite and less commonly chlorite crystals.

Textures: Weakly porphyritic, phenocryst-rich. Interstitial K-feldspar.

Alteration: Weak pervasive clay/sericite alteration of plagioclase phenocrysts.

Mineralization: None observed.

Paragenetic Comments: Interstitial K-feldspar formed late after crystallization of plagioclase, quartz and mafic phenocrysts.

Normalized QAP:

Quartz	38	**Alkali Feldspar**	19	**Plagioclase**	43

Sample: MD070   **Facies:** Bethsaida   **IUGS Classification:** granodiorite

Mineral Name and Abundance	Description
	Primary Mineralogy
Plagioclase 45%	Plagioclase occurs as m.g to c.g. (1.0 to 5.0mm) subhedral tabular and prismatic crystals. Sericitization of crystals is moderate to strong in most cases with sericite occurring in patches throughout crystals and especially concentrated near their cores. The most strongly sericitized crystals are found in contact with the most strongly chlorite altered biotites. Concentric zoning, polysynthetic and deformation twins are common in plagioclase crystals though strong sericitization often disguises these features.
Quartz 28%	Quartz occurs in composite quartz eyes ranging from 3.0 to 7.0mm across which are made of numerous individual f.g. to m.g. (0.1 to 2.5mm) anhedral quartz crystals. Undulatory extinction and subbgrains are common in coarser crystals and finer crystals show little evidence for deformation and strain.
K-feldspar 20%	Orthoclase occurs as f.g. (0.5 to 1.5mm) sub- to anhedral crystals. It is found in the groundmass interspersed with quartz and plagioclase. Minor sercitization has affected most crystals and albite exsolution lamellae are common resulting in perthitic textures.
Chlorite 1.5%	Chlorite occurs as f.g. to c.g. (0.5 to 5.5mm) crystals and is interpreted to be an alteration product of biotite and hornblende. The grainsize of the original biotite and hornblende crystals place a strong control on the size of chlorite crystals. Chlorite is predominantly found in wavy intergrowths with biotite along cleavage planes.
Biotite 1%	Biotite occurs in f.g. to c.g. (0.5 to 5.5.mm) subhedral books intergrown with chlorite along cleavage planes. The biotite is interpreted to have altered to chlorite and anywhere from 40% to 80% of an original biotite book may now be chlorite. This contrasts with what is observed in sample MD069 where chlorite alteration is relatively weak and occurs predominantly along the margins of biotite crystals with only minor replacement along cleavage planes. Lens-shaped bodies of f.g. aggregate quartz are common in many of the more strongly altered biotite-chlorite mica books and are interpreted to be the result of quartz filling the void space left behind after alteration. Other common inclusions include narrow v.f.g. (≤0.1mm) inclusions of titanite aligned parallel to cleavage planes and lenticular aggregates of epidote also aligned parallel to cleavage planes in the micas. Inclusions of opaque minerals (magnetite) are also common. The most strongly altered biotite crystals are associated strongly sericitized plagioclase feldspar either as inclusions or in contact with the biotites along grain boundaries.
Magnetite 2%	

Amphibole <1%	Hornblende occurs as f.g. (0.25 to 1.5mm) subhedral crystals and is often highly fractured. Rare simple twins are observed in some crystals. V.f.g. (≤0.3mm) inclusions of quartz, plagioclase and opaque minerals are common with the hornblende crystals. Most crystals have undergone little to no alteration to chlorite unlike in sample MD069 where most hornblende crystals have been moderately or completely replaced by chlorite. Hornblende is observed in contact with quartz, plagioclase and opaques.
Epidote 1%	Epidote occurs as f.g. (0.1 to 0.3mm) crystals grouped together into lenticular aggregates parallel to cleavage planes in chlorite altered biotite crystals. Crystals show strong pleochroism from pale to lemon yellow.
Titanite 1%	Titanite occurs as v.f.g. (≤0.25mm) inclusions in strongly chlorite altered biotites and less commonly as coarser (0.25 to 0.5mm) sub- to euhedral crystals in the groundmass. Titanite in the groundmass is found along grain boundaries between quartz crystals.

Textures: Weakly porphyritic, phenocryst-rich. Interstitial K-feldspar.

Alteration: Weak pervasive clay/sericite alteration of plagioclase phenocrysts.

Mineralization: None observed.

Paragenetic Comments: Interstitial K-feldspar formed late after crystallization of plagioclase, quartz and mafic phenocrysts.

Normalized QAP:

Quartz	30	**Alkali Feldspar**	22	**Plagioclase**	48

Sample: MD004   **Facies:** Bethsaida   **IUGS Classification:** monzogranite

Mineral Name and Abundance	Description
	Primary Mineralogy
Quartz 42%	Quartz occurs as m.g. to c.g. (3.0 to 8.0mm) ameboid eyes/phenocrysts unevenly distributed throughout a finer-grained matrix as well as more abundant f.g. (0.25 – 1.5mm) crystals which comprise a significant portion of the groundmass. The c.g. quartz eyes characteristically show strain features (undulatory extinction, subgrain boundaries) and contain numerous inclusions of f.g. strain-free quartz crystals as well as f.g. to m.g. strain-free quartz crystals along their margins. The bulk of the f.g. quartz which makes up the groundmass also exhibits indicators of strain. It is interpreted that the majority of the f.g. quartz is primary igneous quartz and the strain – free crystals associated with the c.g. quartz eyes are a result of grainsize reduction.
Plagioclase 25%	Plagioclase occurs as m.g. (1.0 to 5.0mm) tabular, sub- to euhedral crystals. Many of the plagioclase crystals have undergone some degree of sericitization especially the finer-grained crystals. Sericitization is typical of all samples in the Bethsaida phase, being patchy and predominantly focused in the cores of crystals outwards towards the rims. Concentric compositional zoning is common but not ubiquitous. Simple twins and polysynthetic are present in most crystals and combine with zoning to form complex extinction patterns in XPL.
K-Feldspar 25%	Orthoclase occurs as f.g. (0.5 to 1.5mm) sub- to anhedral crystals. It is found in the groundmass interspersed with quartz and plagioclase. Minor sercitization has affected most crystals and albite exsolution lamellae are common resulting in perthitic textures.
Chlorite 3%	Chlorite occurs in f.g. (0.3 to 1.0mm) mica books comprised of biotite and chlorite intergrowths. In individual books, the volumetric ratio of chlorite to biotite is typically greater than 2:1. The two micas are intergrown along cleavage planes and chlorite is interpreted to have replaced biotite as in the other samples from the Bethsaida phase. Rare zircon inclusions are present in some of the chlorite crystals and are easily identified by their pleochroic halos.
Magnetite 2%	
Biotite 1%	Biotite occurs in f.g. (0.3 to 1.0mm) mica books comprised of biotite and chlorite intergrowths. In individual books, the volumetric ratio of chlorite to biotite is typically greater than 2:1. The two micas are intergrown along cleavage planes and chlorite is interpreted to have replaced biotite as in the other samples from the Bethsaida phase.
Titanite 1%	Titanite occurs as f.g. (0.25 to 1.0mm) euhedral crystals in the shape of diamonds. Crystals are seen in isolation surrounded by plagioclase and quartz and also in small clusters with associated

	opaque minerals. Crystal faces of titanite occurring in these clusters are near perfect but the opaque minerals sometimes impinge upon them.
Epidote 1%	Epidote occurs as f.g. (0.1 to 0.3mm) crystals grouped together into lenticular aggregates parallel to cleavage planes in chlorite altered biotite crystals. Crystals show strong pleochroism from pale to lemon yellow.
Zircon (Tr.)	Trace amounts of zircon occurs as v.f.g. (≤0.2mm) inclusions in chlorite crystals. They are most easily discerned by looking for metamict pleochroic halos in chlorite crystals as a result of radiation damage as well as their extremely high relief.

Textures: Weakly porphyritic, phenocryst-rich. Interstitial K-feldspar.

Alteration: Weak pervasive clay/sericite alteration of plagioclase phenocrysts.

Mineralization: None observed.

Paragenetic Comments: Interstitial K-feldspar formed late after crystallization of plagioclase, quartz and mafic phenocrysts.

Normalized QAP:

Quartz	46	**Alkali Feldspar**	27	**Plagioclase**	27

Sample: MD028   **Facies:** FQPC   **Name:** Crowded Quartz- and Feldspar-Phyric, Porphyry Dyke

Hand Sample Description: Crowded porphyritic dyke composed of approximately 40% phenocrysts and 60% groundmass. Elongate to tabular euhedral plagioclase phenocrysts are 1 to 5mm in length and have an earthy lustre and pink colour, likely a result of sericite/clay alteration and Fe-dusting. Quartz phenocrysts (1 to 3mm) are rounded and account for ~7% of the sample. Mafic minerals (hornblende?) predominantly occur as 0.5 to 3mm anhedral phenocrysts with rare outsize crystals up to 7mm in size. Mafic minerals are commonly altered to epidote. When not altered to chlorite, they are altered to chlorite. Plagioclase phenocrysts are also occasionally altered to epidote. The groundmass is aplitic to fine-grained equigranular groundmass. Staining did not reveal any orthoclase present.

Mineral Name and Abundance	Description
	Primary Mineralogy
Plagioclase 45%	Plagioclase phenocrysts are tabular to elongate and subhedral. Crystals are pervasively altered by 10 to 25% muscovite, calcite and epidote. Alteration is not concentrated in cores of crystals as in QFPP and aplite dykes. Remnant polysynthetic twins are present in most crystals and they also appear to lack zoning. V.f.g. plagioclase occurs in the groundmass with quartz.
Epidote 7%	Aggregates of 1mm or less crystals commonly occur with chlorite as a replacement of primary amphibole. Partial replacement of plagioclase crystals is more rare.
Chlorite 8%	Occurs as matts of radiating crystals as well as shreddy replacements after amphibole. Closely associated with epidote in many cases. Has completely replaced all mafic minerals in conjunction with epidote.
Quartz 35%	Rounded phenocrysts evenly distributed throughout the groundmass. Often contain inclusions of altered plagioclase crystals and rarely epidote. Abundant v.f.g. quartz is present in the aplitic groundmass. The only mineral that hasn't been strongly altered.
Titanite 1%	Subhedral sphenoid crystals (<1mm) with corroded margins and anhedral crystals are dispersed throughout the groundmass. Also occurs as replacements of skeletal magnetite.
Opaques 1%	<1mm crystals throughout the groundmass. Smaller crystals are generally euhedral while larger crystals are skeletal and replaced by titanite along fractures. Relict boundaries of skeletal magnetite imply primary magnetite was also euhedral.
Calcite 3%	V.f.g. alteration product of many plagioclase phenocrysts. Replaces a significant amount of a single large, relict amphibole phenocryst where it occurs as a single, optically continuous crystal intergrown with chlorite.

Textures: Crowded, porphyritic texture with an aplitic to fine-grained equigranular groundmass.

Alteration: Chlorite + epidote ± calcite alteration has completely replaced all primary mafic minerals which were most likely hornblende based on crystal shape of relict phenocrysts. Plagioclase phenocrysts have been pervasively altered to muscovite ± calcite ± epidote. Plagioclase alteration is not concentrated in the cores of phenocrysts as observed in the QFPP and aplite dykes.

Mineralization: None observed

Paragenetic Comments: Pervasive chlorite and epidote alteration has completely replaced all igneous mafic phenocrysts. Some quartz phenocrysts contain plagioclase inclusions indicating a later crystallization. Igneous plagioclase is pervasively altered to muscovite, calcite and epidote.

Sample: MD027   **Facies:** FQPC   **Name:** Crowded Quartz- and Feldspar-Phyric, Porphyry Dyke

Hand Sample Description: Crowded porphyritic texture with 40% phenocrysts set in a fine-grained equigranular groundmass. Rounded quartz phenocrysts (2 to 3mm) account for ~5% of the phenocryst population. Plagioclase phenocrysts account for ~25% of the sample and occur in two types. The first is as white, earthy phenocrysts that appear to be altered to clays. The second have a more glassy lustre and pale grey colour, and are less altered. Mafic phenocrysts (1 to 3mm; 10%) are anhedral, interstitial to the quartz and plagioclase phenocrysts and altered to chlorite and epidote. Approximately 5% v.f.g. anhedral K-spar occurs in the groundmass.

Mineral Name and Abundance	Description
	Primary Mineralogy
Plagioclase 30%	Plagioclase phenocrysts are tabular to elongate and subhedral. Crystals are variably affected by pervasive sericite and calcite and more rarely epidote which replaces between 5 to 70% of individual crystals. Alteration is not concentrated in cores of crystals as in QFPP and aplite dykes. Remnant polysynthetic twins are present in most crystals and the largest, least altered phenocrysts display concentric zoning. V.f.g. plagioclase occurs in the groundmass with quartz.
K-feldspar 5%	V.f.g. anhedral, found in interstitial groundmass.
Epidote 3%	Aggregates of 1mm or less crystals commonly occur with chlorite as a replacement of primary amphibole. Also alters from plagioclase, although much less prominent than in other samples of QFPC and FPC dykes.
Chlorite 7%	Occurs as matts of radiating crystals as well as shreddy replacements after amphibole. Closely associated with epidote in many cases. Has completely replaced all mafic minerals in conjunction with epidote.
Quartz 35%	5% 1 to 3mm, rounded phenocrysts occur sporadically throughout the groundmass. Abundant v.f.g. quartz is present in the aplitic groundmass. The only mineral that hasn't been strongly altered. Phenocrysts often contain inclusions of altered plagioclase.
Titanite 2%	Subhedral sphenoid crystals (<1mm) with corroded margins and anhedral crystals are dispersed throughout the groundmass. Sometimes occurs as replacements along fractures in skeletal magnetite grains and also sometimes contains apatite inclusions.
Opaques 3%	0.5 to 1mm crystals throughout the groundmass are relatively rare and often contain apatite inclusions. More abundant, much finer-grained crystals (<0.1mm) are generally anhedral and occur as inclusions in altered relict hornblende phenocrysts.
Calcite 5%	V.f.g. alteration product of many relict hornblende phenocrysts in addition to chlorite and epidote.

Apatite <1%	V.f.g. inclusions in magnetite/titanite and also in the groundmass. Crystals are generally euhedral longitudinal prisms or hexagons in cross-section.

Textures: Crowded, porphyritic texture with a fine-grained equigranular groundmass.

Alteration: Chlorite + epidote alteration has completely replaced all primary mafic minerals which were most likely hornblende based on crystal shape of relict phenocrysts. Plagioclase phenocrysts have been pervasively altered to sericite ± calcite ± epidote. Plagioclase alteration is not concentrated in the cores of phenocrysts as observed in the QFPP and aplite dykes.

Mineralization: None observed

Paragenetic Comments: Pervasive chlorite and epidote alteration has completely replaced all igneous mafic phenocrysts. Some quartz phenocrysts contain plagioclase inclusions indicating a later crystallization. Igneous plagioclase is pervasively altered to sericite, calcite and epidote.

Sample: MD026   **Facies:** FQPC   **Name:** Crowded Quartz- and Feldspar-Phyric, Porphyry Dyke

Hand Sample Description: White to grey coloured sample with a crowded, porphyritic texture with an aplitic to fine-grained equigranular groundmass. Approximately 5% rounded, 1 to 2mm quartz phenocrsysts. Sample contains approximately 40% tabular to elongate, 1 to 3mm plagioclase phenocrysts. Mafic minerals account for ~10% of the sample. Mafics are altered to chlorite and more rarely epidote and predominantly occur interstitially to phenocrysts with rare outsized phenocrysts. Sample is stained and does not show the presence of K-feldspar.

Mineral Name and Abundance	Description
	Primary Mineralogy
Plagioclase 44%	Plagioclase phenocrysts are tabular to elongate and subhedral. Crystals are variable affected by pervasive muscovite, calcite and epidote (5 to 85% of individual crystals). Alteration is not concentrated in cores of crystals as in QFPP and aplite dykes. Remnant polysynthetic twins are present in most crystals and least altered crystals are sometimes zoned. V.f.g., strongly altered plagioclase occurs in the groundmass with quartz.
Epidote 2%	Aggregates of 1mm or smaller crystals commonly occur with chlorite as a replacement of primary amphibole. V.f.g. epidote alteration is common in many plagioclase phenocrysts.
Chlorite 8%	Occurs as matts of radiating crystals as well as shreddy replacements after amphibole. Closely associated with epidote in many cases. Has completely replaced all mafic minerals in conjunction with epidote.
Quartz 35%	5% 1 to 3mm, rounded phenocrysts occur sporadically throughout the groundmass. Phenocrysts often contain inclusions of altered plagioclase. Abundant v.f.g. quartz is present in the aplitic groundmass. The only mineral that hasn't been strongly altered.
Titanite 2%	Subhedral sphenoid crystals (<1mm) with corroded margins and anhedral crystals are dispersed throughout the groundmass, often in close association with magnetite.
Opaques 3%	<1mm crystals throughout the groundmass. Crystals are generally anhedral. Sometimes in association with titanite. Commonly contains inclusions of apatite. Also occurs as inclusions in relict amphibole phenocrysts where it is likely an alteration product of the primary amphibole.
Calcite 5%	V.f.g. alteration product of many plagioclase phenocrysts. Also locallly abundant in the groundmass.
Apatite 1%	V.f.g. euhedral inclusions in magnetite crystals.

Textures: Crowded, porphyritic texture with an aplitic to fine-grained equigranular groundmass.

Alteration: Chlorite + epidote alteration has completely replaced all primary mafic minerals which were most likely hornblende based on crystal shape of relict phenocrysts. Plagioclase phenocrysts have been pervasively altered to muscovite ± calcite ± epidote. Plagioclase alteration is not concentrated in the cores of phenocrysts as observed in the QFPP and aplite dykes.

Mineralization: None observed

Paragenetic Comments: Pervasive chlorite and epidote alteration has completely replaced all igneous mafic phenocrysts. Some quartz phenocrysts contain plagioclase inclusions indicating a later crystallization. Igneous plagioclase is pervasively altered to sericite and calcite with lesser epidote.

Sample: MD022   **Facies:** FPC   **Name:** Crowded Feldspar-Phyric, Porphyry Dyke

Hand Sample Description: Crowded porphyritic rock composed of ~3% rounded quartz (1 to 2mm), ~25% tabular to elongated plagioclase (1 to 3mm) and ~10% mafic (0.5 to 2mm; hornblende?) phenocrysts set in an aplitic matrix. Feldspars have an earthy lustre and are altered to sericite/clays. Sample is stained and no orthoclase is present.

Mineral Name and Abundance	Description
	Primary Mineralogy
Plagioclase 45%	Plagioclase phenocrysts are tabular to elongate and subhedral. Crystals are pervasively altered by 20 to 60% muscovite, calcite and epidote. Alteration is not concentrated in cores of crystals as in QFPP and aplite dykes. Remnant polysynthetic twins are present in most crystals and they also appear to lack zoning. V.f.g. plagioclase occurs in the groundmass with quartz.
Epidote 7%	Aggregates of 1mm or less crystals commonly occur with chlorite as a replacement of primary amphibole. Partial to complete replacement of plagioclase crystals with minor calcite is more rare, but more common than in MD028.
Chlorite 10%	Occurs as matts of radiating crystals as well as shreddy replacements after amphibole. Closely associated with epidote in many cases. Has completely replaced all mafic minerals in conjunction with epidote.
Quartz 30%	3% 1 to 2mm, rounded phenocrysts occur sporadically throughout the groundmass. Abundant v.f.g. quartz is present in the aplitic groundmass. The only mineral that hasn't been strongly altered.
Titanite 1%	Subhedral sphenoid crystals (<1mm) with corroded margins and anhedral crystals are dispersed throughout the groundmass. Also occurs as replacements of skeletal magnetite.
Opaques 2%	<1mm crystals throughout the groundmass. Crystals are generally anhedral and some crystals are skeletal and replaced by titanite along fractures.
Calcite 5%	V.f.g. alteration product of many plagioclase phenocrysts. Also locallly abundant in the groundmass.
Chalcopyrite (Tr.)	V.f.g. inclusions in quartz phenocrysts

Textures: Crowded, porphyritic texture with an aplitic to fine-grained equigranular groundmass.

Alteration: Chlorite + epidote alteration has completely replaced all primary mafic minerals which were most likely hornblende based on crystal shape of relict phenocrysts. Plagioclase phenocrysts have been pervasively altered to muscovite ±

calcite ± epidote. Plagioclase alteration is not concentrated in the cores of phenocrysts as observed in the QFPP and aplite dykes.

Mineralization: Trace pyrite.

Paragenetic Comments: Pervasive chlorite and epidote alteration has completely replaced all igneous mafic phenocrysts. Some quartz phenocrysts contain plagioclase inclusions indicating a later crystallization. Igneous plagioclase is pervasively altered.

Sample: MD029   **Facies:** FPC   **Name:** Crowded Feldspar-Phyric, Porphyry Dyke

Hand Sample Description: Crowded porphyritic texture (~50% phenocrysts) with a reddish, aplititc groundmass. Plagioclase (0.5 to 4mm) phenocrysts are tabular to elongate and account for ~70% of the total phenocrysts population. The remaining 30% of phenocrysts are 0.5 to 1mm anhedral mafics (hornblende?) with rare outsized phenocrysts (3-5mm). Mafic phenocrysts are altered to chlorite and epidote.

Mineral Name and Abundance	Description
	Primary Mineralogy
Plagioclase 40%	Plagioclase phenocrysts are tabular to elongate and subhedral. Crystals are pervasively altered by 20 to 75% calcite, epidote and muscovite. Alteration is not concentrated in cores of crystals as in QFPP and aplite dykes. Remnant polysynthetic twins are rare and they also appear to lack zoning. V.f.g. plagioclase occurs in the groundmass with quartz.
Epidote 5%	Aggregates of 1mm or less crystals commonly occur with chlorite as a replacement of primary amphibole.
Chlorite 10%	Occurs as matts of radiating crystals as well as shreddy replacements after amphibole. Closely associated with epidote in many cases. Has completely replaced all mafic minerals in conjunction with epidote and magnetite.
Quartz 30%	Rarely occurs as 1 to 3mm, rounded phenocrysts throughout the groundmass. Abundant v.f.g. quartz is present in the aplitic groundmass. The only mineral that hasn't been strongly altered.
Titanite 1%	Sub- to anhedral crystals (<1mm) dispersed throughout the groundmass. Also occurs with chlorite inside relict amphibole phenocrysts.
Opaques 3%	<0.5mm crystals throughout the groundmass. Crystals are generally anhedral. Coarser crytsals contain inclusions of apatite. Coarser crystals are often in contact with chlorite.
Calcite 10%	V.f.g. alteration product of many plagioclase phenocrysts. Also locallly abundant in the groundmass.
Apatite 1%	V.f.g. euhedral, hexagonal crystals occur as inclusions in magnetite.

Textures: Crowded, porphyritic texture with an aplitic to fine-grained equigranular groundmass.

Alteration: Chlorite + epidote alteration has completely replaced all primary mafic minerals which were most likely hornblende based on crystal shape of relict phenocrysts. Plagioclase phenocrysts have been pervasively altered to muscovite ± calcite ± epidote. Plagioclase alteration is not concentrated in the cores of phenocrysts as observed in the QFPP and aplite dykes.

Mineralization: None observed.

Paragenetic Comments: Pervasive chlorite and epidote alteration has completely replaced all igneous mafic phenocrysts. Some quartz phenocrysts contain plagioclase inclusions indicating a later crystallization. Igneous plagioclase is pervasively altered.

Sample: MD031 **Facies:** FPC **Name:** Crowded Feldspar-Phyric, Porphyry Dyke

Hand Sample Description: Approximately 15% 0.5 to 5mm, fresh hornblende phenocrysts. Hornblendes are mostly elongate, needle-like prism although clotted, oikocrysts with plagioclase chadacrysts are present. Approximately 40% euhedral, glassy plagioclase phenocrysts 2 to 4mm in size and with tabular to elongate prismatic habit. Rounded quartz phenocrysts (2 to 3mm) are rare (~1%). Groundmass is aplitic and pinkish in colour, most likely K-feldspar (~15%).

Mineral Name and Abundance	Description
	Primary Mineralogy
Plagioclase 35%	Plagioclase phenocrysts are tabular to elongate and subhedral. Crystals are weakly altered by <5% sericite. Alteration is not concentrated in cores of crystals. Polysynthetic twins are present in most crystals and concentric zoning is common. Composite phenocrysts appear to have formed by fusing of two or more smaller crystals and are especially easy to identify when the fused phenocrysts display zoning which is discontinuous across the fused contact. Deformation twinning is common. Some crystals display abnormal 'domained' twinning, where two to three domains exist in a single crystal that contain twinning that is perpendicular to that in adjacent zones. Crystals represent single phenocrysts as many contain concentric zoning that is overprinted by the perpendicular domain twinning. Smaller, altered chadacrysts occur in amphibole oikocrysts.
Amphibole (15%)	1 to 2mm needle shaped longitudinal sections and 2 to 3mm diamond shaped cross-sections. Cross-sections are subhedral, and most often occur as half diamonds with an irregular grain boundary. Rare outsized phenocrysts (up to 6mm) are optically continuous oikocrysts, with inclusions of finer-grained plagioclase chadacrysts
Epidote (Tr.)	V.f.g. trace epidote occurs as replacement of amphibole.
Chlorite (Tr.)	Trace chlorite occurs as alteration of v.f.g. hornblende crystals.
Quartz 35%	Sub-mm (<0.25mm) rounded quartz crystals occur interstitially to the plagioclase and amphibole phenocrysts as well as the groundmass orthoclase. The quartz is aplitic and sugary in texture. 1 to 3mm serrated quartz phenocrysts are rare.
Titanite <1%	Sub- to anhedral sphenoid crystals (<1mm) are dispersed throughout the groundmass.
Opaques 5%	<1 to 2mm crystals throughout the groundmass. Crystals are generally anhedral and coarser crystals are sometimes partially rimmed by chlorite, titanite and contain inclusions of apatite.
Apatite <1%	V.f.g. inclusions in the coarser magnetite crystals.
K-feldspar (orthoclase) 10%	F.g., 0.5 to 1mm anhedral orthoclase occurs interstitial to amphibole and plagioclase phenocrysts. Pervasively altered to clays (~10 to

60% of individual crystals).

Textures: Crowded, porphyritic texture with an aplitic to fine-grained equigranular groundmass. Sparse, oikocrystic, outsized amphibole phenocrysts.

Alteration: Trace chlorite and epidote alteration of amphibole phenocrysts. Trace sericite alteration of plagioclase. 10 to 60% clay alteration of orthoclase.

Mineralization: None observed.

Paragenetic Comments: Trace chlorite and epidote alteration has affected select igneous mafic phenocrysts. Igneous plagioclase is weakly altered (<5%) to sericite. Large amphibole phenocrysts poikilitically enclose finer-grained plagioclase chadarysts.

Sample: MD032 **Facies:** FPC **Name:** Crowded Feldspar-Phyric, Porphyry Dyke

Hand Sample Description: Approximately 10% K-feldspar occurs interstitially. Easily identified by yellow colour as sample is stained for orthoclase.

Mineral Name and Abundance	Description
	Primary Mineralogy
Plagioclase 35%	Plagioclase phenocrysts are tabular to elongate and subhedral. Crystals have been variably affected by pervasive alteration (<5 to 50%) by sericite and calcite. Alteration is not concentrated in cores of crystals as in QFPP and aplite dykes. Polysynthetic and deformation twins are present in most crystals and concentric zoning is common. Fused phenocrysts are common as in MD031.
Epidote (Tr.)	Trace, v.f.g. epidote occurs sparsely scattered throughout the groundmass
Amphibole 5%	1 to 3mm anhedral phenocrysts. Most has been altered to biotite and chlorite. Uncommon outsized phenocrysts (5 to 7mm) that poikilitically enclose plagioclase chadacrysts.
Biotite 3%	Shreddy alteration of amphibole. Lesser, primary biotite may also be present. Often seen being altered to chlorite.
Chlorite 7%	Occurs as alteration of biotite which alters amphibole. Not observed in direct contact with amphibole, but commonly in contact with biotite. Evidence for alteration of amphibole → biotite → chlorite. Sometimes forms clotted masses with magnetite and titanite.
Quartz 50%	Rarely occurs as ~2mm, rounded phenocrysts with serrated grain bondaries. Abundant v.f.g., rounded quartz is present in the aplitic groundmass.
Titanite 2%	Subhedral sphenoid crystals (<1mm) with corroded margins and anhedral crystals are dispersed throughout the groundmass. Also occurs as replacements of skeletal magnetite and in clotted masses with magnetite and chlorite.
Opaques 3%	<1mm magnetite crystals throughout the groundmass. Crystals are generally anhedral and some crystals are skeletal and replaced by titanite along fractures. Often occur in clotted masses with chlorite and titanite. Apatite inclusions are relatively common.
Apatite <1%	V.f.g. inclusions in magnetite
K-feldspar 10%	V.f.g. K-feldspar occurs interstitially to plagioclase phenocrysts. Difficult to distinguish from altered plagioclase in thin section but easily identified in hand sample due to staining. Pervasive clay alteration (60 to 95%).

Textures: Crowded, porphyritic texture with an aplitic to fine-grained equigranular groundmass. Outsized, poikilitic amphibole phenocrysts.

Alteration: Chlorite + biotite alteration has replaced most primary mafic minerals which were most likely hornblende based on crystal shape of relict phenocrysts. Plagioclase phenocrysts have been pervasively altered to sericite ± calcite. Plagioclase alteration is not concentrated in the cores of phenocrysts as observed in the QFPP and aplite dykes. Pervasive clay alteration has affected K-feldspar. Replacement of skeletal magnetite by titanite along fractures.

Mineralization: None observed.

Paragenetic Comments: Pervasive biotite and chlorite alteration has partially replaced all igneous mafic phenocrysts. Igneous plagioclase is pervasively altered by weak sericite and calcite alteration. Titanite replaces skeletal magnetite crystals. Pervasive clay alteration of K-feldspars common.

Sample: MD073   **Facies:** QFPM   **Name:** Quartz- and Feldspar-Phyric, Matrix Supported Porphyry

Hand Sample Description: Matrix supported, porphyritic texture with approximately 30% phenocrysts. Approximately 5% rounded to hexagonal and octahedral euhedral quartz phenocrysts (2 to 7mm), often containing fractures. 25% sub- to euhedral plagioclase phenocrysts with tabular to elongate shapes. Plagioclase phenocrysts have a bimodal size distribution with small 1 to 2mm and large 4 to 10mm crystal populations. Larger phenocrysts contain cores that have a vitreous or waxy lustre and white, chalky rims. The population of small plagioclase phenocrysts are more completely altered to white, earthy clays/sericite. The larger phenocrysts are often composites of smaller, fused plagioclase phenocrysts. Approximately 10% (0.5 to 1mm) mafic phenocrysts with subhedral needle to diamond shapes. The groundmass is aphanitic and grey in colour.

Mineral Name and Abundance	Description
	Primary Mineralogy
Plagioclase 25%	Occurs as phenocrysts with a bimodal size distribution. Populations are ~0.5 to 2mm and 4 to 10mm. Smaller phenocrysts are pervasively altered to sericite (70 to 90%). Larger crystals are often composites composed of numerous finer-grained phenocrysts that have been fused along irregular boundaries. Rims of larger crystals are commonly altered to sericite (~70 to 90%) but do not generally affect most of the interior portion of crystals. Concentric zoning is common in larger phenocrysts but also occurs in smaller ones.
Biotite 1%	Shreddy biotite is largely altered to chlorite along cleavage planes. Often contains epidote between cleavages probably resulting from biotitization of primary amphibole.
Epidote 1%	Rare crystals occur between cleavage planes in biotite and chlorite.
Chlorite 8%	Partial to complete alteration of biotite along cleavage planes. Sometimes contains epidote in between cleavages that is possibly a remnant of biotitization of primary amphiboles. Sometimes partially rimmed by calcite.
Quartz 63%	Rounded to hexagonal and octahedral phenocrysts (5%) and microphenocrysts (0.1 to 0.5mm). Makes up the majority of the groundmass where it occurs as <<0.1mm, rounded crystals.
Tourmaline (Tr.)	Euhedral, 0.1mm prismatic crystals that occur as inclusions in quartz phenocrysts.
Opaques 2%	Sub- to euhedral opaques occur throughout the groundmass and as inclusions in altered amphibole phenocrysts. One crystal observed that is skeletal and replaced by titanite. Generally 0.1 to 1mm.
Calcite 3%	Alteration product of (amphibole?) sometimes seen rimming chlorite. V.f.g. mottled appearance. Also common in patches in the groundmass. More rarely an alteration product of plagioclase phenocrysts.

Textures: Matrix-supported porphyritic texture. Contains used phenocrysts with concentric zoning.

Alteration: Biotitization of primary amphibole as well as chloritization of amphibole and biotite. Sericite alteration is common in plagioclase phenocrysts. Calcite alteration of amphibole is suspected due to spatial association with chlorite and biotite. Calcite is also observed as an alteration product of plagioclase phenocrysts. Replacement by titanite occurs in skeletal magnetite crystals.

Mineralization: None observed

Paragenetic Comments: Quartz and plagioclase phenocrysts formed prior to crystallization of aphanitic groundmass. Most igneous phenocrysts affected by some degree of later alteration with the exception of quartz.

Sample: MD036   **Facies:**QFPP   **Name:** Phenocryst-poor feldspar-phyric porphyry dyke

Hand Sample Description: Tan coloured, holocrystalline porphyritic rock with 1 to 5mm phenocrysts of qz, ksp and pl. Sample is phenocryst poor (~5 to 7%) and supported by an aphanitic tan groundmass. Phenocrysts vary from rounded (mostly qz) to subhedral, tabular prisms (pl + qz).

Mineral Name and Abundance	Description
	Primary Mineralogy
Quartz 2%	1 to 3mm phenocrysts scattered throughout the groundmass. Most crystals are rounded and 'blob' shaped with rarer equant, hexagonal crysals
Plagioclase 3%	1 to 5mm phenocrysts scattered throughout the groundmass. Phenocrysts are variably altered to a mixture of sericite, f.g. muscovite and calcite. Alteration has completely replaced many phenocrysts which are only discernable by relict grain boundaries. Where crystals have not been completely replaced, sericite/muscovite alteration is concentrated in the cores and calcite along fractures. Remnant polysynthetic twins are still visible in the least altered phenocrysts
K-Feldspar 1%	Large ~2 to 5mm phenocrysts with tabular, subhedral shapes. Faint, undulatory albite exsolution lamellae present
Muscovite 5%	0.5 to 1mm phenocrysts. Flaky crystals with "shreddy" grain boundaries. Occurs throughout groundmass. Finer-grained muscovite is a common alteration product of plagioclase whwere it occurs as randomly oriented grains in aggregates concentrated in the cores of phenocrysts with sericite
Groundmass 87%	V.f.g. (<<1mm) mixture of quartz, K-feldspar and plagioclase and their alteration products white mica (sericite + muscovite) and calcite. Flakes of muscovite are coarse enough to be observed. Accurate visual estimation of modal abundances of the constituent minerals impossible due to extremely small crystal size.
Calcite 1%	F.g. patchy alteration in plagioclase phenocrysts concentrated along fractures. Also occurs in groundmass though small crystal size makes accurate estimation of modal abundance difficult.
Sericite/Muscovite 1%	Randomly oriented crystals of v.f.g. sericite to f.g. flaky muscovite alteration is concentrated in the cores of plagioclase phenocrysts. Abundant muscovite is also present in the groundmass, though estimation of its abundance is complicated by small grainsize

Textures: Phenocryst-poor, matrix supported porphyritic

Alteration: Moderate to complete pervasive sericite/muscovite and calcite after plagioclase

Mineralization: None observed

Paragenetic Comments: Sericite/muscovite and calcite alteration overprints igneous plagioclase phenocrysts

Sample: MD037 **Facies:** QFPP **Name:** Phenocryst-poor feldspar-phyric porphyry dyke

Hand Sample Description: Purple-brown coloured, holocrystalline porphyritic rock with 1 to 5mm phenocrysts of qz, ksp and pl. Sample is phenocryst poor (~15%) and supported by an aphanitic, siliceous, purple-brown groundmass. Phenocrysts vary from rounded (mostly qz) to subhedral, tabular prisms (pl + ksp).

Mineral Name and Abundance	Description
	Primary Mineralogy
Quartz 7%	1 to 2mm, hexagonal, sub- to euhedral phenocrysts
Plagioclase 4%	1 to 5mm lath shaped and tabular, sub- to euhedral phenocrysts. Trace to complete pervasive alteration by sericite and v.f.g. calcite concentrated in the cores of crystals. Some crystals are almost completely altered but have thin (<0.25m), unaltered rims. Polysynthetic twinning common in all but the most altered phenocrysts. Small, unaltered crystals occasionally enclosed by larger K-spar phenocrysts
K-Feldspar 2%	2 to 4mm euhedral, tabular phenocrysts. Generally unaltered
Biotite <1%	1mm flaky phenocrysts
Opaques<1%	V.f.g. (~0.25mm) subhedral crystals throughout groundmass and sometimes included in plagioclase phenocrysts
Groundmass 83%	V.f.g. mixture of quartz, plagioclase, K-feldspar and associated alteration products (mostly sericite with lesser v.f.g. muscovite and calcite)
Calcite 1%	V.f.g patchy alteration of plagioclase phenocrysts. Generally <<1mm with largest patches up to 0.25mm
Sericite 2%	Moderate to complete pervasive sericite alteration occurs concentrated in the cores of plagioclase phenocrysts as well as in the groundmass.

Textures: Phenocryst-poor, matrix supported porphyritic

Alteration: Moderate to complete pervasive sericite and patchy calcite after plagioclase

Mineralization: None observed

Paragenetic Comments: Sericite/muscovite and calcite alteration overprints igneous plagioclase phenocrysts. Small plagioclase phenocrysts seen enclosed in one larger K-spar phenocryst. Some inclusions of opaque minerals in feldspar phenocrysts.

Sample: MD038   **Facies:** QFPP   **Name:** Phenocryst-poor feldspar-phyric porphyry dyke

Hand Sample Description: Tan coloured, holocrystalline porphyritic rock with 1 to 2mm phenocrysts of qz, ksp and pl. Sample is phenocryst poor (~7%) and supported by an aphanitic, siliceous, tan groundmass. Phenocrysts vary from rounded (mostly qz) to subhedral, tabular prisms (pl + ksp).

Mineral Name and Abundance	Description
	Primary Mineralogy
Quartz 3%	F.g. rounded phenocrysts dispersed throughout the groundmass. Crystals vary from ~0.25 to 1mm in size. Also found in thin, ~0.25mm veins with calcite where it is the predominant component and as a minor component in thicker veins composed primarily of calcite
Plagioclase 3%	1 to 2mm tabular to lath shaped relict phenocrysts. All phenocrysts have been completely altered to a mixture composed predominantly of cryptocrystalline to sub-mm calcite crystals and f.g. flaky muscovite (typically less than 0.25mm but rarely up to ~1mm)
K-feldspar 1%	1 to 2mm tabular, euhedral phenocrysts. Many contain faint, undulatoryexsolutions of albite (perthitic texture)
Calcite1%	0.25 to 1mm crystals of calcite occur in 0.25 to 1mm thick veins that cut across the groundmass
Muscovite <1%	Trace ~1mm muscovite phenocrysts (after biotite?)
Opaques<1%	Trace opaques occur in the groundmass and as inclusions in relict plagioclase phenocrysts
Groundmass 92%	V.f.g. mixture of quartz, plagioclase, K-feldspar and associated alteration products (mostly calcite with lesser v.f.g. muscovite and sericite)
Calcite 3%	Occurs as pervasive alteration on plagioclase phenocrysts which it completely alters. Crystals are randomly oriented and crystals up to 0.5mm are common and surrounded by patchy, cryptocrystalline aggregates
Muscovite/Sericite <1%	Trace alteration product of plagioclase phenocrysts. Relatively rare compared to other QFPP samples

Textures: Phenocryst-poor, matrix supported porphyritic

Alteration: Moderate to complete pervasive calcite and trace muscovite/sericite after plagioclase

Mineralization: None observed

Paragenetic Comments: Complete replacement of biotite phenocrysts by muscovite. Pervasive calcite and less common sericite/muscovite alteration overprints and completely replaces igneous plagioclase phenocrysts

Sample: MD040   **Facies:** Aplite Dyke   **Name:** Aplite Dyke

Hand Sample Description: Pink coloured, phenocryst-poor porphyritic rock with aplitic, sugary groundmass. Phenocrysts are predominantly 1 to 4mm tabular to lath shaped, relict plagioclase crystals that have been altered to clays giving them a pitted chalky appearance. Lesser 2 to 10mm quartz phenocrysts also occur. The aplitic groundmass contains abundant K-feldspar (40%) and Quartz (40%) with lesser plagioclase (20%). Trace mafic phenocrysts (<1mm) may be biotite.

Mineral Name and Abundance	Description
	Primary Mineralogy
Quartz 47%	3 to 7mm with highly irregular, serrated grain boundaries. Undulatory extinction and subgrain boundaries common, and some phenocrysts contain pods of v.f.g. quartz that show no deformation features. Some of these pods are completely enclosed in the phenocrysts but others are connected to the groundmass and they are interpreted to have formed by ductile deformation and grainsize reduction. Abundant v.f.g. (0.5mm) anhedral quartz is in the groundmass. Phenocrysts are rimmed by v.f.g. quartz and plagioclase (no K-feldspar) in the groundmass which coarsens away from the phenocrysts.
Plagioclase 15%	1 to 4mm randomly oriented phenocrysts distributed throughout the groundmass. Cores of phenocrysts are pervasively altered to sericite with lesser calcite and epidote. Degree of alteration varies from 10 to 85% of individual phenocrysts, primarily affecting the cores of phenocrysts with approximately 0.5mm unaltered rims. Phenocrysts are elongated prisms with serrated, irregular faces that are impinged upon by numerous smaller (<0.25mm) rounded plagioclase crystals. The smaller crystals may have originally been part of the larger phenocrysts and formed by grainsize reduction based on their shape and relationship. V.f.g. (<0.5mm) rounded crystals also occur in the groundmass and are easily identified by their polysynthetic twinning and they lack alteration.Phenocrysts are rimmed by v.f.g. quartz and plagioclase (no K-feldspar) in the groundmass which coarsens away from the phenocrysts.
K-feldspar 35%	Anhedral K-feldspar occurs interstitially to quartz and plagioclase phenocrysts as well as quartz and plagioclase in the groundmass. Tartan twinning is present and crystals are unaltered.
Biotite < 1%	<0.5mm flaky crystals in the groundmass
Pyrite (Tr.)	
Opaques 2%	0.1 to 1mm predominantly subhedral crystals in the groundmass. Some crystals have cubic form.
Rutile (Tr.)	V.f.g. <0.25mm occurs interstitial to quartz and felspars
Zircon (Tr.)	V.f.g. (<0.1mm) crystals in the groundmass
Calcite 1%	Occurs as a cryptocrystalline alteration product of plagioclase

feldspars. Also occurs as infill material in discontinuous, microscopic fractures and one 0.1mm thick vein that can be traced across the entire thin section.

Textures: Phenocryst-poor, porphyritc texture with aplitic groundmass.

Alteration: Pervasive sericite and calcite alteration of plagioclase phenocrysts.

Mineralization: One 5mm blob of massive, f.g. pyrite.

Paragenetic Comments:K-spar is interstitial, most likely formed after quartz and plagioclase phenocrysts and groundmass quartz and plagioclase

Pervasive sericite and calcite alteration of igneous plagioclase phenocrysts.

Quartz (and possibly plagioclase) phenocrysts have undergone grainsize reduction

Sample: MD050   **Facies:** Aplite Dyke   **Name:** Aplite Dyke

Hand Sample Description: Pink coloured with a phaneritic, ineguigranular texture. Sample is composed predominantly of a sugary and aplitic groundmass with slightly coarser (1 to2mm) plagioclase, quartz, K-feldspar and hornblende + biotite crystals. Feldspars are pervasively altered to clays. The sample contains a contact with the Bethlehem facies which it cuts, and there is no chill margin between the two units.

Mineral Name and Abundance	Description
	Primary Mineralogy
Quartz 30%	0.5 to 1mm anhedral quartz occurs intermingled with K-feldspar and plagioclase
Plagioclase 29%	Occurs as 1 to 3mm crystals with irregular, serrate grain boundaries. Crystals are weakly altered by patchy sericite (up to 10%)
K-feldspar 35%	1 to 3mm crystals with irregular, serrate grain boundaries. Weak patchy clay alteration (<5%)
Biotite 4%	Shreddy biotite crystals occur as individual crystals throughout the sample and also as radial aggregates centered on opaqued (magnetite?) crystals. Chlorite alteration occurs along cleavage planes where it replaces ~30 to 50% of the primary biotite
Chlorite 1%	Alteration of biotite concentrated along cleavage planes
Opaques 1%	0.25 to 0.5mm prismatic (cubic and octahedral) sub- to anhedral crystals
Zircon (Tr.)	Prismatic, sub- to euhedral crystals included in biotite/chlorite, generally <0.05mm
Apatite (Tr.)	Euhedral, hexagonal crystals included in biotites and opaques(<0.05mm)

Textures: Inequigranular texture with aplitic groundmass.

Alteration: Pervasive clay alteration of plagioclase phenocrysts.

Mineralization: None observed

Paragenetic Comments: Pervasive clay alteration of igneous plagioclase phenocrysts.

Sample: MD041   **Facies:** Aplite Dyke   **Name:** Aplite Dyke

Hand Sample Description: Pink, phenocryst-poor porphyritic rock with an aplitic groundmass. The groundmass is composed of a mixture of K-feldspar, quartz and plagioclase. Phenocrysts are 1 to 3mm lath-shaped to tabular plagioclase crystals that have been pervasively altered to clays giving them a chalky appearance, 1 to 2mm quartz eyes and <1mm biotite crystals.

Mineral Name and Abundance	Description
	Primary Mineralogy
Quartz 40%	<0.5mm an- to subhedral crystals with rounded hexagonal shapes. Some crystals contain inclusions of zircon.
Plagioclase 20%	Large, 1 to 3mm phenocrysts display oscillatory zoning and complex growth patterns (appears that two or more individual crystals have been fused). Phenocrysts are subhedral and elongate with much finer groundmass quartz and plagioclase growing into grain boundaries resulting in a serrated boundary. Patchy sericite alteration affects between 5 to 10% of individual phenocrysts and is focused in the cores of crystals or along fractures. Finer-grained plagioclase occurs in the groundmass (<0.5m)
K-feldspar 34%	0.25 to 1mm, anhedral crystals in the groundmass. 20 to 60% pervasive alteration to clays affects of most crystals
Biotite 1%	~0.5mm flaky crystals. Some are completely fresh but most have been variably altered to chlorite along cleavage planes.
Chlorite 2%	~0.5 flaky crystals. Occurs as an alteration product along cleavage planes in biotite as well as crystals with no associated biotite. Interpreted to have formed after biotite, even when no direct link to biotite is observed
Opaques 3%	<0.25mm crystals throughout groundmass. Sometimes occur in clusters with epidote and apatite.
Epidote <1%	Occurs as v.f.g. inclusions in chlorite, rarely in clusters with magnetite and as isolated crystals throughout the groundmass.
Apatite <1%	Inclusions in opaque minerals. Euhedral, hexagonal crystsals
Rutile (Tr.)	Isolated intergranular, anhedral crystals
Zircon (Tr.)	V.f.g. (<50um) crystals included in quartz

Textures: Phenocryst-poor, porphyritic rock with an aplitic groundmass

Alteration: Pervasive clay alteration of igneous plagioclase and K-feldspar phenocrysts

Mineralization: None observed

Paragenetic Comments: Plagioclase phenocrysts formed earlier then groundmass, but continued crystallizing during groundmass crystallization as evidenced by irregular grain

boundaries. Pervasive clay alteration of igneous plagioclase and K-feldspar phenocrysts.

APPENDIX C: WHOLE ROCK GEOCHEMISTRY

Sample	MD001	MD002	MD003	MD004	MD005	MD006	MD007	MD008
SiO_2 (wt%)	61.45	55.20	48.77	73.26	66.27	70.79	49.95	67.62
TiO_2	0.81	1.10	1.26	0.17	0.34	0.22	0.79	0.35
Al_2O_3	15.72	17.48	18.19	13.88	16.63	15.11	19.97	15.92
Fe_2O_3*	6.58	8.55	11.09	2.23	3.38	2.52	9.54	2.82
MnO	0.10	0.14	0.17	0.06	0.06	0.04	0.11	0.05
MgO	2.90	3.84	5.44	0.36	1.14	0.76	3.85	1.01
CaO	5.66	7.21	9.33	2.10	4.34	2.83	8.88	2.71
Na_2O	3.28	3.62	3.97	4.14	4.77	4.13	4.66	4.92
K2O	2.17	1.37	0.37	2.81	1.11	2.74	0.35	3.18
P_2O_5	0.14	0.30	0.33	0.06	0.15	0.08	0.35	0.14
LOI	0.90	0.70	0.80	0.70	1.60	0.50	1.20	1.00
Total	99.71	99.51	99.72	99.77	99.79	99.72	99.65	99.72
Ti (ppm)	4856	6595	7554	1019	2038	1319	4736	2098
P	611	1309	1440	262	655	349	1527	611
Cr	14.40	15.80	22.10	3.60	3.10	4.40	10.10	10.60
Co	15.60	19.60	14.20	2.10	6.80	4.30	14.90	4.80
Ni	14.50	15.60	14.30	0.90	3.10	2.50	8.30	5.70
Rb	72.40	31.40	1.60	44.80	12.80	29.50	2.60	71.60
Sr	423.60	720.90	894.50	399.80	680.70	500.10	1243.40	779.10
Cs	4.40	2.50	0.10	0.40	0.20	0.40	0.10	3.40
Ba	597.00	639.00	289.00	1171.00	695.00	1197.00	353.00	1361.00
Sc	16.00	20.00	25.00	2.00	5.00	3.00	18.00	4.00
V	153.00	254.00	274.00	23.00	51.00	43.00	270.00	45.00
Ta	0.30	0.20	0.10	0.20	0.10	0.10	0.10	0.90
Nb	3.50	2.60	3.00	1.60	1.60	1.20	0.90	11.90
Zr	156.80	1480.10	82.60	61.60	69.80	77.50	21.70	141.00
Hf	4.90	35.40	1.90	2.20	2.40	2.20	0.70	3.90
Th	7.70	3.30	0.30	2.40	1.90	1.80	0.20	5.20
U	3.70	2.00	0.10	0.60	0.80	0.50	0.10	1.70
Y	18.40	22.80	19.80	7.30	5.20	5.30	13.80	8.40
La	14.50	16.40	15.50	9.70	8.10	7.50	9.50	24.00
Ce	33.50	34.90	34.70	20.20	17.10	16.60	21.60	41.30
Pr	4.13	4.45	4.66	2.21	1.84	2.06	3.35	4.59
Nd	17.00	21.20	22.40	7.30	7.50	7.00	16.00	16.70
Sm	3.69	4.89	5.09	1.31	1.71	1.51	3.99	2.76
Eu	0.81	1.21	1.25	0.36	0.51	0.35	1.18	0.77
Gd	3.62	4.36	4.62	1.25	1.27	1.24	3.72	2.20
Tb	0.52	0.62	0.62	0.16	0.18	0.19	0.53	0.31
Dy	3.21	3.52	3.67	1.03	1.04	1.04	2.57	1.33
Ho	0.56	0.83	0.66	0.17	0.20	0.19	0.55	0.33
Er	1.90	2.42	2.01	0.48	0.50	0.73	1.35	0.92
Tm	0.29	0.39	0.24	0.10	0.09	0.09	0.17	0.14
Yb	1.93	2.34	1.68	0.73	0.54	0.56	1.17	0.95
Lu	0.33	0.39	0.24	0.12	0.10	0.10	0.16	0.13
Cu	132.24	164.97	188.44	24.54	4.28	8.51	290.84	4.69
Zn	51.40	52.00	41.40	29.10	33.60	24.60	54.60	44.40
Mo	2.52	0.75	0.15	0.16	0.21	0.19	0.12	2.65
Ag	0.07	0.06	0.07	0.04	0.01	0.01	0.08	0.01
Tl	0.12	0.03	0.02	0.02	0.02	0.02	0.02	0.31
Pb	1.53	1.10	0.53	1.65	0.94	1.07	0.50	2.33
Sn	1.00	1.00	1.00	1.00	1.00	1.00	1.00	1.00
Sb	0.12	0.04	0.02	0.03	0.07	0.02	0.02	0.04
Ga	16.20	19.60	19.90	13.20	15.60	14.20	22.90	16.80
Ge	0.20	0.10	0.10	0.10	0.10	0.10	0.10	0.10
As	2.50	1.60	0.90	0.60	1.40	1.60	1.00	0.50
W	1.20	1.30	0.50	0.50	0.50	0.80	0.50	0.50
Bi	0.11	0.04	0.02	0.02	0.02	0.02	0.02	0.06
Be	0.10	0.10	0.10	0.10	0.10	0.30	0.20	0.30
Pt (ppb)	4.00	2.00	5.00	2.00	3.00	2.00	2.00	2.00
Pd (ppb)	10.00	10.00	10.00	10.00	10.00	10.00	10.00	10.00

Sample	MD009	MD010	MD011	MD012	MD013	MD014	MD015	MD016
SiO$_2$ (wt%)	69.08	67.58	67.52	69.08	50.39	58.15	59.52	73.42
TiO$_2$	0.31	0.38	0.40	0.23	1.13	0.72	0.79	0.11
Al$_2$O$_3$	15.52	15.96	15.62	14.98	17.72	16.88	16.83	14.54
Fe$_2$O$_3$*	2.50	2.96	3.25	2.11	10.88	6.30	6.68	1.38
MnO	0.06	0.07	0.06	0.04	0.20	0.10	0.11	0.01
MgO	0.87	1.25	1.21	0.64	4.34	3.13	2.96	0.29
CaO	2.59	2.74	2.88	1.94	9.07	5.25	5.86	0.96
Na$_2$O	4.98	4.90	4.81	4.59	2.79	4.05	3.82	4.37
K2O	3.21	3.20	2.95	3.37	0.82	2.22	2.06	4.02
P$_2$O$_5$	0.13	0.16	0.20	0.09	0.18	0.20	0.23	0.05
LOI	0.40	0.50	0.80	2.70	2.30	2.70	0.80	0.50
Total	99.65	99.70	99.70	99.77	99.82	99.70	99.66	99.65
Ti (ppm)	1858	2278	2398	1379	6774	4316	4736	659
P	567	698	873	393	786	873	1004	218
Cr	9.90	15.00	16.20	10.10	6.10	13.60	11.90	4.90
Co	3.60	6.00	6.00	3.20	13.50	17.10	16.30	1.80
Ni	4.60	7.80	8.90	4.50	3.60	16.00	16.20	3.00
Rb	84.70	76.20	65.00	78.10	17.60	49.80	59.60	57.50
Sr	776.90	715.40	824.60	583.00	406.70	775.70	820.30	479.40
Cs	3.30	2.30	3.50	4.00	0.90	0.70	2.20	1.10
Ba	1274.00	1121.00	1172.00	994.00	311.00	884.00	845.00	1733.00
Sc	4.00	5.00	5.00	3.00	30.00	13.00	13.00	2.00
V	36.00	49.00	52.00	32.00	280.00	166.00	172.00	12.00
Ta	1.20	0.90	0.80	1.00	0.10	0.20	0.20	0.60
Nb	14.70	14.40	12.00	12.00	1.30	3.40	3.50	5.10
Zr	128.00	121.30	153.50	102.20	47.00	124.90	143.40	64.00
Hf	3.30	3.60	4.20	3.30	1.50	3.50	3.50	2.40
Th	5.30	7.20	7.70	8.90	0.70	3.50	4.10	4.90
U	3.50	4.10	2.70	4.30	0.60	1.90	1.80	2.10
Y	9.10	8.30	9.60	6.10	18.70	12.60	15.60	4.70
La	23.10	22.50	28.20	16.20	5.30	13.40	17.60	15.00
Ce	41.40	41.30	49.80	29.50	12.60	29.40	36.90	26.00
Pr	4.59	4.72	5.59	3.13	1.81	3.65	4.87	2.84
Nd	15.30	17.90	19.10	10.70	9.50	15.70	19.30	9.60
Sm	2.82	2.95	3.54	1.89	2.64	3.18	3.90	1.56
Eu	0.76	0.85	0.95	0.53	0.97	0.98	1.06	0.45
Gd	2.10	2.27	2.83	1.35	3.34	3.26	3.51	1.23
Tb	0.33	0.32	0.37	0.20	0.56	0.41	0.52	0.16
Dy	1.73	1.64	1.82	0.98	3.23	2.18	3.25	0.87
Ho	0.30	0.28	0.32	0.20	0.70	0.49	0.57	0.13
Er	0.98	0.85	1.00	0.60	2.15	1.59	1.59	0.48
Tm	0.14	0.13	0.13	0.10	0.29	0.20	0.25	0.06
Yb	0.93	0.89	0.95	0.77	2.21	1.39	1.58	0.51
Lu	0.16	0.15	0.13	0.13	0.30	0.19	0.26	0.09
Cu	12.51	3.12	2.11	6.25	21.50	171.16	73.73	2.72
Zn	40.80	48.90	40.90	38.30	35.00	75.00	62.80	13.10
Mo	0.28	0.20	0.35	0.79	0.31	0.40	0.49	0.10
Ag	0.04	0.02	0.02	0.03	0.02	0.10	0.05	0.00
Tl	0.34	0.37	0.26	0.20	0.06	0.03	0.15	0.05
Pb	1.32	1.81	0.79	2.34	0.56	1.08	0.86	1.45
Sn	2.00	1.00	1.00	1.00	1.00	1.00	1.00	1.00
Sb	0.07	0.02	0.07	0.05	0.02	0.02	0.02	0.02
Ga	17.40	17.10	15.70	16.50	15.40	18.80	18.60	15.80
Ge	0.10	0.10	0.10	0.10	0.10	0.10	0.10	0.10
As	0.80	0.30	0.70	0.70	0.50	1.20	1.40	0.90
W	0.50	1.50	0.80	0.50	0.50	0.50	0.50	0.50
Bi	0.04	0.04	0.08	0.23	0.02	0.11	0.04	0.16
Be	0.20	0.20	0.10	0.10	0.10	0.10	0.10	0.10
Pt (ppb)	2.00	2.00	2.00	2.00	2.00	2.00	2.00	2.00
Pd (ppb)	10.00	10.00	10.00	10.00	10.00	10.00	10.00	10.00

Sample	MD017	MD018	MD019	MD020	MD021	MD022	MD023	MD024
SiO$_2$ (wt%)	72.07	68.76	72.79	51.45	64.52	63.62	64.24	63.73
TiO$_2$	0.40	0.44	0.34	0.96	0.35	0.33	0.32	0.35
Al$_2$O$_3$	14.33	15.24	14.16	18.35	16.45	16.73	16.49	16.42
Fe$_2$O$_3$*	2.79	3.08	3.12	9.99	4.44	3.88	4.55	4.08
MnO	0.03	0.04	0.05	0.19	0.04	0.05	0.03	0.05
MgO	0.85	1.01	0.83	4.27	1.16	1.14	1.12	1.31
CaO	2.63	2.36	3.12	9.32	3.02	4.31	3.16	3.53
Na$_2$O	4.04	4.89	4.13	3.20	4.81	4.39	4.87	5.36
K2O	1.30	3.23	1.13	0.54	1.60	1.88	1.51	1.55
P$_2$O$_5$	0.05	0.22	0.08	0.13	0.13	0.12	0.13	0.14
LOI	1.30	0.40	0.10	1.40	3.30	3.30	3.40	3.30
Total	99.79	99.67	99.85	99.80	99.82	99.75	99.82	99.82
Ti (ppm)	2398	2638	2038	5755	2098	1978	1918	2098
P	218	960	349	567	567	524	567	611
Cr	7.30	11.80	7.00	4.30	5.30	4.50	4.20	4.00
Co	6.40	5.60	4.80	10.80	9.40	6.50	9.70	6.80
Ni	2.90	6.50	2.00	3.40	3.80	3.40	3.50	3.90
Rb	23.00	56.90	29.00	11.70	44.10	35.30	40.50	37.30
Sr	269.80	789.80	280.80	401.00	429.10	693.10	480.70	332.90
Cs	1.30	1.30	1.00	0.50	0.70	0.70	1.00	0.40
Ba	594.00	1387.00	325.00	251.00	656.00	887.00	655.00	538.00
Sc	5.00	3.00	3.00	28.00	5.00	5.00	5.00	5.00
V	57.00	52.00	44.00	226.00	62.00	63.00	67.00	74.00
Ta	0.10	0.40	0.10	0.10	0.10	0.10	0.10	0.10
Nb	1.00	5.70	1.80	2.50	1.50	1.40	1.90	1.40
Zr	170.40	125.10	135.80	64.10	77.30	77.30	71.80	68.90
Hf	3.90	4.00	3.40	1.70	2.30	2.30	1.60	2.00
Th	1.10	7.70	2.10	0.50	1.40	1.30	1.30	1.30
U	1.60	2.40	1.10	0.40	0.90	0.70	1.00	0.80
Y	9.30	5.90	7.40	19.10	5.80	6.00	6.70	6.00
La	11.30	22.80	8.00	6.80	10.50	9.20	7.80	8.10
Ce	20.90	41.70	13.40	14.90	18.60	18.50	17.90	16.40
Pr	2.32	5.18	1.64	2.02	2.35	2.25	2.18	2.03
Nd	10.00	21.40	7.10	10.20	10.80	10.40	9.00	8.50
Sm	1.83	3.88	1.27	2.79	1.95	1.74	1.82	1.69
Eu	0.88	1.00	0.77	0.98	0.50	0.55	0.61	0.53
Gd	1.82	2.50	1.24	3.56	1.38	1.42	1.86	1.33
Tb	0.28	0.27	0.19	0.54	0.19	0.20	0.21	0.20
Dy	1.54	1.29	1.09	3.25	1.07	1.03	1.32	1.16
Ho	0.31	0.16	0.24	0.79	0.22	0.24	0.22	0.21
Er	1.08	0.38	0.71	2.21	0.66	0.70	0.66	0.65
Tm	0.14	0.06	0.11	0.32	0.09	0.09	0.12	0.09
Yb	1.10	0.27	0.91	1.90	0.58	0.73	0.73	0.59
Lu	0.17	0.07	0.16	0.33	0.12	0.11	0.14	0.11
Cu	100.80	4.05	12.82	6.30	76.20	403.07	11.20	1.91
Zn	15.30	67.90	20.00	31.00	20.60	20.10	10.90	19.70
Mo	1.70	0.19	0.24	0.20	5.23	4.78	0.93	0.29
Ag	0.03	0.01	0.01	0.01	0.06	0.03	0.01	0.00
Tl	0.07	0.27	0.11	0.02	0.02	0.02	0.02	0.02
Pb	0.35	1.65	0.30	0.81	0.47	1.12	0.57	0.59
Sn	1.00	1.00	1.00	2.00	1.00	1.00	1.00	1.00
Sb	0.02	0.02	0.02	0.02	0.19	0.15	0.19	0.31
Ga	12.30	20.10	12.30	17.40	16.40	16.30	16.50	17.20
Ge	0.10	0.10	0.10	0.10	0.10	0.10	0.10	0.10
As	0.60	0.70	0.90	0.60	0.80	0.90	1.00	1.30
W	1.30	0.50	0.50	2.00	1.50	0.50	1.10	0.50
Bi	0.04	0.02	0.02	0.02	0.02	0.02	0.03	0.06
Be	0.10	0.10	0.10	0.10	0.20	0.20	0.20	0.20
Pt (ppb)	2.00	2.00	2.00	2.00	2.00	2.00	2.00	2.00
Pd (ppb)	10.00	10.00	10.00	10.00	10.00	10.00	10.00	10.00

Sample	MD025	MD026	MD027	MD028	MD029	MD030	MD031	MD032
SiO$_2$ (wt%)	64.50	65.85	64.88	64.39	64.45	64.20	66.50	66.15
TiO$_2$	0.34	0.32	0.35	0.34	0.33	0.32	0.32	0.32
Al$_2$O$_3$	16.75	16.71	16.55	16.22	16.28	16.06	16.77	16.98
Fe$_2$O$_3$*	3.20	3.91	3.45	3.73	3.40	3.47	3.32	3.12
MnO	0.05	0.03	0.04	0.05	0.05	0.05	0.04	0.03
MgO	1.22	1.13	1.24	1.21	1.07	1.10	1.08	1.06
CaO	3.75	3.79	3.30	3.90	4.36	3.98	4.40	3.72
Na$_2$O	5.07	5.44	6.28	4.69	4.03	3.55	4.77	4.57
K2O	1.56	0.45	0.75	1.60	1.95	2.17	1.35	1.39
P$_2$O$_5$	0.13	0.13	0.14	0.14	0.13	0.15	0.13	0.15
LOI	3.30	2.00	2.80	3.50	3.70	4.90	1.10	2.30
Total	99.87	99.76	99.78	99.77	99.75	99.95	99.78	99.79
Ti (ppm)	2038	1918	2098	2038	1978	1918	1918	1918
P	567	567	611	611	567	655	567	655
Cr	4.80	4.80	4.20	3.60	3.60	3.40	4.10	3.30
Co	5.30	5.50	6.70	7.10	6.10	6.80	3.90	5.80
Ni	3.70	3.80	3.10	3.40	3.20	3.50	2.80	2.80
Rb	41.80	9.70	18.80	34.50	48.60	61.50	18.20	18.90
Sr	521.50	787.10	629.10	605.70	656.80	199.50	813.40	725.10
Cs	0.70	0.40	0.30	0.70	0.90	0.50	0.30	0.70
Ba	219.00	375.00	203.00	875.00	932.00	467.00	882.00	777.00
Sc	5.00	5.00	5.00	5.00	5.00	4.00	4.00	4.00
V	64.00	61.00	69.00	65.00	58.00	60.00	63.00	63.00
Ta	0.10	0.10	0.10	0.10	0.10	0.10	0.10	0.10
Nb	0.80	1.40	1.60	1.60	1.40	1.50	1.40	2.10
Zr	78.20	68.00	75.90	75.00	70.80	66.70	74.80	115.50
Hf	2.20	1.60	1.50	2.40	1.80	2.00	2.00	3.10
Th	1.30	1.30	1.30	1.30	1.20	0.90	1.60	1.30
U	1.00	0.90	0.90	0.70	0.80	0.80	0.80	0.80
Y	6.70	5.90	6.60	6.50	5.90	5.70	6.70	5.30
La	9.50	8.50	8.30	10.00	5.30	7.20	9.00	8.90
Ce	18.80	17.10	17.00	20.90	10.10	14.40	19.20	16.40
Pr	2.16	2.13	2.12	2.75	1.36	1.93	2.22	2.03
Nd	8.20	8.40	9.10	10.60	6.10	8.00	7.90	8.70
Sm	1.64	1.56	1.71	2.04	1.24	1.52	1.49	1.70
Eu	0.58	0.48	0.59	0.60	0.50	0.51	0.55	0.58
Gd	1.44	1.33	1.40	1.57	1.12	1.24	1.53	1.52
Tb	0.19	0.17	0.21	0.22	0.17	0.17	0.20	0.19
Dy	1.09	1.02	1.08	1.23	1.28	1.05	1.22	1.06
Ho	0.22	0.20	0.19	0.20	0.20	0.19	0.23	0.21
Er	0.47	0.48	0.65	0.62	0.65	0.61	0.57	0.63
Tm	0.10	0.08	0.09	0.09	0.08	0.08	0.10	0.12
Yb	0.65	0.69	0.61	0.64	0.70	0.56	0.68	0.50
Lu	0.12	0.11	0.11	0.10	0.11	0.09	0.11	0.13
Cu	111.57	90.04	313.19	38.75	38.80	1.40	75.97	438.27
Zn	12.70	16.90	27.60	25.60	22.00	20.20	7.40	17.80
Mo	0.33	0.60	0.29	2.15	0.70	0.37	0.27	0.31
Ag	0.12	0.02	0.11	0.02	0.02	0.00	0.02	0.05
Tl	0.02	0.02	0.02	0.02	0.02	0.02	0.02	0.02
Pb	0.68	2.04	1.52	0.60	0.62	0.48	1.56	1.00
Sn	1.00	1.00	1.00	1.00	1.00	1.00	1.00	1.00
Sb	0.16	0.10	0.25	0.13	0.09	0.14	0.07	0.02
Ga	17.70	16.20	16.70	16.10	15.60	15.30	16.10	18.60
Ge	0.10	0.10	0.10	0.10	0.10	0.10	0.10	0.10
As	0.70	1.50	2.40	0.80	1.00	0.90	1.30	4.10
W	0.90	0.60	0.50	0.70	0.50	2.50	0.80	1.60
Bi	0.02	0.02	0.06	0.03	0.02	0.06	0.02	0.02
Be	0.20	0.40	0.30	0.10	0.20	0.30	0.30	0.30
Pt (ppb)	2.00	2.00	2.00	2.00	2.00	2.00	2.00	2.00
Pd (ppb)	10.00	10.00	10.00	10.00	10.00	10.00	10.00	10.00

Sample	MD033	MD034	MD035	MD036	MD037	MD038	MD039	MD040
SiO$_2$ (wt%)	65.40	66.28	66.87	74.99	74.35	72.40	37.09	76.57
TiO$_2$	0.35	0.34	0.33	0.06	0.06	0.06	1.91	0.08
Al$_2$O$_3$	17.25	16.84	16.86	13.91	14.04	13.15	10.61	12.35
Fe$_2$O$_3$*	3.53	3.55	3.27	1.00	1.18	0.92	10.75	1.12
MnO	0.03	0.06	0.07	0.02	0.04	0.04	0.15	0.03
MgO	1.05	1.07	1.00	0.24	0.23	0.37	8.60	0.17
CaO	5.80	4.27	4.08	1.01	0.92	3.86	12.69	0.81
Na$_2$O	4.34	4.83	4.78	3.41	4.15	0.28	0.18	3.73
K2O	0.09	1.62	1.74	3.36	3.68	3.82	1.54	4.11
P$_2$O$_5$	0.12	0.13	0.12	0.11	0.11	0.12	1.28	0.03
LOI	1.80	0.90	0.70	1.80	1.10	4.90	14.40	0.90
Total	99.76	99.89	99.82	99.91	99.86	99.92	99.20	99.90
Ti (ppm)	2098	2038	1978	360	360	360	11450	480
P	524	567	524	480	480	524	5586	131
Cr	4.20	4.30	3.30	2.80	3.30	1.40	232.80	3.90
Co	6.50	4.30	4.00	0.70	0.50	0.20	42.90	0.60
Ni	3.70	2.60	2.70	0.70	1.10	0.20	274.10	1.70
Rb	1.20	24.60	26.80	55.80	52.70	71.60	36.50	64.10
Sr	1059.30	721.80	714.90	176.00	185.40	71.10	1296.20	87.40
Cs	0.30	0.60	1.70	1.50	0.60	2.70	24.80	1.50
Ba	170.00	815.00	835.00	505.00	672.00	561.00	2195.00	450.00
Sc	4.00	4.00	3.00	1.00	1.00	1.00	21.00	3.00
V	73.00	62.00	62.00	8.00	8.00	8.00	203.00	8.00
Ta	0.10	0.10	0.20	0.50	0.50	0.40	2.20	0.20
Nb	1.50	1.50	1.70	4.00	3.90	3.50	35.80	2.90
Zr	73.10	68.80	77.20	21.40	21.50	19.50	144.70	50.60
Hf	1.70	2.00	2.80	0.90	0.80	1.00	3.60	2.90
Th	1.10	1.30	1.70	0.20	0.20	0.20	8.20	3.90
U	0.40	0.70	0.60	1.60	1.20	1.30	2.80	0.90
Y	5.40	6.10	5.80	6.70	6.70	5.80	16.90	5.30
La	9.10	9.40	9.90	3.40	3.40	2.80	74.20	19.10
Ce	17.30	18.80	18.00	6.30	6.50	5.40	161.20	30.00
Pr	2.35	2.36	2.24	0.80	1.01	0.78	21.06	2.75
Nd	9.60	9.90	9.30	3.40	3.30	2.70	87.30	7.20
Sm	1.63	1.72	1.66	0.83	0.95	0.72	11.85	0.96
Eu	0.52	0.52	0.49	0.11	0.09	0.08	3.24	0.12
Gd	1.32	1.53	1.39	1.01	0.98	0.83	8.23	0.69
Tb	0.18	0.21	0.19	0.16	0.17	0.14	0.85	0.11
Dy	0.95	1.25	0.95	1.00	0.98	0.87	3.71	0.64
Ho	0.19	0.22	0.20	0.20	0.22	0.17	0.59	0.13
Er	0.48	0.65	0.61	0.51	0.53	0.48	1.29	0.51
Tm	0.09	0.09	0.10	0.08	0.08	0.08	0.19	0.09
Yb	0.61	0.69	0.56	0.63	0.72	0.61	1.14	0.80
Lu	0.11	0.09	0.11	0.09	0.09	0.08	0.15	0.16
Cu	67.37	5.78	16.90	44.05	223.82	37.34	62.30	41.18
Zn	8.30	19.30	30.10	5.80	11.70	4.90	104.80	10.60
Mo	0.59	0.28	0.17	3.46	18.57	2.03	0.21	0.39
Ag	0.02	0.01	0.02	0.01	0.09	0.02	0.04	0.20
Tl	0.02	0.02	0.02	0.02	0.03	0.03	0.02	0.02
Pb	0.53	1.10	1.07	1.02	0.96	0.75	5.90	2.14
Sn	1.00	1.00	1.00	1.00	1.00	1.00	1.00	1.00
Sb	0.23	0.02	0.02	0.02	0.04	0.19	0.13	0.06
Ga	15.60	16.70	17.80	14.70	15.20	14.40	14.40	13.60
Ge	0.10	0.10	0.10	0.10	0.10	0.10	0.20	0.10
As	1.90	0.60	0.40	1.70	1.10	3.30	7.30	5.50
W	0.70	0.50	0.50	0.90	0.60	1.50	1.00	1.00
Bi	0.02	0.02	0.02	0.02	0.07	0.02	0.04	0.02
Be	0.20	0.10	0.20	0.10	0.10	0.30	1.60	0.10
Pt (ppb)	2.00	2.00	2.00	2.00	2.00	2.00	2.00	2.00
Pd (ppb)	10.00	10.00	10.00	10.00	10.00	10.00	10.00	10.00

Sample	MD041	MD042	MD043	MD044	MD045	MD046	MD047	MD048
SiO$_2$ (wt%)	76.36	71.75	63.14	61.43	62.45	52.28	67.13	68.53
TiO$_2$	0.10	0.17	0.52	0.59	0.53	0.95	0.46	0.42
Al$_2$O$_3$	12.80	15.21	16.95	16.98	16.96	18.93	15.12	14.80
Fe$_2$O$_3$*	1.39	1.73	4.79	5.24	4.80	8.12	4.06	3.67
MnO	0.03	0.04	0.08	0.08	0.09	0.10	0.05	0.04
MgO	0.13	0.41	2.19	2.67	2.29	4.60	1.59	1.37
CaO	0.77	2.64	5.10	4.96	5.23	8.96	3.29	2.94
Na$_2$O	3.66	4.44	4.46	4.34	4.37	4.24	3.80	3.70
K2O	4.63	2.72	1.95	2.06	1.93	0.32	3.32	3.29
P$_2$O$_5$	0.05	0.08	0.15	0.16	0.16	0.26	0.11	0.12
LOI	0.00	0.60	0.40	1.30	1.00	1.00	0.80	0.90
Total	99.92	99.79	99.73	99.81	99.81	99.76	99.73	99.78
Ti (ppm)	600	1019	3117	3537	3177	5695	2758	2518
P	218	349	655	698	698	1135	480	524
Cr	3.40	1.80	6.00	9.60	7.90	20.50	8.80	7.70
Co	1.10	2.40	7.30	9.40	8.20	7.90	7.10	6.60
Ni	0.80	1.00	5.70	10.30	6.80	10.50	7.50	7.60
Rb	74.20	46.10	41.20	48.00	46.00	3.90	92.90	98.50
Sr	84.00	485.90	656.90	609.90	679.40	868.90	494.10	438.60
Cs	0.40	0.80	0.80	0.80	0.80	0.30	1.50	1.10
Ba	676.00	1214.00	689.00	677.00	627.00	265.00	809.00	813.00
Sc	2.00	2.00	9.00	10.00	10.00	20.00	7.00	6.00
V	17.00	24.00	114.00	128.00	117.00	244.00	96.00	82.00
Ta	0.40	0.20	0.10	0.20	0.20	0.10	0.20	0.20
Nb	2.60	1.90	1.90	1.90	2.20	1.80	3.50	3.20
Zr	58.10	71.00	96.60	96.50	96.50	101.00	199.50	190.10
Hf	2.90	2.60	3.30	2.30	2.60	2.60	5.80	5.60
Th	5.60	2.80	2.70	3.20	5.50	0.70	8.10	9.60
U	2.20	1.00	1.60	1.70	2.50	0.40	2.30	2.30
Y	5.90	4.40	9.60	8.80	9.80	10.90	12.60	12.50
La	17.20	9.40	11.40	10.90	14.00	8.70	19.20	17.70
Ce	26.70	16.50	24.70	22.10	27.50	20.30	41.60	37.90
Pr	2.59	1.98	3.41	3.17	3.51	2.78	4.85	4.72
Nd	8.60	7.20	14.90	13.30	14.60	13.60	18.00	19.40
Sm	1.04	1.18	2.61	2.45	2.78	2.60	3.68	3.30
Eu	0.14	0.32	0.74	0.73	0.76	0.96	0.76	0.64
Gd	0.79	0.98	2.30	1.99	2.28	2.74	2.96	2.79
Tb	0.12	0.13	0.32	0.28	0.31	0.38	0.41	0.38
Dy	0.84	0.74	1.72	1.72	1.68	2.19	2.54	2.08
Ho	0.17	0.14	0.38	0.23	0.31	0.41	0.44	0.46
Er	0.50	0.47	1.00	0.77	1.11	1.10	1.45	1.29
Tm	0.10	0.06	0.15	0.12	0.15	0.17	0.21	0.20
Yb	0.78	0.51	1.03	0.84	1.00	1.00	1.41	1.37
Lu	0.16	0.09	0.17	0.13	0.16	0.14	0.20	0.21
Cu	4.35	3.61	127.59	75.19	23.86	39.76	120.83	117.13
Zn	11.50	24.40	28.20	32.60	33.20	11.00	23.40	14.50
Mo	0.19	0.10	0.33	0.36	0.32	0.29	0.48	0.45
Ag	0.01	0.00	0.05	0.04	0.01	0.01	0.03	0.02
Tl	0.02	0.02	0.02	0.02	0.03	0.02	0.03	0.02
Pb	2.66	1.04	1.09	1.43	1.06	0.86	1.37	1.68
Sn	1.00	1.00	1.00	1.00	1.00	1.00	1.00	1.00
Sb	0.03	0.02	0.03	0.05	0.04	0.02	0.08	0.06
Ga	13.30	15.10	17.40	18.10	18.20	20.10	15.90	14.80
Ge	0.10	0.10	0.10	0.10	0.10	0.10	0.10	0.10
As	0.30	0.40	0.60	1.30	0.70	1.00	1.90	1.00
W	0.50	0.50	0.50	0.50	0.50	0.50	0.50	0.50
Bi	0.02	0.02	0.04	0.03	0.03	0.02	0.03	0.09
Be	0.20	0.20	0.40	0.20	0.10	0.10	0.20	0.30
Pt (ppb)	2.00	2.00	2.00	2.00	2.00	3.00	2.00	2.00
Pd (ppb)	10.00	10.00	10.00	10.00	10.00	10.00	10.00	10.00

Sample	MD049	MD050	MD051	MD052	MD053	MD054	MD055	MD056
SiO$_2$ (wt%)	65.50	75.79	60.86	65.82	66.05	64.66	65.67	67.50
TiO$_2$	0.39	0.09	0.65	0.37	0.33	0.52	0.35	0.29
Al$_2$O$_3$	16.99	12.96	17.05	16.97	16.97	16.50	17.41	16.71
Fe$_2$O$_3$*	3.65	1.45	5.72	3.53	3.32	4.53	2.80	3.11
MnO	0.06	0.02	0.08	0.04	0.04	0.07	0.04	0.06
MgO	1.32	0.18	2.95	1.28	1.12	1.88	1.16	0.88
CaO	4.45	1.04	5.68	4.63	4.23	4.55	6.18	3.82
Na$_2$O	4.84	3.47	3.93	4.76	4.74	4.26	4.47	4.65
K2O	1.65	4.51	1.68	1.75	1.51	1.91	0.21	1.79
P$_2$O$_5$	0.15	0.03	0.16	0.15	0.14	0.16	0.12	0.12
LOI	0.80	0.40	1.00	0.50	1.40	0.70	1.40	0.90
Total	99.80	99.94	99.76	99.80	99.85	99.74	99.81	99.83
Ti (ppm)	2338	540	3897	2218	1978	3117	2098	1739
P	655	131	698	655	611	698	524	524
Cr	4.00	3.20	18.30	5.00	4.00	10.10	3.50	4.00
Co	5.20	1.40	11.80	3.40	5.10	9.20	5.10	4.00
Ni	2.70	1.00	16.10	2.90	3.20	8.60	3.40	2.20
Rb	27.90	71.30	45.50	29.40	17.90	43.30	1.50	26.70
Sr	758.90	170.30	739.00	750.10	710.40	669.00	994.20	695.00
Cs	0.50	0.60	1.00	0.70	0.20	1.20	0.50	0.90
Ba	1015.00	600.00	593.00	743.00	722.00	664.00	299.00	838.00
Sc	5.00	1.00	12.00	5.00	5.00	9.00	5.00	4.00
V	75.00	18.00	137.00	69.00	62.00	103.00	69.00	57.00
Ta	0.10	0.10	0.30	0.10	0.10	0.10	0.10	0.10
Nb	1.60	0.60	1.90	1.70	1.50	2.20	1.30	1.50
Zr	84.40	43.70	125.40	85.90	70.30	123.60	74.90	70.30
Hf	2.20	1.60	3.60	2.20	1.90	3.20	2.20	2.20
Th	1.80	2.80	4.10	2.20	1.80	4.50	1.30	1.40
U	0.70	1.10	1.80	1.40	0.80	2.30	0.60	0.70
Y	6.40	1.30	11.60	7.10	6.20	10.10	6.10	5.10
La	9.40	3.80	13.30	9.50	9.40	11.70	7.70	10.00
Ce	18.70	4.70	27.90	18.80	18.70	25.50	15.90	19.30
Pr	2.34	0.45	3.52	2.50	2.28	3.24	2.00	2.16
Nd	8.90	1.40	12.20	10.80	8.90	12.50	9.20	8.60
Sm	1.77	0.32	2.65	1.81	1.38	2.54	1.65	1.70
Eu	0.54	0.10	0.80	0.54	0.51	0.67	0.55	0.55
Gd	1.46	0.26	2.50	1.57	1.42	2.12	1.32	1.34
Tb	0.20	0.03	0.33	0.21	0.19	0.31	0.19	0.18
Dy	1.16	0.15	2.02	1.25	1.02	1.74	1.06	0.97
Ho	0.21	0.05	0.37	0.24	0.22	0.32	0.21	0.20
Er	0.63	0.14	1.11	0.78	0.65	1.02	0.69	0.51
Tm	0.09	0.03	0.16	0.11	0.09	0.16	0.10	0.09
Yb	0.65	0.18	1.04	0.74	0.68	0.99	0.69	0.61
Lu	0.10	0.05	0.16	0.09	0.11	0.16	0.11	0.09
Cu	21.25	3.14	100.06	82.76	18.33	131.75	77.25	95.08
Zn	21.70	8.00	26.50	7.30	9.80	28.40	10.40	22.30
Mo	0.29	0.22	1.37	1.52	0.54	2.07	0.20	0.36
Ag	0.02	0.01	0.04	0.03	0.00	0.04	0.01	0.05
Tl	0.02	0.02	0.03	0.02	0.02	0.05	0.02	0.03
Pb	0.89	1.48	1.11	1.20	1.49	1.48	0.77	1.11
Sn	1.00	1.00	1.00	1.00	1.00	1.00	1.00	1.00
Sb	0.02	0.02	0.09	0.07	0.06	0.15	0.37	0.05
Ga	17.50	12.80	17.80	16.30	16.60	15.90	16.40	17.40
Ge	0.10	0.10	0.10	0.10	0.10	0.10	0.10	0.10
As	0.40	0.50	1.50	1.50	1.40	2.00	1.70	0.30
W	0.50	0.80	0.80	0.70	0.50	0.70	1.10	1.90
Bi	0.02	0.02	0.03	0.03	0.02	0.17	0.08	0.08
Be	0.10	0.10	0.10	0.10	0.40	0.20	0.30	0.10
Pt (ppb)	2.00	2.00	2.00	2.00	2.00	2.00	2.00	2.00
Pd (ppb)	10.00	10.00	10.00	10.00	10.00	10.00	10.00	10.00

MD057	MD058	MD059	MD060	MD061	MD062	MD063	MD064
56.32	60.09	65.72	65.83	66.13	68.55	67.19	66.06
0.94	0.79	0.36	0.36	0.50	0.40	0.44	0.54
16.80	16.35	17.34	16.95	15.49	14.83	15.26	15.58
7.84	6.28	3.40	3.39	4.35	3.32	3.74	4.36
0.13	0.08	0.07	0.05	0.06	0.04	0.05	0.07
3.72	2.86	1.17	1.10	2.07	1.41	1.47	2.01
6.25	4.62	4.63	4.46	4.10	3.46	3.67	4.25
4.06	4.25	4.89	4.83	3.80	4.42	4.00	4.08
2.08	2.76	1.57	1.46	2.61	2.13	3.12	2.25
0.25	0.20	0.15	0.14	0.12	0.12	0.12	0.15
1.30	1.50	0.50	1.20	0.50	1.10	0.60	0.40
99.69	99.78	99.80	99.77	99.73	99.78	99.66	99.75
5635	4736	2158	2158	2998	2398	2638	3237
1091	873	655	611	524	524	524	655
18.90	12.90	3.60	4.50	15.40	5.90	6.20	10.60
15.30	9.20	4.10	5.00	8.70	5.90	5.90	8.50
14.30	9.40	2.50	2.50	11.70	5.60	4.80	10.50
73.30	68.90	25.30	20.50	67.30	47.40	56.80	43.90
716.80	555.30	810.60	833.90	534.30	519.50	541.90	507.50
1.50	1.90	0.60	0.30	1.00	0.60	0.90	0.90
637.00	561.00	805.00	846.00	703.00	615.00	1040.00	688.00
17.00	15.00	5.00	5.00	9.00	6.00	7.00	8.00
194.00	138.00	73.00	82.00	107.00	76.00	81.00	99.00
0.30	0.50	0.10	0.20	0.10	0.30	0.30	0.10
3.20	4.00	1.30	1.40	3.20	3.10	3.00	2.60
155.50	162.90	62.90	97.40	110.60	160.10	158.90	150.80
3.90	5.20	2.30	2.20	3.60	4.40	4.70	4.40
4.60	12.30	1.10	1.50	5.30	4.60	2.70	3.60
1.90	7.90	0.60	0.70	2.20	2.10	1.40	1.50
16.50	17.40	6.50	5.80	11.50	15.40	13.90	7.50
16.90	22.10	9.10	9.10	15.90	16.00	14.10	12.90
38.10	46.30	17.80	18.30	34.50	38.20	37.60	25.20
5.00	5.40	2.27	2.17	3.81	5.08	5.05	3.11
20.60	21.50	8.60	9.40	16.00	19.90	21.40	12.40
4.06	3.91	1.66	1.88	2.96	3.95	4.13	2.11
0.94	0.94	0.54	0.61	0.68	0.68	0.81	0.65
3.77	3.59	1.60	1.51	2.44	3.20	3.39	1.72
0.54	0.54	0.21	0.21	0.37	0.48	0.50	0.25
3.14	3.33	1.13	1.32	2.39	2.33	2.85	1.16
0.53	0.64	0.22	0.19	0.37	0.49	0.55	0.27
1.74	1.73	0.56	0.56	1.19	1.48	1.42	0.91
0.24	0.28	0.10	0.11	0.19	0.24	0.21	0.12
1.61	1.99	0.58	0.65	1.22	1.61	1.46	0.80
0.26	0.33	0.10	0.10	0.21	0.23	0.23	0.14
185.66	485.63	9.59	6.11	53.16	28.12	198.74	71.37
42.70	16.10	16.40	15.00	27.00	16.90	19.80	23.80
0.80	2.19	0.23	0.23	0.46	0.57	0.75	0.35
0.05	0.11	0.01	0.00	0.03	0.02	0.08	0.05
0.08	0.02	0.02	0.02	0.09	0.02	0.04	0.07
2.39	2.51	0.67	0.81	0.64	1.53	1.21	1.04
1.00	2.00	1.00	1.00	1.00	1.00	1.00	1.00
0.16	0.29	0.02	0.05	0.02	0.06	0.03	0.03
17.20	16.70	17.90	18.70	14.80	15.00	14.50	14.40
0.10	0.10	0.10	0.10	0.10	0.10	0.10	0.10
3.00	3.70	0.30	0.80	0.40	1.20	0.30	0.90
1.00	0.80	0.50	0.50	0.70	0.50	0.50	0.50
0.09	0.05	0.03	0.02	0.04	0.02	0.07	0.05
0.30	0.30	0.10	0.10	0.10	0.30	0.20	0.10
2.00	3.00	2.00	2.00	2.00	2.00	2.00	2.00
10.00	13.00	10.00	10.00	10.00	10.00	10.00	10.00

Sample	MD065	MD066	MD067	MD068	MD069	MD070	MD071	MD072
SiO$_2$ (wt%)	69.86	63.63	65.00	69.00	68.97	68.70	69.54	68.20
TiO$_2$	0.26	0.53	0.46	0.26	0.26	0.28	0.23	0.30
Al$_2$O$_3$	15.92	16.08	15.99	16.35	16.21	16.29	15.79	16.52
Fe$_2$O$_3$*	2.55	5.10	4.31	2.54	2.59	2.69	2.50	2.90
MnO	0.05	0.08	0.08	0.06	0.05	0.05	0.06	0.06
MgO	0.82	2.42	1.93	0.77	0.83	0.84	0.74	0.93
CaO	3.45	5.09	4.46	3.44	3.31	3.66	3.12	3.82
Na$_2$O	4.39	4.02	4.50	4.73	4.63	4.68	4.61	4.57
K2O	1.98	1.98	1.97	1.92	2.26	1.88	2.09	1.86
P$_2$O$_5$	0.11	0.16	0.14	0.10	0.11	0.10	0.10	0.12
LOI	0.40	0.70	0.90	0.60	0.50	0.60	1.00	0.50
Total	99.79	99.79	99.74	99.77	99.72	99.77	99.78	99.78
Ti (ppm)	1559	3177	2758	1559	1559	1679	1379	1799
P	480	698	611	436	480	436	436	524
Cr	4.10	5.80	8.50	3.90	4.30	3.80	4.40	3.90
Co	4.00	8.10	6.90	4.00	4.00	4.30	3.60	4.30
Ni	2.30	6.00	5.90	2.10	1.90	2.40	1.90	2.30
Rb	32.50	46.00	30.30	32.30	45.60	29.40	35.10	33.00
Sr	614.80	720.90	652.10	623.80	634.60	651.00	583.30	636.20
Cs	0.50	0.90	0.30	0.70	1.00	0.70	0.40	1.10
Ba	893.00	713.00	724.00	828.00	959.00	915.00	861.00	814.00
Sc	3.00	8.00	8.00	4.00	3.00	3.00	3.00	4.00
V	48.00	113.00	101.00	47.00	53.00	50.00	42.00	52.00
Ta	0.20	0.10	0.10	0.20	0.10	0.10	0.20	0.10
Nb	1.90	2.00	2.00	1.50	1.60	1.60	1.60	1.50
Zr	58.70	101.80	99.40	51.80	54.00	68.40	64.40	74.80
Hf	1.50	3.60	2.90	1.80	1.50	2.00	2.10	2.40
Th	1.70	2.40	2.30	1.50	1.50	1.50	2.00	1.80
U	0.60	1.70	1.00	1.00	1.20	0.80	0.80	1.00
Y	8.20	9.70	9.60	4.90	5.00	5.30	4.60	5.60
La	10.20	11.10	12.50	7.80	9.10	8.80	9.10	8.60
Ce	23.40	24.40	26.30	16.10	16.40	16.80	16.10	16.10
Pr	3.03	3.30	3.26	1.81	2.02	1.94	1.81	1.94
Nd	13.10	14.50	15.70	7.10	6.70	7.20	6.30	7.80
Sm	2.14	2.69	2.52	1.24	1.45	1.51	1.21	1.32
Eu	0.50	0.71	0.68	0.45	0.44	0.40	0.43	0.44
Gd	1.80	2.30	2.24	1.11	1.19	1.21	1.05	1.11
Tb	0.25	0.31	0.29	0.15	0.16	0.16	0.14	0.16
Dy	1.36	1.80	1.57	0.88	0.94	0.76	0.58	0.95
Ho	0.33	0.32	0.35	0.19	0.16	0.23	0.18	0.18
Er	0.77	1.06	0.99	0.52	0.57	0.46	0.47	0.51
Tm	0.13	0.15	0.15	0.06	0.08	0.07	0.07	0.09
Yb	0.83	1.06	1.03	0.49	0.60	0.54	0.60	0.70
Lu	0.11	0.17	0.16	0.09	0.10	0.08	0.09	0.09
Cu	1.44	12.33	29.75	31.99	17.19	4.74	3.72	2.86
Zn	17.80	26.00	24.40	29.60	17.80	18.10	33.60	24.00
Mo	0.18	0.29	0.29	0.16	0.28	0.36	0.72	0.20
Ag	0.01	0.01	0.03	0.04	0.01	0.01	0.01	0.01
Tl	0.03	0.03	0.02	0.02	0.04	0.03	0.02	0.03
Pb	0.81	1.06	0.87	1.29	0.64	0.97	1.92	0.93
Sn	1.00	1.00	1.00	1.00	1.00	1.00	1.00	1.00
Sb	0.02	0.06	0.02	0.03	0.02	0.04	0.02	0.04
Ga	15.80	16.40	16.80	16.20	16.30	15.90	16.60	15.60
Ge	0.10	0.10	0.10	0.10	0.10	0.10	0.10	0.10
As	0.60	0.60	0.30	0.50	0.40	0.70	0.60	0.50
W	0.50	0.50	0.50	0.50	0.50	0.60	0.50	0.50
Bi	0.02	0.03	0.03	0.05	0.03	0.02	0.02	0.02
Be	0.10	0.20	0.20	0.10	0.20	0.10	0.40	0.10
Pt (ppb)	2.00	2.00	2.00	2.00	2.00	2.00	2.00	2.00
Pd (ppb)	10.00	10.00	10.00	10.00	10.00	10.00	10.00	10.00

Sample	MD073	MD074	MD075	MD076	MD078
SiO_2 (wt%)	71.65	60.98	61.89	63.1	49.81
TiO_2	0.15	0.62	0.61	0.6	0.96
Al_2O_3	15.24	16.46	16.55	16.09	19.32
Fe_2O_3*	1.89	5.82	5.59	5.36	10.08
MnO	0.06	0.09	0.08	0.08	0.16
MgO	0.40	2.88	2.8	2.62	5.25
CaO	2.32	5.43	5.39	4.95	9.11
Na_2O	4.95	3.88	3.94	3.83	3.77
K2O	1.89	2.16	2.07	2.27	0.49
P_2O_5	0.07	0.14	0.15	0.14	0.3
LOI	1.10	1.3	0.7	0.7	0.5
Total	99.72	99.71	99.73	99.74	99.74
Ti (ppm)	899	3716.9	3656.95	3597	5755.2
P	305	610.96	654.6	610.96	1309.2
Cr	3.80	20.8	19.3	16.2	22.1
Co	1.70	12.1	11.5	10.6	11.7
Ni	0.70	16.3	15.9	14.7	14.9
Rb	29.50	60.2	57	65.1	9.2
Sr	625.80	727.7	695.1	630.3	840.2
Cs	0.70	1.7	1.3	2	0.5
Ba	1077.00	734	688	717	335
Sc	2.00	12	11	11	21
V	19.00	138	138	138	267
Ta	0.10	0.2	0.1	0.2	0.05
Nb	1.60	3	3	2.7	1.6
Zr	54.90	149.7	130.6	146.5	40.4
Hf	1.40	4.1	3.8	4.1	1.1
Th	0.60	5.6	5.5	5.4	0.6
U	0.60	2	1.8	2.2	0.4
Y	4.90	13.4	11.2	12.3	10.9
La	7.80	14.3	13.7	13.8	9.5
Ce	13.60	32.9	30.9	30.9	21.6
Pr	1.53	4.14	3.75	3.83	2.85
Nd	6.10	16.1	16.4	16.7	12.2
Sm	0.96	3.21	3.13	2.99	2.5
Eu	0.28	0.89	0.84	0.79	1.04
Gd	0.82	2.8	2.68	2.63	2.59
Tb	0.13	0.38	0.38	0.38	0.38
Dy	0.74	2.48	2.09	2.1	2.25
Ho	0.16	0.44	0.44	0.47	0.41
Er	0.59	1.28	1.21	1.32	1.16
Tm	0.07	0.2	0.18	0.21	0.16
Yb	0.65	1.27	1.34	1.24	1.09
Lu	0.09	0.21	0.18	0.2	0.16
Cu	9.53	144.96	146.21	123.33	67.11
Zn	16.20	35.1	33.2	39.4	33.4
Mo	0.21	0.93	0.79	0.69	0.81
Ag	0.02	48	51	35	27
Tl	0.02	0.06	0.07	0.06	0.01
Pb	2.37	1.78	1.52	3.35	1.24
Sn	1.00	0.5	0.5	0.5	0.5
Sb	0.10	0.09	0.08	0.1	0.07
Ga	13.40	18	18.4	17.4	19.1
Ge	0.10	0.1	0.05	0.05	0.05
As	0.70	1.4	1.2	1.4	0.9
W	0.50	0.5	0.25	0.25	0.25
Bi	0.02	0.06	0.05	0.06	0.01
Be	0.20	0.2	0.2	0.05	0.05
Pt (ppb)	2.00	1.00	1.00	1.00	1.00
Pd (ppb)	10.00	5.00	5.00	5.00	5.00

APPENDIX D: ELECTRON PROBE MICROANALYZER DATA

Plagioclase Chemistry – based on eight oxygens

Spot	MD001-Pl1-1	MD001-Pl1-2	MD001-Pl1-3	MD001-Pl2-1	MD001-Pl2-2	MD001-Pl2-3
Facies	Border	Border	Border	Border	Border	Border
SiO_2 wt%	56.79	58.08	56.21	59.97	59.18	59.31
Al_2O_3 wt%	28.80	27.92	29.25	26.81	27.68	27.36
CaO wt%	11.08	10.20	11.53	8.81	9.51	9.11
Na_2O wt%	5.04	5.50	4.84	6.39	5.90	6.01
K_2O wt%	0.26	0.31	0.24	0.36	0.38	0.40
BaO wt%	0.05	0.03	0.01	0.00	0.01	0.01
SrO wt%	0.10	0.11	0.08	0.09	0.10	0.08
Total	102.12	102.15	102.15	102.42	102.77	102.28
Si	2.503	2.552	2.479	2.618	2.580	2.594
Al	1.496	1.446	1.521	1.379	1.422	1.411
Ca	0.523	0.480	0.545	0.412	0.444	0.427
Na	0.430	0.469	0.414	0.541	0.499	0.510
K	0.015	0.018	0.013	0.020	0.021	0.022
Ba	0.001	0.000	0.000	0.000	0.000	0.000
Sr	0.003	0.003	0.002	0.002	0.003	0.002
An%	54.0	49.7	56.0	42.4	46.1	44.5
Ab%	44.4	48.5	42.6	55.6	51.7	53.2
Or%	1.5	1.8	1.4	2.0	2.2	2.3

Spot	MD001-Pl3-1	MD001-Pl3-2	MD001-Pl3-3	MD003A-PI1-1	MD003A-PI1-2	MD003A-PI1-3
Facies	Border	Border	Border	Border	Border	Border
SiO_2 wt%	61.00	60.68	58.98	59.62	60.77	60.12
Al_2O_3 wt%	26.26	25.31	27.77	26.77	25.88	26.40
CaO wt%	8.09	7.22	9.69	8.68	7.66	8.22
Na_2O wt%	6.70	7.07	5.79	6.53	7.03	6.65
K_2O wt%	0.27	0.44	0.29	0.20	0.24	0.22
BaO wt%	0.01	0.00	0.00	0.04	0.06	0.06
SrO wt%	0.15	0.10	0.12	0.24	0.17	0.21
Total	102.48	100.81	102.65	102.08	101.81	101.89
Si	2.654	2.682	2.574	2.614	2.662	2.636
Al	1.347	1.318	1.429	1.383	1.337	1.364
Ca	0.377	0.342	0.453	0.408	0.360	0.386
Na	0.565	0.606	0.490	0.555	0.597	0.566
K	0.015	0.025	0.016	0.011	0.013	0.012
Ba	0.000	0.000	0.000	0.001	0.001	0.001
Sr	0.004	0.002	0.003	0.006	0.004	0.005
An%	39.4	35.2	47.2	41.9	37.1	40.1
Ab%	59.0	62.3	51.1	57.0	61.5	58.7
Or%	1.6	2.5	1.7	1.2	1.4	1.3

Spot	MD003A-Pl2-1	MD003A-Pl2-2	MD003A-Pl2-3	MD003A-Pl3-1	MD003A-Pl3-2	MD003A-Pl3-3
Facies	Border	Border	Border	Border	Border	Border
SiO_2 wt%	57.20	58.22	60.77	60.53	60.22	58.55
Al_2O_3 wt%	28.28	27.40	25.82	26.11	26.27	27.46
CaO wt%	10.45	9.52	7.70	7.85	8.17	9.36
Na_2O wt%	5.47	5.95	7.06	6.82	6.76	6.00
K_2O wt%	0.13	0.14	0.19	0.20	0.18	0.19
BaO wt%	0.03	0.05	0.05	0.04	0.06	0.04
SrO wt%	0.20	0.21	0.18	0.17	0.20	0.17
Total	101.77	101.48	101.76	101.71	101.85	101.79
Si	2.527	2.572	2.664	2.654	2.641	2.577
Al	1.472	1.427	1.334	1.349	1.358	1.425
Ca	0.495	0.451	0.361	0.369	0.384	0.442
Na	0.469	0.509	0.600	0.580	0.575	0.512
K	0.007	0.008	0.011	0.011	0.010	0.011
Ba	0.001	0.001	0.001	0.001	0.001	0.001
Sr	0.005	0.005	0.004	0.004	0.005	0.004
An%	51.0	46.6	37.2	38.4	39.6	45.8
Ab%	48.3	52.6	61.7	60.4	59.4	53.1
Or%	0.8	0.8	1.1	1.2	1.0	1.1

Spot	MD004-Pl1-1	MD004-Pl1-2	MD004-Pl1-3	MD004-Pl2-1	MD004-Pl2-2	MD004-Pl2-3
Facies	Bethsaida	Bethsaida	Bethsaida	Bethsaida	Bethsaida	Bethsaida
SiO_2 wt%	61.17	61.89	62.00	61.82	62.03	61.90
Al_2O_3 wt%	25.38	24.71	24.81	25.31	25.17	25.46
CaO wt%	7.05	6.51	6.44	6.91	6.74	7.08
Na_2O wt%	7.15	7.27	7.36	7.36	7.25	7.18
K_2O wt%	0.26	0.36	0.39	0.27	0.33	0.27
BaO wt%	0.07	0.05	0.05	0.03	0.05	0.06
SrO wt%	0.20	0.20	0.21	0.20	0.22	0.17
Total	101.28	100.98	101.26	101.90	101.78	102.12
Si	2.689	2.723	2.721	2.699	2.709	2.696
Al	1.315	1.281	1.283	1.303	1.296	1.307
Ca	0.332	0.307	0.303	0.323	0.315	0.331
Na	0.609	0.620	0.626	0.623	0.614	0.606
K	0.015	0.020	0.022	0.015	0.018	0.015
Ba	0.001	0.001	0.001	0.001	0.001	0.001
Sr	0.005	0.005	0.005	0.005	0.005	0.004
An%	34.7	32.4	31.9	33.6	33.3	34.7
Ab%	63.7	65.5	65.9	64.8	64.8	63.7
Or%	1.5	2.1	2.3	1.6	1.9	1.6

Spot	MD004-Pl3-1	MD004-Pl3-2	MD004-Pl3-3	MD004-Pl4-1	MD004-Pl4-2	MD004-Pl4-3
Facies	Bethsaida	Bethsaida	Bethsaida	Bethsaida	Bethsaida	Bethsaida
SiO_2 wt%	63.34	62.43	62.65	68.12	68.37	68.83
Al_2O_3 wt%	24.36	24.77	24.51	21.03	21.00	20.92
CaO wt%	5.70	6.38	6.07	2.02	2.06	1.72
Na_2O wt%	7.98	7.57	7.70	10.00	10.01	10.47
K_2O wt%	0.35	0.35	0.38	0.34	0.43	0.31
BaO wt%	0.07	0.05	0.05	0.00	0.01	0.00
SrO wt%	0.14	0.17	0.15	0.02	0.06	0.05
Total	101.95	101.72	101.52	101.53	101.94	102.30
Si	2.755	2.727	2.740	2.938	2.939	2.947
Al	1.249	1.275	1.263	1.069	1.064	1.055
Ca	0.266	0.298	0.285	0.093	0.095	0.079
Na	0.673	0.641	0.653	0.837	0.834	0.869
K	0.019	0.019	0.021	0.019	0.024	0.017
Ba	0.001	0.001	0.001	0.000	0.000	0.000
Sr	0.004	0.004	0.004	0.000	0.001	0.001
An%	27.8	31.1	29.7	9.8	9.9	8.2
Ab%	70.2	66.8	68.1	88.2	87.6	90.1
Or%	2.0	2.0	2.2	2.0	2.5	1.8

Spot	MD007-Pl1-1	MD007-Pl1-2	MD007-Pl1-3	MD007-Pl2-1	MD007-Pl2-2	MD007-Pl2-3
Facies	Border	Border	Border	Border	Border	Border
SiO_2 wt%	58.55	58.45	59.64	60.10	60.65	59.51
Al_2O_3 wt%	27.03	27.32	26.44	25.92	25.92	26.62
CaO wt%	8.78	9.09	8.13	7.95	7.51	8.49
Na_2O wt%	6.05	6.05	6.49	6.82	6.75	6.43
K_2O wt%	0.24	0.23	0.26	0.18	0.29	0.25
BaO wt%	0.05	0.04	0.02	0.02	0.05	0.05
SrO wt%	0.20	0.24	0.24	0.21	0.19	0.21
Total	100.90	101.43	101.22	101.20	101.36	101.55
Si	2.596	2.582	2.631	2.650	2.665	2.620
Al	1.412	1.423	1.375	1.347	1.343	1.381
Ca	0.417	0.430	0.384	0.376	0.354	0.400
Na	0.520	0.518	0.555	0.584	0.575	0.549
K	0.014	0.013	0.015	0.010	0.016	0.014
Ba	0.001	0.001	0.000	0.000	0.001	0.001
Sr	0.005	0.006	0.006	0.005	0.005	0.005
An%	43.9	44.7	40.3	38.8	37.4	41.6
Ab%	54.7	53.9	58.2	60.2	60.8	57.0
Or%	1.4	1.4	1.5	1.0	1.7	1.4

Spot	MD007-Pl3-1	MD007-Pl3-2	MD007-Pl3-3	MD007-Pl4-1	MD007-Pl4-2	MD007-Pl4-3
Facies	Border	Border	Border	Border	Border	Border
SiO_2 wt%	60.18	61.44	58.44	59.90	60.40	60.56
Al_2O_3 wt%	26.86	25.91	26.33	26.35	26.10	26.50
CaO wt%	8.23	7.18	8.66	7.94	7.60	8.01
Na_2O wt%	6.53	6.96	6.36	6.57	6.75	6.59
K_2O wt%	0.23	0.26	0.26	0.24	0.28	0.28
BaO wt%	0.05	0.05	0.04	0.04	0.06	0.05
SrO wt%	0.23	0.20	0.16	0.15	0.22	0.18
Total	102.31	102.01	100.26	101.19	101.41	102.16
Si	2.626	2.679	2.610	2.640	2.656	2.644
Al	1.382	1.332	1.386	1.369	1.353	1.364
Ca	0.385	0.335	0.414	0.375	0.358	0.374
Na	0.552	0.589	0.550	0.561	0.576	0.558
K	0.013	0.015	0.015	0.013	0.016	0.015
Ba	0.001	0.001	0.001	0.001	0.001	0.001
Sr	0.006	0.005	0.004	0.004	0.006	0.005
An%	40.5	35.7	42.3	39.5	37.7	39.5
Ab%	58.1	62.7	56.2	59.1	60.6	58.9
Or%	1.4	1.6	1.5	1.4	1.7	1.6

Spot	MD034-Pl1-1	MD034-Pl1-2	MD034-Pl1-3	MD034-Pl2-1	MD034-Pl2-2	MD034-Pl2-3
Facies	Skeena	Skeena	Skeena	Skeena	Skeena	Skeena
SiO_2 wt%	59.30	59.34	60.19	60.55	61.91	58.95
Al_2O_3 wt%	26.18	26.17	25.43	25.28	24.46	26.26
CaO wt%	7.88	7.79	6.98	6.84	5.89	8.41
Na_2O wt%	6.93	6.96	7.38	7.46	7.96	6.64
K_2O wt%	0.28	0.31	0.36	0.28	0.43	0.28
BaO wt%	0.05	0.04	0.06	0.04	0.04	0.04
SrO wt%	0.12	0.16	0.22	0.19	0.17	0.18
Total	100.74	100.78	100.61	100.65	100.86	100.75
Si	2.631	2.632	2.670	2.681	2.729	2.619
Al	1.369	1.368	1.330	1.320	1.271	1.375
Ca	0.374	0.370	0.332	0.324	0.278	0.400
Na	0.596	0.599	0.635	0.641	0.680	0.572
K	0.016	0.017	0.020	0.016	0.024	0.016
Ba	0.001	0.001	0.001	0.001	0.001	0.001
Sr	0.003	0.004	0.006	0.005	0.004	0.005
An%	38.0	37.5	33.6	33.1	28.3	40.5
Ab%	60.5	60.7	64.3	65.3	69.2	57.9
Or%	1.6	1.8	2.1	1.6	2.5	1.6

Spot	MD034-Pl2-4	MD034-Pl3-1	MD034-Pl3-2	MD034-Pl3-3	MD044-Pl1-1	MD044-Pl1-2
Facies	Skeena	Skeena	Skeena	Skeena	Chataway	Chataway
SiO_2 wt%	58.31	60.10	61.88	60.29	62.27	60.77
Al_2O_3 wt%	26.78	25.64	24.31	25.63	24.98	25.86
CaO wt%	8.89	7.35	5.88	7.23	6.57	7.55
Na_2O wt%	6.40	7.12	7.94	7.26	7.60	7.18
K_2O wt%	0.25	0.25	0.40	0.29	0.37	0.24
BaO wt%	0.03	0.05	0.03	0.06	0.05	0.00
SrO wt%	0.15	0.20	0.12	0.16	0.19	0.15
Total	100.81	100.71	100.55	100.91	102.02	101.76
Si	2.592	2.662	2.734	2.665	2.715	2.663
Al	1.403	1.339	1.266	1.335	1.284	1.336
Ca	0.423	0.349	0.279	0.342	0.307	0.355
Na	0.552	0.611	0.680	0.622	0.642	0.610
K	0.014	0.014	0.023	0.016	0.021	0.014
Ba	0.000	0.001	0.001	0.001	0.001	0.000
Sr	0.004	0.005	0.003	0.004	0.005	0.004
An%	42.8	35.8	28.4	34.9	31.6	36.3
Ab%	55.8	62.7	69.3	63.5	66.2	62.4
Or%	1.4	1.5	2.3	1.6	2.1	1.4

Spot	MD044-Pl1-3	MD044-Pl2-1	MD044-Pl2-2	MD044-Pl2-3	MD044-Pl3-1	MD044-Pl3-2
Facies	Chataway	Chataway	Chataway	Chataway	Chataway	Chataway
SiO_2 wt%	61.69	62.47	62.97	60.51	63.13	62.54
Al_2O_3 wt%	25.05	24.75	24.58	26.28	24.42	25.02
CaO wt%	6.67	6.48	6.07	8.04	5.78	6.30
Na_2O wt%	7.66	7.69	8.02	7.04	8.21	8.00
K_2O wt%	0.33	0.29	0.30	0.18	0.27	0.27
BaO wt%	0.02	0.05	0.00	0.00	0.00	0.01
SrO wt%	0.15	0.16	0.12	0.15	0.14	0.09
Total	101.58	101.89	102.07	102.20	101.95	102.23
Si	2.703	2.725	2.739	2.644	2.747	2.719
Al	1.294	1.273	1.260	1.353	1.253	1.282
Ca	0.313	0.303	0.283	0.376	0.269	0.293
Na	0.651	0.651	0.676	0.596	0.692	0.674
K	0.019	0.016	0.017	0.010	0.015	0.015
Ba	0.000	0.001	0.000	0.000	0.000	0.000
Sr	0.004	0.004	0.003	0.004	0.004	0.002
An%	31.9	31.2	29.0	38.3	27.6	29.9
Ab%	66.3	67.1	69.3	60.7	70.9	68.6
Or%	1.9	1.7	1.7	1.0	1.5	1.5

Spot	MD044-Pl3-3	MD046-Pl1-1	MD046-Pl1-2	MD046-Pl1-3	MD046-Pl2-1	MD046-Pl2-2
Facies	Chataway	Border	Border	Border	Border	Border
SiO_2 wt%	60.76	60.24	58.56	58.71	59.02	59.52
Al_2O_3 wt%	25.92	26.39	27.60	27.58	27.37	26.70
CaO wt%	7.67	8.14	9.58	9.45	9.39	8.74
Na_2O wt%	7.09	6.73	5.84	6.06	5.99	6.33
K_2O wt%	0.22	0.13	0.14	0.15	0.16	0.20
BaO wt%	0.02	0.03	0.03	0.04	0.05	0.06
SrO wt%	0.20	0.11	0.15	0.16	0.16	0.14
Total	101.87	101.78	101.91	102.15	102.14	101.69
Si	2.660	2.640	2.574	2.575	2.587	2.617
Al	1.338	1.363	1.430	1.426	1.414	1.383
Ca	0.360	0.382	0.451	0.444	0.441	0.412
Na	0.602	0.572	0.498	0.515	0.510	0.540
K	0.012	0.007	0.008	0.008	0.009	0.011
Ba	0.000	0.001	0.001	0.001	0.001	0.001
Sr	0.005	0.003	0.004	0.004	0.004	0.004
An%	37.0	39.8	47.1	45.9	46.0	42.8
Ab%	61.8	59.5	52.0	53.2	53.1	56.1
Or%	1.3	0.8	0.8	0.8	0.9	1.1

Spot	MD046-Pl2-3	MD049-Pl1-1	MD049-Pl1-2	MD049-Pl1-3	MD049-Pl2-1	MD049-Pl2-2
Facies	Border	Skeena	Skeena	Skeena	Skeena	Skeena
SiO_2 wt%	60.03	62.04	61.65	62.78	64.19	63.19
Al_2O_3 wt%	26.53	25.22	25.56	24.89	23.55	24.37
CaO wt%	8.51	6.82	7.13	6.40	5.19	5.94
Na_2O wt%	6.61	7.26	7.20	7.37	8.07	7.69
K_2O wt%	0.16	0.39	0.33	0.36	0.53	0.51
BaO wt%	0.06	0.06	0.00	0.02	0.06	0.03
SrO wt%	0.10	0.16	0.20	0.21	0.11	0.17
Total	102.00	101.94	102.07	102.03	101.69	101.90
Si	2.629	2.707	2.689	2.731	2.794	2.751
Al	1.369	1.297	1.314	1.276	1.208	1.251
Ca	0.399	0.319	0.333	0.298	0.242	0.277
Na	0.562	0.614	0.609	0.622	0.681	0.649
K	0.009	0.022	0.018	0.020	0.029	0.028
Ba	0.001	0.001	0.000	0.000	0.001	0.001
Sr	0.002	0.004	0.005	0.005	0.003	0.004
An%	41.2	33.4	34.7	31.7	25.4	29.0
Ab%	57.9	64.3	63.4	66.1	71.5	68.0
Or%	0.9	2.3	1.9	2.1	3.1	3.0

Spot	MD049-Pl2-3	MD049-Pl3-1	MD049-Pl3-2	MD049-Pl3-3	MD049-Pl3-4	MD059-Pl1-1
Facies	Skeena	Skeena	Skeena	Skeena	Skeena	Bethlehem
SiO_2 wt%	62.14	65.41	60.04	60.57	60.71	64.14
Al_2O_3 wt%	24.85	23.09	25.67	26.19	25.83	23.24
CaO wt%	6.72	4.41	8.25	8.04	7.80	4.71
Na_2O wt%	7.27	8.67	6.69	6.53	6.73	8.52
K_2O wt%	0.40	0.45	0.33	0.32	0.37	0.54
BaO wt%	0.05	0.01	0.04	0.03	0.03	0.11
SrO wt%	0.19	0.18	0.17	0.23	0.16	0.10
Total	101.61	102.22	101.19	101.93	101.65	101.36
Si	2.719	2.826	2.652	2.651	2.664	2.802
Al	1.282	1.176	1.336	1.351	1.336	1.197
Ca	0.315	0.204	0.390	0.377	0.367	0.220
Na	0.617	0.726	0.573	0.555	0.573	0.722
K	0.022	0.025	0.019	0.018	0.021	0.030
Ba	0.001	0.000	0.001	0.000	0.001	0.002
Sr	0.005	0.004	0.004	0.006	0.004	0.003
An%	33.0	21.4	39.8	39.7	38.2	22.7
Ab%	64.7	76.0	58.4	58.4	59.6	74.2
Or%	2.3	2.6	1.9	1.9	2.2	3.1

Spot	MD059-Pl1-2	MD059-Pl1-3	MD059-Pl2-1	MD059-Pl2-2	MD059-Pl2-3	MD059-Pl3-1
Facies	Bethlehem	Bethlehem	Bethlehem	Bethlehem	Bethlehem	Bethlehem
SiO_2 wt%	60.85	61.76	60.89	64.37	60.90	63.82
Al_2O_3 wt%	25.63	25.23	25.35	23.09	25.38	23.59
CaO wt%	7.44	6.88	7.16	4.56	7.22	5.19
Na_2O wt%	6.95	7.26	7.08	8.47	7.04	8.04
K_2O wt%	0.33	0.34	0.35	0.56	0.34	0.52
BaO wt%	0.03	0.04	0.06	0.07	0.04	0.05
SrO wt%	0.22	0.15	0.17	0.10	0.16	0.18
Total	101.45	101.67	101.07	101.22	101.07	101.39
Si	2.674	2.702	2.684	2.812	2.683	2.788
Al	1.327	1.301	1.317	1.189	1.318	1.214
Ca	0.350	0.322	0.338	0.213	0.341	0.243
Na	0.593	0.616	0.605	0.717	0.601	0.681
K	0.019	0.019	0.020	0.031	0.019	0.029
Ba	0.001	0.001	0.001	0.001	0.001	0.001
Sr	0.006	0.004	0.004	0.003	0.004	0.005
An%	36.4	33.7	35.1	22.2	35.5	25.5
Ab%	61.6	64.3	62.8	74.6	62.6	71.5
Or%	1.9	2.0	2.0	3.2	2.0	3.0

Spot	MD059-Pl3-2	MD059-Pl3-3	MD063-Pl1-1	MD063-Pl1-2	MD063-Pl1-3	MD063-Pl2-1
Facies	Bethlehem	Bethlehem	F.g. GRD	F.g. GRD	F.g. GRD	F.g. GRD
SiO_2 wt%	62.94	62.02	62.48	60.26	60.71	62.82
Al_2O_3 wt%	24.19	24.73	24.43	25.96	25.91	24.38
CaO wt%	5.82	6.51	5.99	7.71	7.69	5.99
Na_2O wt%	7.96	7.41	7.80	7.11	6.98	8.18
K_2O wt%	0.43	0.43	0.49	0.33	0.37	0.36
BaO wt%	0.05	0.05	0.04	0.04	0.03	0.01
SrO wt%	0.19	0.20	0.21	0.21	0.22	0.12
Total	101.58	101.35	101.42	101.62	101.91	101.85
Si	2.751	2.721	2.738	2.650	2.660	2.740
Al	1.247	1.279	1.262	1.346	1.338	1.253
Ca	0.273	0.306	0.281	0.363	0.361	0.280
Na	0.675	0.630	0.663	0.606	0.593	0.692
K	0.024	0.024	0.027	0.019	0.021	0.020
Ba	0.001	0.001	0.001	0.001	0.001	0.000
Sr	0.005	0.005	0.005	0.005	0.006	0.003
An%	28.1	31.9	29.0	36.8	37.0	28.2
Ab%	69.5	65.6	68.2	61.3	60.8	69.8
Or%	2.5	2.5	2.8	1.9	2.1	2.0

Spot	MD063-Pl2-2	MD063-Pl2-3	MD063-Pl3-1	MD063-Pl3-2	MD063-Pl3-3	MD066-Pl1-1
Facies	F.g. GRD	F.g. GRD	F.g. GRD	F.g. GRD	F.g. GRD	Chataway
SiO_2 wt%	63.35	61.47	63.52	59.53	61.73	62.60
Al_2O_3 wt%	24.21	25.54	24.20	26.74	24.97	24.33
CaO wt%	5.73	7.26	5.71	8.60	6.64	6.14
Na_2O wt%	8.03	7.41	8.12	6.50	7.58	7.74
K_2O wt%	0.42	0.29	0.23	0.21	0.43	0.35
BaO wt%	0.02	0.04	0.01	0.03	0.05	0.05
SrO wt%	0.09	0.17	0.10	0.09	0.15	0.17
Total	101.85	102.17	101.88	101.68	101.56	101.36
Si	2.758	2.682	2.762	2.616	2.707	2.742
Al	1.242	1.313	1.240	1.385	1.290	1.256
Ca	0.267	0.339	0.266	0.405	0.312	0.288
Na	0.678	0.627	0.685	0.554	0.645	0.657
K	0.023	0.016	0.013	0.012	0.024	0.020
Ba	0.000	0.001	0.000	0.000	0.001	0.001
Sr	0.002	0.004	0.002	0.002	0.004	0.004
An%	27.6	34.5	27.6	41.7	31.8	29.9
Ab%	70.0	63.8	71.1	57.1	65.7	68.1
Or%	2.4	1.6	1.3	1.2	2.4	2.0

Spot	MD066-Pl1-2	MD066-Pl2-1	MD066-Pl2-2	MD066-Pl2-3	MD066-Pl3-1	MD066-Pl3-2
Facies	Chataway	Chataway	Chataway	Chataway	Chataway	Chataway
SiO_2 wt%	61.87	62.79	61.06	61.25	62.02	60.53
Al_2O_3 wt%	24.27	24.18	25.17	25.34	24.89	25.67
CaO wt%	6.10	6.08	7.34	7.30	6.74	7.79
Na_2O wt%	7.77	7.85	7.07	7.11	7.50	6.96
K_2O wt%	0.40	0.32	0.35	0.34	0.19	0.21
BaO wt%	0.06	0.01	0.08	0.06	0.05	0.05
SrO wt%	0.19	0.09	0.17	0.15	0.23	0.17
Total	100.66	101.33	101.24	101.54	101.61	101.38
Si	2.733	2.749	2.688	2.687	2.714	2.664
Al	1.264	1.248	1.306	1.310	1.284	1.332
Ca	0.289	0.285	0.346	0.343	0.316	0.367
Na	0.665	0.666	0.604	0.605	0.636	0.594
K	0.022	0.018	0.020	0.019	0.011	0.012
Ba	0.001	0.000	0.001	0.001	0.001	0.001
Sr	0.005	0.002	0.004	0.004	0.006	0.004
An%	29.6	29.4	35.7	35.5	32.8	37.8
Ab%	68.1	68.7	62.3	62.6	66.1	61.0
Or%	2.3	1.9	2.0	2.0	1.1	1.2

Spot	MD066-Pl3-3	MD066-Pl3-4	MD069-Pl1-1	MD069-Pl1-2	MD069-Pl1-3	MD069-Pl2-1
Facies	Chataway	Chataway	Bethsaida	Bethsaida	Bethsaida	Bethsaida
SiO_2 wt%	59.97	61.78	62.95	61.50	61.34	64.75
Al_2O_3 wt%	25.24	25.11	23.84	24.63	24.73	21.52
CaO wt%	7.79	7.04	5.62	6.63	6.62	3.30
Na_2O wt%	6.54	7.29	7.84	7.36	7.42	8.80
K_2O wt%	0.15	0.33	0.37	0.29	0.31	0.62
BaO wt%	0.01	0.05	0.08	0.06	0.06	0.01
SrO wt%	0.13	0.14	0.15	0.22	0.17	0.02
Total	99.83	101.74	100.86	100.70	100.65	99.01
Si	2.674	2.702	2.766	2.716	2.711	2.877
Al	1.327	1.295	1.235	1.282	1.288	1.127
Ca	0.372	0.330	0.265	0.314	0.314	0.157
Na	0.566	0.618	0.668	0.631	0.636	0.758
K	0.009	0.018	0.021	0.016	0.018	0.035
Ba	0.000	0.001	0.001	0.001	0.001	0.000
Sr	0.003	0.004	0.004	0.006	0.004	0.000
An%	39.3	34.1	27.8	32.7	32.4	16.5
Ab%	59.8	64.0	70.1	65.6	65.7	79.8
Or%	0.9	1.9	2.2	1.7	1.8	3.7

Spot	MD069-Pl2-2	MD069-Pl2-3	MD069-Pl3-1	MD069-Pl3-2	MD069-Pl3-3	MD071-Pl1-1
Facies	Bethsaida	Bethsaida	Bethsaida	Bethsaida	Bethsaida	Bethsaida
SiO_2 wt%	60.89	62.68	60.79	62.01	62.05	68.60
Al_2O_3 wt%	25.10	23.73	24.63	24.31	24.33	20.94
CaO wt%	7.16	5.62	6.87	6.11	6.18	1.91
Na_2O wt%	7.09	7.88	7.29	7.66	7.58	10.05
K_2O wt%	0.30	0.38	0.28	0.35	0.35	0.41
BaO wt%	0.07	0.05	0.04	0.08	0.04	0.03
SrO wt%	0.17	0.16	0.16	0.22	0.17	0.04
Total	100.77	100.50	100.05	100.74	100.70	101.98
Si	2.691	2.765	2.704	2.735	2.736	2.946
Al	1.308	1.234	1.291	1.264	1.264	1.060
Ca	0.339	0.265	0.327	0.289	0.292	0.088
Na	0.607	0.674	0.629	0.656	0.648	0.837
K	0.017	0.022	0.016	0.020	0.020	0.022
Ba	0.001	0.001	0.001	0.001	0.001	0.000
Sr	0.004	0.004	0.004	0.006	0.004	0.001
An%	35.2	27.6	33.7	30.0	30.4	9.3
Ab%	63.1	70.1	64.7	68.0	67.5	88.4
Or%	1.8	2.2	1.6	2.0	2.1	2.4

Spot	MD071-Pl1-2	MD071-Pl1-3	MD071-Pl2-1	MD071-Pl2-2	MD071-Pl2-3	MD071-Pl3-1
Facies	Bethsaida	Bethsaida	Bethsaida	Bethsaida	Bethsaida	Bethsaida
SiO_2 wt%	60.16	62.94	68.35	62.64	62.33	62.28
Al_2O_3 wt%	26.45	24.96	21.58	25.34	25.40	24.89
CaO wt%	8.36	6.38	2.43	6.68	6.79	6.48
Na_2O wt%	6.56	7.56	9.98	7.47	7.26	7.51
K_2O wt%	0.30	0.40	0.37	0.29	0.37	0.39
BaO wt%	0.06	0.06	0.02	0.06	0.02	0.05
SrO wt%	0.20	0.17	0.05	0.19	0.18	0.18
Total	102.10	102.46	102.79	102.66	102.35	101.77
Si	2.634	2.728	2.918	2.712	2.707	2.720
Al	1.365	1.275	1.086	1.293	1.300	1.282
Ca	0.392	0.296	0.111	0.310	0.316	0.303
Na	0.557	0.635	0.826	0.627	0.611	0.636
K	0.017	0.022	0.020	0.016	0.021	0.022
Ba	0.001	0.001	0.000	0.001	0.000	0.001
Sr	0.005	0.004	0.001	0.005	0.005	0.004
An%	40.6	31.1	11.6	32.5	33.3	31.6
Ab%	57.7	66.6	86.3	65.8	64.5	66.2
Or%	1.7	2.3	2.1	1.7	2.2	2.3

Spot	MD071-Pl3-2	MD071-Pl3-3	MD071-Pl4-1	MD071-Pl4-2	MD071-Pl4-3	MD071-Pl4-4
Facies	Bethsaida	Bethsaida	Bethsaida	Bethsaida	Bethsaida	Bethsaida
SiO_2 wt%	61.49	61.59	62.57	62.52	62.76	62.83
Al_2O_3 wt%	25.67	25.45	25.19	25.05	24.66	24.99
CaO wt%	7.51	7.03	6.54	6.67	6.34	6.44
Na_2O wt%	7.09	7.15	7.54	7.37	7.66	7.51
K_2O wt%	0.32	0.35	0.31	0.34	0.42	0.43
BaO wt%	0.06	0.05	0.05	0.04	0.06	0.04
SrO wt%	0.16	0.18	0.23	0.17	0.17	0.18
Total	102.31	101.79	102.44	102.16	102.06	102.43
Si	2.679	2.693	2.715	2.719	2.733	2.725
Al	1.318	1.311	1.289	1.284	1.266	1.278
Ca	0.351	0.329	0.304	0.311	0.296	0.299
Na	0.599	0.606	0.635	0.622	0.647	0.632
K	0.018	0.019	0.017	0.019	0.023	0.024
Ba	0.001	0.001	0.001	0.001	0.001	0.001
Sr	0.004	0.004	0.006	0.004	0.004	0.005
An%	36.2	34.5	31.8	32.7	30.6	31.4
Ab%	61.9	63.5	66.4	65.3	67.0	66.2
Or%	1.9	2.0	1.8	2.0	2.4	2.5

357

Spot	MD075-Pl1-1	MD075-Pl1-2	MD075-Pl1-3	MD075-Pl2-1	MD075-Pl2-2	MD075-Pl2-3
Facies	Guichon	Guichon	Guichon	Guichon	Guichon	Guichon
SiO_2 wt%	61.91	61.07	61.01	62.17	60.82	60.08
Al_2O_3 wt%	25.36	25.77	25.95	25.45	25.98	26.59
CaO wt%	7.16	7.61	7.82	7.12	7.77	8.59
Na_2O wt%	7.11	6.70	6.68	7.27	6.76	6.41
K_2O wt%	0.44	0.55	0.54	0.42	0.39	0.33
BaO wt%	0.02	0.09	0.07	0.04	0.05	0.07
SrO wt%	0.12	0.17	0.13	0.14	0.21	0.15
Total	102.11	101.96	102.19	102.61	101.97	102.23
Si	2.698	2.672	2.664	2.697	2.661	2.628
Al	1.303	1.329	1.336	1.302	1.340	1.371
Ca	0.334	0.357	0.366	0.331	0.364	0.402
Na	0.600	0.569	0.566	0.611	0.574	0.544
K	0.025	0.030	0.030	0.023	0.022	0.019
Ba	0.000	0.002	0.001	0.001	0.001	0.001
Sr	0.003	0.004	0.003	0.003	0.005	0.004
An%	34.8	37.3	38.0	34.3	37.9	41.7
Ab%	62.6	59.5	58.9	63.3	59.8	56.4
Or%	2.6	3.2	3.1	2.4	2.3	1.9

Spot	MD076-Pl1-1	MD076-Pl1-2	MD076-Pl2-1	MD076-Pl2-2	MD076-Pl2-3	MD076-Pl3-1
Facies	Guichon	Guichon	Guichon	Guichon	Guichon	Guichon
SiO_2 wt%	60.53	59.93	60.66	60.49	60.36	58.88
Al_2O_3 wt%	25.40	25.52	25.00	24.94	25.60	26.05
CaO wt%	7.27	7.35	6.77	6.83	7.45	8.07
Na_2O wt%	7.18	7.22	7.25	7.20	7.10	6.80
K_2O wt%	0.37	0.31	0.53	0.51	0.36	0.32
BaO wt%	0.05	0.00	0.08	0.07	0.08	0.02
SrO wt%	0.20	0.12	0.13	0.13	0.14	0.10
Total	101.01	100.45	100.42	100.16	101.08	100.25
Si	2.674	2.662	2.692	2.691	2.665	2.627
Al	1.323	1.336	1.308	1.308	1.332	1.370
Ca	0.344	0.350	0.322	0.326	0.352	0.386
Na	0.615	0.622	0.624	0.621	0.608	0.588
K	0.021	0.018	0.030	0.029	0.020	0.018
Ba	0.001	0.000	0.001	0.001	0.001	0.000
Sr	0.005	0.003	0.003	0.003	0.003	0.003
An%	35.1	35.4	33.0	33.4	35.9	38.9
Ab%	62.8	62.9	63.9	63.7	62.0	59.3
Or%	2.1	1.8	3.1	3.0	2.1	1.9

Spot	MD076-Pl3-2	MD076-Pl3-3
Facies	Guichon	Guichon
SiO_2 wt%	58.74	57.96
Al_2O_3 wt%	26.58	25.19
CaO wt%	8.83	7.75
Na_2O wt%	6.28	6.60
K_2O wt%	0.32	0.33
BaO wt%	0.08	0.06
SrO wt%	0.16	0.17
Total	100.99	98.05
Si	2.605	2.642
Al	1.390	1.353
Ca	0.420	0.379
Na	0.540	0.583
K	0.018	0.019
Ba	0.001	0.001
Sr	0.004	0.004
An%	42.9	38.6
Ab%	55.2	59.4
Or%	1.8	2.0

Amphibole Chemistry – based on 23 oxygens

Spot	MD046-Hbl2-3	MD034-Hbl3-3	MD059-Hbl3-3	MD034-Hbl1-3	MD063-Hbl2-3	MD069-Hbl4-2
Facies	Border	Skeena	Bethlehem	Skeena	F.g. Granodiorite	Bethsaida
SiO2	54.49	53.19	53.38	53.02	52.89	50.23
Al2O3	3.79	3.84	3.90	4.17	3.97	4.48
TiO2	0.52	0.48	0.46	0.57	0.32	0.37
FeO	9.93	10.10	10.00	10.31	10.48	9.46
MnO	0.30	0.79	0.71	0.80	0.48	0.94
MgO	16.96	16.97	16.40	16.80	16.98	15.29
CaO	11.60	11.63	11.59	11.64	12.03	10.66
Na2O	0.38	0.67	0.73	0.70	0.61	1.10
K2O	0.13	0.25	0.20	0.26	0.30	0.27
F	0.00	0.00	0.00	0.00	0.00	0.00
Cl	0.08	0.03	0.02	0.01	0.02	0.01
Sum	98.18	97.94	97.40	98.27	98.09	92.82
-O=F	0.00	0.00	0.00	0.00	0.00	0.00
-O=Cl	0.02	0.01	0.00	0.00	0.00	0.00
Total	98.17	97.94	97.39	98.27	98.08	92.81
T						
Si	7.600	7.477	7.564	7.436	7.450	7.481
Al-T	0.400	0.523	0.436	0.564	0.550	0.519
Sum T	*8.000*	*8.000*	*8.000*	*8.000*	*8.000*	*8.000*
C						
Al^{vi} (M)	0.223	0.113	0.216	0.125	0.109	0.267
Ti	0.055	0.051	0.049	0.060	0.034	0.042
Fe3+	0.474	0.578	0.367	0.585	0.520	0.396
Fe2+	0.684	0.609	0.819	0.624	0.715	0.782
Mn	0.036	0.094	0.085	0.096	0.057	0.118
Mg	3.527	3.555	3.465	3.511	3.565	3.395
Cr	0.000	0.000	0.000	0.000	0.000	0.000
Sum C	*5.000*	*5.000*	*5.000*	*5.000*	*5.000*	*5.000*
B						
Mg-B	0	0	0	0	0	0
Ca-B	1.733	1.751	1.759	1.749	1.815	1.702
Na-B	0.103	0.183	0.202	0.190	0.167	0.298
Sum B	*1.84*	*1.93*	*1.96*	*1.94*	*1.98*	*2.00*
A						
Na-A	0.000	0.000	0.000	0.000	0.000	0.020
K	0.023	0.046	0.036	0.046	0.054	0.051
Sum A	*0.023*	*0.046*	*0.036*	*0.046*	*0.054*	*0.071*
Total	*14.859*	*14.979*	*14.997*	*14.986*	*15.037*	*15.071*
W						
F	0.000	0.000	0.000	0.000	0.000	0.000
Cl	0.020	0.006	0.005	0.001	0.005	0.004
OH	0.980	0.994	0.995	0.999	0.995	0.996
Sum W	*1.000*	*1.000*	*1.000*	*1.000*	*1.000*	*1.000*

Spot	MD034-Hbl2-3	MD034-Hbl1-2	MD034-Hbl3-2	MD034-Hbl1-1	MD069-Hbl2-2	MD069-Hbl2-1
Facies	Skeena	Skeena	Skeena	Skeena	Bethsaida	Bethsaida
SiO2	53.07	52.93	52.72	52.96	52.96	52.78
Al2O3	3.87	4.08	4.15	4.26	3.35	3.80
TiO2	0.57	0.57	0.57	0.57	0.46	0.53
FeO	10.48	10.43	10.56	10.41	10.12	10.20
MnO	0.79	0.81	0.85	0.80	1.06	1.01
MgO	16.84	16.69	16.84	16.58	16.06	16.14
CaO	11.44	11.49	11.53	11.46	11.21	11.23
Na2O	0.80	0.76	0.72	0.79	0.76	0.76
K2O	0.26	0.25	0.27	0.28	0.25	0.25
F	0.00	0.00	0.00	0.00	0.00	0.00
Cl	0.00	0.02	0.01	0.02	0.00	0.01
Sum	98.11	98.02	98.23	98.14	96.23	96.71
-O=F	0.00	0.00	0.00	0.00	0.00	0.00
-O=Cl	0.00	0.00	0.00	0.00	0.00	0.00
Total	98.11	98.02	98.23	98.13	96.23	96.71
T						
Si	7.452	7.443	7.393	7.441	7.603	7.531
Al-T	0.548	0.557	0.607	0.559	0.397	0.469
Sum T	*8.000*	*8.000*	*8.000*	*8.000*	*8.000*	*8.000*
C						
Al^{vi} (M)	0.091	0.119	0.078	0.147	0.170	0.169
Ti	0.060	0.060	0.060	0.061	0.050	0.056
Fe3+	0.631	0.606	0.700	0.576	0.421	0.495
Fe2+	0.599	0.620	0.539	0.647	0.794	0.722
Mn	0.094	0.097	0.101	0.095	0.129	0.123
Mg	3.525	3.498	3.521	3.474	3.436	3.434
Cr	0.000	0.000	0.000	0.000	0.000	0.000
Sum C	*5.000*	*5.000*	*5.000*	*5.000*	*5.000*	*5.000*
B						
Mg-B	0	0	0	0	0	0
Ca-B	1.721	1.730	1.732	1.725	1.724	1.717
Na-B	0.216	0.207	0.196	0.214	0.211	0.212
Sum B	*1.94*	*1.94*	*1.93*	*1.94*	*1.94*	*1.93*
A						
Na-A	0.000	0.000	0.000	0.000	0.000	0.000
K	0.047	0.044	0.048	0.050	0.046	0.046
Sum A	*0.047*	*0.044*	*0.048*	*0.050*	*0.046*	*0.046*
Total	*14.985*	*14.982*	*14.976*	*14.989*	*14.981*	*14.975*
W						
F	0.000	0.000	0.000	0.000	0.000	0.000
Cl	0.001	0.005	0.001	0.004	0.001	0.002
OH	0.999	0.995	0.999	0.996	0.999	0.998
Sum W	*1.000*	*1.000*	*1.000*	*1.000*	*1.000*	*1.000*

Spot	MD071-Hbl1-1	MD007-Hbl2-2	MD034-Hbl2-1	MD071-Hbl2-1	MD059-Hbl2-2	MD069-Hbl1-1
Facies	Bethsaida	Border	Skeena	Bethsaida	Bethlehem	Bethsaida
SiO2	53.56	49.31	51.97	53.54	51.17	53.26
Al2O3	3.44	7.66	4.67	3.40	6.26	3.81
TiO2	0.44	1.40	0.61	0.35	0.86	0.32
FeO	10.17	10.32	10.47	10.21	10.07	10.21
MnO	1.17	0.30	0.76	1.11	0.51	0.95
MgO	16.07	16.32	16.54	16.09	15.86	15.97
CaO	11.18	11.33	11.49	11.33	10.92	11.48
Na2O	0.71	1.00	0.79	0.67	1.35	0.58
K2O	0.22	0.31	0.29	0.20	0.20	0.20
F	0.00	0.00	0.00	0.00	0.00	0.00
Cl	0.02	0.04	0.01	0.01	0.07	0.01
Sum	96.97	97.98	97.59	96.91	97.26	96.79
-O=F	0.00	0.00	0.00	0.00	0.00	0.00
-O=Cl	0.00	0.01	0.00	0.00	0.02	0.00
Total	96.97	97.97	97.59	96.91	97.25	96.79
T						
Si	7.619	6.923	7.345	7.626	7.256	7.598
Al-T	0.381	1.077	0.655	0.374	0.744	0.402
Sum T	*8.000*	*8.000*	*8.000*	*8.000*	*8.000*	*8.000*
C						
Al^{vi} (M)	0.195	0.190	0.123	0.197	0.301	0.238
Ti	0.047	0.148	0.064	0.037	0.092	0.034
Fe3+	0.448	0.857	0.655	0.423	0.534	0.390
Fe2+	0.761	0.355	0.583	0.793	0.660	0.828
Mn	0.141	0.035	0.091	0.134	0.061	0.115
Mg	3.408	3.415	3.484	3.416	3.352	3.396
Cr	0.000	0.000	0.000	0.000	0.000	0.000
Sum C	*5.000*	*5.000*	*5.000*	*5.000*	*5.000*	*5.000*
B						
Mg-B	0	0	0	0	0	0
Ca-B	1.704	1.704	1.740	1.729	1.659	1.754
Na-B	0.196	0.272	0.216	0.185	0.341	0.161
Sum B	*1.90*	*1.98*	*1.96*	*1.91*	*2.00*	*1.92*
A						
Na-A	0.000	0.000	0.000	0.000	0.030	0.000
K	0.041	0.055	0.052	0.037	0.036	0.037
Sum A	*0.041*	*0.055*	*0.052*	*0.037*	*0.066*	*0.037*
Total	*14.940*	*15.031*	*15.009*	*14.951*	*15.066*	*14.952*
W						
F	0.000	0.000	0.000	0.000	0.000	0.000
Cl	0.004	0.010	0.003	0.002	0.018	0.003
OH	0.996	0.990	0.997	0.998	0.982	0.997
Sum W	*1.000*	*1.000*	*1.000*	*1.000*	*1.000*	*1.000*

Spot	MD007-Hbl2-3	MD069-Hbl4-1	MD069-Hbl1-1	MD034-Hbl2-2	MD007-Hbl1-3	MD071-Hbl1-4
Facies	Border	Bethsaida	Bethsaida	Skeena	Border	Bethsaida
SiO2	49.11	52.90	53.13	52.88	49.28	53.64
Al2O3	7.54	3.53	3.71	4.19	7.46	3.73
TiO2	1.44	0.45	0.34	0.58	1.39	0.49
FeO	10.42	10.35	10.28	10.75	10.51	10.50
MnO	0.27	1.07	0.95	0.78	0.30	1.09
MgO	16.26	16.11	15.95	16.61	16.08	16.05
CaO	11.43	11.27	11.47	11.46	11.53	11.15
Na2O	1.04	0.69	0.58	0.84	1.03	0.77
K2O	0.32	0.24	0.20	0.27	0.31	0.24
F	0.00	0.00	0.00	0.00	0.00	0.00
Cl	0.06	0.01	0.01	0.02	0.07	0.01
Sum	97.89	96.62	96.64	98.38	97.98	97.66
-O=F	0.00	0.00	0.00	0.00	0.00	0.00
-O=Cl	0.01	0.00	0.00	0.00	0.02	0.00
Total	97.88	96.62	96.63	98.37	97.96	97.66
T						
Si	6.919	7.559	7.595	7.418	6.953	7.576
Al-T	1.081	0.441	0.405	0.582	1.047	0.424
Sum T	*8.000*	*8.000*	*8.000*	*8.000*	*8.000*	*8.000*
C						
Al^{vi} (M)	0.170	0.154	0.220	0.111	0.194	0.198
Ti	0.153	0.049	0.037	0.061	0.148	0.052
Fe3+	0.814	0.506	0.401	0.626	0.735	0.496
Fe2+	0.414	0.730	0.828	0.636	0.506	0.745
Mn	0.033	0.130	0.115	0.092	0.036	0.130
Mg	3.416	3.432	3.399	3.475	3.382	3.379
Cr	0.000	0.000	0.000	0.000	0.000	0.000
Sum C	*5.000*	*5.000*	*5.000*	*5.000*	*5.000*	*5.000*
B						
Mg-B	0	0	0	0	0	0
Ca-B	1.725	1.725	1.757	1.723	1.743	1.687
Na-B	0.275	0.191	0.160	0.229	0.257	0.210
Sum B	*2.00*	*1.92*	*1.92*	*1.95*	*2.00*	*1.90*
A						
Na-A	0.009	0.000	0.000	0.000	0.024	0.000
K	0.057	0.043	0.037	0.049	0.056	0.043
Sum A	*0.066*	*0.043*	*0.037*	*0.049*	*0.080*	*0.043*
Total	*15.066*	*14.959*	*14.954*	*15.001*	*15.080*	*14.940*
W						
F	0.000	0.000	0.000	0.000	0.000	0.000
Cl	0.014	0.003	0.004	0.004	0.018	0.002
OH	0.986	0.997	0.996	0.996	0.982	0.998
Sum W	*1.000*	*1.000*	*1.000*	*1.000*	*1.000*	*1.000*

Spot	MD071-Hbl1-3	MD069-Hbl4-3	MD063-Hbl3-2	MD034-Hbl1-4	MD059-Hbl1-3	MD071-Hbl2-2
Facies	Bethsaida	Bethsaida	F.g. Granodiorite	Skeena	Bethlehem	Bethsaida
SiO_2	53.45	52.93	52.22	51.26	50.44	52.28
Al_2O_3	3.71	3.95	4.50	5.51	7.05	4.36
TiO_2	0.43	0.51	0.34	0.72	1.11	0.52
FeO	10.48	10.44	11.09	11.04	10.80	10.90
MnO	1.14	0.98	0.48	0.73	0.47	1.15
MgO	15.97	15.74	16.66	15.90	15.51	15.46
CaO	11.24	11.30	11.89	11.36	10.77	11.28
Na_2O	0.71	0.81	0.85	1.00	1.51	0.76
K_2O	0.20	0.26	0.34	0.31	0.20	0.25
F	0.00	0.00	0.00	0.00	0.00	0.00
Cl	0.01	0.01	0.02	0.02	0.06	0.01
Sum	97.34	96.93	98.38	97.85	97.93	96.98
-O=F	0.00	0.00	0.00	0.00	0.00	0.00
-O=Cl	0.00	0.00	0.00	0.01	0.01	0.00
Total	97.34	96.93	98.38	97.85	97.91	96.98
T						
Si	7.579	7.562	7.356	7.255	7.117	7.472
Al-T	0.421	0.438	0.644	0.745	0.883	0.528
Sum T	*8.000*	*8.000*	*8.000*	*8.000*	*8.000*	*8.000*
C						
Al^{vi} (M)	0.199	0.226	0.103	0.175	0.290	0.207
Ti	0.046	0.055	0.036	0.077	0.118	0.055
Fe3+	0.484	0.373	0.589	0.639	0.650	0.498
Fe2+	0.758	0.875	0.716	0.667	0.624	0.806
Mn	0.137	0.118	0.057	0.087	0.056	0.139
Mg	3.376	3.353	3.499	3.354	3.262	3.295
Cr	0.000	0.000	0.000	0.000	0.000	0.000
Sum C	*5.000*	*5.000*	*5.000*	*5.000*	*5.000*	*5.000*
B						
Mg-B	0	0	0	0	0	0
Ca-B	1.708	1.729	1.794	1.722	1.628	1.728
Na-B	0.194	0.224	0.206	0.275	0.372	0.210
Sum B	*1.90*	*1.95*	*2.00*	*2.00*	*2.00*	*1.94*
A						
Na-A	0.000	0.000	0.026	0.000	0.042	0.000
K	0.036	0.047	0.061	0.057	0.036	0.046
Sum A	*0.036*	*0.047*	*0.087*	*0.057*	*0.078*	*0.046*
Total	*14.939*	*15.000*	*15.087*	*15.054*	*15.078*	*14.984*
W						
F	0.000	0.000	0.000	0.000	0.000	0.000
Cl	0.003	0.002	0.005	0.006	0.016	0.004
OH	0.997	0.998	0.995	0.994	0.984	0.996
Sum W	*1.000*	*1.000*	*1.000*	*1.000*	*1.000*	*1.000*

Spot	MD007-Hbl4-1	MD007-Hbl1-2	MD007-Hbl4-2	MD059-Hbl1-1	MD003A-Hbl4-1	MD059-Hbl2-1
Facies	Border	Border	Border	Bethlehem	Border	Bethlehem
SiO_2	47.86	48.02	47.62	50.43	50.27	50.05
Al_2O_3	8.67	8.92	9.22	6.77	7.59	7.17
TiO_2	1.66	1.75	1.77	0.89	1.01	1.02
FeO	10.90	10.89	10.74	10.89	11.25	10.83
MnO	0.31	0.28	0.30	0.53	0.34	0.57
MgO	15.42	15.38	15.16	15.34	15.83	15.15
CaO	11.47	11.24	11.47	10.84	11.48	11.09
Na_2O	1.11	1.22	1.29	1.46	0.88	1.46
K_2O	0.39	0.40	0.41	0.21	0.30	0.28
F	0.00	0.00	0.00	0.00	0.00	0.00
Cl	0.06	0.05	0.07	0.06	0.08	0.06
Sum	97.86	98.15	98.06	97.41	99.03	97.69
-O=F	0.00	0.00	0.00	0.00	0.00	0.00
-O=Cl	0.01	0.01	0.02	0.01	0.02	0.01
Total	97.85	98.14	98.04	97.40	99.01	97.67
T						
Si	6.786	6.777	6.754	7.166	7.006	7.118
Al-T	1.214	1.223	1.246	0.834	0.994	0.882
Sum T	*8.000*	*8.000*	*8.000*	*8.000*	*8.000*	*8.000*
C						
Al^{vi} (M)	0.234	0.260	0.296	0.300	0.253	0.320
Ti	0.177	0.186	0.189	0.095	0.106	0.110
Fe3+	0.765	0.788	0.654	0.604	0.808	0.508
Fe2+	0.528	0.497	0.620	0.690	0.504	0.780
Mn	0.037	0.033	0.036	0.063	0.041	0.069
Mg	3.259	3.236	3.206	3.249	3.289	3.213
Cr	0.000	0.000	0.000	0.000	0.000	0.000
Sum C	*5.000*	*5.000*	*5.000*	*5.000*	*5.000*	*5.000*
B						
Mg-B	0	0	0	0	0	0
Ca-B	1.743	1.700	1.744	1.650	1.715	1.691
Na-B	0.257	0.300	0.256	0.350	0.238	0.309
Sum B	*2.00*	*2.00*	*2.00*	*2.00*	*1.95*	*2.00*
A						
Na-A	0.048	0.032	0.100	0.052	0.000	0.093
K	0.070	0.071	0.075	0.039	0.053	0.050
Sum A	*0.118*	*0.104*	*0.175*	*0.091*	*0.053*	*0.143*
Total	*15.118*	*15.104*	*15.175*	*15.091*	*15.006*	*15.143*
W						
F	0.000	0.000	0.000	0.000	0.000	0.000
Cl	0.015	0.012	0.018	0.015	0.019	0.014
OH	0.985	0.988	0.982	0.985	0.981	0.986
Sum W	*1.000*	*1.000*	*1.000*	*1.000*	*1.000*	*1.000*

Spot	MD049-Hbl2-2	MD076-Hbl4-3	MD063-Hbl3-3	MD049-Hbl1-3	MD007-Hbl3-2	MD049-Hbl1-2
Facies	Skeena	Guichon	F.g. Granodiorite	Skeena	Border	Skeena
SiO_2	51.60	52.91	51.38	51.66	47.43	52.06
Al_2O_3	5.39	4.21	5.28	5.45	8.34	5.22
TiO_2	0.69	0.36	0.40	0.73	1.60	0.63
FeO	10.97	11.51	11.67	10.93	11.11	11.16
MnO	0.59	0.37	0.46	0.58	0.30	0.59
MgO	15.31	16.02	16.17	15.11	15.32	15.38
CaO	11.69	12.25	11.93	11.77	11.42	11.84
Na_2O	0.89	0.47	0.92	0.82	1.10	0.81
K_2O	0.37	0.21	0.39	0.36	0.39	0.34
F	0.00	0.00	0.00	0.00	0.00	0.00
Cl	0.02	0.10	0.03	0.02	0.06	0.02
Sum	97.51	98.41	98.63	97.43	97.07	98.04
-O=F	0.00	0.00	0.00	0.00	0.00	0.00
-O=Cl	0.00	0.02	0.01	0.01	0.01	0.00
Total	97.51	98.39	98.63	97.43	97.06	98.04
T						
Si	7.374	7.480	7.248	7.398	6.787	7.402
Al-T	0.626	0.520	0.752	0.602	1.213	0.598
Sum T	*8.000*	*8.000*	*8.000*	*8.000*	*8.000*	*8.000*
C						
Al^{vi} (M)	0.281	0.181	0.126	0.317	0.194	0.276
Ti	0.075	0.038	0.043	0.078	0.173	0.067
Fe3+	0.303	0.385	0.615	0.223	0.796	0.295
Fe2+	1.008	0.976	0.761	1.086	0.533	1.032
Mn	0.072	0.044	0.055	0.070	0.036	0.071
Mg	3.262	3.376	3.400	3.225	3.268	3.259
Cr	0.000	0.000	0.000	0.000	0.000	0.000
Sum C	*5.000*	*5.000*	*5.000*	*5.000*	*5.000*	*5.000*
B						
Mg-B	0	0	0	0	0	0
Ca-B	1.790	1.855	1.802	1.807	1.751	1.803
Na-B	0.210	0.130	0.198	0.193	0.249	0.197
Sum B	*2.00*	*1.99*	*2.00*	*2.00*	*2.00*	*2.00*
A						
Na-A	0.037	0.000	0.053	0.033	0.055	0.027
K	0.067	0.038	0.070	0.066	0.072	0.061
Sum A	*0.104*	*0.038*	*0.123*	*0.099*	*0.127*	*0.089*
Total	*15.104*	*15.023*	*15.123*	*15.099*	*15.127*	*15.089*
W						
F	0.000	0.000	0.000	0.000	0.000	0.000
Cl	0.005	0.024	0.007	0.006	0.015	0.005
OH	0.995	0.976	0.993	0.994	0.985	0.995
Sum W	*1.000*	*1.000*	*1.000*	*1.000*	*1.000*	*1.000*

Spot	MD007-Hbl3-4	MD003A-Hbl3-2	MD007-Hbl3-1	MD007-Hbl2-1	MD059-Hbl1-2	MD007-Hbl1-1
Facies	Border	Border	Border	Border	Bethlehem	Border
SiO2	47.69	48.66	47.92	47.33	49.66	47.67
Al2O3	8.82	8.59	8.81	9.55	7.53	9.09
TiO2	1.79	1.48	1.60	1.72	0.97	1.79
FeO	11.04	11.16	11.16	11.15	11.08	11.16
MnO	0.29	0.36	0.29	0.28	0.48	0.29
MgO	15.21	15.33	15.32	15.17	15.05	15.09
CaO	11.35	11.04	11.48	11.35	10.75	11.34
Na2O	1.19	1.11	1.05	1.17	1.59	1.13
K2O	0.37	0.37	0.39	0.43	0.26	0.40
F	0.00	0.00	0.00	0.00	0.00	0.00
Cl	0.06	0.06	0.06	0.07	0.06	0.06
Sum	97.82	98.16	98.09	98.22	97.44	98.02
-O=F	0.00	0.00	0.00	0.00	0.00	0.00
-O=Cl	0.01	0.01	0.01	0.02	0.01	0.01
Total	97.80	98.14	98.08	98.21	97.42	98.01
T						
Si	6.769	6.847	6.776	6.684	7.065	6.750
Al-T	1.231	1.153	1.224	1.316	0.935	1.250
Sum T	*8.000*	*8.000*	*8.000*	*8.000*	*8.000*	*8.000*
C						
Al^{vi} (M)	0.245	0.272	0.244	0.272	0.327	0.268
Ti	0.191	0.156	0.171	0.182	0.104	0.191
Fe3+	0.757	0.870	0.802	0.845	0.635	0.775
Fe2+	0.554	0.443	0.518	0.472	0.683	0.546
Mn	0.035	0.043	0.035	0.034	0.058	0.035
Mg	3.218	3.216	3.230	3.194	3.193	3.185
Cr	0.000	0.000	0.000	0.000	0.000	0.000
Sum C	*5.000*	*5.000*	*5.000*	*5.000*	*5.000*	*5.000*
B						
Mg-B	0	0	0	0	0	0
Ca-B	1.727	1.665	1.739	1.718	1.639	1.721
Na-B	0.273	0.304	0.261	0.282	0.361	0.279
Sum B	*2.00*	*1.97*	*2.00*	*2.00*	*2.00*	*2.00*
A						
Na-A	0.054	0.000	0.028	0.039	0.078	0.032
K	0.067	0.066	0.070	0.077	0.048	0.072
Sum A	*0.121*	*0.066*	*0.097*	*0.116*	*0.126*	*0.104*
Total	*15.121*	*15.034*	*15.097*	*15.116*	*15.126*	*15.104*
W						
F	0.000	0.000	0.000	0.000	0.000	0.000
Cl	0.016	0.015	0.015	0.016	0.015	0.016
OH	0.984	0.985	0.985	0.984	0.985	0.984
Sum W	*1.000*	*1.000*	*1.000*	*1.000*	*1.000*	*1.000*

Spot	MD066-Hbl1-3	MD034-Hbl3-1	MD076-Hbl4-2	MD066-Hbl1-2	MD049-Hbl2-1	MD044-Hbl3-3
Facies	Chataway	Skeena	Guichon	Chataway	Skeena	Chataway
SiO2	48.56	50.74	51.60	48.94	51.97	50.81
Al2O3	8.16	6.46	5.09	7.89	5.30	5.77
TiO2	1.40	0.85	0.85	1.46	0.75	0.72
FeO	11.01	11.58	11.75	11.11	11.40	11.85
MnO	0.34	0.89	0.37	0.42	0.63	0.42
MgO	14.76	15.51	15.66	14.74	15.11	15.68
CaO	11.03	11.17	11.67	11.39	11.78	11.86
Na2O	1.28	1.12	0.92	1.21	0.84	0.79
K2O	0.68	0.22	0.43	0.61	0.32	0.42
F	0.00	0.00	0.00	0.00	0.00	0.00
Cl	0.16	0.04	0.09	0.16	0.03	0.03
Sum	97.38	98.58	98.42	97.92	98.12	98.35
-O=F	0.00	0.00	0.00	0.00	0.00	0.00
-O=Cl	0.04	0.01	0.02	0.03	0.01	0.01
Total	97.35	98.57	98.40	97.89	98.12	98.35
T						
Si	6.957	7.126	7.314	6.995	7.394	7.197
Al-T	1.043	0.874	0.686	1.005	0.606	0.803
Sum T	*8.000*	*8.000*	*8.000*	*8.000*	*8.000*	*8.000*
C						
Al^{vi} (M)	0.336	0.196	0.164	0.324	0.283	0.160
Ti	0.151	0.090	0.091	0.157	0.080	0.077
Fe3+	0.538	0.792	0.469	0.432	0.283	0.596
Fe2+	0.781	0.568	0.924	0.896	1.073	0.808
Mn	0.041	0.106	0.044	0.051	0.075	0.050
Mg	3.153	3.248	3.309	3.141	3.206	3.310
Cr	0.000	0.000	0.000	0.000	0.000	0.000
Sum C	*5.000*	*5.000*	*5.000*	*5.000*	*5.000*	*5.000*
B						
Mg-B	0	0	0	0	0	0
Ca-B	1.693	1.682	1.772	1.744	1.796	1.800
Na-B	0.307	0.304	0.228	0.256	0.204	0.200
Sum B	*2.00*	*1.99*	*2.00*	*2.00*	*2.00*	*2.00*
A						
Na-A	0.049	0.000	0.024	0.080	0.026	0.018
K	0.124	0.039	0.077	0.112	0.059	0.076
Sum A	*0.173*	*0.039*	*0.101*	*0.192*	*0.085*	*0.094*
Total	*15.173*	*15.025*	*15.101*	*15.192*	*15.085*	*15.094*
W						
F	0.000	0.000	0.000	0.000	0.000	0.000
Cl	0.040	0.011	0.022	0.038	0.006	0.008
OH	0.960	0.989	0.978	0.962	0.994	0.992
Sum W	*1.000*	*1.000*	*1.000*	*1.000*	*1.000*	*1.000*

Spot	MD007-Hbl4-3	MD076-Hbl3-3	MD049-Hbl1-4	MD049-Hbl1-1	MD059-Hbl3-2	MD003A-Hbl3-1
Facies	Border	Guichon	Skeena	Skeena	Bethlehem	Border
SiO_2	46.70	50.46	50.88	50.93	50.39	47.71
Al_2O_3	9.69	6.01	6.10	6.17	6.76	9.42
TiO_2	1.90	0.99	0.85	0.78	0.94	1.63
FeO	11.34	11.83	11.40	11.44	11.48	11.53
MnO	0.29	0.42	0.60	0.58	0.71	0.36
MgO	14.94	15.50	14.90	14.81	14.83	14.88
CaO	11.35	11.33	11.56	11.58	11.14	11.17
Na_2O	1.28	1.07	1.06	1.01	1.25	1.13
K_2O	0.41	0.50	0.37	0.30	0.24	0.41
F	0.00	0.00	0.00	0.00	0.00	0.00
Cl	0.08	0.16	0.03	0.03	0.01	0.05
Sum	97.97	98.27	97.74	97.62	97.74	98.30
-O=F	0.00	0.00	0.00	0.00	0.00	0.00
-O=Cl	0.02	0.04	0.01	0.01	0.00	0.01
Total	97.95	98.24	97.73	97.61	97.74	98.29
T						
Si	6.631	7.157	7.272	7.282	7.169	6.729
Al-T	1.369	0.843	0.728	0.718	0.831	1.271
Sum T	*8.000*	*8.000*	*8.000*	*8.000*	*8.000*	*8.000*
C						
Al^{vi} (M)	0.252	0.162	0.299	0.322	0.302	0.295
Ti	0.203	0.106	0.091	0.084	0.101	0.173
Fe3+	0.833	0.641	0.346	0.348	0.544	0.872
Fe2+	0.513	0.762	1.016	1.021	0.822	0.488
Mn	0.035	0.050	0.073	0.070	0.085	0.043
Mg	3.163	3.278	3.175	3.156	3.146	3.129
Cr	0.000	0.000	0.000	0.000	0.000	0.000
Sum C	*5.000*	*5.000*	*5.000*	*5.000*	*5.000*	*5.000*
B						
Mg-B	0	0	0	0	0	0
Ca-B	1.726	1.722	1.770	1.774	1.698	1.688
Na-B	0.274	0.278	0.230	0.226	0.302	0.310
Sum B	*2.00*	*2.00*	*2.00*	*2.00*	*2.00*	*2.00*
A						
Na-A	0.078	0.015	0.064	0.053	0.042	0.000
K	0.073	0.091	0.067	0.054	0.043	0.073
Sum A	*0.151*	*0.106*	*0.131*	*0.107*	*0.085*	*0.073*
Total	*15.151*	*15.106*	*15.131*	*15.107*	*15.085*	*15.071*
W						
F	0.000	0.000	0.000	0.000	0.000	0.000
Cl	0.019	0.039	0.007	0.007	0.003	0.012
OH	0.981	0.961	0.993	0.993	0.997	0.988
Sum W	*1.000*	*1.000*	*1.000*	*1.000*	*1.000*	*1.000*

Spot	MD075-Hbl1-2	MD003A-Hbl2-2	MD076-Hbl3-2	MD003A-Hbl3-4	MD066-Hbl3-2	MD044-Hbl3-2
Facies	Guichon	Border	Guichon	Border	Chataway	Chataway
SiO2	50.92	48.44	50.18	47.37	50.47	50.30
Al2O3	6.35	8.76	6.27	9.71	6.54	6.34
TiO2	0.91	1.61	0.97	1.72	0.87	0.82
FeO	11.72	11.73	11.97	11.53	11.69	12.14
MnO	0.39	0.37	0.42	0.31	0.39	0.42
MgO	15.08	15.06	15.35	14.69	14.81	15.28
CaO	11.26	11.14	11.06	11.46	11.75	11.65
Na2O	1.16	1.09	1.15	1.10	1.00	0.93
K2O	0.53	0.35	0.51	0.41	0.52	0.48
F	0.00	0.00	0.00	0.00	0.00	0.00
Cl	0.17	0.06	0.19	0.07	0.05	0.04
Sum	98.48	98.62	98.07	98.36	98.09	98.40
-O=F	0.00	0.00	0.00	0.00	0.00	0.00
-O=Cl	0.04	0.01	0.04	0.01	0.01	0.01
Total	98.45	98.61	98.03	98.35	98.08	98.39
T						
Si	7.219	6.804	7.126	6.700	7.209	7.132
Al-T	0.781	1.196	0.874	1.300	0.791	0.868
Sum T	*8.000*	*8.000*	*8.000*	*8.000*	*8.000*	*8.000*
C						
Al^{vi} (M)	0.280	0.254	0.176	0.319	0.310	0.192
Ti	0.097	0.170	0.104	0.183	0.093	0.087
Fe3+	0.471	0.891	0.715	0.766	0.325	0.621
Fe2+	0.919	0.487	0.705	0.598	1.071	0.818
Mn	0.047	0.044	0.050	0.037	0.048	0.050
Mg	3.187	3.154	3.250	3.097	3.153	3.231
Cr	0.000	0.000	0.000	0.000	0.000	0.000
Sum C	*5.000*	*5.000*	*5.000*	*5.000*	*5.000*	*5.000*
B						
Mg-B	0	0	0	0	0	0
Ca-B	1.710	1.676	1.683	1.737	1.799	1.769
Na-B	0.290	0.297	0.316	0.263	0.201	0.231
Sum B	*2.00*	*1.97*	*2.00*	*2.00*	*2.00*	*2.00*
A						
Na-A	0.030	0.000	0.000	0.038	0.076	0.024
K	0.097	0.063	0.093	0.074	0.095	0.088
Sum A	*0.127*	*0.063*	*0.093*	*0.112*	*0.172*	*0.111*
Total	*15.127*	*15.035*	*15.093*	*15.112*	*15.172*	*15.111*
W						
F	0.000	0.000	0.000	0.000	0.000	0.000
Cl	0.040	0.015	0.047	0.016	0.011	0.009
OH	0.960	0.985	0.953	0.984	0.989	0.991
Sum W	*1.000*	*1.000*	*1.000*	*1.000*	*1.000*	*1.000*

Spot	MD049-Hbl3-1	MD049-Hbl3-3	MD075-Hbl3-3	MD076-Hbl2-2	MD066-Hbl3-3	MD076-Hbl1-1
Facies	Skeena	Skeena	Guichon	Guichon	Chataway	Guichon
SiO2	50.53	50.84	50.75	50.78	49.29	50.65
Al2O3	6.17	5.92	6.30	5.78	7.61	5.71
TiO2	0.75	0.79	0.89	1.03	1.38	0.91
FeO	11.49	11.66	11.91	12.32	11.74	12.17
MnO	0.58	0.60	0.41	0.39	0.44	0.39
MgO	14.40	14.60	14.87	15.37	14.57	15.08
CaO	11.48	11.73	11.36	11.72	11.45	11.59
Na2O	0.83	0.87	1.04	0.93	1.18	0.94
K2O	0.41	0.38	0.52	0.47	0.68	0.44
F	0.00	0.00	0.00	0.00	0.00	0.00
Cl	0.02	0.03	0.15	0.13	0.16	0.10
Sum	96.67	97.44	98.21	98.92	98.49	97.97
-O=F	0.00	0.00	0.00	0.00	0.00	0.00
-O=Cl	0.00	0.01	0.03	0.03	0.04	0.02
Total	96.66	97.43	98.17	98.89	98.46	97.95
T						
Si	7.304	7.308	7.225	7.182	7.025	7.231
Al-T	0.696	0.692	0.775	0.818	0.975	0.769
Sum T	*8.000*	*8.000*	*8.000*	*8.000*	*8.000*	*8.000*
C						
Al^{vi} (M)	0.355	0.311	0.281	0.145	0.303	0.192
Ti	0.082	0.085	0.095	0.110	0.148	0.098
Fe3+	0.314	0.283	0.454	0.559	0.427	0.497
Fe2+	1.075	1.119	0.964	0.898	0.972	0.957
Mn	0.071	0.073	0.050	0.046	0.053	0.048
Mg	3.102	3.129	3.156	3.241	3.097	3.209
Cr	0.000	0.000	0.000	0.000	0.000	0.000
Sum C	*5.000*	*5.000*	*5.000*	*5.000*	*5.000*	*5.000*
B						
Mg-B	0	0	0	0	0	0
Ca-B	1.778	1.807	1.733	1.776	1.749	1.773
Na-B	0.222	0.193	0.267	0.224	0.251	0.227
Sum B	*2.00*	*2.00*	*2.00*	*2.00*	*2.00*	*2.00*
A						
Na-A	0.010	0.050	0.022	0.032	0.076	0.032
K	0.075	0.070	0.095	0.085	0.124	0.081
Sum A	*0.085*	*0.121*	*0.116*	*0.117*	*0.200*	*0.112*
Total	*15.085*	*15.121*	*15.116*	*15.117*	*15.200*	*15.112*
W						
F	0.000	0.000	0.000	0.000	0.000	0.000
Cl	0.005	0.008	0.037	0.032	0.038	0.024
OH	0.995	0.992	0.963	0.968	0.962	0.976
Sum W	*1.000*	*1.000*	*1.000*	*1.000*	*1.000*	*1.000*

Spot	MD059-Hbl2-3	MD076-Hbl4-1	MD063-Hbl2-1	MD075-Hbl3-2	MD046-Hbl3-2	MD003A-Hbl1-1
Facies	Bethlehem	Guichon	F.g. Granodiorite	Guichon	Border	Border
SiO2	48.64	50.81	50.55	50.45	48.95	47.66
Al2O3	8.62	5.89	6.38	6.65	8.35	9.24
TiO2	1.26	1.00	0.67	0.95	1.65	1.66
FeO	11.60	12.26	12.30	12.03	11.68	12.05
MnO	0.49	0.37	0.49	0.39	0.33	0.31
MgO	14.34	15.14	15.16	14.82	14.38	14.76
CaO	10.77	11.73	11.80	11.13	11.30	11.12
Na2O	1.75	0.92	1.02	1.18	0.90	1.20
K2O	0.31	0.46	0.56	0.56	0.60	0.49
F	0.00	0.00	0.00	0.00	0.00	0.00
Cl	0.06	0.11	0.02	0.19	0.10	0.10
Sum	97.83	98.69	98.95	98.34	98.23	98.59
-O=F	0.00	0.00	0.00	0.00	0.00	0.00
-O=Cl	0.01	0.02	0.00	0.04	0.02	0.02
Total	97.82	98.67	98.94	98.30	98.20	98.57
T						
Si	6.930	7.207	7.153	7.169	6.954	6.724
Al-T	1.070	0.793	0.847	0.831	1.046	1.276
Sum T	*8.000*	*8.000*	*8.000*	*8.000*	*8.000*	*8.000*
C						
Al^{vi} (M)	0.377	0.192	0.216	0.283	0.351	0.260
Ti	0.135	0.106	0.071	0.101	0.177	0.177
Fe3+	0.595	0.483	0.531	0.530	0.545	0.883
Fe2+	0.787	0.971	0.924	0.899	0.842	0.539
Mn	0.059	0.045	0.059	0.047	0.039	0.038
Mg	3.046	3.202	3.198	3.139	3.046	3.104
Cr	0.000	0.000	0.000	0.000	0.000	0.000
Sum C	*5.000*	*5.000*	*5.000*	*5.000*	*5.000*	*5.000*
B						
Mg-B	0	0	0	0	0	0
Ca-B	1.644	1.784	1.789	1.694	1.721	1.682
Na-B	0.356	0.216	0.211	0.306	0.247	0.318
Sum B	*2.00*	*2.00*	*2.00*	*2.00*	*1.97*	*2.00*
A						
Na-A	0.126	0.038	0.068	0.019	0.000	0.010
K	0.057	0.083	0.100	0.102	0.108	0.087
Sum A	*0.183*	*0.121*	*0.168*	*0.121*	*0.108*	*0.098*
Total	*15.183*	*15.121*	*15.168*	*15.121*	*15.076*	*15.098*
W						
F	0.000	0.000	0.000	0.000	0.000	0.000
Cl	0.014	0.026	0.004	0.045	0.024	0.024
OH	0.986	0.974	0.996	0.955	0.976	0.976
Sum W	*1.000*	*1.000*	*1.000*	*1.000*	*1.000*	*1.000*

Spot	MD063-Hbl2-2	MD076-Hbl2-1	MD046-Hbl2-2	MD003A-Hbl3-3	MD063-Hbl1-1	MD076-Hbl3-1
Facies	F.g. Granodiorite	Guichon	Border	Border	F.g. Granodiorite	Guichon
SiO2	50.10	50.45	49.00	47.11	49.99	49.93
Al2O3	6.26	6.17	8.14	9.79	6.61	6.35
TiO2	0.92	1.03	1.56	1.78	0.82	1.11
FeO	12.43	12.35	11.69	11.95	12.44	12.34
MnO	0.50	0.40	0.25	0.36	0.48	0.39
MgO	15.21	15.10	14.27	14.58	15.15	15.00
CaO	11.69	11.42	11.49	11.21	11.71	11.37
Na2O	1.07	0.97	0.93	1.24	1.17	1.10
K2O	0.58	0.51	0.66	0.46	0.59	0.59
F	0.00	0.00	0.00	0.00	0.00	0.00
Cl	0.05	0.08	0.17	0.05	0.10	0.17
Sum	98.81	98.50	98.15	98.51	99.05	98.36
-O=F	0.00	0.00	0.00	0.00	0.00	0.00
-O=Cl	0.01	0.02	0.04	0.01	0.02	0.04
Total	98.80	98.48	98.11	98.50	99.02	98.32
T						
Si	7.105	7.153	6.998	6.656	7.081	7.112
Al-T	0.895	0.847	1.002	1.344	0.919	0.888
Sum T	*8.000*	*8.000*	*8.000*	*8.000*	*8.000*	*8.000*
C						
Al^{vi} (M)	0.151	0.185	0.368	0.286	0.183	0.178
Ti	0.098	0.109	0.167	0.189	0.087	0.119
Fe3+	0.597	0.612	0.405	0.864	0.582	0.590
Fe2+	0.878	0.853	0.991	0.548	0.891	0.880
Mn	0.060	0.048	0.031	0.043	0.057	0.047
Mg	3.216	3.192	3.038	3.071	3.199	3.186
Cr	0.000	0.000	0.000	0.000	0.000	0.000
Sum C	*5.000*	*5.000*	*5.000*	*5.000*	*5.000*	*5.000*
B						
Mg-B	0	0	0	0	0	0
Ca-B	1.777	1.735	1.758	1.698	1.776	1.736
Na-B	0.223	0.265	0.242	0.302	0.224	0.264
Sum B	*2.00*	*2.00*	*2.00*	*2.00*	*2.00*	*2.00*
A						
Na-A	0.070	0.003	0.016	0.036	0.097	0.039
K	0.104	0.092	0.120	0.082	0.106	0.107
Sum A	*0.174*	*0.095*	*0.136*	*0.119*	*0.203*	*0.146*
Total	*15.174*	*15.095*	*15.136*	*15.119*	*15.203*	*15.146*
W						
F	0.000	0.000	0.000	0.000	0.000	0.000
Cl	0.012	0.020	0.041	0.013	0.025	0.042
OH	0.988	0.980	0.959	0.987	0.975	0.958
Sum W	*1.000*	*1.000*	*1.000*	*1.000*	*1.000*	*1.000*

Spot	MD076-Hbl2-3	MD075-Hbl2-2	MD075-Hbl1-1	MD046-Hbl3-3	MD046-Hbl3-1	MD071-Hbl1-2
Facies	Guichon	Guichon	Guichon	Border	Border	Bethsaida
SiO2	49.55	50.28	50.45	49.33	49.54	50.03
Al2O3	6.68	6.59	6.59	8.02	8.22	6.56
TiO2	1.10	1.10	1.02	1.48	1.49	0.82
FeO	12.42	12.10	12.04	11.99	11.91	11.87
MnO	0.44	0.39	0.40	0.31	0.34	1.13
MgO	15.08	14.65	14.59	14.49	14.32	14.25
CaO	11.22	11.36	11.47	11.04	11.31	11.11
Na2O	1.21	1.19	1.11	0.94	0.81	1.14
K2O	0.57	0.57	0.56	0.49	0.54	0.30
F	0.00	0.00	0.00	0.00	0.00	0.00
Cl	0.19	0.16	0.17	0.08	0.09	0.01
Sum	98.45	98.41	98.38	98.18	98.57	97.22
-O=F	0.00	0.00	0.00	0.00	0.00	0.00
-O=Cl	0.04	0.04	0.04	0.02	0.02	0.00
Total	98.41	98.37	98.34	98.16	98.55	97.22
T						
Si	7.041	7.170	7.196	6.986	7.004	7.186
Al-T	0.959	0.830	0.804	1.014	0.996	0.814
Sum T	*8.000*	*8.000*	*8.000*	*8.000*	*8.000*	*8.000*
C						
Al^{vi} (M)	0.160	0.277	0.304	0.325	0.374	0.297
Ti	0.118	0.118	0.109	0.158	0.159	0.088
Fe3+	0.711	0.412	0.369	0.676	0.559	0.546
Fe2+	0.765	1.031	1.068	0.743	0.849	0.880
Mn	0.052	0.048	0.048	0.037	0.040	0.138
Mg	3.194	3.114	3.102	3.060	3.018	3.051
Cr	0.000	0.000	0.000	0.000	0.000	0.000
Sum C	*5.000*	*5.000*	*5.000*	*5.000*	*5.000*	*5.000*
B						
Mg-B	0	0	0	0	0	0
Ca-B	1.708	1.736	1.752	1.675	1.713	1.710
Na-B	0.292	0.264	0.248	0.258	0.222	0.290
Sum B	*2.00*	*2.00*	*2.00*	*1.93*	*1.94*	*2.00*
A						
Na-A	0.041	0.065	0.059	0.000	0.000	0.029
K	0.103	0.104	0.101	0.089	0.097	0.054
Sum A	*0.144*	*0.169*	*0.160*	*0.089*	*0.097*	*0.083*
Total	*15.144*	*15.169*	*15.160*	*15.021*	*15.032*	*15.083*
W						
F	0.000	0.000	0.000	0.000	0.000	0.000
Cl	0.046	0.039	0.041	0.019	0.022	0.001
OH	0.954	0.961	0.959	0.981	0.978	0.999
Sum W	*1.000*	*1.000*	*1.000*	*1.000*	*1.000*	*1.000*

Spot	MD076-Hbl1-3	MD044-Hbl1-2	MD066-Hbl4-2	MD075-Hbl2-1	MD049-Hbl3-2	MD046-Hbl1-3
Facies	Guichon	Chataway	Chataway	Guichon	Skeena	Border
SiO2	50.01	48.61	49.29	50.14	49.72	48.82
Al2O3	6.16	7.80	7.47	6.80	6.90	8.39
TiO2	1.01	1.65	1.27	1.09	1.22	1.69
FeO	12.58	12.38	12.00	12.24	12.03	12.05
MnO	0.43	0.38	0.39	0.34	0.62	0.25
MgO	15.09	14.81	14.27	14.56	14.17	14.16
CaO	11.13	11.25	11.54	11.46	11.60	11.35
Na2O	1.14	1.41	1.21	1.17	1.17	0.95
K2O	0.52	0.61	0.68	0.62	0.25	0.63
F	0.00	0.00	0.00	0.00	0.00	0.00
Cl	0.17	0.19	0.09	0.17	0.06	0.16
Sum	98.23	99.08	98.20	98.59	97.75	98.47
-O=F	0.00	0.00	0.00	0.00	0.00	0.00
-O=Cl	0.04	0.04	0.02	0.04	0.01	0.04
Total	98.20	99.04	98.18	98.55	97.73	98.43
T						
Si	7.111	6.884	7.065	7.147	7.144	6.945
Al-T	0.889	1.116	0.935	0.853	0.856	1.055
Sum T	8.000	8.000	8.000	8.000	8.000	8.000
C						
Al^{vi} (M)	0.145	0.186	0.328	0.289	0.312	0.352
Ti	0.108	0.176	0.137	0.117	0.132	0.181
Fe3+	0.728	0.667	0.329	0.395	0.336	0.502
Fe2+	0.767	0.799	1.109	1.065	1.109	0.931
Mn	0.052	0.046	0.047	0.042	0.076	0.030
Mg	3.200	3.126	3.050	3.093	3.035	3.003
Cr	0.000	0.000	0.000	0.000	0.000	0.000
Sum C	5.000	5.000	5.000	5.000	5.000	5.000
B						
Mg-B	0	0	0	0	0	0
Ca-B	1.696	1.707	1.772	1.750	1.786	1.731
Na-B	0.304	0.293	0.228	0.250	0.214	0.261
Sum B	2.00	2.00	2.00	2.00	2.00	1.99
A						
Na-A	0.010	0.094	0.108	0.074	0.112	0.000
K	0.095	0.109	0.124	0.112	0.046	0.115
Sum A	0.104	0.203	0.232	0.186	0.158	0.115
Total	15.104	15.203	15.232	15.186	15.158	15.107
W						
F	0.000	0.000	0.000	0.000	0.000	0.000
Cl	0.040	0.045	0.023	0.042	0.015	0.039
OH	0.960	0.955	0.977	0.958	0.985	0.961
Sum W	1.000	1.000	1.000	1.000	1.000	1.000

Spot	MD003A-Hbl1-2	MD075-Hbl3-1	MD046-Hbl1-2	MD075-Hbl2-3	MD063-Hbl3-1	MD076-Hbl1-2
Facies	Border	Guichon	Border	Guichon	F.g. Granodiorite	Guichon
SiO_2	47.12	50.01	48.56	50.52	48.36	49.74
Al_2O_3	10.01	6.87	8.35	6.39	7.57	6.62
TiO_2	1.89	1.05	1.74	1.00	1.52	1.19
FeO	12.20	12.24	12.12	12.46	12.45	12.78
MnO	0.36	0.39	0.22	0.38	0.50	0.38
MgO	14.31	14.32	14.14	14.52	14.41	14.73
CaO	10.99	11.42	11.20	11.61	11.48	11.66
Na_2O	1.29	1.08	1.02	1.05	1.45	1.07
K_2O	0.46	0.63	0.64	0.54	0.73	0.52
F	0.00	0.00	0.00	0.00	0.00	0.00
Cl	0.07	0.18	0.16	0.17	0.18	0.13
Sum	98.70	98.18	98.15	98.65	98.65	98.83
-O=F	0.00	0.00	0.00	0.00	0.00	0.00
-O=Cl	0.02	0.04	0.04	0.04	0.04	0.03
Total	98.68	98.14	98.11	98.61	98.61	98.80
T						
Si	6.646	7.159	6.929	7.201	6.928	7.073
Al-T	1.354	0.841	1.071	0.799	1.072	0.927
Sum T	*8.000*	*8.000*	*8.000*	*8.000*	*8.000*	*8.000*
C						
Al^{vi} (M)	0.310	0.317	0.332	0.275	0.206	0.183
Ti	0.201	0.114	0.187	0.108	0.163	0.127
Fe^{3+}	0.886	0.381	0.541	0.374	0.480	0.546
Fe^{2+}	0.552	1.084	0.906	1.111	1.012	0.975
Mn	0.043	0.047	0.026	0.046	0.061	0.046
Mg	3.008	3.056	3.009	3.086	3.078	3.124
Cr	0.000	0.000	0.000	0.000	0.000	0.000
Sum C	*5.000*	*5.000*	*5.000*	*5.000*	*5.000*	*5.000*
B						
Mg-B	0	0	0	0	0	0
Ca-B	1.661	1.751	1.713	1.773	1.763	1.776
Na-B	0.339	0.249	0.282	0.227	0.237	0.224
Sum B	*2.00*	*2.00*	*1.99*	*2.00*	*2.00*	*2.00*
A						
Na-A	0.014	0.049	0.000	0.063	0.164	0.072
K	0.082	0.115	0.117	0.098	0.133	0.095
Sum A	*0.095*	*0.164*	*0.117*	*0.161*	*0.297*	*0.167*
Total	*15.095*	*15.164*	*15.112*	*15.161*	*15.297*	*15.167*
W						
F	0.000	0.000	0.000	0.000	0.000	0.000
Cl	0.018	0.044	0.038	0.040	0.045	0.030
OH	0.982	0.956	0.962	0.960	0.955	0.970
Sum W	*1.000*	*1.000*	*1.000*	*1.000*	*1.000*	*1.000*

Spot	MD003A-Hbl4-2	MD066-Hbl2-2	MD046-Hbl1-1	MD044-Hbl1-1	MD066-Hbl4-1	MD063-Hbl1-2
Facies	Border	Chataway	Border	Chataway	Chataway	F.g. Granodiorite
SiO_2	47.31	48.25	48.62	48.51	49.07	48.56
Al_2O_3	9.84	7.85	8.41	7.84	7.35	7.53
TiO_2	1.69	1.54	1.64	1.59	1.36	1.41
FeO	12.46	12.12	12.30	12.72	12.30	12.75
MnO	0.37	0.42	0.25	0.41	0.41	0.47
MgO	14.31	13.91	14.04	14.45	13.91	14.39
CaO	11.05	11.41	11.43	11.28	11.74	11.51
Na_2O	1.22	1.25	0.95	1.27	0.92	1.35
K_2O	0.46	0.67	0.64	0.59	0.64	0.71
F	0.00	0.00	0.00	0.00	0.00	0.00
Cl	0.06	0.16	0.11	0.17	0.18	0.18
Sum	98.78	97.57	98.40	98.83	97.88	98.87
-O=F	0.00	0.00	0.00	0.00	0.00	0.00
-O=Cl	0.01	0.04	0.02	0.04	0.04	0.04
Total	98.77	97.54	98.37	98.80	97.84	98.83
T						
Si	6.667	6.979	6.930	6.895	7.077	6.936
Al-T	1.333	1.021	1.070	1.105	0.923	1.064
Sum T	*8.000*	*8.000*	*8.000*	*8.000*	*8.000*	*8.000*
C						
Al^{vi} (M)	0.301	0.317	0.342	0.207	0.327	0.203
Ti	0.179	0.167	0.176	0.170	0.148	0.152
Fe^{3+}	0.920	0.360	0.505	0.665	0.298	0.531
Fe^{2+}	0.549	1.106	0.961	0.848	1.186	0.992
Mn	0.044	0.051	0.031	0.049	0.050	0.057
Mg	3.007	2.999	2.984	3.062	2.992	3.065
Cr	0.000	0.000	0.000	0.000	0.000	0.000
Sum C	*5.000*	*5.000*	*5.000*	*5.000*	*5.000*	*5.000*
B						
Mg-B	0	0	0	0	0	0
Ca-B	1.669	1.768	1.746	1.718	1.814	1.761
Na-B	0.331	0.232	0.254	0.282	0.186	0.239
Sum B	*2.00*	*2.00*	*2.00*	*2.00*	*2.00*	*2.00*
A						
Na-A	0.003	0.118	0.008	0.068	0.070	0.135
K	0.082	0.124	0.117	0.107	0.118	0.130
Sum A	*0.085*	*0.241*	*0.125*	*0.176*	*0.188*	*0.264*
Total	*15.085*	*15.241*	*15.125*	*15.176*	*15.188*	*15.264*
W						
F	0.000	0.000	0.000	0.000	0.000	0.000
Cl	0.015	0.039	0.027	0.041	0.045	0.044
OH	0.985	0.961	0.973	0.959	0.955	0.956
Sum W	*1.000*	*1.000*	*1.000*	*1.000*	*1.000*	*1.000*

Spot	MD044-Hbl3-1	MD046-Hbl2-1	MD044-Hbl2-3	MD066-Hbl1-1	MD003A-Hbl1-3	MD049-Hbl2-3
Facies	Chataway	Border	Chataway	Chataway	Border	Skeena
SiO2	48.20	48.83	48.48	48.49	46.45	49.48
Al2O3	7.84	8.46	7.86	7.72	10.76	7.24
TiO2	1.64	1.69	0.84	1.58	2.15	1.21
FeO	12.72	12.40	13.13	12.44	12.68	12.51
MnO	0.42	0.26	0.42	0.44	0.35	0.59
MgO	14.30	13.89	14.66	13.85	14.09	13.90
CaO	11.11	11.38	11.36	11.33	11.00	11.79
Na2O	1.31	1.01	0.63	1.31	1.39	1.08
K2O	0.61	0.56	0.51	0.68	0.47	0.42
F	0.00	0.00	0.00	0.00	0.00	0.00
Cl	0.18	0.15	0.16	0.16	0.08	0.03
Sum	98.32	98.64	98.05	98.01	99.43	98.23
-O=F	0.00	0.00	0.00	0.00	0.00	0.00
-O=Cl	0.04	0.03	0.04	0.04	0.02	0.01
Total	98.28	98.60	98.02	97.97	99.41	98.22
T						
Si	6.887	6.947	6.883	6.988	6.517	7.100
Al-T	1.113	1.053	1.117	1.012	1.483	0.900
Sum T	8.000	8.000	8.000	8.000	8.000	8.000
C						
Al^{vi} (M)	0.206	0.366	0.198	0.299	0.297	0.324
Ti	0.176	0.181	0.089	0.171	0.227	0.130
Fe3+	0.681	0.478	1.017	0.380	0.960	0.315
Fe2+	0.838	0.998	0.541	1.119	0.528	1.187
Mn	0.051	0.032	0.050	0.054	0.041	0.072
Mg	3.047	2.946	3.103	2.976	2.946	2.973
Cr	0.000	0.000	0.000	0.000	0.000	0.000
Sum C	5.000	5.000	5.000	5.000	5.000	5.000
B						
Mg-B	0	0	0	0	0	0
Ca-B	1.701	1.734	1.728	1.750	1.654	1.812
Na-B	0.299	0.266	0.173	0.250	0.346	0.188
Sum B	2.00	2.00	1.90	2.00	2.00	2.00
A						
Na-A	0.063	0.012	0.000	0.115	0.033	0.112
K	0.110	0.101	0.093	0.124	0.084	0.077
Sum A	0.173	0.113	0.093	0.239	0.118	0.188
Total	15.173	15.113	14.994	15.239	15.118	15.188
W						
F	0.000	0.000	0.000	0.000	0.000	0.000
Cl	0.045	0.037	0.039	0.040	0.019	0.007
OH	0.955	0.963	0.961	0.960	0.981	0.993
Sum W	1.000	1.000	1.000	1.000	1.000	1.000

Spot	MD003A-Hbl2-3	MD066-Hbl2-3	MD044-Hbl1-3	MD003A-Hbl2-1	MD063-Hbl1-3	MD044-Hbl2-2
Facies	Border	Chataway	Chataway	Border	F.g. Granodiorite	Chataway
SiO2	46.38	48.34	48.62	46.28	48.76	48.23
Al2O3	10.94	7.94	7.93	10.83	7.43	7.95
TiO2	2.17	1.37	1.39	2.11	1.42	1.65
FeO	12.76	12.77	13.06	12.78	13.10	13.10
MnO	0.34	0.46	0.42	0.35	0.49	0.43
MgO	13.88	13.88	14.17	13.83	14.17	14.17
CaO	11.12	11.27	11.57	10.96	11.68	11.30
Na2O	1.39	0.89	1.15	1.41	1.31	1.30
K2O	0.48	0.61	0.65	0.53	0.70	0.64
F	0.00	0.00	0.00	0.00	0.00	0.00
Cl	0.06	0.17	0.03	0.07	0.22	0.21
Sum	99.51	97.72	99.00	99.15	99.28	98.98
-O=F	0.00	0.00	0.00	0.00	0.00	0.00
-O=Cl	0.01	0.04	0.01	0.02	0.05	0.05
Total	99.50	97.68	98.99	99.14	99.23	98.93
T						
Si	6.515	6.944	6.913	6.522	6.960	6.868
Al-T	1.485	1.056	1.087	1.478	1.040	1.132
Sum T	8.000	8.000	8.000	8.000	8.000	8.000
C						
Al^{vi} (M)	0.325	0.288	0.243	0.322	0.210	0.202
Ti	0.229	0.148	0.148	0.224	0.153	0.177
Fe3+	0.890	0.642	0.585	0.917	0.461	0.652
Fe2+	0.609	0.893	0.969	0.590	1.102	0.909
Mn	0.040	0.056	0.051	0.042	0.059	0.052
Mg	2.906	2.973	3.004	2.906	3.015	3.009
Cr	0.000	0.000	0.000	0.000	0.000	0.000
Sum C	5.000	5.000	5.000	5.000	5.000	5.000
B						
Mg-B	0	0	0	0	0	0
Ca-B	1.674	1.735	1.763	1.656	1.786	1.725
Na-B	0.326	0.248	0.237	0.344	0.214	0.275
Sum B	2.00	1.98	2.00	2.00	2.00	2.00
A						
Na-A	0.052	0.000	0.081	0.041	0.149	0.084
K	0.086	0.111	0.119	0.095	0.127	0.116
Sum A	0.137	0.111	0.200	0.136	0.277	0.199
Total	15.137	15.095	15.200	15.136	15.277	15.199
W						
F	0.000	0.000	0.000	0.000	0.000	0.000
Cl	0.015	0.042	0.006	0.016	0.055	0.051
OH	0.985	0.958	0.994	0.984	0.945	0.949
Sum W	1.000	1.000	1.000	1.000	1.000	1.000

Spot	MD066-Hbl3-1	MD066-Hbl2-1	MD044-Hbl2-1
Facies	Chataway	Chataway	Chataway
SiO2	48.91	48.65	48.28
Al2O3	7.87	7.63	7.67
TiO2	1.18	1.51	1.55
FeO	12.85	12.69	13.26
MnO	0.44	0.46	0.44
MgO	13.72	13.45	14.02
CaO	11.79	11.40	11.47
Na2O	0.98	1.22	1.18
K2O	0.70	0.69	0.60
F	0.00	0.00	0.00
Cl	0.05	0.19	0.14
Sum	98.49	97.91	98.60
-O=F	0.00	0.00	0.00
-O=Cl	0.01	0.04	0.03
Total	98.48	97.87	98.57
T			
Si	7.014	7.040	6.909
Al-T	0.986	0.960	1.091
Sum T	*8.000*	*8.000*	*8.000*
C			
Al^{vi} (M)	0.345	0.341	0.203
Ti	0.127	0.165	0.167
Fe3+	0.364	0.285	0.599
Fe2+	1.177	1.251	0.988
Mn	0.053	0.057	0.053
Mg	2.934	2.902	2.991
Cr	0.000	0.000	0.000
Sum C	*5.000*	*5.000*	*5.000*
B			
Mg-B	0	0	0
Ca-B	1.811	1.767	1.759
Na-B	0.189	0.233	0.241
Sum B	*2.00*	*2.00*	*2.00*
A			
Na-A	0.083	0.110	0.088
K	0.128	0.128	0.110
Sum A	*0.211*	*0.238*	*0.197*
Total	*15.211*	*15.238*	*15.197*
W			
F	0.000	0.000	0.000
Cl	0.012	0.046	0.033
OH	0.988	0.954	0.967
Sum W	*1.000*	*1.000*	*1.000*

Biotite Chemistry – based on 11 oxygens

Spot	MD059-Bt1-1	MD059-Bt1-2	MD059-Bt2-1	MD059-Bt2-2	MD059-Bt3-1	MD059-Bt3-2
Facies	Bethlehem	Bethlehem	Bethlehem	Bethlehem	Bethlehem	Bethlehem
SiO2 wt%	36.61	36.56	35.09	35.34	36.43	35.88
TiO2 wt%	3.77	3.85	3.91	3.96	3.92	4.01
Al2O3 wt%	14.97	15.12	15.05	14.92	15.28	15.20
FeO wt%	15.33	15.35	15.00	14.88	15.01	15.51
MnO wt%	0.43	0.41	0.40	0.39	0.41	0.44
MgO wt%	14.42	14.76	14.90	14.87	15.01	15.03
K2O wt%	9.52	9.62	9.24	9.52	9.39	9.03
F wt%	0.00	0.00	0.00	0.00	0.00	0.00
Cl wt%	0.07	0.04	0.06	0.07	0.04	0.04
H2O*	3.96	3.99	3.90	3.91	4.00	3.97
Subtotal	99.09	99.70	97.55	97.86	99.49	99.13
-O=F,Cl	0.02	0.01	0.01	0.02	0.01	0.01
Total	99.08	99.69	97.54	97.84	99.48	99.12
Si	5.512	5.472	5.374	5.398	5.452	5.399
Al iv	2.488	2.528	2.626	2.602	2.548	2.601
T	*8.000*	*8.000*	*8.000*	*8.000*	*8.000*	*8.000*
Al vi	0.169	0.140	0.090	0.084	0.146	0.096
Ti	0.427	0.434	0.450	0.455	0.441	0.454
Fe$_{tot}$	1.930	1.921	1.921	1.901	1.878	1.952
Fe^{3+}	0.425	0.423	0.423	0.418	0.413	0.429
Fe^{2+}	1.505	1.499	1.499	1.483	1.465	1.522
Mn	0.055	0.051	0.052	0.051	0.052	0.056
Mg	3.237	3.294	3.400	3.386	3.347	3.372
M	*5.818*	*5.841*	*5.915*	*5.877*	*5.864*	*5.931*
K	1.829	1.838	1.806	1.855	1.793	1.734
I	*1.829*	*1.838*	*1.806*	*1.855*	*1.793*	*1.734*
F	0.000	0.000	0.000	0.000	0.000	0.000
Cl	0.018	0.011	0.016	0.018	0.011	0.011
OH*	3.982	3.989	3.984	3.982	3.989	3.989

Spot	MD059-Bt3-3	MD069-Bt1-1	MD069-Bt1-2	MD069-Bt2-1	MD069-Bt2-2	MD069-Bt3-1
Facies	Bethlehem	Bethsaida	Bethsaida	Bethsaida	Bethsaida	Bethsaida
SiO2 wt%	36.03	35.24	35.33	35.15	34.87	34.31
TiO2 wt%	3.35	3.94	3.76	3.70	3.85	3.69
Al2O3 wt%	15.44	15.06	15.19	15.17	15.06	15.07
FeO wt%	15.34	15.85	16.00	15.88	16.18	16.24
MnO wt%	0.39	0.56	0.61	0.63	0.65	0.61
MgO wt%	15.47	13.84	14.23	14.06	13.74	14.18
K2O wt%	8.65	9.62	9.71	9.56	9.59	8.50
F wt%	0.00	0.00	0.00	0.00	0.00	0.00
Cl wt%	0.05	0.04	0.03	0.04	0.04	0.05
H2O*	3.97	3.90	3.93	3.90	3.88	3.84
Subtotal	98.69	98.04	98.80	98.10	97.86	96.49
-O=F,Cl	0.01	0.01	0.01	0.01	0.01	0.01
Total	98.68	98.03	98.80	98.09	97.85	96.48
Si	5.424	5.401	5.379	5.387	5.371	5.335
Al iv	2.576	2.599	2.621	2.613	2.629	2.665
T	*8.000*	*8.000*	*8.000*	*8.000*	*8.000*	*8.000*
Al vi	0.164	0.122	0.106	0.127	0.104	0.098
Ti	0.380	0.454	0.431	0.426	0.446	0.431
Fe_{tot}	1.931	2.032	2.038	2.035	2.084	2.112
Fe^{3+}	0.425	0.447	0.448	0.448	0.459	0.465
Fe^{2+}	1.506	1.585	1.590	1.587	1.626	1.647
Mn	0.050	0.072	0.079	0.082	0.084	0.081
Mg	3.471	3.163	3.231	3.213	3.155	3.287
M	*5.996*	*5.844*	*5.884*	*5.882*	*5.874*	*6.009*
K	1.661	1.881	1.886	1.869	1.885	1.687
I	*1.661*	*1.881*	*1.886*	*1.869*	*1.885*	*1.687*
F	0.000	0.000	0.000	0.000	0.000	0.000
Cl	0.013	0.009	0.006	0.011	0.010	0.013
OH*	3.987	3.991	3.994	3.989	3.990	3.987

Spot	MD069-Bt3-2	MD069-Bt4-1	MD069-Bt4-2	MD071-Bt1-1	MD071-Bt1-2	MD001-Bt1-1
Facies	Bethsaida	Bethsaida	Bethsaida	Bethsaida	Bethsaida	Border
SiO2 wt%	34.59	36.35	36.33	35.67	36.14	35.78
TiO2 wt%	3.85	3.70	3.89	4.01	3.68	4.53
Al2O3 wt%	15.17	14.76	15.12	14.69	14.72	14.84
FeO wt%	16.12	15.85	15.73	15.86	15.74	18.85
MnO wt%	0.60	0.52	0.45	0.60	0.62	0.13
MgO wt%	13.95	14.22	13.89	14.13	14.31	12.31
K2O wt%	9.29	9.56	9.68	9.32	9.59	9.97
F wt%	0.00	0.00	0.00	0.00	0.00	0.00
Cl wt%	0.05	0.03	0.05	0.04	0.03	0.60
H2O*	3.87	3.95	3.96	3.92	3.94	3.80
Subtotal	97.48	98.95	99.10	98.21	98.78	100.82
-O=F,Cl	0.01	0.01	0.01	0.01	0.01	0.14
Total	97.47	98.95	99.09	98.20	98.78	100.68
Si	5.341	5.502	5.487	5.446	5.484	5.422
Al iv	2.659	2.498	2.513	2.554	2.516	2.578
T	8.000	8.000	8.000	8.000	8.000	8.000
Al vi	0.101	0.135	0.179	0.088	0.117	0.072
Ti	0.446	0.421	0.442	0.460	0.420	0.516
Fe_{tot}	2.081	2.007	1.987	2.025	1.998	2.389
Fe^{3+}	0.458	0.441	0.437	0.445	0.440	0.525
Fe^{2+}	1.623	1.565	1.550	1.579	1.558	1.863
Mn	0.078	0.067	0.057	0.077	0.080	0.017
Mg	3.211	3.208	3.127	3.216	3.236	2.779
M	5.918	5.837	5.792	5.866	5.851	5.773
K	1.830	1.846	1.865	1.815	1.857	1.927
I	1.830	1.846	1.865	1.815	1.857	1.927
F	0.000	0.000	0.000	0.000	0.000	0.000
Cl	0.012	0.008	0.012	0.009	0.007	0.155
OH*	3.988	3.992	3.988	3.991	3.993	3.845

Spot	MD001-Bt1-2	MD001-Bt1-3	MD001-Bt2-1	MD001-Bt2-2	MD001-Bt2-3	MD001-Bt3-1
Facies	Border	Border	Border	Border	Border	Border
SiO2 wt%	35.65	36.16	35.90	35.89	35.57	36.04
TiO2 wt%	4.68	4.67	4.64	4.76	4.55	4.76
Al2O3 wt%	14.97	14.84	14.69	15.03	15.17	14.92
FeO wt%	18.37	18.27	18.06	18.21	18.45	18.12
MnO wt%	0.13	0.12	0.10	0.12	0.11	0.14
MgO wt%	12.59	12.50	12.48	12.61	12.45	12.50
K2O wt%	10.01	9.99	9.81	10.01	9.86	9.90
F wt%	0.00	0.00	0.00	0.00	0.00	0.00
Cl wt%	0.57	0.56	0.56	0.57	0.57	0.55
H2O*	3.82	3.84	3.81	3.83	3.81	3.83
Subtotal	100.80	100.95	100.04	101.03	100.53	100.77
-O=F,Cl	0.13	0.13	0.13	0.13	0.13	0.12
Total	100.67	100.82	99.92	100.90	100.40	100.65
Si	5.393	5.450	5.455	5.408	5.391	5.437
Al iv	2.607	2.550	2.545	2.592	2.609	2.563
T	*8.000*	*8.000*	*8.000*	*8.000*	*8.000*	*8.000*
Al vi	0.062	0.086	0.085	0.077	0.100	0.090
Ti	0.532	0.529	0.530	0.539	0.518	0.540
Fe_{tot}	2.324	2.303	2.295	2.294	2.338	2.285
Fe^{3+}	0.511	0.507	0.505	0.505	0.514	0.503
Fe^{2+}	1.813	1.796	1.790	1.789	1.824	1.783
Mn	0.017	0.015	0.013	0.016	0.014	0.019
Mg	2.839	2.809	2.827	2.831	2.814	2.812
M	*5.774*	*5.743*	*5.750*	*5.757*	*5.783*	*5.745*
K	1.932	1.920	1.901	1.924	1.907	1.904
I	*1.932*	*1.920*	*1.901*	*1.924*	*1.907*	*1.904*
F	0.000	0.000	0.000	0.000	0.000	0.000
Cl	0.146	0.144	0.143	0.147	0.145	0.141
OH*	3.854	3.856	3.857	3.853	3.855	3.859

Spot	MD001-Bt3-3	MD001-Bt3-2	MD046-Bt1-1	MD046-Bt1-2	MD046-Bt1-3	MD066-Bt1-1
Facies	Border	Border	Border	Border	Border	Chataway
SiO_2 wt%	35.82	36.30	29.61	29.94	29.67	35.45
TiO_2 wt%	4.65	4.72	3.66	4.10	2.71	4.32
Al_2O_3 wt%	15.14	14.72	18.25	16.80	18.05	15.59
FeO wt%	18.17	18.23	16.95	16.01	17.53	15.92
MnO wt%	0.13	0.13	0.26	0.26	0.28	0.23
MgO wt%	12.25	12.42	18.21	17.07	18.12	14.32
K_2O wt%	9.86	9.81	0.28	0.16	0.32	9.56
F wt%	0.00	0.00	0.00	0.00	0.00	0.00
Cl wt%	0.59	0.57	0.06	0.06	0.08	0.11
H_2O*	3.81	3.83	3.77	3.66	3.73	3.95
Subtotal	100.41	100.74	91.06	88.06	90.49	99.45
-O=F,Cl	0.13	0.13	0.01	0.01	0.02	0.03
Total	100.28	100.61	91.04	88.05	90.47	99.42
Si	5.425	5.475	4.696	4.883	4.749	5.345
Al iv	2.575	2.525	3.304	3.117	3.251	2.655
T	*8.000*	*8.000*	*8.000*	*8.000*	*8.000*	*8.000*
Al vi	0.128	0.091	0.108	0.111	0.155	0.116
Ti	0.529	0.536	0.437	0.502	0.326	0.489
Fe_{tot}	2.302	2.300	2.248	2.184	2.347	2.008
Fe^{3+}	0.506	0.506	0.495	0.481	0.516	0.442
Fe^{2+}	1.795	1.794	1.753	1.704	1.831	1.566
Mn	0.017	0.016	0.035	0.035	0.037	0.029
Mg	2.766	2.793	4.305	4.150	4.323	3.219
M	*5.741*	*5.737*	*7.133*	*6.983*	*7.189*	*5.861*
K	1.905	1.888	0.057	0.034	0.065	1.839
I	*1.905*	*1.888*	*0.057*	*0.034*	*0.065*	*1.839*
F	0.000	0.000	0.000	0.000	0.000	0.000
Cl	0.152	0.147	0.016	0.016	0.022	0.028
OH*	3.848	3.853	3.984	3.984	3.978	3.972

Spot	MD066-Bt1-2	MD066-Bt2-1	MD066-Bt2-2	MD066-Bt3-1	MD066-Bt3-2	MD075-Bt1-1
Facies	Chataway	Chataway	Chataway	Chataway	Chataway	Guichon
SiO2 wt%	35.47	36.34	36.30	35.25	35.56	36.99
TiO2 wt%	3.81	4.31	4.13	4.02	3.83	4.43
Al2O3 wt%	15.71	15.20	15.19	15.81	16.19	14.70
FeO wt%	15.70	15.72	15.73	16.34	15.42	16.43
MnO wt%	0.26	0.27	0.26	0.25	0.24	0.22
MgO wt%	14.11	13.96	13.85	14.15	14.54	14.44
K2O wt%	9.68	9.75	9.69	9.14	9.22	9.74
F wt%	0.00	0.00	0.00	0.00	0.00	0.00
Cl wt%	0.11	0.10	0.09	0.10	0.10	0.19
H2O*	3.92	3.97	3.95	3.93	3.96	4.00
Subtotal	98.76	99.63	99.20	99.00	99.05	101.15
-O=F,Cl	0.02	0.02	0.02	0.02	0.02	0.04
Total	98.74	99.60	99.18	98.98	99.03	101.10
Si	5.381	5.459	5.474	5.337	5.353	5.487
Al iv	2.619	2.541	2.526	2.663	2.647	2.513
T	*8.000*	*8.000*	*8.000*	*8.000*	*8.000*	*8.000*
Al vi	0.191	0.151	0.175	0.159	0.225	0.058
Ti	0.434	0.487	0.469	0.458	0.433	0.494
Fe_{tot}	1.992	1.975	1.984	2.069	1.942	2.039
Fe^{3+}	0.438	0.435	0.436	0.455	0.427	0.448
Fe^{2+}	1.554	1.541	1.547	1.614	1.514	1.590
Mn	0.034	0.034	0.034	0.032	0.031	0.028
Mg	3.192	3.126	3.113	3.194	3.262	3.194
M	*5.843*	*5.774*	*5.775*	*5.912*	*5.893*	*5.812*
K	1.874	1.869	1.864	1.765	1.769	1.843
I	*1.874*	*1.869*	*1.864*	*1.765*	*1.769*	*1.843*
F	0.000	0.000	0.000	0.000	0.000	0.000
Cl	0.028	0.026	0.023	0.026	0.025	0.047
OH*	3.972	3.974	3.977	3.974	3.975	3.953

Spot	MD075-Bt1-2	MD075-Bt1-3	MD075-Bt2-1	MD075-Bt2-2	MD075-Bt3-1	MD075-Bt3-2
Facies	Guichon	Guichon	Guichon	Guichon	Guichon	Guichon
SiO_2 wt%	36.91	37.19	37.19	37.44	36.96	36.82
TiO_2 wt%	4.44	4.27	4.15	4.34	3.98	4.44
Al_2O_3 wt%	14.68	14.40	14.91	14.35	14.57	14.67
FeO wt%	17.01	16.42	16.12	16.25	16.73	16.39
MnO wt%	0.22	0.23	0.19	0.19	0.21	0.21
MgO wt%	13.92	13.99	14.21	14.18	14.07	14.09
K_2O wt%	9.51	9.47	9.77	9.53	9.58	9.66
F wt%	0.00	0.00	0.00	0.00	0.00	0.00
Cl wt%	0.19	0.18	0.15	0.19	0.17	0.16
H_2O*	3.98	3.96	4.00	3.98	3.96	3.97
Subtotal	100.85	100.12	100.71	100.45	100.23	100.42
-O=F,Cl	0.04	0.04	0.03	0.04	0.04	0.04
Total	100.81	100.08	100.67	100.41	100.19	100.38
Si	5.498	5.562	5.526	5.575	5.535	5.499
Al iv	2.502	2.438	2.474	2.425	2.465	2.501
T	*8.000*	*8.000*	*8.000*	*8.000*	*8.000*	*8.000*
Al vi	0.075	0.101	0.138	0.093	0.106	0.081
Ti	0.497	0.481	0.463	0.486	0.449	0.499
Fe_{tot}	2.120	2.053	2.004	2.024	2.095	2.047
Fe^{3+}	0.466	0.452	0.441	0.445	0.461	0.450
Fe^{2+}	1.653	1.602	1.563	1.579	1.634	1.596
Mn	0.028	0.029	0.024	0.024	0.026	0.027
Mg	3.092	3.120	3.148	3.148	3.140	3.137
M	*5.812*	*5.784*	*5.778*	*5.775*	*5.816*	*5.790*
K	1.807	1.807	1.852	1.811	1.829	1.841
I	*1.807*	*1.807*	*1.852*	*1.811*	*1.829*	*1.841*
F	0.000	0.000	0.000	0.000	0.000	0.000
Cl	0.049	0.046	0.039	0.048	0.043	0.040
OH*	3.951	3.954	3.961	3.952	3.957	3.960

Spot	MD076-Bt1-1	MD076-Bt1-2	MD076-Bt2-1	MD076-Bt2-2	MD076-Bt3-1	MD076-Bt3-2
Facies	Guichon	Guichon	Guichon	Guichon	Guichon	Guichon
SiO2 wt%	36.36	36.24	36.11	36.06	36.12	36.04
TiO2 wt%	4.56	4.60	4.36	4.48	4.34	4.44
Al2O3 wt%	14.33	14.65	14.99	14.70	14.65	14.78
FeO wt%	16.11	15.89	16.63	16.39	15.79	16.06
MnO wt%	0.18	0.21	0.21	0.24	0.19	0.19
MgO wt%	14.48	14.48	14.04	14.38	14.30	14.27
K2O wt%	9.65	9.83	9.92	9.40	9.77	9.69
F wt%	0.00	0.00	0.00	0.00	0.00	0.00
Cl wt%	0.26	0.26	0.20	0.21	0.24	0.30
H2O*	3.92	3.93	3.94	3.93	3.91	3.90
Subtotal	99.85	100.08	100.40	99.80	99.31	99.67
-O=F,Cl	0.06	0.06	0.05	0.05	0.05	0.07
Total	99.79	100.03	100.36	99.75	99.26	99.60
Si	5.469	5.438	5.419	5.426	5.459	5.433
Al iv	2.531	2.562	2.581	2.574	2.541	2.567
T	*8.000*	*8.000*	*8.000*	*8.000*	*8.000*	*8.000*
Al vi	0.009	0.029	0.070	0.033	0.068	0.059
Ti	0.516	0.519	0.491	0.507	0.493	0.503
Fe_{tot}	2.026	1.994	2.087	2.063	1.996	2.024
Fe^{3+}	0.446	0.439	0.459	0.454	0.439	0.445
Fe^{2+}	1.581	1.555	1.628	1.609	1.557	1.579
Mn	0.022	0.026	0.026	0.031	0.025	0.024
Mg	3.246	3.239	3.140	3.226	3.221	3.208
M	*5.819*	*5.807*	*5.815*	*5.861*	*5.802*	*5.818*
K	1.851	1.881	1.899	1.805	1.882	1.864
I	*1.851*	*1.881*	*1.899*	*1.805*	*1.882*	*1.864*
F	0.000	0.000	0.000	0.000	0.000	0.000
Cl	0.065	0.066	0.052	0.053	0.062	0.076
OH*	3.935	3.934	3.948	3.947	3.938	3.924

Spot	MD034-Bt1-1	MD034-Bt1-2	MD034-Bt1-3	MD049-Bt1-1	MD049-Bt1-2	MD049-Bt2-1
Facies	Skeena	Skeena	Skeena	Skeena	Skeena	Skeena
SiO_2 wt%	34.59	35.58	35.18	36.19	35.83	35.68
TiO_2 wt%	3.70	3.98	3.81	4.03	3.73	3.46
Al_2O_3 wt%	15.22	15.23	15.38	14.84	14.87	14.85
FeO wt%	15.55	14.60	15.29	15.71	16.01	16.30
MnO wt%	0.50	0.43	0.49	0.36	0.37	0.34
MgO wt%	14.93	14.49	14.52	14.23	14.24	14.42
K_2O wt%	8.73	9.56	9.15	9.80	9.66	9.03
F wt%	0.00	0.00	0.00	0.00	0.00	0.00
Cl wt%	0.05	0.04	0.05	0.07	0.06	0.06
H_2O*	3.88	3.92	3.91	3.95	3.93	3.91
Subtotal	97.16	97.84	97.78	99.18	98.69	98.05
-O=F,Cl	0.01	0.01	0.01	0.02	0.01	0.01
Total	97.14	97.83	97.77	99.16	98.68	98.04
Si	5.325	5.423	5.376	5.469	5.450	5.452
Al iv	2.675	2.577	2.624	2.531	2.550	2.548
T	*8.000*	*8.000*	*8.000*	*8.000*	*8.000*	*8.000*
Al vi	0.087	0.160	0.146	0.113	0.115	0.127
Ti	0.429	0.456	0.438	0.458	0.426	0.397
Fe_{tot}	2.002	1.860	1.954	1.985	2.037	2.082
Fe^{3+}	0.440	0.409	0.430	0.437	0.448	0.458
Fe^{2+}	1.561	1.451	1.524	1.549	1.589	1.624
Mn	0.065	0.056	0.064	0.046	0.047	0.045
Mg	3.426	3.291	3.308	3.205	3.228	3.283
M	*6.008*	*5.823*	*5.909*	*5.807*	*5.853*	*5.934*
K	1.714	1.858	1.784	1.888	1.875	1.759
I	*1.714*	*1.858*	*1.784*	*1.888*	*1.875*	*1.759*
F	0.000	0.000	0.000	0.000	0.000	0.000
Cl	0.013	0.011	0.012	0.018	0.017	0.015
OH*	3.987	3.989	3.988	3.982	3.983	3.985

Spot	MD049-Bt2-2	MD063-Bt1-1	MD063-Bt1-2	MD063-Bt1-3	MD063-Bt2-1
Facies	Skeena	F.g. Granodiorite	F.g. Granodiorite	F.g. Granodiorite	F.g. Granodiorite
SiO2 wt%	35.06	34.45	34.40	33.92	34.05
TiO2 wt%	3.37	3.37	0.00	0.12	3.41
Al2O3 wt%	15.24	15.51	16.82	15.72	15.25
FeO wt%	16.79	15.28	15.31	15.18	15.19
MnO wt%	0.42	0.27	0.00	0.02	0.33
MgO wt%	14.33	15.02	14.80	14.61	14.79
K2O wt%	8.56	9.89	9.87	9.89	9.88
F wt%	0.00	0.00	0.00	0.00	0.00
Cl wt%	0.06	0.11	0.13	0.19	0.25
H2O*	3.89	3.87	3.78	3.67	3.79
Subtotal	97.73	97.77	95.12	93.33	96.94
-O=F,Cl	0.01	0.02	0.03	0.04	0.06
Total	97.71	97.74	95.09	93.29	96.88
Si	5.381	5.297	5.417	5.462	5.293
Al iv	2.619	2.703	2.583	2.538	2.707
T	*8.000*	*8.000*	*8.000*	*8.000*	*8.000*
Al vi	0.138	0.107	0.539	0.446	0.088
Ti	0.389	0.390	0.000	0.015	0.398
Fe_{tot}	2.154	1.964	2.017	2.045	1.974
Fe^{3+}	0.474	0.432	0.444	0.450	0.434
Fe^{2+}	1.680	1.532	1.573	1.595	1.540
Mn	0.054	0.035	0.000	0.003	0.043
Mg	3.278	3.442	3.474	3.507	3.428
M	*6.014*	*5.938*	*6.030*	*6.016*	*5.931*
K	1.676	1.940	1.982	2.032	1.959
I	*1.676*	*1.940*	*1.982*	*2.032*	*1.959*
F	0.000	0.000	0.000	0.001	0.000
Cl	0.015	0.028	0.034	0.051	0.066
OH*	3.985	3.972	3.966	3.948	3.934

Spot	MD063-Bt2-2	MD063-Bt3-1	MD063-Bt3-2
Facies	F.g. Granodiorite	F.g. Granodiorite	F.g. Granodiorite
SiO2 wt%	33.70	34.23	34.91
TiO2 wt%	3.43	3.29	3.20
Al2O3 wt%	15.10	15.63	15.55
FeO wt%	14.90	15.68	15.72
MnO wt%	0.34	0.26	0.29
MgO wt%	14.62	14.95	15.25
K2O wt%	9.83	9.81	9.98
F wt%	0.00	0.00	0.00
Cl wt%	0.23	0.14	0.17
H2O*	3.76	3.86	3.90
Subtotal	95.91	97.84	98.97
-O=F,Cl	0.05	0.03	0.04
Total	95.86	97.81	98.93
Si	5.293	5.269	5.310
Al iv	2.707	2.731	2.690
T	*8.000*	*8.000*	*8.000*
Al vi	0.089	0.105	0.099
Ti	0.405	0.381	0.366
Fe_{tot}	1.957	2.018	1.999
Fe^{3+}	0.431	0.444	0.440
Fe^{2+}	1.527	1.574	1.559
Mn	0.046	0.034	0.037
Mg	3.424	3.432	3.459
M	*5.920*	*5.970*	*5.961*
K	1.969	1.926	1.937
I	*1.969*	*1.926*	*1.937*
F	0.000	0.000	0.000
Cl	0.061	0.037	0.043
OH*	3.939	3.963	3.957

Apatite Chemistry – based on 25 oxygens

Spot	MD059-Ap33	MD059-Ap35.1	MD059-Ap35.2	MD059-Ap36	MD059-Ap37	MD059-Ap38.1
Facies	Bethlehem	Bethlehem	Bethlehem	Bethlehem	Bethlehem	Bethlehem
SiO2 wt%	0.16	0.19	0.06	0.16	0.08	0.12
TiO2 wt%	0.02	<ld	<ld	0.16	0.01	<ld
Al2O3 wt%	<ld	<ld	0.01	<ld	<ld	<ld
FeO wt%	0.23	0.35	0.56	0.74	1.38	0.23
MgO wt%	<ld	<ld	<ld	<ld	<ld	<ld
MnO wt%	0.17	0.15	0.17	0.33	0.16	0.14
CaO wt%	55.13	55.20	55.44	54.47	55.43	56.03
Na2O wt%	0.13	0.17	0.11	0.17	0.07	0.05
P2O5 wt%	39.96	40.13	40.55	39.93	40.77	40.46
SO3 wt%	0.37	0.53	0.21	0.58	0.22	0.23
F wt%	2.04	2.12	2.08	1.23	2.20	2.50
Cl wt%	0.38	0.28	0.26	1.32	0.33	0.28
Total wt%	98.58	99.12	99.46	99.09	100.66	100.04
P	5.822	5.808	5.856	5.796	5.842	5.834
Ca	10.164	10.110	10.131	10.007	10.050	10.224
Si	0.028	0.032	0.011	0.028	0.013	0.020
Al	0.000	0.000	0.001	0.000	0.000	0.000
Fe	0.034	0.050	0.079	0.106	0.195	0.033
Mn	0.025	0.022	0.025	0.047	0.023	0.021
Mg	0.000	0.000	0.000	0.000	0.000	0.000
Na	0.043	0.057	0.038	0.058	0.024	0.015
K	0.000	0.000	0.000	0.000	0.000	0.000
Ti	0.002	0.000	0.000	0.021	0.002	0.000
Sr	0.000	0.000	0.000	0.000	0.000	0.000
Ba	0.000	0.000	0.000	0.000	0.000	0.000
Cl	0.111	0.081	0.076	0.383	0.096	0.081
F	1.110	1.146	1.120	0.669	1.177	1.347
S	0.047	0.068	0.027	0.074	0.028	0.030
X(Fap)	0.56	0.57	0.56	0.33	0.59	0.67
X(Cap)	0.06	0.04	0.04	0.19	0.05	0.04
X(Hap)	0.39	0.39	0.40	0.47	0.36	0.29

Spot	MD059-Ap38.2	MD004-Ap5	MD004-Ap6	MD069-Ap61	MD069-Ap65	MD069-Ap66
Facies	Bethlehem	Bethsaida	Bethsaida	Bethsaida	Bethsaida	Bethsaida
SiO_2 wt%	0.10	0.07	0.08	0.08	0.09	0.05
TiO_2 wt%	0.02	<ld	<ld	0.02	<ld	0.00
Al_2O_3 wt%	<ld	<ld	<ld	<ld	<ld	<ld
FeO wt%	0.14	0.43	0.13	0.04	0.34	0.17
MgO wt%	<ld	<ld	<ld	<ld	<ld	<ld
MnO wt%	0.15	0.43	0.29	0.18	0.19	0.21
CaO wt%	55.84	54.33	55.39	54.31	54.97	54.69
Na_2O wt%	0.04	0.07	0.10	0.04	0.13	0.09
P_2O_5 wt%	40.57	39.81	40.01	40.00	40.01	40.29
SO_3 wt%	0.17	0.22	0.22	0.13	0.21	0.24
F wt%	2.37	2.45	2.81	2.95	2.46	2.46
Cl wt%	0.27	0.14	0.08	0.16	0.19	0.18
Total wt%	99.67	97.96	99.10	97.89	98.59	98.41
P	5.858	5.856	5.835	5.898	5.848	5.883
Ca	10.204	10.112	10.223	10.136	10.169	10.106
Si	0.017	0.013	0.014	0.013	0.016	0.009
Al	0.000	0.000	0.000	0.000	0.000	0.000
Fe	0.020	0.063	0.018	0.006	0.049	0.025
Mn	0.022	0.063	0.043	0.026	0.028	0.031
Mg	0.000	0.000	0.000	0.000	0.000	0.000
Na	0.012	0.024	0.033	0.014	0.043	0.031
K	0.000	0.000	0.000	0.000	0.000	0.000
Ti	0.002	0.000	0.000	0.002	0.000	0.001
Sr	0.000	0.000	0.000	0.000	0.000	0.000
Ba	0.000	0.000	0.000	0.000	0.000	0.000
Cl	0.077	0.042	0.022	0.047	0.057	0.053
F	1.279	1.345	1.529	1.625	1.345	1.342
S	0.021	0.028	0.028	0.017	0.027	0.031
X(Fap)	0.64	0.67	0.76	0.81	0.67	0.67
X(Cap)	0.04	0.02	0.01	0.02	0.03	0.03
X(Hap)	0.32	0.31	0.22	0.16	0.30	0.30

Spot	MD069-Ap67.1	MD069-Ap67.2	MD071-Ap69.1	MD071-Ap69.2	MD071-Ap72	MD071-Ap73.1
Facies	Bethsaida	Bethsaida	Bethsaida	Bethsaida	Bethsaida	Bethsaida
SiO2 wt%	0.13	0.06	0.08	0.12	0.09	0.09
TiO2 wt%	<ld	0.04	0.01	<ld	<ld	<ld
Al2O3 wt%	0.03	<ld	0.00	<ld	<ld	<ld
FeO wt%	0.13	0.10	0.08	0.07	0.51	0.03
MgO wt%	<ld	<ld	<ld	<ld	<ld	<ld
MnO wt%	0.15	0.16	0.25	0.19	0.20	0.15
CaO wt%	55.45	55.42	55.55	55.43	55.55	56.20
Na2O wt%	0.05	0.05	0.09	0.09	0.07	0.03
P2O5 wt%	40.20	40.28	40.10	40.00	40.40	40.30
SO3 wt%	0.16	0.17	0.20	0.24	0.18	0.15
F wt%	2.65	2.67	2.58	2.56	2.74	2.98
Cl wt%	0.16	0.16	0.08	0.09	0.05	0.05
Total wt%	99.10	99.12	99.03	98.78	99.79	99.98
P	5.850	5.861	5.838	5.833	5.847	5.833
Ca	10.212	10.205	10.235	10.230	10.173	10.295
Si	0.022	0.011	0.013	0.020	0.015	0.016
Al	0.007	0.000	0.001	0.000	0.000	0.000
Fe	0.019	0.015	0.012	0.010	0.072	0.004
Mn	0.022	0.023	0.037	0.027	0.029	0.022
Mg	0.000	0.000	0.000	0.000	0.000	0.000
Na	0.016	0.015	0.028	0.030	0.024	0.011
K	0.000	0.000	0.000	0.000	0.000	0.000
Ti	0.000	0.005	0.002	0.000	0.000	0.000
Sr	0.000	0.000	0.000	0.000	0.000	0.000
Ba	0.000	0.000	0.000	0.000	0.000	0.000
Cl	0.045	0.047	0.024	0.026	0.016	0.013
F	1.438	1.452	1.400	1.397	1.480	1.609
S	0.021	0.021	0.026	0.032	0.023	0.020
X(Fap)	0.72	0.73	0.70	0.70	0.74	0.80
X(Cap)	0.02	0.02	0.01	0.01	0.01	0.01
X(Hap)	0.26	0.25	0.29	0.29	0.25	0.19

Spot	MD071-Ap73.2	MD003a-Ap87	MD003a-Ap88	MD003a-Ap95.1	MD003a-Ap95.2	MD007-Ap8.1
Facies	Bethsaida	Border	Border	Border	Border	Border
SiO2 wt%	0.08	0.31	0.38	0.31	0.31	0.15
TiO2 wt%	0.01	0.08	<ld	0.02	0.01	0.04
Al2O3 wt%	0.01	0.00	0.01	0.01	0.00	<ld
FeO wt%	0.45	1.44	1.05	0.77	0.79	0.61
MgO wt%	<ld	<ld	0.01	0.01	0.02	<ld
MnO wt%	0.14	0.08	0.10	0.04	0.07	0.10
CaO wt%	56.01	54.14	54.11	54.30	54.45	54.85
Na2O wt%	0.03	0.06	0.09	0.05	0.06	0.12
P2O5 wt%	40.70	39.30	39.00	39.01	39.70	39.85
SO3 wt%	0.16	0.19	0.17	0.23	0.21	0.46
F wt%	2.78	1.50	1.45	1.57	1.56	2.01
Cl wt%	0.06	1.50	1.18	0.94	0.95	1.09
Total wt%	100.44	98.61	97.56	97.26	98.12	99.28
P	5.850	5.789	5.783	5.787	5.824	5.809
Ca	10.191	10.093	10.154	10.194	10.108	10.118
Si	0.014	0.054	0.066	0.054	0.054	0.025
Al	0.002	0.000	0.002	0.003	0.001	0.000
Fe	0.064	0.210	0.154	0.113	0.114	0.088
Mn	0.020	0.012	0.016	0.007	0.010	0.015
Mg	0.000	0.000	0.003	0.003	0.005	0.000
Na	0.011	0.021	0.031	0.017	0.020	0.039
K	0.000	0.000	0.000	0.000	0.000	0.000
Ti	0.001	0.011	0.000	0.003	0.001	0.005
Sr	0.000	0.000	0.000	0.000	0.000	0.000
Ba	0.000	0.000	0.000	0.000	0.000	0.000
Cl	0.018	0.442	0.350	0.279	0.278	0.319
F	1.493	0.825	0.804	0.870	0.854	1.095
S	0.020	0.024	0.022	0.030	0.027	0.059
X(Fap)	0.75	0.41	0.40	0.43	0.43	0.55
X(Cap)	0.01	0.22	0.17	0.14	0.14	0.16
X(Hap)	0.24	0.37	0.42	0.43	0.43	0.29

Spot	MD007-Ap8.2	MD007-Ap89	MD044-Ap90.1	MD044-Ap90.2	MD044-Ap91	MD066-Ap48
Facies	Border	Border	Chataway	Chataway	Chataway	Chataway
SiO2 wt%	0.17	0.18	0.22	0.23	0.18	0.17
TiO2 wt%	0.03	0.02	0.02	0.00	0.14	0.02
Al2O3 wt%	0.00	0.01	0.07	<ld	<ld	<ld
FeO wt%	1.09	1.66	0.41	0.29	0.56	0.01
MgO wt%	<ld	<ld	0.01	0.01	0.00	<ld
MnO wt%	0.13	0.14	0.10	0.12	0.10	0.04
CaO wt%	55.04	54.57	54.15	54.28	54.72	56.21
Na2O wt%	0.10	0.13	0.21	0.12	0.09	0.05
P2O5 wt%	39.46	39.58	39.33	39.27	39.36	40.51
SO3 wt%	0.42	0.46	0.41	0.45	0.35	0.33
F wt%	2.07	1.86	1.51	1.58	1.68	2.95
Cl wt%	1.11	1.03	0.93	0.89	1.14	0.22
Total wt%	99.62	99.64	97.37	97.23	98.34	100.51
P	5.762	5.765	5.804	5.804	5.788	5.826
Ca	10.171	10.059	10.114	10.152	10.182	10.230
Si	0.029	0.030	0.038	0.040	0.031	0.028
Al	0.001	0.002	0.015	0.000	0.000	0.000
Fe	0.158	0.239	0.060	0.042	0.082	0.001
Mn	0.019	0.020	0.015	0.017	0.015	0.006
Mg	0.000	0.000	0.003	0.002	0.001	0.000
Na	0.032	0.043	0.071	0.039	0.032	0.017
K	0.000	0.000	0.000	0.000	0.000	0.000
Ti	0.003	0.003	0.003	0.000	0.018	0.003
Sr	0.000	0.000	0.000	0.000	0.000	0.000
Ba	0.000	0.000	0.000	0.000	0.000	0.000
Cl	0.325	0.300	0.274	0.262	0.336	0.062
F	1.130	1.010	0.833	0.871	0.924	1.587
S	0.055	0.060	0.053	0.059	0.046	0.042
X(Fap)	0.56	0.51	0.42	0.44	0.46	0.79
X(Cap)	0.16	0.15	0.14	0.13	0.17	0.03
X(Hap)	0.27	0.34	0.45	0.43	0.37	0.18

Spot	MD066-Ap93	MD066-Ap94.1	MD066-Ap94.2	MD075-Ap76	MD076-Ap82.1	MD076-Ap82.2
Facies	Chataway	Chataway	Chataway	Guichon	Guichon	Guichon
SiO2 wt%	0.21	0.14	0.19	0.25	0.22	0.23
TiO2 wt%	<ld	<ld	<ld	0.01	0.03	0.01
Al2O3 wt%	0.00	<ld	0.00	0.03	<ld	<ld
FeO wt%	1.03	0.16	0.09	0.33	0.71	0.86
MgO wt%	<ld	<ld	<ld	0.02	<ld	<ld
MnO wt%	0.11	0.07	0.08	0.08	0.17	0.12
CaO wt%	55.90	56.15	56.18	55.10	54.96	55.18
Na2O wt%	0.12	0.03	0.02	0.11	0.08	0.07
P2O5 wt%	40.19	40.81	40.57	39.42	39.98	39.95
SO3 wt%	0.49	0.28	0.15	0.24	0.20	0.17
F wt%	2.21	2.94	2.87	2.61	1.95	1.88
Cl wt%	0.63	0.23	0.21	0.63	1.40	1.36
Total wt%	100.90	100.81	100.37	98.82	99.71	99.83
P	5.764	5.850	5.843	5.792	5.825	5.815
Ca	10.146	10.185	10.240	10.245	10.133	10.164
Si	0.036	0.024	0.033	0.044	0.039	0.039
Al	0.001	0.000	0.001	0.007	0.000	0.000
Fe	0.146	0.023	0.013	0.047	0.102	0.124
Mn	0.016	0.010	0.011	0.011	0.025	0.018
Mg	0.000	0.000	0.000	0.005	0.000	0.000
Na	0.039	0.009	0.008	0.037	0.027	0.023
K	0.000	0.000	0.000	0.000	0.000	0.000
Ti	0.000	0.000	0.000	0.001	0.004	0.001
Sr	0.000	0.000	0.000	0.000	0.000	0.000
Ba	0.000	0.000	0.000	0.000	0.000	0.000
Cl	0.180	0.065	0.060	0.186	0.410	0.397
F	1.182	1.577	1.543	1.430	1.060	1.019
S	0.063	0.035	0.019	0.031	0.026	0.022
X(Fap)	0.59	0.79	0.77	0.71	0.53	0.51
X(Cap)	0.09	0.03	0.03	0.09	0.20	0.20
X(Hap)	0.32	0.18	0.20	0.19	0.27	0.29

Spot	MD076-Ap83	MD076-Ap84	MD034-Ap12	MD034-Ap12	MD034-Ap14.1	MD034-Ap14.2
Facies	Guichon	Guichon	Skeena	Skeena	Skeena	Skeena
SiO2 wt%	0.22	0.27	0.07	0.14	0.15	0.15
TiO2 wt%	0.01	0.09	<ld	<ld	0.02	<ld
Al2O3 wt%	<ld	0.00	<ld	<ld	<ld	0.01
FeO wt%	1.16	1.83	0.14	0.13	0.11	0.41
MgO wt%	<ld	<ld	<ld	<ld	<ld	<ld
MnO wt%	0.11	0.17	0.16	0.15	0.14	0.22
CaO wt%	54.71	54.14	55.37	55.35	56.05	55.78
Na2O wt%	0.09	0.15	0.07	0.11	0.07	0.08
P2O5 wt%	39.90	39.48	40.01	39.90	40.40	40.21
SO3 wt%	0.12	0.38	0.22	0.35	0.34	0.34
F wt%	1.99	1.75	2.21	2.01	2.61	2.33
Cl wt%	1.11	1.31	0.28	0.37	0.17	0.18
Total wt%	99.43	99.57	98.53	98.50	100.05	99.70
P	5.826	5.766	5.842	5.817	5.963	5.808
Ca	10.109	10.006	10.232	10.212	10.469	10.196
Si	0.039	0.046	0.012	0.025	0.026	0.025
Al	0.000	0.000	0.000	0.000	0.000	0.001
Fe	0.167	0.264	0.020	0.019	0.016	0.058
Mn	0.016	0.026	0.023	0.022	0.020	0.031
Mg	0.000	0.000	0.000	0.000	0.000	0.000
Na	0.030	0.050	0.024	0.037	0.023	0.028
K	0.000	0.000	0.000	0.000	0.000	0.000
Ti	0.001	0.011	0.000	0.000	0.002	0.000
Sr	0.000	0.000	0.000	0.000	0.000	0.000
Ba	0.000	0.000	0.000	0.000	0.000	0.000
Cl	0.325	0.384	0.080	0.108	0.049	0.053
F	1.083	0.955	1.204	1.092	1.441	1.258
S	0.016	0.050	0.028	0.046	0.045	0.043
X(Fap)	0.54	0.48	0.60	0.55	0.72	0.63
X(Cap)	0.16	0.19	0.04	0.05	0.02	0.03
X(Hap)	0.30	0.33	0.36	0.40	0.25	0.34

Spot	MD034-Ap15.1	MD034-Ap15.2	MD034-Ap16.1	MD034-Ap16.2	MD049-Ap25.1
Facies	Skeena	Skeena	Skeena	Skeena	Skeena
SiO2 wt%	0.07	0.06	0.07	0.09	0.07
TiO2 wt%	0.00	0.04	0.03	0.06	0.01
Al2O3 wt%	<ld	<ld	<ld	<ld	<ld
FeO wt%	0.03	0.02	0.03	0.01	0.33
MgO wt%	<ld	<ld	<ld	<ld	<ld
MnO wt%	0.09	0.12	0.14	0.13	0.13
CaO wt%	56.28	56.16	56.22	56.25	55.92
Na2O wt%	0.04	0.04	0.06	0.03	0.06
P2O5 wt%	40.29	40.85	40.47	40.48	39.90
SO3 wt%	0.17	0.14	0.20	0.16	0.23
F wt%	2.56	2.62	3.19	3.08	2.43
Cl wt%	0.18	0.16	0.12	0.15	0.30
Total wt%	99.72	100.20	100.54	100.44	99.39
P	5.831	5.870	5.837	5.839	5.805
Ca	10.308	10.215	10.263	10.269	10.295
Si	0.012	0.010	0.012	0.016	0.012
Al	0.000	0.000	0.000	0.000	0.000
Fe	0.004	0.003	0.004	0.002	0.047
Mn	0.013	0.017	0.021	0.019	0.019
Mg	0.000	0.000	0.000	0.000	0.000
Na	0.014	0.012	0.021	0.010	0.019
K	0.000	0.000	0.000	0.000	0.000
Ti	0.000	0.005	0.004	0.007	0.002
Sr	0.000	0.000	0.000	0.000	0.000
Ba	0.000	0.000	0.000	0.000	0.000
Cl	0.053	0.045	0.033	0.043	0.089
F	1.383	1.405	1.716	1.659	1.322
S	0.022	0.017	0.026	0.020	0.029
X(Fap)	0.69	0.70	0.86	0.83	0.66
X(Cap)	0.03	0.02	0.02	0.02	0.04
X(Hap)	0.28	0.28	0.13	0.15	0.29

Spot	MD049-Ap25.2	MD049-Ap26	MD049-Ap27.1	MD063-Ap45.1	MD063-Ap45.2
Facies	Skeena	Skeena	Skeena	F.g. Granodiorite	F.g. Granodiorite
SiO2 wt%	0.11	0.64	0.16	0.19	0.27
TiO2 wt%	0.02	0.87	0.08	0.04	0.01
Al2O3 wt%	<ld	0.00	0.01	<ld	0.00
FeO wt%	0.47	0.32	0.14	1.34	1.54
MgO wt%	<ld	<ld	<ld	0.01	<ld
MnO wt%	0.13	0.11	0.15	0.09	0.08
CaO wt%	55.67	55.42	55.66	53.98	53.90
Na2O wt%	0.04	0.04	0.07	0.08	0.07
P2O5 wt%	39.91	39.02	39.87	39.49	39.19
SO3 wt%	0.27	0.23	0.34	0.36	0.39
F wt%	2.49	2.23	2.48	2.32	2.31
Cl wt%	0.29	0.31	0.26	0.47	0.44
Total wt%	99.39	99.20	99.22	98.37	98.20
P	5.805	5.677	5.797	5.806	5.778
Ca	10.248	10.203	10.243	10.044	10.058
Si	0.019	0.109	0.027	0.033	0.046
Al	0.000	0.001	0.002	0.000	0.000
Fe	0.067	0.046	0.020	0.194	0.225
Mn	0.019	0.016	0.022	0.013	0.012
Mg	0.000	0.000	0.000	0.002	0.000
Na	0.015	0.014	0.022	0.028	0.024
K	0.000	0.000	0.000	0.000	0.000
Ti	0.002	0.112	0.011	0.005	0.001
Sr	0.000	0.000	0.000	0.000	0.000
Ba	0.000	0.000	0.000	0.000	0.000
Cl	0.084	0.090	0.075	0.140	0.131
F	1.354	1.211	1.348	1.272	1.270
S	0.034	0.030	0.044	0.047	0.051
X(Fap)	0.68	0.61	0.67	0.64	0.64
X(Cap)	0.04	0.05	0.04	0.07	0.07
X(Hap)	0.28	0.35	0.29	0.29	0.30

Spot	MD063-Ap46	MD063-Ap47	MD059-Ap28	MD059-Ap34	MD069-Ap57
Facies	F.g. Granodiorite	F.g. Granodiorite	Bethlehem	Bethlehem	Bethsaida
SiO2 wt%	0.26	0.29	0.20	0.16	0.12
TiO2 wt%	0.01	0.01	0.03	0.02	0.05
Al2O3 wt%	0.01	<ld	0.01	0.00	<ld
FeO wt%	0.68	0.07	0.10	0.06	0.12
MgO wt%	<ld	0.01	<ld	<ld	<ld
MnO wt%	0.10	0.08	0.12	0.14	0.16
CaO wt%	54.25	55.13	55.18	55.42	54.66
Na2O wt%	0.13	0.08	0.19	0.15	0.05
P2O5 wt%	39.66	39.89	39.94	40.33	40.16
SO3 wt%	0.43	0.31	0.54	0.44	0.18
F wt%	2.38	3.13	2.35	2.51	2.67
Cl wt%	0.43	0.18	0.22	0.22	0.12
Total wt%	98.33	99.18	98.88	99.47	98.29
P	5.815	5.823	5.802	5.831	5.879
Ca	10.066	10.184	10.145	10.139	10.128
Si	0.045	0.049	0.034	0.027	0.021
Al	0.002	0.000	0.001	0.000	0.000
Fe	0.098	0.010	0.014	0.009	0.017
Mn	0.014	0.012	0.018	0.021	0.024
Mg	0.000	0.003	0.000	0.000	0.000
Na	0.042	0.025	0.064	0.050	0.017
K	0.000	0.000	0.000	0.000	0.000
Ti	0.001	0.001	0.003	0.003	0.007
Sr	0.000	0.000	0.000	0.000	0.000
Ba	0.000	0.000	0.000	0.000	0.000
Cl	0.127	0.053	0.063	0.065	0.036
F	1.302	1.707	1.277	1.353	1.462
S	0.056	0.040	0.070	0.056	0.024
X(Fap)	0.65	0.85	0.64	0.68	0.73
X(Cap)	0.06	0.03	0.03	0.03	0.02
X(Hap)	0.29	0.12	0.33	0.29	0.25

Spot	MD069-Ap59	MD069-Ap60	MD069-Ap62	MD069-Ap63	MD071-Ap68	MD071-Ap71.1
Facies	Bethsaida	Bethsaida	Bethsaida	Bethsaida	Bethsaida	Bethsaida
SiO2 wt%	0.05	0.13	0.07	0.06	0.07	0.12
TiO2 wt%	0.01	0.03	<ld	<ld	<ld	<ld
Al2O3 wt%	<ld	<ld	<ld	0.00	<ld	<ld
FeO wt%	0.14	0.13	0.17	0.04	0.09	0.11
MgO wt%	<ld	<ld	<ld	<ld	<ld	<ld
MnO wt%	0.17	0.20	0.18	0.19	0.24	0.25
CaO wt%	55.01	54.45	55.24	54.98	55.55	55.64
Na2O wt%	0.09	0.11	0.10	0.08	0.11	0.12
P2O5 wt%	39.92	39.42	40.18	40.23	40.24	39.82
SO3 wt%	0.22	0.28	0.23	0.11	0.23	0.32
F wt%	2.51	2.44	2.67	2.35	2.52	2.72
Cl wt%	0.14	0.15	0.15	0.15	0.13	0.11
Total wt%	98.27	97.33	98.99	98.19	99.18	99.20
P	5.852	5.830	5.854	5.884	5.845	5.802
Ca	10.205	10.193	10.184	10.177	10.211	10.259
Si	0.009	0.023	0.012	0.011	0.012	0.021
Al	0.000	0.000	0.000	0.000	0.000	0.000
Fe	0.020	0.019	0.025	0.006	0.012	0.016
Mn	0.026	0.030	0.026	0.027	0.035	0.036
Mg	0.000	0.000	0.000	0.000	0.000	0.000
Na	0.030	0.037	0.032	0.028	0.036	0.040
K	0.000	0.000	0.000	0.000	0.000	0.000
Ti	0.001	0.004	0.000	0.000	0.000	0.000
Sr	0.000	0.000	0.000	0.000	0.000	0.000
Ba	0.000	0.000	0.000	0.000	0.000	0.000
Cl	0.041	0.044	0.043	0.044	0.039	0.031
F	1.376	1.346	1.455	1.282	1.368	1.479
S	0.028	0.037	0.030	0.015	0.029	0.041
X(Fap)	0.69	0.67	0.73	0.64	0.68	0.74
X(Cap)	0.02	0.02	0.02	0.02	0.02	0.02
X(Hap)	0.29	0.31	0.25	0.34	0.30	0.25

Spot	MD071-Ap71.2	MD001-Ap3	MD003a-Ap1.1	MD003a-Ap1.2	MD003a-Ap2	MD003a-Ap4
Facies	Bethsaida	Border	Border	Border	Border	Border
SiO2 wt%	0.14	0.20	0.22	0.30	0.24	0.34
TiO2 wt%	<ld	0.02	0.02	<ld	<ld	0.02
Al2O3 wt%	<ld	0.01	0.02	0.02	0.03	0.01
FeO wt%	0.18	0.17	0.22	0.30	0.20	0.27
MgO wt%	<ld	<ld	0.03	0.03	0.01	0.02
MnO wt%	0.15	0.03	0.11	0.09	0.08	0.15
CaO wt%	55.84	54.77	54.81	54.51	55.04	54.34
Na2O wt%	0.10	0.05	0.06	0.04	0.05	0.10
P2O5 wt%	40.08	39.70	39.56	39.49	39.60	38.96
SO3 wt%	0.27	0.02	0.20	0.18	0.09	0.14
F wt%	3.33	2.48	1.75	1.68	1.80	1.59
Cl wt%	0.06	0.77	1.28	1.28	1.03	1.55
Total wt%	100.14	98.22	98.28	97.92	98.18	97.48
P	5.814	5.859	5.824	5.827	5.828	5.800
Ca	10.250	10.229	10.211	10.178	10.250	10.237
Si	0.023	0.034	0.037	0.052	0.041	0.059
Al	0.000	0.001	0.005	0.005	0.006	0.001
Fe	0.025	0.025	0.031	0.044	0.030	0.040
Mn	0.021	0.005	0.016	0.013	0.012	0.022
Mg	0.000	0.000	0.009	0.008	0.004	0.004
Na	0.033	0.019	0.021	0.013	0.016	0.033
K	0.000	0.000	0.000	0.000	0.000	0.000
Ti	0.000	0.002	0.002	0.000	0.000	0.003
Sr	0.000	0.000	0.000	0.000	0.000	0.000
Ba	0.000	0.000	0.000	0.000	0.000	0.000
Cl	0.017	0.228	0.378	0.377	0.305	0.463
F	1.806	1.369	0.964	0.928	0.990	0.885
S	0.035	0.003	0.026	0.024	0.012	0.018
X(Fap)	0.90	0.68	0.48	0.46	0.50	0.44
X(Cap)	0.01	0.11	0.19	0.19	0.15	0.23
X(Hap)	0.09	0.20	0.33	0.35	0.35	0.33

Spot	MD007-Ap9.1	MD007-Ap9.2	MD046-Ap21	MD046-Ap22	MD044-Ap17.1	MD044-Ap17.2
Facies	Border	Border	Border	Border	Chataway	Chataway
SiO2 wt%	0.20	0.20	0.17	0.28	0.19	0.22
TiO2 wt%	<ld	<ld	<ld	0.10	<ld	0.02
Al2O3 wt%	<ld	<ld	0.00	0.01	0.01	0.00
FeO wt%	0.26	0.28	0.10	0.06	0.15	0.18
MgO wt%	<ld	<ld	0.01	0.00	0.01	<ld
MnO wt%	0.12	0.13	0.02	0.01	0.09	0.08
CaO wt%	55.07	54.88	55.22	54.97	54.58	54.83
Na2O wt%	0.11	0.07	0.05	0.05	0.14	0.07
P2O5 wt%	39.70	39.71	39.26	39.47	39.47	39.78
SO3 wt%	0.49	0.28	0.22	0.32	0.41	0.34
F wt%	2.09	2.02	2.09	1.87	2.09	2.27
Cl wt%	1.13	1.08	1.31	1.48	0.40	0.33
Total wt%	99.18	98.66	98.45	98.62	97.55	98.13
P	5.796	5.825	5.801	5.802	5.813	5.828
Ca	10.175	10.187	10.324	10.227	10.173	10.165
Si	0.035	0.035	0.029	0.048	0.034	0.038
Al	0.000	0.000	0.001	0.003	0.003	0.001
Fe	0.038	0.041	0.015	0.009	0.022	0.026
Mn	0.017	0.018	0.003	0.002	0.013	0.011
Mg	0.000	0.000	0.003	0.000	0.002	0.000
Na	0.037	0.022	0.015	0.018	0.047	0.022
K	0.000	0.000	0.000	0.000	0.000	0.000
Ti	0.000	0.000	0.000	0.013	0.000	0.003
Sr	0.000	0.000	0.000	0.000	0.000	0.000
Ba	0.000	0.000	0.000	0.000	0.000	0.000
Cl	0.329	0.318	0.388	0.435	0.117	0.096
F	1.140	1.107	1.154	1.028	1.147	1.243
S	0.064	0.037	0.028	0.041	0.054	0.044
X(Fap)	0.57	0.55	0.58	0.51	0.57	0.62
X(Cap)	0.16	0.16	0.19	0.22	0.06	0.05
X(Hap)	0.27	0.29	0.23	0.27	0.37	0.33

Spot	MD044-Ap18	MD044-Ap19	MD066-Ap49	MD066-Ap50.1	MD066-Ap50.2	MD066-Ap51
Facies	Chataway	Chataway	Chataway	Chataway	Chataway	Chataway
SiO2 wt%	0.19	0.22	0.21	0.23	0.21	0.25
TiO2 wt%	<ld	<ld	0.02	0.00	0.01	0.02
Al2O3 wt%	0.00	0.01	<ld	<ld	0.01	0.01
FeO wt%	0.19	0.08	0.18	0.10	0.16	0.19
MgO wt%	<ld	0.01	<ld	<ld	<ld	<ld
MnO wt%	0.06	0.04	0.06	0.06	0.08	0.06
CaO wt%	55.08	54.95	55.76	55.85	55.75	55.31
Na2O wt%	0.09	0.05	0.16	0.17	0.14	0.12
P2O5 wt%	39.62	39.45	40.20	40.09	40.08	40.08
SO3 wt%	0.41	0.44	0.59	0.66	0.55	0.55
F wt%	2.50	2.22	2.87	2.74	2.62	2.42
Cl wt%	0.37	0.22	0.38	0.42	0.42	0.29
Total wt%	98.51	97.69	100.43	100.33	100.03	99.32
P	5.804	5.799	5.790	5.774	5.786	5.802
Ca	10.210	10.224	10.162	10.181	10.185	10.132
Si	0.033	0.039	0.036	0.039	0.036	0.043
Al	0.001	0.002	0.000	0.000	0.002	0.002
Fe	0.028	0.012	0.026	0.015	0.023	0.028
Mn	0.008	0.005	0.009	0.009	0.012	0.009
Mg	0.000	0.002	0.000	0.000	0.000	0.000
Na	0.031	0.015	0.053	0.057	0.047	0.041
K	0.000	0.000	0.000	0.000	0.000	0.000
Ti	0.000	0.000	0.003	0.000	0.002	0.003
Sr	0.000	0.000	0.000	0.000	0.000	0.000
Ba	0.000	0.000	0.000	0.000	0.000	0.000
Cl	0.107	0.066	0.110	0.120	0.120	0.084
F	1.366	1.221	1.542	1.474	1.412	1.311
S	0.053	0.057	0.075	0.084	0.071	0.070
X(Fap)	0.68	0.61	0.77	0.74	0.71	0.66
X(Cap)	0.05	0.03	0.05	0.06	0.06	0.04
X(Hap)	0.26	0.36	0.17	0.20	0.23	0.30

Spot	MD066-Ap53	MD066-Ap54	MD075-Ap77.1	MD075-Ap77.2	MD076-Ap78	MD076-Ap79
Facies	Chataway	Chataway	Guichon	Guichon	Guichon	Guichon
SiO2 wt%	0.21	0.22	0.25	0.23	0.25	0.22
TiO2 wt%	<ld	0.03	0.02	0.03	0.05	0.04
Al2O3 wt%	0.01	<ld	<ld	<ld	0.01	0.00
FeO wt%	0.10	0.13	0.16	0.12	0.27	0.25
MgO wt%	<ld	<ld	0.01	0.04	<ld	<ld
MnO wt%	0.11	0.05	0.10	0.12	0.12	0.08
CaO wt%	55.49	56.07	54.38	54.19	55.14	54.80
Na2O wt%	0.14	0.05	0.13	0.15	0.05	0.09
P2O5 wt%	39.75	40.23	38.96	39.45	39.70	39.74
SO3 wt%	0.59	0.25	0.32	0.25	0.18	0.19
F wt%	2.47	2.84	2.12	2.00	2.12	1.95
Cl wt%	0.35	0.31	1.10	1.10	1.14	1.06
Total wt%	99.22	100.17	97.54	97.68	99.02	98.42
P	5.775	5.814	5.792	5.838	5.816	5.836
Ca	10.203	10.255	10.233	10.148	10.224	10.183
Si	0.037	0.037	0.044	0.041	0.042	0.039
Al	0.003	0.000	0.000	0.000	0.003	0.000
Fe	0.014	0.019	0.024	0.017	0.040	0.037
Mn	0.016	0.007	0.014	0.018	0.018	0.012
Mg	0.000	0.000	0.004	0.009	0.000	0.000
Na	0.046	0.018	0.045	0.052	0.016	0.030
K	0.000	0.000	0.000	0.000	0.000	0.000
Ti	0.000	0.003	0.003	0.003	0.006	0.005
Sr	0.000	0.000	0.000	0.000	0.000	0.000
Ba	0.000	0.000	0.000	0.000	0.000	0.000
Cl	0.101	0.091	0.326	0.327	0.336	0.310
F	1.339	1.533	1.176	1.104	1.158	1.069
S	0.076	0.032	0.043	0.033	0.023	0.025
X(Fap)	0.67	0.77	0.59	0.55	0.58	0.53
X(Cap)	0.05	0.05	0.16	0.16	0.17	0.16
X(Hap)	0.28	0.19	0.25	0.28	0.25	0.31

Spot	MD076-Ap80	MD076-Ap81	MD076-Ap86	MD049-Ap23	MD049-Ap96.1	MD049-Ap96.2
Facies	Guichon	Guichon	Guichon	Skeena	Skeena	Skeena
SiO2 wt%	0.26	0.32	0.19	0.19	0.16	0.39
TiO2 wt%	0.07	0.06	0.03	<ld	<ld	<ld
Al2O3 wt%	0.01	<ld	<ld	<ld	0.00	0.04
FeO wt%	0.28	0.40	0.28	0.14	0.10	0.19
MgO wt%	<ld	<ld	<ld	<ld	<ld	<ld
MnO wt%	0.09	0.07	0.17	0.13	0.13	0.13
CaO wt%	54.54	54.93	55.23	55.48	55.67	55.18
Na2O wt%	0.12	0.15	0.12	0.08	0.10	0.09
P2O5 wt%	39.27	39.74	39.94	40.12	40.31	39.12
SO3 wt%	0.36	0.36	0.22	0.44	0.42	0.34
F wt%	2.14	2.28	2.14	2.59	2.67	2.90
Cl wt%	1.12	1.21	1.25	0.27	0.26	0.16
Total wt%	98.26	99.52	99.58	99.43	99.81	98.53
P	5.795	5.799	5.825	5.815	5.823	5.754
Ca	10.184	10.144	10.194	10.177	10.177	10.272
Si	0.045	0.056	0.032	0.032	0.028	0.068
Al	0.002	0.000	0.000	0.000	0.000	0.009
Fe	0.040	0.057	0.040	0.021	0.014	0.028
Mn	0.014	0.011	0.025	0.018	0.018	0.018
Mg	0.000	0.000	0.000	0.000	0.000	0.000
Na	0.041	0.050	0.041	0.025	0.033	0.029
K	0.000	0.000	0.000	0.000	0.000	0.000
Ti	0.009	0.008	0.003	0.000	0.000	0.000
Sr	0.000	0.000	0.000	0.000	0.000	0.000
Ba	0.000	0.000	0.000	0.000	0.000	0.000
Cl	0.330	0.354	0.365	0.077	0.074	0.047
F	1.179	1.241	1.169	1.401	1.439	1.595
S	0.047	0.046	0.029	0.057	0.053	0.045
X(Fap)	0.59	0.62	0.58	0.70	0.72	0.80
X(Cap)	0.16	0.18	0.18	0.04	0.04	0.02
X(Hap)	0.25	0.20	0.23	0.26	0.24	0.18

Spot	MD063-Ap41	MD063-Ap42	MD063-Ap43	MD059-Ap31	MD059-Ap32
Facies	F.g. Granodiorite	F.g. Granodiorite	F.g. Granodiorite	Bethlehem	Bethlehem
SiO2 wt%	0.23	0.19	0.26	0.17	0.08
TiO2 wt%	0.06	0.01	0.02	<ld	0.01
Al2O3 wt%	0.05	0.01	0.00	0.00	<ld
FeO wt%	0.16	0.26	0.13	0.15	0.06
MgO wt%	0.01	0.02	0.01	<ld	<ld
MnO wt%	0.09	0.12	0.09	0.12	0.16
CaO wt%	54.99	54.95	54.89	54.97	55.63
Na2O wt%	0.16	0.16	0.09	0.20	0.09
P2O5 wt%	39.58	39.87	39.77	39.88	40.28
SO3 wt%	0.57	0.53	0.51	0.55	0.22
F wt%	3.39	3.29	3.40	2.34	2.40
Cl wt%	0.20	0.19	0.09	0.31	0.25
Total wt%	99.48	99.61	99.27	98.70	99.18
P	5.778	5.805	5.806	5.809	5.847
Ca	10.159	10.123	10.141	10.133	10.221
Si	0.039	0.033	0.045	0.029	0.013
Al	0.011	0.001	0.000	0.001	0.000
Fe	0.023	0.038	0.019	0.021	0.009
Mn	0.013	0.018	0.014	0.018	0.023
Mg	0.003	0.006	0.003	0.000	0.000
Na	0.053	0.052	0.032	0.067	0.030
K	0.000	0.000	0.000	0.000	0.000
Ti	0.008	0.002	0.002	0.000	0.001
Sr	0.000	0.000	0.000	0.000	0.000
Ba	0.000	0.000	0.000	0.000	0.000
Cl	0.058	0.055	0.026	0.091	0.073
F	1.851	1.791	1.854	1.273	1.303
S	0.074	0.068	0.066	0.071	0.029
X(Fap)	0.93	0.90	0.93	0.64	0.65
X(Cap)	0.03	0.03	0.01	0.05	0.04
X(Hap)	0.05	0.08	0.06	0.32	0.31

Spot	MD069-Ap64.1	MD069-Ap64.2	MD071-Ap70.1	MD071-Ap70.2	MD066-Ap55	MD075-Ap74
Facies	Bethsaida	Bethsaida	Bethsaida	Bethsaida	Chataway	Guichon
SiO2 wt%	0.08	0.10	0.06	0.07	0.21	0.26
TiO2 wt%	0.01	<ld	<ld	0.00	0.03	0.05
Al2O3 wt%	<ld	<ld	<ld	<ld	0.00	<ld
FeO wt%	0.08	0.04	0.10	0.53	0.13	0.19
MgO wt%	<ld	<ld	<ld	<ld	<ld	0.01
MnO wt%	0.17	0.16	0.20	0.18	0.11	0.08
CaO wt%	54.12	55.34	55.56	55.78	56.24	55.08
Na2O wt%	0.09	0.10	0.08	0.05	0.08	0.14
P2O5 wt%	40.23	40.36	40.24	40.22	40.32	39.54
SO3 wt%	0.25	0.22	0.20	0.17	0.48	0.30
F wt%	2.38	2.46	2.69	2.80	2.93	2.51
Cl wt%	0.23	0.23	0.10	0.09	0.30	0.71
Total wt%	97.64	99.02	99.23	99.89	100.84	98.86
P	5.906	5.864	5.850	5.827	5.788	5.798
Ca	10.055	10.175	10.220	10.229	10.219	10.221
Si	0.014	0.017	0.011	0.013	0.036	0.045
Al	0.000	0.000	0.000	0.000	0.000	0.000
Fe	0.011	0.005	0.014	0.076	0.018	0.027
Mn	0.024	0.023	0.030	0.027	0.016	0.012
Mg	0.000	0.000	0.000	0.000	0.000	0.003
Na	0.031	0.034	0.025	0.015	0.026	0.046
K	0.000	0.000	0.000	0.000	0.000	0.000
Ti	0.001	0.000	0.000	0.001	0.004	0.006
Sr	0.000	0.000	0.000	0.000	0.000	0.000
Ba	0.000	0.000	0.000	0.000	0.000	0.000
Cl	0.067	0.067	0.028	0.025	0.086	0.208
F	1.306	1.337	1.458	1.513	1.572	1.375
S	0.033	0.028	0.026	0.022	0.061	0.039
X(Fap)	0.65	0.67	0.73	0.76	0.79	0.69
X(Cap)	0.03	0.03	0.01	0.01	0.04	0.10
X(Hap)	0.31	0.30	0.26	0.23	0.17	0.21

Spot	MD075-Ap75.1	MD075-Ap75.2	MD034-Ap11	MD034-Ap13	MD049-Ap24	MD063-Ap44
Facies	Guichon	Guichon	Skeena	Skeena	Skeena	F.g. Granodiorite
SiO2 wt%	0.24	0.24	0.08	0.09	0.12	0.26
TiO2 wt%	0.01	0.06	<ld	0.02	<ld	<ld
Al2O3 wt%	<ld	<ld	<ld	<ld	<ld	0.00
FeO wt%	0.24	0.19	0.41	0.48	0.08	0.09
MgO wt%	0.01	<ld	<ld	<ld	<ld	0.01
MnO wt%	0.07	0.08	0.15	0.16	0.10	0.09
CaO wt%	54.61	54.64	55.39	56.00	55.72	55.27
Na2O wt%	0.11	0.13	0.09	0.10	0.08	0.07
P2O5 wt%	39.49	39.47	40.13	40.74	39.56	39.77
SO3 wt%	0.30	0.27	0.18	0.28	0.32	0.37
F wt%	2.13	2.31	2.18	2.53	2.41	3.23
Cl wt%	0.83	0.70	0.25	0.28	0.27	0.17
Total wt%	98.05	98.11	98.85	100.68	98.65	99.34
P	5.818	5.816	5.841	5.838	5.789	5.806
Ca	10.182	10.190	10.205	10.155	10.319	10.211
Si	0.042	0.041	0.013	0.015	0.021	0.045
Al	0.000	0.000	0.000	0.000	0.000	0.001
Fe	0.035	0.028	0.058	0.068	0.012	0.013
Mn	0.010	0.012	0.022	0.023	0.015	0.013
Mg	0.003	0.000	0.000	0.000	0.000	0.004
Na	0.037	0.044	0.029	0.033	0.025	0.024
K	0.000	0.000	0.000	0.000	0.000	0.000
Ti	0.002	0.008	0.000	0.003	0.000	0.000
Sr	0.000	0.000	0.000	0.000	0.000	0.000
Ba	0.000	0.000	0.000	0.000	0.000	0.000
Cl	0.244	0.208	0.073	0.079	0.078	0.049
F	1.172	1.271	1.185	1.354	1.316	1.763
S	0.039	0.036	0.024	0.036	0.042	0.047
X(Fap)	0.59	0.64	0.59	0.68	0.66	0.88
X(Cap)	0.12	0.10	0.04	0.04	0.04	0.02
X(Hap)	0.29	0.26	0.37	0.28	0.30	0.09

Oxide Chemistry – based on four oxygens

Spot	MD001-Mt1-1	MD001-Mt1-2	MD001-Mt1-3	MD001-Mt2-1	MD001-Mt2-2	MD001-Mt3-1
Facies	Border	Border	Border	Border	Border	Border
SiO2 wt%	0.02	< l.d.	0.02	0.02	0.01	< l.d.
TiO2 wt%	0.32	50.84	1.10	0.54	0.35	49.91
Al2O3 wt%	0.19	0.01	0.84	0.72	0.50	0.02
Cr2O3 wt%	0.06	0.01	0.10	0.06	0.12	0.00
FeO wt%	31.48	41.05	32.05	31.79	31.82	41.62
Fe2O3 wt%	67.74	5.50	65.27	66.80	67.83	8.33
MnO wt%	0.09	4.55	0.22	0.12	0.09	2.98
MgO wt%	0.01	0.04	0.03	0.02	0.00	0.15
V2O3 wt%	0.67	0.44	0.64	0.70	0.65	0.45
Total wt%	100.59	102.44	100.25	100.77	101.39	103.46
Si	0.001	0.000	0.001	0.001	0.001	0.000
Ti	0.009	0.944	0.031	0.016	0.010	0.919
Al	0.009	0.000	0.038	0.032	0.022	0.001
Cr	0.002	0.000	0.003	0.002	0.004	0.000
Fe2+	1.006	0.848	1.023	1.011	1.007	0.852
Fe3+	1.949	0.102	1.876	1.912	1.933	0.153
Mn	0.003	0.095	0.007	0.004	0.003	0.062
Mg	0.001	0.001	0.002	0.001	0.000	0.005
V	0.020	0.009	0.019	0.021	0.020	0.009

Spot	MD001-Mt3-2	MD003A-Mt1-1	MD003A-Mt1-2	MD003A-Mt1-3	MD003A-Mt1-4	MD003A-Mt2-1
Facies	Border	Border	Border	Border	Border	Border
SiO2 wt%	< l.d.	0.01	0.00	0.02	0.01	0.00
TiO2 wt%	49.89	0.37	32.07	0.15	45.13	0.06
Al2O3 wt%	0.06	0.12	0.03	0.08	0.01	0.41
Cr2O3 wt%	0.00	0.07	0.01	0.05	0.00	0.07
FeO wt%	41.68	31.81	28.82	31.70	40.35	31.74
Fe2O3 wt%	8.13	68.52	41.91	69.15	13.47	69.12
MnO wt%	2.88	0.05	0.03	0.05	0.26	0.04
MgO wt%	0.15	0.00	0.00	0.00	0.00	0.00
V2O3 wt%	0.45	0.49	0.46	0.53	0.49	0.51
Total wt%	103.26	101.44	103.33	101.74	99.72	101.96
Si	0.000	0.000	0.000	0.001	0.000	0.000
Ti	0.920	0.010	0.601	0.004	0.865	0.002
Al	0.002	0.005	0.001	0.004	0.000	0.018
Cr	0.000	0.002	0.000	0.002	0.000	0.002
Fe2+	0.854	1.009	0.601	1.003	0.860	1.000
Fe3+	0.150	1.956	0.787	1.969	0.258	1.961
Mn	0.060	0.002	0.001	0.002	0.006	0.001
Mg	0.006	0.000	0.000	0.000	0.000	0.000
V	0.009	0.015	0.009	0.016	0.010	0.016

Spot	MD003A-Mt2-2	MD003A-Mt3-1	MD003A-Mt3-2	MD003A-Mt3-3	MD003A-Mt4-1	MD003A-Mt4-2
Facies	Border	Border	Border	Border	Border	Border
SiO2 wt%	0.00	0.01	< l.d.	0.28	0.00	0.01
TiO2 wt%	0.08	0.05	39.06	17.18	0.12	0.58
Al2O3 wt%	0.28	0.02	0.02	0.11	0.18	0.31
Cr2O3 wt%	0.05	0.06	0.02	0.03	0.05	0.12
FeO wt%	31.55	31.54	35.06	15.40	31.69	32.32
Fe2O3 wt%	68.83	69.37	27.85	66.37	69.16	68.41
MnO wt%	0.04	0.05	0.07	0.34	0.04	0.04
MgO wt%	< l.d.	< l.d.	< l.d.	0.03	< l.d.	0.00
V2O3 wt%	0.54	0.48	0.54	0.55	0.50	0.51
Total wt%	101.37	101.58	102.61	100.29	101.74	102.31
Si	0.000	0.000	0.000	0.007	0.000	0.001
Ti	0.002	0.001	0.733	0.336	0.003	0.016
Al	0.012	0.001	0.000	0.003	0.008	0.014
Cr	0.002	0.002	0.000	0.001	0.002	0.003
Fe2+	1.001	1.000	0.731	0.335	1.002	1.015
Fe3+	1.965	1.979	0.523	1.298	1.968	1.934
Mn	0.001	0.002	0.002	0.007	0.001	0.001
Mg	0.000	0.000	0.000	0.001	0.000	0.000
V	0.016	0.015	0.011	0.011	0.015	0.015

Spot	MD004-Mt1-1	MD004-Mt1-2	MD004-Mt1-3	MD004-Mt2-1	MD004-Mt2-2	MD004-Mt3-1
Facies	Bethsaida	Bethsaida	Bethsaida	Bethsaida	Bethsaida	Bethsaida
SiO2 wt%	0.02	0.00	0.01	0.02	0.01	0.07
TiO2 wt%	0.04	0.14	0.17	0.01	0.01	0.23
Al2O3 wt%	0.01	0.15	0.15	0.01	0.02	0.10
Cr2O3 wt%	0.01	0.01	0.01	0.02	0.02	0.01
FeO wt%	29.81	30.84	29.89	30.75	30.84	29.77
Fe2O3 wt%	65.95	67.90	65.74	68.22	68.47	64.59
MnO wt%	0.16	0.21	0.24	0.15	0.17	0.06
MgO wt%	< l.d.	< l.d.	0.00	0.00	< l.d.	0.01
V2O3 wt%	0.33	0.29	0.28	0.27	0.29	0.30
Total wt%	96.33	99.54	96.50	99.46	99.82	95.15
Si	0.001	0.000	0.000	0.001	0.001	0.003
Ti	0.001	0.004	0.005	0.000	0.000	0.007
Al	0.001	0.007	0.007	0.001	0.001	0.005
Cr	0.000	0.000	0.000	0.000	0.001	0.000
Fe2+	0.997	0.997	0.997	0.996	0.995	1.007
Fe3+	1.985	1.976	1.973	1.988	1.988	1.966
Mn	0.005	0.007	0.008	0.005	0.006	0.002
Mg	0.000	0.000	0.000	0.000	0.000	0.001
V	0.010	0.009	0.009	0.008	0.009	0.010

Spot	MD004-Mt3-2	MD004-Mt3-3	MD007-Mt1-1	MD007-Mt2-1	MD007-Mt2-2	MD007-Mt3-1
Facies	Bethsaida	Bethsaida	Border	Border	Border	Border
SiO2 wt%	0.43	0.01	0.00	0.00	< l.d.	0.01
TiO2 wt%	0.37	0.01	0.10	0.75	37.39	0.07
Al2O3 wt%	0.15	0.02	0.36	0.02	0.01	0.51
Cr2O3 wt%	0.02	0.01	0.03	0.03	0.01	0.06
FeO wt%	31.66	30.91	31.32	31.99	33.60	31.49
Fe2O3 wt%	66.36	68.69	68.17	67.73	30.19	68.35
MnO wt%	0.13	0.18	0.04	0.04	0.03	0.04
MgO wt%	0.01	< l.d.	0.00	< l.d.	< l.d.	0.00
V2O3 wt%	0.28	0.28	0.49	0.35	0.53	0.51
Total wt%	99.39	100.11	100.51	100.93	101.77	101.04
Si	0.017	0.000	0.000	0.000	0.000	0.000
Ti	0.011	0.000	0.003	0.022	0.708	0.002
Al	0.007	0.001	0.016	0.001	0.000	0.023
Cr	0.000	0.000	0.001	0.001	0.000	0.002
Fe2+	1.023	0.994	1.002	1.020	0.708	1.001
Fe3+	1.929	1.989	1.962	1.944	0.572	1.955
Mn	0.004	0.006	0.001	0.001	0.001	0.001
Mg	0.000	0.000	0.000	0.000	0.000	0.000
V	0.009	0.009	0.015	0.011	0.011	0.016

Spot	MD007-Mt3-2	MD034-Mt1-1	MD034-Mt1-2	MD034-Mt1-3	MD034-Mt2-1	MD034-Mt2-2
Facies	Border	Skeena	Skeena	Skeena	Skeena	Skeena
SiO2 wt%	1.26	0.08	0.00	0.02	0.01	0.01
TiO2 wt%	48.12	14.24	0.03	0.03	0.02	0.16
Al2O3 wt%	0.55	0.06	0.07	0.07	0.11	0.21
Cr2O3 wt%	0.02	0.01	0.02	0.02	0.02	0.01
FeO wt%	41.63	42.46	31.59	31.53	31.69	31.90
Fe2O3 wt%	3.61	39.43	69.77	69.69	69.96	69.72
MnO wt%	2.19	1.33	0.08	0.13	0.10	0.09
MgO wt%	0.52	0.03	0.01	0.01	0.00	0.00
V2O3 wt%	0.53	0.49	0.37	0.38	0.38	0.38
Total wt%	98.44	98.13	101.94	101.89	102.29	102.50
Si	0.032	0.002	0.000	0.001	0.000	0.000
Ti	0.920	0.311	0.001	0.001	0.001	0.004
Al	0.016	0.002	0.003	0.003	0.005	0.009
Cr	0.000	0.000	0.001	0.001	0.001	0.000
Fe2+	0.885	1.029	0.998	0.996	0.997	1.001
Fe3+	0.069	0.860	1.983	1.982	1.981	1.969
Mn	0.047	0.033	0.003	0.004	0.003	0.003
Mg	0.020	0.001	0.000	0.001	0.000	0.000
V	0.011	0.011	0.011	0.012	0.012	0.012

Spot	MD034-Mt3-1	MD034-Mt3-2	MD044-Mt1-1	MD044-Mt1-2	MD044-Mt1-3	MD044-Mt2-1
Facies	Skeena	Skeena	Chataway	Chataway	Chataway	Chataway
SiO2 wt%	0.01	0.00	0.02	0.51	0.01	0.01
TiO2 wt%	0.02	0.03	0.01	0.06	0.09	0.06
Al2O3 wt%	0.04	0.09	0.05	0.29	0.12	0.08
Cr2O3 wt%	0.02	0.03	0.06	0.06	0.07	0.07
FeO wt%	31.71	31.84	31.82	32.31	31.78	31.77
Fe2O3 wt%	70.04	70.19	70.14	68.16	69.63	69.82
MnO wt%	0.04	0.04	0.03	0.03	0.03	0.02
MgO wt%	0.00	0.00	0.00	0.02	< l.d.	0.00
V2O3 wt%	0.34	0.36	0.32	0.34	0.42	0.34
Total wt%	102.21	102.57	102.46	101.78	102.15	102.16
Si	0.000	0.000	0.001	0.019	0.000	0.000
Ti	0.000	0.001	0.000	0.002	0.002	0.002
Al	0.002	0.004	0.002	0.013	0.005	0.004
Cr	0.001	0.001	0.002	0.002	0.002	0.002
Fe2+	0.999	1.000	1.000	1.019	1.002	1.001
Fe3+	1.986	1.983	1.984	1.934	1.975	1.980
Mn	0.001	0.001	0.001	0.001	0.001	0.001
Mg	0.000	0.000	0.000	0.001	0.000	0.000
V	0.010	0.011	0.010	0.010	0.013	0.010

Spot	MD044-Mt2-2	MD044-Mt2-3	MD044-Mt2-4	MD044-Mt3-1	MD044-Mt3-2	MD044-Mt3-3
Facies	Chataway	Chataway	Chataway	Chataway	Chataway	Chataway
SiO2 wt%	0.01	0.02	0.01	0.01	0.01	< l.d.
TiO2 wt%	0.08	0.08	0.08	20.83	0.02	16.11
Al2O3 wt%	0.09	0.16	0.06	0.09	0.05	0.10
Cr2O3 wt%	0.07	0.07	0.06	0.03	0.07	0.04
FeO wt%	31.62	31.59	30.37	49.93	32.31	45.34
Fe2O3 wt%	69.35	69.13	66.62	27.61	71.08	36.55
MnO wt%	0.03	0.03	0.02	0.25	0.02	0.33
MgO wt%	< l.d.	0.00	0.01	0.05	0.00	0.06
V2O3 wt%	0.37	0.38	0.43	0.59	0.45	0.57
Total wt%	101.62	101.46	97.65	99.39	104.02	99.10
Si	0.000	0.001	0.000	0.000	0.001	0.000
Ti	0.002	0.002	0.002	0.446	0.001	0.347
Al	0.004	0.007	0.003	0.003	0.002	0.004
Cr	0.002	0.002	0.002	0.001	0.002	0.001
Fe2+	1.002	1.002	1.001	1.188	1.000	1.087
Fe3+	1.977	1.973	1.977	0.591	1.980	0.788
Mn	0.001	0.001	0.001	0.006	0.001	0.008
Mg	0.000	0.000	0.000	0.002	0.000	0.003
V	0.011	0.012	0.014	0.013	0.013	0.013

Spot	MD046-Mt1-1	MD046-Mt1-3	MD046-Mt2-1	MD046-Mt2-2	MD046-Mt2-3	MD046-Mt2-4
Facies	Border	Border	Border	Border	Border	Border
SiO2 wt%	0.01	0.02	0.05	0.01	0.02	0.02
TiO2 wt%	0.05	0.31	0.08	0.06	0.06	0.03
Al2O3 wt%	0.07	3.07	0.07	0.12	0.06	0.07
Cr2O3 wt%	0.09	0.08	0.09	0.08	0.08	0.09
FeO wt%	31.18	32.16	30.29	31.59	31.52	31.64
Fe2O3 wt%	68.36	64.55	65.92	69.07	69.05	69.41
MnO wt%	0.05	0.05	0.01	0.03	0.04	0.03
MgO wt%	0.00	0.01	0.02	0.00	0.00	0.00
V2O3 wt%	0.56	0.81	0.68	0.64	0.54	0.51
Total wt%	100.38	101.05	97.21	101.60	101.38	101.80
Si	0.001	0.001	0.002	0.000	0.001	0.001
Ti	0.002	0.009	0.002	0.002	0.002	0.001
Al	0.003	0.135	0.003	0.005	0.003	0.003
Cr	0.003	0.002	0.003	0.002	0.002	0.003
Fe2+	1.000	1.007	1.003	1.001	1.001	1.001
Fe3+	1.973	1.819	1.964	1.969	1.974	1.975
Mn	0.002	0.002	0.000	0.001	0.001	0.001
Mg	0.000	0.001	0.001	0.000	0.000	0.000
V	0.017	0.024	0.021	0.020	0.016	0.015

Spot	MD046-Mt3-3	MD049-Mt1-1	MD049-Mt1-2	MD049-Mt1-3	MD049-Mt2-1	MD049-Mt2-2
Facies	Border	Skeena	Skeena	Skeena	Skeena	Skeena
SiO2 wt%	0.01	0.04	0.01	0.00	0.01	0.01
TiO2 wt%	0.04	0.70	0.10	0.04	0.02	0.17
Al2O3 wt%	0.16	0.78	0.23	0.05	0.04	0.95
Cr2O3 wt%	0.06	0.01	0.01	0.02	0.02	0.02
FeO wt%	31.55	31.82	31.09	31.03	30.95	31.40
Fe2O3 wt%	69.06	66.31	68.06	68.46	68.43	67.42
MnO wt%	0.05	0.07	0.08	0.07	0.12	0.11
MgO wt%	< l.d.	0.01	< l.d.	0.00	< l.d.	0.01
V2O3 wt%	0.61	0.37	0.37	0.37	0.38	0.39
Total wt%	101.53	100.12	99.94	100.04	99.96	100.47
Si	0.000	0.001	0.000	0.000	0.001	0.000
Ti	0.001	0.020	0.003	0.001	0.000	0.005
Al	0.007	0.035	0.010	0.002	0.002	0.043
Cr	0.002	0.000	0.000	0.001	0.000	0.001
Fe2+	1.000	1.019	1.001	0.999	0.997	1.001
Fe3+	1.970	1.910	1.971	1.983	1.984	1.934
Mn	0.001	0.002	0.002	0.002	0.004	0.003
Mg	0.000	0.001	0.000	0.000	0.000	0.000
V	0.018	0.011	0.011	0.011	0.012	0.012

Spot	MD049-Mt3-1	MD049-Mt3-2	MD049-Mt3-4	MD059-Mt1-1	MD059-Mt1-2	MD059-Mt2-2
Facies	Skeena	Skeena	Skeena	Bethlehem	Bethlehem	Bethlehem
SiO2 wt%	0.00	0.01	0.06	0.02	0.01	0.00
TiO2 wt%	0.12	0.05	40.85	0.14	0.27	24.04
Al2O3 wt%	0.06	0.05	0.02	0.61	0.44	0.05
Cr2O3 wt%	0.03	0.02	0.00	0.02	0.02	0.01
FeO wt%	30.07	31.27	36.46	30.94	31.31	47.36
Fe2O3 wt%	65.90	68.82	19.69	67.31	67.63	20.45
MnO wt%	0.05	0.03	0.32	0.21	0.11	5.22
MgO wt%	< l.d.	< l.d.	0.01	0.02	0.01	0.05
V2O3 wt%	0.40	0.39	0.42	0.38	0.37	0.48
Total wt%	96.63	100.64	97.84	99.64	100.17	97.65
Si	0.000	0.000	0.001	0.001	0.000	0.000
Ti	0.004	0.001	0.801	0.004	0.008	0.522
Al	0.003	0.002	0.001	0.028	0.020	0.002
Cr	0.001	0.001	0.000	0.001	0.001	0.000
Fe2+	1.002	1.001	0.795	0.996	1.004	1.142
Fe3+	1.976	1.982	0.386	1.951	1.952	0.444
Mn	0.002	0.001	0.007	0.007	0.004	0.127
Mg	0.000	0.000	0.000	0.001	0.000	0.002
V	0.013	0.012	0.009	0.012	0.011	0.011

Spot	MD059-Mt3-1	MD059-Mt3-2	MD059-Mt3-3	MD063-Mt1-1	MD063-Mt1-2
Facies	Bethlehem	Bethlehem	Bethlehem	F.g. granodiorite	F.g. granodiorite
SiO2 wt%	0.42	1.41	0.01	0.05	0.01
TiO2 wt%	0.07	0.13	0.06	0.01	0.02
Al2O3 wt%	0.30	1.43	0.26	0.08	0.04
Cr2O3 wt%	0.02	0.02	0.02	0.03	0.04
FeO wt%	31.56	32.30	31.25	31.71	30.56
Fe2O3 wt%	67.07	63.47	68.60	69.94	67.46
MnO wt%	0.09	0.10	0.11	0.09	0.06
MgO wt%	0.03	0.53	0.00	0.03	0.00
V2O3 wt%	0.36	0.37	0.38	0.38	0.37
Total wt%	99.91	99.76	100.69	102.33	98.56
Si	0.016	0.053	0.000	0.002	0.000
Ti	0.002	0.004	0.002	0.000	0.001
Al	0.013	0.064	0.012	0.003	0.002
Cr	0.001	0.001	0.001	0.001	0.001
Fe2+	1.014	1.024	0.998	0.997	0.999
Fe3+	1.939	1.810	1.972	1.980	1.984
Mn	0.003	0.003	0.004	0.003	0.002
Mg	0.001	0.030	0.000	0.002	0.000
V	0.011	0.011	0.012	0.012	0.012

Spot	MD063-Mt2-1	MD063-Mt2-2	MD063-Mt3-1	MD063-Mt3-2	MD063-Mt4-1
Facies	F.g. granodiorite	F.g. granodiorite	F.g. granodiorite	F.g. granodiorite	F.g. granodiorite
SiO2 wt%	0.03	0.02	0.01	0.01	0.01
TiO2 wt%	0.02	0.03	0.04	0.04	0.02
Al2O3 wt%	0.00	0.01	0.11	0.10	0.05
Cr2O3 wt%	0.02	0.02	0.04	0.03	0.03
FeO wt%	31.78	31.59	31.78	31.76	31.51
Fe2O3 wt%	70.21	69.86	70.08	70.05	69.81
MnO wt%	0.06	0.06	0.12	0.13	0.18
MgO wt%	0.00	0.00	0.01	0.01	0.02
V2O3 wt%	0.32	0.25	0.43	0.42	0.41
Total wt%	102.43	101.83	102.62	102.54	102.05
Si	0.001	0.001	0.001	0.001	0.000
Ti	0.001	0.001	0.001	0.001	0.001
Al	0.000	0.000	0.005	0.005	0.002
Cr	0.001	0.001	0.001	0.001	0.001
Fe2+	0.999	0.999	0.997	0.997	0.994
Fe3+	1.987	1.989	1.978	1.979	1.982
Mn	0.002	0.002	0.004	0.004	0.006
Mg	0.000	0.000	0.001	0.001	0.001
V	0.010	0.007	0.013	0.013	0.012

Spot	MD063-Mt4-2	MD066-Mt1-1	MD066-Mt1-2	MD066-Mt2-1	MD066-Mt2-2
Facies	F.g. granodiorite	Chataway	Chataway	Chataway	Chataway
SiO2 wt%	0.02	0.01	0.01	0.00	0.01
TiO2 wt%	0.03	0.10	0.10	0.04	0.03
Al2O3 wt%	0.15	0.10	0.10	0.06	0.06
Cr2O3 wt%	0.03	0.04	0.04	0.02	0.02
FeO wt%	31.52	31.41	30.24	30.99	30.99
Fe2O3 wt%	69.61	68.99	66.21	68.75	68.74
MnO wt%	0.19	0.09	0.01	0.20	0.20
MgO wt%	0.02	0.00	0.00	0.00	0.00
V2O3 wt%	0.42	0.35	0.36	0.27	0.28
Total wt%	101.99	101.10	97.08	100.34	100.34
Si	0.001	0.001	0.000	0.000	0.000
Ti	0.001	0.003	0.003	0.001	0.001
Al	0.007	0.004	0.005	0.003	0.003
Cr	0.001	0.001	0.001	0.001	0.001
Fe2+	0.994	1.000	1.003	0.995	0.994
Fe3+	1.976	1.977	1.976	1.986	1.985
Mn	0.006	0.003	0.000	0.006	0.007
Mg	0.001	0.000	0.000	0.000	0.000
V	0.013	0.011	0.011	0.008	0.009

Spot	MD066-Mt2-3	MD066-Mt3-1	MD066-Mt4-1	MD069-Mt1-1	MD069-Mt1-2	MD069-Mt3-1
Facies	Chataway	Chataway	Chataway	Bethsaida	Bethsaida	Bethsaida
SiO2 wt%	0.01	0.05	0.00	0.03	0.01	0.01
TiO2 wt%	0.04	24.93	16.83	0.27	0.29	0.28
Al2O3 wt%	0.06	0.07	0.08	0.03	0.02	0.57
Cr2O3 wt%	0.02	0.03	0.03	0.01	0.00	0.02
FeO wt%	30.94	52.55	45.75	30.94	31.05	30.85
Fe2O3 wt%	68.59	18.52	34.38	67.42	67.86	66.51
MnO wt%	0.20	0.81	0.21	0.13	0.20	0.20
MgO wt%	< l.d.	0.17	0.10	< l.d.	0.00	0.00
V2O3 wt%	0.29	0.64	0.68	0.33	0.32	0.42
Total wt%	100.15	97.79	98.05	99.16	99.76	98.87
Si	0.000	0.002	0.000	0.001	0.001	0.000
Ti	0.001	0.539	0.366	0.008	0.008	0.008
Al	0.003	0.002	0.003	0.001	0.001	0.026
Cr	0.001	0.001	0.001	0.000	0.000	0.001
Fe2+	0.995	1.264	1.107	1.005	1.002	1.002
Fe3+	1.985	0.401	0.748	1.970	1.971	1.943
Mn	0.007	0.020	0.005	0.004	0.006	0.007
Mg	0.000	0.007	0.004	0.000	0.000	0.000
V	0.009	0.015	0.016	0.010	0.010	0.013

Spot	MD069-Mt3-2	MD071-Mt1-1	MD071-Mt1-2	MD071-Mt1-3	MD071-Mt2-1	MD071-Mt2-2
Facies	Bethsaida	Bethsaida	Bethsaida	Bethsaida	Bethsaida	Bethsaida
SiO2 wt%	0.02	0.01	0.01	0.03	0.01	0.01
TiO2 wt%	0.06	0.16	0.16	0.10	0.14	0.08
Al2O3 wt%	0.08	0.20	0.22	0.07	0.35	0.17
Cr2O3 wt%	0.02	0.02	0.01	0.02	0.02	0.01
FeO wt%	30.78	31.13	31.16	31.06	30.84	30.94
Fe2O3 wt%	67.78	67.91	68.00	68.12	67.24	67.93
MnO wt%	0.12	0.05	0.06	0.05	0.13	0.09
MgO wt%	0.00	< l.d.	< l.d.	0.00	0.00	0.00
V2O3 wt%	0.41	0.34	0.33	0.34	0.34	0.35
Total wt%	99.27	99.83	99.96	99.78	99.09	99.59
Si	0.001	0.001	0.000	0.001	0.001	0.001
Ti	0.002	0.004	0.005	0.003	0.004	0.002
Al	0.004	0.009	0.010	0.003	0.016	0.008
Cr	0.001	0.001	0.000	0.000	0.001	0.000
Fe2+	0.998	1.003	1.003	1.002	1.000	1.000
Fe3+	1.978	1.970	1.969	1.978	1.963	1.975
Mn	0.004	0.002	0.002	0.002	0.004	0.003
Mg	0.000	0.000	0.000	0.000	0.000	0.000
V	0.013	0.010	0.010	0.010	0.011	0.011

Spot	MD071-Mt3-1	MD071-Mt3-2	MD071-Mt3-3	MD075-Mt1-1	MD075-Mt1-2	MD075-Mt2-1
Facies	Bethsaida	Bethsaida	Bethsaida	Guichon	Guichon	Guichon
SiO2 wt%	0.00	0.01	0.01	0.02	0.00	0.02
TiO2 wt%	0.01	0.09	0.06	0.03	0.06	0.07
Al2O3 wt%	0.02	0.10	0.05	0.03	0.14	0.09
Cr2O3 wt%	0.02	0.02	0.02	0.15	0.15	0.16
FeO wt%	30.90	30.95	31.07	31.58	31.55	31.47
Fe2O3 wt%	68.41	68.02	68.52	69.34	69.14	68.95
MnO wt%	0.08	0.08	0.08	0.06	0.09	0.09
MgO wt%	< l.d.	0.00	0.00	0.01	0.01	0.01
V2O3 wt%	0.34	0.33	0.33	0.59	0.56	0.53
Total wt%	99.77	99.60	100.14	101.81	101.70	101.39
Si	0.000	0.000	0.000	0.001	0.000	0.001
Ti	0.000	0.003	0.002	0.001	0.002	0.002
Al	0.001	0.004	0.002	0.001	0.006	0.004
Cr	0.001	0.000	0.001	0.005	0.005	0.005
Fe2+	0.998	1.000	0.999	0.999	0.998	0.999
Fe3+	1.988	1.978	1.983	1.974	1.969	1.970
Mn	0.003	0.003	0.003	0.002	0.003	0.003
Mg	0.000	0.000	0.000	0.001	0.001	0.001
V	0.010	0.010	0.010	0.018	0.017	0.016

Spot	MD075-Mt2-2	MD075-Mt2-3	MD075-Mt3-1	MD075-Mt3-2	MD075-Mt3-3	MD076-Mt1-1
Facies	Guichon	Guichon	Guichon	Guichon	Guichon	Guichon
SiO2 wt%	0.01	0.00	0.02	0.02	< l.d.	< l.d.
TiO2 wt%	0.04	0.04	0.08	0.05	23.06	47.33
Al2O3 wt%	0.10	0.04	0.10	0.15	0.01	0.01
Cr2O3 wt%	0.10	0.12	0.09	0.09	0.09	0.01
FeO wt%	31.55	31.33	31.27	31.26	51.21	33.99
Fe2O3 wt%	69.23	68.89	68.53	68.61	22.16	13.25
MnO wt%	0.07	0.09	0.09	0.13	0.47	8.39
MgO wt%	0.00	0.00	0.01	0.01	0.01	0.05
V2O3 wt%	0.58	0.55	0.53	0.54	0.44	0.49
Total wt%	101.68	101.08	100.73	100.87	97.44	103.52
Si	0.000	0.000	0.001	0.001	0.000	0.000
Ti	0.001	0.001	0.002	0.001	0.502	0.873
Al	0.004	0.002	0.004	0.007	0.000	0.000
Cr	0.003	0.004	0.003	0.003	0.002	0.000
Fe2+	0.999	0.998	0.999	0.997	1.240	0.697
Fe3+	1.972	1.975	1.971	1.969	0.483	0.244
Mn	0.002	0.003	0.003	0.004	0.012	0.174
Mg	0.000	0.000	0.001	0.001	0.000	0.002
V	0.018	0.017	0.016	0.017	0.010	0.010

Spot	MD076-Mt1-2	MD076-Mt1-3	MD076-Mt2-1	MD076-Mt2-2	MD076-Mt2-3	MD076-Mt3-1
Facies	Guichon	Guichon	Guichon	Guichon	Guichon	Guichon
SiO2 wt%	0.01	0.02	0.03	0.02	0.01	0.01
TiO2 wt%	0.17	0.21	48.75	0.16	0.16	0.15
Al2O3 wt%	0.44	0.84	0.01	0.38	0.33	0.06
Cr2O3 wt%	0.07	0.05	0.03	0.08	0.08	0.16
FeO wt%	32.14	32.13	30.06	31.74	31.40	32.33
Fe2O3 wt%	69.51	68.77	8.76	68.73	68.08	70.49
MnO wt%	0.04	0.05	13.56	0.04	0.06	0.05
MgO wt%	0.01	0.04	0.05	0.03	0.02	< l.d.
V2O3 wt%	0.55	0.56	0.52	0.56	0.56	0.53
Total wt%	102.95	102.66	101.78	101.74	100.70	103.77
Si	0.001	0.001	0.001	0.001	0.000	0.000
Ti	0.005	0.006	0.912	0.005	0.005	0.004
Al	0.020	0.037	0.000	0.017	0.015	0.002
Cr	0.002	0.002	0.001	0.002	0.002	0.005
Fe2+	1.003	1.003	0.625	1.002	1.002	1.003
Fe3+	1.952	1.931	0.164	1.953	1.955	1.968
Mn	0.001	0.001	0.286	0.001	0.002	0.002
Mg	0.001	0.002	0.002	0.001	0.001	0.000
V	0.016	0.017	0.010	0.017	0.017	0.016

Spot	MD076-Mt3-2	MD076-Mt3-3	MD076-Mt3-4
Facies	Guichon	Guichon	Guichon
SiO2 wt%	0.00	0.01	0.01
TiO2 wt%	49.27	0.19	0.19
Al2O3 wt%	0.01	0.39	0.20
Cr2O3 wt%	0.03	0.11	0.12
FeO wt%	34.81	32.21	32.12
Fe2O3 wt%	9.50	69.70	69.73
MnO wt%	9.34	0.07	0.07
MgO wt%	0.03	0.02	0.00
V2O3 wt%	0.54	0.56	0.55
Total wt%	103.52	103.26	102.98
Si	0.000	0.000	0.000
Ti	0.907	0.005	0.005
Al	0.000	0.017	0.009
Cr	0.001	0.003	0.003
Fe2+	0.712	1.002	1.003
Fe3+	0.175	1.952	1.960
Mn	0.193	0.002	0.002
Mg	0.001	0.001	0.000
V	0.011	0.017	0.016